UNIVERSIDAD COMPLUTENSE DE MADRID
FACULTAD DE CIENCIAS FÍSICAS

TESIS DOCTORAL

Nanostructured, thin film composite and nanocomposite membranes for water treatment

Membranas nanoestructuradas, compuestas de capa fina y nanocompuestas para el tratamiento de aguas

MEMORIA PARA OPTAR AL GRADO DE DOCTORA

PRESENTADA POR

Paula Arribas Fernández

DIRECTORES

Mohamed Khayet Souhaimi
María del Carmen García Payo
Luis Gil Sánchez

Madrid

UNIVERSIDAD
COMPLUTENSE
MADRID

Nanostructured, thin film composite and nanocomposite membranes for water treatment

Membranas nanoestructuradas, compuestas de capa fina y nanocompuestas para el tratamiento de aguas

Doctoral Thesis

PAULA ARRIBAS FERNÁNDEZ

Supervisors

Mohamed Khayet Souhaimi, María del Carmen García Payo and Luis Gil Sánchez

Department of Structure of Matter, Thermal Physics and Electronics

Faculty of Physics

Madrid, 2020

UNIVERSIDAD
COMPLUTENSE
MADRID

Nanostructured, thin film composite and nanocomposite membranes for water treatment

Membranas nanoestructuradas, compuestas de capa fina y nanocompuestas para el tratamiento de aguas

Doctoral thesis presented by Paula Arribas Fernández in fulfillment of the requirements for the degree of Doctor of Philosophy with International Mention in the subject of Physics at Complutense University of Madrid

Department of Structure of Matter, Thermal Physics and Electronics

Faculty of Physics

Madrid, 2020

"Defiende tu derecho a pensar, pues incluso pensar de manera errónea es mejor que no pensar" – Hipatia.

"Por un mundo donde seamos socialmente iguales, humanamente diferentes y totalmente libres" – Rosa Luxemburg.

"Esfuerzo y pasión, creo que éstos son los ingredientes básicos de toda actividad científica. Intentar que tu trabajo tenga siempre un sello de calidad propio, sin olvidar que para todo hace falta un recorrido y que la excelencia no se consigue de un día para otro" – Maribel Arriortua.

A todas mis personas queridas, en especial a mi familia

Agradecimientos

La realización de esta tesis doctoral ha marcado una larga e importante etapa de mi vida. No ha sido un camino fácil, pero me siento muy orgullosa de haberla terminado y muy agradecida por todo lo que me ha aportado en el camino. Mi fuerza de voluntad y mi capacidad de trabajo me han ayudado a enfrentarme a todos los retos y obstáculos que me he ido encontrando por el camino. Mi alegría, mi curiosidad por la vida y mi entusiasmo por aprender cada día una cosa nueva me han ayudado a mantener siempre viva la motivación por la ciencia y la investigación. Esta tesis ha sido un recorrido lleno de aprendizaje y me ha ayudado a desarrollarme tanto en el plano personal como en el profesional.

Todo este tiempo he tenido la suerte de estar rodeada de personas maravillosas que me han ayudado y sostenido en cada paso de mi camino y es a ellas principalmente a las que quiero dirigir unas palabras.

En primer lugar, quiero dar gracias a todas las personas de mi familia: a mis padres, hermanos, hermana, tío abuelo, cuñadas, tíos, tías, primos, primas, abuelos, abuelas, etc. Gracias por apoyarme todo este tiempo, por preocuparos, por ofrecerme conversaciones que me ayudaban a despejar la mente cuando lo necesitaba y otras que me servían para desahogarme y descargar tensiones, gracias por darme ánimos, cariño y amor sin límites, gracias por confiar en mí, gracias por vuestra alegría, por ser un ejemplo a seguir y por enseñarme cada día cómo ser mejor persona. Soy de las que piensa profundamente, de corazón, que el regalo más bonito que le ha dado la vida es su familia, y me siento muy afortunada de poder andar mi camino a vuestro lado. Gracias especialmente a mis padres, por su paciencia y templanza, su cariño incondicional y por su ayuda constante. Gracias por estar en cada bache para poder sostenerme y en cada alegría para saltar de emoción junto a mí. Gracias por enseñarme a ser una mujer fuerte, luchadora y con criterio propio, gracias por los valores humanos que me habéis transmitido y que forman parte de mi ser, gracias por transmitirme que hay que esforzarse para conseguir las metas que uno se propone, gracias por enseñarme a dar siempre lo mejor de mí misma y a ver siempre a todas las personas como iguales. Gracias a mi padre por su sabiduría, su filosofía y la profundidad de sus conversaciones. Gracias a mi madre por sembrar en mí la curiosidad de conocer el porqué de las cosas, gracias por enseñarme a pensar, por tu amistad, por tus consejos y por transmitirme siempre la ilusión y la alegría de haber hecho una tesis en membranas para el tratamiento de aguas. Gracias por recordarme con pasión porqué me encanta la ciencia y porqué soy una buena investigadora. Gracias por ser mi maestra y por mostrarme lo bonito que es aprender entendiendo las cosas. Gracias también a mis hermanos Ignacio, Javi, Rodri y Sasha

por apoyarme tanto en esta última etapa, por escucharme, por darme ánimos y por hacerme reír y disfrutar de cada momento que hemos compartido.

Gracias también a todos mis amigos y amigas, por su apoyo y su alegría. Gracias por entenderme y respetarme cuando he tenido que estar más ausente y gracias por divertiros conmigo cuando he estado disponible.

Gracias a mis amigas de la Navata por ser como una pequeña familia para mí. Gracias por vuestro apoyo durante toda mi tesis, por los viajes, por las risas, por los bailes, por las noches de conversaciones interminables y por vuestros abrazos.

Gracias a mis amigas y compañeras de voley, que me han hecho disfrutar de cada entrenamiento y poder liberar tensiones. Gracias por transmitirme lo bonito y necesario que es el trabajo en equipo. Gracias también por las cañas después de los entrenamientos y los partidos, y por hacerme reír a carcajadas.

La Facultad de Ciencias Físicas ha sido como una segunda casa para mí durante muchos años. Inicié la carrera de Físicas en el 2006, terminé el máster en el 2012 y ahora en el 2020 acabo mi doctorado. Durante la carrera pude hacer bastantes amistades significativas para mí como la de Óscar, Édgar, Ana Pérez, Ana Salamanca, Cristina, Gema, etc. Mención especial a Cristina y Gema, dos de las personas más increíbles que he conocido. Gracias por estar siempre ahí, por vuestra comprensión, apoyo incondicional y vuestras risas, gracias por ser tan bellas personas y por impulsarme a mejorar cada día. Os quiero.

También quiero expresar mi gratitud a mi gran amiga Loreto, que me ha acompañado en el camino desde el colegio hasta terminar hoy el doctorado. No tengo palabras para expresar lo enormemente agradecida y afortunada que me siento de que hayas sido mi compañera de viaje. Gracias por tu amistad, por tu enorme cariño y por ser un ejemplo de superación constante. Personas como tú siempre hacen de este mundo algo mejor. Gracias por tanto.

Todo este tiempo en la facultad me ha brindado la posibilidad de conocer a personas íntegras y con un gran corazón, personas que me han hecho mantener la alegría en mi día a día y han mejorado mi sensación de familia en esta segunda casa. Gracias a Fernando, David, Mariano, José, Mari, Almudena, Isabel, etc. Gracias también a mis amigos de electrónica, con los que he compartido innumerables cafés y celebraciones de cumpleaños. Gracias en especial a Javi por tu apoyo durante la tesis y por ser un gran amigo.

Asimismo, me gustaría agradecer a algunos profesores y profesoras que tuve durante la carrera y el máster, y que han continuado apoyándome, cuidándome y preocupándose por mí de forma constante durante estos años. Gracias a José Luis Contreras, Rafael Mayo y Mari Cruz de Andrés.

En cuanto al ámbito académico y de investigación, me gustaría mostrar mi agradecimiento a mis directores de tesis, Mohamed, Carmen y Luis. Gracias por confiar en mí y darme la oportunidad de llevar a cabo esta tesis doctoral. Mohamed y Carmen, gracias por introducirme en el mundo de la Ciencia y Tecnología de Membranas. Gracias por transmitirme vuestros conocimientos y dedicarme vuestro tiempo. Mohamed, gracias por mostrarme que la constancia y el esfuerzo son claves para alcanzar las metas científicas que me proponga. Carmen, gracias por enseñarme a ser rigurosa con las medidas experimentales y la importancia de hacer un buen análisis de los datos. Gracias igualmente por tu cariño, tu alegría y tu apoyo. Luis, gracias por tus sabios y acertados consejos y por tu buena disposición.

Gracias a mis compañeros de laboratorio, con los que he compartido la mayor parte de mis días durante la tesis. Gracias por acompañarme en este viaje y sobre todo por el buen rollo que hemos tenido siempre entre nosotros. Essalhi, tú eres al primero que conocí y contigo aprendí cómo poder sobrevivir en el laboratorio. Gracias por tu ayuda montando módulos, fabricando membranas y discutiendo sobre resultados. Gracias también a Loreto, Julio, Alia, Catalina, Patxi, Carlos y Jorge por todos los momentos compartidos, las risas, los vaciles, las canciones, los debates, las comidas, los cafés, los paseos por los jardines de física, las charlas, las celebraciones de cumpleaños, etc.

Gracias a todos los miembros del antiguo departamento de Física Aplicada I. He tenido la suerte de ser alumna de muchos de vosotros y también de poder conoceros más personalmente durante mi doctorado, compartiendo pasillo, cafés, charlas e incluso despacho. Gracias a todos por mostrarme vuestro cariño y apoyo durante todos estos años. Siempre me he sentido muy bien acogida por todos y cada uno de vosotros.

Gracias también a otras personas que me han ayudado durante mi doctorado a resolver problemas técnicos, a llevar a cabo algunas de mis ideas, así como a comprender la física y la química escondida detrás de algunos resultados. Gracias a Ana Casado, Antonio Paz, Marcos Rodríguez y José Emilio Fernández.

Me gustaría dedicar también unas palabras de agradecimiento a los miembros del grupo de investigación de la School of Engineering and Applied Sciences of Harvard University, donde he realizado dos estancias de investigación en mi periodo predoctoral: *Thank you Prof. Chad Vecitis for offering me the opportunity to do my research stays in your group and giving me all the support needed during this time. They were very nice and fruitful experiences. Qiaoying, I am very grateful to you for sharing with me your knowledge about bacteria and virus filtration. It was a pleasure working hand in hand with you. I think we make a very good team. Carlo, thanks for your extensive knowledge in the nanomaterials field and your collaboration in several research studies, as well as for your friendship. Special thanks to the rest of my awesome lab-mates, Greg, Andrea, Jiawei, Marielle, Bianca, and Jenny, who always made me feel like a member of their group. I learned a lot from all of you and really enjoyed my time with you.*

Gracias de corazón a Philipp, por recordarme la pasión por la ciencia y la investigación en mis momentos más difíciles. Gracias por ayudarme a creer de nuevo en mí. Gracias por tu apoyo incondicional, tu valiosa ayuda, tu cariño, tu generosidad y tu tiempo.

Soy de las que piensa que la ciencia debe ser interdisciplinar y que el desarrollo humano y tecnológico hacia un mundo mejor es posible cuando se trabaja en equipo y aportando lo mejor de cada uno al conjunto.

¡Gracias a todos por ayudarme a crecer como persona y a ser quien soy!

Esta tesis doctoral ha sido realizada gracias a una beca predoctoral, incluyendo una ayuda para la realización de una estancia predoctoral, concedida por el Campus de Excelencia Internacional dentro del Programa Internacional de Captación de Talento (PICATA) financiado por la Universidad Complutense de Madrid y la Universidad Politécnica de Madrid (UCM-UPM). Asimismo, debo agradecer la financiación de dos contratos de investigación, uno como investigadora invitada a tiempo completo financiado por la empresa ThermoFisher Scientific y la School of Engineering and Applied Sciences of Harvard University, y el otro como ayudante de investigación a tiempo completo con un contrato de Empleo Joven de la Comunidad de Madrid. También, he recibido financiación de los siguientes proyectos de investigación como miembro de mi grupo de investigación Membranas y Energías Renovables: Proyecto I+D+I MAT2010-19249 concedido por el Ministerio de Ciencia e Innovación, Proyecto CTM2015-65348-C2-2-R concedido por el Ministerio de Economía y Competitividad, Proyecto A/032278/10 concedido por la Agencia Española de Cooperación Internacional, y otros proyectos concedidos por la Universidad Complutense de Madrid al grupo de investigación.

Contents

Abstract ……xiii

Resumen……..xvii

Publications, research stays, conferences and awards……xxi

1. Introduction……..1

1.1 Water scarcity problem……...3

1.2 Membranes filtration processes……..4

1.3 Organic and microbial fouling……6

1.4 Fouling mitigation techniques……7

1.4.1 Membrane surface modification……9

1.4.1.1 Interfacial polymerization……9

1.4.1.2 Use of novel membrane materials……10

1.4.2 Electrically-active-based methods: Electrokinetics and electrochemistry……..12

1.5 Thesis overview……13

References……17

2. Novel and emerging membranes for water treatment. Hydrostatic pressure and vapor pressure gradient membrane processes……23

2.1 Introduction……25

2.2 Pressure-driven membrane processes……27

2.2.1 Microfiltration……27

2.2.2 Ultrafiltration……..29

2.2.3 Nanofiltration……34

2.2.4 Reverse osmosis……..37

2.3 Vapor pressure gradient membrane processes……...43

2.3.1 Membrane distillation……..43

2.3.2 Pervaporation……51

2.4 Conclusions……..56

2.5 Future trends……57

References……58

3. Nanostructured membranes. Electrospinning and feed solution conditions effect on structural properties and filtration performance….71

Self-sustained electrospun polysulfone nanofibrous membranes and their surface modification by interfacial polymerization for micro- and ultra-filtration……...73

3.1 Introduction…….73

3.2 Materials and methods……..74

3.2.1 Materials…….74

3.2.2 Preparation of PSU ENMs……..74

3.2.3 Preparation of thin film composite polyester-PSU based ENMs by interfacial polymerization (IP) technique……75

3.2.4 Membranes characterization……....76

3.2.5 Filtration experiments…….77

3.3 Results and discussions…….79

3.3.1 Membranes fabrication and characterization……79

3.3.1.1 PSU ENMs: effect of the electrospinning parameters and heat post-treatment……...79

3.3.1.2 Interfacial polymerization of PSU ENMs……85

3.3.2 Filtration experiments…….88

3.3.2.1 Effects of pH on the HA filtration performance of PSU ENMs…….88

3.3.2.2 Effects of interfacial polymerization on the performance of PSU ENMs….92

3.4 Conclusions……..94

References……96

4. Nanostructured membranes. Heat post-treatment effect on structural properties and filtration performance……..99

Heat-treated optimized polysulfone electrospun nanofibrous membranes for high performance wastewater microfiltration……..101

4.1 Introduction…….....101

4.2 Materials and methods……103

4.2.1 Materials…….....103

4.2.2 Preparation and characterization of the polymer solution……...103

4.2.3 Preparation of PSU ENMs……104

4.2.4 Heat post-treatment (HPT) of PSU ENMs……104

4.2.5 Characterization of PSU ENMs……105

4.2.6 Filtration experiments……....107
4.3 Results and discussions……....108
4.3.1 Polymer solution characterization……..108
4.3.2 PSU ENMs preparation and characterization……108
4.3.2.1 Preliminary evaluation of PSU ENMs prepared with different HPTs and determination of the region of interest of the HPT……108
4.3.2.2 Effects of the HPT temperature and time on the morphology and structure of PSU ENMs……...109
4.3.3 MF tests……116
4.3.3.1 Effects of the HPT temperature and time on the filtration performance of PSU ENMs……..117
4.3.3.2 Comparative study……123
4.4 Conclusions……126
References……....127

5. Thin film composite membranes. Interfacial polymerization conditions effect on physicochemical properties and antifouling performance…..131

Improved antifouling performance of polyester thin film nanofiber composite membranes prepared by interfacial polymerization……133

5.1 Introduction……....133
5.2 Materials and methods……135
5.2.1 Materials……....135
5.2.2 Preparation of PSU ENMs……136
5.2.3 Preparation of polyester and polyamide thin film composite membranes……137
5.2.4 Membranes characterization……..139
5.2.5 Filtration experiments……....141
5.3 Results and discussions……....142
5.3.1 Polyester thin film nanofiber composite membranes prepared with different polymerization reaction times……...142
5.3.1.1 Effects of the polymerization reaction time on the physicochemical properties of polyester thin film nanofiber composite membranes……142
5.3.1.2 Effects of the polymerization reaction time on the filtration performance and antifouling capacity of polyester thin film nanofiber composite membranes……..149

5.3.2 Polyester thin film composite membranes prepared with different supports……...154
5.3.2.1 Effects of the supporting membrane on the physicochemical properties of polyester thin film composite membranes…….155
5.3.2.2 Effects of the supporting membrane on the filtration performance of polyester thin film composite membranes……157
5.3.3 Polyester *versus* polyamide thin film composite membranes……160
5.3.3.1 Physicochemical properties of polyamide thin film composite membranes……..160
5.3.3.2 Comparison of the filtration performance of polyester and polyamide thin film composite membranes……....162
5.4 Conclusions……166
References……....167

6. Nanocomposite membranes. Interlaced CNT electrodes effect on antifouling and filtration performance……173

***Interlaced CNT electrodes for bacterial fouling reduction of microfiltration membranes*……175**

6.1 Introduction……....175
6.2 Materials and methods……176
6.2.1 Materials……....176
6.2.2 Fabrication of ICE on membrane surfaces……177
6.2.3 Membranes characterization……..178
6.2.4 Bacterial filtration experiments……..178
6.2.5 Bacterial density and morphology evaluation ……179
6.2.6 Bacterial fouling trend and BW efficacy evaluation ……179
6.2.7 Bacterial characterization and quantification……..180
6.3 Results and discussions……....180
6.3.1 Membranes characterization……..180
6.3.2 Membrane bacterial removal……181
6.3.3 Membrane surface bacterial density and morphology……181
6.3.4 Fouling trend and BW efficacy……..184
6.3.5 ICE electric field modeling ……...187
6.3.6 Summary of antifouling mechanisms……189
6.4 Conclusions……189
References……....190

7. Nanocomposite membranes. GO-based materials implementation in water treatment applications……195

Graphene oxide standarization and classification: Methods to support the leap from lab to industry……197

7.1 Introduction……....197

7.2 Materials and methods……200

7.2.1 Materials……....200

7.2.2 Characterization……200

7.2.2.1 XPS……..200

7.2.2.2 UV-vis……..201

7.2.2.3 AFM……201

7.2.2.4 XRD……201

7.2.2.5 ATR-FTIR……....201

7.2.2.6 SEM……201

7.2.2.7 Zeta potential and zeta average ……202

7.2.2.8 Raman spectroscopy ……202

7.2.2.9 SCA……..202

7.2.3 GO classification method……..202

7.2.4 GO membrane fabrication and evaluation……203

7.2.4.1 GO membrane fabrication ……...203

7.2.4.2 Bacteria attachment experiments……...203

7.2.4.3 Adsorption experiments ……...204

7.2.4.4 GOM permeability……204

7.3 Results and discussions……....204

7.3.1 GO chemistry……....204

7.3.2 GO morphology……....209

7.3.3 GO characterization tools……212

7.3.4 GO standardization and classification……213

7.3.5 GO applications ……...215

7.4 Conclusions……218

References……....219

8. Other preliminary results……..225

8.1 Surface modification of ENMs by TiO_2 nanoparticles addition……227

8.1.1 Introduction…….227

8.1.2 Preliminary results……227

8.1.2.1 Polymer blended TiO_2−ENMs……...227

8.1.2.2 Surface coated TiO_2−ENMs……...229

8.1.3 Future directions……..231

8.2 Recycling industrial discarded RO membranes: towards a circular economy for sustainable growth……233

8.2.1 Introduction…….233

8.2.2 Materials and methods……..235

8.2.2.1 Discarded RO modules for recycling……...235

8.2.2.2 Preparation of new FO membranes……236

8.2.2.3 Membranes surface characterization……....237

8.2.2.4 FO commercial membranes……237

8.2.2.5 FO experiments……..237

8.2.3 Preliminary results……239

8.2.3.1 Surface characterization of FOMs……...239

8.2.3.2 FO performance…….240

8.2.4 Future directions……..244

References……....246

9. Conclusions……...249

10. Future research projects……..255

11. Appendix A: Supplementary information of Chapter 4……259

12. Appendix B: Supplementary information of Chapter 5……267

13. Appendix C: Supplementary information of Chapter 6……287

14. Appendix D: Supplementary information of Chapter 7……295

Abbreviations and symbols……..301

List of figures……315

List of tables……..327

Abstract

During last decades, population growth, climate change, natural disasters, uncontrolled urbanization, and pollution have left about one third of the world's population without adequate access to drinking water. Water issue is expected to be more exacerbated in the coming decades, with water scarcity occurring globally and affecting even regions currently considered water-rich. Addressing this problem requires a great deal of adequate research to improve the efficiency of water use and wastewater treatment, as well as to mitigate the impacts of a wide variety of factors affecting water availability worldwide. Over the past twenty years, membrane filtration technology has become a significant separation methodology for drinking water production from saltwater (i.e. desalination) and wastewater (or groundwater), providing environmentally friendly and effective alternatives to conventional technologies. The main advantages of membrane filtration technology over conventional separation methods are its high removal capacity of particulates and microorganisms, very low thermal and chemical impact, flexibility of operation, modular design, moderate energy consumption and high cost effectiveness. The growth of the global membranes market is mainly the result of the impressive development of materials used for membrane fabrication and modification, improvements in membrane modules, and the progress of related systems, plants and equipment. However, the application of membranes in water treatment is limited by membrane fouling, which reduces water production rate, increases energy consumption, deteriorates membrane separation capability, and shortens membrane lifespan increasing, consequently, operation and maintenance costs. Particularly, organic and microbial fouling are the initial steps for biofilm formation, resulting in severe fouling problems in many environmental and engineered applications including membrane water filtration. Therefore, it is crucial the preparation of membranes with optimized surface properties, which induce a high fouling resistant capacity.

This PhD thesis is focused on the preparation, characterization, modification and optimization of novel and advanced membranes with enhanced organic and microbial antifouling performance for the treatment, clearance and disinfection of different types of water as a sustainable way to increase drinking water availability and reduce water scarcity. First, an overview of the progress made during last few years on the preparation of novel membranes and their modification for water treatment by hydrostatic pressure and vapor pressure gradient membrane processes (i.e., microfiltration, MF; ultrafiltration, UF; nanofiltration, NF; reverse osmosis, RO; membrane distillation, MD and pervaporation, PV) is outlined in order to better understand the challenges and drawbacks that still need to be overcome for these membrane filtration technologies.

Three different types of membranes were developed throughout this PhD thesis for water treatment applications: i) nanostructured membranes, ii) thin film composite membranes and iii) nanocomposite membranes. Polysulfone electrospun nanofiber membranes (PSU ENMs) (type i) were successfully prepared by electrospinning technique using a mixture of solvents *N,N*-dimethyl formamide (DMF) and tetrahydrofurane (THF). These membranes were intended for the treatment of wastewater containing organic matter. Special attention was paid to the study of the involved electrospinning parameters in membrane fabrication (i.e. polymer solution flow rate, F; electric voltage, V; air gap, G; and electrospinning fabrication time, t_e) and their effects on the structure and morphology of the membranes in order to optimize their filtration performance. Wastewater model solutions of 15 mg/L humic acid (HA) at two different pH conditions (pH 3 and 11) were used to test the filtration performance of the prepared membranes, elucidate their fouling mechanisms and analyze possible changes in both HA–HA molecules interactions and HA–membrane interactions. Although the PSU ENMs demonstrated their suitability for wastewater treatment, the overall filtration performance of the membranes could be improved further by applying a suitable heat post-treatment (HPT) after electrospinning. Therefore, a systematic study about the influence of HPT temperature and time on the structural and morphological properties of the membranes as well as on their fouling tendency and filtration performance was carried out. The optimization of the HPT conditions resulted in heat-treated optimized PSU ENMs with up to 80 % better filtration performance than that of PSU ENMs prepared without HPT and 38% greater filtration performance than that of commercial polyethersulfone (PES) MF membranes. However, the organic irreversible fouling factors of these membranes were very high (FR_W ranged from 81.9 to 99%). The antifouling performance of heat-treated optimized PSU ENMs was enhanced by modifying their surface with interfacial polymerization (IP) of bisphenol A (BPA) and trimesoyl chloride (TMC) to form polyester thin film nanofiber composite (PE TFNC) membranes (type ii). The process of PE thin film layer formation on ENMs was investigated. In addition, the filtration performance and antifouling tendency of these membranes at different IP reaction times were correlated to their physicochemical properties, and the optimum polymerization conditions were obtained. The enhanced antifouling performance of the optimized membrane allowed 90% recovery of its initial water flux after HA filtration process, which may result in a long lifetime of the membrane and the reduction of maintenance costs. PE thin film layers were also prepared under optimum IP conditions on different supporting membranes (lab-made ENMs and commercial MF membranes) to study the impact of the backing material on the physicochemical properties, filtration and antifouling performance of the resulting PE TFC membranes. As most of the prepared thin film composite (TFC) membranes in the literature have a polyamide (PA) active layer instead of a PE active layer, a comparative study of PA and PE TFC membranes was made to evidence and highlight the good filtration and antifouling performance of the PE TFNC membranes developed in this PhD thesis.

Nanocomposite membranes (type iii) were prepared by modifying the surface of commercial MF membranes with carbon-based nanomaterials, particularly carbon nanotubes (CNTs) and graphene oxide (GO). These membranes were used for the disinfection of wastewater containing bacteria. The design of a new experimental set-up to deposit interlaced carbon nanotube electrodes (ICE) on the surface of commercial polyvinylidene fluoride (PVDF) MF membranes was performed first. Then, the resulted ICE-PVDF nanocomposite membranes were used for the electrochemical filtration of water contaminated with *Pseudomonas fluorescens*. The application of a DC or AC voltage on the ICE during filtration was proposed as an active method to mitigate biofouling. The effects of the electrochemically-active ICE on the bacterial density and morphology, as well as on the bacterial fouling tendency and the backwash (BW) efficiency, were discussed and the optimized operation conditions to improve antifouling performance during filtration and BW were also obtained. In addition, a simplified COMSOL model of the ICE electric field in solution was used to elucidate the antifouling mechanisms of the modified membranes. A GO standardization method was proposed by a high-throughput characterization of the chemo-morphological properties of a wide variety of commercial GO materials with the goal of enabling the leap of this nanomaterial from lab to industry. The implementation of GO-based materials in water treatment applications was demonstrated by the preparation of different GO composite membranes (GOMs), which were evaluated in terms of permeability and antifouling performance against *Escherichia Coli* bacterial adhesion. The influence of the initial properties of GO nanomaterial on the macroscopic performance of the prepared membranes was confirmed.

Finally, the incorporation of titanium dioxide (TiO_2) nanoparticles on the surface of PSU ENMs was considered as another possible way to reduce the organic fouling tendency of the membranes. Moreover, forward osmosis membranes (FOMs) were successfully prepared on commercial PES MF membranes using different surface modification IP methods. The good FO performance of these membranes was proved for the treatment of model organic matter wastewaters at low and high concentration conditions. The surface modification of disposed RO membranes from industrial water treatment plants, following the best selected IP method, was also proposed as way to recycle and reuse these membranes in FO technology extending this way RO membranes lifetime and contributing to a circular economy and sustainability in membrane science and related materials.

Resumen

Durante las últimas décadas, el crecimiento demográfico, el cambio climático, los desastres naturales, la urbanización descontrolada y la contaminación han dejado a aproximadamente un tercio de la población mundial sin acceso adecuado al agua potable. Se espera que el problema del agua se agrave aún más en las próximas décadas, habiendo escasez de agua en todo el mundo y afectando incluso a las regiones actualmente consideradas ricas en agua. Abordar este problema requiere una gran cantidad de investigación adecuada para mejorar la eficiencia del uso del agua y el tratamiento de aguas residuales, así como para mitigar los impactos de una amplia variedad de factores que afectan la disponibilidad del agua en todo el mundo. En los últimos veinte años, la tecnología de filtración por membrana se ha convertido en una metodología de separación significativa para la producción de agua potable a partir de agua salada (es decir desalinización) y aguas residuales (o aguas subterráneas), proporcionando alternativas ecológicas y efectivas respecto a las tecnologías convencionales. Las principales ventajas de la tecnología de filtración por membrana sobre los métodos de separación convencionales son su alta capacidad de eliminación de partículas y microorganismos, muy bajo impacto térmico y químico, flexibilidad de operación, diseño modular, consumo moderado de energía y alta rentabilidad. El crecimiento del mercado mundial de membranas es principalmente el resultado del impresionante progreso en los materiales utilizados para la fabricación y modificación de membranas, las mejoras en los módulos de membranas y la evolución de los sistemas, plantas y equipos relacionados. Sin embargo, la aplicación de membranas para el tratamiento de agua está limitada por el ensuciamiento de la membrana, lo que reduce la tasa de producción de agua, aumenta el consumo de energía, deteriora la capacidad de separación de la membrana y acorta la vida útil de la misma aumentando, en consecuencia, los gastos de operación y mantenimiento. Particularmente, el ensuciamiento orgánico y microbiano conforman las etapas iniciales para la formación de biopelículas, lo que da lugar a graves problemas de ensuciamiento en muchas aplicaciones ambientales y de ingeniería, incluida la filtración de agua por membrana. Por consiguiente, resulta crucial preparar membranas con propiedades superficiales optimizadas que induzcan una alta capacidad de resistencia al ensuciamiento.

Esta tesis doctoral se centra en la preparación, caracterización, modificación y optimización de membranas novedosas y avanzadas con una eficiencia de anti-ensuciamiento "antifouling" orgánico y microbiano mejorada para el tratamiento, depuración y desinfección de diferentes tipos de agua como una forma sostenible de aumentar la disponibilidad de agua potable y reducir la escasez de agua. Primero, se ofrece una visión general del progreso realizado durante los

últimos años en la preparación de nuevas membranas y su modificación para el tratamiento de agua mediante procesos de membrana con gradiente de presión hidrostática y presión de vapor (incluyendo microfiltración, MF; ultrafiltración, UF; nanofiltración, NF; ósmosis inversa, OI; destilación en membrana, DM y pervaporación, PV) con el objetivo de comprender mejor los desafíos y los inconvenientes que aún deben ser superados por estas tecnologías de filtración de membrana.

A lo largo de esta tesis se desarrollaron tres tipos diferentes de membranas para aplicaciones de tratamiento de agua: i) membranas nanoestructuradas, ii) membranas compuestas de capa fina y iii) membranas nanocompuestas. Las membranas nanofibrosas electrohiladas de polisulfona (MNE PSU) (tipo i) se prepararon con éxito mediante la técnica de electrohilatura utilizando una mezcla de disolventes *N*, *N*-dimetilformamida (DMF) y tetrahidrofurano (THF). Estas membranas se destinaron al tratamiento de aguas residuales con materia orgánica. Una especial atención se dirigió al estudio de los parámetros de electrohilatura involucrados en la fabricación de este tipo de membranas (es decir, flujo de la disolución polimérica, *F*; voltaje eléctrico, *V*; hueco de aire, *G*; y tiempo de electrohilatura, t_e) y de sus efectos sobre la estructura y la morfología de las membranas para optimizar su eficiencia de filtración. Se usaron disoluciones modelo de aguas residuales de 15 mg/L de ácido húmico (AH) en dos condiciones de pH diferentes (pH 3 y 11) para probar el rendimiento de filtración de las membranas, dilucidar sus mecanismos de ensuciamiento, y analizar posibles cambios en las interacciones entre moléculas de AH y las interacciones entre las moléculas de AH y la membrana. Aunque las membranas MNE PSU demostraron ser adecuadas para el tratamiento de aguas residuales, su eficiencia de filtración podía mejorarse aún más aplicando un post-tratamiento térmico (PTT) adecuado después de la electrohilatura. Por lo tanto, se llevó a cabo un estudio sistemático sobre la influencia de la temperatura y el tiempo del PTT en las propiedades estructurales y morfológicas de las membranas, así como en su tendencia al ensuciamiento y en su eficiencia de filtración. La optimización de las condiciones del PTT resultó en membranas MNE PSU térmicamente tratadas y optimizadas con una eficiencia de filtración hasta un 80% mejor que la de las membranas MNE PSU preparadas sin PTT y un 38% mayor que el de las membranas comerciales de MF de polietersulfona (PES). Sin embargo, los factores de ensuciamiento orgánico irreversible de estas membranas eran muy altos (FR_{IR} varió de 81.9 a 99%). La eficiencia anti-ensuciamiento de las membranas MNE PSU térmicamente tratadas y optimizadas mejoró al modificar su superficie con polimerización interfacial (PI), utilizando bisfenol A (BPA) y cloruro de trimesoilo (TMC) para formar membranas nanofibrosas compuestas de capa fina de poliéster (NCCF PE) (tipo ii). Se investigó el proceso de formación de las láminas de poliéster (PE) de capa fina sobre las membranas nanofibrosas electrohiladas (MNE). Además, la eficiencia de filtración y la tendencia anti-ensuciamiento de estas membranas para diferentes tiempos de reacción de la PI se correlacionaron con sus propiedades fisicoquímicas, y se

obtuvieron las condiciones óptimas de la polimerización interfacial. La eficiencia anti-ensuciamiento mejorada de la membrana así preparada permitió la recuperación del 90% de su flujo de agua inicial después del proceso de filtración de AH, lo que puede resultar en una larga vida útil de la membrana y en la reducción de los gastos de mantenimiento. También se prepararon láminas de PE de capa fina bajo las condiciones óptimas de PI sobre diferentes membranas usadas como soporte (MNE hechas en el laboratorio y membranas de MF comerciales) para estudiar el impacto del soporte en las propiedades fisicoquímicas y en la eficiencia de filtración y anti-ensuciamiento de las membranas NCCF PE resultantes. Como la mayoría de las membranas compuestas de capa fina (CCF) preparadas en la bibliografía tienen una capa activa de poliamida (PA) en lugar de una capa activa de PE, se realizó un estudio comparativo de membranas CCF de PA y PE para evidenciar y resaltar la buena eficiencia de filtración y ant-ensuciamiento de las membranas NCCF PE desarrolladas en esta tesis doctoral.

Se prepararon membranas nanocompuestas (tipo iii) modificando la superficie de membranas comerciales de MF con nanomateriales con base de carbono, particularmente nanotubos de carbono (NTC) y óxido de grafeno (OG). Estas membranas se utilizaron para la desinfección de aguas residuales con bacterias. Se llevó a cabo primero el diseño de un nuevo sistema experimental para depositar electrodos de nanotubos de carbono entrelazados (ENE) en la superficie de membranas comerciales de fluoruro de polivinilideno (PVDF). Las membranas nanocompuestas resultantes (PVDF-ENE) se usaron para la filtración electroquímica de agua contaminada con *Pseudomonas fluorescens*. Se propuso la aplicación de un voltaje de CC o CA en el ENE durante la filtración como un método activo para mitigar el bio-ensuciamiento "biofouling". Se discutieron los efectos del ENE electroquímicamente activo sobre la densidad de bacterias y su morfología, así como sobre su tendencia al ensuciamiento bacteriano y su eficacia del retro-lavado (RL) y también se obtuvieron las condiciones de operación óptimas para mejorar la eficiencia de anti-ensuciamiento durante la filtración y el RL. Además, se utilizó un modelo COMSOL simplificado del campo eléctrico del ENE en disolución para dilucidar los mecanismos anti-ensuciamiento de las membranas modificadas. Se propuso un método de estandarización del OG mediante una caracterización altamente eficiente de las propiedades quimico-morfológicas de una amplia variedad de materiales comerciales de OG con el objetivo de permitir el salto de este nanomaterial del laboratorio a la industria. La implementación de materiales basados en OG en aplicaciones de tratamiento de agua fue demostrada mediante la preparación de diferentes membranas compuestas de OG (MOG), que se evaluaron en términos de permeabilidad y eficiencia de anti-ensuciamiento hacia la adhesión bacteriana de *Escherichia Coli*. Se confirmó la influencia de las propiedades iniciales del nanomaterial de OG en el rendimiento macroscópico de las membranas preparadas.

Por último, la incorporación de nanopartículas de dióxido de titanio (TiO_2) en la superficie de las membranas MNE PSU fue considerada como otra forma posible de reducir la tendencia

de las membranas al ensuciamiento orgánico. Además, se prepararon con éxito membranas de ósmosis directa (MOD) sobre membranas de MF comerciales de PES utilizando diferentes métodos de modificación superficial por PI. La buena prestación de estas membranas en la OD para tratar aguas residuales modelo con materia orgánica fue probada en condiciones de baja y alta concentración. También se propuso la modificación superficial de membranas de OI desechadas de plantas de tratamiento de aguas industriales, siguiendo el mejor método de PI seleccionado, como una forma de reciclar y reutilizar estas membranas en la tecnología de OD extendiendo de esta manera su vida útil y contribuyendo a una economía circular y a la sostenibilidad en la ciencia de membranas y de materiales relacionados.

Publications, research stays, conferences and awards

Scientific publications derived from the PhD Thesis

1. P. Arribas, M.C. García-Payo, M. Khayet, L. Gil, Improved antifouling performance of polyester thin film nanofiber composite membranes prepared by interfacial polymerization, Journal of Membrane Science, 598 (2020) 117774.

2. P. Arribas, M.C. García-Payo, M. Khayet, L. Gil, Heat-treated optimized polysulfone electrospun nanofibrous membranes for high performance wastewater microfiltration, Separation and Purification Technology, 226 (2019) 323-336.

3. C. A. Amadei, P. Arribas, C. D. Vecitis, Graphene oxide standardization and classification: Methods to support the leap from lab to industry, Carbon 133 (2018) 398-409.

4. Q. Zhang, P. Arribas, M.R. Remillard, M.C. García-Payo, M. Khayet, C.D. Vecitis, Interlaced CNT electrodes for bacterial fouling reduction of microporous membranes, Environmental Science and Technology 51 (2017) 9176-9183.

5. P. Arribas, M. Khayet, M.C. García-Payo, L. Gil, Self-sustained electro-spun polysulfone nano-fibrous membranes and their surface modification by interfacial polymerization for micro- and ultra-filtration, Separation and Purification Technology 138 (2014) 118-129.

Scientific book chapters derived from the PhD Thesis

6. P. Arribas, M. Khayet, M.C. García-Payo, L. Gil, Novel and emerging membranes for water treatment by hydrostatic pressure and vapor pressure gradient membrane processes, Chapter 8 in book "Advances in membrane technologies for water treatment: materials, processes and applications", Woodhead Publishing, (2015) 239-285, ISBN: 978-1-78242-121-4.

7. P. Arribas, M. Khayet, M.C. García-Payo, L. Gil, Novel and emerging membranes for water treatment by electric potential and concentration gradient membrane processes, Chapter 9 in book "Advances in membrane technologies for water treatment: materials, processes and applications", Woodhead Publishing, (2015) 287-325, ISBN: 978-1-78242-121-4.

Patent applications derived from the PhD Thesis

8. P. Arribas, Q. Zhang, C.D. Vecitis, Membranes with Interlaced Electrodes and Methods of forming the same, 002806-086780 US Provisional Patent (2016).

Other scientific publications related to the PhD Thesis

9. J. Contreras-Martínez, M.C. García-Payo, P. Arribas, L. Rodríguez-Sáez, A. Lejarazu-Larrañaga, E. García-Calvo, M. Khayet, Recycled reverse osmosis membranes for forward osmosis technology, Desalination (2020) submitted, under revision.

10. C. A. Amadei, P. Arribas, L. Cruzado, C. D. Vecitis, Graphene oxide membranes on a hierarchical elemental carbon-based support, Environmental Science: Nano, 7 (2020) 891-902.

11. M. Essalhi, M. Khayet, C. Cojocaru, M.C. García-Payo, P. Arribas-Fernández, Response Surface Modeling and Optimization of Electrospun Nanofiber Membranes, The Open Nanoscience Journal 7 (2013) 8-17.

12. M. Essalhi, L. Fernández, P. Arribas, M.C. García-Payo, M. Khayet, Spinning an optimized hollow fiber membrane for desalination by membrane distillation using experimental statistical designs, Procedia Engineeiring 44 (2012) 1786-1787.

Journal details: Impact factor JCR (year) / Quartile (category)

Journal of Membrane Science: 7.183 (2019)/Q1 (Engineering, Chemical)/Q1 (Polymer Science)

Separation and Purification Technology: 5.774 (2019); 3.091 (2014)/Q1(Engineering, Chemical)

Carbon: 7.466 (2018)/Q1 (Chemistry, Physical)/Q1 (Materials Science, Multidisciplinary)

Environmental Science and Technology: 6.653 (2017)/Q1(Engineering Environmental)/ Q1 (Environmental Sciences)

Environmental Science: Nano: 7.683 (2019)/Q1 (Chemistry, Multidisciplinary)/Q1 (Environmental Sciences)/Q1 (Nanoscience & Nanotechnology)

Desalination: 7.098 (2019)/ Q1 (Engineering, Chemical)/Q1 (Water Resources)

Research stays during the PhD Thesis

1. Host Institution: Harvard University, John A. Paulson School of Engineering and Applied Sciences.

Supervisor: Professor Chad David Vecitis

Temporary stay: from 01/05/15 to 18/09/15

Project: "Development of carbon nanomaterial-based coatings for electroactive biofouling reduction of micro- and ultra-filtration membranes"

2. Host Institution: Harvard University, John A. Paulson School of Engineering and Applied Sciences.

Supervisor: Professor Chad David Vecitis

Temporary stay: from 01/11/16 to 15/04/17

Project: "Electrochemical carbon nanotube filtration of cell culture media for viral and bacterial clearance"

Scientific conferences

1. P. Arribas, Q. Zhang, M.C. García-Payo, M. Khayet, C. D. Vecitis, Improved bacterial removal through interlaced CNT electrodes on membrane surfaces, Oral communication, Euromembrane 2018, July 2018, Valencia (Spain).

2. P. Arribas, J. Contreras-Martínez, M.C. García-Payo, M. Khayet, Interfacial polymerization study for recycling RO membranes in FO wastewater treatment, Poster, Euromembrane 2018, July 2018, Valencia (Spain).

3. J. Contreras-Martínez, P. Arribas, M. Khayet, M.C. García-Payo, Recycling RO membrane modules for the treatment of high saline solutions by membrane distillation, Poster, Euromembrane 2018, July 2018, Valencia (Spain).

4. Loreto García-Fernández, Paula Arribas, Carmen García-Payo and Mohamed Khayet, Thermodynamic and kinetic effects on the fabrication of hydrophobic porous membranes for membrane distillation, Poster, 12th International Meeting on Thermodiffusion, May–June 2016, Madrid (Spain). Best poster award.

5. P. Arribas, M. Khayet, M.C. García-Payo, L.Gil, Antifouling thin film composite electrospun nanofiber membranes for wastewater treatment, Poster, Euromembrane 2015, September 2015, Aachen (Germany).

6. P. Arribas, M. Khayet, M.C. García-Payo, L.Gil, Interfacial polymerization of electrospun polysulfone nanofibrous membranes for micro- and ultra-filtration: irreversible fouling study, Poster, 25th Annual North American Membrane Society Meeting (NAMS), May–June 2015, Boston, Massachusetts (USA).

7. P. Arribas, M. Khayet, M.C. García-Payo, L.Gil, Effects of heat treatment on the characteristics of self-sustained electrospun polysulfone nanofibrous membranes, Poster, 25th Annual North American Membrane Society Meeting (NAMS), May–June 2015, Boston, Massachusetts (USA).

8. P. Arribas, M.C. García-Payo, M. Khayet, Modification and optimization of polysulfone nano-structured membranes for micro/ultra-filtration, Oral communication, XXXIV Biennial Meeting of the Royal Spanish Society of Physics, July 2013, Valencia (Spain).

9. P. Arribas, M.C. García-Payo, M. Khayet, Novel nano-structured membranes for micro/ultra-filtration, Poster, 1st International Conference on Desalination using Membrane Technology, April 2013 Sitges (Spain).

10. M. Essalhi, L. García-Fernández, P. Arribas, M.C. García-Payo, M. Khayet, Spinning an optimized hollow fiber membrane for desalination by membrane distillation using experimental statistical designs, Poster, Euromembrane 2012, September 2012, London (UK).

11. L. García-Fernández, P. Arribas, M.C. García-Payo, M. Khayet, Effects of solvent type on the structural morphology and membrane distillation performance of PVDF-HFP hollow fiber membranes, Poster, International Workshop on Membrane Distillation and Related Technologies, October 2011, Ravello (Italy).

12. P. Arribas, M.C. García-Payo, M. Khayet, Microfiltration with sheet polysulfone nano-structured membranes, Oral communication, XXXIII Biennial Meeting of the Royal Spanish Society of Physics, September 2011, Santander (Spain).

Scientific awards

1. First position award for the research study entitled "New membranes for water treatment: towards circular economy to increase water resources" presented at the 2nd edition of the PhDay Complutense, November 2018, Madrid (Spain).

2. Poster award for the research study entitled "Thermodynamic and kinetic effects on the fabrication of hydrophobic porous membranes for membrane distillation" presented at the 12th International Meeting on Thermodiffusion, May–June 2016, Madrid (Spain).

3. "Archimedes" award for the introduction to scientific research with the study entitled "Desalination with hollow fibers: membrane distillation", November 2011, Palencia (Spain).

1

Introduction

1.1. Water scarcity problem

1.2. Membrane filtration processes

1.3. Organic and microbial fouling

1.4. Fouling mitigation techniques

1.5. Thesis overview

1.1 Water scarcity problem

Water scarcity has become a crucial environmental issue worldwide. The intensive population growth, the economic development, and the increasing irrigation activities have resulted in a significant increase in water demand over the last century (i.e. the global water withdrawals increased from 600 to 3900 km^3 [1]). The change in land use and hydraulic engineering have also altered the water supply [2]. This huge abstraction of water resources has resulted in many regions suffering from pervasive water scarcity conditions. Nowadays, 4.3 billion people live in water-stressed areas for at least 1 month a year (an area is considered water-stressed when the amount of available freshwater per person per year is between 1000–1700 m^3 [3]). Another extensive water problem afflicting people throughout the world is the lack of access to clean water and sanitation. Currently, 2.1 billion people throughout the world suffer from lack access to safe drinking water while 4.5 billion people lack safely managed sanitation service [4]. The lack of access to clean water results in economic losses, environmental effects, and social costs that negatively affect public health. In addition, the lack of sanitation services increases exposure to waterborne bacteria and enteric viruses, which cause intestinal parasitic infections and diarrheal diseases. For instance, millions of people die annually (i.e. about 3900 children a day) from diseases transmitted through unsafe water [5]. Water issue is also expected to be further exacerbated in the coming decades driven by socio-economic and climatic changes [6], affecting developing and industrialized nations [5]. On one hand, climate change scenarios project spatial and temporal variations of water cycle dynamics, affecting the distribution and availability of water resources in all parts of the world and exacerbating the discrepancies between water supply and demand [7]. On the other hand, it is estimated that the world population will grow from the current 7.2 billion people to 9.6 billion in 2050 and to 10.9 billion in 2100 [8]. The global water requirement is projected to increase by 55% in 2050 mainly due to the growing demands from industry, irrigation, thermal electricity generation and domestic uses [9]. Therefore, global water withdrawal will increase by a staggering 150% by 2095 [10].

Addressing the above cited problems requires a great deal of adequate research to identify new methods and innovative technologies to purify water at low cost, less energy and with minimal use of chemicals and environmental impact. In this sense, membrane technology has become increasingly important in providing effective solutions to the global water scarcity problem as it allows an efficient, economic and environmentally friendly treatment of different types of contaminated waters

1.2 Membrane filtration processes

Membrane filtration is a physical separation process in which a semipermeable material (i.e. membrane) acts as a barrier to selectively separate water molecules (in liquid or gaseous phase) from undesired substances (e.g. particulates, bacteria, microorganisms, salts, natural organic material, etc.) by means of a driving force applied between both sides of the membrane giving rise to a transmembrane water chemical potential. Several driving forces can be considered, namely, hydrostatic pressure, vapor pressure, electric potential and concentration. In Table 2.1 of Chapter 2 it is shown a classification of the membrane separation processes according to the applied transmembrane driving force together with their main fields of application. The main advantages of membrane filtration technology over conventional separation methods are its high removal capacity of particulates and microorganisms, very low thermal and chemical impact, flexibility of operation, modular design, moderate energy consumption and high cost effectiveness [11, 12]. Among all membrane separation processes, pressure-driven membrane processes are the most widely used for water treatment.

Membrane filtration processes can be classified into four categories based on the membrane pore size, which dictates the size of the particles or molecules capable of crossing the membrane pore or being retained: i) microfiltration (MF) membranes are used to remove large suspended solids ranging from 0.1 to 10 μm and larger microorganisms like protozoa and bacteria, ii) ultrafiltration (UF) membranes are used to reject viruses, proteins, colloids and organic solids ranging from 1 to 100 nm, iii) nanofiltration (NF) membranes, having a pore size between 0.5 and 2 nm, are able to separate smaller dissolved solids and multivalent ions, and iv) reverse osmosis (RO) membranes, characterized by a sub-nanometer pore size < 0.5 nm, are suitable to remove all monovalent ions. Table 2.2 in Chapter 2 summarizes the main characteristics of the different pressure-driven membrane processes together with the typical materials used for membrane preparation.

Pressure-driven membrane filtration processes can be operated in cross-flow or dead-end configurations (see Fig. 1.1). In cross-flow filtration, which is the most common configuration, the fluid on the upstream side of the membrane (i.e. feed) moves parallel to the membrane surface while the fluid on the downstream side of the membrane (i.e. permeate) moves away from the membrane in the direction normal to the membrane surface. The portion of the feed that leaves the membrane module without passing through the membrane to the downstream is called retentate. Compared to the dead-end configuration, one advantage of the cross-flow configuration is the possibility to recirculate the retentate through the membrane module enhancing therefore water recovery and reducing fouling susceptibility of the membrane surface [13]. In dead-end filtration, the direction of the feed flow is normal to the membrane surface and the only outlet for feed is through the membrane [14]. This configuration is easy to

implement in the laboratory and the process is usually cheaper than the cross-flow filtration. The main disadvantage of the dead-end filtration process is the extensive membrane fouling and concentration polarization phenomena [15].

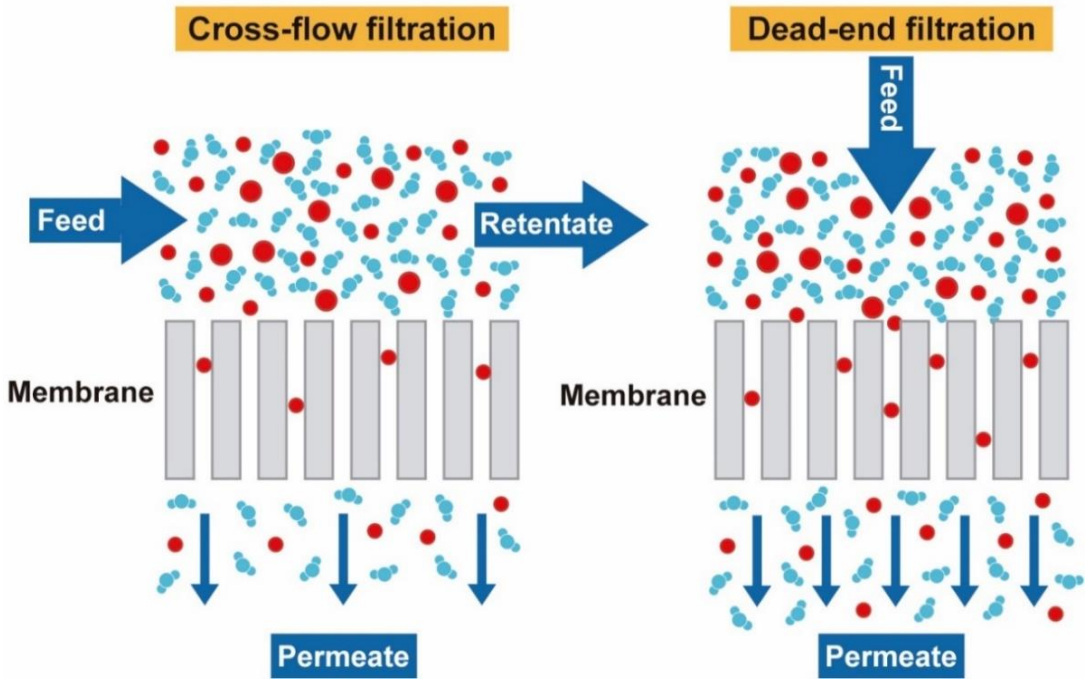

Figure 1.1. Cross-flow and dead-end configurations for a membrane filtration process.

There are three key factors affecting the performance of a membrane filtration process: permeability, selectivity and membrane lifetime. The permeate flux and the separation factor are the main parameters influencing the filtration performance. The permeate flux describes the quantity of clean water produced by the membrane and the separation factor, which is related to the quality of the produced water, indicates the ability of the membrane to separate the contaminants from water. The higher the permeation flux and separation factor, the higher is the membrane filtration performance. During last decades a lot of efforts have been made to develop novel membranes with enhanced properties for water treatment applications using new materials and different membrane preparation and modification techniques. However, in spite of the improvements achieved in membrane properties and performance, it is still challenging to develop membranes with both high water production rate and good water quality due to the well-known trade-off between permeability and selectivity [16].

The third factor affecting membrane separation processes is membrane lifetime. Membranes with high lifespan reduce the replacement frequency of the membrane modules in water treatment plants and consequently lower its maintenance costs. Membrane lifetime strongly depends on fouling phenomena. This refers to the undesired deposition of foulants or solutes on the membrane surface or inside its pores during filtration. It is the major obstacle limiting the application of membranes in water treatment as it directly affects the previously mentioned

main three factors. It drops the water production rate and increases the energy consumption, it deteriorates the membrane separation capability reducing the permeate quality and it shortens the membrane lifespan increasing the operation and maintenance costs [17-22]. It is therefore of great importance to design and develop new and advanced membranes with high filtration performance and optimized antifouling surface properties that could overcome these limitations. Details about the last progresses made on the preparation and modification of novel membranes for water treatment field can be found in Chapter 2.

1.3 Organic and microbial fouling

Membrane fouling results from the interactions between the membrane surface and the foulants as well as the interactions between foulants. It is strongly influenced by [17-22]:

i) the physicochemical properties of the membrane surface (i.e. pore size and its geometry, charge density, roughness, hydrophilicity, chemical composition and morphology),
ii) the nature of the foulants (i.e. organic and inorganic compounds like humic and fluvic acids, colloids, salts, etc.; or biological substances like bacteria, algae, viruses, etc.),
iii) the characteristics of the foulants (i.e. size, hydrophobicity, surface charge and surface structure),
iv) the operating conditions of the filtration system (i.e. permeate flux, cross-flow velocity, applied pressure, temperature, feed solution characteristics such as pH, ionic strength and solute concentration, etc.).

Depending on the foulant species, membrane fouling can be classified into organic fouling, biofouling, inorganic fouling (i.e. scaling) and colloidal fouling [21]. The difficulty to mitigate fouling is different depending on the foulant type. For instance, inorganic scaling can easily be reduced by chemical and/or physical methods, whereas organic fouling and biofouling are more difficult to control due to the complexity of the formed structure of the fouling layer [23]. Generally, membrane fouling is caused by a combination of different foulants. Particularly, the major fouling types in wastewater treatment plants are the organic fouling and biofouling, which have been found to be synergistic and interconnected [24].

The organic fouling is mainly caused by natural organic matter (NOM), which consists of humic substances (humic acids, fluvic acids and humins), polysaccharides, proteins, lipids, nucleic acids, amino acids, carbohydrates, and cell components [20, 25-27]. It is a main problem in wastewater treatment provided that the concentration (10–20 ppm) of the effluent organic matter (EfOM) is much higher than that of typical NOM concentration in surface waters (2–5 ppm) [28]. Biofouling occurs in all membrane treatment facilities, being the result of the adhesion and proliferation of microorganisms on the membrane surface and forming a biofilm

that results in unacceptable losses in the process performance [29, 30]. The biofilm may comprise populations of different types of microorganisms (e.g., bacteria, algae, protozoa and fungi) and the extracellular polymeric substances (EPS), which are excreted by bacteria during the metabolism process (mainly polysaccharides and proteins) [31-33]. The EPS form supportive and protective structures for bacteria, making the biofilm stronger and more difficult to remove. The sequence of biofouling formation includes [21, 33-35] (see Fig. 1.2):

i) adhesion and adsorption of organic matter and suspended particles as a conditioning film within minutes,
ii) bacteria attachment and assembly into a slime biofilm layer within hours (i.e. micro-fouling),
iii) bacteria reproduction and macrofouling community formation comprising algae, invertebrates and EPS over days or even longer timescales,
iv) limitation of biofilm growth and bacteria detachment due to lack of nutrients and increase of population density (i.e. steady state fouling resistance) over months.

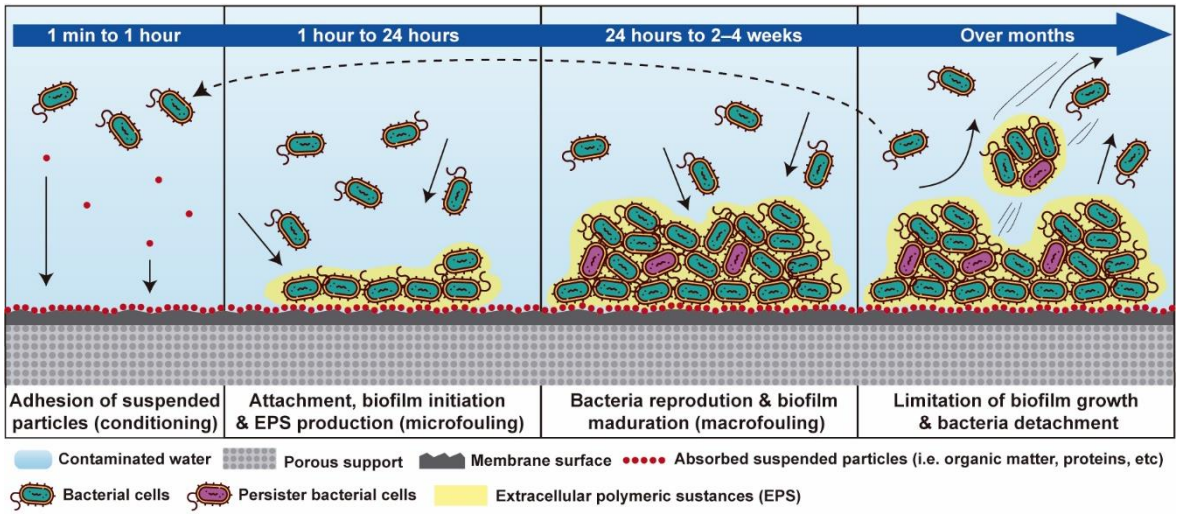

Figure 1.2. Biofouling formation sequence.

A proper control of the initial organic and microbial fouling could therefore reduce the chance of biofouling.

1.4 Fouling mitigation techniques

Adhesion and adsorption are the first steps of both organic and microbial fouling. These are determined by the interactions between the membrane surface and the foulants. The three major characteristics of the membrane surface that affect these primary processes are charge density, hydrophilicity, and roughness [36]. Most bacteria [37] and organic matter [38] are negatively charged under natural conditions. Therefore, apart from the universal and relatively weak van

der Waals forces, the foulant-membrane surface electrostatic interaction plays a very significant role in fouling mitigation. A negatively charged surface is generally preferred to repel foulants and reduce organic and bacterial fouling [36]. A greater charge density of a membrane surface is usually associated with a greater membrane hydrophilicity [18]. Most of the polymers used to prepare porous membranes have high thermal, chemical, and mechanical stabilities but are hydrophobic in nature and prone to the adsorption of fouling substances. Hydrophilic membranes are characterized by the presence of active groups that have the ability to form hydrogen-bonds with water (i.e. tendency to adsorb water) [18]. Since proteins and most of the foulants in aqueous media are hydrophobic in nature, a hydrophilic surface is generally favourable towards organic and microbial fouling mitigation [39]. Smoother surfaces have also been demonstrated to experience less fouling, presumably because foulant particles are more likely to be entrained through smoother topologies than by rougher ones [21, 40]. In addition, the adhesion of foulants to the membrane surface can be influenced by the hydrodynamics of the filtration process (Fig. 1.3). For instance, the improvement of boundary layer conditions with high cross-flow rates and the introduction of spacers can effectively reduce fouling [19, 33, 41]. It is worth quoting that biofilm development on a membrane surface requires active bacterial growth after adhesion. Therefore, mechanisms promoting bacteria inactivation and bacteria detachment from the membrane surface would contribute to long-term biofouling mitigation [42]. Fig. 1.3 summarizes the fouling mitigation strategies adopted to reduce organic and microbial adhesion on the membrane surface.

Taking into consideration all above mentioned mechanisms, fouling mitigation strategies can be divided into two main categories, passive and active methods, depending on whether the external physicochemical or energetic inputs are introduced into the system during the operating process. A common passive method for fouling control is the modification of the membrane surface. Surface modification techniques include polymer blending, grafting, coating, interfacial polymerization and addition of nanoparticles [36, 43]. The use of novel materials resistant to a certain fouling type in membrane preparation was also proved to be convenient for fouling mitigation [21, 36]. However, a designed membrane surface is unable to reduce biofouling for all microorganisms because microbial cells have a complicated and species-dependent surface chemistry, which usually decreases membrane antifouling performance in complex environments. A possible solution may be the use of active fouling control methods that tune *in situ* both the membrane surface properties and the interfacial interactions. For instance, inducing electrically-active electrokinetic and electrochemical effects is among the most effective methods for fouling control and it has also shown the advantages of easy-automation and low environmental impacts [44, 45].

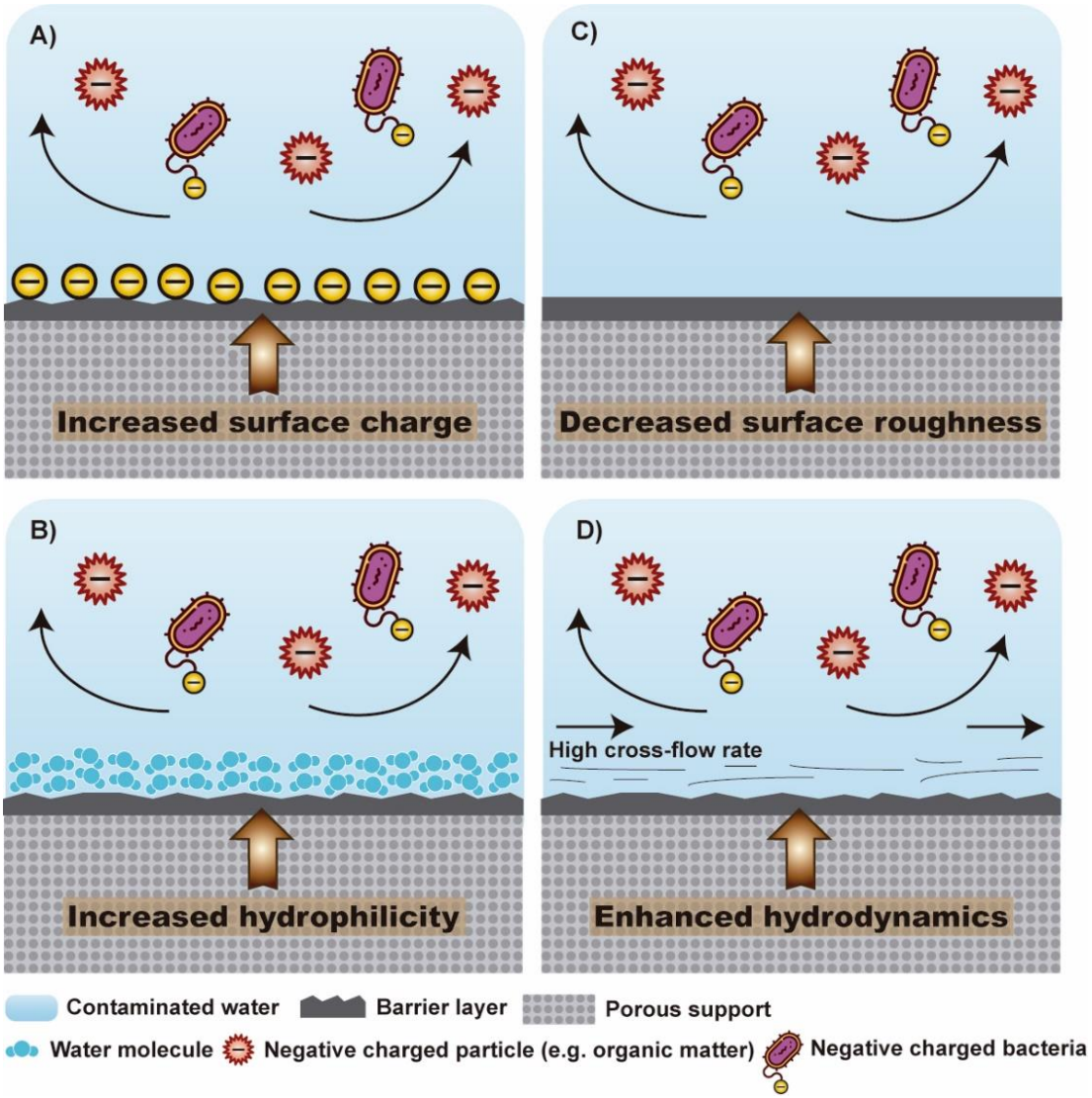

Figure 1.3. Strategies to reduce organic and microbial adhesion on the membrane surface to mitigate fouling. These strategies include: A) increased surface charge density, B) increased surface hydrophilicity, C) reduced surface roughness, and D) enhanced hydrodynamics conditions.

1.4.1 Membrane surface modification

Membrane surface modification is a promising strategy that prevents and reduces membrane fouling. It provides the membrane surface with antifouling properties by hydrophilization, smoothing, and the introduction of charged or bactericide groups to minimize specific undesired interactions with potential foulant(s) [46].

1.4.1.1 Interfacial polymerization

The interfacial polymerization (IP) technique has been widely used to improve the filtration and antifouling performance of a membrane by the synthesis of a polymeric ultrathin functional layer on its surface (i.e. thin film composite, TFC). This technique is based on the polymerization that occurs between two reactive monomers at the interface of two immiscible solvents, water

and an organic solvent (see Fig. 1.4) [47]. The support layer, which is generally an UF or MF membrane, is immersed in an aqueous solution containing a reactive monomer. The membrane is then immersed in a second solution containing a water-immiscible solvent (i.e. organic solvent) in which another reactive monomer is dissolved. The two monomers react with each other during a specific time, known as polymerization reaction time, to form a thin and denser polymeric top layer on the UF or MF membrane surface. One of the advantages of this technique is that the thin layer can be optimized by using different monomer combinations, ratios and concentrations, utilizing additives in either the aqueous and/or the organic phases, and varying the polymerization reaction time [48]. Generally, the IP technique produces changes in the physicochemical properties of the membranes, which significantly influence the membrane filtration performance (i.e. permeability, rejection and antifouling character).

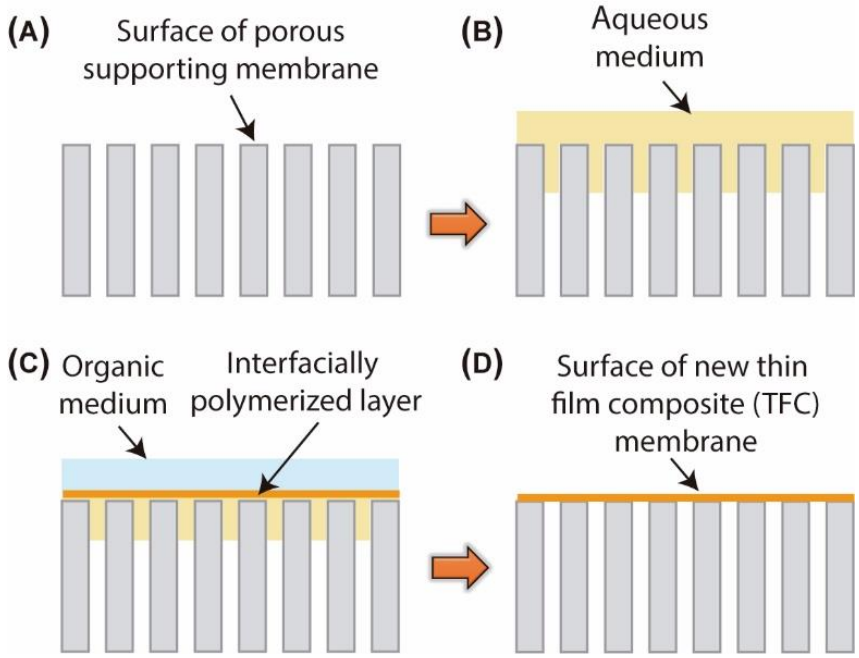

Figure 1.4. Mechanism of interfacial polymerization (A–D).

1.4.1.2 Use of novel membrane materials

Numerous studies have been carried out on improving the membrane antifouling performance by incorporating novel nanomaterials on the membranes including metal oxide nanoparticles [49], carbon nanotubes (CNT) [50], and graphene oxide (GO) [51].

The use of nanoparticles to prepare and modify polymeric membranes has received much attention during the last few years in order to enhance their water permeability and permeate water quality as well as to reduce their fouling [49, 52]. Some studies included antimicrobial nanoparticles like silver (Ag) and chitosan, and other inorganic nanoparticles such as titanium dioxide (TiO_2), silicon dioxide (SiO_2), alumina (Al_2O_3), zirconium dioxide (ZrO_2), zinc oxide (ZnO), and zeolite to improve membrane fouling resistance [53-55]. Among them, TiO_2

nanoparticles hold great potential due to their innocuity, low-cost, low environmental impact, stability, and commercial availability, other than their excellent photocatalytic, antibacterial and self-cleaning ultra-hydrophilic properties under ultraviolet (UV) light [54]. Two approaches have been considered to prepare these nanocomposite membranes. One is the blend of the nanoparticles in the membrane matrix by adding the nanoparticles to the polymeric casting solution. This method can improve the hydrophilicity, strength and stiffness, water permeability and antifouling properties of the membranes. It also has the advantages of simplicity, stable performance, reproducibility, facile processability, modularity and scale-up [46, 56]. The other approach is by coating or depositing the nanoparticles on the membrane surface via dipping the porous support in an aqueous suspension of nanoparticles. However, when using this approach, a release of nanoparticles has been observed in some cases due to the difficulty to immobilize them on the membrane surface without using any binding agent, which raise questions about the properties of the modified membrane during long–term filtration [49, 56].

The use of carbon-based nanomaterials such as carbon nanotubes (CNT) and graphene oxide (GO) nanosheets have attracted much attention to prepare novel membranes for filtration applications due to their effective antibiofouling and antimicrobial properties. These are able to inactivate bacteria upon direct cell contact by inducing membrane damage through physical disruption, charge transfer and formation of reactive oxygen species [57-60].

CNT are one-dimensional nanomaterials known for their excellent surface adsorption, chemical, mechanical, electrical and thermal properties. CNT have also the advantages of stability and intrinsic biotoxicity. They can be fabricated in a free-standing membrane or a thin porous layer on a substrate with nm scale pore size. In addition, CNT are ideal reinforcing fibers for nanocomposites due to their high aspect ratio and high in-axis strength [61]. A key advantage of using CNT, especially multiwalled CNT (MWCNT), is their easy scale-up, high purity and low production cost (i.e. bulk CNT price < 100 US$/kg [62]). The use of CNT layer alone can reduce organic fouling in pressure-driven membrane systems due to the adsorption of foulant(s) before reaching the membrane surface [50, 63]. Their biotoxicity can inactivate bacteria upon contact with CNT surface [64]. Due to their electrical conductivity and stability, CNT membranes were also investigated as an anode filter for bacteria and virus removal and an active electrode layer for biofouling reduction in RO filtration systems using alternating currents [65].

GO is a monolayer of highly oxidized graphite. It is basically a wrinkled two-dimensional carbon sheet with various oxygen-containing functional groups (i.e. epoxy, hydroxyl, carboxyl) on its basal planes and at the edges, with about one nanometer thickness and lateral dimensions ranging from nanometers up to a few micrometers [66]. The presence of polar hydroxyl and carboxyl groups endows it a hydrophilic nature. Apart from its antibacterial character, GO has recently been studied as a membrane material because of its high mechanical strength, chemical stability, and possibility to tune the primary GO properties (i.e. flake size and quantity of oxy-

functionalities), other than its accessibility, versatility and scalable synthesis process. In addition, because of its high aspect ratio, GO nanosheets can be assembled to form thin film laminate membranes with remarkable separation performance for separation applications such as gas separation [67], pervaporation [68] and membrane filtration [51, 69, 70]. Specifically, the great potential of GO membranes in water treatment field is attributed to the ultrafast characteristics of water flow inside the well-defined carbon nanochannels. GO membranes have been self-assembled on a variety of substrates by filtration of aqueous GO solutions, spin coating , vacuum filtration, drop casting, layer-by-layer (LbL) dip coating, doctor blade printing and evaporation at the liquid-air interface [66, 71, 72].

1.4.2 Electrically-active-based methods: Electrokinetics and electrochemistry

Electrokinetic and electrochemical methods represent an important class of fouling mitigation techniques. These methods are implemented using electrodes at the membrane surface-solution interface and require the generation of an electric field. They can prevent bacteria attachment, contribute to bacteria detachment once bacteria have attached to the membrane surface, and promote bacteria inactivation. The electric field can directly damage bacteria by decomposing DNA or RNA of their cells, which results in the death of the microorganisms [35]. The electric field can also create oxidizing species that degrade the microorganisms [36]. In a conventional electrically-active system, the surface is used as an anode or a cathode with a counter electrode using a direct current (DC) input or an alternating current (AC) input between the two electrodes [73]. Some advantages of the electro-active methods used for water disinfection include their lower energy requirements compared to the conventional thermal techniques and the ability to avoid producing a new generation of microorganisms that are tolerant to electrical treatment [74].

Electrokinetic effects are phenomena collectively referred to "the liquid flow that occurs along a solid/liquid interface as a result of an applied potential gradient, and conversely to the potential developed when a liquid is made to flow along an interface" [75]. Electrokinetic effects are associated with the electrostatics at the electrode surface and the electric field generated between the electrodes, and both can affect bacterial attachment [45]. Electrophoresis (EP), dielectrophoresis (DEP), and electroosmosis (EO) are common phenomena resulting from electrokinetics. Particularly:

i) EP refers to the movement of a charged particle or macromolecule in solutions with an external electric field,
ii) DEP is the movement of polarizable particles in a non-uniform electric field,
iii) EO is the migration of solution on a stationary charged surface in the electric field.

Electrophoretic and electroosmotic mechanisms together with electrostatic interactions play an important role in biofouling reduction of electrical filtration systems since most bacteria are negative charged in natural aqueous conditions. DEP is an alternative detachment mechanism typically used for bacterial cell separation more than for bacterial fouling reduction. Recently, DEP was reported to reduce particle fouling and concentration polarization phenomena in MF cross-flow systems, which improved permeate flow and prolonged membrane lifetime at a lower energy consumption compared to the filtration process without DEP [76].

Electrochemical mechanism is also considered as an effective electro-active antifouling method. Electrochemical reactions take place on the electrode surface in a Faradaic system. The influence of the electric current or potential on bacterial adhesion, detachment, and inactivation was demonstrated [44, 77, 78]. The cathode, with a negative surface charge, can reduce bacterial and organic adhesion via electrostatic repulsion interactions, whereas the anode inactivates bacteria through direct and indirect oxidation [79, 80], all resulting in the reduction of the bacteria growth and thus, the long-term fouling. Other than the inactivation phenomenon and as a result of electrochemical reactions, the formation of microbubbles at the electro-active membrane surface demonstrated to remove organic and microbial fouling on the electrode surface via physical cleaning [81].

Electrode material is a key factor determining the success of electro-active microbial and organic fouling control. It needs to be anti-corrosive, inexpensive, and capable of serving as both an electrode and a separation membrane [41]. Among all considered materials, recent development of a CNT electrochemical filter provides a possible solution to electrode fabrication [82] since CNT exhibits both high chemical stability and high electrical conductivity. Its nanosize also facilitates the fabrication of CNT-polymer composites of low material cost, uniform structure, and tuneable Faradaic properties. In addition, the formed CNT network has a pore size of ~100 nm, so that it can act simultaneously as a filter and an electrode for removal and inactivation of bacteria [82].

1.5 Thesis overview

This thesis focuses on the preparation and modification of different types of membranes with enhanced organic and microbial antifouling performance for the treatment and disinfection of different types of water using different filtration processes (see Fig. 1.5).

Chapter 2 describes the previously mentioned pressure-driven membranes processes (MF, UF, NF and RO) and shows an overview of the progress made during the last few years on the preparation of novel membranes and their modification for water treatment. In particular, this chapter focuses on flat-sheet and hollow-fiber membranes made with innovative materials (i.e., nanoparticles, additives, polymers, etc.) and improved characteristics (i.e. enhanced mechanical

properties, porosity, thermal stability, etc.) and filtration performance (i.e. high hydrophilicity and water permeability, better solute rejection factors, enhanced antifouling and antibacterial ability, etc.). The same attention is also paid to the emerging membranes developed for water treatment by other important and attractive membrane separation technologies such as membrane distillation (MD) and pervaporation (PV). The end of this chapter is devoted to some challenges and drawbacks that still need to be overcome for these membrane filtration technologies.

The membranes developed in chapters 3, 4 and 5 are lab-made electrospun nanostructured-based membranes for the treatment of wastewater containing organic matter. Emphasis is placed on the chemical and morphological properties of these membranes and their effects on filtration and antifouling performance. In particular, Chapter 3 focuses on the influence of the electrospinning fabrication conditions on the structure and morphology of polysulfone electrospun nanofiber membranes (PSU ENMs). Some heat post-treatment (HPT) effects on membrane characteristics are also elucidated. The filtration performance of the membranes when treating humic acid (HA) solutions at different pH conditions is studied and the changes in both HA–HA and HA–membrane interactions is thoroughly analysed.

Chapter 4 is focused on the improvement of the filtration performance of PSU ENMs for wastewater treatment by the application of a suitable HPT. The influence of the HPT temperature and time on the structural and morphological properties of the membranes as well as on their fouling tendency and filtration performance is systematically investigated to obtain the optimum conditions of the HPT.

Chapter 5 reports the enhancement of the antifouling performance of heat-treated optimized PSU ENMs by modifying their surface with the interfacial polymerization (IP) technique to form polyester thin film nanofiber composite (PE TFNC) membranes. A new insight into the PE thin film layer formation on ENMs is given. In addition, the filtration performance and antifouling tendency of these membranes at different IP reaction times are correlated to their physicochemical properties to select the optimum polymerization conditions. PE thin film layers are also prepared under optimum IP conditions on different supporting membranes (lab-made ENMs and commercial MF membranes) to study the impact of the backing materials on the physicochemical properties, filtration and antifouling performance of the resulting PE TFC membranes. As most of the prepared TFC membranes have a polyamide (PA) active layer instead of a PE active layer, a comparative study of PA and PE TFC membranes is presented at the end of this chapter.

The membranes investigated in chapters 6 and 7 are nanocomposite membranes prepared by modifying the surface of commercially available membranes with carbon-based nanomaterials, particularly carbon nanotubes (CNT) and graphene oxide (GO). These

membranes are intended for the disinfection of wastewater containing bacteria. Electrokinetic and electrochemical systems are proposed in Chapter 6 as an active method to mitigate biofouling. A new set-up, for the deposition of interlaced carbon nanotube electrodes (ICE) on the surface of commercial polyvinylidene fluoride (PVDF) MF membranes, is shown. The resulted nanocomposite membranes are used for the electrochemical filtration of water contaminated with bacteria. The application of a DC or AC voltage on the ICE during filtration not only inactivates and degrades bateria, but reduces also its attachement to the surface of the modified membranes. The effects of the electrochemically-active ICE on the bacterial density and morphology as well as on the bacterial fouling tendency and the backwash (BW) efficiency are discussed. Optimized operation conditions to minimize microbial fouling during filtration and backwash are also summarized. In addition, the antifouling mechanism of the modified membranes is elucidated with a simplified COMSOL model of the ICE electric field in solution.

Chapter 7 gives an overview of the implementation of GO-based materials in water treatment applications. The lack of a GO standardization process and the highly variable properties of the GO starting material result in different performances of the devices prepared by different research groups. This chapter describes a high-throughput characterization of the chemo-morphological properties of a wide variety of industrial available GO materials and proposes a GO standardization method to enable the leap of this nanomaterial from lab to industry. In addition, different GO composite membranes (GOMs) are prepared to highlight the effects of the starting GO nanomaterial properties on the macroscopic performance of the prepared device. The different GOM samples are tested and evaluated in terms of permeability and antifouling performance against bacterial adhesion.

Finally, Chapter 8 discusses different future research directions and a vision of the next steps to follow based on some preliminary results. On one hand, the addition of titanium dioxide (TiO_2) nanoparticles via blending to form mixed matrix membranes or via coating on a membrane surface support is considered as another possible way to reduce organic fouling tendency of the PSU ENMs. On the other hand, in order to boost a circular economy in water filtration with membranes, recycling of disposed RO membranes from industrial water treatment plants is assessed as a way to increase the sustainability of water treatment systems, improve the durability of the membranes, and reduce membrane discharge to the environment and the associated costs. IP technique is proposed to modify the surface of disposed RO membranes and transform them into polymeric TFC membranes for forward osmosis (FO) wastewater treatment.

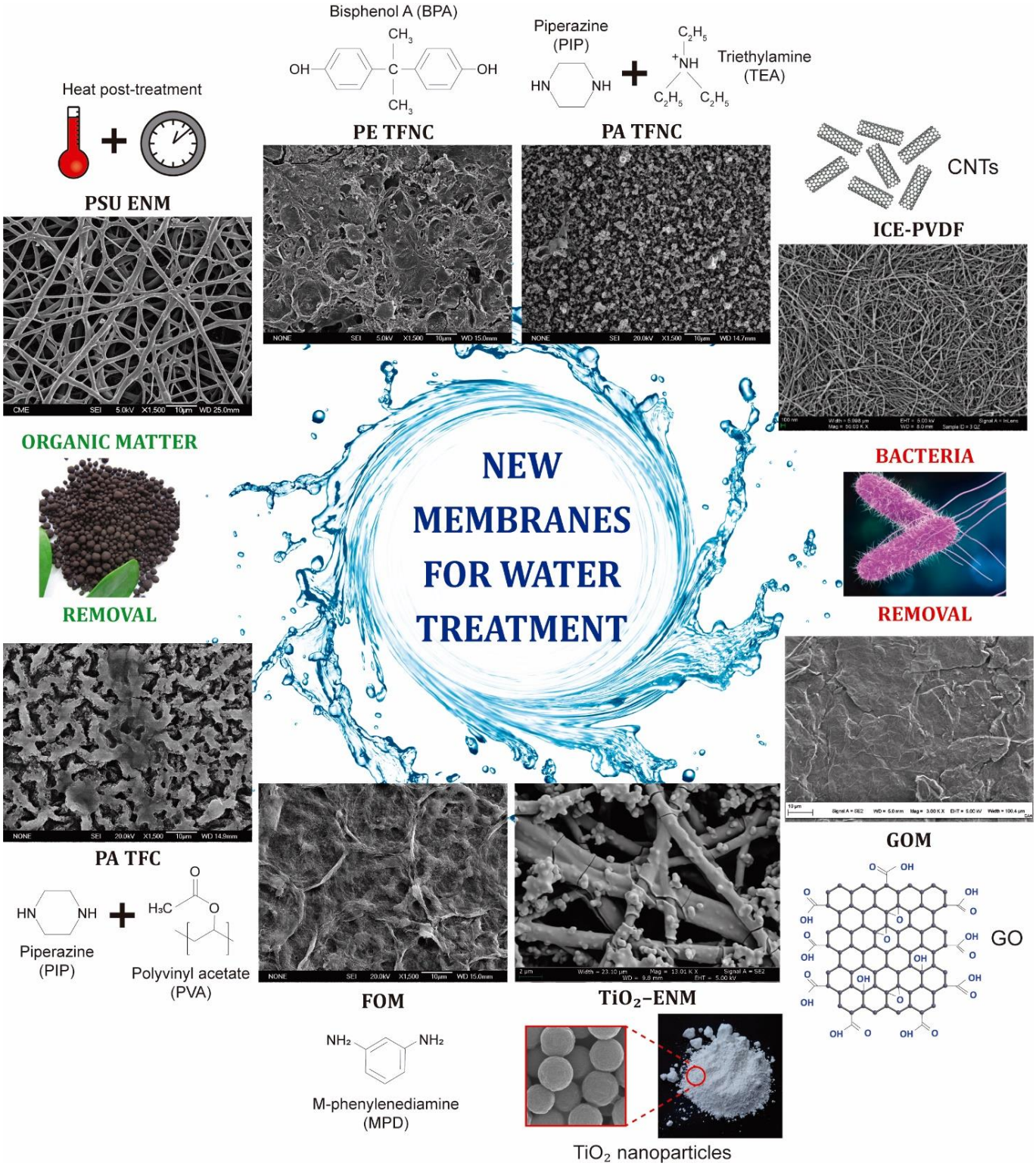

Figure 1.5. Membranes developed in this PhD thesis for the treatment and disinfection of different types of waters containing organic matter and bacteria.

References

[1] I.A. Shiklomanov, Appraisal and assessment of world water resources, Water International, 25 (2000) 11-32.

[2] N.L. Poff, J.D. Olden, D.M. Merritt, D.M. Pepin, Homogenization of regional river dynamics by dams and global biodiversity implications, Proceedings of the National Academy of Sciences, 104 (2007) 5732.

[3] M.M. Mekonnen, A.Y. Hoekstra, Four billion people facing severe water scarcity, Science Advances, 2 (2016) e1500323.

[4] WHO-UNICEF, Progress on drinking water, sanitation and hygiene: 2017 update and SDG baselines, WHO-UNICEF, 2017.

[5] M.A. Shannon, P.W. Bohn, M. Elimelech, J.G. Georgiadis, B.J. Mariñas, A.M. Mayes, Science and technology for water purification in the coming decades, Nature, 452 (2008) 301-310.

[6] P. Greve, T. Kahil, J. Mochizuki, T. Schinko, Y. Satoh, P. Burek, G. Fischer, S. Tramberend, R. Burtscher, S. Langan, Y. Wada, Global assessment of water challenges under uncertainty in water scarcity projections, Nature Sustainability, 1 (2018) 486-494.

[7] UNESCO-WWAP, The United Nations world water development report, 2017: Wastewater: an untapped resource, Paris: UNESCO, 2017.

[8] P. Gerland, A.E. Raftery, H. Ševčíková, N. Li, D. Gu, T. Spoorenberg, L. Alkema, B.K. Fosdick, J. Chunn, N. Lalic, G. Bay, T. Buettner, G.K. Heilig, J. Wilmoth, World population stabilization unlikely this century, Science, 346 (2014) 234.

[9] UNESCO-WWAP, The United Nations world water development report 2015: Water for a sustainable world, Paris: UNESCO, 2015.

[10] E.G.R. Davies, P. Kyle, J.A. Edmonds, An integrated assessment of global and regional water demands for electricity generation to 2095, Advances in Water Resources, 52 (2013) 296-313.

[11] J.H. Jhaveri, Z.V.P. Murthy, A comprehensive review on anti-fouling nanocomposite membranes for pressure driven membrane separation processes, Desalination, 379 (2016) 137-154.

[12] A. Ambrosi, N.S.M. Cardozo, I.C. Tessaro, Membrane separation processes for the beer industry: A review and state of the art, Food and Bioprocess Technology, 7 (2014) 921-936.

[13] D. Couto, A. Laverdiere, Methods of tangential flow filtration and an apparatus therefore, in: European Patent Office, EP1601788A1, 2005.

[14] W.J. Koros, Y.H. Ma, T. Shimidzu, Terminology for membranes and membrane processes (IUPAC Recommendations 1996), in: Pure and Applied Chemistry, 1996, pp. 1479.

[15] S. Roy, Innovative use of membrane technology in mitigation of GHG emission and energy generation, Procedia Environmental Sciences, 35 (2016) 474-482.

[16] H.B. Park, J. Kamcev, L.M. Robeson, M. Elimelech, B.D. Freeman, Maximizing the right stuff: The trade-off between membrane permeability and selectivity, Science, 356 (2017) eaab0530.

[17] N. Yang, X. Wen, T.D. Waite, X. Wang, X. Huang, Natural organic matter fouling of microfiltration membranes: Prediction of constant flux behavior from constant pressure materials properties determination, Journal of Membrane Science, 366 (2011) 192-202.

[18] A. Abdelrasoul, H. Doan, A. Lohi, Fouling in membrane filtration and remediation methods, in: Mass Transfer - Advances in Sustainable Energy and Environment Oriented Numerical Modeling, Hironori Nakajima, 2013.

[19] X. Cui, K.-H. Choo, Natural organic matter removal and fouling control in low-pressure membrane filtration for water treatment, Environmental Engineering Research, 19 (2014) 1-8.

[20] X. Shi, G. Tal, N.P. Hankins, V. Gitis, Fouling and cleaning of ultrafiltration membranes: A review, Journal of Water Process Engineering, 1 (2014) 121-138.

[21] S. Jiang, Y. Li, B.P. Ladewig, A review of reverse osmosis membrane fouling and control strategies, Science of The Total Environment, 595 (2017) 567-583.

[22] L.K. Jepsen, V.M. Bram, S. Pedersen, Z. Yang, Membrane fouling for produced water treatment: A review study from a process control perspective, Water, 10 (2018) 847.

[23] J. Shen, A.I. Schäfer, Factors affecting fluoride and natural organic matter (NOM) removal from natural waters in Tanzania by nanofiltration/reverse osmosis, Science of The Total Environment, 527-528 (2015) 520-529.

[24] S. Jeong, S.-J. Kim, L. Hee Kim, M. Seop Shin, S. Vigneswaran, T. Vinh Nguyen, I.S. Kim, Foulant analysis of a reverse osmosis membrane used pretreated seawater, Journal of Membrane Science, 428 (2013) 434-444.

[25] W. Yuan, A.L. Zydney, Humic acid fouling during microfiltration, Journal of Membrane Science, 157 (1999) 1-12.

[26] I. Sutzkover-Gutman, D. Hasson, R. Semiat, Humic substances fouling in ultrafiltration processes, Desalination, 261 (2010) 218-231.

[27] A.W. Zularisam, A.F. Ismail, R. Salim, Behaviours of natural organic matter in membrane filtration for surface water treatment – a review, Desalination, 194 (2006) 211-231.

[28] L. Malaeb, G.M. Ayoub, Reverse osmosis technology for water treatment: State of the art review, Desalination, 267 (2011) 1-8.

[29] J.S. Baker, L.Y. Dudley, Biofouling in membrane systems – A review, Desalination, 118 (1998) 81-89.

[30] J.C.-T. Lin, D.-J. Lee, C. Huang, Membrane fouling mitigation: Membrane cleaning, Separation Science and Technology, 45 (2010) 858-872.

[31] H.C. Flemming, Biofouling in water systems – cases, causes and countermeasures, Applied Microbiology and Biotechnology, 59 (2002) 629-640.

[32] H.C. Flemming, Microbial biofouling: Unsolved problems, insufficient approaches, and possible solutions, in: H.C. Flemming, J. Wingender, U. Szewzyk (Eds.) Biofilm Highlights, Springer Berlin Heidelberg, 2011, pp. 81-109.

[33] T. Nguyen, F.A. Roddick, L. Fan, Biofouling of water treatment membranes: a review of the underlying causes, monitoring techniques and control measures, Membranes, 2 (2012) 804-840.

[34] M.E. Callow, J.E. Callow, Marine biofouling: a sticky problem, Biologist, 49 (2002) 10-14.

[35] H. Maddah, A. Chogle, Biofouling in reverse osmosis: phenomena, monitoring, controlling and remediation, Applied Water Science, 7 (2017) 2637-2651.

[36] J. Kucera, Biofouling of polyamide membranes: Fouling mechanisms, current mitigation and cleaning strategies, and future prospects, Membranes, 9 (2019) 1-81.

[37] M. Rosenberg, S. Kjelleberg, Hydrophobic interactions: Role in bacterial adhesion, in: K.C. Marshall (Ed.) Advances in Microbial Ecology, Springer US, Boston, MA, 1986, pp. 353-393.

[38] A.E. Childress, M. Elimelech, Effect of solution chemistry on the surface charge of polymeric reverse osmosis and nanofiltration membranes, Journal of Membrane Science, 119 (1996) 253-268.

[39] J. Rezania, V. Vatanpour, A. Shockravi, M. Ehsani, Preparation of novel carboxylated thin-film composite polyamide-polyester nanofiltration membranes with enhanced antifouling property and water flux, Reactive and Functional Polymers, 131 (2018) 123-133.

[40] G.-d. Kang, Y.-m. Cao, Development of antifouling reverse osmosis membranes for water treatment: A review, Water Research, 46 (2012) 584-600.

[41] S.N. Jagannadh, H.S. Muralidhara, Electrokinetics methods to control membrane fouling, Industrial & Engineering Chemistry Research, 35 (1996) 1133-1140.

[42] S. Nakasono, J.G. Burgess, K. Takahashi, M. Koike, C. Murayama, S. Nakamura, T. Matsunaga, Electrochemical prevention of marine biofouling with a carbon-chloroprene sheet, Applied and Environmental Microbiology, 59 (1993) 3757.

[43] N. Hilal, M. Khayet, C.J. Wright, Membrane Modification : Technology and Applications, CRC Press, 2012.

[44] S.H. Hong, J. Jeong, S. Shim, H. Kang, S. Kwon, K.H. Ahn, J. Yoon, Effect of electric currents on bacterial detachment and inactivation, Biotechnology and Bioengineering, 100 (2008) 379-386.

[45] S. Ibeid, M. Elektorowicz, J.A. Oleszkiewicz, Novel electrokinetic approach reduces membrane fouling, Water Research, 47 (2013) 6358-6366.

[46] V. Kochkodan, Reduction of membrane fouling by polymer surface modification, in: N. Hilal, M. Khayet, C.J. Wright (Eds.) Membrane Modification: Technology and Applications, CRC Press, 2012, pp. 41-76.

[47] M.N. Abu Seman, M. Khayet, N. Hilal, Development of antifouling properties and performance of nanofiltration membranes by interfacial polymerization and photografting techniques, in: N. Hilal, M. Khayet, C.J. Wright (Eds.) Membrane Modification: Technology and Applications, CRC Press, 2012, pp. 119-131.

[48] M.N.A. Seman, M. Khayet, N. Hilal, Nanofiltration thin-film composite polyester polyethersulfone-based membranes prepared by interfacial polymerization, Journal of Membrane Science, 348 (2010) 109-116.

[49] L.Y. Ng, A. Mohammad, N. Hilal, Modifications of polymeric membranes by incorporating metal/metal oxide nanoparticles, in: N. Hilal, M. Khayet, C.J. Wright (Eds.) Membrane Modification: Technology and Applications, CRC Press, 2012, pp. 77-118.

[50] G.S. Ajmani, D. Goodwin, K. Marsh, D.H. Fairbrother, K.J. Schwab, J.G. Jacangelo, H. Huang, Modification of low pressure membranes with carbon nanotube layers for fouling control, Water Research, 46 (2012) 5645-5654.

[51] M. Fathizadeh, W.L. Xu, F. Zhou, Y. Yoon, M. Yu, Graphene oxide: A novel 2-dimensional material in membrane separation for water purification, Advanced Materials Interfaces, 4 (2017) 1600918.

[52] J. Kim, B. Van der Bruggen, The use of nanoparticles in polymeric and ceramic membrane structures: Review of manufacturing procedures and performance improvement for water treatment, Environmental Pollution, 158 (2010) 2335-2349.

[53] D.A. Gopakumar, A.R. Pai, D. Pasquini, L. Shao-Yuan, A.K. H.P.S, S. Thomas, Chapter 1 - Nanomaterials – State of art, new challenges, and opportunities, in: S. Thomas, D. Pasquini, S.-Y. Leu, D.A. Gopakumar (Eds.) Nanoscale Materials in Water Purification, Elsevier, 2019, pp. 1-24.

[54] Z. Xu, T. Wu, J. Shi, K. Teng, W. Wang, M. Ma, J. Li, X. Qian, C. Li, J. Fan, Photocatalytic antifouling PVDF ultrafiltration membranes based on synergy of graphene oxide and TiO_2 for water treatment, Journal of Membrane Science, 520 (2016) 281-293.

[55] P. Arribas, M. Khayet, M.C. García-Payo, L. Gil, 8 - Novel and emerging membranes for water treatment by hydrostatic pressure and vapor pressure gradient membrane processes, in: A. Basile, A. Cassano, N.K. Rastogi (Eds.) Advances in Membrane Technologies for Water Treatment, Woodhead Publishing, Oxford, 2015, pp. 239-285.

[56] J.P. Méricq, J. Mendret, S. Brosillon, C. Faur, High performance PVDF-TiO_2 membranes for water treatment, Chemical Engineering Science, 123 (2015) 283-291.

[57] A. Tiraferri, C.D. Vecitis, M. Elimelech, Covalent binding of single-walled carbon nanotubes to polyamide membranes for antimicrobial surface properties, ACS Applied Materials & Interfaces, 3 (2011) 2869-2877.

[58] A.S. Brady-Estévez, S. Kang, M. Elimelech, A single-walled-carbon-nanotube filter for removal of viral and bacterial pathogens, Small, 4 (2008) 481-484.

[59] O. Akhavan, E. Ghaderi, Toxicity of graphene and graphene oxide nanowalls against bacteria, ACS Nano, 4 (2010) 5731-5736.

[60] F. Perreault, M.E. Tousley, M. Elimelech, Thin-film composite polyamide membranes functionalized with biocidal graphene oxide nanosheets, Environmental Science & Technology Letters, 1 (2014) 71-76.

[61] V. Vatanpour, S.S. Madaeni, R. Moradian, S. Zinadini, B. Astinchap, Novel antibifouling nanofiltration polyethersulfone membrane fabricated from embedding TiO_2 coated multiwalled carbon nanotubes, Separation and Purification Technology, 90 (2012) 69-82.

[62] M.F.L. De Volder, S.H. Tawfick, R.H. Baughman, A.J. Hart, Carbon nanotubes: Present and future commercial applications, Science, 339 (2013) 535.

[63] L. Bai, H. Liang, J. Crittenden, F. Qu, A. Ding, J. Ma, X. Du, S. Guo, G. Li, Surface modification of UF membranes with functionalized MWCNTs to control membrane fouling by NOM fractions, Journal of Membrane Science, 492 (2015) 400-411.

[64] C.D. Vecitis, K.R. Zodrow, S. Kang, M. Elimelech, Electronic-structure-dependent bacterial cytotoxicity of single-walled carbon nanotubes, ACS Nano, 4 (2010) 5471-5479.

[65] C.-F. de Lannoy, D. Jassby, K. Gloe, A.D. Gordon, M.R. Wiesner, Aquatic biofouling prevention by electrically charged nanocomposite polymer thin film membranes, Environmental Science & Technology, 47 (2013) 2760-2768.

[66] B.M. Yoo, H.B. Park, Graphene membranes, in: E. Drioli, L. Giorno, E. Fontananova (Eds.) Comprehensive Membrane Science and Engineering, Elsevier, Oxford, 2017, pp. 358-385.

[67] H.W. Kim, H.W. Yoon, S.-M. Yoon, B.M. Yoo, B.K. Ahn, Y.H. Cho, H.J. Shin, H. Yang, U. Paik, S. Kwon, J.-Y. Choi, H.B. Park, Selective gas transport through few-layered graphene and graphene oxide membranes, Science, 342 (2013) 91.

[68] W.-S. Hung, Q.-F. An, M. De Guzman, H.-Y. Lin, S.-H. Huang, W.-R. Liu, C.-C. Hu, K.-R. Lee, J.-Y. Lai, Pressure-assisted self-assembly technique for fabricating composite membranes consisting of highly ordered selective laminate layers of amphiphilic graphene oxide, Carbon, 68 (2014) 670-677.

[69] Y. Han, Z. Xu, C. Gao, Ultrathin graphene nanofiltration membrane for water purification, Advanced Functional Materials, 23 (2013) 3693-3700.

[70] M. Hu, B. Mi, Enabling graphene oxide nanosheets as water separation membranes, Environmental Science & Technology, 47 (2013) 3715-3723.

[71] C.A. Amadei, P. Arribas, C.D. Vecitis, Graphene oxide standardization and classification: Methods to support the leap from lab to industry, Carbon, 133 (2018) 398-409.

[72] Y. Zhang, T.-S. Chung, Graphene oxide membranes for nanofiltration, Current Opinion in Chemical Engineering, 16 (2017) 9-15.

[73] Q. Zhang, Electrokinetic and electrochemical methods for microbial and organic fouling mitigation at liquid-solid interfaces, in: John A. Paulson School of Engineering and Applied Sciences, Harvard University, 2016, pp. 1-229.

[74] R.A. Al-Juboori, T. Yusaf, Biofouling in RO system: Mechanisms, monitoring and controlling, Desalination, 302 (2012) 1-23.

[75] P. Sennett, J.P. Olivier, Colloidal dispersions,electrokinetic effects and the concept of zeta potential, Industrial & Engineering Chemistry, 57 (1965) 32-50.

[76] F. Du, A. Hawari, M. Baune, J. Thöming, Dielectrophoretically intensified cross-flow membrane filtration, Journal of Membrane Science, 336 (2009) 71-78.

[77] A. Borden, H. Werf, H. van der Mei, H. Busscher, Electric current-induced detachment of Staphylococcus epidermidis biofilms from surgical stainless steel, Applied and Environmental Microbiology, 70 (2004) 6871-6874.

[78] A.T. Poortinga, R. Bos, H.J. Busscher, Reversibility of bacterial adhesion at an electrode surface, Langmuir, 17 (2001) 2851-2856.

[79] T. Matsunaga, T. Nakayama, H. Wake, M. Takahashi, M. Okochi, N. Nakamura, Prevention of marine biofouling using a conductive paint electrode, Biotechnology and Bioengineering, 59 (1998) 374-378.

[80] K. Hori, S. Matsumoto, Bacterial adhesion: From mechanism to control, Biochemical Engineering Journal, 48 (2010) 424-434.

[81] Z. Wu, H. Chen, Y. Dong, H. Mao, J. Sun, S. Chen, V.S.J. Craig, J. Hu, Cleaning using nanobubbles: Defouling by electrochemical generation of bubbles, Journal of Colloid and Interface Science, 328 (2008) 10-14.

[82] C.D. Vecitis, M.H. Schnoor, M.S. Rahaman, J.D. Schiffman, M. Elimelech, Electrochemical multiwalled carbon nanotube filter for viral and bacterial removal and inactivation, Environmental Science & Technology, 45 (2011) 3672-3679.

2

Novel and emerging membranes for water treatment

Hydrostatic pressure and vapor pressure gradient membrane processes

Hydrostatic pressure (microfiltration, ultrafiltration, nanofiltration and reverse osmosis) and vapor pressure gradient membrane processes (membrane distillation and pervaporation) have received an increased attention since 1980s for different water treatment applications. This chapter describes the significant progress achieved during the last few years regarding the fabrication of novel membranes and their modification for these separation processes. In particular, the chapter focuses on novel flat sheet and hollow-fiber membranes made with innovative materials and improved properties suitable for specific applications.

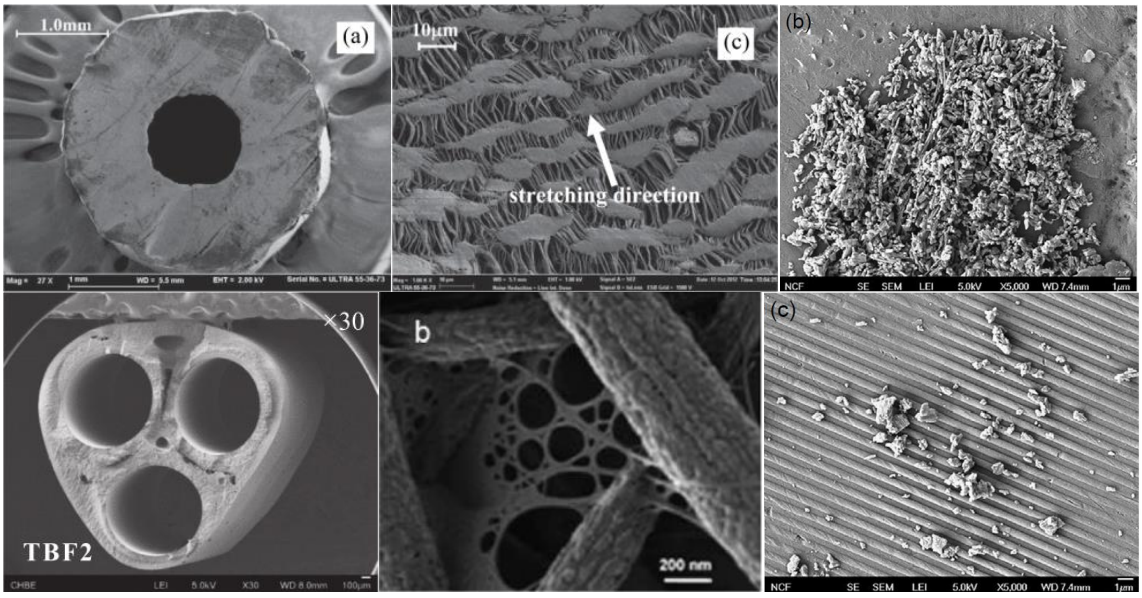

Adapted from Wang et al. [4], Wang et al. [6], Maruf et al [70] and Zhu et al. [78], with permission of Elsevier.

Novel and emerging membranes for water treatment by hydrostatic pressure and vapor pressure gradient membrane processes

2.1 Introduction

Membrane-based separation technologies are environmentally-friendly separation processes that are designed to provide effective and economic solutions to a wide variety of environmental issues related to water and energy use, including climate change and global warming. The growth of membrane science and technology is mainly due to the impressive developments in materials used for membrane fabrication and modification, improvements in membrane modules and the evolution of related systems, plants and equipment.

In general, membranes are semi-permeable barriers used for selective permeation of the desired species in liquid or gaseous phases by means of an appropriate driving force(s). One of the provided classifications of membrane separation processes is according to the nature of the membrane and the applied transmembrane driving force. Each membrane process exhibits its advantages and drawbacks, and as consequence it has its fields of applications. Providing that the present chapter book is focused on water treatment, Table 2.1 summarizes the common considered membrane separation processes in this field together with the corresponding driving forces and their applications.

It is worth quoting that membranes of different forms and characteristics are generally made from a wide variety of chemically and thermally stable polymers. Both single and polymer blends are considered. Other materials such as ceramics, metals and glasses are also used and mixed matrix membranes (MMMs) are fabricated. Various membrane fabrication techniques are being proposed and improved (i.e. phase inversion, sintering, stretching, track-etching, electro-spinning, etc.). In addition, various methods have been developed for membrane modification (i.e. chemical modification, surface coating, grafting, etc.) in order to improve its performance. Novel membranes with innovative materials and improved properties suitable for specific applications as well as compact module designs with better hydrodynamic flow channels and new areas of applications are continuously reported.

Table 2.1. Membrane separation processes used for water treatment together with their driving force and main fields of applications.

Membrane process	Transmembrane driving force	Main fields of applications
Microfiltration (MF)	Hydrostatic pressure gradient	Pre-treatment for other processes Clarification and biological stabilization in the beverage industry Analysis Sterilization in food and pharmaceutical industries Removal of bacteria, clarification
Ultrafiltration (UF)	Hydrostatic pressure gradient	Pre-treatment for other processes Separation of oil/water emulsion Dewaxing Deasphalting Electrophoretic paint Removal of macromolecules and virus
Nanofiltration (NF)	Hydrostatic pressure gradient	Drinking water production Removal of ions and small organics Chemical and pharmaceutical industry Concentration/dewatering Water softening Fractionation of monovalent and divalent cations
Reverse osmosis (RO)	Hydrostatic pressure gradient	Sea and brackish water desalination Drinking water production Wastewater treatment (industrial and municipal, pulp and paper, textile) Petroleum industry
Membrane distillation (MD)	Vapour pressure gradient (temperature gradient, downstream pressure)	Desalination and concentration of brines Ultra-pure water production Near 100% separation of non-volatile solutes present in water Extraction of volatile organic compounds Recovery of valuable compounds Food, medical, radioactive wastewaters
Pervaporation (PV)	Vapour pressure gradient (downstream pressure)	Dehydration of organic solvents Removal of organics from water Organic/organic separation
Electrodialysis (ED)	Electric potential gradient	Sea and brackish water desalination Ultrapure water production Demineralization of food products Table salt production Concentration of brines
Reverse Electrodialysis (RED)	Electric potential gradient	Power generation Sea and brackish water desalination
Osmotic distillation (OD)	Vapour pressure gradient (concentration gradient)	Near 100% separation of non-volatile solutes present in water Recovery of valuable compounds Food wastewaters
Forward osmosis (FO)	Concentration gradient	Sea and brackish water desalination Drinking water production
Pressure retarded osmosis (PRO)	Concentration gradient	Power generation Sea and brackish water desalination

Besides the high process performance of a given membrane that includes both the high liquid or vapor production rate and selectivity or separation efficiency, there are other basic properties that must be taken into account such as operational simplicity, high energy efficiency, low cost, good stability under wide operating conditions, long-term durability, less fouling and scaling susceptibility, environment compatibility, customizable and adaptive between different membrane operations in integrated systems, easy control of its structure and scale-up.

2.2 Pressure-driven membrane processes

In general, pressure-driven membrane processes (PDMPs) include microfiltration (MF), ultrafiltration (UF), nanofiltration (NF) and reverse osmosis (RO). These filtration processes can be distinguished by the size of the particles or molecules that the corresponding membrane is capable to retain or pass through it [1]. This is roughly related to the membrane pore size, which is the main responsible parameter dictating the field of the process applications.

The membranes fabricated for each of the PDMPs exhibit specific characteristics according to the operating conditions and the subjected application. A common characteristic of the PDMP membranes is the high mechanical property to bear the applied hydrostatic pressure, especially for NF and RO. In what follows, the recent progress made in each individual PDMP is thoroughly described together with its novel and emerging membranes proposed for water treatment.

2.2.1 Microfiltration

As it is shown in Table 2.2, the pore size of a MF membrane ranges between 0.1 and 10 μm. The MF membranes must have a high porosity and a pore size distribution as narrow as possible. A large number of materials were considered for fabrication of MF membranes, both organic (hydrophilic or hydrophobic polymers) and inorganic materials (ceramics, metals, glasses). Some of the fabrication techniques such as sintering, stretching, track-etching and phase inversion were employed for fabrication of polymeric MF membranes.

The main problems of MF are the concentration polarization and fouling phenomena. Both reduce the water production rate and the efficiency of the whole process. Therefore, MF membranes are designed or modified taking into consideration both phenomena and MF modules are cleaned periodically. It must be pointed out that the selection of a suitable material for MF is an important factor because solute(s) adsorption phenomenon plays also an important role on irreversible fouling effects.

Dong et al. [2] used hydrophilic $Mg(OH)_2$ nanoparticles (NPs) as inorganic fillers to prepare PVDF/$Mg(OH)_2$ MF hybrid membranes with enhanced antifouling property. Due to the addition of $Mg(OH)_2$ NPs, large amount of hydroxyl (–OH) groups were formed. This results

in an increase of the hydrophilicity of the prepared hybrid membrane reducing the permeate flux losses caused by membrane biofouling of *Escherichia coli* and bovine serum albumin (BSA).

Table 2.2. Characteristics of the different pressure-driven membrane processes.

	Microfiltration (MF)	**Ultrafiltration (UF)**	**Nanofiltration (NF)**	**Reverse osmosis (RO)**
Pore size (nm)	100–10000	1–100	0.5–2	< 0.5
MWCO[a] (Da)	$> 5 \cdot 10^5$	$2–5 \cdot 10^5$	$5 \cdot 10^2–2 \cdot 10^3$	$< 5 \cdot 10^2$
Pressure (MPa)	0.1–2	1–10	10–30	15–30 (brackish) 40–80 (seawater)
Permeability (kg/m^2s)	<278	2.5–278	0.5–8.5	<0.5
Membrane materials[b]	Ceramic, PSU, PES, PVDF, CA	Ceramic, PSU, PES, PVDF, CA, TF	CA, TF	CA, TF
Rejection	Particles Bacteria	Macromolecules Proteins Virus Colloids	High *Mw* compounds Multivalent ions Glucose	High and low *Mw* compounds Mono-valent ions Inorganic ions Amino acids
Separation mechanism	Sieving	Sieving	Sieving, charge effects, diffusion	Solution-diffusion

[a]MWCO = molecular weight cut-off of the membrane (corresponding solute rejection 90%).
[b]PSU = polysulfone; PES = polyethersulfone; PVDF = polyvinyl fluoride; CA = cellulose acetate; TF = thin film.

Wu et al. [3] developed a novel silica (SiO_2)–graphene oxide (GO) nanohybrid/polysulfone (PSU) membrane, which exhibited excellent antifouling ability along with improved water permeability maintaining high the rejection factor to egg albumin. These results were attributed to the specific properties of SiO_2–GO nanohybrid such as the high hydrophilicity and the good dispersion derived from SiO_2 NPs.

Wang et al. [4] developed novel nanofibrous MF composite membranes, consisting of a two-layered electrospun polyacrylonitrile (PAN)/polyethylene terephthalate (PET) fibrous scaffold infused with oxidized or modified cellulose nanofibers, which were subsequently grafted by amine, such as polyvinylamine (PVAm), polyethyleneimine (PEI), or ethylenediamine (see Fig. 2.1). These membranes have a web-like structure with very high charge density, high porosity and large surface area per unit volume. These characteristics enabled the membranes to simultaneously remove bacteria, viruses and/or toxic heavy metal ions maintaining a very good permeation flux.

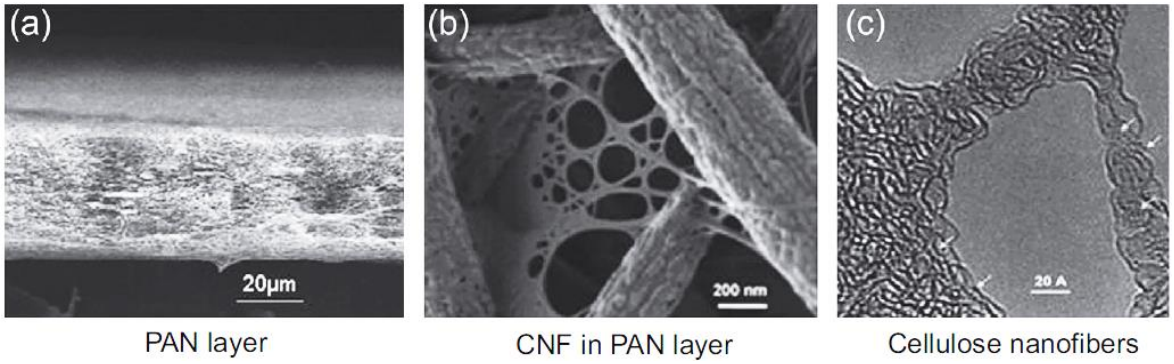

Figure 2.1. SEM images of electrospun polyacrylonitrile/polyethylene terephthalate (PAN/PET) membrane: (a) PAN/PET membrane (cross-section) and (b) PAN/PET membrane infused with polyvinylamine (PVAm) grafted cellulose nanofiber (CNF) (top view). (c) TEM image taken at a small section of the cellulose network containing pores and individual polymer chains with spaghetti-like configuration. Reprinted from Wang et al. [4], with permission from Elsevier.

2.2.2 Ultrafiltration

UF is a PDMP placed between MF and NF. However, MF and UF both involve similar membrane processes based on the same separation principle, being the difference between both the structure of the membrane, which is asymmetric for UF membrane with a much denser top layer, and consequently a much higher hydrodynamic resistance than MF. UF is commonly used to retain macromolecules and colloids from aqueous solutions and to remove un-dissolved, suspended or emulsified solids from water. Cellulose acetate (CA) and polyelectrolytes are among the first synthetic polymers used for UF membranes. Today, UF membranes are made from a wide variety of chemically and thermally stable synthetic polymers, including PSU, PAN, polyethersulfone (PES), polyvinyl chloride (PVC), polycarbonate (PC), aliphatic and aromatic polyamides (PAs), polyimides (PIs), polyarylsulfone (PAS), and PVDF.

Kong et al. [5] studied the effect of adding hydrophilic TEMPO-oxidized cellulose nanofibrils (TOCNs) as a modifying agent on the structure and performance of cellulose triacetate (CTA) UF membranes. The obtained results showed that the incorporation of TOCNs to CTA membranes enhanced its mechanical properties (tensile strength and break–elongate ratio) and its hydrophilicity, resulting in higher permeate fluxes and better antifouling performance.

Another innovative and interesting study was performed by Wang et al. [6], who developed tri-bore UF hollow fiber membranes made from Matrimid® and PES polymers with round-shape bore channels and a regular triangle-shape outer geometry. Fig. 2.2 shows the mechanism of formation of these UF membranes together with their scanning electron microscopy (SEM) cross-section images. This particular geometry is claimed to be advantageous in terms of uniform mechanical strength and enhanced permeation properties due to the evenly distributed membrane wall thickness.

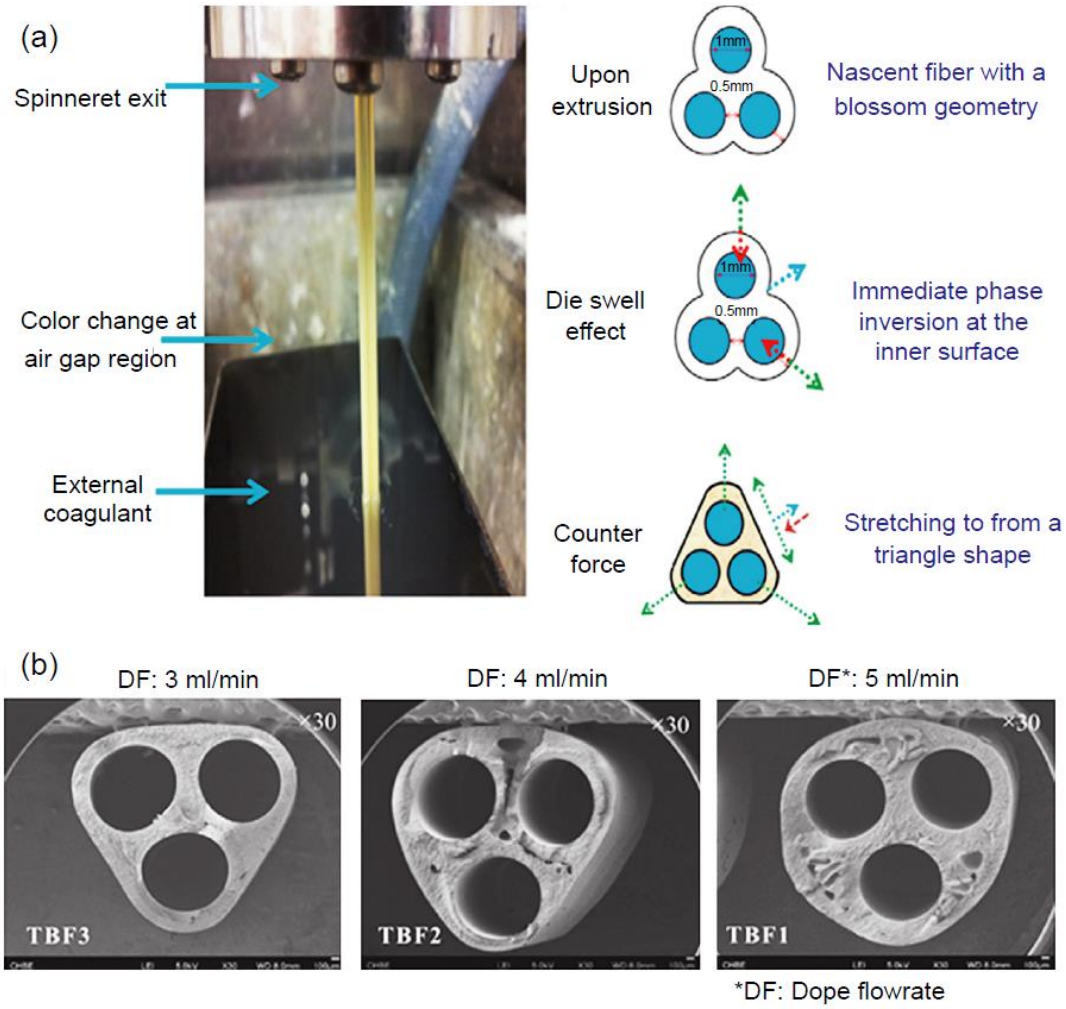

Figure 2.2. (a) Mechanisms of formation of triangle-shape tri-bore hollow fiber membranes. (b) SEM images of Matrimid® tri-bore hollow fiber membranes using different dope compositions. Adapted from Wang et al. [6], with permission from Elsevier.

Recently, a variety of inorganic particles or fillers such as SiO_2 [7-9], silver (Ag) [10], ferrous ferric oxide (Fe_3O_4), alumina (Al_2O_3) [11], zirconia (ZrO_2) [11-13], titania (TiO_2) [11, 14-18], zinc oxide (ZnO) [19], and zeolites [20] have been used to develop novel UF MMMs or organic–inorganic hybrid membranes with improved permeabilities, mechanical strengths, and fouling resistant ability.

Among the different inorganic NPs blended with polymeric membranes, TiO_2 has also been used in numerous studies due to its superhydrophilic, photocatalytic, and antibacterial properties under ultraviolet (UV) irradiation. Rahimpour et al. [21] performed an approach to improve the properties, structure, and performance of PVDF/sulfonated polyethersulfone (SPES) blend UF membranes by using self-assembly of TiO_2 NPs on the membrane surface followed by UV irradiation to activate their photocatalytic property. The water contact angle measurements showed that the hydrophilicity of PVDF/SPES membranes was strongly improved by TiO_2 deposition and UV irradiation. The initial permeate fluxes of both pure water and BSA aqueous

solutions were lower for the TiO_2 deposited membranes compared to the PVDF/SPES membranes. However, the fouling propensity (bacterial activity) was significantly reduced, and the long-term permeate flux stability was enhanced.

As was mentioned previously, SiO_2 is another common NP used for membrane modification. SiO_2 has the advantage to improve the membrane mechanical properties and membrane porosity. Yu et al. [8] used modified SiO_2 NPs grafted with N-Halamine to develop novel hydrophilic PES UF membranes. By SEM image analysis and contact angle measurements, it was confirmed that the addition of this modified SiO_2 exerted a slight influence on the microstructure of the PES membrane, but significantly improved its surface hydrophilicity and permeability.

Song and Kim [22] prepared PSU composites UF membranes with poly(1-vinylpyrrolidone) (PVP)-grafted SiO_2 NPs (PVP-g-SiO_2) by phase inversion method (see Fig. 2.3). The resulted UF membranes exhibited higher water permeate flux than PSU membranes without scarifying the solute rejection factors when the amount of PVP-g-SiO_2 was less than or equal to 5 wt% in the casting solution. The hydrophilicity of the PVP-g-SiO_2 membranes was increased with increasing PVP-g-SiO_2 content, and the PVP-g-SiO_2 membranes exhibited enhanced fouling resistance toward non-ionic surfactants.

Multifunctional inorganic ZnO NP has also attracted a significant attention due to its outstanding physical and chemical properties, including promising catalytic activity and efficient antibacterial and bactericidal capabilities. ZnO as an additive NP is more economical than TiO_2 and Al_2O_3 [23]. Hong and He [19] successfully prepared PVDF UF membrane blended with ZnO NP via phase inversion method. The photocatalysis tests clearly showed that the modified PVDF membranes had significant photocatalysis self-cleaning capability, which was due to the addition of nano-ZnO on the inner surface of the membrane (i.e., the pore wall). The water permeate flux of nano-ZnO/PVDF blend membranes was higher than that of single PVDF membrane, decreasing the membrane fouling resistance.

Mehrparvar et al. [24] prepared novel modified PES UF membrane for humic acid removal by blending different concentrations of two hydrophilic organic monomers, 3,5-diaminobenzoic acid (DBA) and gallic acid (GA), with PES. Experimental results showed that the different component ratios of each monomer affected the structural property of the blended membranes and the top surface roughness. As can be seen in Fig. 2.4, with the addition of DBA and GA, the size of the macrovoids became smaller, and a denser surface was formed at the top membrane surface. The addition of DBA and GA monomers in the casting solution increased the water content and the hydrophilicity of the membranes. Moreover, the modified membranes exhibited better antifouling properties, and the best membrane was prepared with 8 wt% DBA and 6 wt% GA.

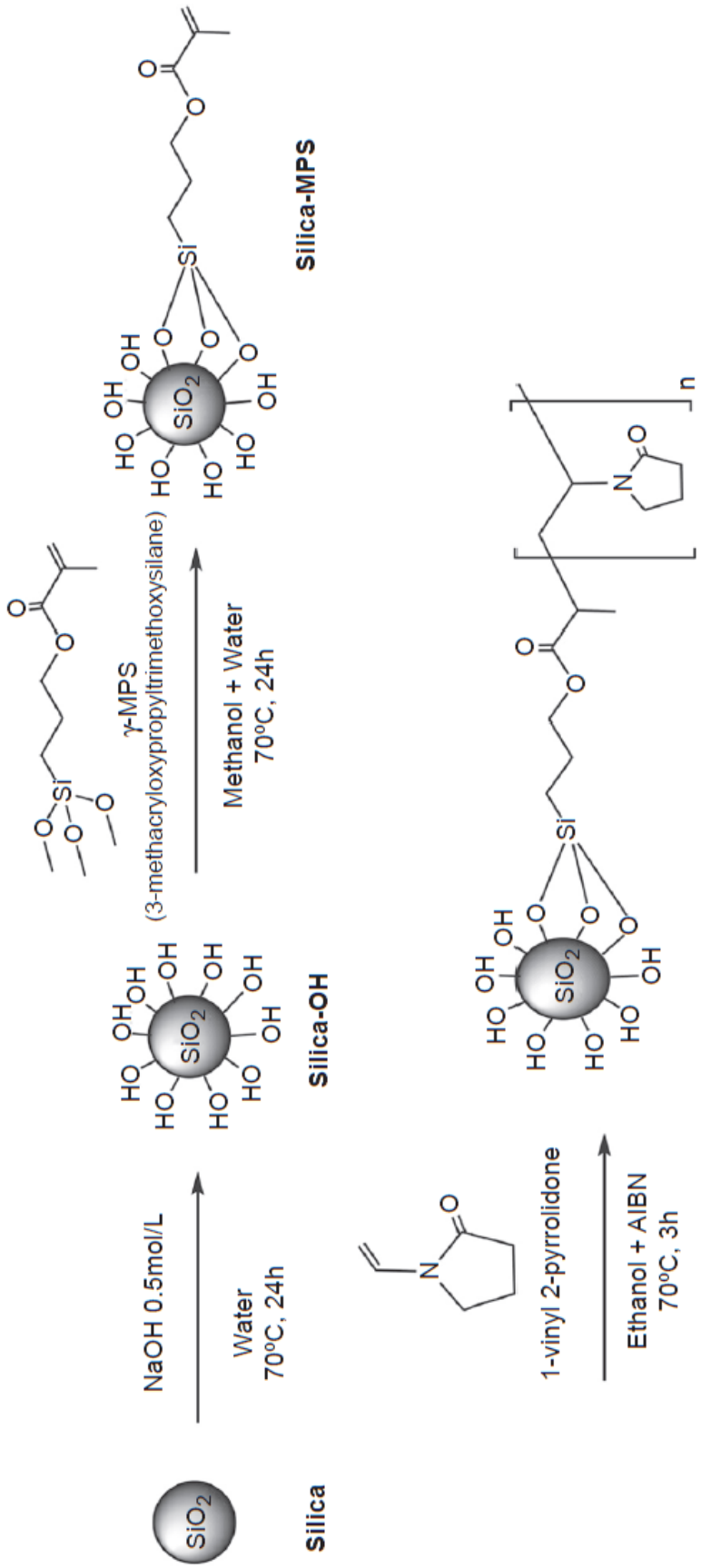

Figure 2.3. Reaction procedure for preparation of PVP grafted silica nanoparticles (PVP-g-SiO_2). Reprinted from Song and Kim [22], with permission from Elsevier.

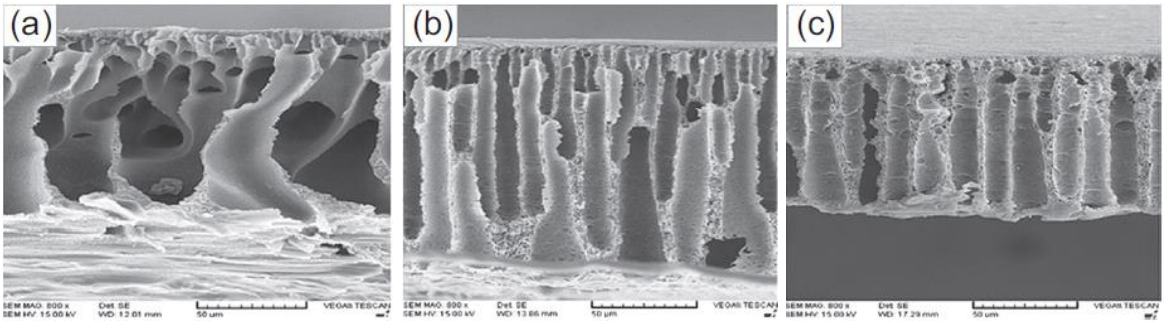

Figure 2.4. SEM cross-section images of: (a) neat polyethersulfone (PES) membrane and PES membrane with (b) 15 wt% diaminobenzoic acid (DBA) and (c) 15 wt% gallic acid (GA). Reprinted from Mehrparvar et al. [24], with permission from Elsevier.

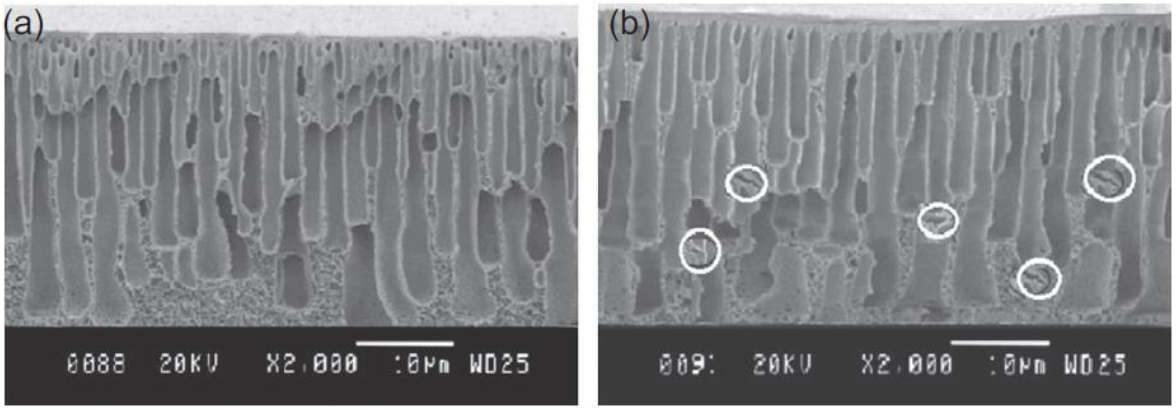

Figure 2.5. SEM cross-section images of the GO-blended polyvinylidene fluoride (PVDF) membranes with (a) 0 and (b) 0.3 wt% graphene oxide (GO). Reprinted from Wang et al. [25], with permission from Elsevier.

During the last 5 years, GO nanosheets, a two-dimensional carbon material, have received tremendous attentions thanks to its fantastic properties, such as good hydrophilicity, easy to be modified, and its ability to be dispersed in water, yielding to a prolonged and stable suspension. Wang et al. [25] used GO nanosheets to develop novel organic e inorganic nanocomposite GO/PVDF-blended UF membranes. The GO addition played an important role in the membrane microstructure due to the affinity of GO with many types of hydrophilic groups, which increase the rapid mass transfer between the solvent and non-solvent during phase inversion. When the GO content increased up to 0.30 wt%, lateral pore structures appeared within the GO-blended PVDF membranes (Fig. 2.5). These features enhanced the hydrophilicity, mechanical properties, and water permeate flux recovery ratio compared to the PVDF membrane. Yu et al. [26] also developed a novel hyperbranched polyethylenimine (HPEI)-GO/PES blend UF membrane with enhanced antifouling and antibacterial performance via the phase inversion method.

2.2.3 Nanofiltration

NF is a PDMP using semipermeable membranes with a molecular weight cut-off (MWCO) in the range of 0.5–2 kDa and pore sizes in the range of 0.5–2.0 nm (see Table 2.2). The origin of NF dates back to 1970s, when efforts started to be made developing RO membranes with reasonable water permeate fluxes at relatively low pressures [27]. The NF process exhibits separation characteristics between RO and UF. The specific features of NF membranes are mainly the combination of very high rejection factors for multivalent ions (99%) with low to moderate rejection factors for monovalent ions (0–70%), and high rejection factors (90%) for organic compounds with molecular weights above that of the membrane MWCO. The major separation mechanisms of NF involve a steric (i.e., size exclusion) effect and an electrostatic partitioning interaction (i.e., Donnan exclusion) between a given NF membrane and a feed aqueous solution [28]. In general, the traditional materials used for fabrication of NF membranes are polymers using the phase inversion or the interfacial polymerization (IP) techniques. The phase inversion membranes are homogeneous and asymmetric, and they are often made of CA or PES, while the NF membranes made by IP are heterogeneous, consisting of a thin film composite (TFC) layer on the top of an UF substrate. Typically used polymers are (aromatic) PA, PI, PSU, PES, sulfonated PSU, and poly(piperazine amide), among others.

Recently, there has been a growing interest in developing novel NF hollow fiber membranes because of their flexibility and they are self-supporting and easy to pack in modules with high membrane area per unit module volume [29, 30]. Most NF membranes have a TFC structure because of various key advantages compared to asymmetric membranes. Sun et al. [28] developed a TFC NF dual-layer hollow fiber membrane via IP of HPEI and isophthaloyl chloride on a Torlon® polyamide-imide (PAI) dual-layer hollow fiber substrate. This NF membrane exhibited a double repulsion effect, a negatively charged substrate and a positively charged selective layer, resulting in superior rejection factors (>99%) for both positively and negatively charged dye molecules. This type of membrane was suggested to recycle valuable products and reuse water for textile, pharmaceutical, and other industries. Fang et al. [31] prepared TFC NF hollow fiber membranes for water softening under low operating pressure (<2 bar) using IP of PEI and trymesoyl chloride (TMC) on the inner surface of a PES UF membrane substrate. The prepared membrane showed a pure water permeability (*PWP*) of about 17 L/m^2 h bar, an MWCO of around 500 Da (i.e., effective pore radius of about 0.65 nm), an $MgCl_2$ rejection factor of 96.7%, and an $MgSO_4$ rejection factor of 80.6%. Wei et al. [32] prepared also TFC NF hollow fiber membranes by IP of piperazine (PIP) and TMC on PSU/PES UF supporting membranes. The fabricated composite NF hollow fiber membranes had a relatively hydrophilic surface with an MWCO of approximately 520 Da, a *PWP* of 11.9 L/m^2 h bar, and rejection factors of 39.8% and 96.2% to NaCl and Na_2SO_4, respectively. Zheng et al. [33] followed the dip-coating method to prepare positively charged TFC NF hollow fiber

membranes for cationic dyes removal using polypropylene (PP) hollow fiber MF membrane as support, PVA and polyquaternium-10 as coating materials, and glutaraldehyde (GLA) as a crosslinking agent. The prepared membrane had an MWCO of 650 Da, a *PWP* of 8.6 L/m^2 h bar, and rejection factors of 92.8% and 35.0% to $CaCl_2$ and NaCl, respectively.

Not only hollow fiber membranes have been proposed for NF, but also flat sheet membranes. Guan et al. [34] developed TFC NF flat sheet membranes with improved thermal stability and high performance by coating sulfonated copoly (phthalazinone biphenyl ether sulfone; SPPBES) on poly(phthalazinone ether sulfone ketone) UF membranes used as support. The prepared SPPBES composite membranes exhibited a *PWP* of 7.3 L/m^2 h bar and 84% Na_2SO_4 rejection factor. TFC NF flat sheet membranes were also prepared by Han [35] following the IP of melamine and TMC on a PEI UF membrane reinforced on PP non-woven fabric as a backing material. The membranes prepared under the optimum preparation conditions achieved a *PWP* of 3.4 L/m^2 h bar and a rejection factor to Na_2SO_4 of 77.8%.

As occurred with membranes designed for UF, different polymers and inorganic NPs have been used to improve the NF performance of TFC membranes. For instance, to solve the biofouling problem, Ag NPs were used. Kim et al. [36] used Ag NPs to enhance the antifouling and antibacterial property of the surface of NF membranes. Recently, a stable Ag-doped fly ash/polyurethane (Ag-FA/PU) nanocomposite multifunctional spider-web-like membrane was prepared by Pant et al. [37] via one-step electrospinning process using FA particles. It was suggested that the direct reduction of the Ag metal precursor ($AgNO_3$) into Ag NPs caused by the solvent of PU (*N,N*-dimethylformamide) in the blend solution could be the responsible of the simultaneous formation of spider-web-like nanonets and deposition of Ag NPs on the surface of the fibers during electrospinning (Fig. 2.6). These features enhanced absorption capacity to remove carcinogenic arsenic and toxic organic dyes, with the antibacterial properties reducing biofouling of the membrane. Mollahosseini and Rahimpour [38] tried to improve the antibacterial and antifouling property of TFC NF membranes by first coating TiO_2 NPs on an UF PSU membrane support followed by the IP of *m*-phenylenediamine (MPD) and TMC monomers on the coated TiO_2 layer. With increasing TiO_2 content in TFC membranes, smoother and thicker surfaces appeared on the selective PA layer, reducing the probability of membrane fouling by macromolecules.

A novel β-cyclodextrin (β-CD)/polyester TFC NF membrane was prepared by Wu et al. [39] via in situ IP of TMC and triethanolamine (TEOA) in presence of β-CD. By adding an appropriate amount of β-CD, the membrane NF performance was improved in terms of water permeability, hydrophilicity, water permeate flux, rejection factor, and antifouling property. To enhance acid stability of TFC NF membranes, Yu et al. [40] followed the IP of TMC and naphthalene-1,3,6-trisulfonylchloride (NTSC), and PIP to modify a PSU UF membrane used as support. It was observed that the increase of the NTSC content in TMC-organic solution

resulted in a more hydrophilic and negatively charged membrane surface, with an increase of both MWCO and *PWP* up to 660 Da and 10.6 L/m^2 h bar, respectively. Wu et al. [41] performed an improved process to develop high-performance thin film nanocomposite (TFN) membranes using IP of TEOA and TMC on PSU UF supporting membrane in presence of multiwalled carbon nanotubes (MWCNTs). By using an adequate amount of MWCNTs, an appropriate surfactant, and a proper reaction time, MWCNTs/polyester nanocomposite membranes can be fabricated with both high permeation flux and excellent selectivity.

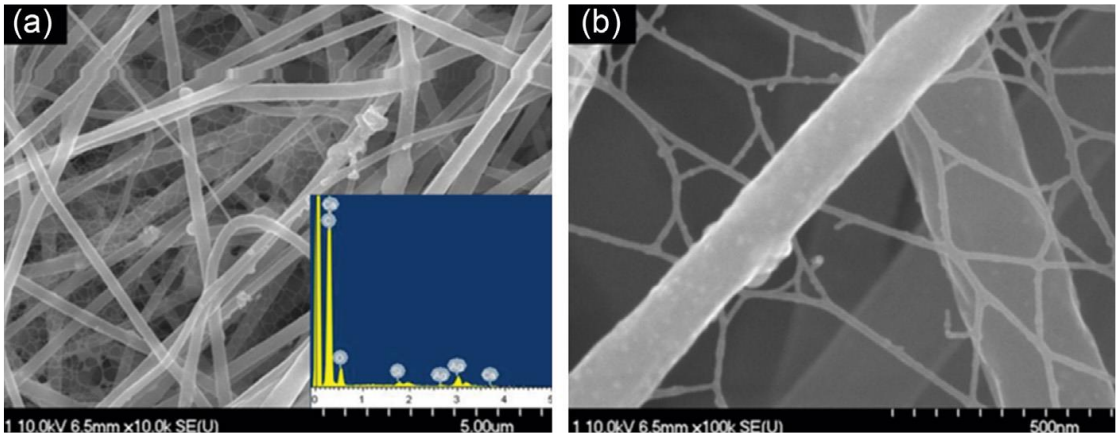

Figure 2.6. Field emission scanning electron microscopy (FESEM) images of Ag/FA/PU (M1) mat (obtained from 1 h stirring solution) at different magnifications (a) lower magnification, (b) higher magnification (inset is FESEM EDX of Ag/FA/PU (M1) mat). Reprinted from Pant et al. [37], with permission from Elsevier.

A novel antifouling mixed matrix PES NF membrane was prepared by Zinadini et al. [42] by embedding GO nanoplates in PES matrix. The modified GO/PES membranes showed a wider finger-like structure in comparison to those of the unmodified PES membrane, with a significantly higher water permeate flux, higher hydrophilicity, higher dye removal capacity, and higher retention factor. In addition, it was found that the membrane prepared with 0.5 wt% GO exhibited the best antibiofouling property with the highest mean pore size, porosity, and therefore the greater water permeate flux.

Recently, positively charged composite NF membranes were prepared via crosslinking modification with an active PEI layer and a PAN substrate [43]. The PAN/PEI membrane with a PEI layer crosslinked with 12.0 wt% epichlorohydrin at 65°C for 15 h exhibited an optimum NF performance with relatively high salt rejection factor and a high permeate flux (i.e., salt rejection factors of 92.82%, 69.76%, and 61.31% for feed aqueous solutions containing 2000 mg/L of $MgCl_2$, $MgSO_4$, and NaCl, respectively, with the corresponding *PWP*: 1.63, 1.60, and 1.79 L/m^2 h bar).

Another type of NF membranes, aquaporin (AQP)-based biomimetic membrane, has attracted increasing attention during the last two years because of its potential application for

water purification and seawater desalination, attributed to the exceptionally high permeability and selectivity of AQPs. In late 2013, Li et al. [44] introduced a novel and simple method to prepare an aquaporin Z (AQP-Z)-based biomimetic NF membrane consisting first on the deposition of polydopamine (PDA)-coated proteoliposomes on the surface of a substrate and then crosslinking PEI with the PAI substrate to encapsulate these deposited proteoliposomes (Fig. 2.7). The resultant AQP-Z-based membrane prepared under the optimal conditions achieved 95% $MgCl_2$ rejection factor and a *PWP* of 3.7 L/m^2 h bar (50% higher than the control membrane with inactive AQPs). This type of membrane could preserve its activity even under harsh environmental conditions such as a high thermal treatment at 343 K for 2 h [44].

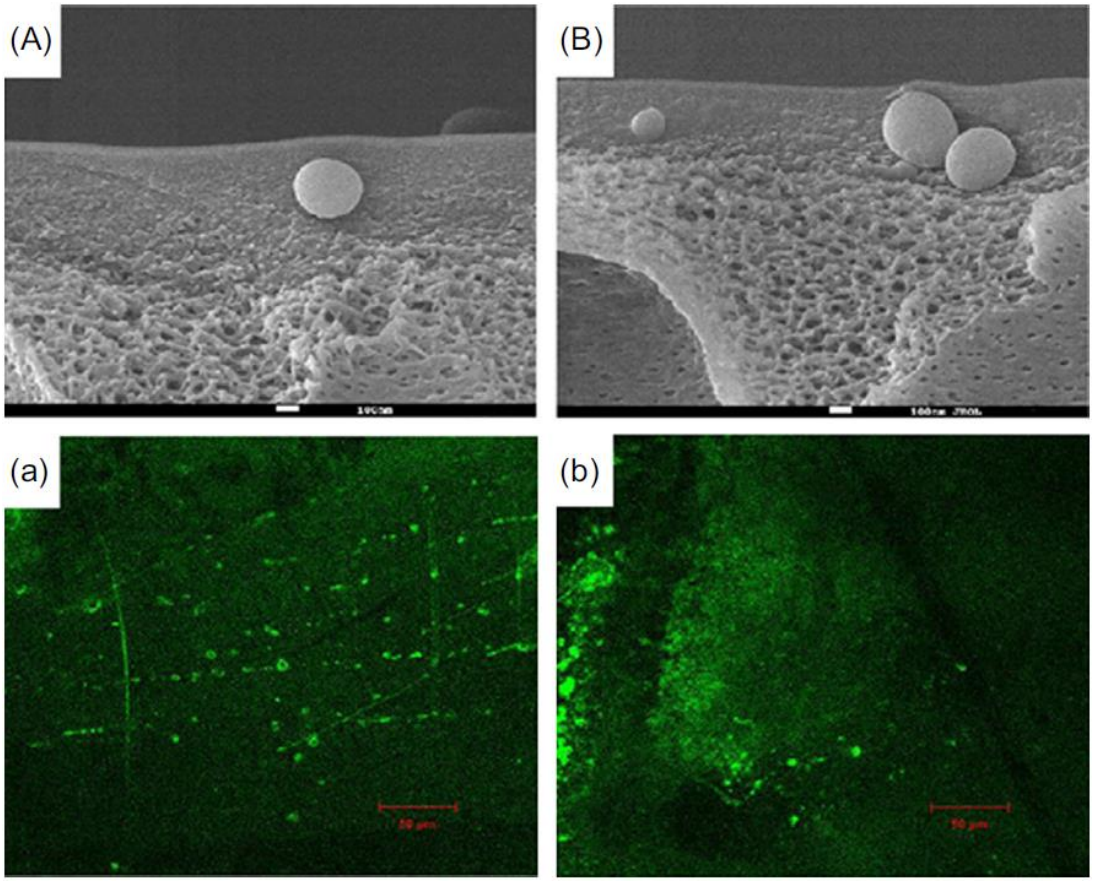

Figure 2.7. FESEM images (A and B, scale bar 100 nm) and confocal fluorescence microscopy images (a and b, scale bar 50 mm) of different membranes with AQP-Z incorporated membrane (called LPR 400). Reprinted from Li et al. [44], with permission from Elsevier.

2.2.4 Reverse osmosis

RO is a PDMP used to separate dissolved solids, such as ions, high and low molecular weight compounds, and amino acids from water-based solutions. More details on RO membrane and process applications are summarized in Tables 2.1 and 2.2. Currently, RO is the most important desalination technology. Different types of membranes were proposed for the RO process, but the most common ones are CA membranes and aromatic PA composite membranes. The first

was an asymmetric CA-based RO membrane invented by Loeb and Sourirajan in 1960 [45]. Today, TFC membranes are the most used in RO applications. However, the main drawbacks of RO membranes are the "trade-off" between permeability and salt rejection factors, the membrane fouling, and the chlorination problem resulting in a significant membrane degradation by the presence of chlorine in feed water solutions [46]. As a consequence, research studies considered these three obstacles in developing novel suitable membranes for different RO applications [47].

Innovative RO membrane engineering is still required because of the continuous increasing demands of desalination and membrane wastewater treatments with enhanced water production rates, greater salt rejection factors, and overall higher resistance to fouling [48]. Various strategies have been explored to tackle these needs, among which surface modifications (e.g., surface coating) and incorporation of specific additives, nanoparticles, and/or co-solvents in the aqueous/organic phase during the IP have been identified to be the most effective [46]. Wang et al. [49] prepared TFC RO membranes through IP of TMC, 2,4,4´,6-biphenyl tetraacyl chloride, 2,3´,4,5´,6-biphenyl pentaacyl chloride, and 2,2´,4,4´,6,6´-biphenyl hexaacyl chloride with MPD. The RO membrane skin layer became more negatively charged, thinner, and smoother as the functionality of the acid chloride monomer increased. The lower permeate flux of the highly functional acid chloride-based membrane owing to the greater extent of carboxylic acid groups on the membrane surface, lower surface roughness, and lower mobility of the crosslinked PA chains was observed. A novel high permeability PA TFC RO membrane was synthesized by Zhao et al. [50] by introducing four different hydrophilic additives (*o*-aminobenzoic acid-triethylamine salt, *m*-aminobenzoic acid-triethylamine salt, 2-(2-hydroxyethl) pyridine, and 4-(2-hydroxyethyl) morpholine) in the MPD aqueous solution for IP. The obtained optimum membrane exhibited a stable desalination performance over a one-month test with a salt rejection factor of 98.8% and a permeate flux of 107.2 L/m^2 h.

Functionalized polyethylene glycol (PEG)-based polymers also have been synthesized and used to modify the PA TFC RO membrane surface to enhance its antifouling properties. A comb-like amphiphilic copolymer, methylmethacrylate-hydroxypoly(oxyethylene) methacrylate, was synthesized by Choi et al. [51] via free-radical polymerization and used to modify the surface of the PA TFC RO membrane by the dip-coating method. In addition, to introduce antifouling quality in RO membranes without compromising their separation properties, a new type of polymer coating made from hydrophilic dendritic polymers was used to modify the surface of PA TFC RO membrane, rendering it more hydrophilic [52]. As it can be seen in Fig. 2.8, the hydrophilic dendritic polymers were crosslinked to form a network, and this was modified with hydrophilic linear chains (e.g., PEG, polyvinyl alcohol (PVA), and polyacrylamide) to form polymer brushes, which can help to prevent formation of biofilm. Moreover, antimicrobial metal ions such as Ag, Zn, or potassium could be chelated into the polymer network to further

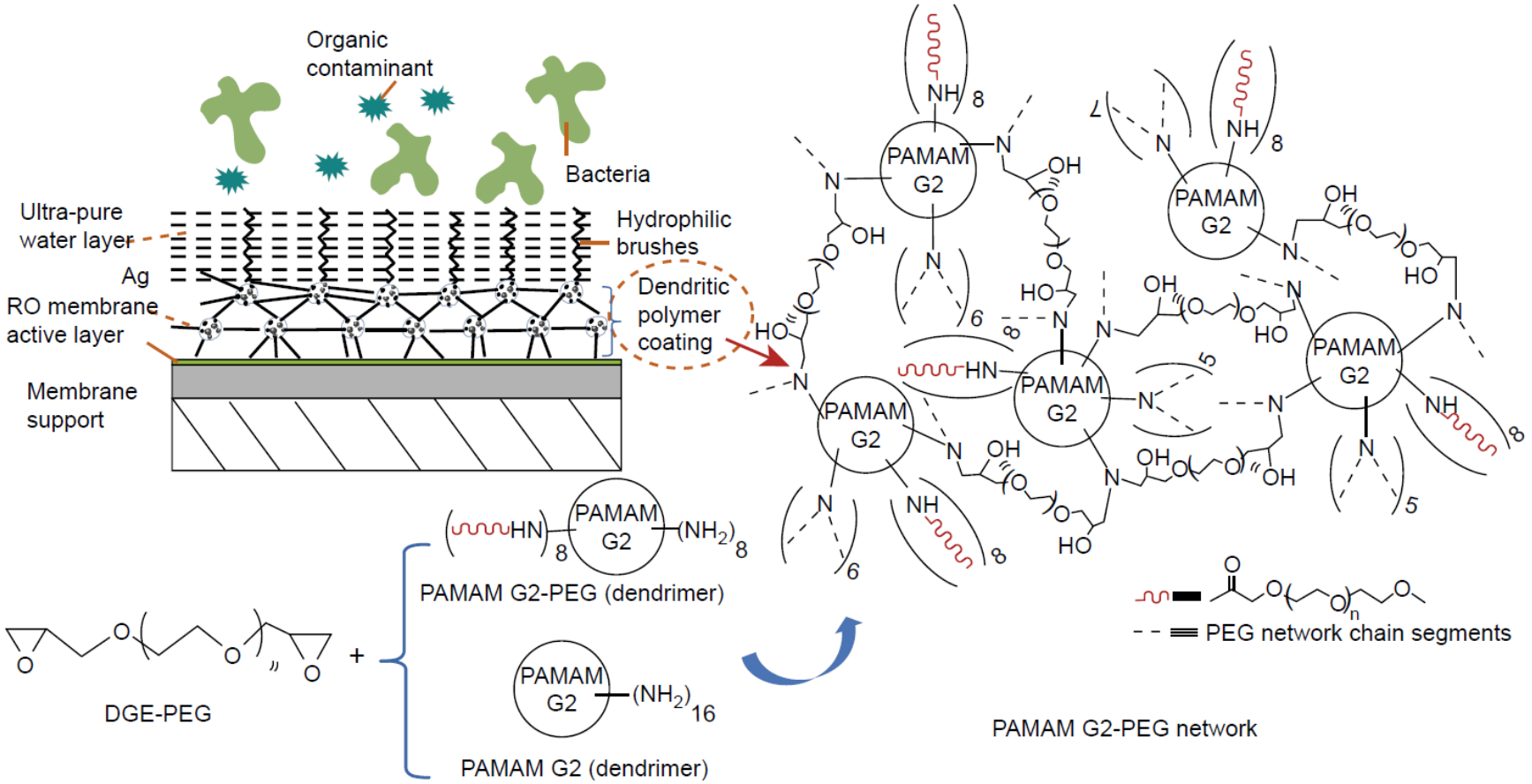

Figure 2.8. Schematic illustration of hydrophilic coating with dendritic polymers on the polyamide (PA) active layer of thin film composite reverse osmosis (TFC RO) membrane. Reprinted from Xu et al. [46] and Sarkar et al. [52], with permission from Elsevier.

prevent biofouling. Examples of dendritic polymers are hyperbranched polymers or dendrimers. The chosen dendrimers were NH_2-terminated PAMAM (PAMAM G2) and PAMAM G2-PEG. Both dendrimers polymers can be crosslinked with glycidyl ether-functionalized α,ω-telechelic PEG to from the PAMAM G2-PEG networks, which were then used as hydrophilic coating layers.

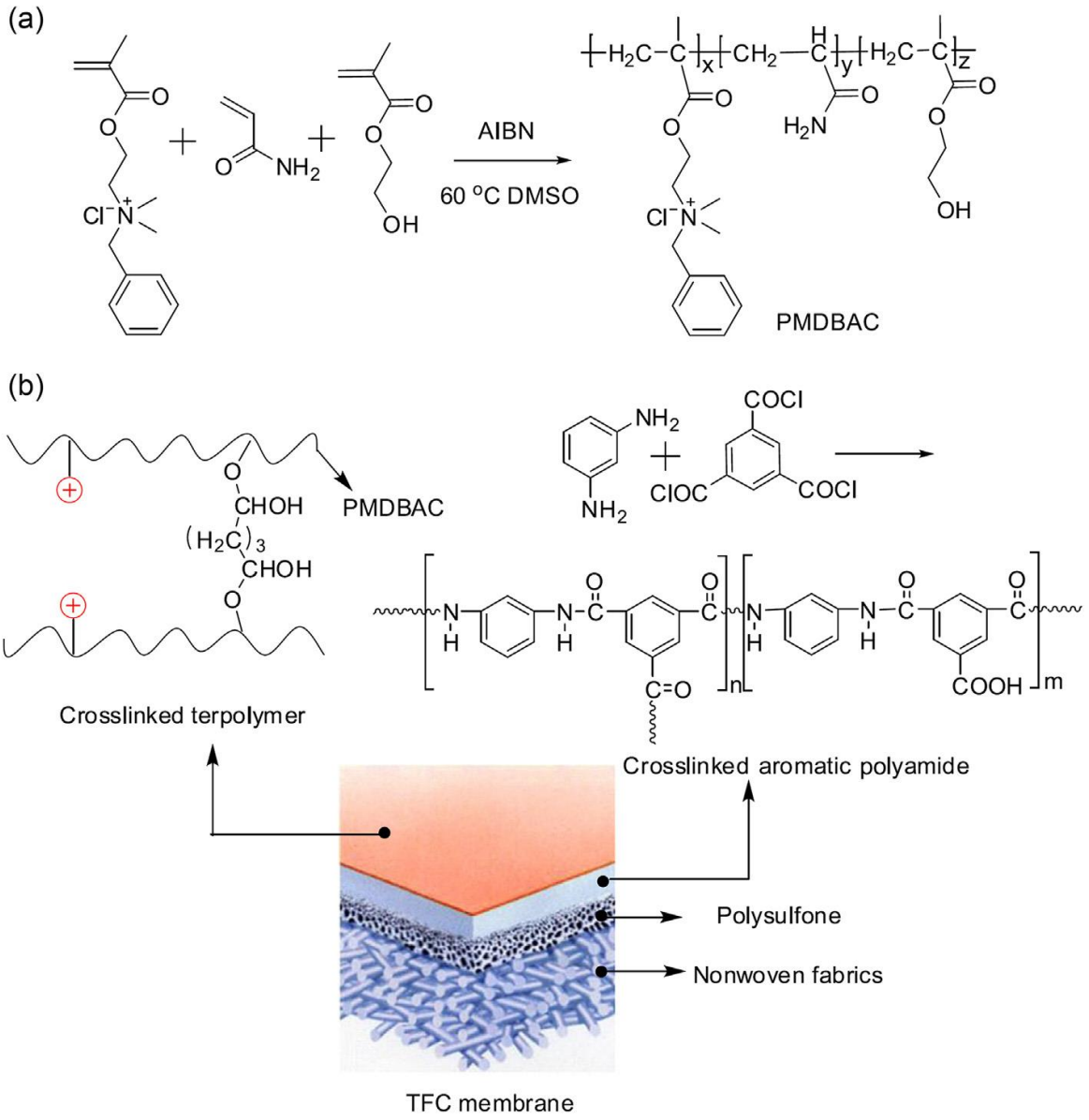

Figure 2.9. Schematic diagram for synthesis of the terpolymer P(MDBAC-r-Am-r-HEMA) (a) and surface modification of reverse osmosis (RO) membranes (b). Reprinted from Ni et al. [53], with permission from Elsevier.

Zwitterionic materials can bind water molecules more strongly than other hydrophilic materials via electrostatically induced hydration. Therefore, zwitterionic-based materials have been developed as promising candidates for preparation of antifouling surfaces [46]. In this sense, Azari and Zou [54] incorporated red-ox functional amino acid 3-(3,4-dihydroxyphenyl)-

L-alanine onto commercial PA TFC RO membranes to create a zwitterionic surface resistant to membrane fouling. It was found that the coated membranes exhibited remarkably improved hydrophilicity, which resulted in an increase of the membrane water permeability preserving the salt rejection factor.

For the purpose of improving the antifouling properties of RO membranes, Ishigami et al. [55] used the layer-by-layer (LbL) assembly to modify their surfaces by poly (sodium 4-styrenesulfate) (PSS) and poly(allylamine hydrochloride) forming a thin polyelectrolyte coating layer. This antifouling capability increased with increasing the number of layers due to the enhanced hydrophilicity and smoothness of the membrane surface. The obtained optimal layer number, based on the highest obtained water permeability when BSA was used as a foulant solute in water, was found to be four. It was concluded that LbL assembly on a membrane surface could reduce fouling not only by electrostatic repulsion between foulant and membrane surface, but also by electrostatic attraction due to the fact that the surface charge could be controlled by alternatively choosing the outer polyelectrolyte.

As was pointed out previously, chlorination is another trade-off for PA TFC RO membranes. Several researchers focused their studies to enhance chlorine tolerance of PA TFC RO membranes. For instance, Zhang et al. [56] modified a commercial TFC aromatic PA RO membrane (RE2521-TL, Woongjin Chemical Co., Ltd., Korea) via free-radical graft polymerization of 3-allyl-5,5-dimethylhydantoin (ADMH) followed by crosslinking by *N,N´*-methylenebis(acrylamide) (MBA). After graft polymerization, it was observed that the ADMH/MBA modified membrane was more hydrophilic, with higher salt rejection factors but lower permeate flux than the unmodified membrane. Recently, Ni et al. [53] synthesized a novel hydrophilic random terpolymer, poly(methylacryl-oxyethyldimethyl benzyl ammonium chloride-r-acryl-amide-r-2-hydroxyethyl methacrylate), via simple free-radical copolymerization using as a coating material a commercial PA TFC RO membranes (LCLE and BW30, DOW Chemical Co. Ltd., Minneapolis, USA) to improve their membrane antifouling performance and chlorine resistance (Fig. 2.9). This innovative membrane modification method was demonstrated to be an effective way to render the PA TFC RO membrane more hydrophilic with antimicrobial properties and more resistance to chlorine and fouling.

The introduction of NPs with multifunctionalities in RO TFC membranes could lead to another breakthrough in membrane desalination by further enhancing water permeability without scarifying the salt rejection factors [47]. Recently, a number of organic–inorganic TFC nanocomposite membranes containing NPs such as zeolite [57, 58], SiO_2 [59, 60], Ag [61], TiO_2 [62], ZnO [63], organo-selenium compounds [64], and carbon nanotubes (CNTs) [65, 66] have been investigated for their potential use in RO applications. Hydrophilic polyether-block-polyamide copolymer solutions with different contents of Ag NPs were used to prepare dense

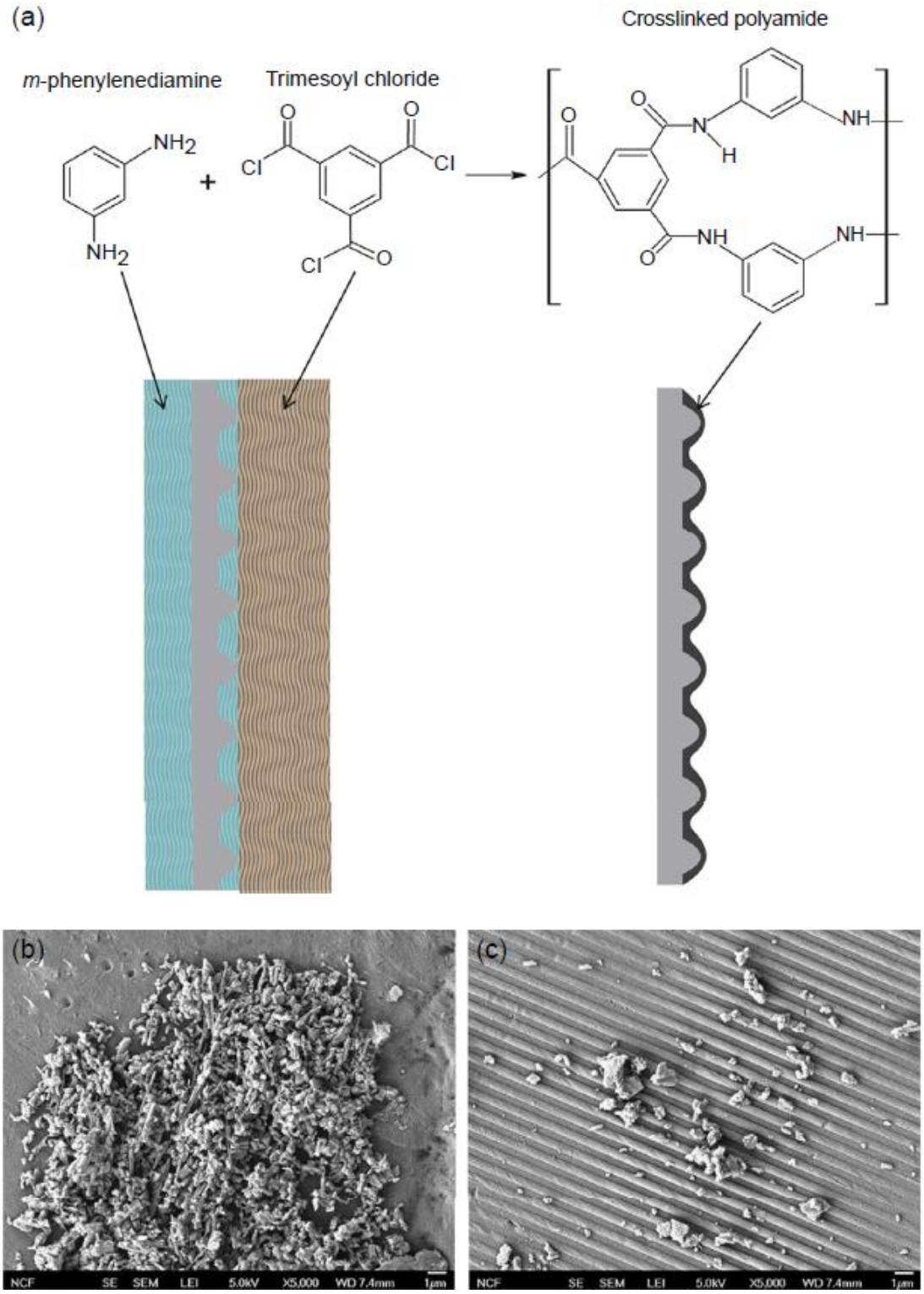

Figure 2.10. (a) Schematic diagram of the interfacial polymerization process used to fabricate the patterned thin film composite (TFC) membranes. The monomers *m*-phenylenediamine (MPD) and trymesoyl chloride (TMC) react to form a highly crosslinked polyamide (PA) layer at top of the patterned polyethersulfone (PES) ultrafiltration (UF) membrane used as a support. SEM images of the non-patterned (b) and patterned (c) TFC membrane surface after 24 h of $CaSO_4$ filtration experiment. Reprinted from Maruf et al. [67], with permission from Elsevier.

films and coating layers to improve the biofouling resistance of commercial PSU UF membranes [61]. ZnO NPs in biocompatible poly(*N*-isopropylacrylamide) (PNIPAAm) hydrogel layers were used by Schwartz et al. [63] to prepare novel antimicrobial composite membranes via mixing the PNIPAAm pre-polymer with ZnO NPs, followed by spin-coating and photo-crosslinking. It was also found that these ZnO/hydrogel nanocomposite coated films exhibited differential toxicity between bacterial and cellular species, which qualified them as promising candidates for novel biomedical device coatings.

It must be pointed out that different types of zeolite NPs such as NaA zeolite [68], NaX zeolite [69] and A zeolite [70] have been added in PA active layer of TFC RO membranes to improve their RO performance.

Carboxy-functionalized MWCNTs were incorporated by Zhao et al. [66] in PA TFC RO membranes via IP of MPD and TMC to improve their RO performance. The developed nanocomposite membranes were more negatively charged than the MWCNTs-free PA membrane, and the increase of MWCNTs concentration in the membrane resulted in a higher permeate flux (50% higher) with almost the same solute rejection factor.

Surface topography modification of TFC RO membranes has been shown to be another potential approach for fouling mitigation. Functional TFC RO membrane with well-controlled surface patterns was reported by Maruf et al. [67]. As it shown in Fig. 2.10, this membrane fabrication procedure consisted on the formation of a dense PA layer via IP with TMC and MPD solutions on a nano-imprinted commercial PES UF support membrane (PW, GE Water and Infrastructure). The results showed that the patterned TFC membrane had a separation performance comparable to the current commercial TFC RO/NF membranes (i.e., commercial TFC RO membranes: XLE-440 (DOW Filmtec), CPA 3 (Hydranautics), ACM 2 (Trisep), TM-700 (Toray), and commercial TFC NF membranes: NF 270 (Hydranautics) and ES-10 (Nitto Denko). It is important to note that the surface patterns induced hydrodynamic secondary flow at the membrane-feed interface, which is an effective way to decrease concentration polarization and reduce scaling effects.

2.3 Vapor pressure gradient driven membrane processes

2.3.1 Membrane distillation

In contrast to the previous reported PDMPs (MF, UF, NF, and RO) technology, which is isothermal, membrane distillation (MD) is a non-isothermal separation process in which only molecules in the vapor phase are transported from the feed to the permeate through a porous hydrophobic membrane, being the driving force the transmembrane vapor pressure [71, 72]. Simultaneous heat and mass transfer occur in MD, and different MD configurations can be used

to establish the driving force. The difference between the MD configurations is localized only in the permeate side of the membrane module. In direct contact MD (DCMD), sweeping gas MD (SGMD), and air gap MD (AGMD), the temperature difference induces the necessary vapor pressure difference. There is also another configuration termed vacuum MD (VMD), in which the permeate side of the membrane is kept at lower pressure by a vacuum pump to establish the transmembrane vapor pressure.

MD is applied in different fields (desalination, treatment of wastewaters containing non-volatile contaminants including radioactive wastes, recovery of valuable compounds, production of distilled and ultrapure water, food, medical, etc.). Compared to RO separation process, MD does not require the application of a high hydrostatic pressure (atmospheric pressure is enough), can process very high salinity brines including those generated by RO, and produce water with very high quality, which means almost total rejection factors of non-volatile contaminants. Moreover, MD can be combined with other processes in integrated systems such as MF, UF, NF, RO, and forward osmosis among others, making MD promising for various industrial applications [72]. However, MD technology also suffers some drawbacks such as the low membrane permeability, low thermal efficiency, high water production cost, temperature and concentration polarization effects, risk of membrane pore wetting, fouling, and scaling phenomena [71, 72].

MD membranes are porous with a high porosity (void volume fractions), low pore tortuosity, low thermal conductivity, and hydrophobic. More details of the membrane requirements for an effective MD application were outlined by Khayet [73]. The most common used techniques for preparation of MD membranes are phase inversion, stretching, track-etching, sintering, dry/wet spinning or wet spinning, electrospinning, or membrane surface modification by physical or chemical techniques such as coating, grafting, and plasma polymerization. Most of the MD membranes are made via phase inversion methods because of its simplicity.

Some authors focused their MD membrane engineering toward the preparation of dual-layered membranes. Wang et al. [74] investigated the morphological architecture of dual-layer PVDF hollow fiber membranes consisting of a fully finger-like macrovoid inner-layer and a totally sponge-like outer-layer. Edwie and Chung [75] also designed novel hollow fiber membranes with improved wetting resistances for desalination and salt recovery from highly concentrated NaCl aqueous solution by DCMD and crystallization. Three types of hollow fiber membranes were fabricated, single-layer PVDF, dual-layer hydrophobic–hydrophobic PVDF, and dual-layer hydrophobic–hydrophilic PVDF/PAN membranes. The single-layer PVDF membrane had a superior wetting resistance compared to other types of dual-layer membranes, in addition to the smallest reduction of membrane permeability (17.7%) and the highest purity of product water (1.1–1.3 μS/cm).

Su et al. [76] performed experimental and theoretical studies to investigate the effect of the inner-layer thermal conductivity on the DCMD permeate flux of hydrophobic–hydrophilic dual-layer hollow fiber membranes prepared by dry/wet spinning technique. Graphite particles and MWCNTs were embedded in the inner hydrophilic layer (Fig. 2.11). It was found that incorporating graphite alone led to only a minor improvement of the thermal conductivity, but using both graphite and MWCNTs, the thermal conductivity was increased from 0.59 to 1.30 W/m K. This enhancement of the thermal conductivity was attributed to the network formed by the MWCNTs, which bridges the polymer nodules. As a consequence of the improved thermal conductivity of the inner-layer, a higher vapor pressure difference was established between both sides of the hydrophobic porous layer (see Fig. 2.11(b) and (c)), and therefore a significant increase of the DCMD permeate flux was observed from 41.2 to 66.9 kg/m^2 h when using an inlet feed temperature of 80.4°C.

Polytetrafluoroethylene (PTFE) is an attractive membrane material for MD due to its superior hydrophobicity, chemical resistance, thermal stability, and mechanical strength compared to PP and PVDF. It has also excellent stability in many organic and inorganic solvents. Teoh et al. [77] prepared PVDF/PTFE dual-layer composite hollow fiber membranes for seawater desalination by DCMD. The incorporation of PTFE particles in the PVDF spinning solution could efficiently suppress the formation of macrovoids and enhance the outer surface hydrophobicity of the membranes. Recently, Zhu et al. [78] also used PTFE for the preparation of novel PTFE hydrophobic hollow fiber membranes for VMD by a cold pressing method including extrusion, stretching, and sintering. It was observed that the PTFE hollow fiber membranes with four stretching ratios (120%, 160%, 180%, and 220%) showed microstructures of nodes interconnected by fibrils (Fig. 2.12) and achieved salt rejection factors of 99.9%. The increase of the stretching ratio significantly increased the pore size and porosity and therefore improved the permeate flux, but decreased the water entry pressure in the pores and reduced the mechanical property of the membrane.

It is well known that ceramic membranes exhibit excellent chemical, structural, and thermal stabilities. Therefore, it would be interesting to explore this type of membranes in MD applications. Fang et al. [79] developed a novel hydrophobic porous alumina ceramic hollow fiber membrane by phase inversion and sintering method for desalination by VMD process. When using a feed salt aqueous solution (4 wt% NaCl) at 80°C and a vacuum pressure of 4 kPa applied in the lumen side of the hollow fibers, a water permeate flux as high as 42.9 L/m^2 h was achieved, with a salt rejection factor over 99.5%, which was comparable to polymeric membranes.

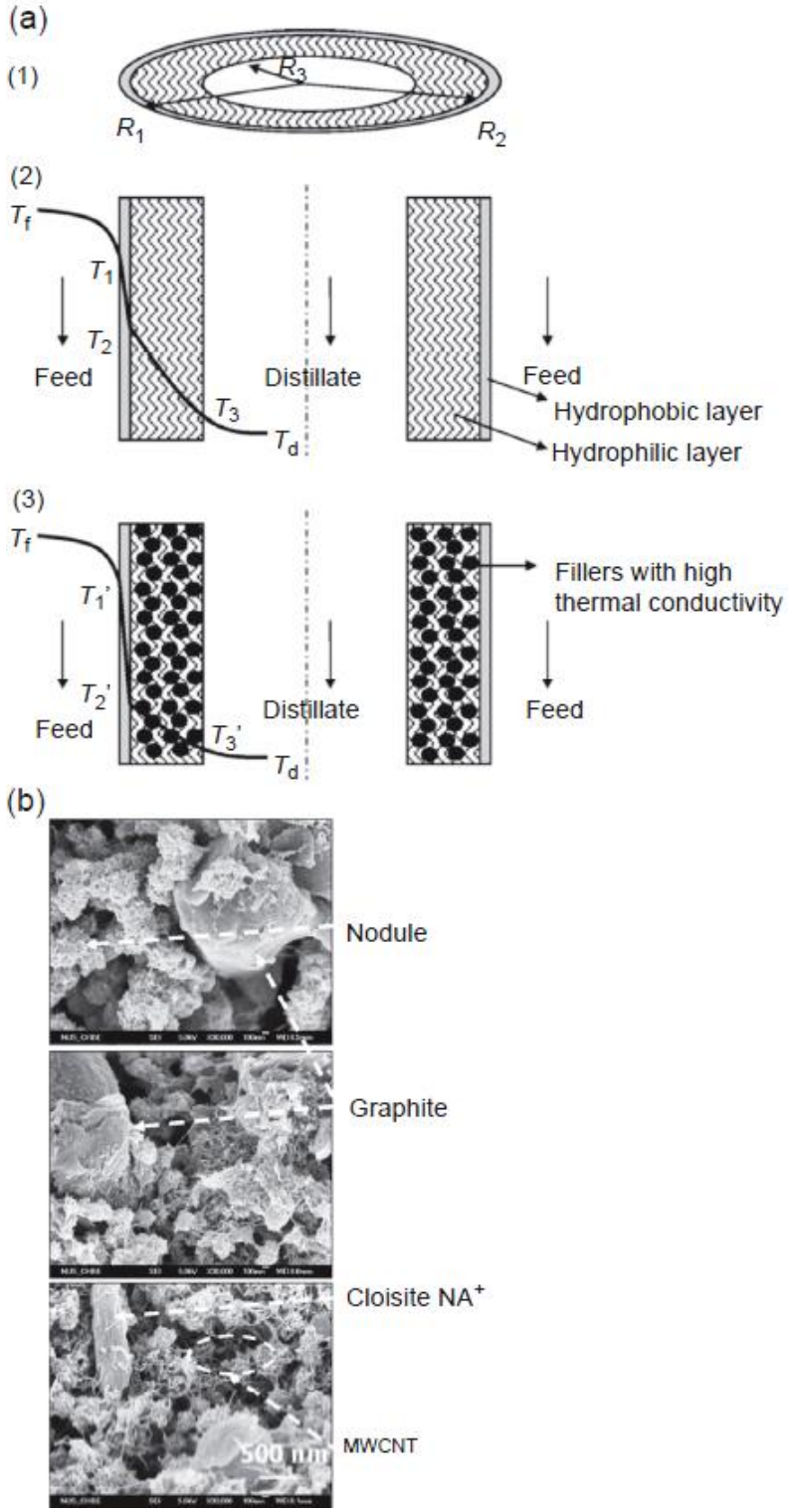

Figure 2.11. (a) Schematic dual-layer hydrophobic/hydrophilic hollow fiber membranes: (1) Cross-section of dual-layer hollow fiber membranes, (2) temperature distribution across dual-layer hydrophobic/hydrophilic membranes, and (3) temperature distribution across dual-layer hydrophobic/hydrophilic membranes filled with high thermal conductivity fillers blended into the inner-layer. (b) SEM images of the inner-layer filled with graphite, Cloisite NA^+ and MWCNTs. Reprinted from Su et al. [76], with permission from Elsevier.

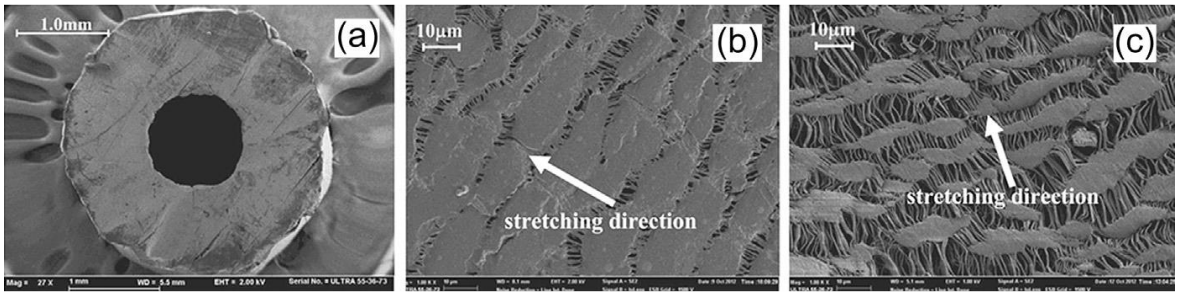

Figure 2.12. SEM images of the polytetrafluoroethylene (PTFE) hollow fiber membrane prepared by a stretching ratio of 220%: (a) X27 cross-section, (b) X1000 inner-surface, and (c) X1000 outer-surface. Reprinted from Zhu et al. [78], with permission from Elsevier.

Yang et al. [80] proposed plasma or chemical modification of the surface of PVDF hollow fiber-based membranes. The plasma coating involved a surface activation by exposing the membrane to a continuous plasma and a polymerization with the vapor of activated monomer. On the other hand, the chemical modification involved the hydroxylation of the PVDF membrane by an aqueous lithium hydroxide solution and successive reduction with an organic sodium borohydride ($NaBH_4$) solution followed by crosslinking with a perfluoro-compound of perfluoropolyether containing ethoxysilane terminal groups. Compared to the unmodified PVDF hollow fiber membrane, both modified membranes showed a greater hydrophobicity, higher liquid entry pressure (*LEP*) values, better mechanical strengths, smaller maximum pore sizes, and narrower pore size distributions with reasonably high DCMD permeate fluxes over a long-term operation (one month) as well as a high water quality. Wei et al. [81] also used plasma surface modification approach to develop suitable membranes for MD. The surface of asymmetric hydrophilic PES flat sheet and hollow fiber membranes were modified by CF_4 plasma polymerization to form a hydrophobic layer with a water contact angle up to 120°. DCMD results proved that these plasma-modified PES membranes were good membranes for MD, with high water permeate fluxes up to 66.7 kg/m^2 h using 4 wt% NaCl as feed aqueous solution, and the salt rejection factors were as high as 99.97%. A comparative compilation of DCMD performance for different novel hollow fiber membranes is summarized in Table 2.3.

Novel and emerging flat sheet membranes were also developed for MD. Khayet et al. [82] proposed for the first time the use of double-layered porous hydrophobic/hydrophilic composite membranes for DCMD using fluorinated surface modifying macromolecules (SMMs) and the phase inversion method. This promising type of membrane exhibited a thin hydrophobic layer of about 10 μm, higher permeate flux than the commonly used commercial membranes, and very high salt rejection factors. Then a series of studies were performed using different types of SMMs and hydrophilic host polymers, such as PES and PSU [72, 83-87]. Recently, Khayet [84] used this type of membrane in nuclear technology for the treatment of low and intermediate-level radioactive liquid wastes.

Table 2.3. DCMD performance of different single and dual layer hollow fiber membranes fabricated in the literature.

Membrane	Thickness (μm)	Hollow fiber porosity (%)	Mean pore size (μm)	Feed parameters			Distillate parameters		DCMD flux (kg/m² h)	Ref
				Solution	Inlet temperature (°C)	Flow rate (m/s)	Inlet temperature (°C)	Flow rate (m/s)		
Accurel PP S6/2[a]	400	73.0	0.22	Concentrated tap water	90	0.96	20	0.29	34.0	[88]
PVDF single-layer HF[b]	140	86.0	0.16	3.5 wt.% NaCl	79.5	1.9	17.5	0.9	46.1	[89]
PVDF single-layer HF	180	86.7	-	3.5 wt.% NaCl	81.3	1.8	17.5	1.2	79.2	[90]
PVDF single-layer HF	275	83.0	0.145	3.5 wt.% NaCl	70	-	25	-	54.0	[80]
PVDF single-layer HF	127.5	69.6	0.23[c]	3.5 wt.% NaCl	80	0.7	17	0.7	35.1	[75]
PVDF single-layer HF	130	79.7	0.28	3.5 wt.% NaCl	81.8	0.5	20	0.15	40.5	[91]
PVDF single-layer HF	180	71.9	0.28	3.5 wt.% NaCl	80.0		20	0.04	27.5	[92]
PVDF single-layer HF	120	80.0	0.44	3.5 wt.% NaCl	79.9	1.6	19.4	0.8	54.3	[93]
PVDF single-layer HF	230	83.4	0.32	Distillate water	70	-	25	-	22.0	[94]
Si_3N_4 single-layer HF	-	50	0.74	4 wt.% NaCl	80	-	20	-	10.8	[95]
PES single-layer HF	210	79.0	<0.07	4 wt.% NaCl	73.8	2	20	0.68	66.7	[81]
PVDF/PAN dual-layer HF	340	80.0	0.41	3.5 wt.% NaCl	78.2	1.6	16.6	0.8	37.4	[96]
PVDF/PAN dual-layer HF	271	70.0	0.41	3.5 wt.% NaCl	80.4	1.8	15.3	0.7	66.9	[76]
PVDF/PAN dual-layer HF	153	75.4	0.47[c]	3.5 wt.% NaCl	80	1.4	17	0.7	83.4	[97]
PVDF/PTFE dual-layer HF	141	84.0	-	3.5 wt.% NaCl	79.8	1.4	17	0.7	98.6	[74]
PVDF/PTFE dual-layer HF	145	82.5	0.26[c]	3.5 wt.% NaCl	80	1.9	17.5	0.9	50.9	[77]

[a]Accurel PP S6/2: Commercial membrane from GmbH, Germany; [b]HF = hollow fiber; [c]Maximal pore size, others are mean pore size.

Dumée et al. [98] explored the possibility of developing novel self-supporting CNT Bucky-Paper (BP) membranes via vacuum filtration for DCMD desalination. CNTs have exceptional mechanical, electrical, and thermal properties. It was reported that the CNT-BP membranes exhibited a high water contact angle (113°), a high porosity (90%), and relatively low thermal conductivity (i.e., 2.7 kW/m^2 h). However, a decline of the DCMD permeate flux and delamination of BP membranes due to the formation of micro-cracks were observed. To optimize this type of BP membrane, Dumée et al. [99] developed novel CNT-BP-based composite and supported membranes with significantly improved MD performance. Furthermore, the same researchers also coated the CNT-BP membranes with a thin layer of PTFE to enhance their hydrophobicity and improve their mechanical stability without drastically changing their average pore size and porosity [100].

Various studies have been focused on the preparation of more hydrophobic membranes for MD to reduce the risk of pore wetting. A variety of techniques such as plasma treatment, lithography, sol-gel technology, NP deposition on both smooth and rough substrates, fluoroalkylsilane coatings, and phase separation of a multicomponent mixture were considered for fabrication of superhydrophobic surfaces (i.e., water contact angles higher than 150°). Razmjou et al. [101] prepared a superhydrophobic PVDF membrane for MD applications with a 163° water contact angle, by generating a hieralchical structure with multilevel roughness and reducing the surface free energy of the membranes via TiO_2 coating through a low-temperature hydrothermal process followed by fluorosilanization of the surface with 1H, 1H, 2H, 2H-perfluorododecyltrichlorosilane (FTCS) (Fig. 2.13). The multilevel hierarchical structure was attributed to the templating agent, which was found to be decisive in the final wettability of the membrane surface. Moreover, TiO_2 coating layer on the membrane provided sites for covalent bonding with hydrolyzed silane coupling agents. The modified FTCS–TiO_2–PVDF membranes showed good thermal and mechanical resistance, while both the *LEP* and water contact angle of the membrane were increased.

During last five years, novel flat sheet nanofibrous membranes prepared by electrospinning were proposed for MD because of their attractive characteristics for MD, such as the high void volume fraction, high hydrophobicity, high roughness, high surface-to-mass (volume) ratio, interconnected open space between nanofibers, low thermal conductivity, etc. [102]. Self-sustained electrospun nanofibrous membranes (ENMs) were prepared varying the PVDF concentrations in the solvent mixture acetone (Ac)/*N,N*-dimethylacetamide from 15 to 30 wt% and the electrospinning time [103, 104]. The optimum PVDF concentration and electrospinning time for ENM formation was found to be 25 wt% and 2 h, respectively. This ENM exhibited a DCMD permeate flux of 12.15×10^{-3} kg/m^2 s, and the NaCl rejection factor was higher than 99.99%. The permeate flux of the ENMs was lower for longer electrospinning time. Essalhi and

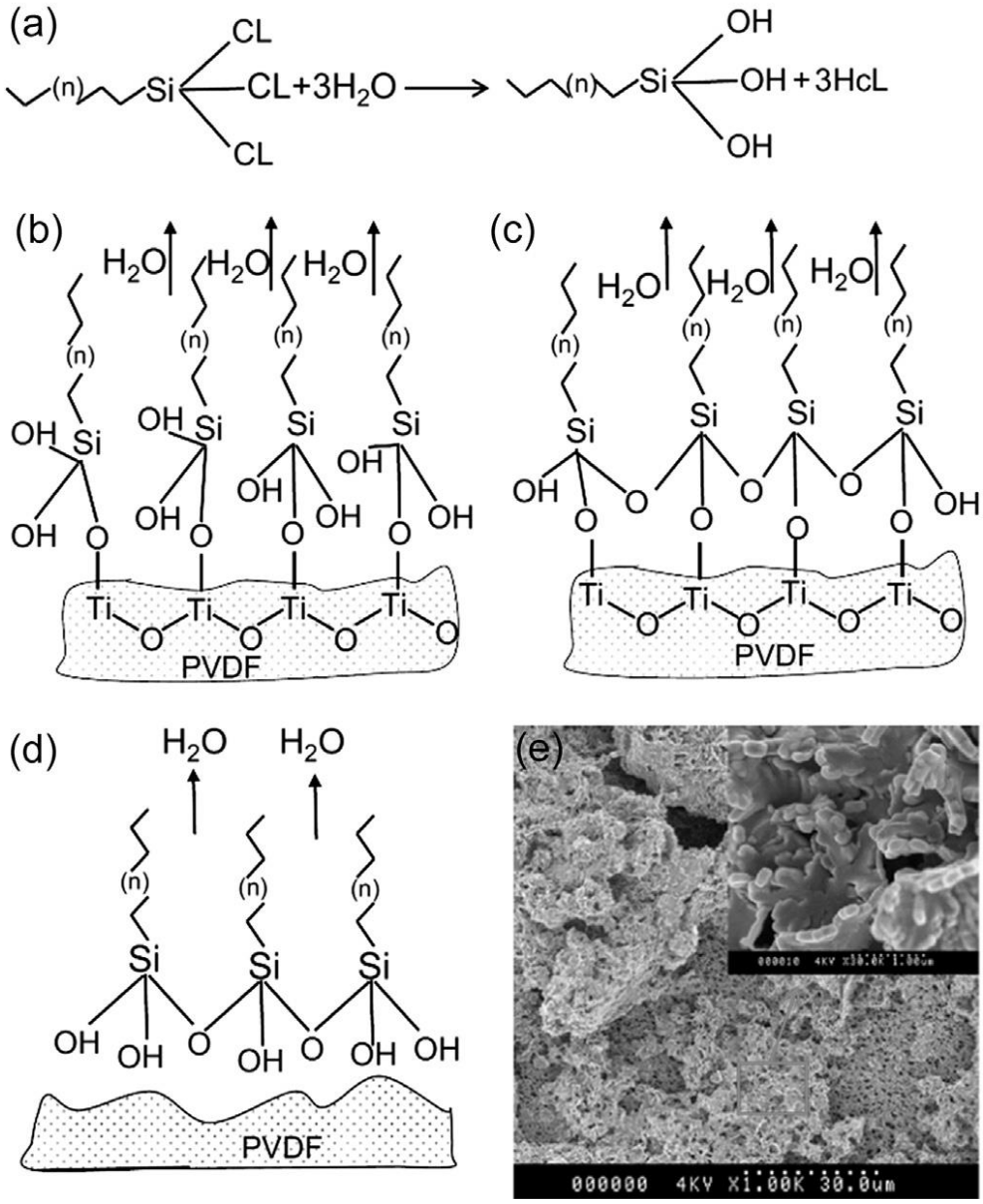

Figure 2.13. Mechanism for the fluorosilanization on the surface of polyvinylidene fluoride (PVDF) membranes with and without TiO_2. (a) Hydrolyzation of 1H, 1H, 2H, 2H-perfluorododecyltrichlorosilane (FTCS), (b) interaction of the hydroxyl groups with the surface of TiO_2 can form covalent bonds of Si–O–Ti, (c) the intermolecular crosslinking between the tri-silanols can lead to a 2D network of polysiloxane, (d) condensation of tri-silanols in the solution in absence of TiO_2 coating, and (e) surface SEM image of FTCS–PVDF membrane. Reprinted from Razmjou et al. [101], with permission from Elsevier.

Khayet [105] developed a novel theoretical model that considered the gas transport mechanisms through the inter-fiber space of ENMs to predict the DCMD permeate flux of ENMs.

Maab et al. [106] used both the phase inversion technique and the electrospinnig method to prepare a novel flat sheet porous membrane for MD based on hydrophobic synthesized aromatic fluorinated polyoxadiazoles and polytriazoles. By combining the high polymer

hydrophobicity (i.e., 162° water contact angle), the high void volume fraction, and the *LEP* of about 0.9 bar, the salt rejection factors of these membranes were as high as 99.95%, and the water permeate fluxes were as high as 85 L/m^2 h for a feed temperature of 80°C and a permeate temperature of 22°C. Similarly, Prince et al. [107] developed novel ENMs consisting of PVDF blended with clay nanocomposite for DCMD. An increase of the surface hydrophobicity with the addition of clay nanocomposite was also observed, and the prepared PVDF-clay ENMs showed good DCMD performance.

Lalia et al. [108] also prepared ENMs for MD using the copolymer polyvinylidene fluoride-co-hexafluoropropylene (PVDF-HFP). To fuse the fibers together and enhance the ENMs structural integrity with the mechanical properties, the ENMs were hot pressed. Among all prepared ENMs, the one fabricated with 10 wt% PVDF-HFP in the electrospinning solution had the optimum properties for MD application with 0.26 μm mean pore size, 58% porosity, 125° water contact angle, and a *LEP* value of 131.7 kPa.

To further improve the hydrophobicity of the PVDF ENMs used in MD, the electrospinning technique was followed by surface modification [109]. As shown in Fig. 2.14, this procedure included PDA surface activation to improve the adhesive force between the fibers and Ag NPs, Ag NP deposition to optimize the morphology and roughness of the membrane, and hydrophobic treatment with 1-dodecanethiol. Compared to the unmodified ENM, the integrally-modified membrane could achieve a stable MD permeate flux of 31.6 L/m^2 h using a 3.5 wt% NaCl feed aqueous solution at 60°C and permeate temperature of 20°C.

To enhance the MD performance of the ENMs, Prince et al. [110] prepared PVDF ENM on a porous PVDF supported membrane fabricated by the immersion precipitation method and used it for desalination by AGMD configuration. The addition of the nanofiber layer on the PVDF supported membrane was found to increase the permeate flux, the salt rejection factor, and the AGMD long-term performance.

2.3.2 Pervaporation

PV is a membrane process in which an organic solvent/water mixture or an organic solvent mixture can be selectively separated by a dense membrane placed between the liquid feed mixture and a downstream permeate maintained by a vacuum pump. PV technology is similar to VMD, the difference being the characteristics of the membrane used, which is porous and hydrophobic for VMD. There is also a similarity between PV and SGMD when PV is carried out by gas stripping. Both a solution diffusion model and a pore flow model were considered in PV, in which the phase change of the diffused species takes place inside the membrane, and the desorption step occurs at the permeate side of the membrane. There are mainly two PV applications, those involving hydrophilic membranes used for the dehydration of organic/water

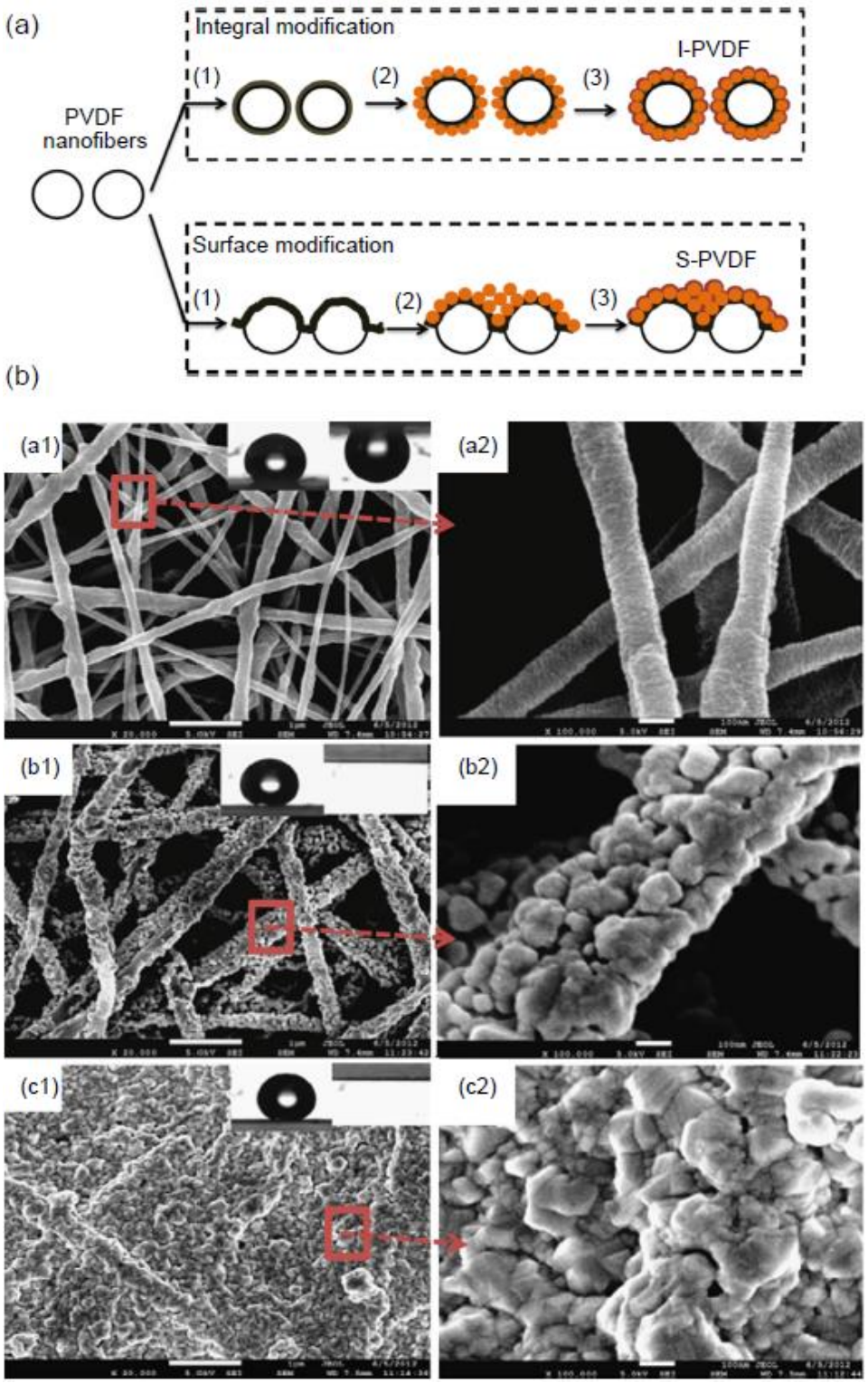

Figure 2.14. (a) Schematic method used for preparation of superhydrophobic polyvinylidene fluoride electrospun nanofibrous membranes (PVDF ENMs) ((1) PDA-modification; (2) silver nanoparticle coating; (3) 1-dodecanethiol hydrophobic modification). (b) SEM images of un-modified PVDF ENMs ((a1), (a2)), integral modified PVDF ENMs (I-PVDF (b1), (b2)), and surface modified PVDF ENMs (S-PVDF (c1), (c2)). Reprinted from Liao et al. [109], with permission from Elsevier.

mixtures such as PVA and NaA zeolite membranes [111], and those involving hydrophobic membranes used to extract organic solvents or volatile organic compounds from water such as polydimethylsiloxane (PDMS) and silicalite-1 membranes [111].

Zuo et al. [112] developed high-performance hollow fiber membranes for PV dehydration of isopropanol (IPA) consisting of a TFC PA selective layer and a porous Torlon® 4000T-MV PAI (Solvay Advanced Polymers) substrate prepared via IP of MPD or HPEI with TMC. The TFC membrane prepared from HPEI showed a higher hydrophilicity and fractional free volume than that made from MPD, which exhibited a better permeability. The TFC membrane fabricated under the optimum IP conditions from HPEI having a molecular weight of 2 kg/mol showed the best selectivity (i.e., 624), with a total permeate flux of 1.3 kg/m^2 h and a permeate water concentration of 99.1 wt% using a feed composition of 85/15 wt% IPA/water at 50°C.

Wang et al. [113] developed high-performance dual-layer polybenzimidazole (PBI)/PEI hollow fiber membranes for ethylene glycol dehydration by PV process. Three types of membranes were prepared: PBI flat sheet dense membranes, which had the lowest PV separation performance due to its severe swelling; PBI single-layer hollow fiber membranes, which showed better PV separation performance, but had very low tensile strains; and PBI/PEI dual-layer hollow fiber membranes, which exhibited the best PV separation performance. An enhancement of the separation performance of PBI/PEI dual-layer hollow fiber membrane after exposing it to 75°C thermal treatment was also detected. A novel approach to prepare multilayered membranes with excellent PV dehydration of different solvent/water mixtures has been performed by Zhang et al. [114]. This approach is based on a dynamic pressure-driven LbL technique to obtain a covalent assembly of GLA-crosslinked PEI multilayers on the inner surfaces of PAN hollow fiber porous substrate membranes. The dynamic pressure-driven LbL assembly was demonstrated to be an effective way to fabricate a defect-free selective layer only on a single side of the hollow fiber, which has the advantage of reducing the membrane transport resistance compared to the membranes made with traditional LbL process. Zhang et al. [115] prepared novel polyacrylic acid (PAA)/PEI multilayer polyelectrolyte complex (PEC) films on the inner side of hydrolyzed PAN hollow fiber membranes by the dynamic negative pressure LbL technique. Others papers also proposed an electric field enhanced method to fabricate multilayered PEC membranes by using modified PA RO membranes as supports, and poly(diallyl dimethylammoniumchloride) (PDDA), PEI, PSS, PAA as assembly components [116-119]. Zhao et al. [120] used charged PEC colloidal aggregates as novel LbL building blocks to prepare LbL multilayered membranes for PV dehydration.

As mentioned previously, the hydrophilicity of the PV membrane is necessary for the dehydration of organic solvents. The more hydrophilic the membrane is, the higher are the water sorption selectivity and water permselectivity. To improve the membrane hydrophilicity,

many polymer materials were modified using different methods, such as sulfonation, quaternization, grafting, etc. However, an increase of the membrane hydrophilicity might increase the membrane swelling excessively, leading to a membrane with an open structure, which reduces the membrane strength. Crosslinking with an organic chemical reagent, such as GA, PAA, maleic acid, formaldehyde, or fumaric acid is an effective way to reduce membrane swelling. Zhang et al. [121] synthesized quaternized PVA by grafting with (2,3-epoxypropyl) trimethylammonium chloride, to enhance the hydrophilicity, and then crosslinked by GLA to restrict its swelling in an aqueous ethanol solution. Rachipudi et al. [122] also developed PV membranes for IPA dehydration by crosslinking sulfonated-PVA membranes with sulfophthalic acid (SPTA). The membrane prepared with 15 wt% of SPTA showed the highest water separation selectivity of 3452 with a total permeate flux of 3.51×10^{-2} kg/m^2 h.

Novel chitosan (CS)/TiO_2 nanocomposite membranes were prepared by Yang et al. [123] using an in situ sol-gel process using tetrabutyl titanate as precursor and acetyl acetone as chelating agent controlling the forming rate of TiO_2 NPs. Compared to CS and CS/TiO_2 blended membranes, CS/TiO_2 nanocomposite membranes exhibited better PV performance for ethanol dehydration. CS-wrapped MWCNTs incorporated in sodium alginate membranes were prepared by Sajjan et al. [124] for the separation of water/IPA mixtures. CS was chosen to wrap MWCNTs to improve their hydrophilicity. The PV membranes containing the highest amount of CS-wrapped MWCNTs (2 wt%) showed a water selectivity of 6419 and a permeate flux of 21.76×10^{-2} kg/m^2 h at 30°C and 10 wt% of water in the feed solution.

UV/O_3 surface modification technology was used by Lai et al. [125] to develop PDMS PV membranes for the treatment of 90 wt% aqueous ethanol mixture. Water contact angle measurements demonstrated that the hydrophilicity of PDMS membranes surface was significantly improved due to the change in its chemical structure from siloxane to silica. PV results indicated that both the treatment time and the working distance during the UV/O_3 treatment were important variables affecting the PV performance of the PDMS membrane.

To improve the PV permeate flux of polymeric membranes, Xiangli et al. [126] prepared PDMS/ceramic composite membrane by depositing uniformly a crosslinked PDMS layer on the top of tubular non-symmetric ZrO_2/Al_2O_3 porous ceramic supports. The resulted PDMS/ceramic composite membranes exhibited a total permeate flux of 19.5 kg/m^2 h and an ethanol selectivity of 5.7 when using a 4.3 wt% ethanol feed aqueous mixture. Liu et al. [127] used these PDMS/ceramic composite membrane for butanol removal from its dilute aqueous solution and obtained a total permeate flux of 0.457 kg/m^2 h with an acceptable butanol selectivity of 26.1 using a 1 wt% butanol in the feed solution at 40°C. Because of the good long-term stability of these PDMS/ceramic composite membranes, Liu et al. [128] decided to use them for recovering biobutanol from biomass acetone-butanol-ethanol (ABE) fermentation broth exhibiting a high average total flux of 0.670 kg/m^2 h and an applicable ABE selectivity of

16.7. The performance of PDMS/ceramic composite PV membranes was improved by a homogeneous dispersion of ZSM-5 zeolite in PDMS via a surface graft/coating approach [129]. Lue et al. [130] also prepared a heterogeneous PDMS MMMs containing 10 μm sized zeolite (TZP-9023, Tricate Zeolites, Bitterfeld, Germany) for PV of ethanol/water solutions.

Zhu et al. [131] synthesized hydrophilic crosslinked PVA/CS layers on tubular asymmetric ZrO_2/Al_2O_3 ceramic supports and demonstrated that these ceramic-supported PVA/CS composite membranes were suitable candidates for PV dehydration of alcohol/water and ester/water mixtures. The composite membrane exhibited excellent PV performance, achieving a permeate flux of 1.25 kg/m^2 h and a water selectivity larger than 10,000 for 3.5 wt% ethyl acetate/water mixture.

To achieve higher membrane stability and improve the PV performance, various attempts have been made to develop blend membranes of PVA with other polymers. Mixed matrix blend membranes of PVA/PVP loaded with phosphomolybdic acid (PMA) were prepared for ethanol dehydration by Magalad et al. [132]. It was demonstrated that the extent of PMA loaded in the membrane affected the PV performance. 4 wt% of PMA particles in PVA/PVP blended matrix resulted in an enhancement of the PV performance, but higher PMA amounts (8 and 12 wt%) did not result in any improvement of PV performance.

It is worth mentioning that there are few research studies on homogeneous polyelectrolyte complex membranes (HPECMs), although these membranes exhibit good PV performance for dehydration of different organic aqueous solutions containing IPA, ethanol, Ac, etc. The required PECs to prepare HPECMs were synthesized by PAA, sodium carboxymethyl cellulose (CMCNa) as anionic polyelectrolyte, and PDDA, CS, poly(2-methacryloyloxy ethyl trimethylammonium chloride) (PDMC), and poly(*N*-ethyl-4-vinylpyridiniumbromide) (PEVP) as cationic polyelectrolyte. For example, the PECs were first synthesized in aqueous hydrochloric acid. Then, the obtained solid PECs were dissolved in aqueous NaOH, and subsequently the HPECMs were made by casting the solution on a clean and smooth porous PSU UF membrane. All the fabricated HPECMs from CMCNa–PDDA PECs [133, 134], PAA–PDDA PECs [135], CMCNa–CS PECs [136], CMCNa–PDMC [137], and CMCNa–PEVP [138] were used in PV dehydration of aqueous IPA or ethanol solutions and showed very high water selectivity and high permeability (see Table 2.4). Attempts were also made to improve the mechanical properties of the HPECMs by modification using inorganic SiO_2 [139] and MWCNTs [140], but even under the optimal membrane fabrication conditions the elongations at break were maintained low, whereas the tensile strengths increased. In addition, CMCNa–PDDA PEC [141], PDDA–PAANa PEC [142], and CMCNa–PDMC PEC [143] were blended with the commercial PVA to increase both the mechanical properties and the PV performance of the HPECMs. It was found that the PEC/PVA blended membrane with PVA content of 30 wt% (PEC/PVA70-30) achieved the best mechanical properties with a tensile strength, Young's

modulus, and elongation at break of about 1.5, 3.6, and 1.4 times those of the original HPECM, respectively.

Table 2.4. Pervaporation performance of various polyelectrolyte membranes (PECMs) for dehydration of isopropanol (IPA) and ethanol (EtOH) at 70°C.

Membrane	Feed solution	Water selectivity	Permeation flux (kg/m² h)	Ref
CMCNa-PDDA HPECM5.5	10 wt.% water-IPA	960	2.47	[133]
CMCNa-PDDA HPECM2.6	10 wt.% water-IPA	1791	1.92	[133]
CMCNa-PDDA HPECM0.19	10 wt.% water-IPA	1049	2.47	[134]
CMCNa-PDDA TPECM	10 wt.% water-IPA	148.4	1.49	[134]
PDMC-CMCNa PECM0.46	10 wt.% water-IPA	1641	4.25	[137]
PDMC-CMCNa PECM0.36	10 wt.% water-IPA	1641	3.85	[137]
CMCNa-PDDA/5 wt.% SiO_2	10 wt.% water-IPA	2186	2.1	[139]
CMCNa-PDDA/5 wt.% MWCNTs	10 wt.% water-IPA	2565	2.35	[140]
PDDA-PAANa/30 wt.% PVA	10 wt.% water-IPA	978	2.36	[142]
CMCNa-PDMC/30 wt.% PVA	10 wt.% water-IPA	2084	2.12	[143]
CS-CMCNa HPECM0.39	10 wt.% water-IPA	1657	2.17	[135]
PERVAP 2510[a]	10 wt.% water-IPA	810	0.75	[144]
CMCNa-PDDA TPECM	10 wt.% water-EtOH	188	0.49	[136]
CS-CMCNa HPECM0.025	10 wt.% water-EtOH	1062	1.14	[136]
PECM0.284	10 wt.% water-EtOH	1419	0.93	[138]
PECM0.440	10 wt.% water-EtOH	782	1.32	[138]

[a]PERVAP 2510: commercial membrane from Sulzer Chemtech GmbH, Linden, Germany.

2.4 Conclusions

The growth of membrane science and technology for water treatment is mainly due to the developments of materials used for membrane fabrication and for their modification. A wide variety of innovative materials such as chemically and thermally stable polymers, ceramics, metallics, etc., are used for preparing novel membranes of different configurations and characteristics. Moreover, various membrane fabrication techniques are being proposed and improved (i.e., phase inversion, sintering, stretching, track-etching, dry/wet spinning or wet spinning, electrospinning, LbL assembly, lithography, sol-gel, etc.), and various methods have been developed for membrane modification (i.e., IP, chemical modification, surface coating, grafting, crosslinking, plasma polimerization, polymer sulfonation or quaternization,

nanoparticles (NPs) deposition, etc.) to improve both the properties of the membranes and the performance of the specific processes and their applications.

It has been observed that the incorporation of different additives, polymers, and inorganic NPs or fillers (i.e., zeolite, organo-selenium compounds, SiO_2, Fe_3O_4, Al_2O_3, ZrO_2, TiO_2, ZnO, CNTs, MWCNTs, GO, TOCNs, β-CD, zwitterionic materials, etc.) on the MF, UF, NF, and RO membranes has improved their antifouling and antibacterial ability, has increased their hydrophilicity and water permeability preserving or improving the solute rejection factors, and in some cases has enhanced membrane mechanical properties, porosity, and thermal stability.

In contrast to PDMP technology, MD is a non-isothermal separation process, which uses porous hydrophobic membranes for water treatment. In general, there is a growing interest on MD membrane engineering. In particular, various researchers are developing composite hollow fiber membranes for MD with a dual-layered configuration (hydrophobic–hydrophobic or hydrophobic–hydrophilic) to reduce membrane pore wetting, temperature and concentration polarization effects, fouling, and scaling phenomena. The addition of different materials and NPs (i.e., graphite particles, PTFE, Al_2O_3, ZrO_2, TiO_2, ZnO, CNTs, MWCNTs, SMMs, etc.) resulted in greater membrane hydrophobicity and thermal conductivity, higher *LEP* values, water quality, and long-term operation, and also better mechanical strengths, permeate fluxes, and salt rejections.

High permeate fluxes and water selectivities were achieved when ceramic-supported composite membranes and HPECMs have been used for PV dehydration of organic alcohol/water and ester/water mixtures containing solvents such as IPA, ethanol, Ac, etc. Some attempts were made to improve the mechanical properties of HPECMs using inorganic SiO_2 and MWCNTs or blending their PEC with PVA.

2.5 Future trends

Although the current use of membrane technology for water treatment is constantly growing thanks to the discovery and development of novel and advanced materials for membrane fabrication and modification, there are still some involved phenomena with effects that need to be reduced further (e.g., temperature and concentration polarization phenomena, membrane fouling, long-term operation, etc.).

Innovative membrane engineering is required because of the still continuous increasing demands of desalination and treatments of different and emerging types of wastewaters with improved water production rates, greater salt rejection factors, and higher resistance to fouling.

PMDPs and MD technologies can be adequately integrated for water production offering a wide range of industrial water treatment applications.

References

[1] M.C. Porter, Handbook of Industrial Membrane Technology, Noyes Publications, Westwood, New Jersey, U.S.A., 1988.

[2] C. Dong, G. He, H. Li, R. Zhao, Y. Han, Y. Deng, Antifouling enhancement of poly(vinylidene fluoride) microfiltration membrane by adding $Mg(OH)_2$ nanoparticles, Journal of Membrane Science, 387-388 (2012) 40-47.

[3] H. Wu, B. Tang, P. Wu, Development of novel SiO_2–GO nanohybrid/polysulfone membrane with enhanced performance, Journal of Membrane Science, 451 (2014) 94-102.

[4] R. Wang, S. Guan, A. Sato, X. Wang, Z. Wang, R. Yang, B.S. Hsiao, B. Chu, Nanofibrous microfiltration membranes capable of removing bacteria, viruses and heavy metal ions, Journal of Membrane Science, 446 (2013) 376-382.

[5] L. Kong, D. Zhang, Z. Shao, B. Han, Y. Lv, K. Gao, X. Peng, Superior effect of TEMPO-oxidized cellulose nanofibrils (TOCNs) on the performance of cellulose triacetate (CTA) ultrafiltration membrane, Desalination, 332 (2014) 117-125.

[6] P. Wang, L. Luo, T.-S. Chung, Tri-bore ultra-filtration hollow fiber membranes with a novel triangle-shape outer geometry, Journal of Membrane Science, 452 (2014) 212-218.

[7] H. Wu, J. Mansouri, V. Chen, Silica nanoparticles as carriers of antifouling ligands for PVDF ultrafiltration membranes, Journal of Membrane Science, 433 (2013) 135-151.

[8] H. Yu, X. Zhang, Y. Zhang, J. Liu, H. Zhang, Development of a hydrophilic PES ultrafiltration membrane containing SiO_2@N-Halamine nanoparticles with both organic antifouling and antibacterial properties, Desalination, 326 (2013) 69-76.

[9] S. Zhang, R. Wang, S. Zhang, G. Li, Y. Zhang, Treatment of wastewater containing oil using phosphorylated silica nanotubes (PSNTs)/polyvinylidene fluoride (PVDF) composite membrane, Desalination, 332 (2014) 109-116.

[10] X. Li, R. Pang, J. Li, X. Sun, J. Shen, W. Han, L. Wang, In situ formation of Ag nanoparticles in PVDF ultrafiltration membrane to mitigate organic and bacterial fouling, Desalination, 324 (2013) 48-56.

[11] J.M. Arsuaga, A. Sotto, G. del Rosario, A. Martínez, S. Molina, S.B. Teli, J. de Abajo, Influence of the type, size, and distribution of metal oxide particles on the properties of nanocomposite ultrafiltration membranes, Journal of Membrane Science, 428 (2013) 131-141.

[12] G. Arthanareeswaran, P. Thanikaivelan, Fabrication of cellulose acetate–zirconia hybrid membranes for ultrafiltration applications: Performance, structure and fouling analysis, Separation and Purification Technology, 74 (2010) 230-235.

[13] R. Pang, X. Li, J. Li, Z. Lu, X. Sun, L. Wang, Preparation and characterization of ZrO_2/PES hybrid ultrafiltration membrane with uniform ZrO_2 nanoparticles, Desalination, 332 (2014) 60-66.

[14] N.A.A. Hamid, A.F. Ismail, T. Matsuura, A.W. Zularisam, W.J. Lau, E. Yuliwati, M.S. Abdullah, Morphological and separation performance study of polysulfone/titanium dioxide (PSF/TiO_2) ultrafiltration membranes for humic acid removal, Desalination, 273 (2011) 85-92.

[15] A. Razmjou, J. Mansouri, V. Chen, The effects of mechanical and chemical modification of TiO_2 nanoparticles on the surface chemistry, structure and fouling performance of PES ultrafiltration membranes, Journal of Membrane Science, 378 (2011) 73-84.

[16] A. Razmjou, A. Resosudarmo, R.L. Holmes, H. Li, J. Mansouri, V. Chen, The effect of modified TiO_2 nanoparticles on the polyethersulfone ultrafiltration hollow fiber membranes, Desalination, 287 (2012) 271-280.

[17] G. Zhang, S. Lu, L. Zhang, Q. Meng, C. Shen, J. Zhang, Novel polysulfone hybrid ultrafiltration membrane prepared with TiO_2-g-HEMA and its antifouling characteristics, Journal of Membrane Science, 436 (2013) 163-173.

[18] S. Zhao, P. Wang, C. Wang, X. Sun, L. Zhang, Thermostable PPESK/TiO_2 nanocomposite ultrafiltration membrane for high temperature condensed water treatment, Desalination, 299 (2012) 35-43.

[19] J. Hong, Y. He, Polyvinylidene fluoride ultrafiltration membrane blended with nano-ZnO particle for photo-catalysis self-cleaning, Desalination, 332 (2014) 67-75.

[20] C.P. Leo, N.H. Ahmad Kamil, M.U.M. Junaidi, S.N.M. Kamal, A.L. Ahmad, The potential of SAPO-44 zeolite filler in fouling mitigation of polysulfone ultrafiltration membrane, Separation and Purification Technology, 103 (2013) 84-91.

[21] A. Rahimpour, M. Jahanshahi, A. Mollahosseini, B. Rajaeian, Structural and performance properties of UV-assisted TiO_2 deposited nano-composite PVDF/SPES membranes, Desalination, 285 (2012) 31-38.

[22] H.J. Song, C.K. Kim, Fabrication and properties of ultrafiltration membranes composed of polysulfone and poly(1-vinylpyrrolidone) grafted silica nanoparticles, Journal of Membrane Science, 444 (2013) 318-326.

[23] S. Liang, K. Xiao, Y. Mo, X. Huang, A novel ZnO nanoparticle blended polyvinylidene fluoride membrane for anti-irreversible fouling, Journal of Membrane Science, 394-395 (2012) 184-192.

[24] A. Mehrparvar, A. Rahimpour, M. Jahanshahi, Modified ultrafiltration membranes for humic acid removal, Journal of the Taiwan Institute of Chemical Engineers, (2013).

[25] Z. Wang, H. Yu, J. Xia, F. Zhang, F. Li, Y. Xia, Y. Li, Novel GO-blended PVDF ultrafiltration membranes, Desalination, 299 (2012) 50-54.

[26] L. Yu, Y. Zhang, B. Zhang, J. Liu, H. Zhang, C. Song, Preparation and characterization of HPEI-GO/PES ultrafiltration membrane with antifouling and antibacterial properties, Journal of Membrane Science, 447 (2013) 452-462.

[27] N.N. Li, A.G. Fane, W.S.W. Ho, T. Matsuura, Advanced Membrane Technology and Applications, John Wiley & Sons, Inc., Hoboken, New Jersey, 2008.

[28] S.P. Sun, T.A. Hatton, S.Y. Chan, T.-S. Chung, Novel thin-film composite nanofiltration hollow fiber membranes with double repulsion for effective removal of emerging organic matters from water, Journal of Membrane Science, 401-402 (2012) 152-162.

[29] S.P. Nunes, K.V. Peinemann, Membrane Technology in the Chemical Industry, Wiley-VCH Verlag GmbH, Weinheim, 2001.

[30] S. Yu, Q. Cheng, C. Huang, J. Liu, X. Peng, M. Liu, C. Gao, Cellulose acetate hollow fiber nanofiltration membrane with improved permselectivity prepared through hydrolysis followed by carboxymethylation, Journal of Membrane Science, 434 (2013) 44-54.

[31] W. Fang, L. Shi, R. Wang, Interfacially polymerized composite nanofiltration hollow fiber membranes for low-pressure water softening, Journal of Membrane Science, 430 (2013) 129-139.

[32] X. Wei, X. Kong, C. Sun, J. Chen, Characterization and application of a thin-film composite nanofiltration hollow fiber membrane for dye desalination and concentration, Chemical Engineering Journal, 223 (2013) 172-182.

[33] Y. Zheng, G. Yao, Q. Cheng, S. Yu, M. Liu, C. Gao, Positively charged thin-film composite hollow fiber nanofiltration membrane for the removal of cationic dyes through submerged filtration, Desalination, 328 (2013) 42-50.

[34] S. Guan, S. Zhang, R. Han, B. Zhang, X. Jian, Preparation and properties of novel sulfonated copoly (phthalazinone biphenyl ether sulfone) composite nanofiltration membrane, Desalination, 318 (2013) 56-63.

[35] R. Han, Formation and characterization of (melamine–TMC) based thin film composite NF membranes for improved thermal and chlorine resistances, Journal of Membrane Science, 425-426 (2013) 176-181.

[36] E.-S. Kim, G. Hwang, M. Gamal El-Din, Y. Liu, Development of nanosilver and multi-walled carbon nanotubes thin-film nanocomposite membrane for enhanced water treatment, Journal of Membrane Science, 394-395 (2012) 37-48.

[37] H.R. Pant, H.J. Kim, M.K. Joshi, B. Pant, C.H. Park, J.I. Kim, K.S. Hui, C.S. Kim, One-step fabrication of multifunctional composite polyurethane spider-web-like nanofibrous membrane for water purification, Journal of Hazardous Materials, 264 (2013) 25-33.

[38] A. Mollahosseini, A. Rahimpour, Interfacially polymerized thin film nanofiltration membranes on TiO_2 coated polysulfone substrate, Journal of Industrial and Engineering Chemistry, 20 (2014) 1261-1268.

[39] H. Wu, B. Tang, P. Wu, Preparation and characterization of anti-fouling β-cyclodextrin/polyester thin film nanofiltration composite membrane, Journal of Membrane Science, 428 (2013) 301-308.

[40] S. Yu, Q. Zhou, S. Shuai, G. Yao, M. Ma, C. Gao, Thin-film composite nanofiltration membranes with improved acid stability prepared from naphthalene-1,3,6-trisulfonylchloride (NTSC) and trimesoyl chloride (TMC), Desalination, 315 (2013) 164-172.

[41] H. Wu, B. Tang, P. Wu, Optimization, characterization and nanofiltration properties test of MWNTs/polyester thin film nanocomposite membrane, Journal of Membrane Science, 428 (2013) 425-433.

[42] S. Zinadini, A.A. Zinatizadeh, M. Rahimi, V. Vatanpour, H. Zangeneh, Preparation of a novel antifouling mixed matrix PES membrane by embedding graphene oxide nanoplates, Journal of Membrane Science, 453 (2014) 292-301.

[43] C. Feng, J. Xu, M. Li, Y. Tang, C. Gao, Studies on a novel nanofiltration membrane prepared by cross-linking of polyethyleneimine on polyacrylonitrile substrate, Journal of Membrane Science, 451 (2014) 103-110.

[44] X. Li, R. Wang, F. Wicaksana, C. Tang, J. Torres, A.G. Fane, Preparation of high performance nanofiltration (NF) membranes incorporated with aquaporin Z, Journal of Membrane Science, 450 (2014) 181-188.

[45] D. Hasson, In memory of Sidney Loeb, Desalination, 261 (2010) 203-204.

[46] G.-R. Xu, J.-N. Wang, C.-J. Li, Strategies for improving the performance of the polyamide thin film composite (PA-TFC) reverse osmosis (RO) membranes: Surface modifications and nanoparticles incorporations, Desalination, 328 (2013) 83-100.

[47] N. Misdan, W.J. Lau, A.F. Ismail, Seawater Reverse Osmosis (SWRO) desalination by thin-film composite membrane – Current development, challenges and future prospects, Desalination, 287 (2012) 228-237.

[48] D. Li, H. Wang, Recent developments in reverse osmosis desalination membranes, Journal of Materials Chemistry, 20 (2010) 4551-4566.

[49] T. Wang, L. Dai, Q. Zhang, A. Li, S. Zhang, Effects of acyl chloride monomer functionality on the properties of polyamide reverse osmosis (RO) membrane, Journal of Membrane Science, 440 (2013) 48-57.

[50] L. Zhao, P.C.Y. Chang, W.S.W. Ho, High-flux reverse osmosis membranes incorporated with hydrophilic additives for brackish water desalination, Desalination, 308 (2013) 225-232.

[51] H. Choi, J. Park, T. Tak, Y.N. Kwon, Surface modification of seawater reverse osmosis (SWRO) membrane using methyl methacrylate-hydroxy poly(oxyethylene) methacrylate (MMA-HPOEM) comb-polymer and its performance, Desalination, 291 (2012) 1-7.

[52] A. Sarkar, P. Carver, T. Zhang, A. Merrington, K. Bruza, J. Rousseau, S. Keinath, P. Dvornic, Dendrimer-based coatings for surface modification of polyamide reverse osmosis membranes, Journal of Membrane Science, 349 (2010) 421-428.

[53] L. Ni, J. Meng, X. Li, Y. Zhang, Surface coating on the polyamide TFC RO membrane for chlorine resistance and antifouling performance improvement, Journal of Membrane Science, 451 (2014) 205-215.

[54] S. Azari, L. Zou, Using zwitterionic amino acid l-DOPA to modify the surface of thin film composite polyamide reverse osmosis membranes to increase their fouling resistance, Journal of Membrane Science, 401-402 (2012) 68-75.

[55] T. Ishigami, K. Amano, A. Fujii, Y. Ohmukai, E. Kamio, T. Maruyama, H. Matsuyama, Fouling reduction of reverse osmosis membrane by surface modification via layer-by-layer assembly, Separation and Purification Technology, 99 (2012) 1-7.

[56] Z. Zhang, Z. Wang, J. Wang, S. Wang, Enhancing chlorine resistances and anti-biofouling properties of commercial aromatic polyamide reverse osmosis membranes by grafting 3-allyl-5,5-dimethylhydantoin and N,N'-Methylenebis(acrylamide), Desalination, 309 (2013) 187-196.

[57] S.G. Kim, D.H. Hyeon, J.H. Chun, B.-H. Chun, S.H. Kim, Nanocomposite poly(arylene ether sulfone) reverse osmosis membrane containing functional zeolite nanoparticles for seawater desalination, Journal of Membrane Science, 443 (2013) 10-18.

[58] Y. Liu, X. Chen, High permeability and salt rejection reverse osmosis by a zeolite nano-membrane, Physical Chemistry Chemical Physics, 15 (2013) 6817–6824.

[59] M. Bao, G. Zhu, L. Wang, M. Wang, C. Gao, Preparation of monodispersed spherical mesoporous nanosilica–polyamide thin film composite reverse osmosis membranes via interfacial polymerization, Desalination, 309 (2013) 261-266.

[60] S.Y. Park, S.G. Kim, J.H. Chun, B.-H. Chun, S.H. Kim, Fabrication and characterization of the chlorine-tolerant disulfonated poly(arylene ether sulfone)/hyperbranched aromatic polyamide-grafted silica composite reverse osmosis membrane, Desalination and Water Treatment, 43 (2012) 221-229.

[61] G.M. Nisola, J.S. Park, A.B. Beltran, W.-J. Chung, Silver nanoparticles in a polyether-block-polyamide copolymer towards antimicrobial and antifouling membranes, RSC Advances, 2 (2012) 2439.

[62] S.H. Kim, S.-Y. Kwak, B.-H. Sohn, T.H. Park, Design of TiO_2 nanoparticle self-assembled aromatic polyamide TFC membrane as an approach to solve bio-fouling problem, Journal of Membrane Science, 211 (2003) 157–165.

[63] V.B. Schwartz, F. Thétiot, S. Ritz, S. Pütz, L. Choritz, A. Lappas, R. Förch, K. Landfester, U. Jonas, Antibacterial surface coatings from zinc oxide nanoparticles embedded in poly(N-isopropylacrylamide) hydrogel surface layers, Advanced Functional Materials, 22 (2012) 2376–2386.

[64] T. Vercellino, A. Morse, P. Tran, L. Song, A. Hamood, T. Reid, T. Moseley, Attachment of organo-selenium to polyamide composite reverse osmosis membranes to inhibit biofilm formation of S. aureus and E. coli, Desalination, 309 (2013) 291-295.

[65] G.N.B. Baroña, J. Lim, M. Choi, B. Jung, Interfacial polymerization of polyamide-aluminosilicate SWNT nanocomposite membranes for reverse osmosis, Desalination, 325 (2013) 138-147.

[66] H. Zhao, S. Qiu, L. Wu, L. Zhang, H. Chen, C. Gao, Improving the performance of polyamide reverse osmosis membrane by incorporation of modified multi-walled carbon nanotubes, Journal of Membrane Science, 450 (2014) 249-256.

[67] S.H. Maruf, A.R. Greenberg, J. Pellegrino, Y. Ding, Fabrication and characterization of a surface-patterned thin film composite membrane, Journal of Membrane Science, 452 (2014) 11-19.

[68] H. Huang, X. Qu, H. Dong, L. Zhang, H. Chen, Role of NaA zeolites in the interfacial polymerization process towards a polyamide nanocomposite reverse osmosis membrane, RSC Advances, 3 (2013) 8203-8207.

[69] M. Fathizadeh, A. Aroujalian, A. Raisi, Effect of added NaX nano-zeolite into polyamide as a top thin layer of membrane on water flux and salt rejection in a reverse osmosis process, Journal of Membrane Science, 375 (2011) 88-95.

[70] M.M. Pendergast, A.K. Ghosh, E.M.V. Hoek, Separation performance and interfacial properties of nanocomposite reverse osmosis membranes, Desalination, 308 (2013) 180-185.

[71] A. Alkhudhiri, N. Darwish, N. Hilal, Membrane distillation: A comprehensive review, Desalination, 287 (2012) 2-18.

[72] M. Khayet, T. Matsuura, Membrane Distillation: Principles and Applications, 2011.

[73] M. Khayet, Membranes and theoretical modeling of membrane distillation: a review, Advances in Colloid and Interface Science, 164 (2011) 56-88.

[74] P. Wang, M.M. Teoh, T.S. Chung, Morphological architecture of dual-layer hollow fiber for membrane distillation with higher desalination performance, Water Research, 45 (2011) 5489-5500.

[75] F. Edwie, T.S. Chung, Development of hollow fiber membranes for water and salt recovery from highly concentrated brine via direct contact membrane distillation and crystallization, Journal of Membrane Science, 421-422 (2012) 111-123.

[76] M. Su, M.M. Teoh, K.Y. Wang, J. Su, T.-S. Chung, Effect of inner-layer thermal conductivity on flux enhancement of dual-layer hollow fiber membranes in direct contact membrane distillation, Journal of Membrane Science, 364 (2010) 278-289.

[77] M.M. Teoh, T.-S. Chung, Y.S. Yeo, Dual-layer PVDF/PTFE composite hollow fibers with a thin macrovoid-free selective layer for water production via membrane distillation, Chemical Engineering Journal, 171 (2011) 684-691.

[78] H. Zhu, H. Wang, F. Wang, Y. Guo, H. Zhang, J. Chen, Preparation and properties of PTFE hollow fiber membranes for desalination through vacuum membrane distillation, Journal of Membrane Science, 446 (2013) 145-153.

[79] H. Fang, J.F. Gao, H.T. Wang, C.S. Chen, Hydrophobic porous alumina hollow fiber for water desalination via membrane distillation process, Journal of Membrane Science, 403-404 (2012) 41-46.

[80] X. Yang, R. Wang, L. Shi, A.G. Fane, M. Debowski, Performance improvement of PVDF hollow fiber-based membrane distillation process, Journal of Membrane Science, 369 (2011) 437-447.

[81] X. Wei, B. Zhao, X.-M. Li, Z. Wang, B.-Q. He, T. He, B. Jiang, CF4 plasma surface modification of asymmetric hydrophilic polyethersulfone membranes for direct contact membrane distillation, Journal of Membrane Science, 407-408 (2012) 164-175.

[82] M. Khayet, J.I. Mengual, T. Matsuura, Porous hydrophobic/hydrophilic composite membranes, Journal of Membrane Science, 252 (2005) 101-113.

[83] M. Essalhi, M. Khayet, Surface segregation of fluorinated modifying macromolecule for hydrophobic/hydrophilic membrane preparation and application in air gap and direct contact membrane distillation, Journal of Membrane Science, 417-418 (2012) 163-173.

[84] M. Khayet, Treatment of radioactive wastewater solutions by direct contact membrane distillation using surface modified membranes, Desalination, 321 (2013) 60-66.

[85] Y. Peng, Y. Dong, H. Fan, P. Chen, Z. Li, Q. Jiang, Preparation of polysulfone membranes via vapor-induced phase separation and simulation of direct-contact membrane distillation by measuring hydrophobic layer thickness, Desalination, 316 (2013) 53-66.

[86] M. Qtaishat, D. Rana, M. Khayet, T. Matsuura, Preparation and characterization of novel hydrophobic/hydrophilic polyetherimide composite membranes for desalination by direct contact membrane distillation, Journal of Membrane Science, 327 (2009) 264-273.

[87] D.E. Suk, T. Matsuura, H.B. Park, Y.M. Lee, Development of novel surface modified phase inversion membranes having hydrophobic surface-modifying macromolecule (nSMM) for vacuum membrane distillation, Desalination, 261 (2010) 300-312.

[88] M. Gryta, Influence of polypropylene membrane surface porosity on the performance of membrane distillation process, Journal of Membrane Science, 287 (2007) 67-78.

[89] M.M. Teoh, T.-S. Chung, Membrane distillation with hydrophobic macrovoid-free PVDF–PTFE hollow fiber membranes, Separation and Purification Technology, 66 (2009) 229-236.

[90] K.Y. Wang, S.W. Foo, T.S. Chung, Mixed matrix PVDF hollow fiber membranes with nanoscale pores for desalination through direct contact membrane distillation, Industrial & Engineering Chemistry Research, 48 (2009) 4474-4483.

[91] D. Hou, Wei, W., Xia, S.S., Xiangli, F.J., Chen, Y.W., Jin, W.Q., Influence of inorganic salts on pervaporation performance of PDMS/ceramic composite membranes, Journal of the Chemical Industry and Engineering Society of China, 60 (2009) 389-393.

[92] Z. Song, M. Xing, J. Zhang, B. Li, S. Wang, Determination of phase diagram of a ternary PVDF/γ-BL/DOP system in TIPS process and its application in preparing hollow fiber

membranes for membrane distillation, Separation and Purification Technology, 90 (2012) 221-230.

[93] S. Bonyadi, T.S. Chung, R. Rajagopalan, A novel approach to fabricate macrovoid-free and highly permeable PVDF hollow fiber membranes for membrane distillation, AIChE Journal, 55 (2009) 828-833.

[94] E. Drioli, A. Ali, S. Simone, F. Macedonio, S.A. Al-Jlil, F.S. Al Shabonah, H.S. Al-Romaih, O. Al-Harbi, A. Figoli, A. Criscuoli, Novel PVDF hollow fiber membranes for vacuum and direct contact membrane distillation applications, Separation and Purification Technology, 115 (2013) 27-38.

[95] J.-W. Zhang, H. Fang, J.-W. Wang, L.-Y. Hao, X. Xu, C.-S. Chen, Preparation and characterization of silicon nitride hollow fiber membranes for seawater desalination, Journal of Membrane Science, 450 (2014) 197-206.

[96] S. Bonyadi, T.S. Chung, Flux enhancement in membrane distillation by fabrication of dual layer hydrophilic–hydrophobic hollow fiber membranes, Journal of Membrane Science, 306 (2007) 134-146.

[97] F. Edwie, M.M. Teoh, T.S. Chung, Effects of additives on dual-layer hydrophobic–hydrophilic PVDF hollow fiber membranes for membrane distillation and continuous performance, Chemical Engineering Science, 68 (2012) 567-578.

[98] L. Dumée, K. Sears, N. Finn, M. Duke, S. Gray, Carbon nanotube based composite membranes for water desalination by membrane distillation, Desalination and Water Treatment, 17 (2010) 72-79.

[99] L.F. Dumée, K. Sears, J. Schütz, N. Finn, C. Huynh, S. Hawkins, M. Duke, S. Gray, Characterization and evaluation of carbon nanotube Bucky-Paper membranes for direct contact membrane distillation, Journal of Membrane Science, 351 (2010) 36-43.

[100] L. Dumée, J.L. Campbell, K. Sears, J. Schütz, N. Finn, M. Duke, S. Gray, The impact of hydrophobic coating on the performance of carbon nanotube bucky-paper membranes in membrane distillation, Desalination, 283 (2011) 64-67.

[101] A. Razmjou, E. Arifin, G. Dong, J. Mansouri, V. Chen, Superhydrophobic modification of TiO_2 nanocomposite PVDF membranes for applications in membrane distillation, Journal of Membrane Science, 415-416 (2012) 850-863.

[102] M. Khayet, M.C. García-Payo, Nanostructured flat membranes for direct contact membrane distillation, in: WO2011/117443 (Ed.), Universidad Complutense de Madrid, 2011.

[103] M. Essalhi, M. Khayet, Self-sustained webs of polyvinylidene fluoride electrospun nanofibers at different electrospinning times: 1. Desalination by direct contact membrane distillation, Journal of Membrane Science, 433 (2013) 167-179.

[104] M. Essalhi, M. Khayet, Self-sustained webs of polyvinylidene fluoride electrospun nanofibers: Effects of polymer concentration and desalination by direct contact membrane distillation, Journal of Membrane Science, 455 (2014) 133-143.

[105] M. Essalhi, M. Khayet, Self-sustained webs of polyvinylidene fluoride electrospun nanofibers at different electrospinning times: 2. Theoretical analysis, polarization effects and thermal efficiency, Journal of Membrane Science, 433 (2013) 180-191.

[106] H. Maab, L. Francis, A. Al-saadi, C. Aubry, N. Ghaffour, G. Amy, S.P. Nunes, Synthesis and fabrication of nanostructured hydrophobic polyazole membranes for low-energy water recovery, Journal of Membrane Science, 423-424 (2012) 11-19.

[107] J.A. Prince, G. Singh, D. Rana, T. Matsuura, V. Anbharasi, T.S. Shanmugasundaram, Preparation and characterization of highly hydrophobic poly(vinylidene fluoride)–clay nanocomposite nanofiber membranes (PVDF–clay NNMs) for desalination using direct contact membrane distillation, Journal of Membrane Science, 397-398 (2012) 80-86.

[108] B.S. Lalia, E. Guillen-Burrieza, H.A. Arafat, R. Hashaikeh, Fabrication and characterization of polyvinylidenefluoride-co-hexafluoropropylene (PVDF-HFP) electrospun membranes for direct contact membrane distillation, Journal of Membrane Science, 428 (2013) 104-115.

[109] Y. Liao, R. Wang, A.G. Fane, Engineering superhydrophobic surface on poly(vinylidene fluoride) nanofiber membranes for direct contact membrane distillation, Journal of Membrane Science, 440 (2013) 77-87.

[110] J.A. Prince, V. Anbharasi, T.S. Shanmugasundaram, G. Singh, Preparation and characterization of novel triple layer hydrophilic–hydrophobic composite membrane for desalination using air gap membrane distillation, Separation and Purification Technology, 118 (2013) 598-603.

[111] G. Liu, W. Wei, W. Jin, N. Xu, Polymer/ceramic composite membranes and their application in pervaporation process, Chinese Journal of Chemical Engineering, 20 (2012) 62-70.

[112] J. Zuo, Y. Wang, S.P. Sun, T.-S. Chung, Molecular design of thin film composite (TFC) hollow fiber membranes for isopropanol dehydration via pervaporation, Journal of Membrane Science, 405-406 (2012) 123-133.

[113] Y. Wang, M. Gruender, T.S. Chung, Pervaporation dehydration of ethylene glycol through polybenzimidazole (PBI)-based membranes. 1. Membrane fabrication, Journal of Membrane Science, 363 (2010) 149-159.

[114] G. Zhang, L. Dai, S. Ji, Dynamic pressure-driven covalent assembly of inner skin hollow fiber multilayer membrane, AIChE Journal, 57 (2011) 2746-2754.

[115] G. Zhang, X. Song, S. Ji, N. Wang, Z. Liu, Self-assembly of inner skin hollow fiber polyelectrolyte multilayer membranes by a dynamic negative pressure layer-by-layer technique, Journal of Membrane Science, 325 (2008) 109-116.

[116] M. Yin, J. Qian, Q. An, Q. Zhao, Z. Gui, J. Li, Polyelectrolyte layer-by-layer self-assembly at vibration condition and the pervaporation performance of assembly multilayer films in dehydration of isopropanol, Journal of Membrane Science, 358 (2010) 43-50.

[117] P. Zhang, J. Qian, Y. Yang, Q. An, X. Liu, Z. Gui, Polyelectrolyte layer-by-layer self-assembly enhanced by electric field and their multilayer membranes for separating isopropanol–water mixtures, Journal of Membrane Science, 320 (2008) 73-77.

[118] P. Zhang, J. Qian, Q. An, X. Liu, Q. Zhao, H. Jin, Surface morphology and pervaporation performance of electric field enhanced multilayer membranes, Journal of Membrane Science, 328 (2009) 141-147.

[119] Q. Zhao, Q.F. An, Y. Ji, J. Qian, C. Gao, Polyelectrolyte complex membranes for pervaporation, nanofiltration and fuel cell applications, Journal of Membrane Science, 379 (2011) 19-45.

[120] Q. Zhao, J. Qian, Q. An, Z. Sun, Layer-by-layer self-assembly of polyelectrolyte complexes and their multilayer films for pervaporation dehydration of isopropanol, Journal of Membrane Science, 346 (2010) 335-343.

[121] Q.G. Zhang, Q.L. Liu, A.M. Zhu, Y. Xiong, L. Ren, Pervaporation performance of quaternized poly(vinyl alcohol) and its crosslinked membranes for the dehydration of ethanol, Journal of Membrane Science, 335 (2009) 68-75.

[122] P.S. Rachipudi, M.Y. Kariduraganavar, A.A. Kittur, A.M. Sajjan, Synthesis and characterization of sulfonated-poly(vinyl alcohol) membranes for the pervaporation dehydration of isopropanol, Journal of Membrane Science, 383 (2011) 224-234.

[123] D. Yang, J. Li, Z. Jiang, L. Lu, X. Chen, Chitosan/TiO_2 nanocomposite pervaporation membranes for ethanol dehydration, Chemical Engineering Science, 64 (2009) 3130-3137.

[124] A.M. Sajjan, B.K. Jeevan Kumar, A.A. Kittur, M.Y. Kariduraganavar, Novel approach for the development of pervaporation membranes using sodium alginate and chitosan-wrapped multiwalled carbon nanotubes for the dehydration of isopropanol, Journal of Membrane Science, 425-426 (2013) 77-88.

[125] C.-L. Lai, Y.-J. Fu, J.-T. Chen, Q.-F. An, K.-S. Liao, S.-C. Fang, C.-C. Hu, K.-R. Lee, Pervaporation separation of ethanol/water mixture by UV/O_3-modified PDMS membranes, Separation and Purification Technology, 100 (2012) 15-21.

[126] F. Xiangli, Y. Chen, W. Jin, N. Xu, Polydimethylsiloxane (PDMS)–ceramic composite membrane with high flux for pervaporation of ethanol−water mixtures, Industrial & Engineering Chemistry Research, 46 (2007) 2224-2230.

[127] G. Liu, D. Hou, W. Wei, F. Xiangli, W. Jin, Pervaporation separation of butanol-water mixtures using polydimethylsiloxane/ceramic composite membrane, Chinese Journal of Chemical Engineering, 19 (2011) 40-44.

[128] G. Liu, W. Wei, H. Wu, X. Dong, M. Jiang, W. Jin, Pervaporation performance of PDMS/ceramic composite membrane in acetone butanol ethanol (ABE) fermentation–PV coupled process, Journal of Membrane Science, 373 (2011) 121-129.

[129] G. Liu, F. Xiangli, W. Wei, S. Liu, W. Jin, Improved performance of PDMS/ceramic composite pervaporation membranes by ZSM-5 homogeneously dispersed in PDMS via a surface graft/coating approach, Chemical Engineering Journal, 174 (2011) 495-503.

[130] S.J. Lue, C.-F. Chien, K.P.O. Mahesh, Pervaporative concentration of ethanol–water mixtures using heterogeneous polydimethylsiloxane (PDMS) mixed matrix membranes, Journal of Membrane Science, 384 (2011) 17-26.

[131] Y. Zhu, S. Xia, G. Liu, W. Jin, Preparation of ceramic-supported poly(vinyl alcohol)–chitosan composite membranes and their applications in pervaporation dehydration of organic/water mixtures, Journal of Membrane Science, 349 (2010) 341-348.

[132] V.T. Magalad, G.S. Gokavi, K.V.S.N. Raju, T.M. Aminabhavi, Mixed matrix blend membranes of poly(vinyl alcohol)–poly(vinyl pyrrolidone) loaded with phosphomolybdic acid used in pervaporation dehydration of ethanol, Journal of Membrane Science, 354 (2010) 150-161.

[133] Q. Zhao, J.-W. Qian, Q.-F. An, Q. Yang, P. Zhang, A facile route for fabricating novel polyelectrolyte complex membrane with high pervaporation performance in isopropanol dehydration, Journal of Membrane Science, 320 (2008) 8-12.

[134] Q. Zhao, J. Qian, Q. An, Z. Gui, H. Jin, M. Yin, Pervaporation dehydration of isopropanol using homogeneous polyelectrolyte complex membranes of poly(diallyldimethylammonium chloride)/sodium carboxymethyl cellulose, Journal of Membrane Science, 329 (2009) 175-182.

[135] Q. Zhao, J. Qian, Q. An, Q. Yang, Z. Gui, Synthesis and characterization of solution-processable polyelectrolyte complexes and their homogeneous membranes, ACS Applied Materials & Interfaces, 1 (2009) 90-96.

[136] Q. Zhao, J. Qian, Q. An, C. Gao, Z. Gui, H. Jin, Synthesis and characterization of soluble chitosan/sodium carboxymethyl cellulose polyelectrolyte complexes and the pervaporation dehydration of their homogeneous membranes, Journal of Membrane Science, 333 (2009) 68-78.

[137] Q. Zhao, Q. An, Z. Sun, J. Qian, K.-R. Lee, C. Gao, J.-Y. Lai, Studies on structures and ultrahigh permeability of novel polyelectrolyte complex membranes, The Journal of Physical Chemistry B, 114 (2010) 8100-8106.

[138] H. Jin, Q. An, Q. Zhao, J. Qian, M. Zhu, Pervaporation dehydration of ethanol by using polyelectrolyte complex membranes based on poly (*N*-ethyl-4-vinylpyridinium bromide) and sodium carboxymethyl cellulose, Journal of Membrane Science, 347 (2010) 183-192.

[139] Q. Zhao, J. Qian, C. Zhu, Q. An, T. Xu, Q. Zheng, Y. Song, A novel method for fabricating polyelectrolyte complex/inorganic nanohybrid membranes with high isopropanol dehydration performance, Journal of Membrane Science, 345 (2009) 233-241.

[140] Q. Zhao, J. Qian, M. Zhu, Q. An, Facile fabrication of polyelectrolyte complex/carbon nanotube nanocomposites with improved mechanical properties and ultra-high separation performance, Journal of Materials Chemistry, 19 (2009) 8732-8740.

[141] Q. Zhao, J. Qian, Q. An, M. Zhu, M. Yin, Z. Sun, Poly(vinyl alcohol)/polyelectrolyte complex blend membrane for pervaporation dehydration of isopropanol, Journal of Membrane Science, 343 (2009) 53-61.

[142] M. Zhu, J. Qian, Q. Zhao, Q. An, J. Li, Preparation method and pervaparation performance of polyelectrolyte complex/PVA blend membranes for dehydration of isopropanol, Journal of Membrane Science, 361 (2010) 182-190.

[143] M. Zhu, J. Qian, Q. Zhao, Q. An, Y. Song, Q. Zheng, Polyelectrolyte complex (PEC) modified by poly(vinyl alcohol) and their blend membranes for pervaporation dehydration, Journal of Membrane Science, 378 (2011) 233-242.

[144] P.D. Chapman, T. Oliveira, A.G. Livingston, K. Li, Membranes for the dehydration of solvents by pervaporation, Journal of Membrane Science, 318 (2008) 5-37.

3

Nanostructured membranes

Electrospinning and feed solution conditions effect on structural properties and filtration performance

Polysulfone electrospun nanofibrous membranes (PSU ENMs) were prepared using a mixture of solvents *N, N*-dimethyl formamide (DMF) and tetrahydrofurane (THF) for microfiltration and ultrafiltration. The involved electrospinning parameters, namely, the polymer solution flow rate (*F*), the electric voltage (*V*) and the distance between the needle tip and the collector or gap (*G*) were varied in the range within which it was possible to obtain bead-free PSU ENMs. Their effects on the morphology and structure of the PSU ENMs were studied. Interfacial polymerization technique was applied to develop novel thin film composite polyester-PSU based ENMs. The prepared membranes were characterized by means of different techniques such as scanning electron microscopy, contact angle measurements, X-ray diffraction, attenuated total reflectance Fourier transform spectroscopy, etc. Micro/ultra-filtration tests were conducted using humic acid (HA) model solutions with a concentration of 15 mg/L at two different pH values (3 and 11). It was observed that PSU ENMs were not selective under acidic conditions, whereas the thin film composite polyester-PSU based ENMs achieved better separation factors and lower irreversible fouling factors than those of the un-modified PSU ENMs.

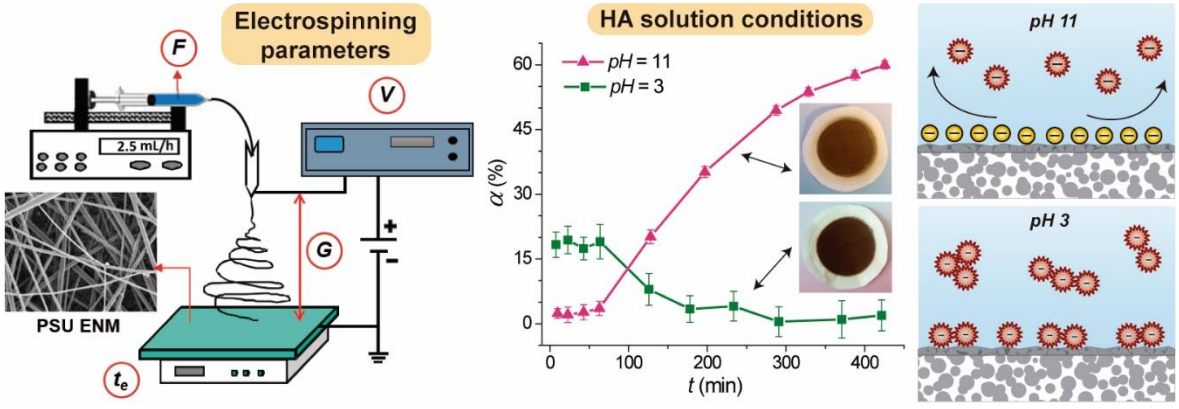

Self-sustained electrospun polysulfone nanofibrous membranes and their surface modification by interfacial polymerization for micro- and ultra-filtration

3.1 Introduction

Electrospinning is recognized as an efficient technique for the fabrication of polymer sub-micron to nano-scale fibers by applying electric forces. Electrospun nanofibrous membranes (ENMs) exhibit a great potential in membrane filtration technology due to several attractive attributes, such as their highly porous and interconnected pore structure, micron scaled interstitial space, controllable thickness and a large surface area to volume ratio [1, 2]. These outstanding properties render ENMs to be one of the most cost-effective alternatives to successfully compete with conventional separation processes for the treatment of different types of wastewaters. Other advantages of using ENMs for wastewater treatment include high permeability and acceptable separation factor [3].

Among the used synthetic polymers for preparation of membranes for different separation processes, polysulfone (PSU) has been widely considered because of its excellent physicochemical properties (i.e. chemical resistance, thermal stability and mechanical strength as well as good processability). In general, PSU membranes have a broad operating temperature and pH ranges, excellent chlorine tolerance and ability to retain their mechanical properties in both hot and wet environments [4]. However, PSU membranes are not immune to fouling problem, which results in serious decline of permeate flux with changes of the separation characteristic during filtration operations. Various techniques such as surface coating, plasma treatment and surface grafting have been considered in order to overcome this drawback by improving the antifouling characteristics of the membrane and reducing therefore the foulant(s) adsorption to its surface [5].

The main purposes of the present study are the preparation and characterization of PSU ENMs using different electrospinning parameter conditions. Attempts are made to prepare a thin film composite (TFC) membrane by interfacial polymerization (IP) technique in order to improve the filtration performance of PSU ENMs. This technique is based on the polymerization that occurs between two reactive monomers at the interface of two immiscible

solvents. The skin or thin layer produced by this technique will determine the overall solute retention, permeate flux and, in general, will control the efficiency of the membrane process. One of the advantages of the interfacial polymerization technique is that the thin layer can be optimized for particular function by varying the monomer concentration in each solution (both aqueous and organic solutions), the monomer ratios or the reaction time of the polymerization step [6].

3.2 Materials and methods

3.2.1 Materials

The spinning solution was prepared from the polymer polysulfone (PSU, UDEL P-3500 LCD, Solvay Specialty Polymers; Mw = 79,000 g/mol; ϱ_{PSU} = 1.24 g/cm^3) and the mixture of solvents *N, N*-dimethyl formamide (DMF, Sigma-Aldrich) and tetrahydrofuran (THF, Sigma-Aldrich). The monomers bisphenol A (BPA, Sigma-Aldrich) and trimesoyl chloride (TMC, Sigma-Aldrich) along with the solvent hexane (Panreac) were used for the IP of the prepared PSU ENMs. Humic acid (HA, Fluka) of molecular weight 4.1 kDa was chosen as the model organic foulant. Hydrochloric acid (HCl, Sigma-Aldrich) and sodium hydroxide (NaOH, Panreac) were employed to adjust the pH of the feed humic acid solutions to the required values (3 or 11).

3.2.2 Preparation of PSU ENMs

Due to the possible influence of ambient humidity on PSU polymer, this was first dried at 120°C overnight using a vacuum desiccator composed of a vacuum pump (Vacuubrand brand, model MZ2C), a desiccant (Afora) and a heating mantle (Selecta).

For the preparation of the polymer solution, DMF (64 wt.%) and THF (16 wt.%) were first mixed during 2 min at 80 rpm using a magnetic stirrer (IKA, RCT basic). Subsequently, 20 wt.% PSU was added to this mixture and the whole solution was stirred at 60ºC and 80 rpm during 15 h until the polymer solution becomes homogeneous.

Once the spinning solution was prepared, electrospinning technique was used for the fabrication of the PSU ENMs. The electrospinning set-up schematized in Fig. 3.1 consists of a glass syringe (50 mL, Nikepal) to hold the polymer solution, a circulation pump (KDS-200, Scientific) to control the polymer solution flow rate, two electrodes (a metallic Hamilton needle of 0.60/0.90 mm internal/external diameter and a grounded copper collector covered with aluminum foil to facilitate the extraction of the as electrospun) and a DC voltage supply in the kV range (Iseg, TCIP300 304p).

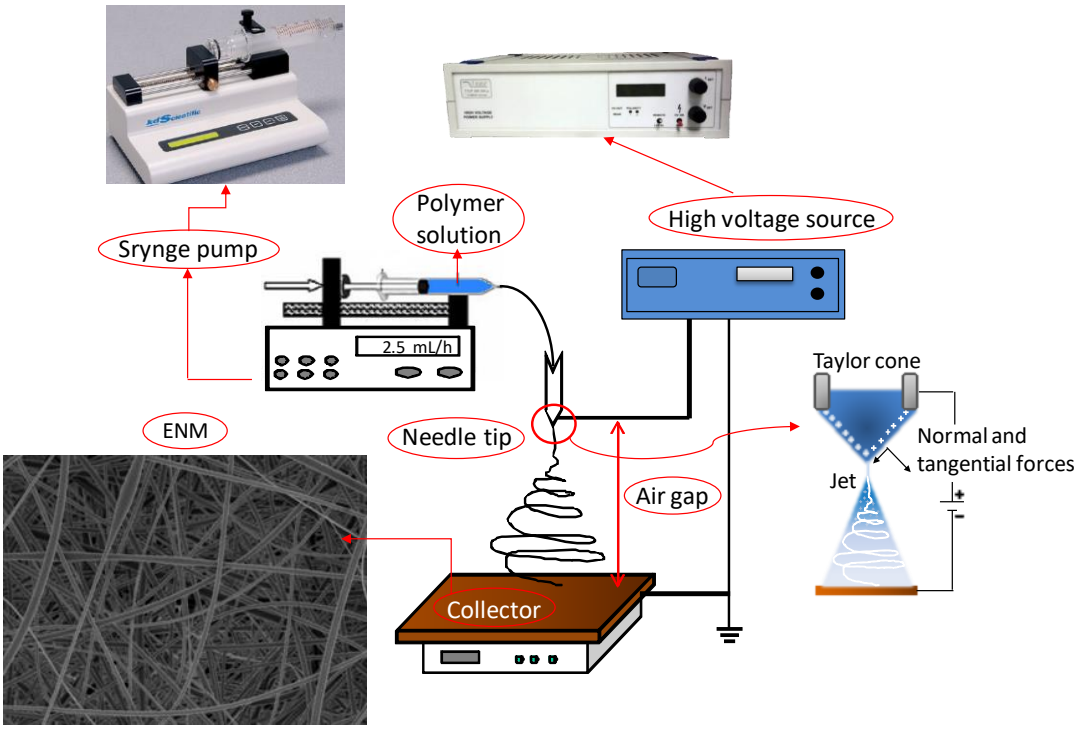

Figure 3.1. Schematic diagram of electrospinning set-up.

The involved electrospinning parameters (i.e. polymer solution flow rate, *F*; electric voltage, *V*; and distance between the needle tip and the collector or gap, *G*) were varied in the range within which it was possible to obtain bead free nanofibers. These ranges were 1 to 3 mL/h, 16 to 20 kV and 10 to 15 cm, respectively. The electrospinning time (t_e) was varied to obtain the desired thickness of the ENM. Furthermore, in order to increase the mechanical resistance and the structural integrity of the ENMs, a heat post-treatment was carried out at 220°C for 2 h. It must be mentioned that the post-treatment temperature must be higher than the boiling point of the used solvents in order to ensure their complete evaporation from the formed ENMs. This temperature must be also above the glass transition temperature of the used polymer (185ºC for PSU) in order to form good contact and junction points between nanofibers. Finally, the post-treated ENM was immersed in a bath containing distilled water for a short time to peel them out of the aluminum foil and subsequent drying at room temperature for 24 h.

3.2.3 Preparation of thin film composite polyester-PSU based ENMs by interfacial polymerization (IP) technique

The prepared PSU ENM was first immersed in a 0.5 w/v.% BPA aqueous solution for 15 min. Since the monomer BPA has very low solubility in water, it was dissolved in an aqueous solution of 2M NaOH at basic pH. The soaked ENM taken out from the aqueous solution was positioned vertically for 2 min to drain the excess monomer on its surface [6]. Then, this ENM was dipped during 30 s in the organic solution prepared by mixing 0.15 w/v.% TMC in hexane.

The reaction of the monomers BPA and TMC occurs at the ENM surface forming a thin film polyester layer of a few microns thickness. All these steps were carried out at ambient temperature, about 23ºC. Finally, the ENM was dried in air for 24 h before the characterization tests.

3.2.4 Membranes characterization

The thickness of the ENMs was measured using a micrometer equipped with a feeler (Millitron). 44 measurements were taken at different positions of each ENM sample. The final thickness was determined as the mean value with its corresponding standard deviation.

The surface of the PSU ENMs was examined by a field emission scanning electron microscope (FESEM, JEOL Model JSM-6335F) operating at a voltage of 5 kV. The samples were first sputter-coated with a thin gold layer (5 nm) using an evaporator (EMITECH K550 X) during one minute under a current of 25 mA. The diameters of the nanofibers were evaluated from the SEM images using the UTHSCSA Image Tool free software. The mean nanofiber diameter ($\overline{\lambda_w}$) together with weighted standard deviation ($\overline{s_w}$) and the distribution of the nanofiber diameter were determined. About 100 nanofibers of each ENM sample were considered. More details can be found in our previous work [7].

The water contact angle (θ_w) measurements of the ENMs were measured using CAM100 device (Sb) with the software Cam200usb, enabling to acquire photographs of the drop on the surface of the sample and to calculate the contact angle value. A Hamilton stainless steel needle allowed controlling the volume of the drops, which was about 17 µL. For the unmodified ENMs, which are hydrophobic, the water drops deposited on the surface remained static. For each drop, five images were recorded during 4 s and for each ENM sample at least 10 different drops were considered to determine the average θ_w value together with its standard deviation. For the modified ENMs by IP, which are more hydrophilic, the volume of the water drops deposited on their surfaces decreased with time and consequently the measured θ_w changed. In this case, an average θ_w value with its corresponding standard deviation were obtained at each time (0, 1.1, 2.2, 3.3 and 4.3 s) for at least 10 drops.

X-ray diffractograms of the samples were obtained using a diffractometer X'Pert-MPD (Philips) at a wavelength of the Cu Kα (λ = 1.54 Å). The scanning range was varied from 5° to 90° in steps of 0.4°, with a scanning speed of 1 step/s. The operating conditions were 45 kV and 40 mA using an aperture of 0.15 mm. The interplanar distance (d) was calculated using Bragg's law:

$$d = \frac{\lambda}{2 \cdot \sin \theta} \tag{3.1}$$

where θ is the middle of the diffraction angle.

The samples were also analyzed by attenuated total reflectance Fourier transform infrared spectroscopy (ATR-FTIR) with a Nicolet device (Magna-IR 750 Series II) equipped with a detector DTGS-KBr (sulfate triglycerin deuterated with KBr window), a beam splitter KBr and an infrared source (Ever-Glo). The H-ATR Multiple Bounce (Spectra Tech) accessory with a ZnSe crystal and 13 steps was used for analysis. ATR-FTIR measurements were carried out at 128 scans and 8 cm^{-1} resolution.

3.2.5 Filtration experiments

The experimental device used for microfiltration/ultrafiltration (MF/UF) tests was designed and assembled as schematized in Fig. 3.2. The effective filtration area of the membrane is $(217.58 \pm 0.14) \times 10^{-5}$ m^2. The feed solution kept at a temperature of 23ºC was circulated from the double jacketed feed container through the feed channel of the membrane module by a magnetic gear pump (DANFOSS, APP 0.6). The retentate was turned back to the feed container. To control the feed flow and pressure at the inlet of the membrane module a frequency variator (ABB industrial drives, ACS355), a three steps stopcock and two ball valves were used. The pressure at the inlet and outlet of the membrane module was measured by means of the manometers (WIKA Alexander Wiegand GMBH & Co.KG) connected to two digital indicators (Junior20 brand-Kosmos PRC). The feed flow rate was also measured by a flowmeter (RS-Amidata, 5111-3892). In all experiments the feed flow rate was maintained at 1.6–1.8 L/min.

A pre-filter module (Dassel FP050, Schleicher&Schull, W.Germany) with a nylon pre-filter (Nylon Millipore, NY20) having a pore size of 20 μm was placed between the pump and the membrane module in order to filter the large particles produced by the magnetic gear pump and therefore protect the membrane. It is important to note that this pre-filter does not affect the permeate flow measurements nor the HA concentration of the feed solution circulated tangentially to the membrane.

Diluted solutions of 15 mg/L HA at two different pH values (3 and 11) from a standard HA concentrated solution of 1 g/L were prepared to carry out the filtration tests. Solution pH was measured using a pH/Ion meter (692, Metrohm) and adjusted to 3 and 11 by adding 2M HCl as needed. A spectrophotometer (UV/VIS 7315, Jenway) was used to analyze the HA concentration of the permeate, feed and retentate samples. It is worth noting that the HA absorption spectrum has no characteristic peak. It is worth quoting that, in the literature, different views were found on the wavelength at which the HA samples must be analyzed [8, 9]. Therefore, HA aqueous solutions with different concentrations (5, 10, 15, 20, 25 and 30 mg/L) and pH values (3 and 11) were measured at different wavelengths (656, 565, 465, 365, 280 and 254 nm) for calibration. It was observed, regardless on the pH, the absorption values of the calibration curves were more accurate at low wavelengths. Therefore, the HA

concentration measurements were taken at 254 nm. The same criteria was considered by Yuan and Zydney [10-12] when studying HA fouling phenomenon during MF.

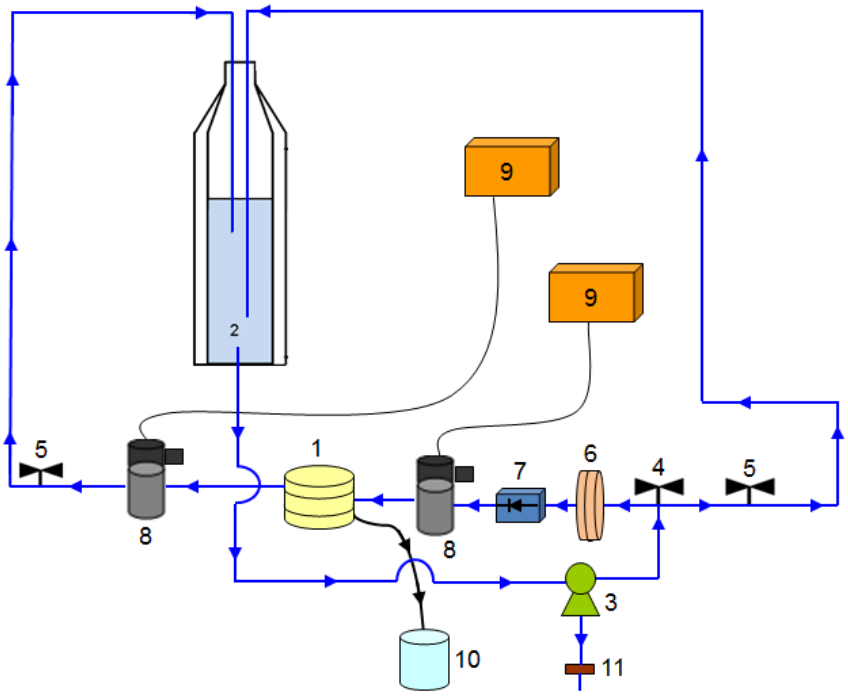

Figure 3.2. Scheme of the micro/ultra-filtration experimental set-up: (1) Membrane module; (2) double jacketed container; (3) circulation pump; (4) three steps stopcock; (5) pressure and flow control valves; (6) pre-filter; (7) flow-meter; (8) manometer; (9) pressure indicator; (10) permeate container; (11) emptying valve.

Before carrying out the filtration measurements, the membranes were first compacted applying a pressure difference of 4×10^5 Pa for about 5 h using distilled water as feed. Then, permeation tests were carried out with distilled water and HA feed aqueous solutions at 10^5 Pa. Permeate fluxes of both HA solution (J_{HA}) and distilled water before (J_{w0}) and after (J_{wf}) each HA test were measured and the irreversible membrane fouling factor (FR_W) was evaluated.

The permeate fluxes were determined by weighing the produced permeate during a predetermined time on an electronic balance (AND GF-1200) and using the following equation:

$$J\ (\mathrm{kg/m^2\,h}) = \frac{m}{A_{ef} \cdot \Delta t} \tag{3.2}$$

where m is the mass of the obtained permeate during a predetermined time (Δt) and A_{ef} is the effective filtration membrane area.

FR_W was determined as follows [6]:

$$FR_W\ (\%) = \frac{J_{w0} - J_{wf}}{J_{w0}} \cdot 100 \tag{3.3}$$

The separation factor (α) of the membranes was calculated as follows:

$$\alpha\,(\%) = \left(1 - \frac{C_p}{C_f}\right)\cdot 100 \tag{3.4}$$

where C_p and C_f are the HA concentration of the permeate and the feed solutions, respectively.

3.3 Results and discussions

3.3.1 Membranes fabrication and characterization

3.3.1.1 PSU ENMs: effect of the electrospinning parameters and heat post-treatment

Various PSU ENMs were prepared with different electrospinning parameters (F, V, G) as it is summarized in Table 3.1. It is well known that F determines the quantity of the polymer solution available for electrospinning and affects the volume charge density and the involved electrical current. There is a minimum polymer flow rate to produce nanofibers [13, 14]. In the present study, a minimum value of 1 mL/h was found. When F was lower than this value, the polymer solution solidified at the needle tip and small droplets of the polymer were formed and then ejected to the surface of the membrane. However, when F was higher than 3 mL/h the solvents present in the polymer solution have not enough time for evaporation along the distance between needle tip and the collector and the probability to produce beaded ENMs became higher.

Table 3.1. Electrospinning parameters used to prepare PSU ENMs using a polymer solution mixture of 20% PSU + 16% THF + 64% DMF: polymer solution flow rate (F), electric voltage (V), distance between the needle tip and the collector or gap (G), electric current or intensity (I) and electrospinning time (t_e).

Membrane	F (mL/h)	V (kV)	G (cm)	I (μA)	t_e (min)
ENM 1	1	18	15	2–2.7	60
ENM 2	1.5	18	15	1.8–2	60
ENM 3	2	18	15	1–1.9	60
ENM 4	2	18	10	2.1–3.5	60
ENM 5	2.5	18	10	2.4–3.6	60
ENM 6	2.5	20	10	3.2–3.9	80
ENM 7	2.5	20	10	3.2–3.9	120
ENM 8	2.5	18	10	2.2–3.4	130
ENM 9	2.5	20	10	3.1–3.8	130

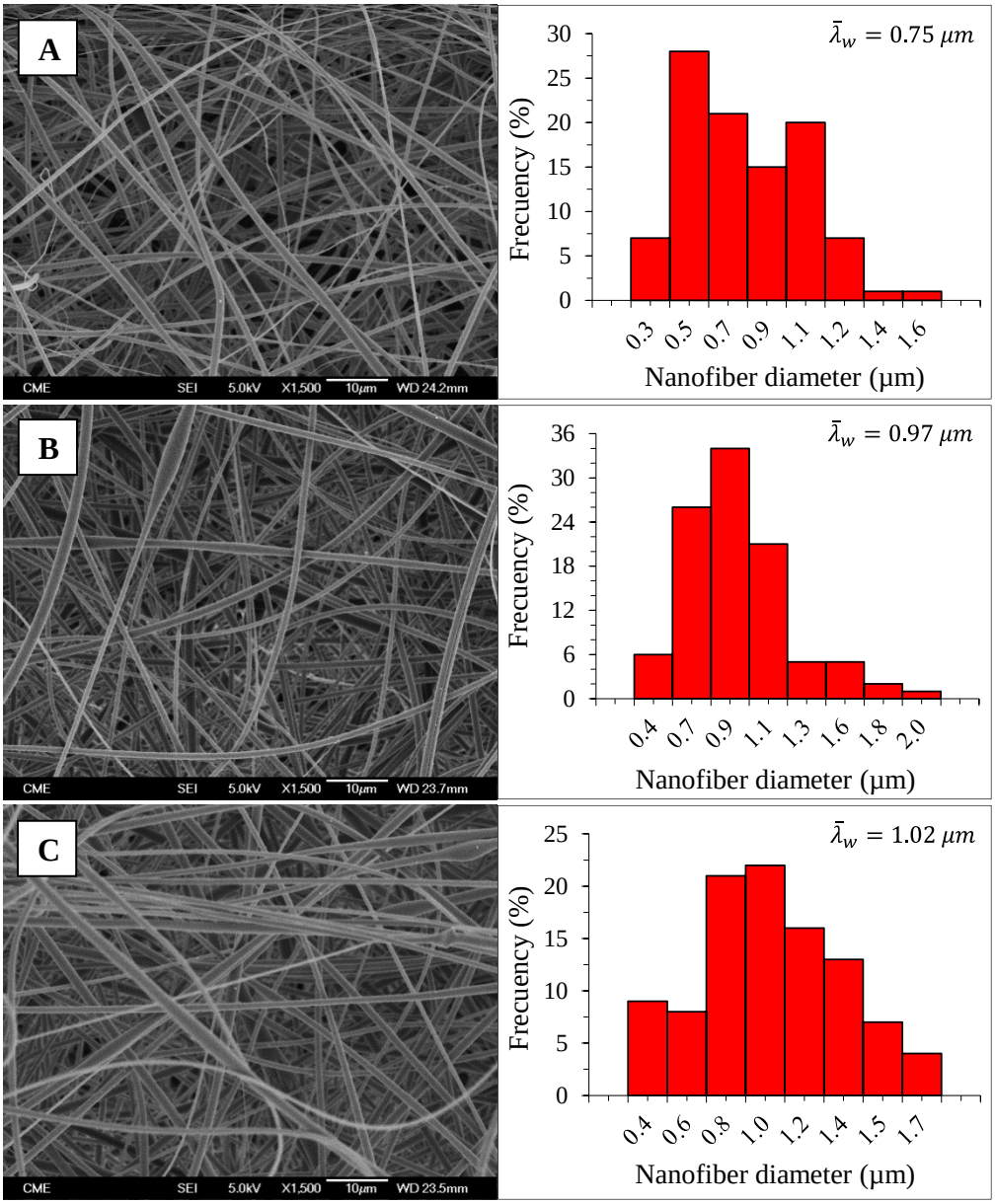

Figure 3.3. SEM images of PSU ENMs without heat post-treatment for three different polymer solution flow rates (V = 18 kV and G = 15 cm): A) ENM 1 (F = 1 mL/h), B) ENM 2 (F = 1.5 mL/h) and C) ENM 3 (F = 2 mL/h). All images were taken at the same magnification X1500.

The increase of F from 1 to 2 mL/h resulted in a continuous enhancement of the diameter of the nanofibers as can be seen in Fig. 3.3. This is expected because of the greater available polymer solution volume at the needle tip [14, 15].

Fig. 3.4 shows as an example the reduction of the diameter of the nanofibers (from 1.10 to 0.85 μm) with the increase of V from 18 to 20 kV. This result is due to the increase of the generated electrostatic repulsive forces on the polymer solution jet along with a stronger electric field present between the needle tip and the collector, which causes greater stretching of the electrified jet resulting in smaller diameters of the nanofibers [13, 14].

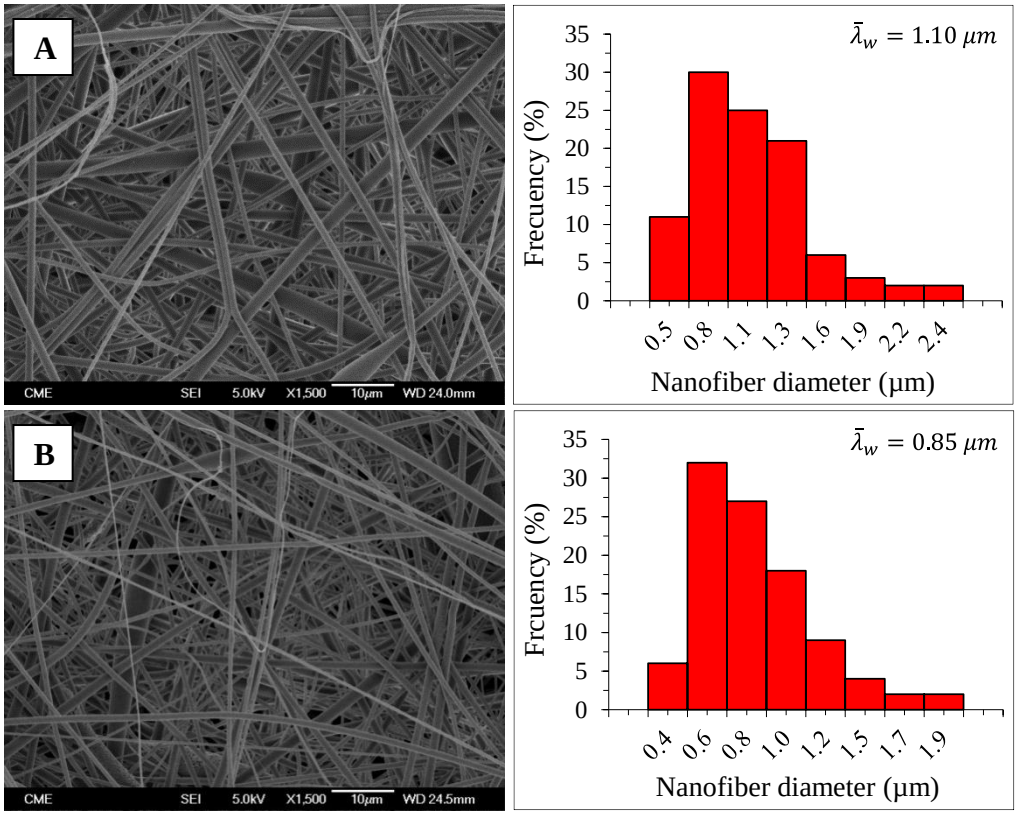

Figure 3.4. SEM images of PSU ENMs without heat post-treatment for two electric voltages (F = 2.5 mL/h and G = 10 cm): A) ENM 5 (V = 18 kV), B) ENM 6 (V = 20 kV). Both images were taken at the same magnification X1500.

The distance between the needle tip and the collector (i.e. air gap distance, G) has been also studied in order to control the nanofiber diameter and the morphology of the ENMs. However, compared to F and V, G is of less effect. It was observed that decreasing G exerted the same effect as increasing V (i.e. inducing higher electric field strength). Fig. 3.5 shows as an example the increase of the nanofiber diameter when decreasing G from 15 to 10 cm. Besides, when G was maintained under 8 cm, the instability of the jet due to the strong electric field resulted in the formation of beads and often the solvents have no sufficient time to evaporate completely resulting in nanofibers with flattened structures [15].

Comparing the absorption spectra of the PSU ENMs obtained by means of ATR-FTIR analysis, it can be seen in Fig. 3.6 that all peaks coincide indicating that the studied electrospinning parameters do not cause any compositional change of the PSU ENMs. It is to be noted that the peaks appeared at 3300 cm^{-1} and 1650 cm^{-1} for the ENMs 6 and 7 are due to the presence of water in the ENMs.

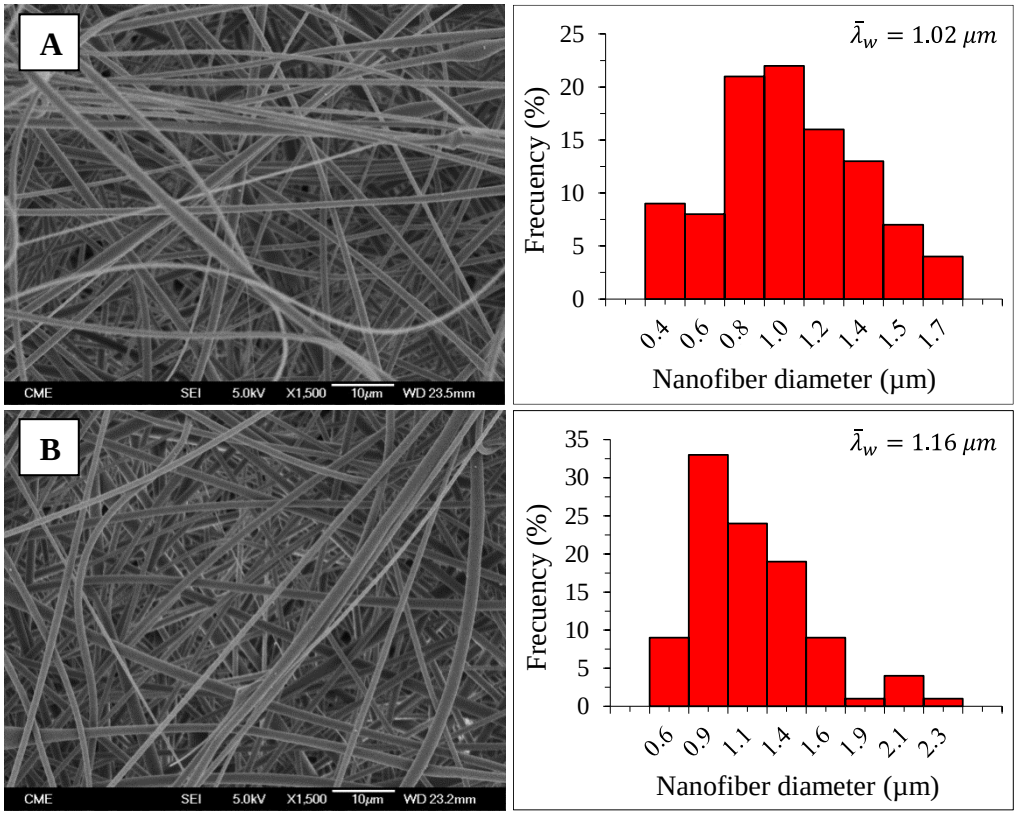

Figure 3.5. SEM images of PSU ENMs without heat post-treatment for two different air gap distances (F = 2 mL/h and V = 18 kV): A) ENM 3 (G = 15 cm) and B) ENM 4 (G = 10 cm). Both images were taken at the same magnification X1500.

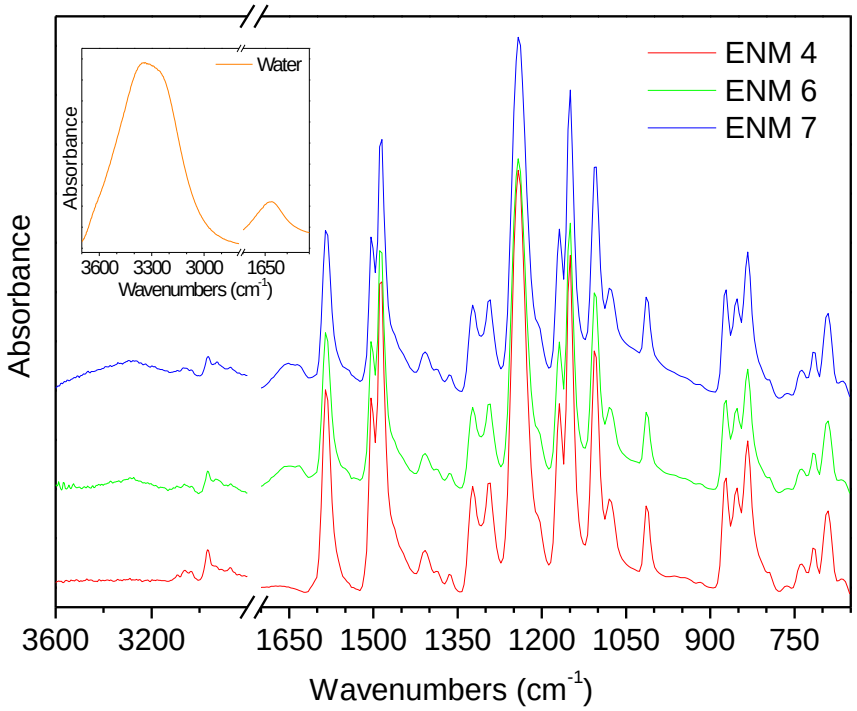

Figure 3.6. ATR-FTIR spectra of 20% PSU ENMs with different fabrication parameters and water absorbance spectra.

From the SEM images presented in Fig. 3.7, it can be seen the appearance of a large number of contact points between PSU nanofibers indicating that these are fused together as a result of the application of the heat post-treatment. This junction between nanofibers improves the compact structure, integrability and mechanical properties of the PSU ENMs. In addition, as it is summarized in Table 3.2, the diameters of the nanofibers of all prepared PSU ENMs are reduced after being exposed to the heat post-treatment.

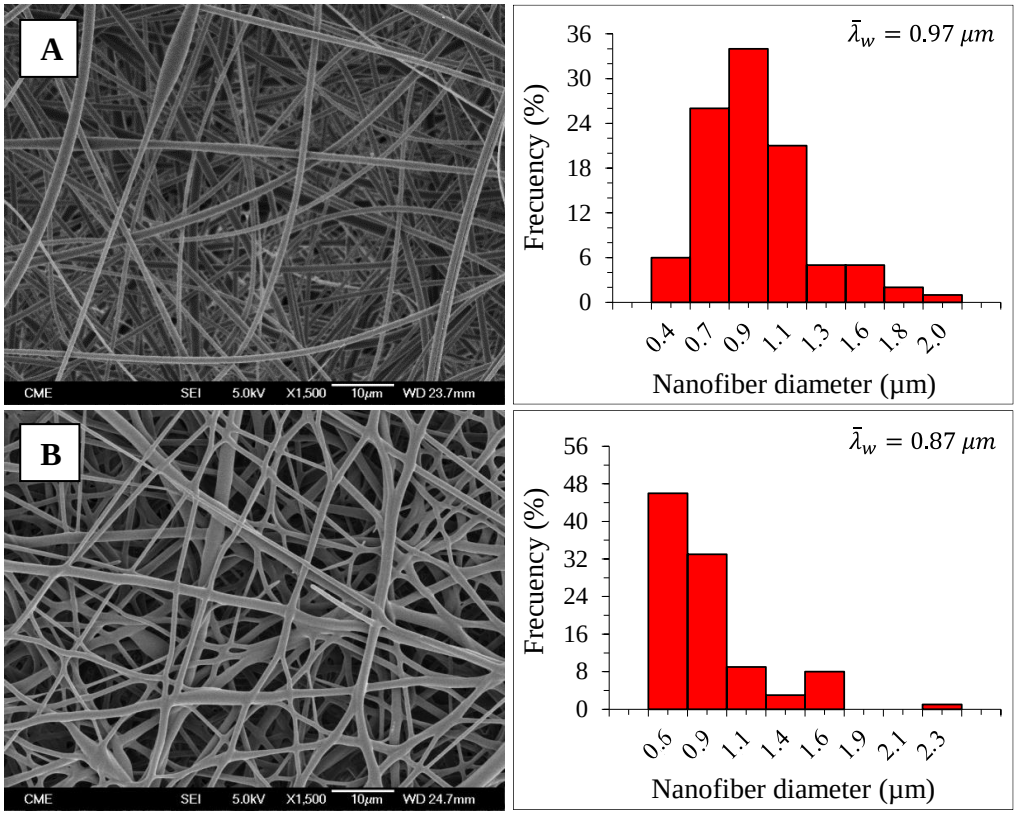

Figure 3.7. SEM images of ENM 2 (F = 1.5 mL/h, V = 18 kV and G = 15 cm) taken at X1500: A) Without heat post-treatment, B) with heat post-treatment and their respective nanofiber diameter distributions.

It is worth noting that the absorption peaks obtained by ATR-FTIR for the ENMs prepared with and without heat post-treatment were the same as shown in Fig. 3.8. This indicates that the membrane composition did not change and the PSU polymer maintained its characteristics despite the high temperature to which it was exposed (220°C).

In Table 3.3 are summarized the water contact angles (θ_w) of the PSU ENMs exposed to heat post-treatment. No significant changes can be detected for θ_w values of the ENMs. However, a slight reduction of θ_w after heat post-treatment was observed. This may be attributed partly to the reduction of the membrane surface roughness. It is well known that PSU is a hydrophilic polymer. In order to check the hydrophilicity of the PSU polymer, a phase inversion membrane was prepared from the same polymer solution used to prepare ENMs and the measured θ_w was

found to be 82.3° ± 2.1°. Therefore, the high θ_w of the ENMs is due to the nanofibrous structure, to their higher surface roughness and air entrapped between the nanofibers.

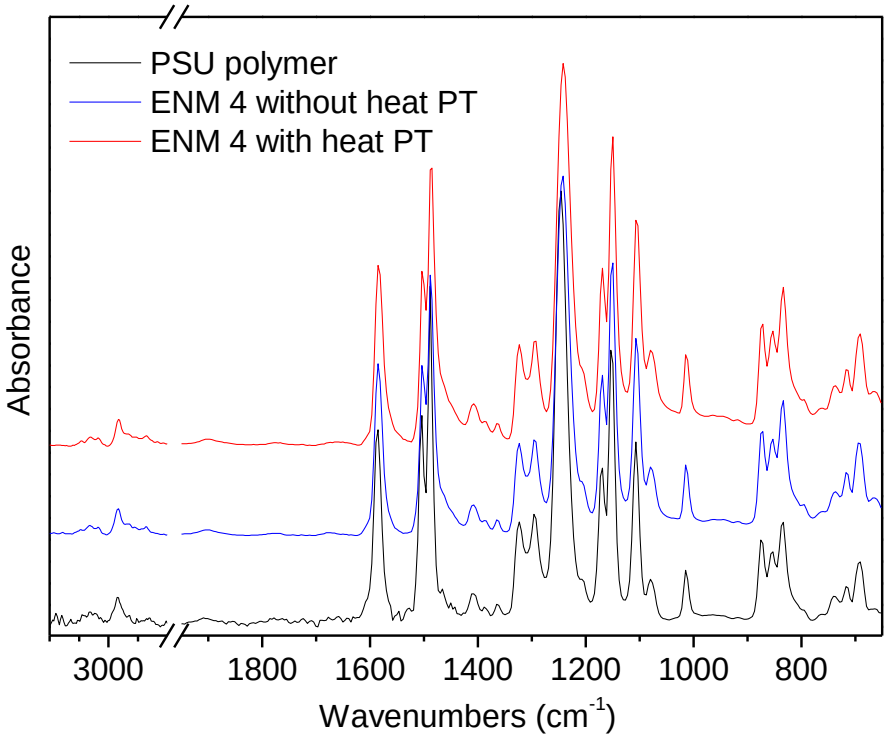

Figure 3.8. ATR-FTIR spectra of the PSU polymer and ENM 4 with and without heat post-treatment (HPT) at 220°C for 2 h.

Table 3.2. Mean nanofiber diameter of the PSU ENMs prepared with and without heat post-treatment and their corresponding weighted standard deviation.

Membrane	$\overline{\lambda_w} \pm \overline{s_w}$ (μm)	
	Without heat-treatment	With heat-treatment
ENM 1	0.75 ± 0.04	0.67 ± 0.05
ENM 2	0.97 ± 0.05	0.87 ± 0.05
ENM 3	1.02± 0.05	0.83 ± 0.04
ENM 4	1.16 ± 0.07	0.86 ± 0.04
ENM 5	1.10 ± 0.08	0.91 ± 0.06
ENM 6	0.85 ± 0.05	0.70 ± 0.05
ENM 7	0.88 ± 0.08	0.72 ± 0.03
ENM 8	1.20 ± 0.06	1.11 ± 0.05
ENM 9	0.89 ± 0.05	0.82 ± 0.03

Table 3.3. Water contact angles (θ_w) of PSU ENMs prepared with heat post-treatment.

Membrane	θ_w (°)
ENM 1	116.8 ± 4.5
ENM 2	119.0 ± 1.5
ENM 3	122.6 ± 4.6
ENM 4	122.0 ± 4.3
ENM 5	121.4 ± 4.9
ENM 6	122.9 ± 2.0
ENM 7	117.1 ± 3.1
ENM 8	128.7 ± 4.3
ENM 9	125.6 ± 4.5

3.3.1.2 Interfacial polymerization of PSU ENMs

Fig. 3.9 confirms the performed IP and the change of the surface morphology of the PSU ENMs. A thin polyester layer is formed on the surface of the PSU ENM (see Fig. 3.9 D and E) and its estimated thickness from Fig. 3.9-C was about 0.5 µm. After surface modification, θ_w was reduced considerably indicating the surface of the ENMs became hydrophilic. The measured water contact angles of the surface modified PSU ENMs were declined with time from 57.7° to 47.0° during 3.3 s (i.e. the water drop on the surface did not remain static). This significant reduction of θ_w also corroborated that the IP was effective. Therefore, it may be expected less fouling for the surface modified PSU ENMs.

Both the unmodified and the surface modified PSU ENMs were characterized by means of ATR-FTIR spectroscopy and their spectra are shown in Fig. 3.10. New absorption peaks appeared at 1724 and 1215 cm^{-1} corresponding to C=O and C–O ester group bands, respectively. Both peaks are associated to the formed polyester layer as it was reported elsewhere [16, 17].

The X-ray diffractograms of PSU polymer, PSU phase inversion membrane, PSU ENM 9, and modified PSU ENM 9 by IP are presented in Fig. 3.11. The angles at which the maximum diffraction occurs, 2θ, along with the full width at half-maximum (*FWHM*) and the interplanar distance (d) are presented in Table 3.4. The PSU polymer presented a typical diffractogram of an amorphous polymer having a maximum intensity peak at 17.9° and a secondary peak at 43.7°. This peak disappeared from all membranes diffractograms. In other words, all membranes are

amorphous and showed only the single peak at around 17.9º and this was narrower compared to the peak of the PSU polymer.

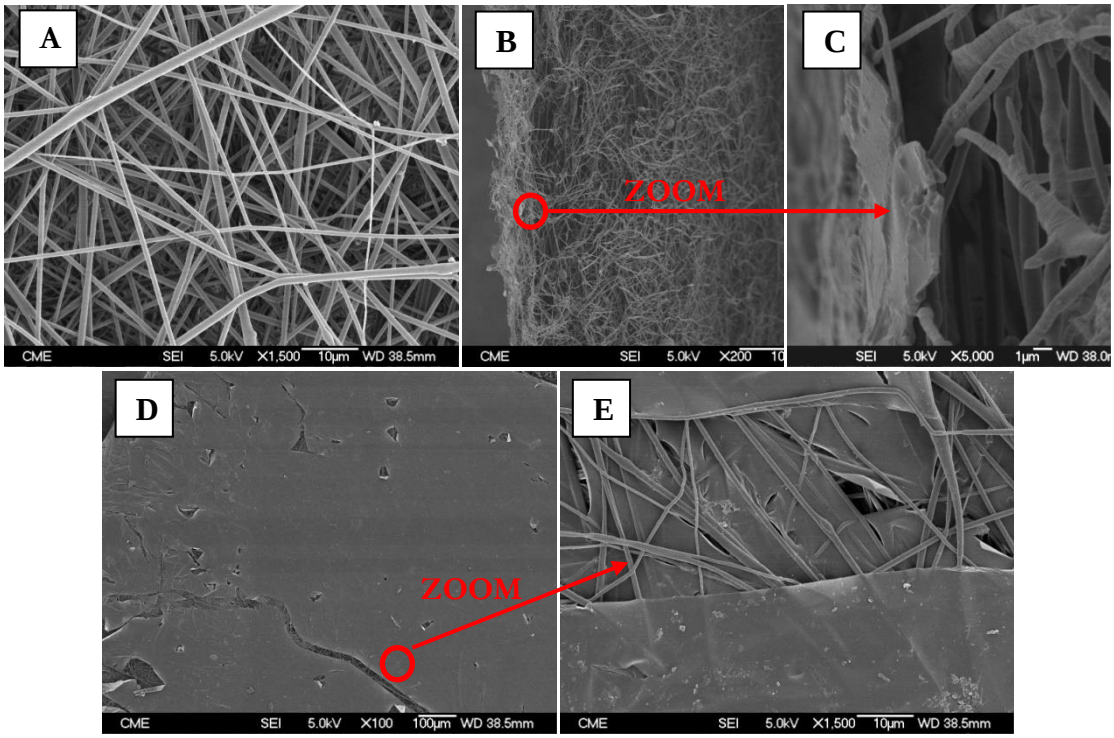

Figure 3.9. SEM images of ENM 9 (F = 2.5 mL/h, V = 20 kV and G = 10 cm): A) Without IP at X1500, D) E) with IP at X80 and X1500 respectively, B) and C) Cross section of ENM 9 with IP at X200 and X5000 respectively.

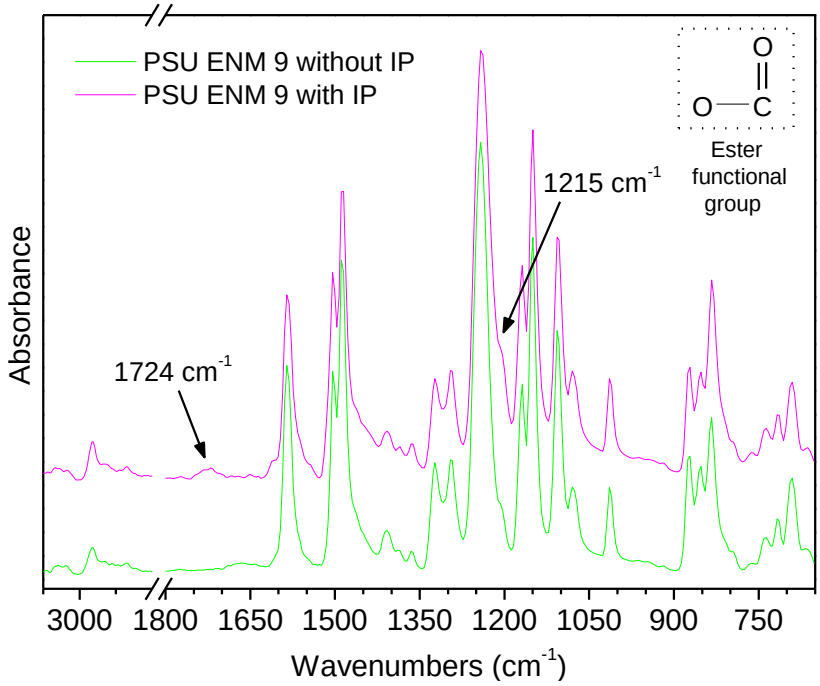

Figure 3.10. ATR-FTIR spectra of the PSU ENM 9 unmodified and modified by IP (F = 2.5 mL/h, V = 20 kV and G = 10 cm).

Compared to PSU polymer and PSU phase inversion membrane, the *FWHM* of the maximum intensity peak of the PSU ENM 9 became slightly narrower indicating a small increase in crystallinity. This is because the presence of elongational flow fields during electrospinning of polymeric solutions causes preferred orientation of polymer molecular chains along the nanofiber axis [18, 19]. Nevertheless, the amorphous character of the nanofibrous membranes indicates that most of the molecular chains are in a non-crystalline state, which occurs because during the electrospinning, stretched chains do not have enough time to organize into ordered crystalline structures before they were solidified. This effect has been also observed and confirmed by other authors in the literature [20].

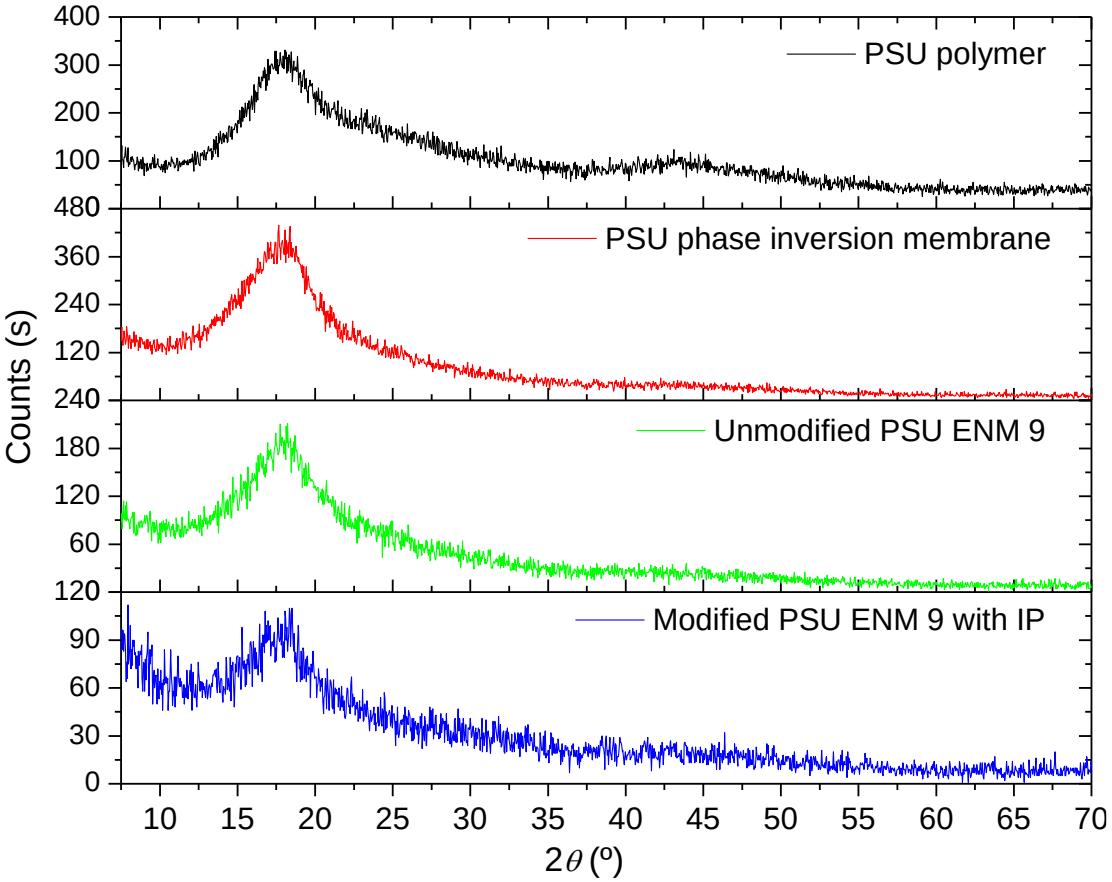

Figure 3.11. XRD patterns of PSU polymer, phase inversion PSU membrane and PSU ENM 9 unmodified and modified by IP.

After surface modification of the PSU ENM 9, the intensity and width of the main peak became slightly smaller and narrower than that of the unmodified PSU ENM 9 indicating a minor change of the amorphous nature of the membrane. This is due to the polyester layer formed on the membrane surface. It must be pointed out that both the unmodified and modified PSU ENMs are amorphous despite its slight change of the XRD spectra derived from the manufacturing electrospinning process and the modification surface technique employed, respectively.

Table 3.4. Diffraction angles of each diffractogram (2θ), full width at half-maximum (*FWHM*) and inter-planar distance (*d*).

Sample	2θ	*FWHM* (°)	*d* (Å)
PSU polymer*	17.91	6.41	4.95
PSU phase inversion membrane	17.80	5.20	4.99
PSU ENM 9 without IP	17.98	5.06	4.94
PSU ENM 9 with IP	17.71	4.42	5.01

*At 43.7° it was detected a secondary peak with 13% relative intensity with respect to the maximum intensity peak shown at 17.9°.

3.3.2 Filtration experiments

3.3.2.1 Effects of pH on the HA filtration performance of PSU ENMs

The PSU ENMs were used for the treatment of HA aqueous solutions at two pH values 3 and 11. The pH effects on the filtration performance of PSU ENMs were studied analysing the permeate flux, separation factor and irreversible fouling factor. As it can be seen in Figs. 3.12 and 3.13, given as an example, the PSU ENMs showed completely different behaviours in acid or basic aqueous solutions. This pH-dependent behaviour can be explained by changes in both HA-HA and HA-membrane interactions under different environmental conditions [6, 21, 22]. For instance, the macromolecular structure and particle size of HA strongly depend on the degree of charge neutralization and therefore vary with the pH, ionic strength and degree of complexation with metal ions [23]. At acidic media HA particles tend to aggregate forming chains or networks favoured by attractive forces of hydrogen bonding, Van der Waals interactions and π-electron interactions. Besides, a higher HA aggregation phenomenon occurs at low pH due to the reduction of the intra- or intermolecular electrostatic repulsive forces and/or the increase of the hydrophobicity of the HA molecules associated with the reduced electrical charge [11] (e.g. at pH 3 the average of HA particles heights range from 1 to 27 nm [24]). In contrast, under alkaline condition, deprotonation of HA functional groups result in higher intra- and intermolecular electrostatic repulsive forces where HA forms stretched linear and flat structures but not aggregates (e.g. at pH 8 the average particle heights range from 0.3 to 4 nm [24]).

From Fig. 3.12 it can be seen that the PSU ENM is not capable to concentrate the feed HA solution at pH 3 indicating that this type of membrane is not selective in acidic media. Under this condition, a simultaneous reduction of both the feed and permeate concentration were observed suggesting the adsorption of the HA macromolecules to the PSU ENM surface. It is known that the isoelectric point of PSU microfiltration membranes is around 3.1 [25, 26].

Therefore, the PSU ENM is electrically neutral at pH 3. In addition, inter- and intra-molecular electrostatic repulsive forces of HA are also very low or close to zero [11]. As consequence, the electrostatic repulsive forces between the PSU ENM and the HA particles and/or between HA particles become negligible, being the hydrophobic interaction rather than the electrostatic interaction the predominant mechanism affecting adsorption phenomenon [27]. The observed initial 20% separation factor in Fig. 3.13 at pH 3 is attributed to the adsorption of HA at the surface of PSU ENM resulting in a thick and blackish HA deposit or cake layer as can be seen from the corresponding photograph. This initial deposit accelerated the subsequent rate of HA fouling, possibly serving as a nucleation site for deposition of macromolecular HA [10]. In Fig. 3.12-A it can also be seen that after certain filtration time both permeate and feed concentrations reached an equal stationary state. This indicates the end of the cake growth on the membrane surface.

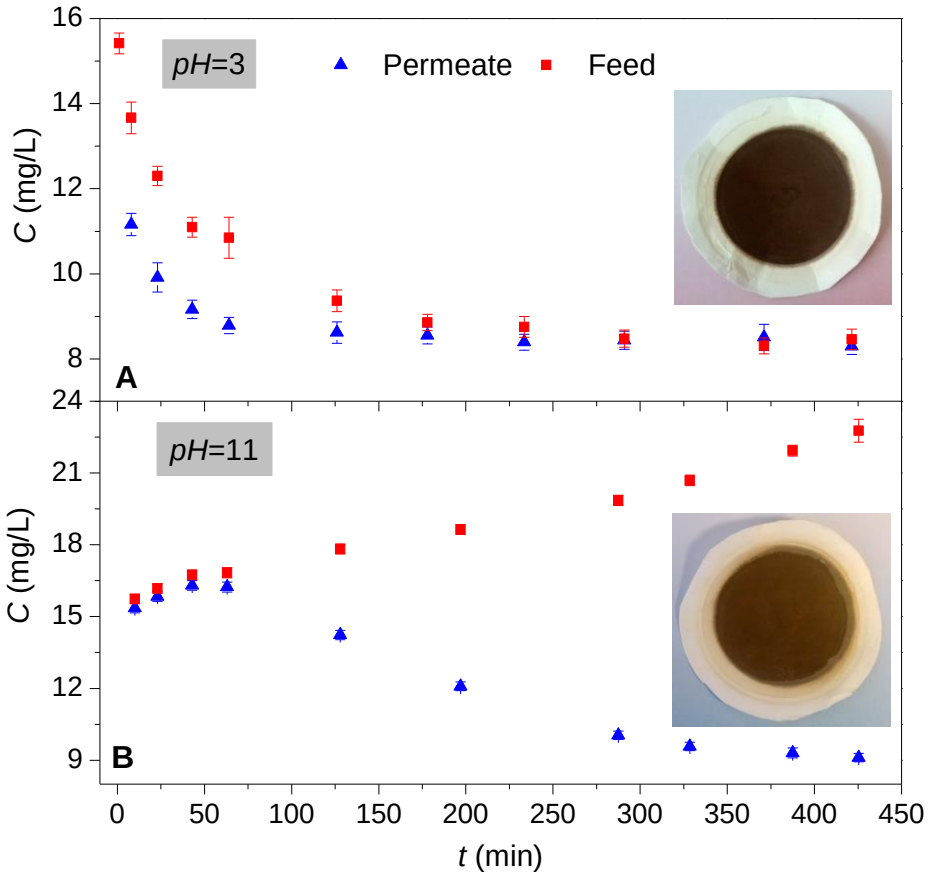

Figure 3.12. Feed and permeate concentration measurements during the filtration test of PSU ENM 8 with a heat post-treatment at 205°C for 30 min using 15 mg/L HA solution at different environment conditions: A) pH = 3; B) pH = 11. The shown images in A and B correspond to the surface of PSU ENM 8 after HA filtration tests.

When using HA solutions at basic pH, an opposite behaviour of the HA separation factor and concentrations were detected as plotted in Figs. 3.12-B and 3.13. In these figures, the HA feed concentration and separation factor of the PSU ENMs increased with time, whereas the

permeate concentration decreased approaching asymptotic values. In this case, the separation factor of the membranes reached 60%. Under pH 11, lower adsorption on the membrane surface occurs because of the increase of the electrostatic repulsive forces between HA macromolecules and between HA-membrane surface (i.e. both HA and PSU membrane are negatively charged) along with the increased hydrophilicity of the HA molecules [21, 28]. In this case, electrostatic interaction is the predominant mechanism affecting separation phenomenon. Moreover, the deposition of HA on the membrane surface during filtration process increases further the negative charge of the membrane surface and the electrostatic repulsion effect becomes greater with increasing filtration time, contributing consequently to the increase of the separation factor of the membrane (see Fig. 3.13). As a result, a yellowish and thinner HA deposit or cake layer is formed on the membrane surface compared to the cake formed at pH 3. The same behaviors at both pH 3 and pH 11 were obtained for others ENMs prepared in this study. Similar results were also observed by Yuan and Zydney [11] when using polyethersulfone (PES) membranes for MF of HA aqueous solutions.

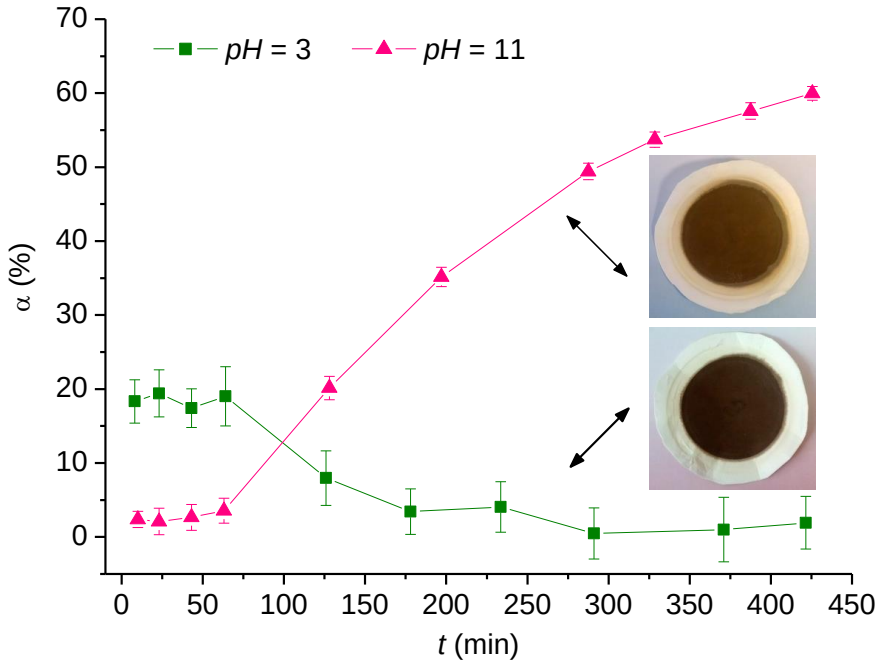

Figure 3.13. Separation factor (α) of PSU ENM 8 with heat post-treatment at 205°C for 30 min during the filtration tests of 15 mg/L HA solution at different pH values, 3 and 11.

HA fouling in membrane MF process involves not only chemical interactions but also physical (i.e. hydrodynamic) interactions. Permeate flux decline of PSU ENMs plotted in Fig. 3.14-A as an example, during MF of 15 mg/L HA solutions at both pH 3 and 11, can be described using the combined pore blockage and cake filtration model recently used by Ho and Zydney [29], Yuan et al. [12] and Astaraee et al. [30] for the analysis of fouling during MF of proteins and HA. As it can be seen in Fig. 3.14-A, at the beginning of the filtration process a rapid permeate flux decline is observed and then the rate of flux decline decreases.

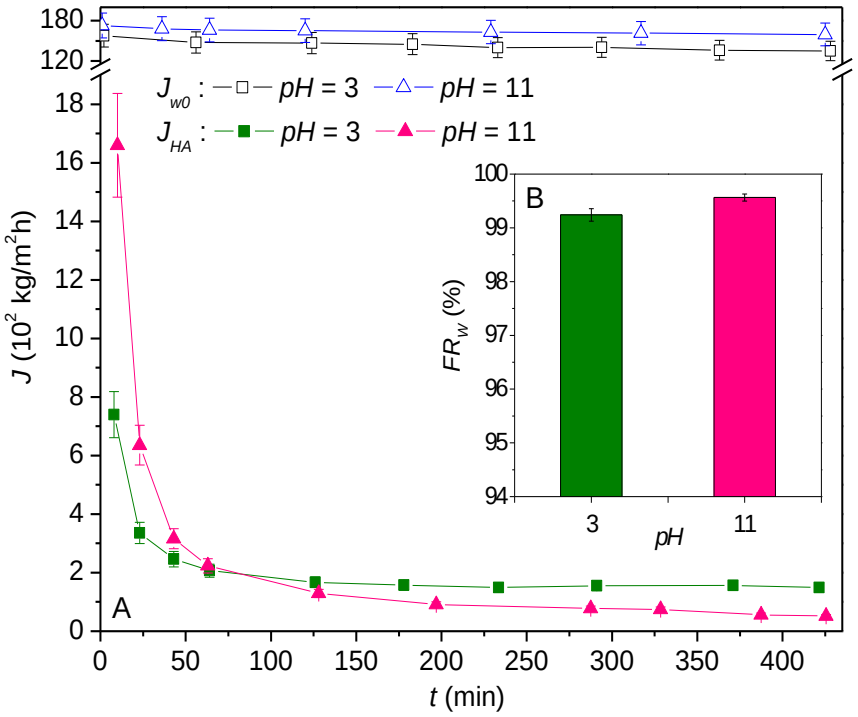

Figure 3.14. A) Permeate fluxes (J_{w0},J_{HA}) and B) irreversible fouling factors (FR_W) of PSU ENM 8 with heat post-treatment at 205°C for 30 min during the filtration test of 15 mg/L HA solution at different pH values, 3 and 11. (ΔP = 10^5 Pa; J_{wf}(pH 3) = 1.03 × 10^2 kg/m² h; J_{wf}(pH 11) = 0.69 × 10^2 kg/m² h).

The transition between these two stages, pore blockage and cake filtration, is determined by the change in the slope of the permeate flux with time [30]. Based on this model, the initial fouling of the membrane is due to pore blockage caused by the physical deposition of large HA aggregates on the surface of the MF membrane and then, a HA deposit or cake is formed on those regions of the membrane that have first been covered by an aggregate. In the last stage, the cake layer resistance is the main mass transport resistance of the filtration process [29]. From Fig. 3.14-A it can be seen the higher reduction of the initial permeate flux for HA at pH 3 (i.e. HA permeate flux/initial water flux ratio (J_{HA}/J_{w0}) of 0.05 at a filtration time of 9 min compared to J_{HA}/J_{w0} of 0.19 at pH 11 after the same filtration time). This behavior is due to the higher affinity and absorption phenomenon of the HA molecules with respect to the PSU ENM surface at lower pH as it was explained previously. This is consistent with results obtained by Yuan and Zydney in their studies of HA fouling during MF [10, 11]. In Fig. 3.14-A it can also be observed the change of the slope of the permeate flux decline in both acidic and basic media after 100 min filtration tests. The specific time at which this change occurred depends mainly on the physical characteristics of each PSU ENM (e.g. mean pore size, pore size distribution, porosity, thickness, etc.). It must be indicated that this specific time coincides with the filtration moment corresponding to the change of the HA separation tendency of the PSU ENMs (see Fig. 3.13). As it was reported by Yuan and Zydney [11], asymptotic permeate fluxes are reached

for long filtration times (in Fig. 3.14-A: 148.9 kg/m^2 h at pH 3 and 51.3 kg/m^2 h at pH 11). On the other hand, irreversible fouling factors up to 99% were observed for both acid and alkaline media (see Fig. 3.14-B). These values are higher than those obtained by Schäfer et al. [31], 80% and 73%, during MF of 5 mg/L of HA with a commercial GVWP membrane (Millipore, nominal pore sizes of 0.22 μm) at pH 4.5 and 10 respectively. Therefore, the irreversible fouling factor of PSU ENMs must be reduced. One possible way is by means of surface modification using IP as it is indicated previously.

Based on the above reported and discussed results, in order to compare the HA separation factor and the irreversible fouling factor, only filtration tests at pH 11 will be considered for the surface modified PSU ENMs. Any PSU ENM prepared under the indicated range of the studied electrospinning parameters *F*, *V* and *G* is suitable for IP. In what follows, for sake of comparison, the ENM 8 and ENM 9 are selected for IP because of their different nanofiber diameters (Table 3.2) and thicknesses (178 ± 42 μm for ENM 8 and 98 ± 14 μm for ENM 9).

3.3.2.2 Effects of interfacial polymerization on the performance of PSU ENMs

The surface modified PSU ENMs by IP were used for the treatment of HA aqueous solution at pH 11 and the results (permeate flux, separation factor and irreversible fouling factor) were compared to those of the unmodified PSU ENMs.

The modified PSU ENMs showed much lower pure water permeability (*PWP*), 1689 kg/m^2 h bar, than that of the unmodified PSU ENMs, 19,467 kg/m^2 h bar. This is attributed to the formed polyester layer on the surface of PSU ENM. Similar results were observed by Mohammad et al. [32], Yung et al. [33] and Abu Seman et al. [16].

Figs. 3.15-A, 3.15-B and 3.16 show, as an example, a comparison between the unmodified and the surface modified PSU ENM 9 in terms of the permeate flux, irreversible fouling factor and HA separation factor, respectively. It can be seen that the polyester layer formed on the membrane surface by IP results in a decrease of both the permeate flux and the irreversible fouling factor along with a great improvement of the separation factor. These results are related to the improvement of the hydrophilicity of the membrane after surface modification as it was discussed previously. Other authors have also observed similar results when modifying the top surface of porous membranes by different techniques for filtration tests [33-35]. For instance, Chu et al. [34] modified the surface of ceramic-supported PES membranes by synthesizing a poly(vinyl alcohol) (PVA)/polyamide (PA) composite thin surface layer by IP technique, and developed hydrophilic membrane surfaces with much lower contact angles compared to the unmodified ones and consequently, could reduce the membrane fouling effectively. Liu et al. [35] by grafting the hydrophilic polymers PVA, polyethylene glycol (PEG), and chitosan onto PES UF flat sheet membranes via IP, observed reduction of water contact angles by 25 to 40% and an enhancement of antifouling property of the PES membrane surface.

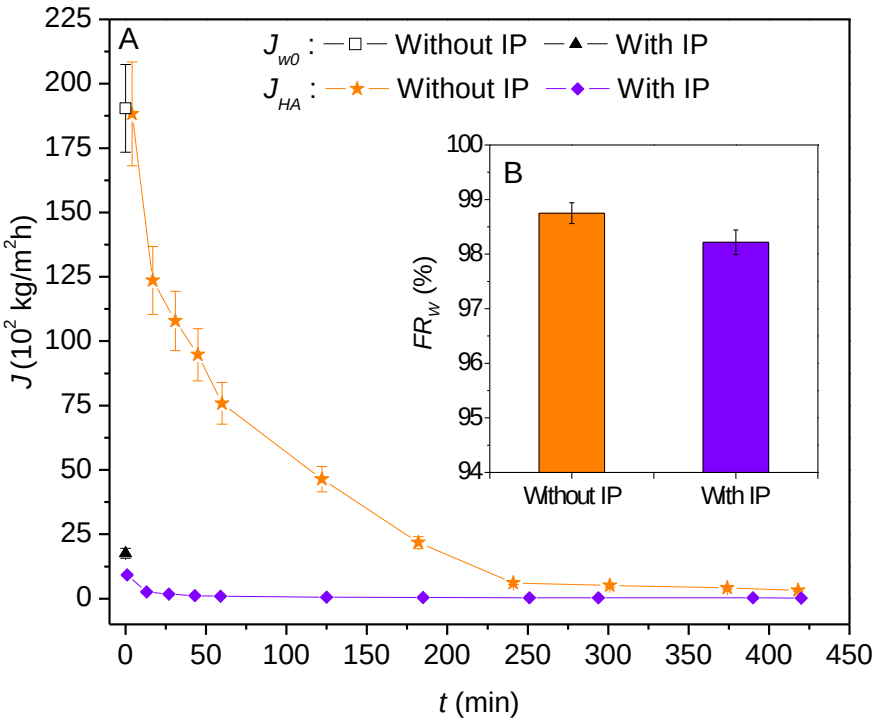

Figure 3.15. A) Permeate fluxes (J_{w0}, J_{HA}) and B) irreversible fouling factors (FR_W) of PSU ENM 9 unmodified and modified by interfacial polymerization (IP) with a heat post-treatment at 200°C for 75 min during the filtration test of 15 mg/L HA solution at pH 11. (ΔP = 10^5 Pa; J_{wf}(ENM 9 without IP) = 2.53 × 10^2 kg/m^2 h; J_{wf}(ENM 9 with IP) = 0.31 × 10^2 kg/m^2 h).

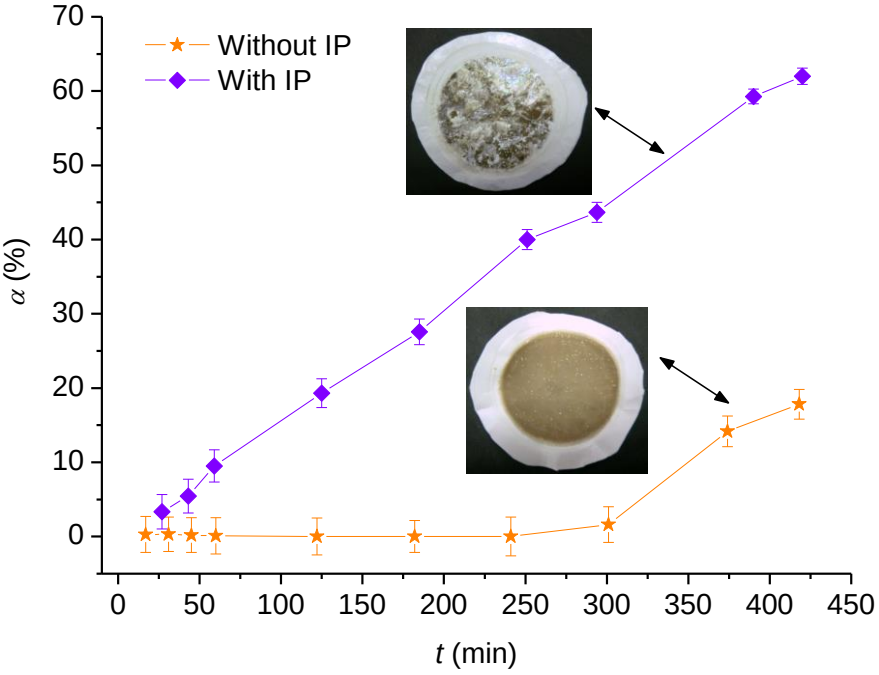

Figure 3.16. Separation factor (α) of PSU ENM 9 unmodified and modified by IP with heat post-treatment at 200°C for 75 min during the filtration tests of 15 mg/L HA solution at pH 11. The shown images correspond to the surface of the unmodified and modified PSU ENM 9 after HA filtration test.

The decrease of the permeate flux along with the increase of the separation factor after IP shown in Figs. 3.15 and 3.16 was also observed previously by other authors when using other monomers and supports [17, 33, 36]. Yung et al. [33] developed a new type of thin film nanofiber composite membrane (TFNC) prepared by IP of piperazine (PIP) on highly porous electrospun PES nanofibrous scaffold, and demonstrated that TFNC membrane exhibited lower permeation flux (up to 131%) and higher rejection factor (up to 6%) than the electrospun PES nanofibrous scaffold. They suggested that the decrease of the permeate flux could be due to the increase of the PA thickness layer that increases the hydraulic membrane resistance. Experimental results obtained by Yoon et al. [36] and Tang et al. [17] also confirmed that the apparently denser PA or polyester layer led to a distinct decrease in water permeability and an increase in salt rejection factor.

By analyzing the permeate fluxes of Fig. 3.15, it can be observed a rapid permeate flux decline at the beginning of the filtration process and then a decrease of the rate of this reduction tending to steady-state permeate fluxes. In this case, the specific time corresponding to the predominant change of the permeate flux decline with time is 40 min for the modified PSU ENM 9, whereas that of the unmodified membrane PSU ENM 9 is higher. The photographs shown in Fig. 3.16 correspond to the surface of the unmodified and the modified PSU ENM 9 after the HA filtration test. A clear reduction of membrane fouling can be observed on the membrane surface of the modified membrane by IP. At first sight, white sections free of HA deposition appear on the surface of the modified PSU ENM 9.

3.4 Conclusions

Various PSU ENMs were prepared by varying the electrospinning parameters (polymer flow rate, *F*; electric voltage, *V*; distance between the needle tip and the collector or gap, *G*) in the ranges: 1 to 3 mL/h, 16 to 20 kV and 15 to 10 cm, respectively. Out of these ranges beaded ENMs were formed. It was observed an increase of the diameter of the nanofiber with the increase of *F* and the decrease of *V* or *G*.

By applying a heat post-treatment to the prepared ENMs more nanofibers were fused together improving the compact structure of the PSU ENMs and reducing the diameter of the nanofibers.

Thin film composite polyester ENMs were successfully prepared by interfacial polymerization (IP) of BPA and TMC as it was confirmed by SEM, water contact angle measurements and ATR-FTIR spectra analysis. After surface modification the PSU ENMs become more hydrophilic.

HA MF results showed that the unmodified PSU ENMs were not selective in acidic media but clear HA separation factors of the unmodified PSU ENMs were observed when using HA

alkaline solutions reaching a separation factor value of 60%. Although higher reduction of the initial permeate flux of HA solution was observed at pH 3 compared to that at pH 11, the achieved steady-state permeate flux at pH 3 was higher than that at pH 11.

The modified PSU ENMs by IP showed much lower pure water permeability but greater HA separation factors, almost 4 times higher, than that of the unmodified PSU ENMs. This was attributed to the polyester layer formed on the PSU ENM surface, which produced a decrease of both the permeate flux and the HA irreversible fouling factor.

To further optimize the surface characteristics of the modified PSU ENMs by IP and improve their fouling resistance, systematic studies on the effects of the parameters involved in IP should be carried out (e.g. BPA and TMC concentrations, reaction time of BPA and TMC). These are the objectives of our current research studies.

References

[1] L. Huang, J.T. Arena, S.S. Manickam, X. Jiang, B.G. Willis, J.R. McCutcheon, Improved mechanical properties and hydrophilicity of electrospun nanofiber membranes for filtration applications by dopamine modification, Journal of Membrane Science, 460 (2014) 241-249.

[2] Z. Ma, M. Kotaki, S. Ramakrishna, Surface modified nonwoven polysulphone (PSU) fiber mesh by electrospinning: A novel affinity membrane, Journal of Membrane Science, 272 (2006) 179-187.

[3] H.-C. Kim, B.G. Choi, J. Noh, K.G. Song, S.-H. Lee, S.K. Maeng, Electrospun nanofibrous PVDF–PMMA MF membrane in laboratory and pilot-scale study treating wastewater from Seoul Zoo, Desalination, 346 (2014) 107-114.

[4] H.J. Song, C.K. Kim, Fabrication and properties of ultrafiltration membranes composed of polysulfone and poly(1-vinylpyrrolidone) grafted silica nanoparticles, Journal of Membrane Science, 444 (2013) 318-326.

[5] Y.-F. Zhao, L.-P. Zhu, Z. Yi, B.-K. Zhu, Y.-Y. Xu, Improving the hydrophilicity and fouling-resistance of polysulfone ultrafiltration membranes via surface zwitterionicalization mediated by polysulfone-based triblock copolymer additive, Journal of Membrane Science, 440 (2013) 40-47.

[6] M.N. Abu Seman, M. Khayet, N. Hilal, Nanofiltration thin-film composite polyester polyethersulfone-based membranes prepared by interfacial polymerization, Journal of Membrane Science, 348 (2010) 109-116.

[7] M. Essalhi, M. Khayet, C. Cojocaru, M.C. García-Payo, P. Arribas, Response surface modeling and optimization of electrospun nanofiber membranes, The Open Nanoscience Journal, 7 (2013) 8-17.

[8] D. Ghernaout, B. Ghernaout, A. Saiba, A. Boucherit, A. Kellil, Removal of humic acids by continuous electromagnetic treatment followed by electrocoagulation in batch using aluminium electrodes, Desalination, 239 (2009) 295-308.

[9] A. Maartens, P. Swart, E.P. Jacobs, Humic membrane foulants in natural brown water: characterization and removal, Desalination, 115 (1998) 215-227.

[10] W. Yuan, A.L. Zydney, Humic acid fouling during microfiltration, Journal of Membrane Science, 157 (1999) 1-12.

[11] W. Yuan, A.L. Zydney, Effects of solution environment on humic acid fouling during microfiltration, Desalination, 122 (1999) 63-76.

[12] W. Yuan, A. Kocic, A.L. Zydney, Analysis of humic acid fouling during microfiltration using a pore blockage–cake filtration model, Journal of Membrane Science, 198 (2002) 51-62.

[13] N. Bhardwaj, S.C. Kundu, Electrospinning: a fascinating fiber fabrication technique, Biotechnology Advances, 28 (2010) 325-347.

[14] M. Khayet, T. Matsuura, Membrane Distillation: Principles and Applications, Elsevier, The Netherlands, 2011.

[15] V. Pillay, C. Dott, Y.E. Choonara, C. Tyagi, L. Tomar, P. Kumar, L.C. Du Toit, V.M.K. Ndesendo, A review of the effect of processing variables on the fabrication of electrospun nanofibers for drug delivery applications, Journal of Nanomaterials, (2013) 1-22.

[16] M.N. Abu Seman, M. Khayet, N. Hilal, Development of antifouling properties and performance of nanofiltration membranes by interfacial polymerization and photografting techniques, in: N. Hilal, M. Khayet, C.J. Wright (Eds.) Membrane Modification: Technology and Apllications, CRC Press, Taylor & Francis Group, U.S.A., 2012, pp. 119-131.

[17] B. Tang, Z. Huo, P. Wu, Study on a novel polyester composite nanofiltration membrane by interfacial polymerization of triethanolamine (TEOA) and trimesoyl chloride (TMC), Journal of Membrane Science, 320 (2008) 198-205.

[18] W.-W. Cui, D.-Y. Tang, Z.-L. Gong, Electrospun poly(vinylidene fluoride)/poly(methyl methacrylate) grafted TiO_2 composite nanofibrous membrane as polymer electrolyte for lithium-ion batteries, Journal of Power Sources, 223 (2013) 206-213.

[19] L. Larrondo, M.R. St John, Electrostatic fiber spinning from polymer melts. I. Experimental observations on fiber formation and properties, Journal of Polymer Science: Part B: Polymer Physics, 19 (1981) 909-920.

[20] X. Zong, S. Ran, D. Fang, B.S. Hsiao, B. Chu, Control of structure, morphology and property in electrospun poly(glycolide-co-lactide) non-woven membranes via post-draw treatments, Polymer, 44 (2003) 4959-4967.

[21] A.E. Childress, M. Elimelech, Effect of solution chemistry on the surface charge of polymeric reverse osmosis and nanofiltration membranes, Journal of Membrane Science, 119 (1996) 253-268.

[22] S. Hong, M. Elimelech, Chemical and physical aspects of natural organic matter (NOM) fouling of nanofiltration membranes, Journal of Membrane Science, 132 (1997) 159-181.

[23] R.S. Swift, Humic substances II, in: M.H.B. Hayes, P.M. Carthy, R.L. Malcolm, R.S. Swift (Eds.), John Wiley and Sons, New York, 1989, pp. 449-465.

[24] M. Plaschke, J. Römer, R. Klenze, J.I. Kim, In situ AFM study of sorbed humic acid colloids at different pH, Colloids and Surfaces: Part A: Physicochemical and Engineering Aspects, 160 (1999) 269-279.

[25] M.J. Ariza, J. Benavente, Streaming potential along the surface of polysulfone membranes: a comparative study between two different experimental systems and determination of electrokinetic and adsorption parameters, Journal of Membrane Science, 190 (2001) 119-132.

[26] K.J. Kim, A.G. Fane, M. Nystrom, A. Pihlajamaki, W.R. Bowen, H. Mukhtar, Evaluation of electroosmosis and streaming potential for measurement of electric charges of polymeric membranes, Journal of Membrane Science, 116 (1996) 149-159.

[27] K. Xiao, X. Wang, X. Huang, T.D. Waite, X. Wen, Combined effect of membrane and foulant hydrophobicity and surface charge on adsorptive fouling during microfiltration, Journal of Membrane Science, 373 (2011) 140-151.

[28] R.F. Spinette, Fouling of a hydrophobic microfiltration membrane by algae and algal organic matter: mechanisms and prevention, in: Department of Geography and Environmental Engineering Johns Hopkins University, Maryland, 2008.

[29] C.-C. Ho, A.L. Zydney, A combined pore blockage and cake filtration model for protein fouling during microfiltration, Journal of Colloid and Interface Science, 232 (2000) 389-399.

[30] R. Seifollahy Astaraee, T. Mohammadi, N. Kasiri, Analysis of BSA, dextran and humic acid fouling during microfiltration, experimental and modeling, Food and Bioproducts Processing, 94 (2015) 331-341.

[31] A.I. Schäfer, U. Schwicker, M.M. Fischer, A.G. Fane, T.D. Waite, Microfiltration of colloids and natural organic matter, Journal of Membrane Science, 171 (2000) 151-172.

[32] A.W. Mohammad, N. Hilal, M.N. Abu Seman, A study on producing composite nanofiltration membranes with optimized properties, Desalination, 158 (2003) 73-78.

[33] L. Yung, H. Ma, X. Wang, K. Yoon, R. Wang, B.S. Hsiao, B. Chu, Fabrication of thin-film nanofibrous composite membranes by interfacial polymerization using ionic liquids as additives, Journal of Membrane Science, 365 (2010) 52-58.

[34] L.-Y. Chu, S. Wang, W.-M. Chen, Surface modification of ceramic-supported polyethersulfone membranes by interfacial polymerization for reduced membrane fouling, Macromolecular Chemistry and Physics, 206 (2005) 1934-1940.

[35] S.X. Liu, J.-T. Kim, S. Kim, M. Singh, The effect of polymer surface modification via interfacial polymerization on polymer–protein interaction, Journal of Applied Polymer Science, 112 (2009) 1704-1715.

[36] K. Yoon, B.S. Hsiao, B. Chu, High flux nanofiltration membranes based on interfacially polymerized polyamide barrier layer on polyacrylonitrile nanofibrous scaffolds, Journal of Membrane Science, 326 (2009) 484-492.

4

Nanostructured membranes

Heat post-treatment effect on structural properties and filtration performance

The structure and morphology of self-sustained electrospun nanofibrous membranes (ENMs) are key factors determining membrane performance for filtration applications. In this study, heat post-treatment (HPT) method was applied to modify the structural and morphological properties of polysulfone (PSU) ENMs, to improve their filtration performance and to obtain membranes suitable for wastewater treatment. The influence of the HPT temperature and time on the morphological structure of the PSU ENMs as well as on fouling and filtration performance was investigated. Microfiltration (MF) tests were conducted using humic acid model solutions with a concentration of 15 mg/L at pH 11. Increasing the HPT temperature or time, led to an increase of the mean nanofiber diameter along with a decrease of the mean size of the inter-fiber space, the void volume fraction and the water contact angle. ENMs treated with a higher HPT temperature and a longer time exhibited higher nanofibers interconnectivity and a more compact structure with a smaller size of inter-fiber spaces. Under the same MF operating conditions, a commercial polyethersulfone (PES) MF membrane (HPWP, Millipore) had lower filtration performance (i.e. lower performance index, *PI,* 82 kg/m^2 h) than the treated-optimized PSU ENMs (i.e. 147 and 133 kg/m^2 h for ENMs 9 and 10, respectively). The obtained results confirm the good performance of the developed PSU ENMs for MF applications.

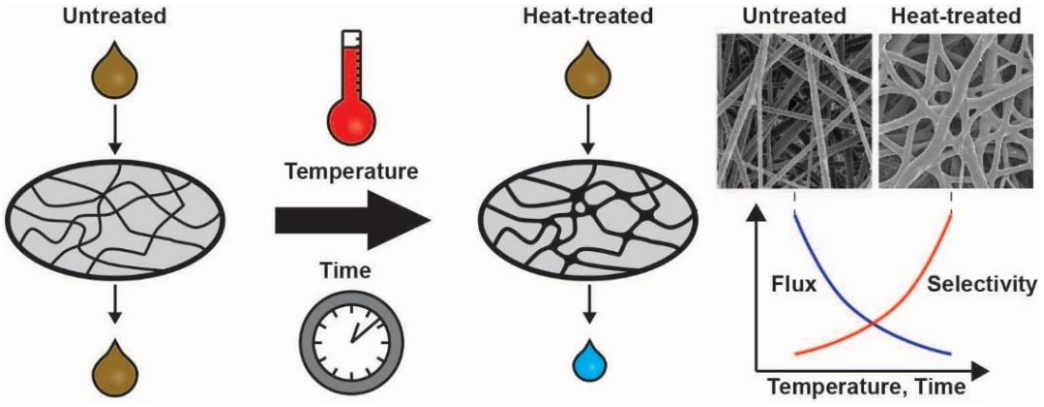

Heat-treated optimized polysulfone electrospun nanofibrous membranes for high performance wastewater microfiltration

4.1 Introduction

The development of efficient membrane filtration technologies is especially important as water shortage has become a growing global problem in recent years [1]. The improved compactness, low cost operation, high energy efficiency and high throughput enable membrane separation processes to compete successfully with conventional separation processes. In fact, membranes are an environmentally-friendly method highly utilized in waste treatment, water purification and in clarification and concentration processes [2]. However, the fabrication of adequately designed membranes for a specific application is challenging [3]. Electrospinning is an attractive and efficient technique for polymer solution processing that provides a simple and versatile way to prepare ultrafine polymeric fibers with micro- to nano-scale diameters, ranging from 50 nm to 10 μm thickness [4, 5]. Electrospun fibers are typically collected in the form of a non-woven mesh, which is of importance for a variety of applications including semi-permeable membranes, filters, composite reinforcement and scaffolding used in tissue engineering [6]. Electrospun nanofibrous membranes (ENMs) have a great potential for membrane filtration due to their attractive structural features, such as high porosity and interconnected open pore structure, micro-scale interstitial space, controllable thickness and a large surface area to volume ratio [7]. In ENMs the pores are induced by the entanglement of interconnected nanofibers (i.e. inter-fiber space). The mean pore size of ENMs correlates with the nanofiber diameter [8]. Thus, the pore size of ENMs can be tuned to meet different filtration requirements by changing the nanofiber diameter.

Advantages of using ENMs for water treatment include high permeability, mainly related to their high void volume fraction (i.e. porosity), and good separation factor due to the highly tortuous path through the nanofibrous structure and the remaining static charge in the nanofibers after electrospinning, which helps to separate different contaminants [9-11]. In recent years, microfiltration (MF) has attracted increasing attention in the field of wastewater treatment and reclamation as an alternative to conventional water treatment processes (i.e. coagulation, sedimentation and sand filtration) [12]. MF offers several advantages including

easier control of operation, and reduced maintenance and sludge production. However, a major factor that limits the use of membranes in water treatment is membrane fouling, which reduces water production rates and increases energy consumption [13]. Fouling reduces the effective membrane surface for filtration leading to a strong decline of permeate flux and worse separation performance [7, 14, 15]. Given that membrane properties have a high impact on fouling, it is important to understand their effects well in order to develop adequate membranes that are capable to mitigate fouling. For instance, it has been demonstrated that membrane hydrophobicity, roughness, pore size and pore morphology affect membrane-foulant-interactions and consequently, fouling effects [16].

In the literature, there is a large number of studies using nanofibrous scaffolds or ENMs as pre-filters for particulate removal through MF/UF applications. Some of the most mentioned drawbacks of ENMs are the low mechanical strength and the difficulty of handling them after electrospinning [17]. Several methods were proposed to overcome these problems before their application in filtration: plasticization [18]; polymer blending [19]; solvent induced inter-nanofiber bonding [9]; hot-pressing [20-22]; heat treatment [5-7, 23-26]; addition of nanoparticles [27, 28]; use of crosslinking agents [29]. One of the most effective approaches is to enhance the bonding at junction points in the nanofiber mat by welding the nanofibers together, as for example by applying a heat post-treatment (HPT) (i.e. heating the mat between the glass transition temperature of the electrospun polymer and its melting temperature). Compared to plasticizing and polymer blending, an appropriate heat treatment may be more environmental friendly and less energy consuming. The incorporation of nanoparticles in the membrane matrix, such as titanium dioxide, usually needs a post-treatment of the membrane (e.g. hydrothermal bath, annealing), which increases the membrane fabrication costs [27]. Moreover, although hot-pressing has been reported to increase the structural integrity and mechanical strength of the ENMs, heat treatment can also induce a change in the molecular structure of the polymer, leading to a higher degree of nanofibers crystallinity [30] and, consequently, to a greater elastic modulus of the ENMs [2, 23].

In this study, the filtration properties of polysulfone electrospun nanofibrous membranes (PSU ENMs) were improved by the application of HPT. The effects of the HPT temperature and the HPT time on the structural and morphological properties of the membranes (i.e. porosity, pore size and its distribution, wettability, thickness) were investigated, because these factors affect the membrane filtration performance [2, 31]. The filtration performance index (*PI*) was considered to select the optimum heating conditions for the application of the ENMs in wastewater treatment by MF.

4.2 Materials and methods

4.2.1 Materials

The polymer polysulfone (PSU, UDEL P-3500 LCD, Solvay Specialty Polymers; *Mw* = 79,000 g/mol; ρ_{PSU} = 1.24 g/cm^3) and the mixture of solvents *N, N*-dimethyl formamide (DMF, Sigma-Aldrich) and tetrahydrofuran (THF, Sigma-Aldrich) were used to prepare the spinning solution. The organic foulant humic acid (HA, Fluka) with a molecular weight of 4.1 kDa was utilized to prepare the feed solution for the MF tests. Sodium hydroxide (NaOH, Panreac) was used to prepare a concentrated HA stock solution of 1 g/L. Hydrochloric acid (HCl, Sigma-Aldrich) was employed to adjust the pH of the diluted HA feed solutions (15 mg/L) to 11. Isopropyl alcohol (IPA, Sigma-Aldrich) was used to determine the void volume fraction (ε) of the PSU ENMs. POREFIL®, a fluorinated hydrocarbon (chemical nature: pefluoroether; surface tension: 16 mN/m, vapor pressure: 3.33 Pa; viscosity: 4.4 mPa·s, POROMETER) was used as a wetting liquid to perform the inter-fiber space measurements.

4.2.2 Preparation and characterization of the polymer solution

The polymer solution was prepared by mixing DMF (64 wt.%) and THF (16 wt.%) at room temperature with a magnetic stirrer (IKA, RCT basic) for 2 min at 80 rpm. Subsequently, 20 wt.% PSU was added to the solvent mixture and the solution was stirred at 60°C and 80 rpm for 10 h until the PSU was completely dissolved and the resulting polymer solution homogeneous.

The polymer solution was characterized by measuring its surface tension, viscosity and electrical conductivity. The surface tension of the spinning solution was determined at room temperature by the pendant drop shape analysis using an Optical Contact Angle Meter (CAM 200) and a stainless-steel needle with an outer diameter of 1.825 mm. The volume of all drops was maintained constant at 16.08 ± 0.82 µL. The viscosity of the spinning solution was measured with a Digital Viscometer (Brookfield, Model DV-I+) in a cylindrical sample container and using the SC4-31 spindle at 30 rpm and a shear rate of 10.2 s^{-1}. The temperature of the spinning solution was maintained constant at 25°C by a thermostat (Techne, Model TU-16D). The electrical conductivity of the polymer solution was measured at 25°C using a conductivity meter (CyberScan con11 Conductivity/TDS/°C, Eutech Instruments).

4.2.3 Preparation of PSU ENMs

PSU ENMs were prepared by electrospinning using the polymer solution indicated in the previous section. The used electrospinning system was described elsewhere [7]. In this study, all PSU ENMs were prepared under the previously obtained optimum electrospinning parameter conditions: a polymer solution flow rate of 2.5 mL/h, an electric voltage of 16 kV, a distance between the needle tip and the collector or air gap of 10 cm and an electrospinning time of 45 min [7]. The ambient conditions during electrospinning fabrication were a temperature between 20–25°C and a relative humidity in the range 38–41%.

4.2.4 Heat post-treatment (HPT) of PSU ENMs

The silky, fluffy and loose structure of the PSU ENMs complicated their handling after the electrospinning step. In addition, it was observed that PSU ENMs without any HPT were not useful for filtration application as the membranes were not capable to achieve any separation. Thus, a HPT step was carried out to get membranes with improved structural integrity and greater filtration performance.

The HPT was carried out in a ceramic oven (CWF 13/13, Carbolite®). Before being placed into the oven, the ENMs deposited on the aluminum foil were attached to a smaller rounded copper support to avoid shrinkage of the membrane during heating. The samples were first heated from 70°C to the established HPT temperature (i.e. 190–250°C) at a rate of 30°C/min (this process took between 6–8 min, depending on the final temperature) and then exposed to the HPT temperature for a specific HPT time (i.e. 20–300 min). HPT temperatures above the boiling point of the used solvents were chosen to guarantee their complete evaporation from the formed ENMs. To induce good bonding points between nanofibers (i.e. points in which nanofibers were fused together) the applied temperatures were also higher than the glass transition temperature of the used polymer (185°C for PSU). After the HPT step, ENMs were wetted with DI water, peeled off from the aluminum foil, dried at room temperature for 24 h and stored until use.

In order to perform a systematic and accurate study on the effect of the HPT on the morphological structure of PSU ENMs, all membranes were obtained from the same manufacturing batch, avoiding as many steric dissimilarities (in terms of, for example, pore size, structure, porosity and surface roughness) between them as possible. In addition, SEM images of membranes with an initial thickness of 900 ± 50 μm were used to select those ENMs with similar initial nanofibrous structure (i.e. uniformity of the nanofiber web).

It was observed that not all the heat post-treatments (HPTs) led to the same morphology and structure of the membranes. In order to fully understand the influence of the applied HPT on the morphological and structural changes of PSU ENMs, a preliminary study with 90

membranes and 30 different HPTs was conducted to determine the operational working area (i.e. region of interest) of the HPT as shown later on. Then, a systematic study in this region of interest was conducted and eleven PSU ENMs were evaluated and compared in terms of their morphological characteristics (i.e. mean nanofiber diameter, mean size of the inter-fiber space, water contact angle, void volume fraction, etc.). Moreover, MF tests were carried out with these eleven ENMs to determine the optimum region of the HPT, in which the treated membranes exhibit the highest filtration performance indexes.

4.2.5 Characterization of PSU ENMs

The thickness (δ) of each PSU ENM was measured at 40 different spots on the sample using a micrometer equipped with a feeler (ISL Isocontrol). The final thickness of each sample was determined as the average value of the measured thicknesses with its corresponding standard deviation.

The morphology of the surface of the PSU ENMs was evaluated with a field emission scanning electron microscope (FESEM, JEOL Model JSM–6335F) operating at 5 kV. Before conducting the SEM analysis, a thin gold layer of approximately 5 nm was sputter-coated on the membrane surface using an evaporator (EMITECH K550 X) for one minute under 25 mA. SEM images were analyzed with the UTHSCSA Image Tool 3.0 software to determine the nanofiber diameter. For each membrane, at least three SEM images were analyzed and the diameters of a total number of 100 nanofibers/per image were measured. Statistical analyses were applied to determine the nanofiber diameter distribution (i.e. nanofiber diameter histogram). The weighted arithmetic mean of the nanofiber diameters (λ_w) along with its corresponding weighted standard deviation (s_w) were evaluated as follows:

$$\lambda_w = \lambda_0 + \frac{h}{N}\sum_{j=1}^{m} u_j \cdot FC_j \tag{4.1}$$

$$s_w = \sqrt{\left(\frac{1}{N}\sum_{j=1}^{m}\left(u_j^2 \cdot FC_j\right) - \left(\frac{1}{N}\sum_{j=1}^{m}\left(u_j \cdot FC_j\right)\right)^2\right) \cdot h^2} \tag{4.2}$$

where m denotes de number of bins (disjoint categories), h is the width, $h = (\lambda_{max} - \lambda_{min})/m$, FC is the frequency count, N is the number of samples in the statistical set (in our case $N = 100$), λ_0 is the dominant characteristic of the statistical set that corresponds to the highest peak, u is a variable defined as $u = (\lambda_c - \lambda_0)/h$ and λ_c is the bin characteristic (or bin center).

The final value of the weighted arithmetic mean of the nanofiber diameters ($\overline{\lambda_w}$) with its corresponding weighted standard deviation ($\overline{s_w}$) for the PSU ENMs was determined as the arithmetic mean and standard deviation of all SEM samples evaluated for each membrane.

The water contact angle (θ_w) values on the surface of the PSU ENMs were measured at room temperature using a computerized optical system (CAM100 device, Sb) equipped with a CCD camera and an image analysis software (Cam200usb). This system enables the acquisition of photographs of the water drop on the sample surface and to evaluate the contact angle. A Hamilton stainless steel needle was used to control the volume of the drops, which was between 12 and 14 μL. Every drop was recorded taking five images within 4 s. For each ENM sample at least 10 different drops were considered to determine the final averaged θ_w value together with its standard deviation.

The void volume fraction (i.e. porosity, ε) is defined as the ratio between the volume of the inter-fiber space and the total volume of the membrane. The value of ε was determined by measuring the density of the polymer material (ϱ_{pol}) using isopropyl alcohol (IPA), which penetrates inside the inter-fiber space, and the density of the membrane (ϱ_m) using distilled water, which does not get into the inter-fiber space, according to equation (3) [32]:

$$\varepsilon\,(\%) = \left(1 - \frac{\varrho_m}{\varrho_{pol}}\right) \cdot 100 \tag{4.3}$$

The inter-fiber space (d_f) of the PSU ENMs was measured with capillary flow porometry (CFP) using a gas–liquid displacement Porometer (POROLUX™ 100, Porometer). CFP uses the displacement of a wetting liquid inside a porous network by means of an inert gas flow to measure d_f. In this study, POREFIL® (Porometer) was used as the wetting liquid agent, compressed air was employed as the inert gas and the applied hydrostatic pressure was varied in the range of 0–0.7 MPa at room temperature (~23°C). The ENMs were first wetted by the POREFIL® and the gas permeation flow was measured by increasing the transmembrane pressure to obtain the S shaped wet curve. Subsequently, the dry curve was obtained by measuring the gas flow through the dry sample as a function of the applied pressure. Both, the wet and the dry curves were used to determine the mean size of the inter-fiber space ($\overline{d_f}$, which corresponds to the size of the inter-fiber space at which the wet curve intersects the half-dry curve that corresponds to 50% gas flow through the dry membrane), the inter-fiber space distribution or differential filter flow (*DFF*, which represents the increase in flow rate per unit increase in inter-fiber space), and the cumulative filter flow distribution (*CFF*, i.e. percentage of the total gas flow that goes through inter-fiber spaces of a certain size and larger) of the PSU EMNs.

4.2.6 Filtration experiments

The experimental set up used for MF tests was described elsewhere [7]. The effective filtration area of the membrane was (21.76 ± 0.01) 10^{-4} m^2. The feed solution was kept at room temperature (~23°C) and the feed flow rate was maintained at 1.6–1.8 L/min.

To carry out the MF tests, diluted HA feed solutions of 15 mg/L were prepared from a concentrated HA stock solution of 1 g/L. In our previous study, it was demonstrated that PSU ENMs were not selective to HA in acidic media (pH = 3), whereas clear HA separation factors were observed when using alkaline HA solutions (pH = 11) [7]. Thus, in this study the solution pH was adjusted to 11 by adding 2 M NaOH as needed using a pH/Ion meter (692, Metrohm). A spectrophotometer (UV/VIS 7315, Jenway) was used to determine the HA concentration of the permeate, the retentate and the feed samples at a wavelength of 254 nm.

Before carrying out the MF tests, all membranes were pre-compacted by circulating distilled water at a transmembrane pressure (ΔP) of 3 × 10^5 Pa for 3 h. Subsequently, MF tests were conducted at a transmembrane pressure of 10^5 Pa using first distilled water for 1 h to determine the pure water permeability (*PWP*), then the aqueous HA feed solution for 7 h (i.e. HA test), and finally distilled water again for 1 h. The permeate fluxes of both HA solution (J_{HA}) and distilled water before (J_{w0}) and after (J_{wf}) each HA test were measured and the irreversible fouling factor (FR_W) of the membrane was evaluated as follows [33]:

$$FR_W\,(\%) = \frac{J_{w0} - J_{wf}}{J_{w0}} \cdot 100 \tag{4.4}$$

The permeate fluxes were calculated using the weight of the permeate produced during a specific time on an electronic balance (AND GF-1200) as follows:

$$J\,(\mathrm{kg/m^2\,h}) = \frac{m}{A_{ef} \cdot \Delta t} \tag{4.5}$$

where m is the mass of the obtained permeate over a period of time Δt, and A_{ef} is the effective filtration membrane area.

The separation factor (α) of the membranes was evaluated using the following equation:

$$\alpha\,(\%) = \left(1 - \frac{2C_p}{C_r + C_f}\right) \cdot 100 \tag{4.6}$$

where C_p, C_r and C_f are the HA concentration of the permeate, retentate and feed solutions, respectively.

The initial HA permeate flux decline (FD_0), which relates to the beginning of the fouling of the membranes, was determined as follows:

$$FD_0 = 1 - \frac{J_{HA_0}}{J_{w0}} \tag{4.7}$$

where J_{HA_0} corresponds to the HA permeate flux at the beginning of the filtration test.

The filtration performance of the membranes was evaluated considering the performance index (*PI*), which takes into account the final values of both the HA permeate flux (J_{HA_f}) and the HA separation factor (α_f) obtained at the end of the HA test (after about 420 min of experiment):

$$PI\ (\mathrm{kg/m^2\,h}) = \frac{J_{HA_f} \cdot \alpha_f}{100} \tag{4.8}$$

4.3 Results and discussions

4.3.1 Polymer solution characterization

The surface tension of the PSU electrospun solution is 35.8 ± 1.8 mN/m, its viscosity is 485.3 ± 0.8 mPa·s and its electrical conductivity is 9.12 ± 0.15 μS/cm. Similar values for the surface tension (35.47 mN/m) and the viscosity (520 mPa·s) of the PSU dope solution (20% wt/v PSU in DMAC/acetone (9:1) mixed solvents) were reported by Yuan et al. [34] when preparing ultrafine PSU fibers by electrospinning.

4.3.2 PSU ENMs preparation and characterization

4.3.2.1 Preliminary evaluation of PSU ENMs prepared with different HPTs and determination of the region of interest of the HPT

A preliminary HPT study (see Fig. 4.1) was carried out to evaluate 90 membranes treated with 30 different HPTs in terms of damage, thickness homogeneity and degree of networking (i.e. quantity of bonding points between nanofibers) after the HPT. A visual criterion was used to evaluate the damage of the membranes due to the HPT (see Fig. 11.1 in Appendix A), giving 0 points to membranes that were burned on most of the surface, 5 points to membranes with only few small burned spots or 10 points to membranes without any burned spot on the surface. The final thickness homogeneity of the membrane was evaluated by means of the relative error of the thickness ($E_r = (\Delta\delta/\delta)\cdot 100$), giving 0, 1.5, 3.5, 5, 6.5, 8.5 or 10 points to membranes with a relative error of the thickness between 40–100, 30–40, 20–30, 15–20, 10–15, 5–10 and 0–5%, respectively. Finally, SEM images of the PSU ENMs surfaces were used to evaluate the degree

of networking and interconnectivity of the PSU ENMs, giving 0, 2.5, 5, 7.5 or 10 points to membranes with a percentage of nanofiber intersections bonded < 20, 20–40, 40–60, 60–80 and > 80%, respectively (see Fig. 11.2 in Appendix A). The individual scores from the three evaluations were averaged to obtain a normalized score from 0 to 10 for each membrane. The scores of all membranes fabricated under the same HPT condition were averaged to obtain a single score for that condition.

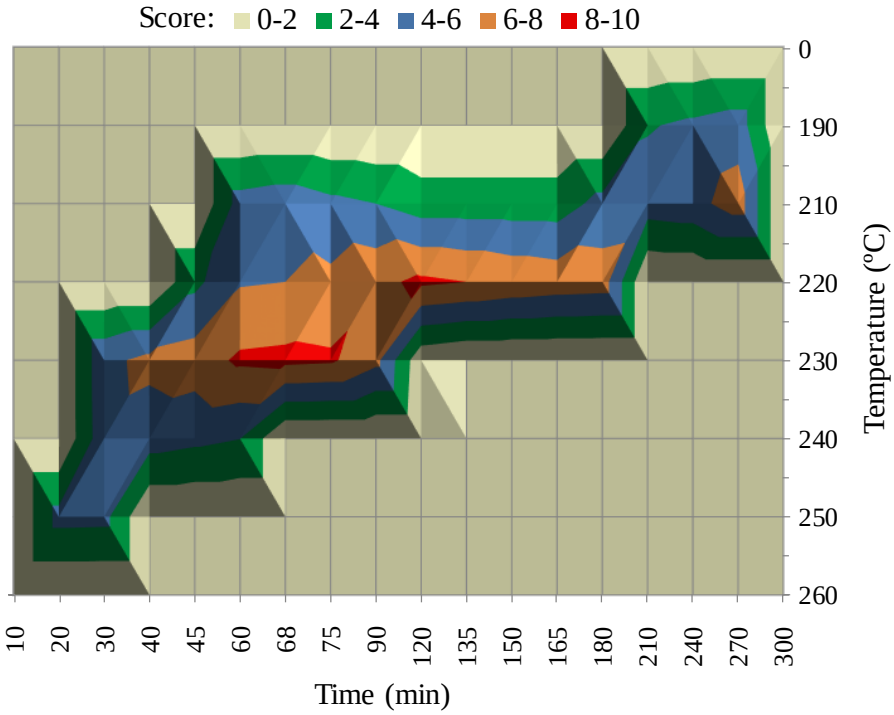

Figure 4.1. 3D surface graph showing the result of the preliminary evaluation of the PSU ENMs treated with different heat post-treatments (HPTs).

Fig. 4.1 shows a three-dimensional representation of the average scores of the different HPTs. A region of interest for further investigation was identified (average score > 6, orange and red colors), which corresponded to (210°C, t > 250 min), (220°C, 65 < t < 180 min) and (230°C, 35 < t < 90 min). Eleven different HPTs within the region of interest were used to systematically study the effects of the HPT temperature and time on the morphology and structure of the PSU ENMs as well as on their filtration performance.

4.3.2.2 Effects of the HPT temperature and time on the morphology and structure of PSU ENMs

Table 4.1 summarizes the morphological characteristics of the eleven PSU ENMs treated with different HPTs. It must be pointed out that the HPTs used to treat the ENM 1 (210°C/60 min), ENM 2 (210°C/90 min) and ENM 3 (220°C/60 min) were not within the region of interest, but they were useful to systematically study the effects of the changes of the HPT temperature. Figs. 4.2–4.5 show the morphological and structural properties of the PSU ENMs

prepared with the different HPTs. One of the main effects of the application of the HPT was the reduction of the thickness of the ENMs, which decreased from 900 to 80–380 μm, depending on the applied HPT.

Table 4.1. Prepared PSU ENMs with different heat post-treatments and their corresponding morphological characteristics: thickness (δ), weighted arithmetic mean of the nanofiber diameters ($\overline{\lambda_w}$) with its corresponding weighted standard deviation ($\overline{s_w}$), water contact angle (θ_w), void volume fraction (ε) and mean size of the inter-fiber space ($\bar{d}_f$).

Membrane	Heat treatment		Morphological characteristics				
	T (°C)	t (min)	δ (μm)	$\overline{\lambda_w} \pm \overline{s_w}$ (μm)	θ_w (°)	ε (%)	$\bar{d}_f$ (μm)
ENM 1	210	60	338 ± 15	0.69 ± 0.03	137.4 ± 1.7	94.1 ± 0.2	3.35 ± 0.03
ENM 2	210	90	373 ± 24	0.70 ± 0.06	135.9 ± 2.1	92.8 ± 0.4	3.12 ± 0.02
ENM 3	220	60	380 ± 69	0.70 ± 0.03	135.0 ± 3.2	90.2 ± 1.1	2.98 ± 0.03
ENM 4	220	90	251 ± 47	0.73 ± 0.02	128.1 ± 3.3	83.6 ± 1.7	2.89 ± 0.05
ENM 5	220	120	116 ± 33	0.74 ± 0.07	125.2 ± 2.8	79.5 ± 2.5	2.80 ± 0.05
ENM 6	220	150	106 ± 18	0.77 ± 0.04	121.0 ± 2.8	77.1 ± 2.2	2.72 ± 0.05
ENM 7	220	180	92 ± 18	0.85 ± 0.04	120.4 ± 2.6	72.3 ± 1.5	2.65 ± 0.05
ENM 8	230	45	257 ± 17	0.69 ± 0.06	135.4 ± 3.3	92.3 ± 1.2	3.20 ± 0.04
ENM 9	230	60	213 ± 65	0.72 ± 0.02	125.7 ± 3.1	81.7 ± 2.1	3.04 ± 0.05
ENM 10	230	75	82 ± 29	0.76 ± 0.03	119.3 ± 1.7	80.8 ± 1.7	2.85 ± 0.03
ENM 11	230	90	147 ± 17	0.83 ± 0.04	115.4 ± 3.6	78.2 ± 2.6	2.67 ± 0.03

The changes of the surface of the PSU ENMs when increasing the HPT temperature from 210 to 230°C can be observed in Fig. 4.2. For both 60 and 90 min of HPT time, an increase of the mean nanofiber diameter ($\overline{\lambda_w}$) (see Table 4.1 and Fig. 4.4) and nanofibers interconnectivity was observed when increasing the HPT temperature, resulting in membranes with improved integrity and a more compact structure [1, 5]. The same morphological and structural changes (i.e. increase of $\overline{\lambda_w}$ and the number of interconnected nanofibers) were observed by Liang. et al. [25] on PVDF ENMs when increasing the applied heat treatment temperature from 150 to 160°C. The increase of $\overline{\lambda_w}$ is attributed to the shrinkage of the nanofibers at high temperatures [6, 23, 25].

By comparing the SEM images of 60 min of HPT time with those of 90 min (Fig. 4.2), it can be noticed that the effect of increasing the HPT temperature was stronger at higher HPT time.

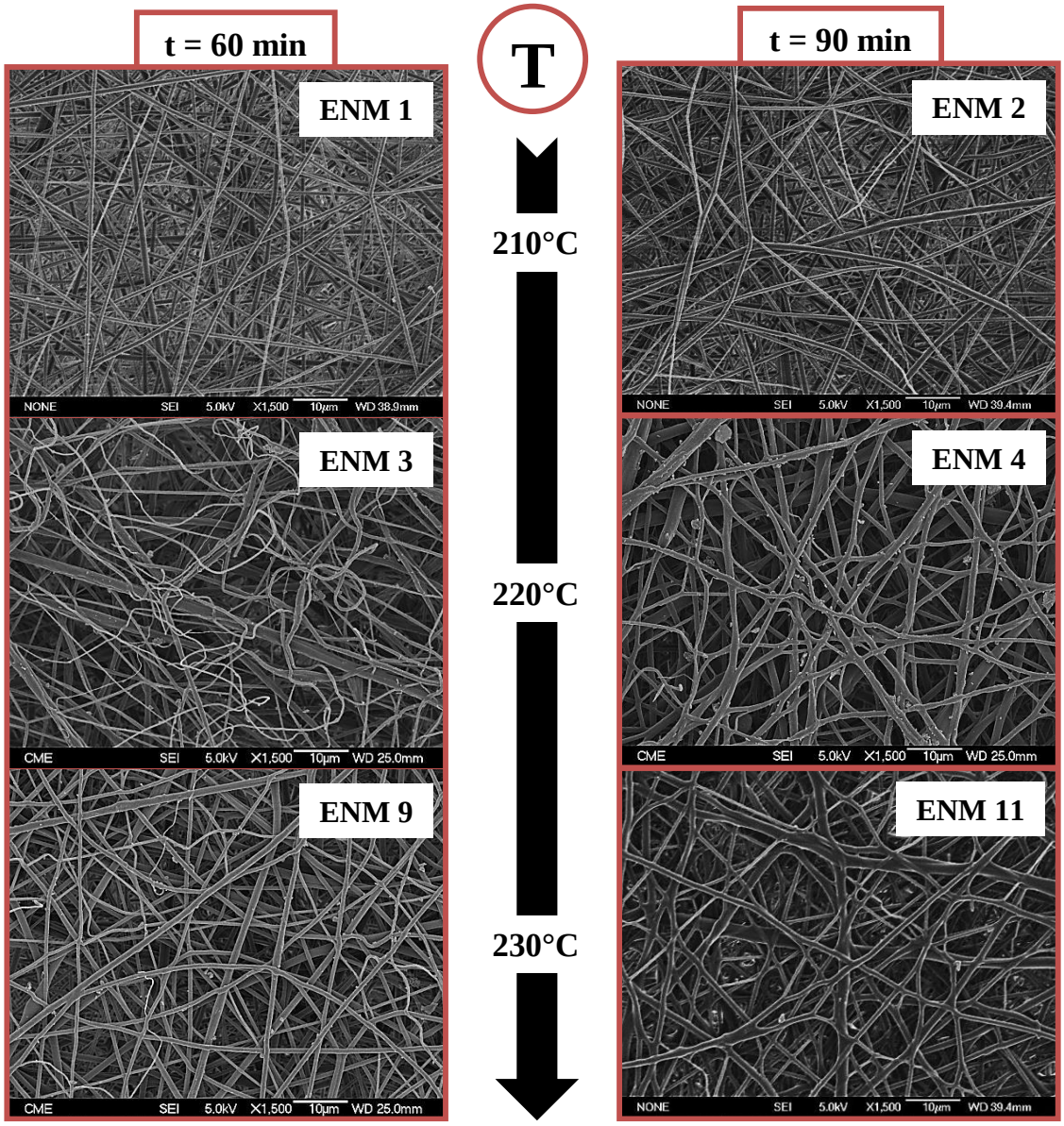

Figure 4.2. SEM images of the surface of PSU ENMs prepared with a HPT time of 60 and 90 min at a HPT temperature of 210, 220 and 230°C. All images were taken at X1500 magnification.

For instance, ENMs 4 and 11 resulted in larger values of $\overline{\lambda_w}$ (i.e. thicker nanofibers, see Table 4.1 and Fig. 4.4) and higher degree of networking than that of the ENMs 3 and 9, respectively. Furthermore, ENMs 4 and 11 had more and larger junctions between nanofibers compared with those of the ENMs 3 and 9.

As can be seen in Fig. 4.3, different increments of the HPT time (30 and 15 min) for the membranes treated at 220 and 230°C, respectively, were established to avoid burning the membranes, as the effects of increasing the HPT time on the structure and morphology of the membranes were notably stronger when the applied temperature was higher. In fact, the maximum applied HPT time without observing any burned spot on the membrane was 180 min at 220°C, twice as long as that for the membranes treated at 230°C (90 min).

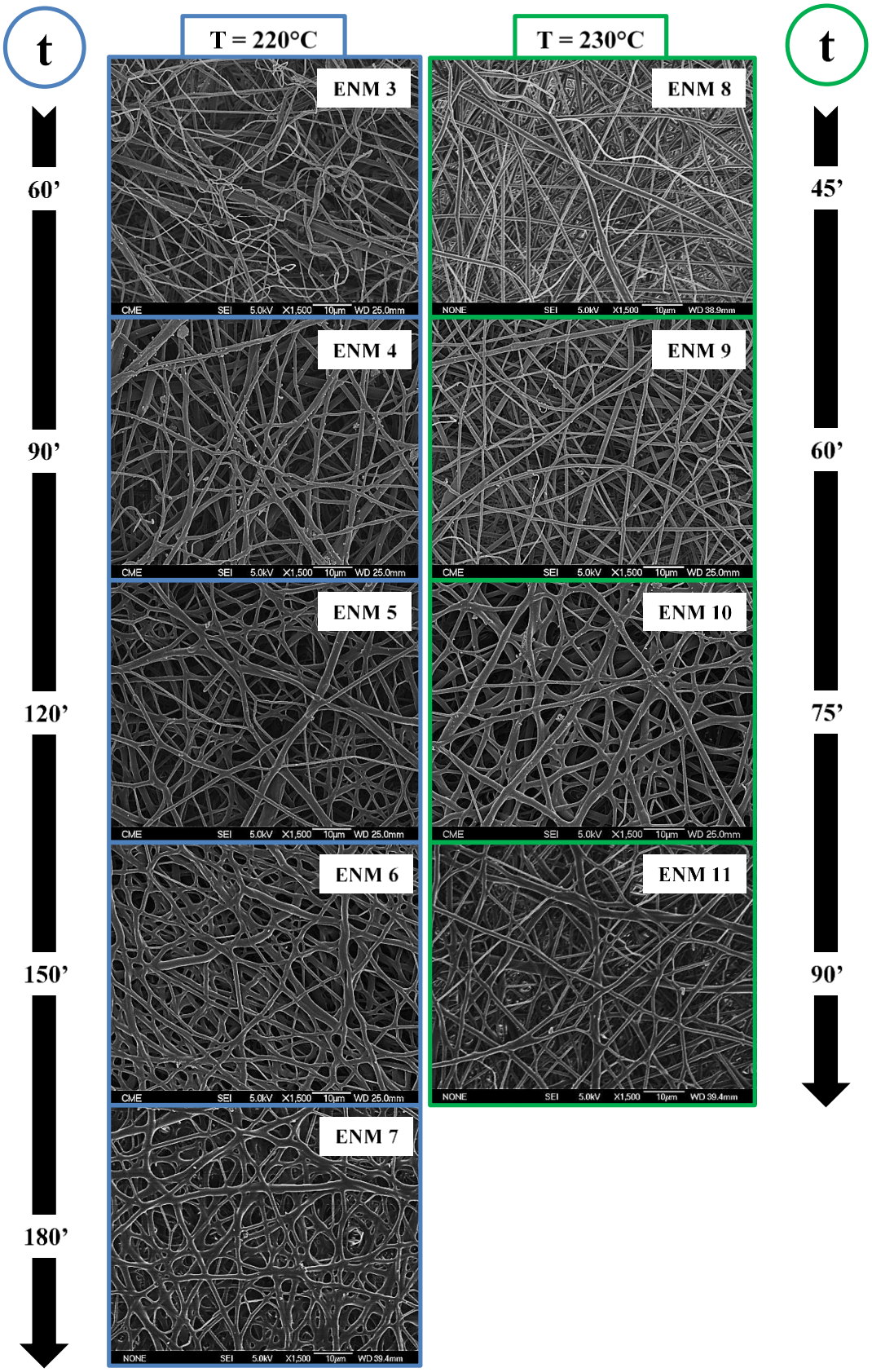

Figure 4.3. SEM images of the surface of PSU ENMs prepared with a HPT temperature of 220 and 230°C at different HPT times (from 45 to 180 min). All SEM images were taken at X1500 magnification.

No connection points between nanofibers could be detected on the surface of the membranes prepared with the lowest HPT times (ENM 3, 60 min at 220°C, and ENM 8, 45 min at 230°C). In these cases, the nanofibers were smaller in diameter (i.e. thinner nanofibers), cylindrical and curled. Similar nanofiber structures were also reported by Homaeigohar et al. [24] on polyethersulfone (PES) ENMs without heat-treatment.

When increasing the HPT time at 220 or 230°C, an enhancement of the degree of networking was observed and the nanofibers became thicker and flatter, resulting in membranes with a more compact structure. In addition, the inter-fiber spaces of the PSU ENMs, which were large and without any specific geometrical shape for low HPT times, became smaller with rounder edges when the HPT time was increased. For instance, the nanofiber network of the membrane prepared with the highest HPT time, 180 minutes at 220°C (see SEM image of ENM 7 in Fig. 4.3), had relatively small and rounded inter-fiber spaces together with more fused nanofibers. Similar membrane morphologies were also observed in electrospun poly (lactic acid) (PLA) membranes treated for 120 min at 90°C [26].

Increasing the HPT temperature from 210 to 230°C led to an increase of $\overline{\lambda_w}$ by 4.6 and 18.9%, respectively, for the applied HPT times of 60 and 90 min (Fig. 4.4-A left). It is worth noting that increasing the HPT time by only 30 min, resulted in ~4 times greater enhancement of $\overline{\lambda_w}$ at the highest HPT temperature. Higher increases of $\overline{\lambda_w}$ were achieved by increasing the HPT time from 60 to 180 min at 220°C and from 45 to 90 min at 230°C (22.4 and 19.7%, respectively, Fig. 4.4-A right). Furthermore, the nanofiber diameter distribution histograms of the PSU ENMs (Fig. 11.3 in Appendix A) became broader when increasing both the HPT temperature and the HPT time as claimed by Liang et al. [25]. For example, the nanofiber diameter distribution of the ENM 7 treated at 220°C for 180 min (0.5 to 1.6 μm) was wider than that of the ENM 3 treated at 220°C for 60 min (0.3 to 1.2 μm).

The increase of the HPT temperature or time also resulted in a left shift of both the cumulative (*CFF*, Fig. 4.5 A and B left) and the differential (*DFF*, Fig. 4.5 A and B right) inter-fiber space distributions along with a decrease of the mean size of the inter-fiber space ($\overline{d_f}$) of the membranes. When the HPT temperature was increased from 210 to 230°C, $\overline{d_f}$ decreased by 15.5%, and when the HPT time was increased from 45 to 90 min, $\overline{d_f}$ decreased by 18.7%. The detected reduction of $\overline{d_f}$ was mainly caused by the increase of $\overline{\lambda_w}$ and the degree of networking (Fig. 11.4 in Appendix A). The latter effect was also reported in other previous studies [1, 26].

The obtained values of $\overline{\lambda_w}$ (from 690 ± 30 to 850 ± 40 nm) and $\overline{d_f}$ (from 2.6 to 3.3 μm) for all PSU ENMs in this study (Table 4.1) are comparable to those reported by both Gopal et al. [3] for PSU ENMs treated at 188°C for 180 min (470 ± 150 nm; 2.1 μm) and Lui et al. [35] for PSU ENMs treated at 190°C for 120 min (663 ± 254 nm; 4.5 μm).

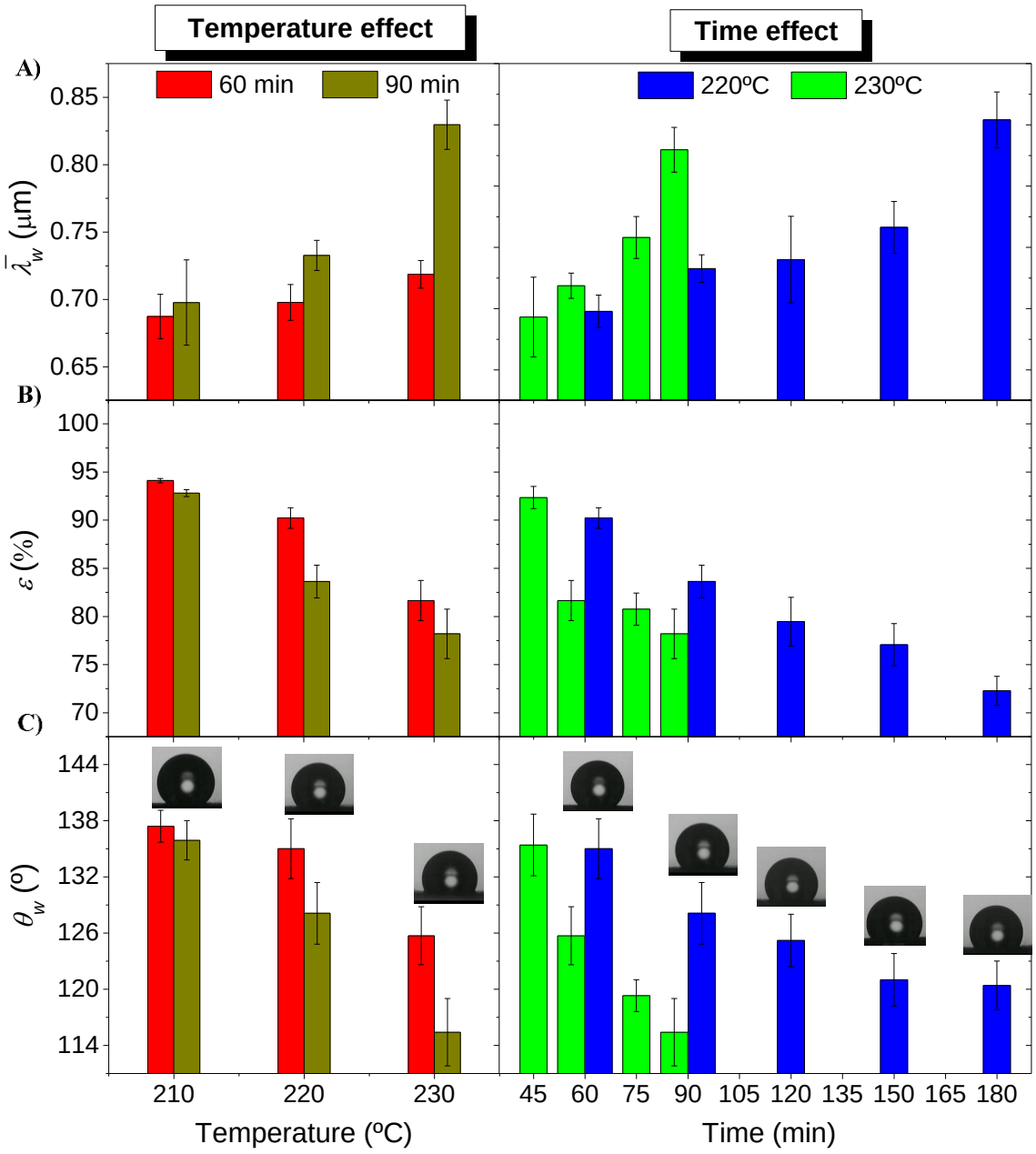

Figure 4.4. Effects of HPT temperature and time on the morphological characteristics of PSU ENMs: A) weighted arithmetic mean of the fiber diameters ($\bar{\lambda}_w$), B) void volume fraction (ε) and C) water contact angle (θ_w). Contact angles micrographs in C) are added as supporting information of the graphics.

It was expected that the changes in the size of the nanofibers and the inter-fiber spaces of the PSU ENMs resulted in notable effects on the total void volume fraction and permeation properties of the membranes [36]. In fact, a gradual decrease of both the void volume fraction (ε) and the water contact angle (θ_w) of the PSU ENMs was observed with the increase of the HPT temperature and time (Figs. 4.4 B and C). The increase of the HPT temperature from 210 to 230°C caused a reduction of ε by 13.2 and 15.7% when the applied HPT time was 60 and 90 min, respectively (Fig. 4.4-B left). Meanwhile, a reduction of ε by 19.9 and 15.4% was detected

when the applied HPT time was varied from 60 to 180 min at 220°C and from 45 to 90 min at 230°C, respectively (Fig. 4.4-B right).

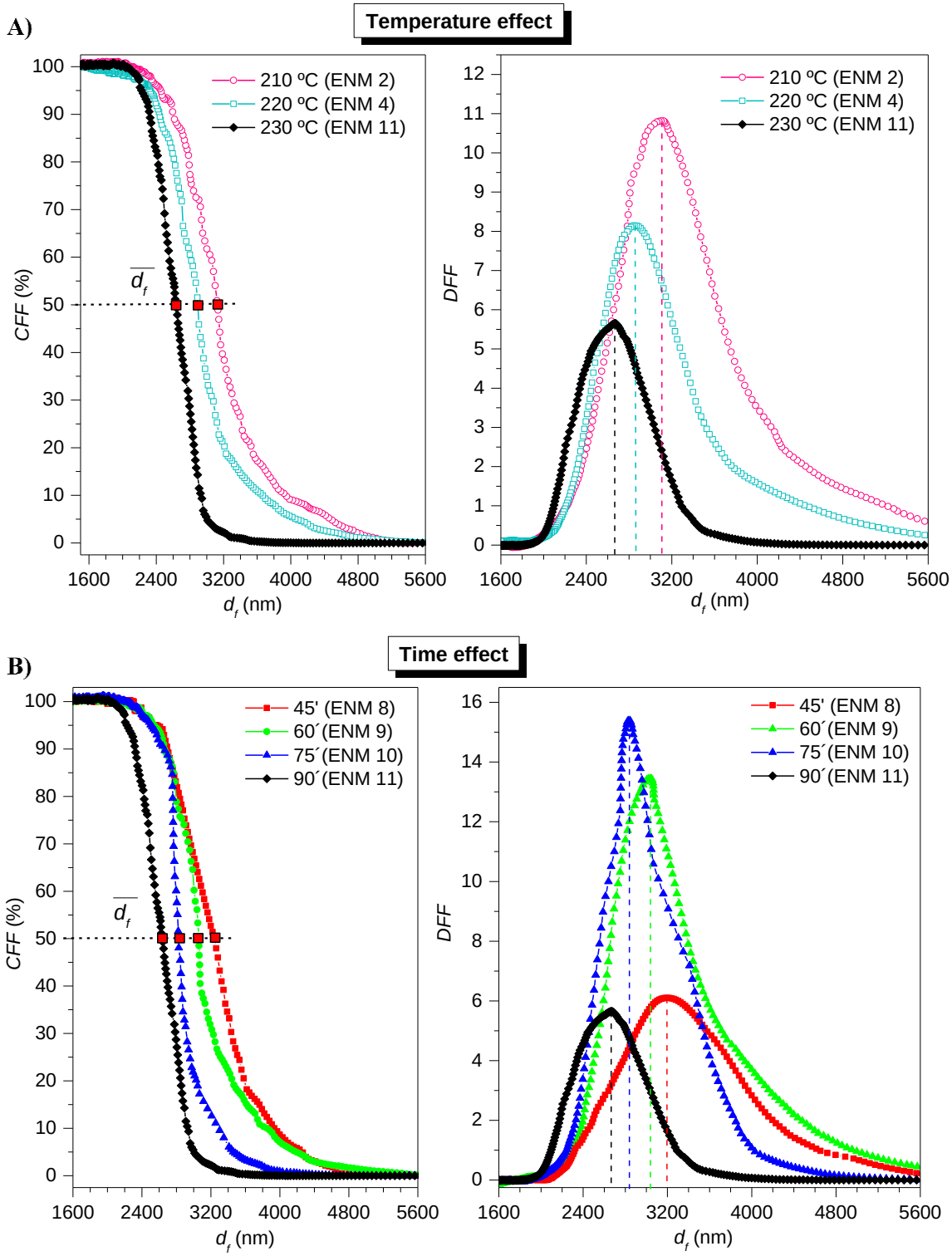

Figure 4.5. Effects of HPT temperature (A) and time (B) on the mean size of the inter-fiber space ($\overline{d_f}$), the inter-fiber space distribution or differential filter flow (*DFF*) and the cumulative filter flow distribution (*CFF*) of the PSU ENMs.

It is worth noting that although ε was reduced, it still remained sufficiently high (above 70%, see Table 4.1). The values of ε of the prepared PSU ENMs ranged between 72.3 (ENM 7, 220°C/180 min) and 94.2% (ENM 1, 210°C/60 min), which is well within the range reported for non-woven PSU ultrafine fiber mats treated at 188°C for 360 min (80–85%) [5] and PVDF ENMs treated at 80°C for 30 min (85–93%) [37].

The reduction of θ_w of PSU ENMs (Fig. 4.4-C) could be due to the gradual flattening of the nanofibers when increasing the HPT temperature or time, resulting in smoother membrane surfaces [38, 39]. Increasing the HPT temperature from 210 to 230°C at a HPT time of 60 min decreased the values of θ_w from 137.4 to 125.7°; at a HPT time of 90 min it decreased the value of θ_w from 135.9 to 115.4° (Fig. 4.4-C left). When increasing the HPT time from 60 to 180 min at 220°C, θ_w was reduced from 135.0 to 120.4°, whereas by increasing the HPT time from 45 to 90 min at 230°C, θ_w was reduced from 135.4 to 115.4° (Fig. 4.4-C right). During the applied HPT, the hydrophobic character of the ENMs decreased reducing the membrane water contact angles by up to 15%. However, the surfaces of all heat-treated ENMs retained their hydrophobic character with contact angles θ_w >115° (see Table 4.1). Similar θ_w values were reported for PSU ultrafine ENMs heat-treated at 188°C for 360 min (135 ± 5°) [5]. It is to be noted that the hydrophobic character was also maintained in PVDF ENMs heat-treated at 120°C for 120 min (127.0 ± 1.1°) [40] and PVDF-HFP ENMs hot-pressed at 200°C for 2 s (125.0 ± 2.5°) [21].

All observed trends of the morphological characteristics ($\uparrow\overline{\lambda_w}$, $\downarrow\overline{d_f}$, $\downarrow\varepsilon$, $\downarrow\theta_w$) of the PSU ENMs when increasing the HPT temperature or time, correlated well with the changes of the surface and the morphology of the PSU ENMs (higher interconnectivity and more compacted structure), which were larger for the ENMs 7 and 11.

The SEM images and the morphological characteristics of the membranes treated at a HPT temperature of 220°C and the membranes treated at 230°C but for half the HPT time were similar. For instance, the differences of $\overline{\lambda_w}$, $\overline{d_f}$, ε and θ_w between the ENMs 5 and 9 (220°C/120 min and 230°C/60 min) were smaller than 2.7% while for the ENMs 6 and 10 (220°C/180 min and 230°C/90 min) the differences were smaller than 4.8%. Therefore, similar filtration properties (i.e. selectivity and permeation fluxes) of these membranes are expected.

4.3.3 MF tests

As mentioned above, electrospun nanofibers exhibit, due to their nanostructure, very large water contact angles compared to polymeric films made from the same material (i.e. phase inversion flat membrane prepared with the same polymer). In this study, PSU ENMs exhibited contact angles between 115 and 137°. However, phase-inversion PSU membranes are reported to exhibit contact angle values around 70–80° [7]. Therefore, there is an initial 'resistance' for water to enter a completely dry ENM. Once the ENM is wetted, the high void volume fraction

of the ENM leads to relatively high flow rates. ENMs are prone to be compressed during filtration because of their high void volume fraction and their relatively poor nanofiber adhesion. Therefore, to open and wet all the inter-fiber spaces of the PSU ENMs and to ensure that the water permeate flux kept constant with filtration time at an applied pressure, a water compaction step was carried out before the MF tests. Subsequently, HA MF tests were conducted with a 15 mg/L HA solution at pH 11 for all the PSU ENMs. The filtration results of all the PSU ENMs are summarized in Table 4.2.

4.3.3.1 Effects of the HPT temperature and time on the filtration performance of PSU ENMs

The effects of the HPT temperature and time on the filtration performance of the PSU ENMs were evaluated analysing the changes of the HA permeate fluxes (J_{HA}), the HA separation factor (α) and the irreversible fouling factors (FR_{IR}) (Figs. 4.6 A and B, shown as an example) with the filtration time, and by comparing their performance indexes (PI) (Fig. 4.8).

Fig. 4.6-A shows the effects of increasing the HPT temperature (at a fixed HPT time of 90 min) from 210 to 230°C (PSU EMNs 2, 4, and 11). A considerable decrease of J_{HA} along with a gradual increase of α and FR_{IR} was observed. The final HA permeate flux (J_{HA_f}) of the PSU ENMs decreased by 82.2% when increasing the HPT temperature from 210 to 220°C (ENM 2 to ENM 4) and by 70.6%, when increasing the HPT temperature from 220 to 230°C (ENM 4 to ENM 11). The final HA separation factor (α_f) of ENM 4 (220°C) was 88.9% larger than that of ENM 2 (220°C) and that of ENM 11 (230°C) was 55.9% larger than that of ENM 4. However, the respective changes of FR_{IR} (3.6 and 2.7%) were not as noticeable as those of J_{HA} and α.

The initial permeate flux decline (FD_0) was 0.15, 0.19 and 0.92 for ENM 2, ENM 4 and ENM 11, respectively. This means that the permeate flux of the membrane prepared with the lowest HPT temperature (210°C, ENM 2) was reduced only by 15% during the first minutes of HA filtration whereas that of the membrane prepared with a higher HPT temperature (230°C, ENM 11) was declined by 92%.

These differences in the filtration performance of the membranes are mainly related to their different structural morphology. For instance, the membrane prepared with low HPT temperature (210°C, ENM 2) exhibited the largest $\overline{d_f}$ (3.1 μm) and ε (92.8%) and, therefore had the highest mean HA permeate flux (i.e. average of all the HA permeate fluxes during the MF test; $\overline{J_{HA}}$ = 8406 kg/m^2 h) with the lowest α_f value (3.7%). On the other hand, the membrane treated with the highest temperature (230°C, ENM 11) had the smallest $\overline{d_f}$ (2.6 μm) and ε (78.2%) values and exhibited the lowest $\overline{J_{HA}}$ (358 kg/m^2 h) with the highest α_f (75%) values.

It is worth nothing that although the ENM 11 had a $\overline{J_{HA}}$ value of 92.3% lower than that of ENM 2, its *PI* value resulted to be higher (74 kg/m^2 h) than that of the ENM 2 (70 kg/m^2 h) because of its larger separation factor. Similar results were reported by Li et al. [26] with PLA ENMs when increasing the HPT temperature from 90 to 95°C (at a fixed HPT time of 30 min). A decrease in the inter-fiber space of these membranes (from 2.3 to 2.0 μm) resulted in a permeate flux decline (from about 26,000 to 8500 L/m^2 h) along with an increase of the separation factor of TiO_2 particles (from 61 to 85%).

Table 4.2. Filtration performance of PSU ENMs prepared with different heat post-treatments: initial water permeate flux (J_{w0}), mean humic acid (HA) permeate flux ($\overline{J_{HA}}$), final HA permeate flux (J_{HAf}), final HA separation factor (α_f), irreversible fouling factor (FR_W) and performance index (*PI*).

Membrane	Heat treatment		Filtration characteristics					
	T (°C)	t (min)	J_{w0} $\left(10^2 \frac{kg}{m^2 h}\right)$	$\overline{J_{HA}}$ $\left(10^2 \frac{kg}{m^2 h}\right)$	J_{HAf} $\left(\frac{kg}{m^2 h}\right)$	α_f (%)	FR_W (%)	*PI* $\left(\frac{kg}{m^2 h}\right)$
ENM 1	210	60	196 ± 21	116 ± 12	8590 ± 919	0.8 ± 1.0	81.9 ± 2.8	65 ± 22
ENM 2	210	90	199 ± 22	84.1 ± 9.0	1899 ± 203	3.7 ± 1.2	93.1 ± 1.1	70 ± 14
ENM 3	220	60	205 ± 22	66.6 ± 7.1	1923 ± 206	0.8 ± 1.1	91.7 ± 1.3	16 ± 10
ENM 4	220	90	204 ± 22	27.7 ± 3.0	337 ± 36	33.1 ± 2.0	96.4 ± 0.5	111 ± 14
ENM 5	220	120	194 ± 19	10.0 ± 0.7	222 ± 18	57.2 ± 0.6	98.3 ± 0.3	127 ± 10
ENM 6	220	150	182 ± 19	4.5 ± 0.5	170 ± 18	65.3 ± 0.5	96.8 ± 0.5	111 ± 12
ENM 7	220	180	153 ± 17	3.2 ± 0.3	104 ± 11	65.5 ± 0.4	98.9 ± 0.2	68 ± 7
ENM 8	230	45	184 ± 20	34.8 ± 3.7	306 ± 33	37.0 ± 0.6	97.7 ± 0.4	113 ± 12
ENM 9	230	60	206 ± 22	20.0 ± 2.1	232 ± 26	63.6 ± 0.7	95.9 ± 0.6	147 ± 17
ENM 10	230	75	203 ± 22	9.9 ± 1.1	188 ± 20	70.9 ± 0.4	96.8 ± 0.5	133 ± 14
ENM 11	230	90	156 ± 17	3.6 ± 0.4	99 ± 11	75.0 ± 0.3	99.0 ± 0.1	74 ± 8

Fig. 4.6-B shows the effects of the HPT time (at a fixed HPT temperature of 230°C) on the filtration performance of the PSU EMNs 8 (45 min), 9 (60 min), 10 (75 min) and 11 (90 min). In this case, the effects on J_{HA} and α when increasing the HPT time from 45 to 90 min were not as noticeable as those observed when the HPT temperature was increased from 210 to 230°C. For instance, a gradual reduction of J_{HA_f} (20.9, 22.3 and 47.3%) and an increase of α_f (41.8, 10.3 and 5.6%) were observed when increasing the HPT time from 45 to 60, from 60 to

75 and from 75 to 90 min, respectively. The FR_W values did not follow a clear trend. The membrane with the lowest value of FR_W (95.9%) was the one treated for 60 min (ENM 6).

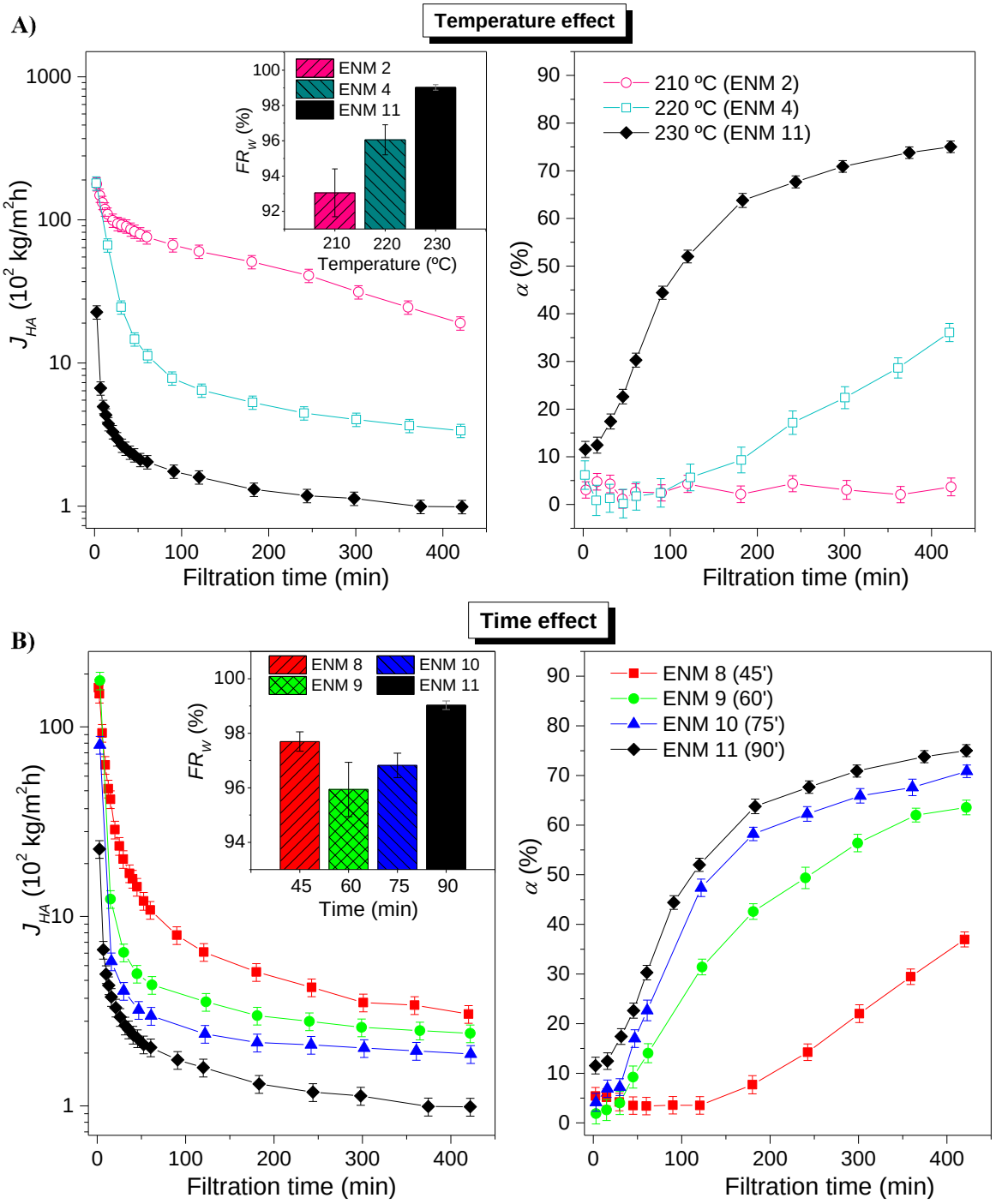

Figure 4.6. Humic acid permeate flux (J_{HA}), separation factor (α) and irreversible fouling factor (FR_W) of the PSU ENMs prepared with a HPT temperature of 210, 220 and 230°C for 90 min HPT time (A), and with 230°C HPT temperature for 45, 60, 75 and 90 min HPT time (B). The filtration tests were conducted with 15 mg/L HA feed aqueous solution at pH 11 and 10^5 Pa transmembrane pressure (ΔP).

The values of FD_0 for the ENMs 8, 9, 10 and 11 were 0.40, 0.55, 0.79 and 0.92, respectively, indicating that the initial permeate flux decline increased progressively when increasing the HPT time. It can also be noticed in Fig. 4.6-B that all membranes reached a relatively constant J_{HA} value after 360 min of filtration time. As mentioned before, the changes in filtration performance of the PSU ENMs are directly related to their morphological and structural changes. The longer the HPT time, the more compacted was the membrane structure and the thicker and more interconnected were their nanofibers (i.e. higher $\overline{\lambda_w}$ and smaller $\overline{d_f}$; see Table 4.1, Fig. 4.3, and Fig. 4.5-B). These resulted in a reduction of $\overline{J_{HA}}$ from 3481 kg/m^2 h for ENM 8 (45 min) to 358 kg/m^2 h for ENM 11 (90 min) and an enhancement of α_f from 37.0 to 75.0%, respectively (see Table 4.2). The membranes prepared at 230°C with the lowest HPT time (ENM 8, 113 kg/m^2 h) and the highest HPT time (ENM 11, 74 kg/m^2 h) both had smaller *PI* values than those treated for intermediate HPT times (ENM 9, 147 kg/m^2 h, and ENM 10, 133 kg/m^2 h).

As mentioned in the introduction, fouling is a major factor limiting the application of membranes in water treatment. Thus, a characterization analysis of the organic fouling generated on the membranes after MF tests was conducted. FTIR, SEM imaging and EDS mapping were used to confirm the presence of HA across the PSU ENMs, to compare the surface morphology of the membranes before and after filtration and to measure the change of the atomic composition of the membranes due to the organic fouling (Fig. 11.5 in Appendix A).

The J_{HA} and α curves plotted in Fig. 4.6 can be used to study the fouling phenomenon of the PSU ENMs. HA fouling in MF membranes has two stages: i) a pore blockage that corresponds to a rapid HA permeate flux decline due to the deposition of large HA aggregates on the surface and in the pores (inter-fiber space for ENMs) of the membrane; ii) a cake filtration that induces a slow decrease of the HA permeate flux with filtration time until a relatively constant value of the permeate flux (known as steady-state value or asymptotic permeate flux) is reached. During this second stage a HA deposit or cake layer forms on those regions of the membrane that were covered by HA aggregates during the first stage [14, 41-44].

The transition between the pore blockage and the cake filtration stage is usually determined by the change of the slopes of both the permeate flux and separation factor curves with filtration time. The time (t_c) at which this change occurs is known as the "critical point". A smaller t_c indicates a shorter length of the initial pore blocking stage, and hence a faster fouling evolution rate. The value of t_c depends mainly on the morphological and structural characteristics of each PSU ENM (e.g. mean size of the inter-fiber space, inter-fiber space distribution, void volume fraction, mean nanofiber diameter, hydrophobicity, etc.).

From Fig. 4.6-B it can be seen that the pore blockage of the PSU ENMs prepared with higher HPTs (i.e. ENMs 9, 10 and 11) occurred faster, during the first half an hour of filtration (t_c < 30

min). This is attributed to their more compact structure and smaller size of the inter-fiber space, which promotes the pore blockage phenomenon [45, 46]. For these membranes, the slope of the α curve was relatively small until the critical time t_c (i.e. beginning of pore blockage stage) was reached. Subsequently, a considerable increase of α was observed (due to the reduction of the membrane inter-fiber space during the pore blockage stage and during the formation and growth of the cake layer in the second stage), followed by a slower increase of α (attributed to the reached cake layer mature stage). A relatively steady-state value of the HA separation factor (α_f) was obtained at the end of the filtration test (70.9, 75.0 and 77.6% for the ENMs 9, 10 and 11, respectively).

For the membranes prepared with low HPTs (i.e. ENMs 4 and 8, see Figs. 4.6 A and B), the slope of the α curve was relatively constant and close to zero during the first 125 minutes of filtration (i.e. pore blockage stage with $t_c \approx 125$ min). Then it increased considerably during the next 300 min of filtration time (i.e. cake filtration), reaching values up to 37%. The membrane prepared with the lowest HPT (i.e. ENM 2) did not retain HA, most likely due to the low quantity of bonding points between nanofibers (see SEM image in Fig. 4.2). Unbounded nanofibers may be displaced by the hydrostatic water pressure leading to a broad inter-fiber space of the ENM and allowing HA particles to penetrate through the membrane resulting in no separation. The α_f values of all the PSU ENMs ranged from 1 to 78% (see Table 4.2). This elucidates the clear differences of the morphological characteristics of the PSU ENMs and confirms the important influence of the HPT on the filtration performance of the membranes.

In the previous section it was reported that the morphological and structural characteristics of the membranes treated at a HPT temperature of 220°C during a time t and those treated at 230°C during a time $t/2$ were very similar. For this reason, a comparison of the filtration properties (i.e. J_{HA}, α and FR_W) of the membrane pairs ENMs 4-8, 5-9, 6-10 and 7-11 was performed (Fig. 4.7). Their J_{HA_f} values were approximately the same (see Table 4.2) with deviations below 10.2%. Similarly, the same tendency was observed for the curves of α as a function of filtration time for each pair of membranes. In particular, the α curves of the membranes prepared with lower HPTs (i.e. ENMs 4 and 8) overlapped, while only small differences were detected for the pairs of membranes prepared with higher HPTs (i.e. ENMs 5-9, 6-10 and 7-11). Taking into account their mean α for the entire filtration process ($\bar{\alpha}$), the deviation between these values was low and ranged between 4.1 and 11.9%, the maximum deviation corresponding to the membranes prepared with the highest HPTs (i.e. EMN 7 ($\bar{\alpha} =$ 39.6%) and ENM 11 ($\bar{\alpha} = 45.0\%$). It is worth noting that despite the similarities in the filtration behaviour of the pairs of membranes, higher α_f values were obtained for all the membranes treated at 230°C compared to those treated at 220°C for a double HPT time. By comparing the values of FR_W of the different pairs of membranes (Table 4.2 and Fig. 4.7) no clear conclusion

could be drawn. The deviation of the FR_W values of the pairs of membranes prepared with higher HPTs (i.e. ENMs 6-10 and 7-11) was smaller than 0.2%, while the highest deviation (2.5%) was reached for the pair of ENMs 5-9.

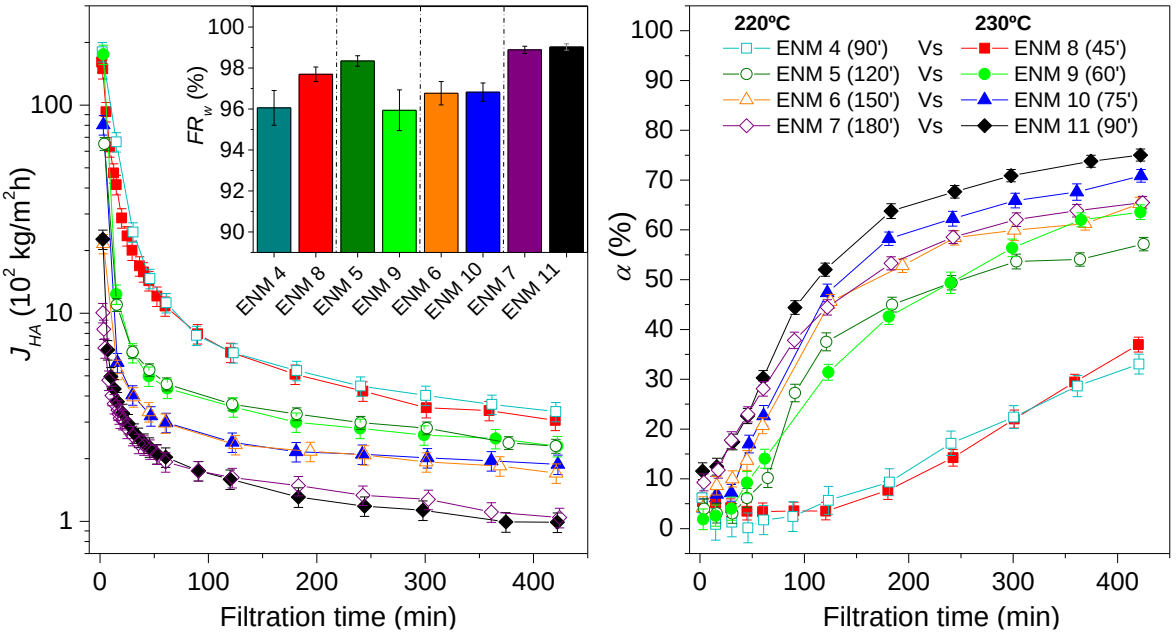

Figure 4.7. Humic acid permeate flux (J_{HA}), separation factor (α) and irreversible fouling factor (FR_W) of the PSU ENMs prepared at different HPT conditions. The filtration tests were conducted with 15 mg/L HA feed aqueous solution at pH 11 and 10^5 Pa transmembrane pressure (ΔP).

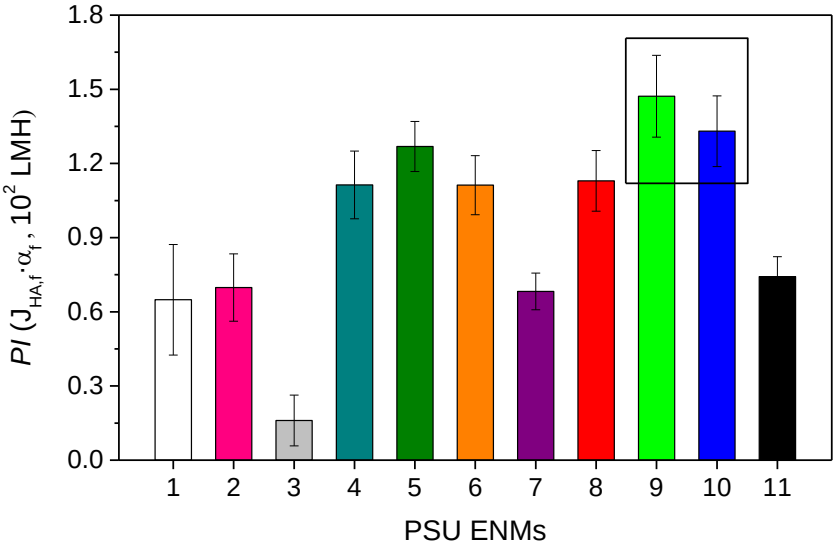

Figure 4.8. Performance index (PI) of the PSU ENMs prepared with different HPT conditions.

Despite the similarities in the filtration characteristics between the pairs of membranes, PSU ENMs treated at 230°C had up to 16.4% greater PI values than PSU ENMs treated at 220°C (see Fig. 4.8). Therefore, it is advisable to increase the HPT temperature by 10°C and reduce the HPT time by half as it permits energy and cost savings.

4.3.3.2 Comparative study

The pure water permeability (*PWP*) of all prepared PSU ENMs measured after compaction ranged from 15,260 to 20,563 kg/m^2 h bar, which is 3-fold to 100-fold higher than those achieved by highly porous lab-made PSU ENMs (1472–5648 kg/m^2 h bar) [3] and PVDF ENMs (232–1984 kg/m^2 h bar) [2] used for particulate removal, and similar or greater than those reported for mechanically enhanced lab-made PES ENMs (16,006 kg/m^2 h bar) [47]. In addition, the *PWP* values obtained in the present study for PSU ENMs were larger than those of commercial flat sheet membranes typically used in MF processes (i.e. PVDF MF: 2436 kg/m^2 h bar, Model V0.2, Synder Membrane Technology [47]; PES tight MF: 327 kg/m^2 h bar, Model LX, Synder Membrane Technology [47]; GVHP MF: 8875 kg/m^2 h bar, Millipore [43]; PES OMEGA MF: 6783 kg/m^2 h bar, Filtron Technology [12]; PVDF DURAPORE MF: 5217 kg/m^2 h bar, Millipore [12]; PES HPWP MF: 14,761 kg/m^2 h bar, Millipore; see Table 4.3). These values confirm the structural advantages of the ENMs over traditional water filtration membranes, such as their three-dimensional-inter-pore connectivity and high void volume fractions (i.e. higher porosity leads to more channels for water flow) [46, 48]. In addition, the treated PSU ENMs had a small water entry pressure (below 1 bar), which is convenient for low-pressure water purification and therefore for MF applications.

In this study, the final permeate fluxes (J_f) measured after 7 hours of filtration for the PSU ENMs with the highest *PI* values (i.e. ENMs 9 and 10) are 188 and 232 kg/m^2 h (Table 4.3). These values are 3.7 to 4.5 times greater than the value obtained in our previous study (51.3 kg/m^2 h) [7]. In addition, the values of α_f of ENMs 9 and 10 are 6.5 and 18.2% greater than the highest value obtained in our former work (60%) [7]. Thus, the optimized HPT improved the filtration *PI* of the membranes up to 5-fold [7].

The final normalized permeate fluxes (J_f) by the applied pressure (ΔP) of the ENMs 9 and 10 (232 and 188 kg/m^2 h bar) are 63 and 32% greater than that of the eco-efficient, micro-porous, lab-made PLA ENM 1 (143 kg/m^2 h bar) [26]. The values of α_f measured for ENMs 9 and 10 are also 5 and 16% higher than that of the PLA ENM 1. The values of *PI* of ENMs 9 and 10 are therefore 53 and 69% greater than that of PLA ENM 1, which confirms the high filtration performance of the heat-treated optimized ENMs.

The commercial MF membranes (PES MF, PVDF MF and PCTE MF) used by Yuan and Zydney [12] for the treatment of 2 mg/L HA solutions had up to 33% smaller J_f values than those of the PSU ENMs 9 and 10, which were used to treat higher concentrated HA solutions (15 mg/L). This is probably due to their lower porosity and smaller mean pore size. However, the commercial MF membranes exhibited higher α_f values (up to 49%) when compared with the PSU ENMs 9 and 10, mainly caused by their smaller mean pore size. Considering that the

average size of HA particles in a basic environment ranges from 0.3 to 4 nm [7] and the mean size of the inter-fiber space of the PSU ENMs ranges from 2 to 4 μm, the values of α_f obtained for the ENMs 9 and 10 (63.9 and 70.9%, respectively) can be considered reasonably good. The measured values of α_f are probably affected by both the high tortuosity of the ENMs (i.e. HA molecules are expected to be more prone to mechanical entrapment in the thread-like network of an ENM [46]) and the rejection mechanism in a fibrous structured membrane, which includes sieving, electrostatic attraction, diffusion and inertia [47].

For sake of comparison, a commercial PES MF membrane (HPWP, hydrophilic, Millipore) was tested in this study following exactly the same filtration procedure than that of the PSU ENMs. The results are summarized in Table 4.3. The PES MF commercial membrane has lower J_f value (up to 55%) but a higher α_f (up to 18%) than the ENMs 9 and 10. However, its *PI* value (82 kg/m^2 h) is 44 and 38% lower than that of the ENMs 9 and 10 (i.e. 147 and 133 kg/m^2 h, respectively) (Fig. 11.6 in Appendix A). This result elucidates the good performance of the treated-optimized PSU ENMs for MF applications.

The values of FR_W obtained for all PSU ENMs ranged from 81.9 to 99%, and are higher than those reported by Schäfer et al. [43] during MF of 20 mg/L HA solution at pH 8 (81%) and 5 mg/L HA solution at pH 10 (73%) with a MF commercial hydrophilic membrane (GVWP, 0.22 μm pore size; Millipore). The reduction of the irreversible fouling factor of PSU ENMs is important to extend the membrane lifetime for filtration application. Different ways have been adopted to improve the FR_W including surface modification of ENMs by interfacial polymerization (IP) technique [33, 49].

Compared to other ENMs with HPT used for filtration [2, 5, 7, 24, 26, 37, 50, 51], the total manufacturing time of PSU ENMs of the present study was shorter. For other reported membranes the electrospinning process took between 1 and 8 hours, up to 10 times longer than the electrospinning fabrication time (t_e) used in this study (45 min). In addition, the HPT times used for the treated-optimized PSU ENMs of the present study were 60–75 min, up to 18-fold shorter than the time (120–1080 min) reported for other membranes.

Table 4.3. Morphological characteristics and filtration performance of lab-made ENMs and commercial MF membranes: thickness (δ), void volume fraction (ε), mean pore size (*MPS*), mean nanofiber diameter ($\overline{\lambda_w}$), transmembrane pressure (ΔP), pure water permeability (*PWP*), initial water permeate flux (J_{w0}), initial permeate flux (J_i), final permeate flux (J_f), final water flux (J_{wf}), final separation factor (α_f) and irreversible fouling factor (FR_W).

Membrane[1]	Morphological characteristics				Filtration performance											Ref
	δ (μm)	ε (%)	*MPS* (μm)	$\overline{\lambda_w}$ (nm)	Filtration mode	ΔP (bar)	*PWP*[2] (LMH /bar)	Solution[3]	Particle size (μm)	J_{w0} (LMH)	J_i^4 (LMH)	J_f (LMH)	J_{wf} (LMH)	α_f (%)	FR_W (%)	
PSU ENM^L	135	-	2.1	470	Dead-end	0.5	4568	10 ppm PS Ms	1	2284	1000	538	675	92	70	[3]
							4924		0.5	2462	1867	1433	1120	47	55	
							5544		0.1	2772	2667	2438	2684	14	3	
PVDF ENM^L	300	-	4-10.6	360	Dead-end	0.57	351	500 ppm PS Ms	5	200	200	133	200	91	0	[2]
						0.66	1970	100 ppm PS Ms	1	1300	1066	530	530	98	59	
PES ENM^L	200	76.5	0.42	600	Dead-end	1	16006	Kaolin Ms	1.6	16006	15990	3143	11844	100	26	[47]
PES tight MF^C	220	-	0.1	-	Dead-end	1	2436	Kaolin Ms	1.6	2436	2421	1000	-	99.4	-	
PVDF MF^C	205	-	0.2	-	Dead-end	1	327	Kaolin Ms	1.6	327	312	143	-	98.8	-	
GVWP MF^C	125	70	0.22	-	Dead-end	1	6378	5 mg/L HA (pH 10)	-	6378			1722	29	73	[43]
							7874	20 mg/L HA (pH 8)	-	7874	-	-	1496	6	81	
GVHP MF^C	125	75	0.22	-	Dead-end	1	7924	5 mg/L HA (pH 8)	-	7924	-	-	1981	16	75	
PSU ENM^L	178	-	-	1110	Cross-flow	1	16513	15 mg/L HA (pH 11)	~0.004	16513	-	51	69	60	99	[7]
PVDF ENM 1^L	86	87.2	4.78	163	Dead-end	1	23880*	100 ppm PS Ms	1	23880*	-	-	-	87	-	[52]
PVDF ENM 2^L	78	85.7	3.30	163	Dead-end	1	15590*	100 ppm PS Ms	1	15590*	-	-	-	91	-	
PLA ENM 1^L	180	31.4	2.3	≥ 900	Dead-end	0.75	78000	0.12 wt% TiO_2	0.01-0.5	58500**	25947*	107*	-	61.0*	-	[26]
PLA ENM 2^L	130	27.6	1.4	≥ 900	Dead-end	0.75	78000	0.12 wt% TiO_2	0.01-0.5	58500**	8463*	52*	-	84.3*	-	
PLA ENM 3^L	120	18.0	2.0	≥ 900	Dead-end	0.75	78000	0.12 wt% TiO_2	0.01-0.5	58500**	1002*	27*	-	85.6*	-	
PES MF^C	-	≈ 70	0.16	-	Dead-end	0.69	6783	2 mg/L HA	-	4680	3865	202	-	95	-	[12]
PVDF MF^C	125	≈ 70	0.22	-	Dead-end	0.69	5217	2 mg/L HA	-	3600	3600	159*	-	93*	-	
PCTE MF^C	25	13.8	0.22	-	Dead-end	0.69	4957	2 mg/L HA	-	3420	1565	155	-	87	-	
PSU ENM 9^L	213	81.7	3.06	720	Cross-flow	1	20563	15 mg/L HA (pH 11)	~0.004	20563	17540	232	834	63.9	95.9	This study
PSU ENM 10^L	89	80.8	2.82	760	Cross-flow	1	20269	15 mg/L HA (pH 11)	~0.004	20269	8036	188	643	70.9	96.8	
PES HPWP MF^C	137	70-84	0.45	-	Cross-flow	1	14761	15 mg/L HA (pH 11)	~0.004	14761	1120	106	216	77.6	98.5	

[1] PSU = polysulfone; ENM = electrospun nanofiber membrane; ^{L} = lab-made membrane; ^{C} = commercial membrane; PVDF = polyvinylidene fluoride; PES = polyethersulfone; UF = ultrafiltration; MF = microfiltration; PLA = poly (lactic acid).

[2] LMH = L/m^2 h

[3] PS = polystyrene; Ms = microparticles; HA = humic acid.

[4] The initial permeate flux for the membranes of this study corresponds to the HA permeate flux after 2.5 min of the filtration test.

*Estimated values taken from figures plotted in the corresponding reference; **Average value.

4.4 Conclusions

Different HPTs were investigated to improve the filtration performance of PSU ENMs. The effects of the HPT temperature (i.e. 210, 220, 230°C) and time (i.e. 45, 60, 75, 90, 120, 150, 180 min) on their morphology and structure were studied systematically. It was observed that increasing either the HPT temperature or time resulted in a reduction of $\overline{d_f}$ along with an increase of both $\overline{\lambda_w}$ and the number of connections between nanofibers, which led to an improvement of the structural integrity of the membranes. A gradual decrease of the ε and θ_w values of the PSU ENMs was obtained when the HPT temperature or the HPT time was increased, which resulted in membranes with smoother surfaces. No connection points between nanofibers could be detected when the membranes were prepared at a low HPT temperature (ENMs 1-2 (210°C)) or for a short HPT time (ENMs 3 (60 min) and 8 (45 min)).

The main effects of increasing either the HPT temperature or the HPT time on the filtration properties of the membranes were a reduction of the HA permeate flux and an improvement of the HA separation factor.

It was observed that the fouling evolution rate of the PSU ENMs prepared with higher HPTs (i.e. ENMs 10 and 11) was faster. Pore blockage occurred earlier (t_c < 30 min) in these membranes compared to those prepared with lower HPTs (i.e. ENMs 4 and 8), in which pore blockage took place during the first 125 minutes of the filtration process.

Similar morphological characteristics as well as filtration performance were observed for the membranes treated at 220°C and those treated at 230°C for half the heating time. Despite these similarities, the values of α_f of the membranes treated at 230°C were up to 14.6% higher than those of the membranes treated at 220°C, resulting in up to 16.4% better performance indexes. From these results it can be concluded that it is better to perform HPT at a higher temperature, because the reduction in HPT time permits energy and cost savings.

Compared to the best PSU ENMs (i.e. ENMs 9 and 10), up to 44% lower *PI* value was obtained for the commercial PES MF membrane (HPWP, Millipore) tested under the same filtration procedure to that followed for the PSU ENMs. This confirms the good performance of the prepared PSU ENMs for MF applications.

The significantly higher *PWP* of PSU ENMs compared to commercial flat sheet filtration membranes allows the use of lower pressures and thus reduces energy consumption during filtration. Together with their short manufacturing time, this property makes PSU ENMs fabricated with the optimized HPT conditions very promising candidates to reduce the overall costs and energy consumption of MF applications.

References

[1] Y. Huang, Q.L. Huang, H. Liu, C.X. Zhang, Y.W. You, N.N. Li, C.F. Xiao, Preparation, characterization, and applications of electrospun ultrafine fibrous PTFE porous membranes, Journal of Membrane Science, 523 (2017) 317-326.

[2] R. Gopal, S. Kaur, Z. Ma, C. Chan, S. Ramakrishna, T. Matsuura, Electrospun nanofibrous filtration membrane, Journal of Membrane Science, 281 (2006) 581-586.

[3] R. Gopal, S. Kaur, C.Y. Feng, C. Chan, S. Ramakrishna, S. Tabe, T. Matsuura, Electrospun nanofibrous polysulfone membranes as pre-filters: Particulate removal, Journal of Membrane Science, 289 (2007) 210-219.

[4] J. Doshi, D.H. Reneker, Electrospinning process and applications of electrospun fibers, Journal of Electrostatics, 35 (1995) 151-160.

[5] Z. Ma, M. Kotaki, S. Ramakrishna, Surface modified nonwoven polysulphone (PSU) fiber mesh by electrospinning: A novel affinity membrane, Journal of Membrane Science, 272 (2006) 179-187.

[6] S.-S. Choi, Y.S. Lee, C.W. Joo, S.G. Lee, J.K. Park, K.-S. Han, Electrospun PVDF nanofiber web as polymer electrolyte or separator, Electrochimica Acta, 50 (2004) 339-343.

[7] P. Arribas, M. Khayet, M.C. García-Payo, L. Gil, Self-sustained electro-spun polysulfone nano-fibrous membranes and their surface modification by interfacial polymerization for micro- and ultra-filtration, Separation and Purification Technology, 138 (2014) 118-129.

[8] Y. Liu, R. Wang, H. Ma, B.S. Hsiao, B. Chu, High-flux microfiltration filters based on electrospun polyvinylalcohol nanofibrous membranes, Polymer, 54 (2013) 548-556.

[9] S. Homaeigohar, J. Koll, E.T. Lilleodden, M. Elbahri, The solvent induced interfiber adhesion and its influence on the mechanical and filtration properties of polyethersulfone electrospun nanofibrous microfiltration membranes, Separation and Purification Technology, 98 (2012) 456-463.

[10] H.-C. Kim, B.G. Choi, J. Noh, K.G. Song, S.-H. Lee, S.K. Maeng, Electrospun nanofibrous PVDF–PMMA MF membrane in laboratory and pilot-scale study treating wastewater from Seoul Zoo, Desalination, 346 (2014) 107-114.

[11] A. Baji, Y.-W. Mai, S.-C. Wong, M. Abtahi, P. Chen, Electrospinning of polymer nanofibers: Effects on oriented morphology, structures and tensile properties, Composites Science and Technology, 70 (2010) 703-718.

[12] W. Yuan, A.L. Zydney, Humic acid fouling during microfiltration, Journal of Membrane Science, 157 (1999) 1-12.

[13] N. Yang, X. Wen, T.D. Waite, X. Wang, X. Huang, Natural organic matter fouling of microfiltration membranes: Prediction of constant flux behavior from constant pressure materials properties determination, Journal of Membrane Science, 366 (2011) 192-202.

[14] R. Seifollahy Astaraee, T. Mohammadi, N. Kasiri, Analysis of BSA, dextran and humic acid fouling during microfiltration, experimental and modeling, Food and Bioproducts Processing, 94 (2015) 331-341.

[15] Y. Su, C. Li, W. Zhao, Q. Shi, H. Wang, Z. Jiang, S. Zhu, Modification of polyethersulfone ultrafiltration membranes with phosphorylcholine copolymer can remarkably improve the antifouling and permeation properties, Journal of Membrane Science, 322 (2008) 171-177.

[16] A.-R. Cho, D.M. Shin, H.W. Jung, J.C. Hyun, J.S. Lee, D. Cho, Y.L. Joo, Effect of annealing on the crystallization and properties of electrospun polylatic acid and nylon 6 fibers, Journal of Applied Polymer Science, 120 (2011) 752-758.

[17] L. Huang, S.S. Manickam, J.R. McCutcheon, Increasing strength of electrospun nanofiber membranes for water filtration using solvent vapor, Journal of Membrane Science, 436 (2013) 213-220.

[18] X. Ran, Z. Jia, C. Han, Y. Yang, L. Dong, Thermal and mechanical properties of blends of polylactide and poly(ethylene glycol-co-propylene glycol): Influence of annealing, Journal of Applied Polymer Science, 116 (2010) 2050-2057.

[19] H.-C. Chen, C.-H. Tsai, M.-C. Yang, Mechanical properties and biocompatibility of electrospun polylactide/poly(vinylidene fluoride) mats, Journal of Polymer Research, 18 (2011) 319-327.

[20] S. Kaur, R. Barhate, S. Sundarrajan, T. Matsuura, S. Ramakrishna, Hot pressing of electrospun membrane composite and its influence on separation performance on thin film composite nanofiltration membrane, Desalination, 279 (2011) 201-209.

[21] B.S. Lalia, E. Guillen-Burrieza, H.A. Arafat, R. Hashaikeh, Fabrication and characterization of polyvinylidenefluoride-co-hexafluoropropylene (PVDF-HFP) electrospun membranes for direct contact membrane distillation, Journal of Membrane Science, 428 (2013) 104-115.

[22] Y. Liao, R. Wang, M. Tian, C. Qiu, A.G. Fane, Fabrication of polyvinylidene fluoride (PVDF) nanofiber membranes by electro-spinning for direct contact membrane distillation, Journal of Membrane Science, 425-426 (2013) 30-39.

[23] Y. You, S. Won Lee, S. Jin Lee, W.H. Park, Thermal interfiber bonding of electrospun poly(l-lactic acid) nanofibers, Materials Letters, 60 (2006) 1331-1333.

[24] S.S. Homaeigohar, K. Buhr, K. Ebert, Polyethersulfone electrospun nanofibrous composite membrane for liquid filtration, Journal of Membrane Science, 365 (2010) 68-77.

[25] Y. Liang, S. Cheng, J. Zhao, C. Zhang, S. Sun, N. Zhou, Y. Qiu, X. Zhang, Heat treatment of electrospun Polyvinylidene fluoride fibrous membrane separators for rechargeable lithium-ion batteries, Journal of Power Sources, 240 (2013) 204-211.

[26] L. Li, R. Hashaikeh, H.A. Arafat, Development of eco-efficient micro-porous membranes via electrospinning and annealing of poly (lactic acid), Journal of Membrane Science, 436 (2013) 57-67.

[27] S.S. Homaeigohar, H. Mahdavi, M. Elbahri, Extraordinarily water permeable sol–gel formed nanocomposite nanofibrous membranes, Journal of Colloid and Interface Science, 366 (2012) 51-56.

[28] S.S. Homaeigohar, M. Elbahri, Novel compaction resistant and ductile nanocomposite nanofibrous microfiltration membranes, Journal of Colloid and Interface Science, 372 (2012) 6-15.

[29] Y. Liao, C.H. Loh, M. Tian, R. Wang, A.G. Fane, Progress in electrospun polymeric nanofibrous membranes for water treatment: Fabrication, modification and applications, Progress in Polymer Science, 77 (2018) 69-94.

[30] C. Migliaresi, D. Cohn, A. De Lollis, L. Fambri, Dynamic mechanical and calorimetric analysis of compression-molded PLLA of different molecular weights: Effect of thermal treatments, Journal of Applied Polymer Science, 43 (1991) 83-95.

[31] D. Aussawasathien, C. Teerawattananon, A. Vongachariya, Separation of micron to sub-micron particles from water: Electrospun nylon-6 nanofibrous membranes as pre-filters, Journal of Membrane Science, 315 (2008) 11-19.

[32] K. Smolders, A.C.M. Franken, Terminology for Membrane Distillation, Desalination, 72 (1989) 249-262.

[33] M.N.A. Seman, M. Khayet, N. Hilal, Nanofiltration thin-film composite polyester polyethersulfone-based membranes prepared by interfacial polymerization, Journal of Membrane Science, 348 (2010) 109-116.

[34] X. Yuan, Y. Zhang, C. Dong, J. Sheng, Morphology of ultrafine polysulfone fibers prepared by electrospinning, Polymer International, 53 (2004) 1704-1710.

[35] L. Liu, Z. Pan, Properties of hydrophilic chitosan/polysulfone nanofibrous filtration membrane, Journal of Engineered Fibers and Fabrics, 9 (2014) 76-86.

[36] D. Hussain, F. Loyal, A. Greiner, J.H. Wendorff, Structure property correlations for electrospun nanofiber nonwovens, Polymer, 51 (2010) 3989-3997.

[37] M. Essalhi, M. Khayet, Self-sustained webs of polyvinylidene fluoride electrospun nanofibers at different electrospinning times: 1. Desalination by direct contact membrane distillation, Journal of Membrane Science, 433 (2013) 167-179.

[38] A. Marmur, Wetting on hydrophobic rough surfaces: to be heterogeneous or not to be?, Langmuir, 19 (2003) 8343-8348.

[39] B. Bhushan, Y. Chae Jung, Wetting study of patterned surfaces for superhydrophobicity, Ultramicroscopy, 107 (2007) 1033-1041.

[40] H. Savoji, D. Rana, T. Matsuura, S. Tabe, C. Feng, Development of plasma and/or chemically induced graft co-polymerized electrospun poly(vinylidene fluoride) membranes for solute separation, Separation and Purification Technology, 108 (2013) 196-204.

[41] S. Hong, M. Elimelech, Chemical and physical aspects of natural organic matter (NOM) fouling of nanofiltration membranes, Journal of Membrane Science, 132 (1997) 159-181.

[42] C.-C. Ho, A.L. Zydney, A combined pore blockage and cake filtration model for protein fouling during microfiltration, Journal of Colloid and Interface Science, 232 (2000) 389-399.

[43] A.I. Schäfer, U. Schwicker, M.M. Fischer, A.G. Fane, T.D. Waite, Microfiltration of colloids and natural organic matter, Journal of Membrane Science, 171 (2000) 151-172.

[44] W. Yuan, A. Kocic, A.L. Zydney, Analysis of humic acid fouling during microfiltration using a pore blockage–cake filtration model, Journal of Membrane Science, 198 (2002) 51-62.

[45] K. Xiao, Y. Shen, X. Huang, An analytical model for membrane fouling evolution associated with gel layer growth during constant pressure stirred dead-end filtration, Journal of Membrane Science, 427 (2013) 139-149.

[46] K. Xiao, J. Sun, Y. Mo, Z. Fang, P. Liang, X. Huang, J. Ma, B. Ma, Effect of membrane pore morphology on microfiltration organic fouling: PTFE/PVDF blend membranes compared with PVDF membranes, Desalination, 343 (2014) 217-225.

[47] J. Bae, I. Baek, H. Choi, Mechanically enhanced PES electrospun nanofiber membranes (ENMs) for microfiltration: The effects of ENM properties on membrane performance, Water Research, 105 (2016) 406-412.

[48] L. Marbelia, M. Mulier, D. Vandamme, K. Muylaert, A. Szymczyk, I.F.J. Vankelecom, Polyacrylonitrile membranes for microalgae filtration: Influence of porosity, surface charge and microalgae species on membrane fouling, Algal Research, 19 (2016) 128-137.

[49] M.N. Abu Seman, M. Khayet, N. Hilal, Development of antifouling properties and performance of nanofiltration membranes modified by interfacial polymerisation, Desalination, 273 (2011) 36-47.

[50] A.M. Bazargan, M. Keyanpour-rad, F.A. Hesari, M.E. Ganji, A study on the microfiltration behavior of self-supporting electrospun nanofibrous membrane in water using an optical particle counter, Desalination, 265 (2011) 148-152.

[51] S. Kaur, Z. Ma, R. Gopal, G. Singh, S. Ramakrishna, T. Matsuura, Plasma-induced graft copolymerization of poly(methacrylic acid) on electrospun poly(vinylidene fluoride) nanofiber membrane, Langmuir, 23 (2007) 13085-13092.

[52] X. Zhuang, L. Shi, K. Jia, B. Cheng, W. Kang, Solution blown nanofibrous membrane for microfiltration, Journal of Membrane Science, 429 (2013) 66-70.

5

Thin film composite membranes

Interfacial polymerization conditions effect on physicochemical properties and antifouling performance

Membrane technology is becoming increasingly important to solve the global water scarcity problem because it allows an efficient, economic and environmental friendly treatment of water. However, the long-term use of a filtration membrane is limited by fouling, which reduces water production rates and increases energy consumption. In this chapter, polyester thin film nanofiber composite (PE TFNC) membranes with improved antifouling performance were developed for wastewater treatment. The membranes were prepared by interfacial polymerization (IP) of bisphenol A (BPA) and trimesoyl chloride (TMC) on the surface of polysulfone electrospun nanofiber membranes (PSU ENMs). The antifouling properties of the membranes were improved by varying the polymerization reaction time. All membranes were characterized with scanning electron microscope (SEM), attenuated total reflectance-Fourier transform infrared spectroscopy (ATR-FTIR), porometry and zeta potential measurements. Humic acid (HA) permeation tests were carried out to relate their physicochemical properties to their filtration and antifouling performance. The best PE TFNC membrane (polymerized for 15 min) was compared with polyester based thin film composite membranes prepared on other supports and polyamide based thin film composite membranes formed by IP of piperazine (PIP) and TMC in the presence of trimethylamine (TEA). The best PE TFNC membrane exhibited a permeability of 213.0 L/m² h bar, two orders of magnitude greater than previously reported PE thin film composite membranes, a HA separation factor of 72.5% and an irreversible fouling factor of 10.2%.

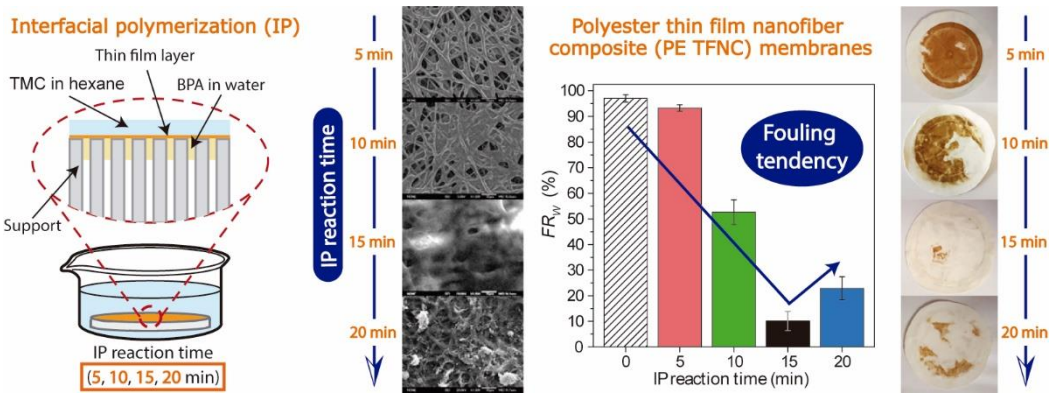

Improved antifouling performance of polyester thin film nanofiber composite membranes prepared by interfacial polymerization

5.1 Introduction

Membrane filtration technology has demonstrated extensive practical applications in separation processes such as water purification, wastewater treatment and seawater desalination. The numerous advantages of membrane technology in filtration applications include the low cost, high efficiency, simplicity, insignificant chemical consumption and environmental friendliness [1]. However, the main obstacle that restricts the application of membranes in water treatment is membrane fouling, which usually lowers the water productivity, deteriorates membrane separation capability (i.e. reduction of the permeate quality), shortens membrane lifespan and consequently, increases the operation and maintenance costs [1-4]. Fouling originates from the interaction between a membrane surface and foulant(s), thus, it is strongly influenced by the physicochemical properties of the membrane surface such as pore size and its geometry, charge density, roughness and hydrophilicity [3-6]. Therefore, it is of a great importance to design and develop new membranes with optimized surface properties to reduce fouling in order to overcome the aforementioned limitations.

Interfacial polymerization (IP) is an effective membrane surface modification technique widely used to improve both the filtration and antifouling performance of membranes [2, 3, 5-10]. After IP, the resulting thin film composite (TFC) membrane is comprised of a thin polymeric active layer on top of a porous supporting membrane. The key advantage of the TFC approach is the possible separate optimization of the active layer and the support layer to get membranes with high filtration performance. Most of the research studies have been focused on: i) optimizing the physicochemical properties of the TFC active layer to improve the permeability, selectivity and antifouling capacity of the resulting membranes [11-17], and ii) improving the intrinsic morphological structure and chemical properties of the support layer suitable for the active layer formation with enhanced mechanical strength and low resistance to permeate flow [18-25].

Several parameters are involved in the IP procedure like the monomer type and its concentration in the aqueous and the organic phases, the used additives in both phases and the polymerization reaction time. It was shown that the IP reaction time plays an important role in determining the structural morphology and composition of the active layer as it affects the extent of polymerization and thus the density and thickness of the active layer [14, 16, 26-30]. Different types of water-soluble monomers have been considered such as the commonly used polyamines to form polyamide (PA) TFC membranes [10-16, 24-28] and the less used polyols or polyphenols to form polyester (PE) TFC membranes [7-9, 31, 32]. These last membranes exhibit higher antifouling performance against hydrophobic contaminants because of their abundant surface hydroxyl groups, whereas PA TFC membranes have better salt rejection properties due to their highly cross-linked structure**.** For instance, PE TFC membrane prepared by IP using tannic acid (TA) and trimesoyl chloride (TMC) on a porous polyethersulfone (PES) ultrafiltration (UF) support [8] exhibited 56% greater water permeability (*PWP* = 23.4 L/m^2 h bar) and much better antifouling capacity against humic acid (HA) (i.e. lower irreversible fouling factor, FR_W = 1%) than that of a PA TFC membrane prepared by IP of piperazine (PIP) and TMC on a PES UF support (*PWP* = 10.3 L/m^2 h bar and FR_W = 48%, respectively) [6]. However, the salt rejection of $MgSO_4$ of the PE TFC membrane (50.2%) was lower than that of the PA TFC membrane (97.4%).

The most common used porous supports to develop the TFC membranes are commercial microfiltration (MF) and UF membranes or lab-made membranes prepared by the phase inversion method, which usually have a low surface porosity [33]. Polysulfone (PSU) [3-5, 15-17] and PES [6-8, 11-13] are the most employed supporting materials, mainly due to their low price, ease of processing, and good chemical, thermal and mechanical resistance. Recently, electrospun nanofiber membranes (ENMs) were successfully used as an alternative support to fabricate TFC membranes [22, 33-35]. Compared with the conventional MF/UF supporting membranes, ENMs offer unique advantages such as a higher porosity, an interconnected nanofiber structure with an open pore morphology and a larger surface area to volume ratio, a low flow resistance and a high permeability. The resulting thin film nanofiber composite (TFNC) membranes exhibited significantly higher permeation fluxes and comparable rejection factors than the commercial nanofiltration (NF) membranes and conventional TFC membranes. For instance, the PA TFNC membrane developed by Yung et al. [33] achieved a superior filtration performance over a conventionally prepared PA TFC membrane, with a salt rejection factor of 99.1% and a permeation flux about 2 times higher than that of the PA TFC membrane having a salt rejection factor of 97.3%. Recently, Kaur et al. [34] reported PA TFNC membranes with up to 256% larger permeate fluxes than those of commercial NF membranes and only 8–12% lower salt rejection factors. Compared to PA TFNC membranes, very few studies have been reported on the development of PE TFNC membranes.

In the present study, PE TFNC membranes were prepared by IP of bisphenol A (BPA) and TMC. The effects of the polymerization reaction time on the antifouling performance and the physicochemical properties of the PE TFNC membranes were studied and the optimum IP reaction time was determined. Furthermore, the formation process of the PE layer was elucidated by means of FTIR spectra. PE layers were also prepared on different supports under the optimum IP conditions to investigate the influence of the supporting membrane on the physicochemical properties, the filtration performance and the antifouling capacity of the resulting PE TFC membranes. Different PA TFC membranes were also prepared by IP reaction of PIP and TMC in the presence of the acid acceptor trimethylamine (TEA) and their filtration and antifouling performance was compared to that of the PE TFC membranes. New insight on the formation of the PE thin film layer on ENMs was emphasized in this study showing the relationship between the polymerization reaction time and the physicochemical, filtration and antifouling properties of the PE TFNC membranes.

5.2 Materials and methods

5.2.1 Materials

The spinning solution was prepared from the polymer polysulfone (PSU, UDEL P-3500 LCD, Solvay Specialty Polymers; Mw = 79,000 g/mol; ϱ_{PSU} = 1.24 g/cm^3) and a mixture of the solvents *N, N*-dimethyl formamide (DMF, Sigma-Aldrich) and tetrahydrofuran (THF, Sigma-Aldrich). The monomer trimesoyl chloride (TMC, Sigma-Aldrich) and the solvent hexane (Sigma-Aldrich, puriss., ≥99% (GC)) were used to prepare the organic phase for the modification of the surface of the membranes by interfacial polymerization (IP). For the aqueous phase, the monomers bisphenol A (BPA, Sigma-Aldrich), *m*-phenylenediamine (MPD, Sigma-Aldrich), triethylamine (TEA, Sigma-Aldrich), piperazine (PIP, Sigma-Aldrich) and polyvinyl acetate (PVA, Sigma-Aldrich) were used either separately or combined to form a polyester (PE) or polyamide (PA) layer on the membrane surface. The organic foulant humic acid (HA, Fluka) having a molecular weight of 4.1 kDa was employed to prepare the feed solution of the filtration tests. Sodium hydroxide (NaOH, Panreac) was used to prepare a standard HA concentrated solution of 1 g/L. Hydrochloric acid (HCl, Sigma-Aldrich) was used to adjust to 11 the pH of the HA feed solution of 15 mg/L. Isopropyl alcohol (IPA, Sigma-Aldrich) was used to determine the void volume fraction (ε) of the membranes. POREFIL®, a fluorinated hydrocarbon (chemical nature: perfluoro-ether, surface tension: 16 mN/m, vapor pressure: 3.33 Pa; viscosity: 4.4 mPa·s, POROMETER), was used as a wetting liquid to perform the pore size measurements. Commercial polyethersulfone (PES) microfiltration (MF) membrane (HPWP, hydrophilic, Millipore) was used as a support.

5.2.2 Preparation of PSU ENMs

The spinning solution was prepared by dissolving 20 wt.% PSU into the solvent mixture DMF/THF (80/20 wt.%). The solvent mixture with PSU was kept at 60ºC and stirred at 80 rpm for 10 h until the polymer was completely dissolved and the solution became homogeneous. The PSU electrospun solution had 35.8 ± 1.8 mN/m surface tension, 485.3 ± 0.8 mPa·s viscosity and 9.12 ± 0.15 μS/cm electrical conductivity at 25°C. More details can be found elsewhere [36].

Electrospinning was applied to prepare the PSU ENMs using the system described elsewhere [37, 38]. All PSU ENMs were prepared under the optimum electrospinning parameter conditions [37]: a polymer solution flow rate of 2.5 mL/h, an electric voltage of 16 kV, an air gap of 10 cm and an electrospinning time of 45 min. The electrospinning ambient conditions were kept in the ranges 20–25ºC and 38–41% relative humidity.

After electrospinning, PSU ENMs had a silky, fluffy and loose structure, which required delicate handling. Several studies [36, 37, 39-41] demonstrated the importance of the application of a heat post-treatment (HPT) on ENMs to improve their structural integrity, mechanical stability and filtration performance. Thus, in this study, two different conditions of the HPT were carried on the PSU ENMs after electrospinning. The PSU ENMs were treated either for 75 min at 230ºC (ENM1) or for 120 min at 220ºC (ENM2) (see Table 5.1). These were the optimized conditions resulting in very high filtration performances in our previous study [36].

Table 5.1. Morphological and filtration properties of the unmodified supporting membranes: heat post-treatment temperature (*T*), heat post-treatment time (*t*), thickness (δ), weighted arithmetic mean of the nanofiber diameters ($\overline{\lambda_w}$) and its corresponding weighted standard deviation ($\overline{s_w}$), water contact angle (θ_w), void volume fraction (ε), mean pore size ($\bar{d}_f$) and pure water permeability (*PWP*).

Membrane	Heat treatment		Morphological characteristics					Filtration properties
	T **(ºC)**	***t*** **(min)**	δ **(μm)**	$\overline{\lambda_w} \pm \overline{s_w}$ **(μm)**	θ_w **(°)**	ε **(%)**	$\bar{d}_f$ **(μm)**	***PWP*** **(LMH/bar)**
ENM1	230	75	135 ± 19	0.76 ± 0.03	119.5 ± 1.8	80.6 ± 1.8	3220 ± 20	20248± 2151
ENM2	220	120	129 ± 20	0.73 ± 0.07	125.0 ± 2.6	79.3 ± 2.5	3084 ± 30	19914 ± 1801
PES	-	-	137 ± 14	-	26.8 ± 3.4	77.0 ± 7.0*	573 ± 3	15217± 1667

*Averaged data from Millipore supplier.

5.2.3 Preparation of polyester and polyamide thin film composite membranes

IP is based on the formation of a dense polymeric top layer (thin film composite) on the membrane surface (support) as a result of the reaction between two monomers at the interface of two immiscible solvents (i.e. aqueous and organic phases). In this study, IP was employed to prepare polyester (PE) and polyamide (PA) thin film composite (TFC) membranes. Fig. 5.1 shows a schematic illustration of the process: 1) the supporting membrane was immersed for 60 min in an aqueous solution containing a reactive monomer; 2) the soaked membrane was taken out from the aqueous solution and positioned vertically for 2 min to drain the excess of monomer on its surface; 3) the membrane was then dipped for 5, 10, 15 or 20 min in a second solution containing 0.25% w/v TMC in hexane; 4) the soaked membrane was extracted from the organic solution and drained vertically for 1 min; 5) finally, the membrane was dried in open-air for 24 h before characterization. All these steps were carried out at room temperature (~23ºC).

Table 5.2. Interfacial polymerization conditions used to prepare the polyester and polyamide thin film composite membranes.

Membrane	Support	TFC type[1]	Aqueous phase			Organic phase		
			Material[2]	w/w (%)	t_{ap}[3] (min)	Material[2]	w/v (%)	t_{IP}[3] (min)
PE TFNC1_5	ENM1	PE	BPA	2	60	TMC	0.25	5
PE TFNC1_10	ENM1	PE	BPA	2	60	TMC	0.25	10
PE TFNC1_15	ENM1	PE	BPA	2	60	TMC	0.25	15
PE TFNC1_20	ENM1	PE	BPA	2	60	TMC	0.25	20
PE TFNC2_15	ENM2	PE	BPA	2	60	TMC	0.25	15
PE TFC_15	PES	PE	BPA	2	60	TMC	0.25	15
PA TFNC1_5	ENM1	PA	PIP—TEA	1—1	60	TMC	0.25	5
PA TFC_5	PES	PA	PIP—TEA	1—1	60	TMC	0.25	5

[1]PE: polyester; PA: polyamide.
[2]BPA: bisphenol A; PIP: piperazine; TEA: triethylamine; TMC: trimesoyl chloride.
[3]t_{ap}: aqueous phase time; t_{IP}: polymerization reaction time.

In this study, the monomers BPA and TMC were used to form a dense and thin layer of PE on the membrane surface, whereas the combination of monomers PIP and TMC in presence of the acid acceptor TEA was used to form a PA thin film on the membrane surface. Fig. 5.2 shows the schematic reaction mechanisms of these different IP approaches. The thin film layers were formed on the prepared PSU ENMs (i.e. TFNC) and on PES commercial membranes (i.e. TFC) for sake of comparisons. Table 5.2 summarizes the preparation conditions of all developed membranes in this study.

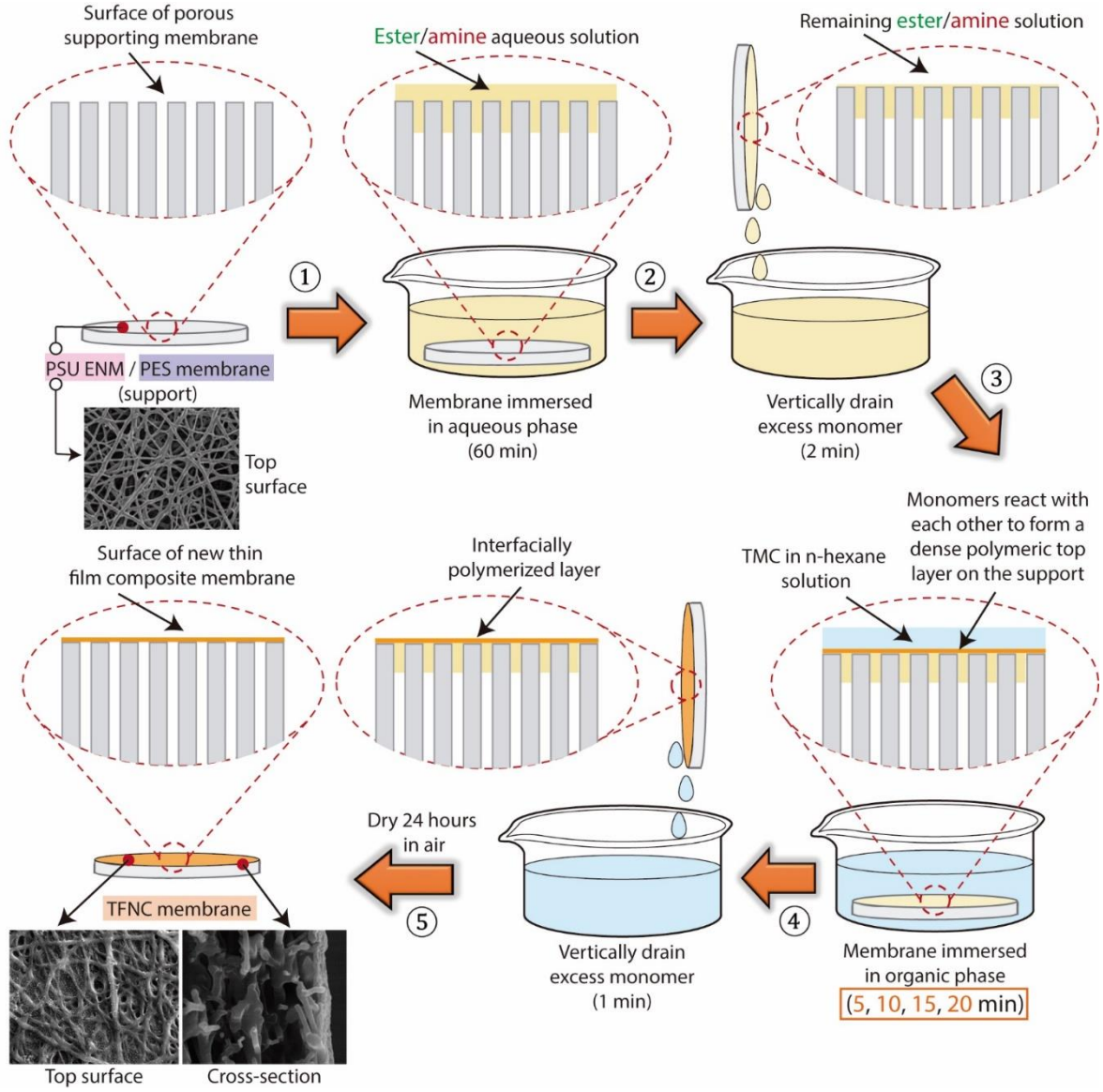

Figure 5.1. Schematic illustration of the preparation process of polyester and polyamide thin film composite membranes by interfacial polymerization.

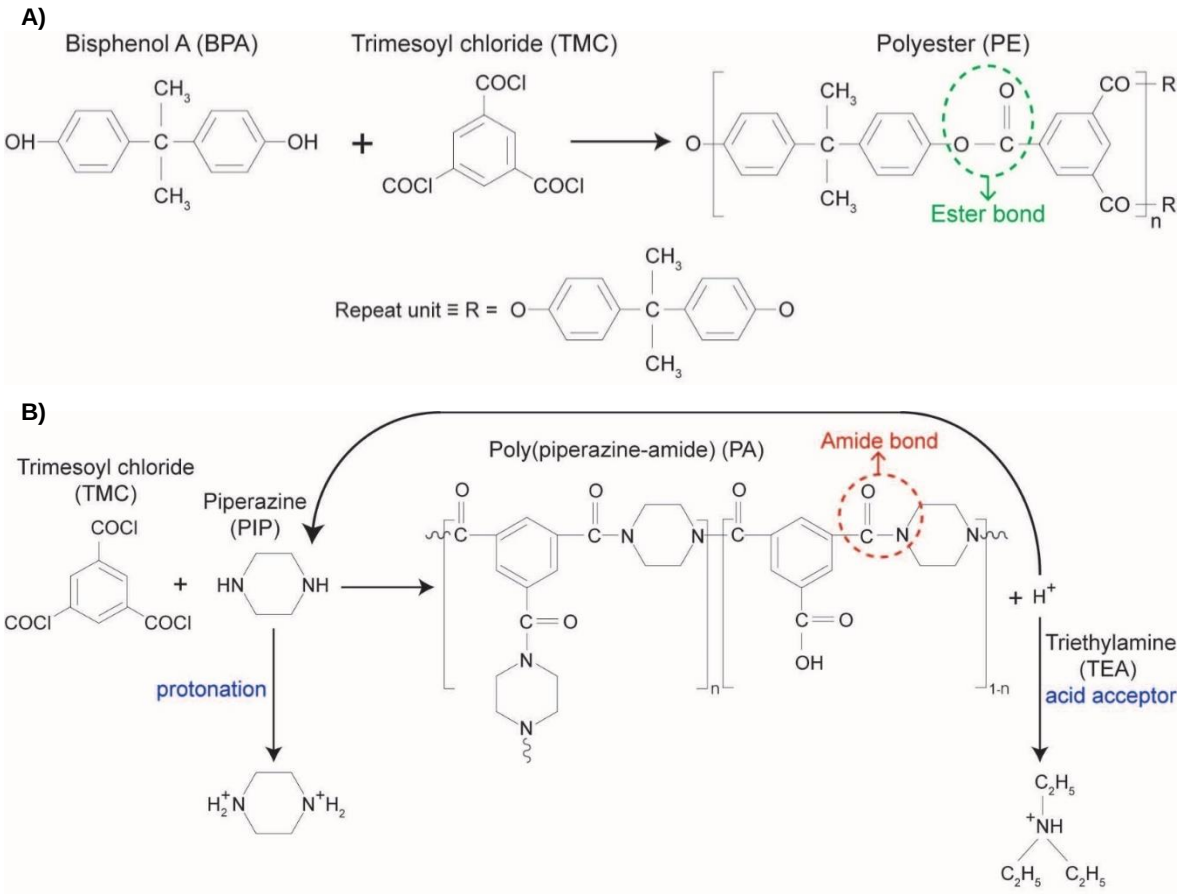

Figure 5.2. Schematic of the interfacial polymerization reaction of different monomers. A) Bisphenol A and trimesoyl chloride react to form polyester (PE) and B) piperazine and trimesoyl chloride in presence of acid acceptor triethylamine to form polyamide (PA).

5.2.4 Membranes characterization

The average thickness (δ) of the unmodified supporting membranes and its standard deviation were calculated from 41 different points measured along the membrane surface using a micrometer equipped with a feeler (ISL Isocontrol).

The water contact angles (θ_w) of the unmodified supporting membranes were measured at room temperature using a CAM100 device (Sb) with the Cam200usb software, which was used to acquire photographs of the water drop on the sample surface and to calculate the contact angle value. A Hamilton stainless steel needle was used to control the volume of the drops, which ranged between 12 and 14 µL. For each ENM sample at least 10 different drops were considered to determine the average value of the θ_w together with its standard deviation.

The void volume fraction (porosity, ε) of all unmodified ENM supporting membranes was determined by measuring the density of the polymer material (ρ_{pol}) using isopropyl alcohol (IPA), which penetrates into the pores, and the density of the membrane (ρ_m) using distilled water, which does not go into the pores, according to equation (1) [42]:

$$\varepsilon\,(\%) = \left(1 - \frac{\varrho_m}{\varrho_{pol}}\right) \cdot 100 \tag{5.1}$$

The surface morphology of the membranes was analyzed by a field emission scanning electron microscope (FESEM, JEOL Model JSM-6335F) operated at 5 kV. Before conducting the SEM analysis, a thin gold layer of about 5 nm was sputtered on the membrane surface using an evaporator (EMITECH K550 X) for one minute under 25 mA. SEM images were evaluated with the software UTHSCSA Image Tool 3.0 to measure the diameter of the nanofibers of the PSU ENMs. At least 3 SEM images/per ENM sample were considered and the diameters of a total number of 100 nanofibers/per image were measured. Statistical analysis was used to determine the nanofiber diameter distribution (i.e. nanofiber diameter histogram) and to estimate the arithmetic weighted mean of the nanofiber diameters ($\overline{\lambda_w}$) with its corresponding weighted standard deviation ($\overline{s_w}$). More details can be found elsewhere [36].

The pore size of the membranes (i.e. inter-fiber space for ENMs, d_f) was measured at room temperature (~23ºC) with the capillary flow porometry method using a gas–liquid displacement Porometer (POROLUX™ 100, Porometer). POREFIL® (Porometer) was employed as the wetting liquid agent and compressed air as the inert gas. The applied hydrostatic pressure was varied in the range 0–0.45 MPa. At least 3 tests were performed for each membrane. The mean pore size ($\overline{d_f}$), the pore size distribution or differential filter flow (*DFF*) and the cumulative filter flow distribution (*CFF*) of the membranes were determined using the wet and dry curves.

The chemical structure of the membranes was analysed by attenuated total reflectance Fourier transform infrared (ATR-FTIR) spectroscopy with a Nicolet device (Magna-IR 750 Series II) equipped with the detector DTGS-KBr (sulfate triglycerin deuterated with KBr window), a beam splitter KBr and an infrared source (Ever-Glo). The H-ATR Multiple Bounce (Spectra Tech) accessory with a ZnSe crystal and 13 steps was used for analysis. ATR-FTIR measurements were carried out at 128 scans and 8 cm^{-1} resolution.

The surface charge characteristics of the membranes were measured using a SurPASS streaming potential analyzer (Anton Paar GmbH, Austria). The Zeta potential (ζ-potential) measurement was carried out at 25 ± 2 ºC using 1 mM KCl solution as background electrolyte at a pH 10.0 ± 0.2 adjusted with a 0.1 M NaOH solution. For each measurement, two membrane samples with dimensions 20 × 10 mm^2 were placed into the measuring cell. The gap of the flow channel between their surfaces was set at 100 μm. Before starting the measurement, the samples were thoroughly rinsed with the measuring electrolyte. Three measurements were performed for each membrane to determine the mean and the standard deviation of the ζ-potential.

5.2.5 Filtration experiments

A crossflow experimental device previously designed in our research group was used for the filtration tests [37]. Before carrying out the filtration tests, all membranes were compacted by circulating distilled water for 3 h at a transmembrane pressure (ΔP) of 3×10^5 Pa. Distilled water was used first as feed for 1 h and the pure water permeability (*PWP*) of the membranes was determined at a transmembrane pressure of 10^5 Pa. The effective filtration area of the membrane was 21.76 ± 0.01 cm^2 and the feed solution was circulated at a constant flow rate of 1.6–1.8 L/min. Subsequently, filtration test was conducted using a HA solution of 15 mg/L at pH 11 (~23ºC) as feed for 7 h (i.e. HA test). Then, the filtration system was washed with distillated water without removing the membrane and distilled water was circulated again for 1 h.

During each step, the produced permeate was measured as a function of time by weighing the permeate in discrete time steps on an electronic balance (AND GF-1200). The permeate fluxes of the HA solution (J_{HA}) and distilled water before (J_{w0}) and after (J_{wf}) the HA filtration test were calculated from the measured mass (m) collected over a period of time (Δt) as:

$$J\ (\mathrm{kg/m^2\,h}) = \frac{m}{A_{ef} \cdot \Delta t} \tag{5.2}$$

where A_{ef} is the effective filtration area of the membrane.

The irreversible fouling factor (FR_W) was used to evaluate the antifouling performance of the membranes. This was calculated in terms of pure water flux reduction [43]:

$$FR_W\ (\%) = \frac{J_{w0} - J_{wf}}{J_{w0}} \cdot 100 \tag{5.3}$$

Permeate, retentate and feed samples were extracted from the filtration system during the HA test and a spectrophotometer (UV/VIS 7315, Jenway) was used to determine their HA concentration at 254 nm wavelength. These values were used to calculate the separation factor (α) of the membranes as follows:

$$\alpha\ (\%) = \left(1 - \frac{2C_p}{C_r + C_f}\right) \cdot 100 \tag{5.4}$$

where C_p, C_r and C_f are the HA concentration of the permeate, retentate and feed solutions, respectively.

The filtration performance of the membranes was evaluated by means of the performance index (*PI*), which takes into account the final values of both the HA permeate flux (J_{HA_f}) and the HA separation factor (α_f) obtained at the end of the HA test:

$$PI\ (\mathrm{kg/m^2\,h}) = \frac{J_{HA_f} \cdot \alpha_f}{100} \tag{5.5}$$

5.3 Results and discussions

5.3.1 Polyester thin film nanofiber composite membranes prepared with different polymerization reaction times

The polymerization reaction time strongly affects the physicochemical properties of the developed thin film layer (e.g. surface morphology, roughness, chemical structure and hydrophilicity) as it significantly influences the degree of polymerization and therefore, the thickness and the crosslinking density of the thin film [7, 9, 14, 16, 26-30]. In this study, the effects of the IP reaction time (t_{IP}) on the physicochemical properties, the antifouling capacity (irreversible fouling factor) and the filtration performance (water permeability, permeation fluxes and separation factor) of polyester thin film nanofiber composite (PE TFNC) membranes were investigated. In our previous work [36], a systematic study of the heat post-treatment applied to PSU ENMs was conducted to optimize their morphological structure and obtain membranes with improved filtration performance (i.e. up to 38% better filtration performance than that of commercial PES MF membranes). Those heat-treated optimized PSU ENMs were used in this study as supporting membranes to prepare the PE TFNC membranes. The fabrication conditions, morphological properties and pure water permeability (*PWP*) of the supporting membranes are summarized in Table 5.1. ENM1 was the supporting membrane used in this section. A thin PE layer was formed on the membrane surface by reacting the monomers BPA and TMC with varying reaction times as described in the Materials and Methods section. The surface modified membranes were named according to the IP reaction time: PE TFNC1_5 (t_{IP} = 5 min), PE TFNC1_10 (t_{IP} = 10 min), PE TFNC1_15 (t_{IP} = 15 min) and PE TFNC1_20 (t_{IP} = 20 min) (see Table 5.2).

5.3.1.1 Effects of the polymerization reaction time on the physicochemical properties of polyester thin film nanofiber composite membranes

SEM images of the surface morphologies of the unmodified supporting membrane and the surface modified PE TFNC membranes are shown in Fig. 5.3-A. The polymerization time clearly affected the surface morphology of the resulting PE TFNC membranes. Before IP, the surface of the ENM1 support was rough due to its nanofiber structure. During the first 15 min of polymerization, the thickness of the formed PE layer increased with time and the inter-fiber space of the membrane was progressively covered with the PE film (PE TFNC1_5, PE TFNC1_10) leading to a less rough membrane surface until almost the entire surface of the membrane was covered by a smooth PE layer (PE TFNC1_15). When increasing the IP reaction

time over 15 min (PE TFNC1_20), the PE layer became rougher with nodular structure and without any visible open inter-fiber space (see also Fig. 12.1 in Appendix B). Other authors [14, 16, 27, 28, 44] observed the increase of both the roughness and thickness of the top layer of thin film composite (TFC) membranes as a function of the polymerization reaction time.

The SEM observed morphological differences between the unmodified supporting membrane and the surface modified PE TFNC membranes explained the measured size of the inter-fiber space of the membranes and its distributions (Fig. 5.3 B and C). Increasing the IP

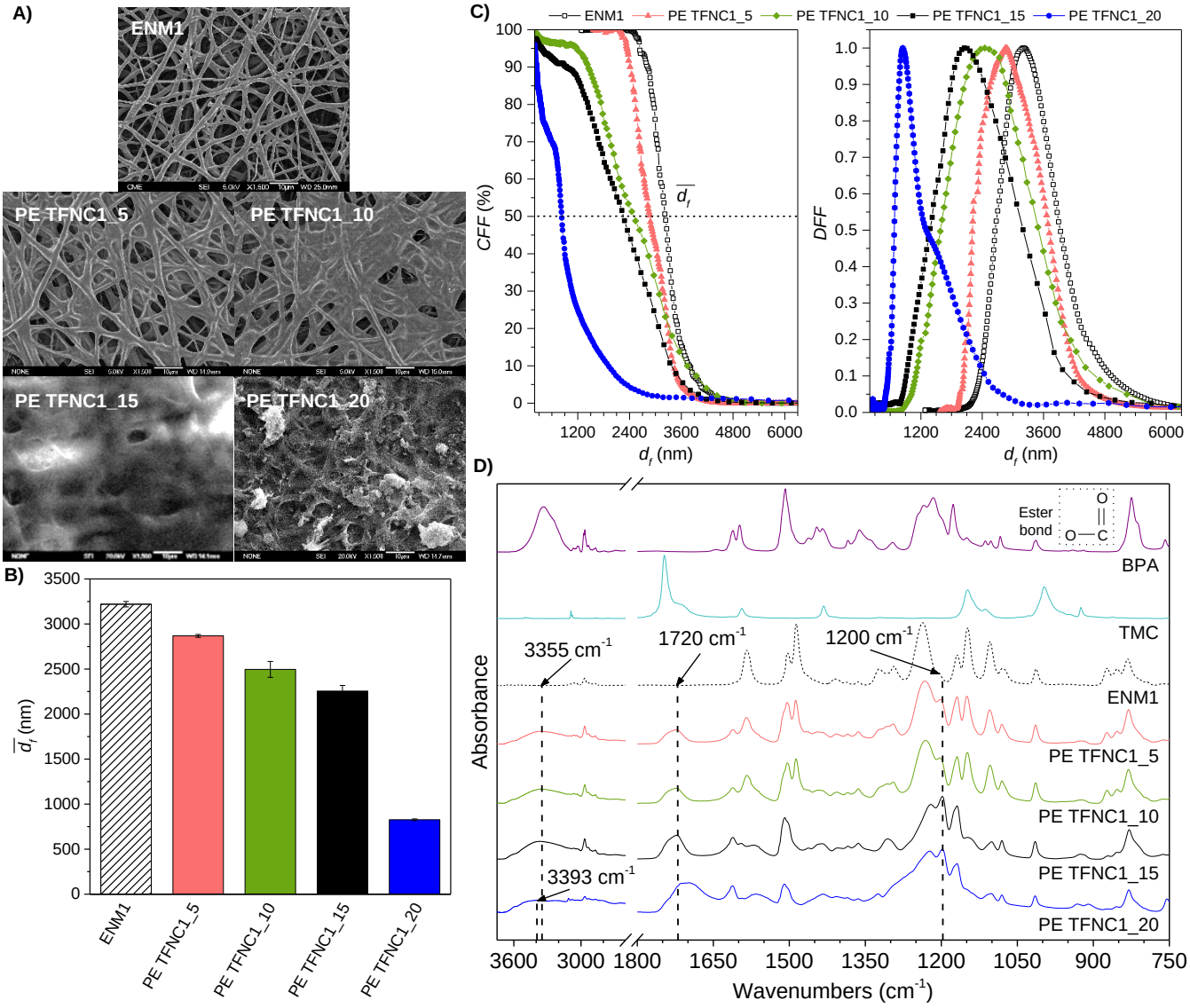

Figure 5.3. Influence of the polymerization reaction time on the morphological and structural characteristics of polyester thin film nanofiber composite membranes. A) SEM surface images at X1500 magnification, B) mean pore size ($\overline{d_f}$), C) normalized differential (*DFF*) and cumulative (*CFF*) pore size distributions, and D) FTIR spectra of the unmodified supporting membrane (ENM1) and the surface modified PE TFNC membranes prepared with reaction times of 5 min (PE TFNC1_5), 10 min (PE TFNC1_10), 15 min (PE TFNC1_15) and 20 min (PE TFNC1_20). The PE TFNC membranes were prepared by reacting BPA and TMC as described in Fig. 5.2-A.

Table 5.3. Physicochemical properties and filtration performance of the unmodified supporting membranes and the polyester and polyamide thin film composite membranes: mean pore size ($\bar{d}_f$), zeta potential (ζ-potential), initial water permeate flux (J_{w_0}), mean humic acid (HA) permeate flux ($\overline{J_{HA}}$), final HA permeate flux (J_{HA_f}), mean HA separation factor ($\bar{\alpha}$), final HA separation factor (α_f), irreversible fouling factor (FR_W) and performance index (PI).

Membrane	Physicochemical properties		Filtration characteristics						
	$\bar{d}_f$ (nm)	ζ-potential * (mV)	J_{w_0} $\left(10^2 \frac{kg}{m^2h}\right)$	$\overline{J_{HA}}$ $\left(10^2 \frac{kg}{m^2h}\right)$	J_{HA_f} $\left(\frac{kg}{m^2h}\right)$	$\bar{\alpha}$ (%)	α_f (%)	FR_W (%)	PI $\left(\frac{kg}{m^2h}\right)$
ENM1	3220 ± 20	-59.4 ± 0.4	203 ± 22	9.3 ± 1.0	188 ± 20	39.1 ± 1.0	70.9 ± 0.4	96.8 ± 1.4	133 ± 14
ENM2	3084 ± 30	-63.2 ± 0.6	194 ± 19	13.7 ± 1.3	222 ± 18	29.3 ± 0.9	57.2 ± 0.6	98.5 ± 1.2	127 ± 10
PES	573 ± 6	-46.4 ± 0.1	152 ± 17	2.69 ± 0.30	117 ± 13	56.4 ± 1.4	84.0 ± 1.2	98.3 ± 1.3	98 ± 11
PE TFNC1_5	2868 ± 16	-59.9 ± 1.6	160 ± 17	6.94 ± 0.74	178 ± 19	42.4 ± 1.5	69.0 ± 1.5	93.3 ± 1.3	123 ± 13
PE TFNC1_10	2496 ± 88	-63.8 ± 0.8	3.5 ± 0.3	3.06 ± 0.17	117 ± 4	42.1 ± 1.4	70.3 ± 1.2	52.6 ± 4.8	82.4 ± 3.4
PE TFNC1_15	2255 ± 63	-72.5 ± 0.4	2.1 ± 0.2	1.51 ± 0.06	97.1 ± 3.7	42.3 ± 1.5	72.5 ± 1.2	10.2 ± 3.8	70.4 ± 2.9
PE TFNC1_20	827 ± 9	-70.2 ± 1.0	1.06 ± 0.04	0.26 ± 0.01	20.3 ± 0.8	61.6 ± 1.5	91.5 ± 1.2	22.9 ± 4.5	18.6 ± 0.7
PE TFNC2_15	1492 ± 30	-73.0 ± 1.0	0.99 ± 0.06	0.50 ± 0.02	42.5 ± 1.6	33.0 ± 1.6	62.5 ± 1.3	20.1 ± 5.0	26.6 ± 1.1
PE TFC_15	462 ± 4	-48.1 ± 1.2	0.26 ± 0.01	0.52 ± 0.02	79.1 ± 3.0	68.5 ± 1.3	86.9 ± 1.1	-220 ± 30**	68.7 ± 2.8
PA TFNC1_5	2844 ± 79	-49.2 ± 0.1	3.2 ± 0.2	2.89 ± 0.18	127 ± 6	36.4 ± 1.5	69.0 ± 1.3	46.4 ± 4.1	87.4 ± 4.7
PA TFC_5	521 ± 3	-34.8 ± 0.2	0.044 ± 0.002	0.057 ± 0.002	6.4 ± 0.2	70.1 ± 4.7	91.0 ± 1.1	-33.0 ± 8.0**	5.8 ± 0.2

*Values at pH=10; **The negative values of the FR_W are due to the partial detachment of the thin film layer from the supporting membrane.

reaction time resulted in a left shift of both the cumulative (*CFF*) and normalized differential (*DFF*) inter-fiber space distributions of the membranes along with a decrease of their mean size of the inter-fiber space ($\overline{d}_f$) (see also data in Table 5.3). The $\overline{d}_f$ value of the surface modified membranes decreased by up to 74.3% with respect to that of the unmodified membrane. This reduction was significantly greater for 20 min of reaction time, which is likely related to the previously mentioned structural change of the formed PE thin film (i.e. from thin and smooth to thick and rough). Seman et al. [45] reported a similar left shift of the pore size distribution curves with a decrease of the mean pore size up to 45.6% for surface modified BPA TFC and tetramethyl BPA TFC membranes compared to the unmodified membrane.

Fig. 5.3-D displays the FTIR spectra of the unmodified supporting membrane, the surface modified PE TFNC membranes, BPA and TMC. In addition, Table 5.4 [5, 6, 9-13, 16-18, 20, 29, 46-50] provides the corresponding peak assignments of the IR bands. For the FTIR spectrum of the ENM1 support, the bands at 1322 and 1148 cm^{-1} showed the asymmetric and symmetric stretching vibration of S=O bonds of the base polymer PSU. Other characteristic strong IR bands of PSU substrate appeared at 1584, 1486 and 1237 cm^{-1}, which correspond to the C=C aromatic in-plane ring stretching vibration, the C–H stretching vibration of the methyl group (CH_3–C–CH_3), and the C–O–C asymmetric stretching of aryl–O–aryl group, respectively. In addition, the two weak bands at 1387 and 1364 cm^{-1} are assigned to the presence of methyl groups in the PSU matrix.

The PE TFNC membranes exhibited a weak adsorption peak at about 1612 cm^{-1} and large peaks at 1509 and 832 cm^{-1}, which are likely due to the presence of excess BPA in the membranes (see FTIR spectrum of BPA). The presence of absorption peaks at 1612 and 1509 cm^{-1} was attributed to the C=C aromatic stretching vibrations of the ring of the BPA moiety [51]. Beside the PSU bands of the substrate and BPA, the spectrum of the PE TFNC membranes exhibited absorption peaks at 1720 and 1200 cm^{-1}, which correspond to C=O and C–O stretching vibrations of the ester groups, respectively. The presence of these peaks verified the successful formation of the PE thin film layer on top of the ENM1 support for all IP reaction times. Additionally, a broad adsorption peak appeared in the range 3150–3700 cm^{-1} with a center at ~3355 cm^{-1} due to the stretching vibration of the hydroxyl groups (–OH), which could arise from the unreacted hydroxyl groups of BPA in the membranes as well as from the partial hydrolysis of the acyl chloride unit of TMC.

The FTIR spectrum of the membrane PE TFNC1_20 differed from that of the rest of the modified membranes. The changes in the peak corresponding to the C=O stretching vibration of the ester group at 1720 cm^{-1} (i.e. became broader due to a new contribution centered at 1698 cm^{-1}), the appearance of a broad contribution in the range 2300–2700 cm^{-1} and a narrow peak at 3110 cm^{-1} revealed the presence of carboxylic acid group (see Fig. 12.2-A in Appendix B). In addition, the centre of the broad adsorption peak attributed to the stretching vibration of the

–OH groups shifted to higher wavenumbers (3396 cm^{-1}). All this confirmed the change in the chemical structure of the membrane as it will be explained later on.

Table 5.4. Peak assignments of the IR spectra of the unmodified supporting membranes and the polyester and polyamide thin film composite membranes.

Peak assignments	Wavenumbers (cm^{-1})	Polymers*	Ref.
In-phase out-of-plane hydrogen deformation of para-substituted phenyl groups/Aliphatic C–H rocking	832, 853, 835, 858	PSU, PES	[20, 48]
Skeletal aliphatic C–C/aromatic hydrogen bending/ rocking	873, 1013, 1080, 1104, 1169, 872, 1011, 1073, 1104	PSU, PES	[20, 49]
C–SO_2–C symmetric stretching vibration	1148, 1148	PSU, PES	[20, 48, 49]
C–O–C asymmetric stretching of aryl–O–aryl group	1237, 1239	PSU, PES	[20, 48, 49]
S=O stretching vibration	1294, 1298	PSU, PES	[20, 48, 49]
C–SO_2–C asymmetric stretching vibration	1322, 1321	PSU, PES	[20, 48, 49]
C–H symmetric deformation of CH_3–C–CH_3 group	1364, 1387	PSU	[20, 48, 49]
C=C aromatic in-plane ring stretching vibration	1409, 1407	PSU, PES	[20]
C–H stretching vibration of CH_3–C–CH_3 group	1486, 1485	PSU, PES	[20, 48, 49]
C=C aromatic in-plane ring stretching vibration	1504, 1584, 1577	PSU, PES	[20, 48, 49]
C–O stretching vibration of ester bonds (–COO–)	1200	PE	[29]
C=O stretching vibration of ester bonds (–COO–)	1720	PE	[6, 9, 29]
O–H stretching vibration of hydroxyl group (–OH) and carboxylic acid group (–COOH)	3355, 3393	PE	[6, 9, 50]
Stretching vibration of sulfonic group/C–O stretching vibration of ester groups	1027	PA	[48]
N–H in-plane bending coupled with C–N stretching/ C–H and N–H deformation vibration of amide bond formation (–CONH) (amide III band)	1283	PA	[46]
C–O stretching/O–H bending vibration of carboxylic acid/bending vibration of methylene group (–CH_2–)	1442, 1441	PA	[5, 10]
C–C and C–N in plane stretching vibration/ C=O stretching vibration of carboxylic acid salt	1584, 1580 (shoulder)	PA	[11, 12, 47]
C=O stretching/C–N stretching vibration of amide bond formation (–CONH) (amide I band)	1616, 1614 (peak) 1630, 1625 (shoulder)	PA	[5, 12, 16, 18, 47, 48]
C=O stretching vibration of carboxylic acid group	1697	PA	[5, 10, 47]
O–H stretching of carboxylic acid group (–COOH)/ N–H stretching vibration of residual amine groups	3426, 3393 (broad)	PA	[12, 13, 16, 17, 48]

*PSU: polysulfone; PES: polyethersulfone; PE: polyester; PA: polyamide. The colors are used to clarify the link between a specific wavenumber and its corresponding polymer.

The analysis of the areas under the peak at 1720 cm^{-1} attributed to the –C=O group (i.e. CO bonding) and under the peak at 3355 cm^{-1} corresponding to the –OH group (i.e. OH bonding) and their ratio as a function of the IP reaction time can be used to explain the process of monomer crosslinking and film growth on the membrane surface (Fig. 5.4 A–C). The intensity of the peak attributed to the –C=O group increased continuously with the reaction time (Fig. 5.4-A), indicating that both the film thickness and the degree of crosslinking of the membrane layer increased with the reaction time [16, 26-28]. The intensity of the peak corresponding to the –OH group also increased with IP reaction time from 5 to 15 min (Fig. 5.4-B), but it was slower than that of the –C=O group, so that their ratio (OH/CO) decreased as plotted in Fig. 5.4-C. This behaviour can be explained based on the corresponding SEM images. At the beginning of the IP process, BPA molecules could freely diffuse through the organic phase, facilitated by the loose and open pore structure of the membrane, and react with TMC forming the initial PE film (PE TFNC1_5 in Fig. 5.3-A). The number of BPA molecules available for IP reaction was so large that only part could react with TMC increasing the amount of polyester bonds (–C=O) in the PE film with time while the rest remained un-reacted. The hydroxyl groups of the un-reacted BPA caused the increase with time of the intensity of the peak corresponding to the –OH bonds.

The diffusion of BPA towards TMC slowed down with increasing polymerization time due mainly to the continuous growth of the PE layer that progressively covered the inter-fiber space at the surface of the membrane (PE TNFC1_10 and PE TFNC1_15 in Fig. 5.3-A) and acted as barrier limiting BPA diffusion [14, 16, 52]. Over 15 min reaction time, the entire surface of the membrane was so covered by the PE film (PE TFNC1_20 in Fig. 5.3-A) that hindered the diffusion of BPA, which is confirmed by the reduction of the intensity of the peaks corresponding to pure BPA (1612, 1509 and 832 cm^{-1}) in the FTIR spectrum of the membrane PE TFNC1_20. At this stage of the IP process, two reactions occurred simultaneously: i) TMC reacted with the previously un-reacted hydroxyl groups of the BPA in the membrane. As a result, the number of OH bonds on the surface decreased by 29.8%. ii) The excess concentration of TMC in the solution led to the hydrolysis of TMC with water to form carboxylic acids. The presence of carboxylic acid group in the FTIR spectrum of the membrane PE TFNC1_20 was confirmed by the broadening of the peak at 1720 cm^{-1} together with the appearance of a larger contribution in the range 2300–2700 cm^{-1}, and was hypothesized to be due to a mixture of 1,3,5-benzene tricarboxylic acid and 1,3-benzene dicarboxylic acid (see Fig. 12.2-A in Appendix B). Both reactions led to a 71.8% increase of the CO bonding value (Fig. 5.4-A). Consequently, the membrane PE TFNC1_20 exhibited much lower OH/CO bonding ratio than the other membranes prepared with shorter IP reaction times.

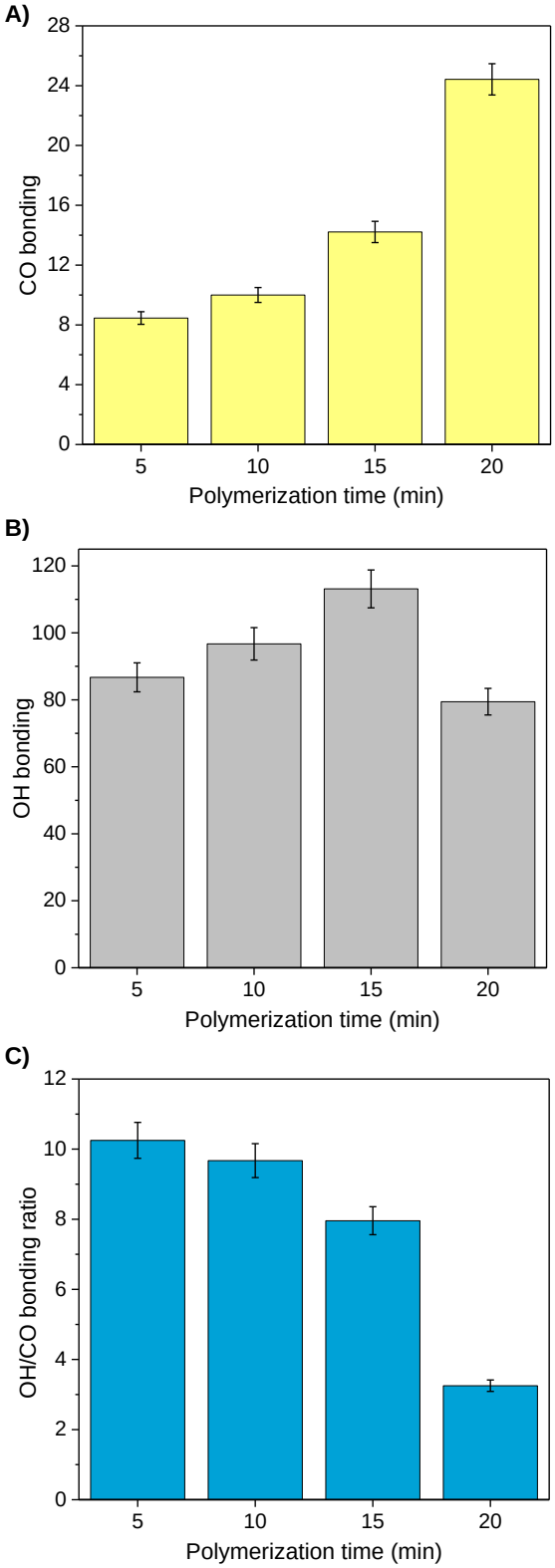

Figure 5.4. Influence of the polymerization reaction time on the bondings and bonding ratio of polyester thin film nanofiber composite membranes. A) Area under the peak at 1720 cm^{-1} corresponding to the –C=O fuctional group (i.e. CO bonding), B) area under the peak at 3355 cm^{-1} corresponding to the –OH fuctional group (i.e. OH bonding), and C) area bonding ratio of these two functional groups (i.e. OH/CO).

5.3.1.2 Effects of the polymerization reaction time on the filtration performance and antifouling capacity of polyester thin film nanofiber composite membranes

Fig. 5.5 A and B shows the HA permeate flux (J_{HA}) and the HA separation factor (α) of the unmodified supporting membrane (ENM1) and the PE TFNC membranes prepared with different polymerization times as a function of the filtration time. Compared to ENM1, J_{HA} was decreased with the increase of the IP reaction time. This reduction was quantified with the change of the mean HA permeate flux (i.e. average J_{HA} over the whole filtration test; $\overline{J_{HA}}$) (see Table 5.3). The value of $\overline{J_{HA}}$ decreased almost linearly with the increase of the reaction time from 5 to 15 min (i.e. 1.5 to 6 times lower) but changed sharply for 20 min (i.e. up to 36 times lower). This trend in flux reduction agrees well with the reduction of the mean size of the inter-fiber space ($\overline{d_f}$) of the membranes and the changes observed in their surface due to the film formation process (see Fig. 5.3 A–C). A substantial reduction of the permeate flux of TFC membranes after a critical reaction time of the polymerization process was previously reported by other authors [14, 16, 27, 30]. This behaviour was generally related to a significant increase of the degree of crosslinking, which increased the thickness of the formed thin film, increasing the permeability resistance of the membrane.

The observed changes of the HA separation factor (α) of the PE TFNC membranes with the increase of the polymerization reaction time followed a different trend than that reported for the permeate flux (see Fig. 5.5-B). From 5 to 15 min IP reaction time, no significant enhancement of the separation factor was detected. The α values of the membranes PE TFNC1_5, PE TFNC1_10 and PE TFNC1_15 were very similar to that of the ENM 1 support and the mean value of the HA separation factor ($\bar{\alpha}$ in Table 5.3) was increased by only 8.4, 7.7 and 8.1%, respectively. These membranes were not fully covered by the PE thin film. However, a noticeable enhancement (57.6%) was observed for the α value of the membrane PE TFNC1_20 compared to ENM1 due to the fact that the membrane PE TFNC1_20 was entirely covered with the PE layer, which strongly decreased its $\overline{d_f}$ value. This phenomenon was also reported previously by other researchers who developed TFC membranes using different monomers and supports [6, 9, 27]. For instance, a significant increase in rejection of $MgSO_4$ (from 21.2 to 83.9%) was also observed by Zhang et al. [6] when a sharply decrease in the water permeability (from 15.1 to 6.0 L/m^2 h bar) of polyesteramide (PEA) TFC membranes occurred at prolonged IP reaction time.

It is worth noting that the filtration performance index (*PI*) of the membranes (Table 5.3) decreased with increasing the IP reaction time following the same trend as the final HA permeate flux (J_{HA_f}) (Table 5.3). This highlights the predominant effect of the J_{HA_f} on the *PI* of the membrane over its final separation factor (α_f). For instance, despite the considerable

enhancement of α_f of the membrane PE TFNC1_20, its *PI* decreased 73.6% with respect to the membrane PE TFNC1_15 due mainly to the strong reduction of its permeate flux.

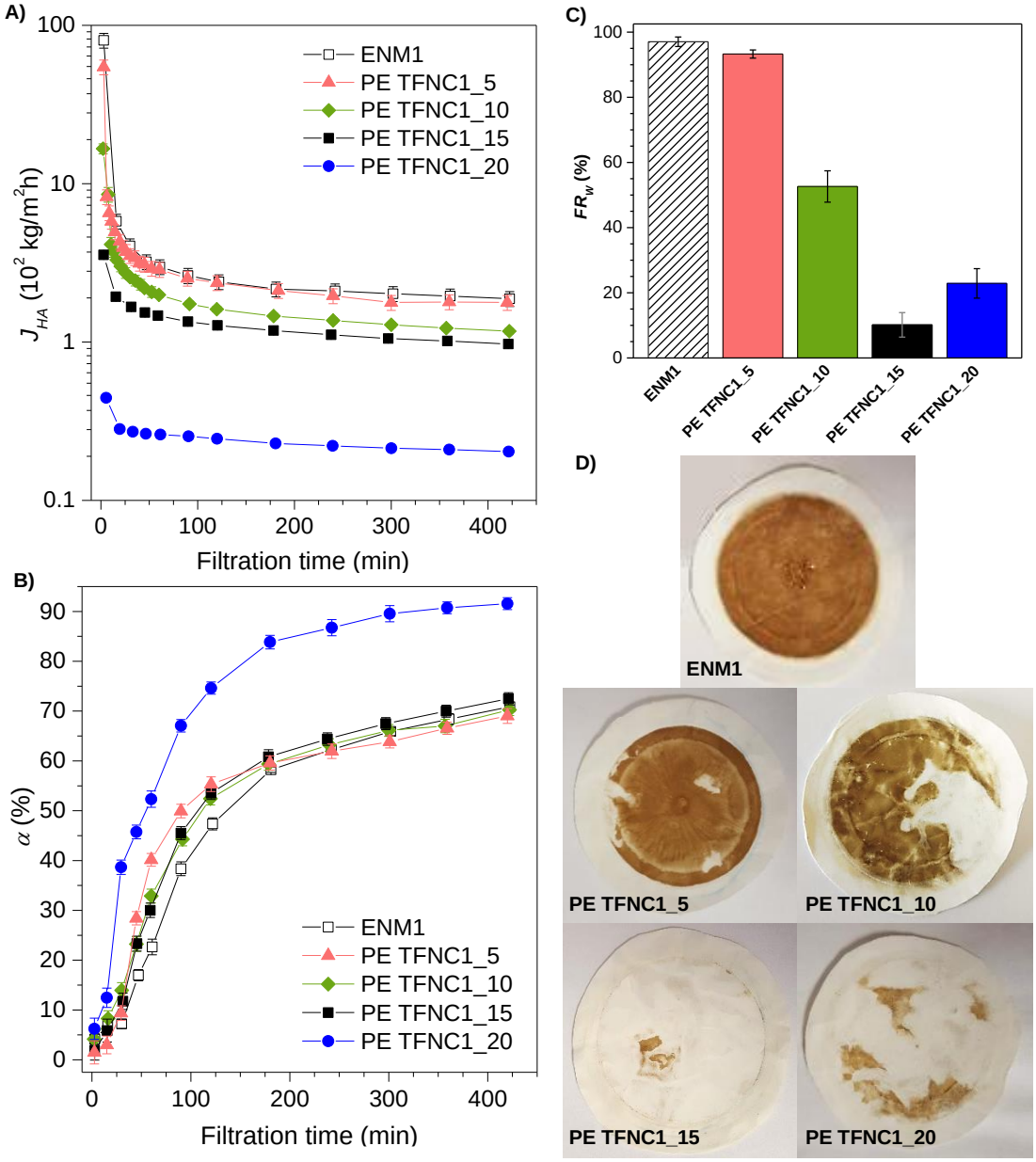

Figure 5.5. Influence of the polymerization reaction time on the filtration properties of polyester thin film nanofiber composite membranes. A) Humic acid permeate flux (J_{HA}) and B) separation factor (α) as a function of filtration time of the unmodified supporting membrane (ENM1) and the surface modified PE TFNC membranes prepared with reaction times of 5 min (PE TFNC1_5), 10 min (PE TFNC1_10), 15 min (PE TFNC1_15) and 20 min (PE TFNC1_20). C) Irreversible fouling factors (FR_W), and D) photographs of the membranes after the filtration tests carried out with 15 mg/L HA feed aqueous solution at pH 11 and 10^5 Pa transmembrane pressure.

The antifouling properties of the membranes were evaluated by determining their irreversible fouling factor (FR_W) after the HA filtration tests as described earlier. The results are summarized in Table 5.3 and plotted in Fig. 5.5-C. All surface modified PE TFNC membranes exhibited lower fouling tendency than that of the ENM1 support. Compared to this membrane (FR_W = 96.8%), the FR_W value of the PE TFNC membranes decreased with the IP reaction time to 10.2% for the membrane PE TFNC1_15 (i.e. ~90% of the initial water permeate flux (J_{w0}) was recovered after cleaning the membrane with pure water). An increase of the FR_W value was detected when further increasing the IP reaction time to 20 min (22.9%), but it remained smaller than that of the membranes PE TFNC1_5 (93.3%) and PE TFNC1_10 (52.6%). Photographs of the ENM1 support and the PE TFNC membranes after performing the HA filtration tests (Fig. 5.5-D) are consistent with the mentioned FR_W results. The membrane with the best antifouling performance (PE TFNC1_15) showed the lowest HA deposition on its surface.

The trend of the fouling tendency with IP reaction time can be explained by the changes in the morphological structure of the PE TFNC membranes (Table 5.3). It is well known that membrane surface roughness, hydrophilicity and charge density are the three major factors affecting fouling phenomena [3-6]. Foulants preferentially accumulate and adhere to a hydrophobic and rough membrane surface while those deposited on a hydrophilic and smooth surface are easily removed [5]. The PE layer formed during the first 15 min of the IP process made the surface of the membrane less rough (Fig. 5.3-A), which therefore reduced its fouling tendency (i.e. FR_W value was reduced from 96.8 to 10.2%). With a further increase of the IP reaction time to 20 min, the membrane surface became rougher than that obtained for 15 min and the FR_W value was increased ($FR_{W,\ 20\ min}$ = 22.9%, see Table 5.3). Seman et al. [45] also found a clear correlation between the roughness of BPA PE TFC membranes and the obtained FR_W values.

Additionally, the unreacted residual hydroxyl groups (–OH) on the membrane surface can effectively enhance the membrane hydrophilicity and therefore its antifouling capacity against hydrophobic foulants [3, 5, 6]. The increasing number of the –OH groups on the membrane surface with the increase of the IP reaction time from 5 to 15 min (Fig. 5.4-B) agrees well with the reduction of the FR_W of the corresponding PE TFNC membranes. For 20 min reaction time, the membrane PE TFNC1_20 exhibited a reduced OH bonding, which together with its rougher surface decreased its fouling resistance compared to the membrane PE TFNC1_15.

The electrostatic interaction between the membrane surface and solutes in the feed solution also affects particles deposition and fouling tendency [6, 29]. At pH 11, both HA particles and PSU ENMs are negatively charged [37]. According to the values of the ζ-potential shown in Table 5.3, all PE TFNC membranes exhibited higher negative surface charge (i.e. lower ζ-potential values) than that of the ENM1 support. Therefore, the electrostatic repulsion between

Table 5.5. Interfacial polymerization conditions, physicochemical properties and filtration and antifouling performance of different reported polyester and polyamide thin film composite membranes: molecular weight cut off (*MWCO*), mean pore size (*MPS*), zeta potential (ζ-potential), transmembrane pressure (Δ*P*), pure water permeability (*PWP*), final separation factor (α_f) and irreversible fouling factor (FR_W).

Membrane[1] (monomer AP-monomer OP /support)	IP conditions[2]			Physicochemical properties		Filtration performance[3]				Antifouling performance[4]		Ref
	TFC type	AP/OP (% w/v)	t_{IP}	*MWCO* *MPS*	ζ-potential (mV) (pH)	Δ*P* (bar)	*PWP* (LMH /bar)	Solution	α_f (%)	Solution (pH)	FR_w (%)	
TEOA-TMC/PSU MF^C	PE	5/0.5^{oc}	35 min	-	-1.75* (9)	6	0.82*	0.6 g/L $MgSO_4$	56.8*	-	-	[29]
PEN-TMC/PES UF^C	PE	5/0.2^{oc}	20 min	820 Da	-57.4* (10)	5	1.3	1 g/L $MgSO_4$	67.9	-	-	[32]
(HPE-SDS)-TMC/PAN UF^C	PE	2.7-0.3/0.5	30 min	4000 Da	-14.1* (8)	6	6.2*	1 g/L $MgSO_4$	48.9*	-	-	[50]
TMBPA-TMC/PES NF^C	PE	0.1/0.15	30 s	1.32 nm	-	6	4.6	-	-	15 mg/L HA (7)	5.4	[7]
BPA-TMC/PES NF^C	PE	2/0.15	10 s	1.00 nm	-	6	2.6	-	-	15 mg/L HA (7)	-13.6*	[53]
TA-TMC/PES UF^C	PE	0.05/0.01^{oc}	3 min	-	-	2	23.4	1.2 g/L $MgSO_4$	50.2*	1 g/L HA	1.0	[8]
(SE-DMAP)-TMC/PES UF^C	PEA	1/0.05^{oc}	70 s	474 Da	-43.2* (10)	5	6.0	1 g/L $MgSO_4$	83.9	0.5 g/L HA (7.4)	24.0	[6]
PIP-TMC/PES UF^C	PA	1/0.05^{oc}	70 s	309 Da	-79.2 (9.8)	5	10.3	1 g/L $MgSO_4$	97.4	0.5 g/L HA (7.4)	48.0	
CDADO-TMC/PSU UF^L	PEA	2/0.3^{oc}	2 min	-	-23.3* (10)	10	5.3	2 g/L Na_2SO_4	91.0	0.5 g/L BSA	26.2	[5]
PIP-TMC/PSU UF^L	PA	2.5/0.3	2 min	-	-13.6* (10)	10	3.0	2 g/L Na_2SO_4	90.0	0.5 g/L BSA	58.6	
(PIP-BPID-TEA)-TMC/PAN ENM^L	PA	0.7-0.3-1/0.1	1 min	-	-	4.8	20.4$_p$	2 g/L $MgSO_4$	87.0	-	-	[34]

(PIP-TEA)-TMC/PES ENM[L]	PA	1-1/0.1	1 min	-	-	4.8	6.7_p	2 g/L $MgSO_4$	99.1	-	-	[33]
(PIP-TEA)-TMC/PAN UF[C]	PA	1-1/0.1	1 min	-	-	4.8	3.0_p	2 g/L $MgSO_4$	97.3	-	-	
NF270[C]	PA	-	-	-	-41.3 (9)	13.8	14.5	2 g/L $MgSO_4$	97.4	-	-	[33, 54]
NF90[C]	PA	-	-	-	-37.0 (9)	13.8	11.2	2 g/L $MgSO_4$	99.0	-	-	
(PIP-DABSA)-TMC/PAN MF[L]	PA	1-1/0.1[oc]	1 min	-	-	3	20.4*	1 g/L Na_2SO_4	95.6*	1.5 g/L CTAB	15.4	[10]
PIP-TMC/PAN MF[L]	PA	2/0.1	1 min	-	-	3	15.2	1 g/L Na_2SO_4	95.2*	1.5 g/L CTAB	46.7	
PIP-TMC/PSU UF[L]	PA	2/0.05	30 s	294* Da	-28.9* (6.5)	7	4.1_p	2 g/L $MgSO_4$	89.6	1 g/L BSA (7.4)	16.0	[4]
PIP-TMC/PSU UF[L]	PA	0.2/0.15	50 s	280 Da	-65.2 (7)	5	14.2	0.5 g/L Na_2SO_4	98.3	0.5 g/L BSA (7)	24.8	[3]
BPA-TMC/PSU ENM[L]	PE	2/0.25[oc]	15 min	2.26 µm	-72.5 (10)	1	213	15 mg/L HA	72.5	15 mg/L HA (11)	10.2	This study
BPA-TMC/PES MF[C]	PE	2/0.25	15 min	0.46 µm	-48.1 (10)	1	25.6	15 mg/L HA	86.9	15 mg/L HA (11)	-220**	
(PIP-TEA)-TMC/PSU ENM[L]	PA	1-1/0.25	5 min	2.84 µm	-49.2 (10)	1	324	15 mg/L HA	69.0	15 mg/L HA (11)	46.4	
(PIP-TEA)-TMC/PES MF[C]	PA	1-1/0.25	5 min	0.52 µm	-34.8 (10)	1	4.4	15 mg/L HA	91.0	15 mg/L HA (11)	-33.0**	

[1]AP = aqueos phase; OP = organic phase; [C] = commercial support; [L] = Lab-made support; TEOA = triethanolamine; TMC = trimesoyl chloride; PSU = polysulfone; MF = microfiltration; PEN = pentaerythritol; PES = polyethersulfone; UF = ultrafiltration; HPE = hyperbranched polyester; SDS = sodium dodecyl sulfate; PAN = polyacrylnitrile; TMBPA = tetramethyl bisphenol A; NF = nanofiltraton; BPA = bisphenol A; TA = tannic acid; SE = seriol (2-Amino-1, 3-propanediol); DMAP = 4-dimethylaminopyridine; PIP = piperazine; CDADO = carboxylated aromatic diamine-diol; BPID = bipiperidine; TEA = trimethylamine; ENM = electrospun nanofiber membrane; DABSA = 2,5-diaminobenzene sulfonic acid.

[2]IP = interfacial polymerization; PE = polyester; PEA = polyesteramide; PA = polyamide; [oc] = optimized conditions; t_{IP} = IP reaction time.

[3]The subscript p indicates that these values correspond to permeate fluxes instead of pure water fluxes.

[4]HA = humic acid; CTAB = cyltrimethylammonium bromide; BSA = bovine serum albumin.

*Estimated values taken from figures plotted in the corresponding reference.

**The negative values of the FR_W are due to the partial detachment of the thin film layer from the supporting membrane.

the HA particles and the membrane surface increased, resulting in a lower HA fouling tendency. The increase of the negative surface charge was caused by the presence of the –OH and –COOH groups on the membrane surface, or which is the same by the phenoxide and carboxylate ions ($–O^-$, $–COO^-$) at a basic pH [5, 18]. The membrane PE TFNC1_15 had the lowest ζ-potential value (-72.5 mV) and the lowest FR_W value (10.2%) as well indicating its greatest antifouling performance.

Taking into account the results of both the filtration and the antifouling performance of all PE TFNC membranes, the membrane PE TFNC1_15 was selected as the best membrane and therefore, 15 min was considered as the optimum IP reaction time to prepare these PE TFNC membranes. Compared to other reported PE TFC membranes [7, 8, 29, 32, 50, 53] (see Table 5.5), the optimized PE TFNC1_15 exhibited very good filtration performance, with an extremely high water permeability (213.0 L/m^2 h bar at 23°C, up to 2 orders of magnitude higher) and a competitive final HA separation (72.5%). For instance, the PE TFC membrane developed by Cheng et al. [32] with a similar optimum IP reaction time (20 min) and a comparable negative surface charge (ζ-potential = -57.4 mV) to that of the membrane PE TFNC1_15, exhibited a much lower water permeability (1.34 L/m^2 h bar at 25°C) and only a $MgSO_4$ rejection of 67.9%. In terms of antifouling performance, the optimized membrane PE TFNC1_15 in the present study exhibited a FR_W value as low as 10.2%, comparable to that of the PE TFC membrane prepared by Seman et al. [7] (FR_W = 5%) used also for the treatment of 15 mg/L HA solutions under basic conditions.

5.3.2 Polyester thin film composite membranes prepared with different supports

The effects of the supporting membrane on the formation of the PE thin film layer and on the physicochemical and filtration properties of PE TFC membranes were investigated. A second heat-treated optimized PSU ENM (ENM2) and a commercial PES MF membrane (PES) were used as supports to prepare PE TFC membranes following the same IP procedure to get the best PE TFNC membrane in the previous section (PE TFNC1_15: 2% w/v BPA reacts with 0.25% w/v TMC for 15 min IP reaction time). The morphological properties and *PWP* values of all different supporting membranes are summarized in Table 5.1. Although the morphological properties of the three selected supports (ENM1, ENM2, PES) are different, their filtration performance under the same conditions are high as reported in our previous study [36].

.

5.3.2.1 Effects of the supporting membrane on the physicochemical properties of polyester thin film composite membranes

The physicochemical properties of the supporting membranes and the corresponding PE TFC membranes are displayed in Fig. 5.6. The observed differences between the surface morphology of the PE TFC membranes (Fig. 5.6-A) suggested that the supporting membrane affected the formation of the PE film layer. While the membrane PE TFNC1_15 exhibited a smooth surface, the membranes PE TFNC2_15 and PE TFC_15 had rougher surfaces with nodular structure similar to that of the membrane PE TFNC1_20 (Fig. 5.3-A). Compared to their supports, a clear reduction of the mean pore size ($\overline{d_f}$) of all surface modified membranes was observed. The $\overline{d_f}$ values decreased by 30.0, 51.6 and 19.3% for the membranes PE TFNC1_15, PE TFNC2_15 and PE TFC_15, respectively (see Fig. 5.6 B and C, and data in Table 5.3).

It worth quoting that during IP, the hydrophilicity and the pore size of a supporting membrane are key parameters affecting film formation [20, 21, 23, 24, 35]. For instance, Singh et al. [20] studied the structural variations of PA TFC membranes prepared over PSU porous membranes with different pore sizes. It was reported that a two-fold thicker PA thin film layer was formed on the supporting membrane with a smaller pore size. Kaur et al. [35], who studied the influence of the nanofiber diameter ($\overline{\lambda_w}$) of ENMs supports on the formation of the PA thin film layer, claimed that the ENMs with larger $\overline{\lambda_w}$ resulted in a thinner PA layer with a smoother structure, whereas when the value of $\overline{\lambda_w}$ was smaller, the packing density of the nanofibers was higher and the inter-fiber space was lower, favouring a rougher PA layer with a more cross-linked and packed structure. Ghosh and Hoek [21] investigated the influence of the physical and chemical properties of different porous PSU supports on the PA thin film layer characteristics. More hydrophobic supports resulted in a thicker and rougher PA thin film layer. The above mentioned results agree well with the different morphological structures of the membranes PE TFNC1_15 and PE TFNC2_15 (Fig. 5.6-A). The ENM2 support had a smaller inter-fiber space and nanofiber diameters, and a higher water contact angle (i.e. more hydrophobic) than ENM1 (Table 5.1). Therefore, a thicker and rougher PE layer was expected for the membrane PE TFNC2_15 compared to the membrane PE TFNC1_15. After IP, the reduction of the $\overline{d_f}$ value of the membrane PE TFNC2_15 was almost 2 times higher than that of the membrane PE TFNC1_15. In addition, the membrane PE TFC_15 had a rougher surface than the membrane PE TFNC1_15, which was also consistent with the results reported in previous studies as the PES support had 5.6 times smaller $\overline{d_f}$ value than ENM1 [21].

FTIR spectra of the unmodified supporting membranes together with their respective surface modified membranes are displayed in Fig. 5.6-D. An excess of BPA was detected in all surface modified membranes, as their FTIR spectra showed a weak adsorption peak at about

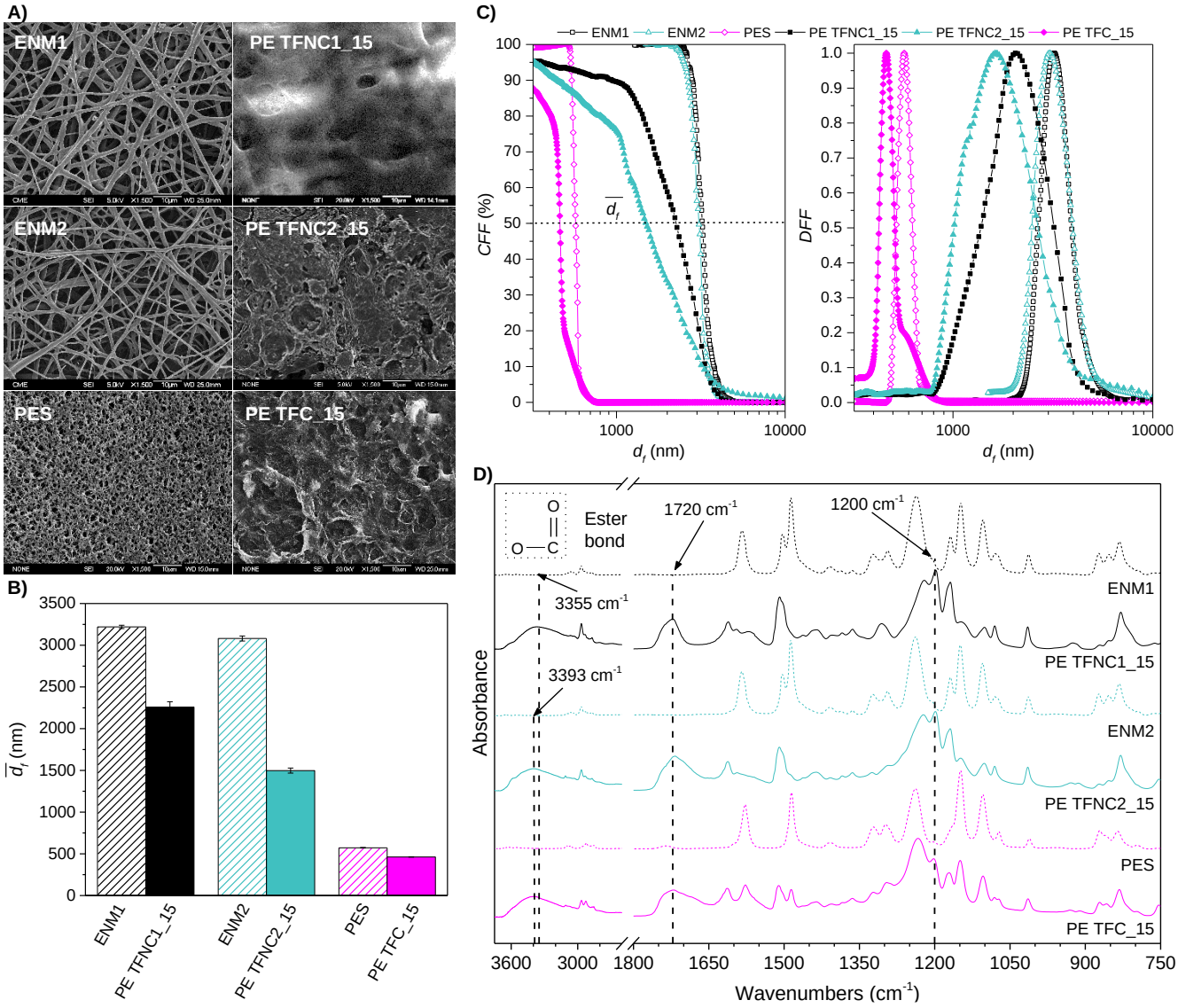

Figure 5.6. Influence of the supporting membrane on the morphological and structural characteristics of polyester thin film composite membranes. A) SEM surface images at X1500 magnification, B) mean pore size ($\overline{d_f}$), C) normalized differential (*DFF*) and cumulative (*CFF*) pore size distributions, and D) FTIR spectra of the unmodified supporting membranes (ENM1, ENM2, PES) and the surface modified membranes (PE TFNC1_15, PE TFNC2_15, PE TFC_15, respectively). All membranes were prepeared with 15 min reaction time of BPA and TMC as described in Fig. 5.2-A.

1612 cm^{-1} and a larger contribution of the peaks at 1509 and 832 cm^{-1} compared to the FTIR spectra of their supports, mainly attributed to the C=C aromatic stretching vibration of the ring of the BPA moiety. However, the BPA excess in the membranes PE TFNC2_15 and PE TFC_15 was lower than that of the membrane PE TFNC1_15, as the respective intensities of the peaks were lower than those observed in the FTIR spectrum of the membrane PE TFNC1_15. New absorption peaks of the ester group bands at 1720 and 1200 cm^{-1} were observed for all surface modified membranes confirming the successful formation of the PE thin film layer regardless of the supporting membrane used. The peak assigned to the C=O

stretching vibration of the ester group at 1720 cm^{-1} of the membranes PE TFNC2_15 and PE TFC_15 was much wider than that of the membrane PE TFNC1_15, mainly due to a new contribution centered at 1698 cm^{-1}, which revealed the presence of carboxylic acid groups (–COOH). These –COOH groups for the membranes PE TFNC2_15 and PE TFC_15 were responsible for the shift of the center of the broad absorption peak between 3150–3700 cm^{-1} (stretching vibration of the hydroxyl groups (–OH) of the membranes) to higher wavenumbers (~3393 cm^{-1}) compared to that of the membrane PE TFNC1_15 (~3355 cm^{-1}) (Fig. 12.2-B). In addition, similar to the FTIR spectrum of the membrane PE TFNC1_20, a broad contribution between 2300 and 2700 cm^{-1} and a narrow peak at 3110 cm^{-1} also emerged in the FTIR spectra of the membranes PE TFNC2_15 and PE TFC_15 due to the presence of –COOH groups (Fig. 12.2 A and B). The chemical structural differences in the FTIR spectra of the membranes PE TFNC2_15 and PE TFC_15 compared to that of the membrane PE TFNC1_15 agreed with the morphological structural differences observed in the SEM surface images of their formed PE thin film layers (Fig. 5.6-A). As it was explained in section 5.3.1.1, the surface modified membrane having carboxylic acid groups (PE TFNC1_20) reached a higher degree of crosslinking during IP, resulting in a denser, thicker and rougher PE film layer. Based on the similarities between the surface morphology and the FTIR spectra of the membranes PE TFNC2_15 and PE TFC_15 (Fig. 5.6 A and D) and that of the membrane PE TFNC1_20 (Fig. 5.3 A and D), it could be deduced that the smaller pore size of the ENM2 and PES supports favoured a faster IP reaction compared to ENM1 and resulted in the formation of a thick and rough PE layer with high crosslinking degree in only 15 min IP reaction time.

5.3.2.2 Effects of the supporting membrane on the filtration performance of polyester thin film composite membranes

All surface modified membranes exhibited lower J_{HA} and greater α values than those of their respective supports (Fig. 5.7 A and B). The reduction of the permeate flux was expected because of the reduction of the mean pore size ($\overline{d_f}$) of the PE TFC membranes and the subsequent increase of the permeate resistance due to the formation of the PE layer. The greatest reduction of $\overline{J_{HA}}$ was observed for the membrane PE TFNC2_15 (97%), which also experienced the greatest reduction of its $\overline{d_f}$ compared to its support. In general, it is expected a decline of J_{HA} with the filtration time due mainly to fouling phenomena. However, J_{HA} of the membrane PE TFC_15 increased with time. Its water permeate flux after conducting HA filtration test was 3.2 times higher than its initial water permeate flux. This unexpected behavior may be due to the partial detachment of the PE layer from the PES support during HA filtration test, decreasing the permeate resistance of the membrane. Bui et al. [49] also found adhesion problems of the PA layer to the PES support when developing PA TFNC membranes on PSU ENMs and PES ENMs. Compared to PSU ENM support, a weaker adhesion of the PA layer to the PES ENM

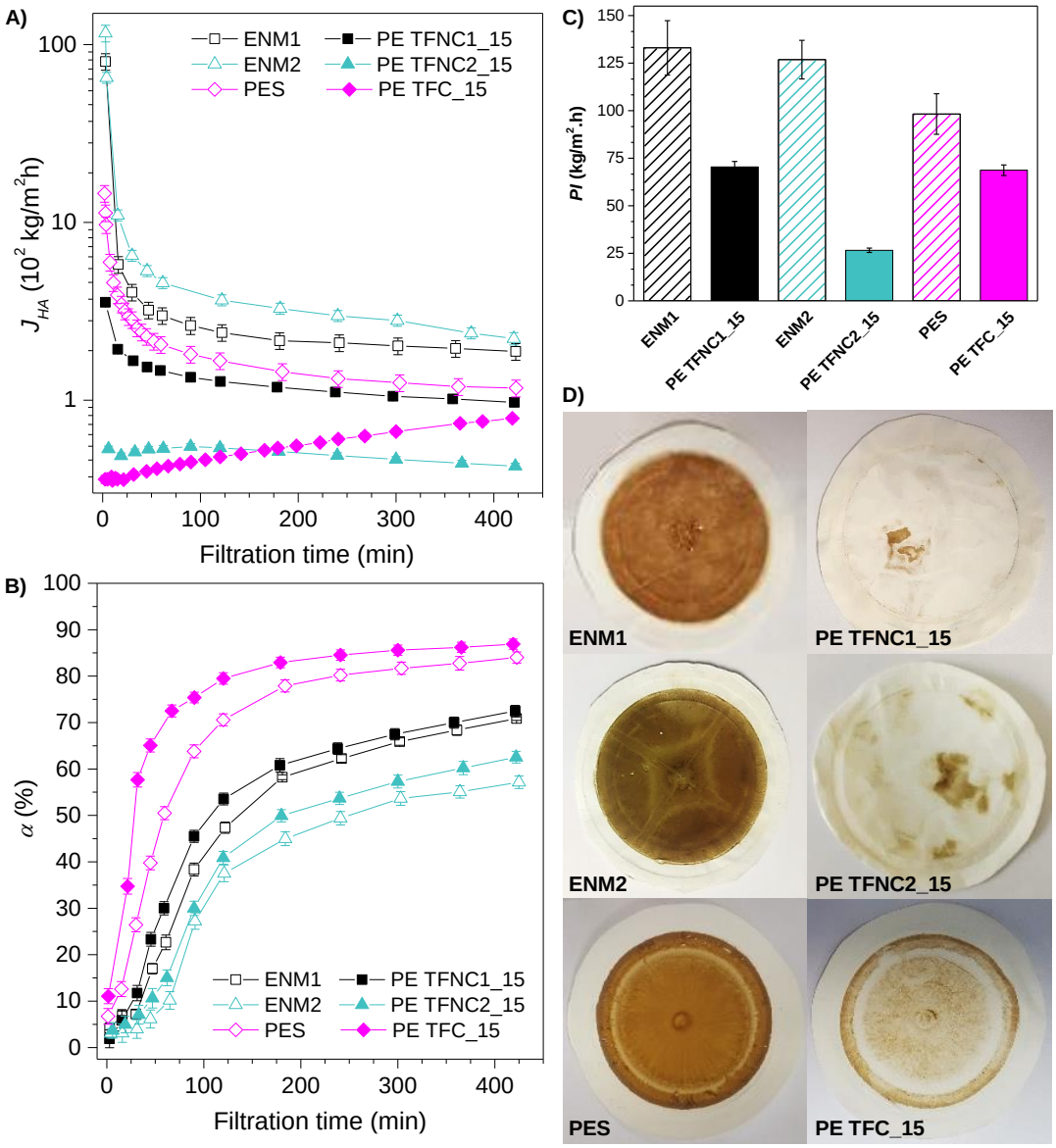

Figure 5.7. Influence of the supporting membrane on the filtration properties of polyester thin film composite membranes. A) Humic acid permeate flux (J_{HA}) and B) separation factor (α) as a function of filtration time of the unmodified supporting membranes (ENM1, ENM2, PES) and the surface modified membranes (PE TFNC1_15, PE TFNC2_15, PE TFC_15, respectively). C) Performance index (*PI*) and D) photographs of the membranes after filtration tests carried out with 15 mg/L HA feed aqueous solution at pH 11 and 10^5 Pa transmembrane pressure.

support was observed so that delamination and, in some cases, detachment of the PA layer from the PES support occurred. It was hypothesized that the BPA moiety difference between the chemical composition of PSU and PES together with the higher water contact angle of the PSU support contributed to the good adhesion of the PA layer to PSU. In the present study, the PES support exhibited up to 4.7 times lower water contact angle value than the PSU ENM1 and ENM2 supports, which basically may reduce the adhesion capability of PE layer to PES support. Moreover, taking into consideration that ENM1 and ENM2 are electrospun nanofibrous PSU

supports with inter-fiber spaces bigger than the pore size of the PES phase inversion membrane support, the BPA in the aqueous phase may penetrate easily through part of the nanofiber network favoring the formation and growth of the PE layer from the inter-fiber space and resulting in a better adhesion.

The enhancement of α for all surface modified membranes compared to their corresponding supports (Fig. 5.7-B) was mainly related to the formation of the PE layer and reduction of their $\overline{d_f}$. In addition, the surface modified membranes exhibited lower ζ-potential values (i.e. higher negative surface charge, see Table 5.3) than their supports, which resulted in an enhancement of the electrostatic repulsion forces between the HA particles and the membrane surface favouring the HA separation as consequence.

All surface modified membranes exhibited better antifouling capacity (i.e. lower FR_W values, Table 5.3) than their respective supports. The negative FR_W value determined for the membrane PE TFC_15 resulted from the increase of the water permeate flux from its initial value after the HA filtration test. The FR_W value of the membrane PE TFNC2_15 (20.1%) was larger than that of the membrane PE TFNC1_15 (10.2%). Both membranes exhibited quite similar ζ-potential values (Table 5.3), but the membrane PE TFNC2_15 had a rougher PE layer, which contributed to its higher fouling tendency (higher FR_W value).

The photographs shown in Fig. 5.7-D of the unmodified and surface modified membranes after HA filtration tests are consistent with the mentioned results of the FR_W. The surface of the membrane PE TFNC1_15 with the lowest HA deposition is the membrane with the best antifouling performance (i.e. lowest FR_W value). It is to be noted that although the FR_W value calculated for the membrane PE TFC_15 was negative, HA was deposited on its entire surface indicating that this membrane also experienced fouling.

The filtration performance of the different membranes used as supports as well as the surface modified membranes were evaluated using their *PI* values (see Fig. 5.7-C and Table 5.3). The membrane PE TFNC2_15 exhibited the lowest *PI* value (26.6 kg/m^2 h), whereas membranes PE TFNC1_15 and PE TFC_15 achieved similar *PI* values (70.4 and 68.7 kg/m^2 h, respectively). Although the membranes PE TFNC1_15 and PE TFC_15 exhibited similar *PI* values, their physicochemical and morphological properties together with other filtration parameters were different. For instance, the initial water permeate flux (J_{w0}) of the membrane PE TFNC1_15 (213 kg/m^2 h) was 8 times higher than that of the membrane PE TFC_15 (26 kg/m^2 h). The HA filtration test showed that the $\overline{J_{HA}}$ value of the membrane PE TFNC1_15 (151 kg/m^2 h) was 3 times higher than that of the membrane PE TFC_15 (51 kg/m^2 h), but its HA separation factor (α_f = 72.5%) was worse than that of the membrane PE TFC_15 (α_f = 86.9%). In addition, from the photographs of the membranes taken after HA filtration tests (Fig. 5.7-D), less HA deposition was observed on the surface of the membrane PE TFNC1_15 compared to

that of the membrane PE TFC_15. Taking into account both the filtration performance and antifouling capacity of these membranes and considering the lack of stability of the PE thin layer of the membrane PE TFC_15 (i.e. detachment due to poor adhesion of PE to its support), the membrane PE TFNC1_15 was chosen as the best PE TFC membrane developed in this study.

5.3.3 Polyester *versus* polyamide thin film composite membranes

It is worth quoting that most TFC membranes have been prepared with IP that involved amine monomers in the aqueous phase to form a PA thin film layer on a supporting membrane. Compared to PA TFC membranes, very few research studies have been focused on PE TFC membranes. This may be due to the greater salt rejection of the PA TFC membranes compared to that of PE TFC membranes attributed to their denser structure with a high crosslinking degree although the PE TFC membranes exhibited better antifouling capacity against hydrophobic contaminants because of the presence of abundant hydroxyl groups on their surface [5, 6]. In this section, PA TFC membranes were prepared and their filtration and antifouling properties were compared to those of the previously prepared PE TFC membranes that exhibited a high filtration performance (PE TFNC1_15 and PE TFC_15 in Table 5.3).

Different combinations of monomers and conditions of the IP process were considered to form the PA thin film layer. Details of the followed procedure to select the final IP approach can be found in the Appendix B (see Figs. 12.3–12.9 and Tables 12.1–12.4). The selected IP consists of 1% w/w PIP that reacted with 2% w/v TMC in presence of 1% w/w TEA (acid acceptor) during 5 min IP reaction time. The schematic mechanism of this IP reaction is shown in Fig. 5.2-B. Both ENM1 and the MF commercial PES membrane were used as supports to form the membranes PA TFNC1_5 and PA TFC_5, respectively.

5.3.3.1 Physicochemical properties of polyamide thin film composite membranes

The structure of the PA TFC membranes (PA TFNC1_5 and PA TFC_5) was studied by means of SEM (Fig. 5.8-A). The surface morphology of these membranes was different from the corresponding PE TFC membranes (PE TFNC1_15 and PE TFC_15). The PA thin film layer of the membrane PA TFNC1_5 was formed in the inter-fiber space wrapping the PSU nanofibers and preserving the nanofiber structure of the support and its roughness (see also Fig. 12.10 in Appendix B). A similar surface morphology of PA TFNC membranes was observed by other authors [35, 49]. The membrane PA TFC_5 showed a rough PA layer that covered completely the surface of the PES support. The granular structure formed throughout the PA layer of both membranes is typically attributed to the crosslinking of the used monomers PIP and TMC [16, 18, 55]. From the SEM images, the thin film layer of the membrane

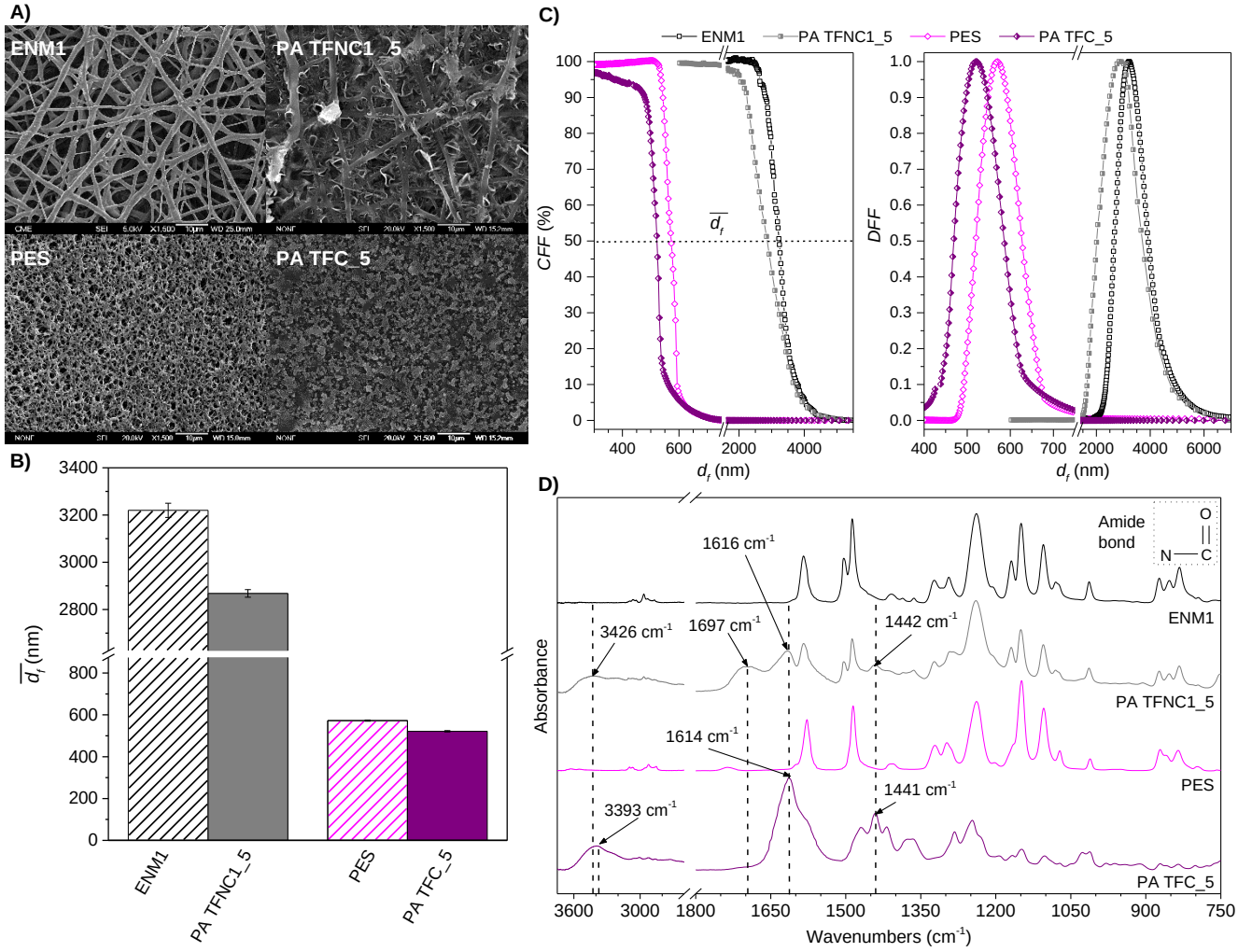

Figure 5.8. Morphological and structural characteristics of polyamide thin film composite membranes prepared on different supports. A) SEM surface images at X1500 magnification, B) mean pore size ($\overline{d_f}$), C) normalized differential (*DFF*) and cumulative (*CFF*) pore size distributions, and D) FTIR spectra of the unmodified supporting membranes (ENM1, PES) and their respective surface modified membranes (PA TFNC1_ 5, PA TFC_5). The PA TFC membranes were prepared with 5 min reaction time of PIP and TMC in presence of the acid acceptor TEA as described in Fig. 5.2-B.

PA TFC_5 seemed to be denser than that of the membrane PA TFNC1_5. The porometry measurements confirmed the reduction of the $\overline{d_f}$ value of the membranes PA TFNC1_5 and PA TFC_5 with respect to their supports due to the addition of the PA layer (Fig. 5.8 B and C, and Table 5.3).

The differences in the chemical structure of the PA TFC membranes were studied by FTIR spectra shown in Fig. 5.8-D. Table 5.4 summarizes the assignments of IR bands for the ENM1 and PES supports as well as for the PA TFC membranes. Beside the typical IR bands of the PSU and PES substrates, the spectra of the PA TFC membranes exhibited absorption peaks at about 1442 and 1616 cm^{-1}. The peak at 1442 cm^{-1} was assigned to the C–O stretching and the O–H bending vibration of the carboxylic acid group as well as to the bending vibration of the

methylene group (–CH_2–). Whereas the peak at 1616 cm^{-1} was attributed to the C=O and the C–N stretching vibrations of the amide bond formation (–CONH) (amide I band). Furthermore, the broad adsorption peak between 3150–3700 cm^{-1} centred at about 3426 cm^{-1} for the membrane PA TFNC1_5 and at 3393 cm^{-1} for the membrane PA TFC_5 was mainly attributed to the O–H stretching vibration of the carboxylic acid group (–COOH) formed by the partial hydrolysis of the acyl chloride unit of TMC. It was reported that some contribution to the latter peak could also correspond to the N–H stretching vibration of residual amine bonds [6, 13, 48]. The membrane PA TFC_5 also displayed a peak at 1283 cm^{-1}, which could be assigned to the N–H in-plane bending coupled with the C–N stretching or to the C–H and N–H deformation vibration of amide III band. The membrane PA TFNC1_5 exhibited a peak at about 1697 cm^{-1} attributed to the C=O stretching vibration of the carboxylic acid group. The presence of all the above cited peaks verified the successful formation of the PA thin layer on the surface of both supports, ENM1 and PES. The intensity of the peak at about 1616 cm^{-1} (previously ascribed to the amide bond formation) was higher for the membrane PA TFC_5 compared to the membrane PA TFNC1_5, indicating a thicker, denser and more cross-linked PA thin layer of the membrane PA TFC_5. This result was also confirmed by the characteristic IR bands of the PES support that were much more attenuated (some peaks even disappeared) in the FTIR spectrum of the membrane PA TFC_5 than those of the PSU support in the FTIR spectrum of the membrane PA TFNC1_5. These results agree well with those reported by Singh et al. [20], who claimed the formation of a thicker PA thin film layer over a supporting membrane with smaller pore sizes.

5.3.3.2 Comparison of the filtration performance of polyester and polyamide thin film composite membranes

The filtration performance of the PA TFC membranes (PA TFNC1_5, PA TFC_5) was evaluated and compared with that of the previously prepared PE TFC membranes (PE TFNC1_15, PE TFC_15) and the corresponding supporting membranes (ENM1, PES).

The change of the HA permeate flux (J_{HA}) and the HA separation factor (α) with the filtration time were plotted in Fig. 5.9 A and B. The membrane PA TFNC1_5 exhibited lower J_{HA} than that of the ENM1 support. The value of $\overline{J_{HA}}$ decreased by 68.9% compared to that of the ENM1 (from 929.5 to 289.1 $kg/m^2\,h$). This reduction of the permeate flux was mainly attributed to the reduction of the $\overline{d_f}$ value of the modified membrane. However, unlike the other surface modified TFC membranes developed in this study, the α value of the membrane PA TFNC1_5 decreased (by 6.9%) in relation to ENM1 instead of increasing. Not only the pore size of the membrane (i.e. stereo-hindrance or sieving effect) affects its separation capacity, but also the electrostatic interaction between the HA molecules and the membrane surface (i.e. electrostatic repulsion effect). After IP modification, the membrane PA TFNC1_5 exhibited a

higher ζ-potential value (-49.2 mV) compared to ENM1 (-59.4 mV). The lower negative surface charge of the membrane PA TFNC1_5 resulted in a reduction of the electrostatic repulsion

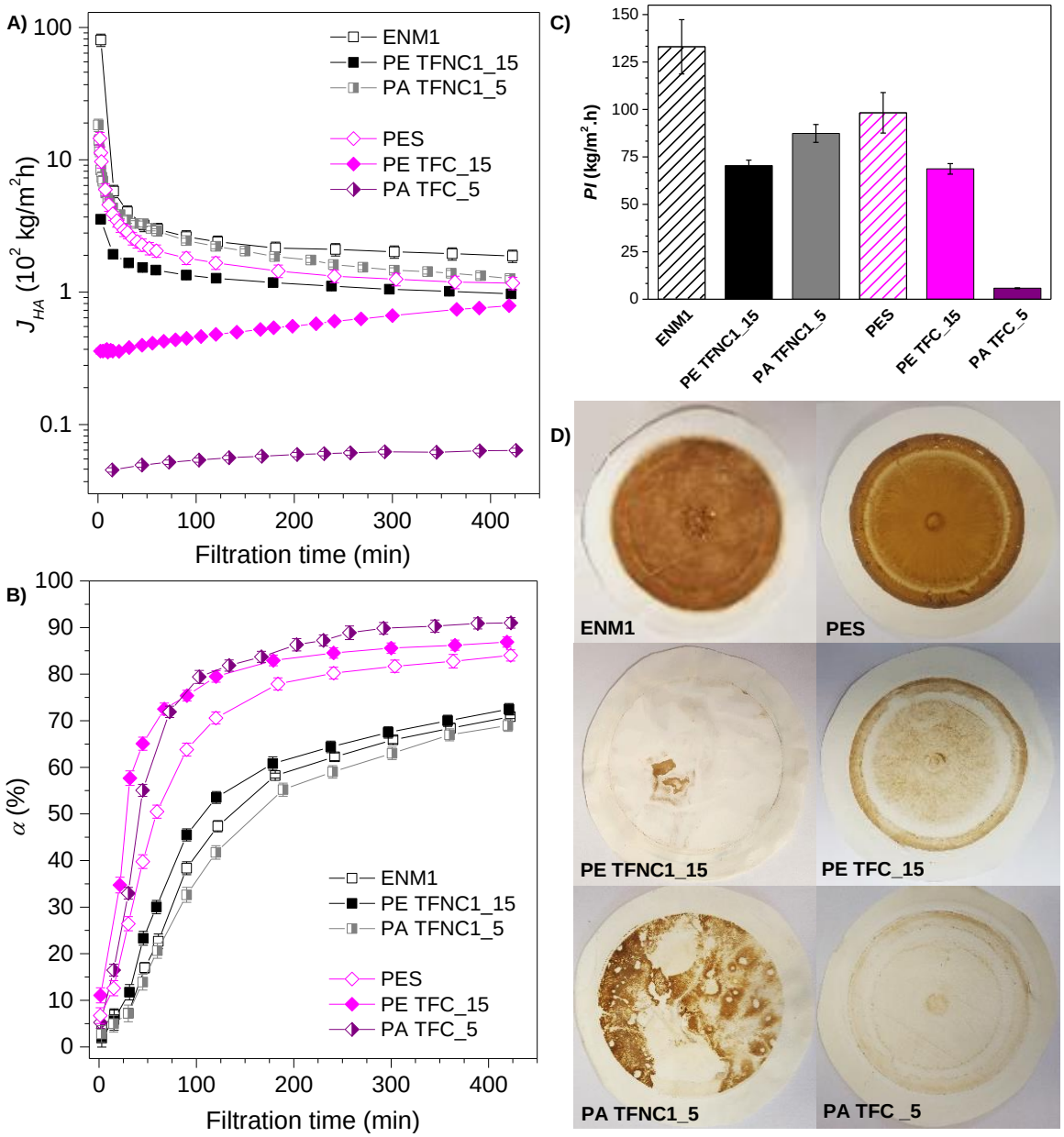

Figure 5.9. Comparison of the filtration properties of polyester and polyamide thin film composite membranes prepared on different supports. A) Humic acid permeate flux (J_{HA}) and B) separation factor (α) as a function of filtration time of the unmodified supporting membranes (ENM1, PES) and their respective surface modified polyester (PE TFNC1_15, PE TFC_15) and polyamide (PA TFNC1_5, PA TFC_5) TFC membranes. C) Performance index (*PI*), and D) photographs of the membranes after the filtration tests carried out with 15 mg/L HA feed aqueous solution at pH 11 and 10^5 Pa transmembrane pressure.

between the HA molecules and the membrane surface. In this case, both the electrostatic repulsion and size exclusion reduced the HA separation factor of the membrane PA TFNC1_5.

Despite its lower negative surface charge (i.e. a higher ζ-potential value), the membrane PA TFNC1_5 showed a better antifouling performance (FR_W = 46.4%) than that of the ENM1 (FR_W = 96.8%). As stated previously, the antifouling properties of the membranes depend mainly on the roughness, charge density and hydrophilicity of the membrane surface. After IP modification, the surface of the membrane PA TFNC1_5 contained carboxylic acid group and amine end groups, which improved its hydrophilicity compared to ENM1 [5, 16, 55]. This could be the reason of the improved antifouling properties of the membrane PA TFNC1_5. The photographs of the membranes PA TFNC1_5 and ENM1 after HA filtration tests shown in Fig. 5.9-D are consistent with the better antifouling performance of the membrane PA TFNC1_5 because less HA was deposited on its surface.

A significant decrease of J_{HA} was observed for the membrane PA TFC_5 compared to the PES support, leading to a reduction of its $\overline{J_{HA}}$ value by 97.9%. In addition, surface modification improved the separation capacity of the membrane PA TFC_5 in relation to PES by 24.3% from $\bar{\alpha}$ = 56.4% to $\bar{\alpha}$ = 70.1%. The strong decrease of the permeate flux together with the increase of the separation factor of the membrane PA TFC_5 was attributed mainly to the reduction of the $\overline{d_f}$ of the membrane due to the highly cross-linked PA layer formed on its surface. The membrane PA TFC_5 displayed also a lower negative surface charge (ζ-potential = -34.8 mV) than PES (ζ-potential = -46.4 mV), but the combining effect of the electrostatic repulsion and the size exclusion together with the high density of the PA layer improved the HA separation of the membrane PA TFC_5. The antifouling performance of the membrane PA TFC_5 was also improved compared to that of its support as it can be seen from Fig. 5.9-D where much less HA was deposited on its surface after filtration. The reduction of the fouling tendency of the membrane PA TFC_5 was likely due to the enhancement of its surface hydrophilicity after IP modification. An increase of J_{HA} with the filtration time was also observed for the membrane PA TFC_5 and its final water permeate flux after HA filtration test was larger than its initial water flux. As a result, the membrane PA TFC_5 exhibited a negative FR_W value (see Table 5.3). Similar to the membrane PE TFC_15 (section 5.3.2.2), this phenomenon could be explained by the partial detachment of the PA thin layer during the HA filtration test, which reduced the permeate resistance of the membrane.

A 74-fold higher *PWP* value was achieved by the membrane PA TFNC1_5 (i.e. 324 L/m^2 h bar) compared to the membrane PA TFC_5 (i.e. 4.4 L/m^2 h bar) (Table 5.3). The higher permeate flux of the membrane PA TFNC1_5 was likely due to the interconnected nanofibrous structure of the ENM1 support having a higher porosity than the PES support and to the

formation of water channels through the interface between the nanofibers and the PA thin layer of the membrane PA TFNC1_5 [33].

From the HA tests, the reduction of $\overline{J_{HA}}$ for the membrane PA TFC_5 compared to its support (97.9%) was higher than that of the membrane PA TFNC1_5 (68.9%). This is consistent with the previously mentioned chemical and structural differences of these membranes. The thicker, denser and more cross-linked PA thin layer of the membrane PA TFC_5 caused a higher reduction of the permeate fluxes and an improved HA separation performance. Moreover, the increase of the ζ-potential of this membrane from that of its support (25.0%) was also greater than that of the PA TFNC1_5 (17.2%). This justified the more cross-linked PA thin film layer of the membrane PA TFC_5. It is well known that the negative surface charge of this type of poly(piperazine-amide) TFC membranes is mainly attributed to the deprotonation of carboxyl groups (–COOH → $–COO^-$) dissociated from the unreacted acid chlorides of TMC [10, 18]. Therefore, the greater crosslinking degree of the PA layer of the membrane PA TFC_5 indicated the lower amount of carboxyl groups available to be deprotonated and the subsequent lower negative surface charge of the membrane PA TFC_5 compared to that of the membrane PA TFNC1_5 [18].

The data summarized in Table 5.5 for different reported PE and PA TFC membranes showed the good filtration performance of the prepared PA TFC membranes in this study. For instance, the permeability of the membrane PA TFNC1_5 was up to two orders of magnitude higher than that of lab-made PA TFNC membranes prepared with similar IP conditions [33, 34], whereas its separation factor was 21 to 30% lower. The membrane PA TFC_5 exhibited a very similar separation factor (only 1.5% higher α_f value) than that of the lab-made PA TFC membranes with 7 to 32% higher permeability [4, 5].

Regardless of the type of polymer of the thin film layer (i.e. PE or PA), all surface modified membranes exhibited lower fouling tendency (i.e. FR_W values from 10.2 to 93.3%, see Table 5.3) than their supports (i.e. FR_W values from 96.8 to 98.5%) than their supports.

All surface modified membranes prepared on ENM1 support (PE TFNC1_15, PA TFNC1_5) exhibited greater *PI* values (70.4 and 87.4 $kg/m^2 h$, respectively) than those prepared on PES support (68.7 $kg/m^2 h$ for PE TFC_15 and 5.8 $kg/m^2 h$ for PA TFC_5) (see Fig. 5.9-C and Table 5.3). The improved *PI* values of the TFNC membranes resulted mainly from their much larger permeability, which is directly related to the interconnected open pore structure and the high porosity of the nanofiber support.

In order to select the best membrane between PE TFNC1_15 and PA TFNC1_5, both the filtration and antifouling performance should be considered. The *PI* of the membrane PE TFNC1_15 (70.4 $kg/m^2 h$) was 20% lower than that of the membrane PA TFNC1_5 (87.4

kg/m^2 h). This was caused mainly by its lower J_{HA_f} value, 97.1 kg/m^2 h, compared to 126.7 kg/m^2 h of the membrane PA TFNC1_5 although its HA separation factor was higher (72.5%) than that of the membrane PA TFNC1_5 (69.0%). In addition, the membrane PE TFNC1_15 had better antifouling performance, exhibiting a 4.5 times lower FR_W value (10.2%) than that of the membrane PA TFNC1_5 (46.4%). Due to its enhanced antifouling properties, the water permeability of the membrane PE TFNC1_15 after HA filtration test was larger (i.e. 191.3 kg/m^2 h bar) than that of the membrane PA TFNC1_5 (i.e. 173.7 kg/m^2 h bar). The lower fouling tendency of the membrane PE TFNC1_15 guarantees it a longer lifetime and reduces maintenance costs. Taking into account all the above mentioned points, the membrane PE TFNC1_15 was chosen as the best TFC membrane developed in this study. This membrane exhibited comparable antifouling performance to previously reported PE TFC membranes with two orders of magnitude greater water permeability [29] and 6–33% better separation factor [32, 50]. Compared to other PA TFC membranes, it exhibited 34–83% greater antifouling performance [5, 10] and 10–71 times higher water permeability [5, 34] with only 17–27% lower separation efficiency [33, 34] (Table 5.5).

5.4 Conclusions

The effects of the polymerization reaction time on the physicochemical, filtration and antifouling characteristics of the PE TFNC membranes were studied. The optimum IP reaction time was found to be 15 min. The so prepared membrane PE TFNC1_15 had a smooth surface and exhibited a water permeability as high as 213.0 L/m^2 h bar with a 72.5% HA separation factor. The enhanced antifouling performance of this membrane against HA foulant permitted 90% recovery of its initial water flux after HA filtration.

The surface of the PE layer formed on the ENM2 supporting membrane with a smaller mean size of the inter-fiber space and a higher hydrophobicity was rougher and denser than that prepared on ENM1. The PE layer prepared on the commercial PES supporting membrane had a very similar surface morphology to that formed on ENM2. The PE TFC membranes formed on ENM2 and PES supports (i.e. PE TFNC2_15 and PE TFC_15, respectively) exhibited lower filtration performance indexes and worse antifouling properties than that of the PE TFC membrane prepared on ENM1 (i.e. PE TFNC1_15).

The PA layer formed on PES support was denser and higher cross-linked than that prepared on ENM1. Regardless of the type of polymer of the thin layer, PE or PA, all surface modified TFC membranes prepared on ENM1 support (PE TFNC1_15, PA TFNC1_5) exhibited greater filtration performance indexes than that of the TFC membranes prepared on PES support (PE TFC_15, PA TFC_5). The membrane PE TFNC1_15, prepared with 15 min IP reaction time of BPA and TMC on ENM1, was chosen as the best TFC membrane developed in this study as it exhibited the best antifouling capacity with a high filtration performance.

References

[1] S. Zinadini, S. Rostami, V. Vatanpour, E. Jalilian, Preparation of antibiofouling polyethersulfone mixed matrix NF membrane using photocatalytic activity of ZnO/MWCNTs nanocomposite, Journal of Membrane Science, 529 (2017) 133-141.

[2] Y. Mo, A. Tiraferri, N.Y. Yip, A. Adout, X. Huang, M. Elimelech, Improved antifouling properties of polyamide nanofiltration membranes by reducing the density of surface carboxyl groups, Environmental Science and Technology, 46 (2012) 13253-13261.

[3] F. Yan, H. Chen, Y. Lü, Z. Lü, S. Yu, M. Liu, C. Gao, Improving the water permeability and antifouling property of thin-film composite polyamide nanofiltration membrane by modifying the active layer with triethanolamine, Journal of Membrane Science, 513 (2016) 108-116.

[4] H. Li, W. Shi, Q. Du, R. Zhou, H. Zhang, X. Qin, Improved separation and antifouling properties of thin-film composite nanofiltration membrane by the incorporation of cGO, Applied Surface Science, 407 (2017) 260-275.

[5] J. Rezania, V. Vatanpour, A. Shockravi, M. Ehsani, Preparation of novel carboxylated thin-film composite polyamide-polyester nanofiltration membranes with enhanced antifouling property and water flux, Reactive and Functional Polymers, 131 (2018) 123-133.

[6] R. Zhang, S. Yu, W. Shi, W. Wang, X. Wang, Z. Zhang, L. Li, B. Zhang, X. Bao, A novel polyesteramide thin film composite nanofiltration membrane prepared by interfacial polymerization of serinol and trimesoyl chloride (TMC) catalyzed by 4-dimethylaminopyridine (DMAP), Journal of Membrane Science, 542 (2017) 68-80.

[7] M.N. Abu Seman, M. Khayet, N. Hilal, Development of antifouling properties and performance of nanofiltration membranes modified by interfacial polymerisation, Desalination, 273 (2011) 36-47.

[8] Y. Zhang, Y. Su, J. Peng, X. Zhao, J. Liu, J. Zhao, Z. Jiang, Composite nanofiltration membranes prepared by interfacial polymerization with natural material tannic acid and trimesoyl chloride, Journal of Membrane Science, 429 (2013) 235-242.

[9] C. Zhou, Y. Shi, C. Sun, S. Yu, M. Liu, C. Gao, Thin-film composite membranes formed by interfacial polymerization with natural material sericin and trimesoyl chloride for nanofiltration, Journal of Membrane Science, 471 (2014) 381-391.

[10] A. Akbari, E. Aliyarizadeh, S.M. Mojallali Rostami, M. Homayoonfal, Novel sulfonated polyamide thin-film composite nanofiltration membranes with improved water flux and anti-fouling properties, Desalination, 377 (2016) 11-22.

[11] N.K. Saha, S.V. Joshi, Performance evaluation of thin film composite polyamide nanofiltration membrane with variation in monomer type, Journal of Membrane Science, 342 (2009) 60-69.

[12] J. Xiang, Z. Xie, M. Hoang, K. Zhang, Effect of amine salt surfactants on the performance of thin film composite poly(piperazine-amide) nanofiltration membranes, Desalination, 315 (2013) 156-163.

[13] Y. Li, Y. Su, Y. Dong, X. Zhao, Z. Jiang, R. Zhang, J. Zhao, Separation performance of thin-film composite nanofiltration membrane through interfacial polymerization using different amine monomers, Desalination, 333 (2014) 59-65.

[14] C. Klaysom, S. Hermans, A. Gahlaut, S. Van Craenenbroeck, I.F.J. Vankelecom, Polyamide/polyacrylonitrile (PA/PAN) thin film composite osmosis membranes: Film optimization, characterization and performance evaluation, Journal of Membrane Science, 445 (2013) 25-33.

[15] J. Xu, H. Yan, Y. Zhang, G. Pan, Y. Liu, The morphology of fully-aromatic polyamide separation layer and its relationship with separation performance of TFC membranes, Journal of Membrane Science, 541 (2017) 174-188.

[16] N. Misdan, W.J. Lau, A.F. Ismail, Physicochemical characteristics of poly(piperazine-amide) TFC nanofiltration membrane prepared at various reaction times and its relation to the performance, Journal of Polymer Engineering, 35 (2015) 71-78.

[17] A.L. Ahmad, B.S. Ooi, Properties–performance of thin film composites membrane: study on trimesoyl chloride content and polymerization time, Journal of Membrane Science, 255 (2005) 67-77.

[18] Y. Li, Y. Su, J. Li, X. Zhao, R. Zhang, X. Fan, J. Zhu, Y. Ma, Y. Liu, Z. Jiang, Preparation of thin film composite nanofiltration membrane with improved structural stability through the mediation of polydopamine, Journal of Membrane Science, 476 (2015) 10-19.

[19] Z. Tang, C. Qiu, J.R. McCutcheon, K. Yoon, H. Ma, D. Fang, E. Lee, C. Kopp, B.S. Hsiao, B. Chu, Design and fabrication of electrospun polyethersulfone nanofibrous scaffold for high-flux nanofiltration membranes, Journal of Polymer Science Part B: Polymer Physics, 47 (2009) 2288-2300.

[20] P.S. Singh, S.V. Joshi, J.J. Trivedi, C.V. Devmurari, A.P. Rao, P.K. Ghosh, Probing the structural variations of thin film composite RO membranes obtained by coating polyamide over polysulfone membranes of different pore dimensions, Journal of Membrane Science, 278 (2006) 19-25.

[21] A.K. Ghosh, E.M.V. Hoek, Impacts of support membrane structure and chemistry on polyamide–polysulfone interfacial composite membranes, Journal of Membrane Science, 336 (2009) 140-148.

[22] K. Yoon, B.S. Hsiao, B. Chu, High flux nanofiltration membranes based on interfacially polymerized polyamide barrier layer on polyacrylonitrile nanofibrous scaffolds, Journal of Membrane Science, 326 (2009) 484-492.

[23] M. Tian, C. Qiu, Y. Liao, S. Chou, R. Wang, Preparation of polyamide thin film composite forward osmosis membranes using electrospun polyvinylidene fluoride (PVDF) nanofibers as substrates, Separation and Purification Technology, 118 (2013) 727-736.

[24] M. Fathizadeh, A. Aroujalian, A. Raisi, Effect of lag time in interfacial polymerization on polyamide composite membrane with different hydrophilic sub layers, Desalination, 284 (2012) 32-41.

[25] N. Misdan, W.J. Lau, A.F. Ismail, T. Matsuura, D. Rana, Study on the thin film composite poly(piperazine-amide) nanofiltration membrane: Impacts of physicochemical properties of substrate on interfacial polymerization formation, Desalination, 344 (2014) 198-205.

[26] L. Hu, S. Zhang, R. Han, X. Jian, Preparation and performance of novel thermally stable polyamide/PPENK composite nanofiltration membranes, Applied Surface Science, 258 (2012) 9047-9053.

[27] B.S. Ooi, J.Y. Sum, S.O. Lai, Investigation on membrane morphological and chemical properties changes at different reaction times and its effect on dye removal, Desalination and Water Treatment, 45 (2012) 250-255.

[28] A. Soroush, J. Barzin, M. Barikani, M. Fathizadeh, Interfacially polymerized polyamide thin film composite membranes: Preparation, characterization and performance evaluation, Desalination, 287 (2012) 310-316.

[29] B. Tang, Z. Huo, P. Wu, Study on a novel polyester composite nanofiltration membrane by interfacial polymerization of triethanolamine (TEOA) and trimesoyl chloride (TMC), Journal of Membrane Science, 320 (2008) 198-205.

[30] X.-Z. Wei, J. Yang, G.-L. Zhang, Preparation and characterization of nanofiltration membranes synthesized by hyperbranched polyester and terephthaloyl chloride (TPC), Polymers and Polymer Composites, 20 (2012) 261-270.

[31] X.-Z. Wei, L.-P. Zhu, H.-Y. Deng, Y.-Y. Xu, B.-K. Zhu, Z.-M. Huang, New type of nanofiltration membrane based on crosslinked hyperbranched polymers, Journal of Membrane Science, 323 (2008) 278-287.

[32] J. Cheng, W. Shi, L. Zhang, R. Zhang, A novel polyester composite nanofiltration membrane formed by interfacial polymerization of pentaerythritol (PE) and trimesoyl chloride (TMC), Applied Surface Science, 416 (2017) 152-159.

[33] L. Yung, H. Ma, X. Wang, K. Yoon, R. Wang, B.S. Hsiao, B. Chu, Fabrication of thin-film nanofibrous composite membranes by interfacial polymerization using ionic liquids as additives, Journal of Membrane Science, 365 (2010) 52-58.

[34] S. Kaur, R. Barhate, S. Sundarrajan, T. Matsuura, S. Ramakrishna, Hot pressing of electrospun membrane composite and its influence on separation performance on thin film composite nanofiltration membrane, Desalination, 279 (2011) 201-209.

[35] S. Kaur, S. Sundarrajan, D. Rana, T. Matsuura, S. Ramakrishna, Influence of electrospun fiber size on the separation efficiency of thin film nanofiltration composite membrane, Journal of Membrane Science, 392-393 (2012) 101-111.

[36] P. Arribas, M.C. García-Payo, M. Khayet, L. Gil, Heat-treated optimized polysulfone electrospun nanofibrous membranes for high performance wastewater microfiltration, Separation and Purification Technology, 226 (2019) 323-336.

[37] P. Arribas, M. Khayet, M.C. García-Payo, L. Gil, Self-sustained electro-spun polysulfone nano-fibrous membranes and their surface modification by interfacial polymerization for micro- and ultra-filtration, Separation and Purification Technology, 138 (2014) 118-129.

[38] M. Essalhi, M. Khayet, C. Cojocaru, M.C. García-Payo, P. Arribas, Response surface modeling and optimization of electrospun nanofiber membranes, The Open Nanoscience Journal, 7 (2013) 8-17.

[39] Z. Ma, M. Kotaki, S. Ramakrishna, Surface modified nonwoven polysulphone (PSU) fiber mesh by electrospinning: A novel affinity membrane, Journal of Membrane Science, 272 (2006) 179-187.

[40] L. Li, R. Hashaikeh, H.A. Arafat, Development of eco-efficient micro-porous membranes via electrospinning and annealing of poly (lactic acid), Journal of Membrane Science, 436 (2013) 57-67.

[41] Y. Liang, S. Cheng, J. Zhao, C. Zhang, S. Sun, N. Zhou, Y. Qiu, X. Zhang, Heat treatment of electrospun Polyvinylidene fluoride fibrous membrane separators for rechargeable lithium-ion batteries, Journal of Power Sources, 240 (2013) 204-211.

[42] K. Smolders, A.C.M. Franken, Terminology for Membrane Distillation, Desalination, 72 (1989) 249-262.

[43] M.N.A. Seman, M. Khayet, N. Hilal, Nanofiltration thin-film composite polyester polyethersulfone-based membranes prepared by interfacial polymerization, Journal of Membrane Science, 348 (2010) 109-116.

[44] Y. Mansourpanah, M. Samimi, Preparation and characterization of a low-pressure efficient polyamide multi-layer membrane for water treatment and dye removal, Journal of Industrial and Engineering Chemistry, 53 (2017) 93-104.

[45] M.N. Abu Seman, M. Khayet, N. Hilal, Development of antifouling properties and performance of nanofiltration membranes by interfacial polymerization and photografting techniques, in: N. Hilal, M. Khayet, C.J. Wright (Eds.) Membrane Modification: Technology and Apllications, CRC Press, Taylor & Francis Group, U.S.A., 2012, pp. 119-131.

[46] B.R. Singh, D.B. DeOliveira, F.-N. Fu, M.P. Fuller, Fourier transform infrared analysis of amide III bands of proteins for the secondary structure estimation, Proc. SPIE 1890, Biomolecular Spectroscopy III, 1993.

[47] N.-W. Oh, J. Jegal, K.-H. Lee, Preparation and characterization of nanofiltration composite membranes using polyacrylonitrile (PAN). II. Preparation and characterization of polyamide composite membranes, Journal of Applied Polymer Science, 80 (2001) 2729-2736.

[48] C.Y. Tang, Y.-N. Kwon, J.O. Leckie, Effect of membrane chemistry and coating layer on physiochemical properties of thin film composite polyamide RO and NF membranes: I. FTIR

and XPS characterization of polyamide and coating layer chemistry, Desalination, 242 (2009) 149-167.

[49] N.-N. Bui, M.L. Lind, E.M.V. Hoek, J.R. McCutcheon, Electrospun nanofiber supported thin film composite membranes for engineered osmosis, Journal of Membrane Science, 385-386 (2011) 10-19.

[50] X. Wei, X. Kong, J. Yang, G. Zhang, J. Chen, J. Wang, Structure influence of hyperbranched polyester on structure and properties of synthesized nanofiltration membranes, Journal of Membrane Science, 440 (2013) 67-76.

[51] S.G. Sanadhya, S. Oswal, K.C. Parmar, Synthesis and characterization of aliphatic-aromatic polyesters using interfacial polycondensation technique, Journal of Chemical and Pharmaceutical Research, 6 (2014) 705-714.

[52] Y. Jin, Z. Su, Effects of polymerization conditions on hydrophilic groups in aromatic polyamide thin films, Journal of Membrane Science, 330 (2009) 175-179.

[53] M.N. Abu Seman, M. Khayet, N. Hilal, Nanofiltration thin-film composite polyester polyethersulfone-based membranes prepared by interfacial polymerization, Journal of Membrane Science, 348 (2010) 109-116.

[54] C.Y. Tang, Y.-N. Kwon, J.O. Leckie, Effect of membrane chemistry and coating layer on physiochemical properties of thin film composite polyamide RO and NF membranes: II. Membrane physiochemical properties and their dependence on polyamide and coating layers, Desalination, 242 (2009) 168-182.

[55] M. Jahanshahi, A. Rahimpour, M. Peyravi, Developing thin film composite poly(piperazine-amide) and poly(vinyl-alcohol) nanofiltration membranes, Desalination, 257 (2010) 129-136.

6

Nanocomposite membranes

Interlaced CNT electrodes effect on antifouling and filtration performance

Interlaced carbon nanotube electrodes (ICE) were prepared by vacuum filtering a well-dispersed carbon nanotube-Nafion solution through a laser-cut acrylic stencil onto a commercial polyvinylidene fluoride (PVDF) microfiltration (MF) membrane. Dead-end filtration was carried out using 10^7 and 10^8 CFU mL^{-1} *Pseudomonas fluorescens* to study the effects of the electrochemically-active ICE on bacterial density and morphology, as well as to evaluate the bacterial fouling trend and backwash (BW) efficacy, respectively. Finally, a simplified COMSOL model of the ICE electric field was used to help elucidate the antifouling mechanism in solution. At 2 V DC and AC (total cell potential), the average bacterial log removal of the ICE-PVDF increased by ~1 log compared to the control PVDF (3.5–4 log). Bacterial surface density was affected by the presence and polarity of DC electric potential, being 87–90% lower on the ICE cathode and 59–93% lower on the ICE anode than on the PVDF after filtration, and BW further reduced the density on the cathode significantly. The optimal operating conditions (2 V AC) reduced the fouling rate by 75% versus the control and achieved up to 96% fouling resistance recovery (*FRR*) during BW at 8 V AC using 155 mM NaCl. The antifouling performance should mainly be due to electrokinetic effects and the electric field simulation by COMSOL model suggested electrophoresis and dielectrophoresis as likely mechanisms.

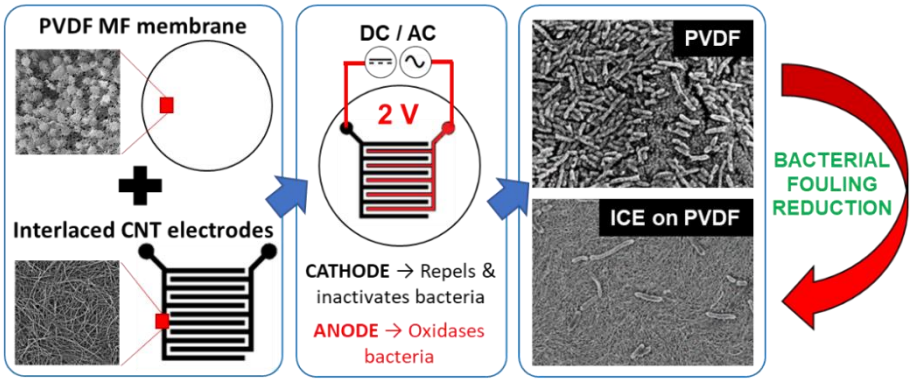

Interlaced CNT electrodes for bacterial fouling reduction of microfiltration membranes

6.1 Introduction

Microfiltration (MF) is a separation technique widely used in water treatment and industrial processing. MF membranes typically have a pore size ranging from 100 nm to 10 μm and remove suspended particles and microbial cells by mechanical sieving [1]. Accumulation of bacteria on MF membrane surfaces is common. At short timescales, high concentration bacteria e.g., during recovery of biochemicals [2] or in membrane bioreactor systems [3], results in concentration polarization and cake layer formation reducing permeability. At long timescales, even low bacterial concentrations may result in biofilm formation on the membrane surface reducing both permeability and backwash (BW) efficacy [4]. Since biofouling increases operation & maintenance (O&M) costs and reduces membrane lifetime, fouling mitigation is of practical importance and research interest.

Bacterial fouling control can be divided into categories such as membrane surface/structure modification, boundary condition control, and external force application [5]. For instance, modification of microporous polysulfone membrane with a sulfonated polyether-ethersulfone/ polyethersulfone block copolymer [6], and with the addition of silver nanoparticles [7, 8] as well as operation at critical flux [9, 10], sonication [11], and electric-field application [12-16] have all been reported to reduce membranes microbial fouling. Among these, electrokinetic and electrochemical methods have the advantages of real-time automation and control.

The electrokinetics is associated with the electrostatics at the electrode surface and the electric field between the electrodes, and both could affect bacterial attachment. Electrostatic [17], electrophoretic, and electroosmotic [18] mechanisms play an important role in biofouling reduction since most bacteria are negatively charged in aquatic systems [19]. Dielectrophoresis [20, 21] is an alternative detachment mechanism, although it has been seldom used for bacterial fouling reduction. The electrochemistry in liquid phase can result in direct or indirect bacterial inactivation reducing bacterial growth, thus long-term fouling [17, 22], and producing gaseous products, e.g., the formation of micro-bubbles at an electro-active membrane surface has also been demonstrated to remove the cake layer [13]. Among the above mechanisms,

dielectrophoresis works under both DC and AC potentials, yet the others are more for DC potential studies.

The electrode material largely determines the performance of electro-active methods. For membrane applications, the electrode needs to be anti-corrosive, inexpensive, and porous [5]. A carbon nanotube (CNT) electrochemical filter [14, 22-24] provides a possible solution to membrane surface electrode fabrication. CNT electrodes have been observed to inactivate bacteria in the presence of oxidizing [22, 23] or reducing [17] potentials. The bulk CNT price has decreased to 100 US$/kg [25] making large scale applications possible, also the CNT network has a pore size of 25~100s nm and is relatively stable at low electrochemical voltages making it compatible for microfiltration applications.

In a conventional electrochemical filtration system, the two electrodes are placed parallel, on opposite sides [5, 26, 27], or both on the feed side [28, 29] of the membrane, complicating filter design and hindering scale-up. Additionally, only one electrode is functional whereas the other is an unutilized counter electrode. An alternative is an interlaced electrode design. Du et al. placed 0.6 mm diameter metal wires with a 0.03 mm insulating polyurethane coating in an alternating-anode/cathode configuration beneath the MF membrane to reduce clay particle fouling at 200 V AC (200 kHz) by dielectrophoresis [30]. However, the insulating layer necessitated the application of high voltages and frequencies and the membrane weakened the dielectrophoretic force.

In this work, interlaced CNT electrodes (ICE) on a membrane surface are hypothesized as a potential solution to the issues of interlaced metal electrodes below the membrane. First, ICE were fabricated by vacuum filtration of a CNT-Nafion solution through a stencil onto a MF membrane. Next, the effects of the ICE on bacterial density distribution and morphology were evaluated by dead-end filtration of 10^7 CFU mL^{-1}. Then, ICE anti-biofouling performance was challenged by filtration of 10^8 CFU mL^{-1}. Finally, a COMSOL model of the ICE electric field was used to elucidate the underlying anti-biofouling mechanisms.

6.2 Materials and methods

6.2.1 Materials

CNT (C-grade, multiwalled, powder, >95% purity) was purchased from NanoTechLabs, Inc. (Yadkinville, NC) (properties detailed in Appendix C). Nafion 117 solution (~5% in a mixture of lower aliphatic alcohols and water) and formaldehyde (ACS reagent, 37 wt.% in water) were purchased from Sigma-Aldrich (St. Louis, MO). *Pseudomonas fluorescens* (*P. fluorescens*) ATCC 700830 (ATCC, Manassas, VA) was utilized in the bacterial fouling experiments. BD Bacto™ tryptic soy broth (TSB), tryptic soy agar (TSA), NaCl (reagent grade), isopropyl alcohol (IPA;

laboratory grade), and ethanol (EtOH; laboratory grade) were purchased from VWR International (West Chester, PA). The fluorescence staining reagent 4', 6-diamidino-2-phenyindole dilactate (DAPI) was acquired from Life Technologies (Grand Island, NY). Deionized (DI) water (>18 MΩ) was produced by a Nanopure Infinity ultrapure water system (Barnstead/Thermolyne) and was used to prepare solutions and rinse containers.

Polyvinylidene fluoride (PVDF) membranes (0.3 μm pore size; GE Osmonics JX; hydrophobic) and grey polycarbonate (PC) membranes (0.2 μm pore size; 47 mm diameter; hydrophilic) were purchased from Sterlitech (Kent, WA). The PVDF membrane was cleaned by ultrasonication in IPA for 5 min, then in DI for 5 min, and kept in IPA prior to use. The PC membrane was used directly without pre-treatment (details in Appendix C). The PVDF membranes were used in most of the fouling experiments while the PC membranes were only used for fluorescence microscopy analysis since the former had a too bright fluorescence background.

6.2.2 Fabrication of ICE on membrane surfaces

ICE were fabricated by vacuum filtering the CNT-Nafion solution through an acrylic stencil onto a commercial MF membrane as shown in Fig. 6.1. The CNT-Nafion solution was prepared by probe ultrasonicating 60 mg CNT and 300 mg Nafion solution in 30 g IPA at 50% magnitude (~1000 W/L) for 15 min (Branson Sonifier S450-D). Since the density of the IPA was 0.80 g/mL, the resulting solution has a concentration of 1.6 mg/mL CNT and 0.4 mg/mL Nafion.

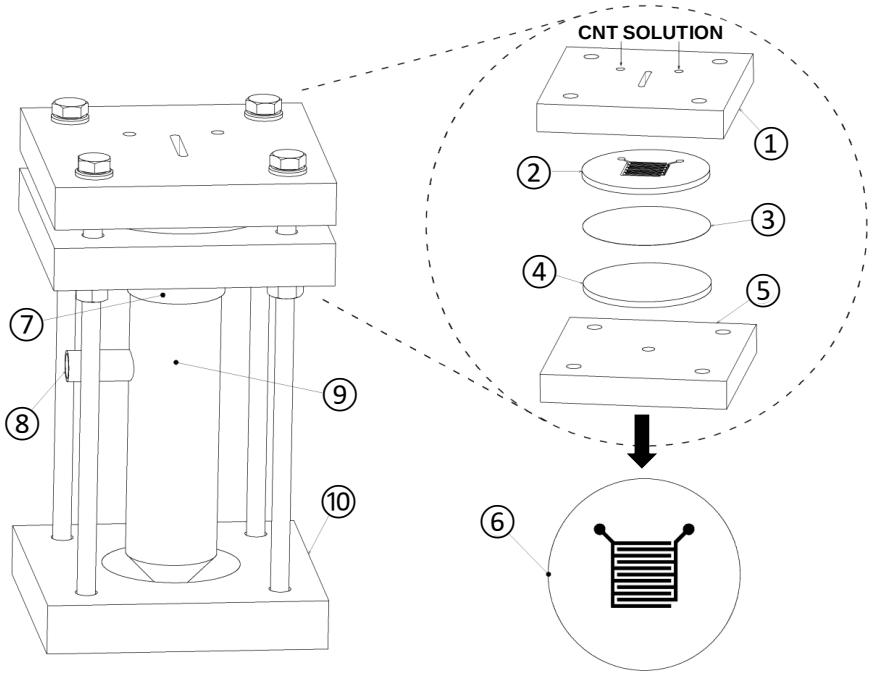

Figure 6.1. Schematic for interlaced CNT electrodes (ICE) fabrication on MF membranes. 1) Top casing, 2) stencil, 3) MF membrane, 4) porous sinter, 5) bottom casing, 6) MF membrane with ICE post-fabrication, 7) container casing, 8) pump connection, 9) filtrate container, and 10) base.

A piece of aluminum foil was used to cover the container to avoid excessive solvent evaporation. The solution was well-dispersed and stable for up to 2 months. The acrylic stencil was prepared by a laser cutter (VersaLaser). The thickness of the acrylic plate was 3 mm, and the filament dimensions were 18 × 1.5 mm^2 with 0.5 mm edge-to-edge spacing. The pattern without the two antenna leads covers a total area of 2.1 × 2.1 cm^2 of which ~80% is covered by ICE. The protective wax paper was kept on the acrylic plate during cutting as well as CNT-Nafion solution filtration to help seal the system. After a specific volume (1.0 to 2.2 mL) of the CNT-Nafion solution was added to the stencil, ~0.5 bar vacuum was applied and maintained for 5–10 min. The samples were then dried in a sterile petri dish at room temperature.

6.2.3 Membranes characterization

Membranes were evaluated for differential and cumulative pore size distributions (*DFF* and *CFF*, respectively), volumetric mean pore size (d_V), and wet curve flow with a gas-liquid displacement porometer (POROLUX™ 100) [31], for volumetric porosity (ε_V) with a pycnometer and a balance [32], and for superficial mean pore size (d_S), superficial porosity (ε_S), and thickness (δ) with a Zeiss UltraPlus field emission SEM. Analysis of the SEM images was completed using Image J (National Institutes of Health, Bethesda, MD).

6.2.4 Bacterial filtration experiments

The MF membranes undergo compaction during filtration [33, 34], thus mechanical pre-compaction was utilized here by compressing the membrane with or without ICE for 45 min (Carver 4386) between two pieces of 1.6 mm silicon rubber at a pressure of 4 MPa (40 bar) (the rubber provided a smooth compaction surface and reduced the actual pressure exerted on the membranes; parchment paper was placed between the membrane and rubber to protect the membrane surface). Compacted membranes had a relative constant permeability within the pressure range of 0–1.0 bar for >60 min (Fig. 13.1 in Appendix C).

P. fluorescens was cultured in TSB by seeding from a TSA plate at 30°C and harvested at mid-to-late exponential phase (18 h) (Fig. 13.2 in Appendix C). After centrifugation and resuspension twice in 155 mM NaCl, the bacterial stock solution was diluted to an optical density of 0.15 at 600 nm (OD_{600} = 0.15) in saline (~10^8 CFU mL^{-1} by fluorescence microscopy [17]). Finally, the solution was either used directly or diluted to 10^7 CFU mL^{-1}.

All filtration experiments were completed in dead-end mode using a peristaltic pump at a constant flow rate of 1.2 mL/min with an effective membrane filtration area of 4.4 cm^2, thus a filtration flux of J = 163.6 L/m^2 h. The membranes were first wetted with ~8 mL of EtOH:DI (v/v) 50:50 and then rinsed with DI water for 10–30 min. The inlet pressure was monitored and the outlet was open to the atmosphere.

Prior to bacterial filtration, the pure water permeability (*PWP,* L/m^2 h bar) of the membranes was determined by the following equation:

$$PWP = \frac{\Delta V}{(\Delta t \, A_{ef} \, \Delta P)} \tag{6.1}$$

where ΔV (mL) is the permeate volume collected over a time Δt (min), A_{ef} (cm^2) is the effective filtration area, and ΔP (bar) is the transmembrane (inlet) pressure.

Bacterial filtration experiments were carried out with either 10^7 or 10^8 CFU mL^{-1} in 155 mM NaCl, with or without ICE, in the presence or absence of applied voltage. DC was applied by a power supply (Agilent N5750A) and AC was generated by a customized inverter (DC to square-wave AC) with V_{rms} (2 or 8 V) and frequency (10 kHz) set by an arbitrary waveform generator (Agilent 33120A). The current of the system was monitored by the power supply with 1 mA limit of detection. The ΔP was recorded during bacterial filtration at 2, 10, and every 10 min afterwards. As the influent concentration was high (10^7–10^8 CFU mL^{-1}), a 10 min BW was carried out every 60 min or when the ΔP reached 1.1 ± 0.1 bar. Permeate and feed aliquots were collected in sterile glass vials at 30 min of filtration to count CFUs, thus determine bacteria removal.

6.2.5 Bacterial density and morphology evaluation

Bacterial filtration experiments were carried out by filtering 10^7 CFU mL^{-1} in 155 mM NaCl solution for 60 min, in the absence (control PVDF membrane) or presence (ICE-DC membranes) of 2 V DC applied voltage. BW with DI water without voltage or at 8 V DC (DC polarity inversed with respect to filtration) was performed for 10 min after bacteria filtration (see Fig. 13.3 in Appendix C, Protocol 1). Both the filtration and BW flow rates were kept at 1.2 mL/min (i.e. J = 163.6 L/m^2 h).

6.2.6 Bacterial fouling trend and BW efficacy evaluation

Bacterial filtration experiments were carried out by filtering 10^8 CFU mL^{-1} in 155 mM NaCl solution for 60 min, in the absence (control PVDF and ICE-0 V membranes) or presence of 2 V DC or AC applied voltage (ICE-DC and ICE-AC membranes, respectively). Up to 2 bacterial filtration cycles were performed in each experiment, and each cycle included a 60-min filtration, a 10-min BW, and a 10-min DI water filtration. The BW solution was either DI water or 155 mM NaCl. For filtration in the presence of voltage, the BW was carried out in the presence of voltage as well with V_{rms} = 8 V (DC or AC). The DC polarity was reversed in comparison to filtration for the first 5 min and then reversed again for the final 5 min to clean both electrodes. In the end, DI water was filtered for 10 min to determine the fouling resistance recovery (*FRR*) following Eq. 6.2 below [35, 36]:

$$FRR\ (\%) = \frac{(\Delta P_f - \Delta P_c)}{(\Delta P_f - \Delta P_0)} \cdot 100 \tag{6.2}$$

where ΔP_0, ΔP_f, and ΔP_c (bar) are the ΔP before fouling, after fouling before BW, and after BW, respectively.

For all bacteria filtration, BW filtration and DI water filtration, the flow rates were kept at 1.2 mL/min (i.e. J = 163.6 L/m^2 h). Experimental procedure diagram is displayed in Fig. 13.3 in Appendix C, Protocol 2.

6.2.7 Bacterial characterization and quantification

The bacterial concentration in the feed solution prior to fouling experiment was determined by OD_{600}. To quantify the bacterial rejection, the feed and permeate aliquots were characterized by the colony forming unit (CFU) method.

After 10^7 CFU mL^{-1} filtration and BW, membranes were examined by fluorescence microscopy (PC membranes) and SEM (PVDF membranes) to determine surface bacterial density and morphology. After 10^8 CFU mL^{-1} filtration and BW, PVDF membranes were only examined by SEM. Fluorescence microscopy was completed after staining the samples with DAPI (excitation/emission 358/461 nm) for 2–5 min using an inverted microscope (Olympus BX60). SEM of bacterial samples was completed after they were fixed with formaldehyde vapor for at least 12 h, dehydrated with 40-to-100% EtOH/DI solutions, dried at room temperature, and coated with 2 nm of Pt/Pd (80/20) (EMS 300T D Dual Head Sputter Coater).

6.3 Results and discussions

6.3.1 Membranes characterization

The PVDF and ICE-PVDF membranes were characterized by SEM for cross-sectional and superficial morphology (Fig. 13.4 A–E in Appendix C), by two-point probe for electric conductivity (Fig. 13.4-F in Appendix C), and by capillary flow porometry for volumetric pore size distributions and mean pore size (Fig. 13.4-G in Appendix C), with results summarized in Table 13.1 in Appendix C.

From the SEM images, the unpressed PVDF membrane had a thickness (δ) of about 181 ± 6 μm, a surface porosity (ε_S) of 15.7 ± 1.4%, and a mean pore size (d_S) of 44 ± 4 nm. After mechanical compaction, the PVDF membrane δ, ε_S, and d_S decreased to 119 ± 3 μm, 8.1 ± 0.9%, and 31 ± 4 nm, respectively. The CNT network after compaction had a thickness of 14 ± 3 μm and was more porous than the PVDF regarding surface porosity (ε_S = 25.5 ± 4.1%) and pore size (d_S = 52 ± 10 nm).

From *DFF*, the unpressed PVDF had a large wide peak (d_V = 722 ± 59 nm), while the pressed PVDF peak was narrower and shifted towards smaller values (d_V = 412 ± 13 nm). The pressed ICE-PVDF had two peaks, one similar to the pressed PVDF (d_V = 407 ± 15 nm), and the other from the ICE (d_V = 175 ± 7 nm). The mean pore size of the pressed ICE-PVDF (d_V = 245 ± 14 nm) was between the two. The volumetric porosity decreased from 39.0 ± 4.5 to 31.4 ± 7.5% upon the addition of ICE.

The compaction reduced the *PWP* of the PVDF membranes from 2950 ± 323 to 935 ± 71 L/m^2 h bar. The pressed PVDF had a stable and similar permeability to the DI-filtration-compacted PVDF (Fig. 13.1). The ICE deposition on the PVDF did not significantly change the permeability (902 ± 12 L/m^2 h bar; P value of 0.31; Welch's t test). The minor decrease in permeability upon ICE deposition (~33 L/m^2 h bar, ~4%) was further confirmed by the wet curve flow (Fig. 13.4-G, right).

The ICE electrical resistance is displayed in Fig. 13.4-F. CNT filament resistance decreased linearly from 130 ± 18 to 59 ± 6 **Ω** (2.2-fold) when the volume of the CNT-Nafion solution increased from 1.0 to 2.2 mL (1.6 to 3.5 mg CNT). For the filtration experiments, 2.9 mg CNT was deposited on a pattern area of 2.1 × 2.1 cm^2 and the filaments were l = 18 mm, w = 1.5 mm, h = 14 μm, and 0.5 mm apart. The CNT network bulk resistivity ρ (**Ω** cm) was 0.008 **Ω** cm, lower than 0.029 **Ω** cm for a previous CNT-Nafion coating[17] due to the reduced Nafion/CNT ratio (3-fold). At a resistance of 72.9 **Ω**, the potential drop over a single filament will be negligible (0.07 V given a maximum current of 1 mA at 2 V), indicating ICE are sufficiently conductive for electrochemical filtration.

6.3.2 Membrane bacterial removal

The compacted PVDF membrane (d_S = 31 ± 4 nm) removes bacteria by sieving. The control PVDF log removal (Fig. 13.5 in Appendix C) was 3.5 ± 0.6 and 4.1 ± 0.9 for 10^7 and 10^8 CFU mL^{-1}, respectively. In the absence of electric potential, the addition of ICE did not significantly alter the log removal, being higher at 4.6 ± 0.8 for 10^7 CFU mL^{-1} and lower at 3.6 ± 0.6 for 10^8 CFU mL^{-1}. At 2 V DC and AC, the log removal increased by ~1 log from the control PVDF to 4.5 ± 0.5 and 4.7 ± 0.6 for 10^7 CFU mL^{-1} and 5.1 ± 0.6 and 5.2 ± 0.9 for 10^8 CFU mL^{-1}, respectively. However, Welch's t-test (Table 13.2 in Appendix C) indicated none of the results had a P-value <0.05, thus additional experimental data is required to determine a statistical difference.

6.3.3 Membrane surface bacterial density and morphology

The bacterial density distribution on the membrane surface was affected by the applied ICE electric potential as displayed in Fig. 6.2, and in Fig. 13.6 and Table 13.3 in Appendix C.

From SEM image analysis (Fig. 13.6, Table 13.3), the bacterial density on the control PVDF was 202.1 ± 29.1 and 86.6 ± 6.2 × 10^5 CFU/cm^2 before and after BW. In comparison, the bacterial density on the ICE anode and the ICE cathode after electrochemical filtration at 2 V DC was 62.8 ± 5.6 and 25.9 ± 3.2 × 10^5 CFU/cm^2, 69 and 87% lower than the control PVDF, respectively. Similarly, electrically charged CNTs ultrafiltration (UF) membranes at 1.5 V were reported to have a bacterial detachment 2.6-fold higher (thus lower remained cells attached on the surface) than that of the control membrane without applied potential [15]. After BW, the bacterial density on the anode (21.7 ± 2.1 × 10^5 CFU/cm^2) and cathode (2.7 ± 1.1 × 10^5 CFU/cm^2) was again 75 and 97% lower than the control PVDF, respectively. Theoretically, 1.64 × 10^8 (1640 × 10^5) CFU/cm^2 should be sieved by the membrane considering the influent (10^7 CFU mL^{-1}) and effluent (10^2–10^3 CFU mL^{-1}) concentration, 8 times greater than the control PVDF, of which the majority were probably not well deposited after filtration or not fixed during SEM sample preparation.

In resume, the bacterial surface density was control > anode > cathode for the PVDF before and after BW. In an attempt to verify the results, another set of experiments were completed with PC membranes and the bacterial densities were measured with fluorescence microscopy (discussion in Appendix C). For the membrane surface before BW, the bacterial densities on the anode and the control did not follow a clear relation i.e., ICE anode density being smaller on PVDF and greater on PC than the control PVDF and PC, respectively. However, there was a consistently higher bacterial density on the anode than the cathode before and after BW independent of the membrane material, suggesting a likely electrokinetic mechanism between the electrode and the deposited bacteria (zeta potential = -10.8 mV) [17], which generally includes electrostatic repulsion by the cathode surface [17], electroosmotic motion on electrode surface [18], as well as electrophoretic and dielectrophoretic motions in the solution (will be discussed in **ICE electric field modeling**). Air bubble evolution due to water splitting $2H_2O \rightarrow 2H_2 + O_2$, 1.23 eV NHE and other electrochemical reactions can reduce bacteria on both electrodes [37, 38], yet no visible air bubble or gas accumulation could be observed during filtration at 2 V DC. In contrast, during BW at 8 V DC, gas bubbles (<1 mm in diameter, see supplementary videos in https://doi.org/10.1021/acs.est.7b00966) were observed from both electrodes.

The bacterial morphology was also affected by electrofiltration and BW (Fig. 6.2 insets). The filtered bacteria on the control PVDF membrane had a rod-like structure with some stretched and broken cells. After 60 min filtration at 2 V DC, the bacteria on the ICE anode appeared flattened and dehydrated, similar to the morphology change after 30 s electro-oxidization of *E. Coli* on CNT filters at 2 V that resulted in >80% inactivation [22]. Comparable cell damage and bacterial structure changes were also reported on electrically charged CNT UF membranes subjected to a potential of ± 1.5 V [15]. Therefore, notable inactivation of the deposited bacteria

on the anode can be expected in this study. The bacteria on the ICE cathode retained membrane integrity and morphology after 60 min filtration, in agreement with previous findings [17]. The morphology change of bacteria partly supported the observed improvement in bacterial removal at 2 V DC.

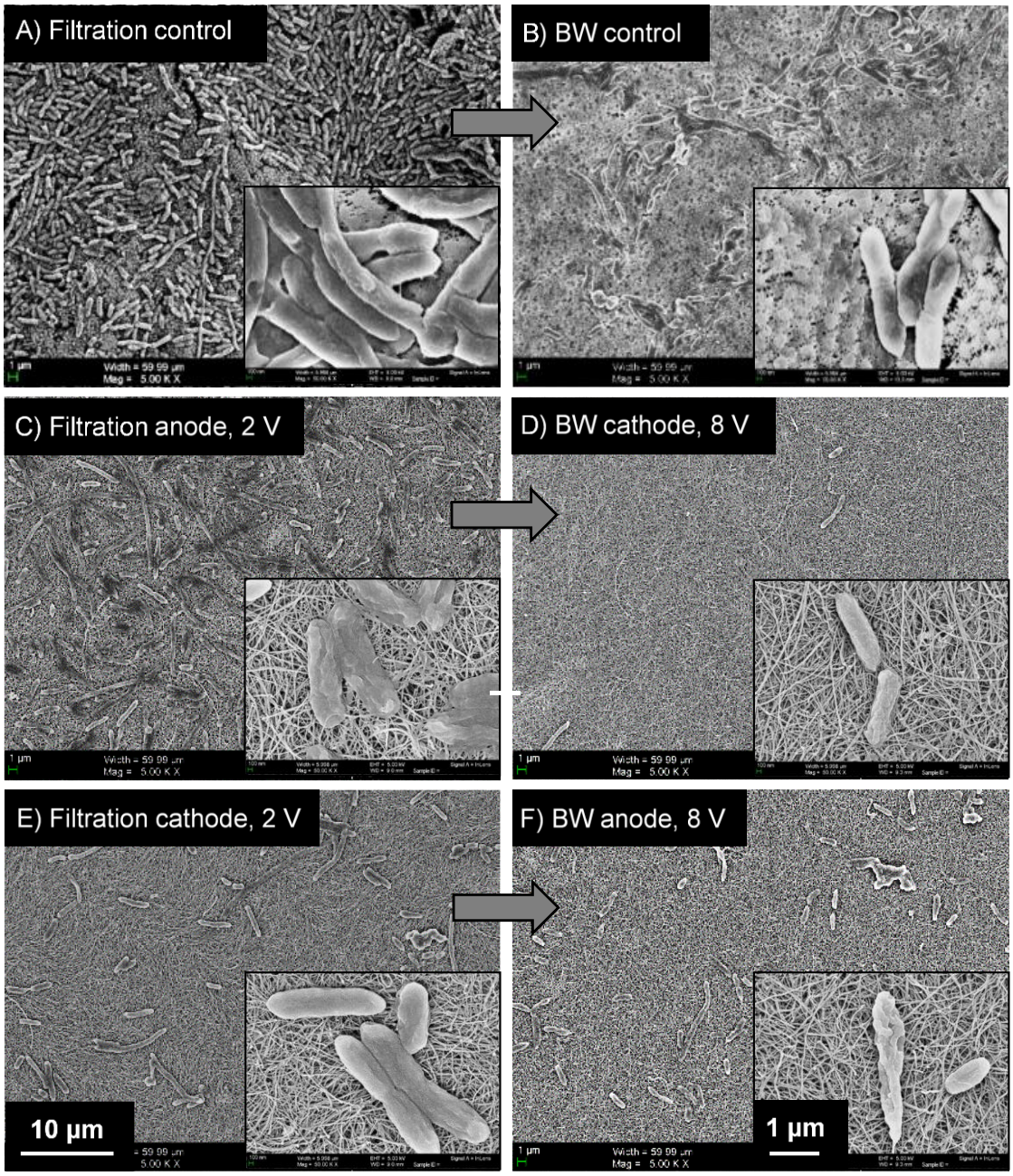

Figure 6.2. Bacterial density and morphology on membrane surfaces with or without ICE after filtration and BW. SEM images of the control PVDF and ICE surfaces: A) Filtration control PVDF, B) BW control PVDF, C) filtration ICE anode, D) cathodic BW of ICE anode during filtration, E) filtration ICE cathode, and F) anodic BW of ICE cathode during filtration. Experiments were completed by filtering 10^7 CFU mL^{-1} in 155 mM NaCl solution for 60 min at the flow rate of 1.2 mL/min (i.e. J = 163.6 L/m^2 h) and BW at the same flow rate for 10 min with DI water. For the ICE-PVDF, 2 V DC and 8 V DC (with the reversed polarity) were applied during filtration and BW, respectively.

After BW without voltage, the bacteria remaining on the control PVDF membrane surface were still mostly rod-like. In contrast, after electrochemical BW at 8 V DC, cells on the BW anode were significantly degraded and those on the BW cathode looked quite rough, but less degraded than the anode bacteria. The ICE anode consistently had a greater bacterial density than the cathode in all experiments, suggesting that the anodic oxidation did not affect the bacterial density, e.g., by breaking down cells, as much as the electrokinetic effects.

6.3.4 Fouling trend and BW efficacy

The ΔP values did not change notably during 10^7 CFU mL^{-1} filtration and BW experiments used to determine bacterial density and morphology changes. Thus, filtration experiments using a higher bacterial concentration of 10^8 CFU mL^{-1} were completed under similar conditions (i.e., F = 1.2 mL/min, A_{ef} = 4.4 cm^2 and J = 163.6 L/m^2h) to evaluate the ICE antifouling performance. In an attempt to improve performance and test different mechanisms, the experiments were done with 2 V DC and AC. The biofouling test sequence was: DI filtration (**DI-0**, 10–30 min) → bacteria filtration (**F-1**, 60 min) → **BW-1** (10 min) → **DI-1** (10 min) → **F-2** (60 min or ΔP = 1.1 bar) → **BW-2** (10 min) → **DI-2** (10 min) (see Fig. 13.3 in Appendix C, Protocol 2). Fouling trends and ΔP values recorded during filtration experiment are shown in Fig. 6.3-A and Table 6.1, respectively. Additionally, an empirical exponential fitting of the pressure increase was completed to quantitatively compare fouling rates using Eq. 6.3 [29, 39]:

$$\Delta P = \Delta P_0 \exp(kt) \tag{6.3}$$

where ΔP_0 and ΔP (bar) are the transmembrane pressure at time 0 and t (min), and k (min^{-1}) is the fouling rate constant (fitting results summarized in Table 13.4 in Appendix C).

For all membranes prior to fouling, the *PWP* was determined (ΔP_{PWP} = 0.13 ± 0.02 bar). Over the first bacterial filtration cycle (**F-1**), the ΔP increased to 0.75, 0.66, 0.54, and 0.25 bar with a fouling rate constant k of 0.029, 0.033, 0.019, and 0.012 min^{-1} for the control PVDF, ICE-0 V, ICE-DC, and ICE-AC, respectively. It is noteworthy that the highest ΔP, and thus the fouling, was obtained using the control PVDF membrane, being 1.4 and 3 times higher than the ICE-DC and ICE-AC, respectively. Otherwise, the fouling rate of the ICE-0 V was slightly greater than that of the control PVDF, but that of the ICE-DC and ICE-AC was 34 and 68% lower, respectively.

BW-1 with DI water was then conducted for 10 min to recover the flux in the absence (PVDF and ICE-0 V) and presence (ICE-DC and ICE-AC) of 8 V electric potential. Afterwards, **DI-1** was performed and the ΔP decreased to 0.64, 0.36, 0.36, and 0.22 bar for the control PVDF, ICE-0 V, ICE-DC, and ICE-AC (Fig. 6.3-A, between two plots), respectively. The ΔP value decreased even more (another 6-33%) when starting the second bacterial filtration cycle in 155 mM NaCl (see ΔP_0 for **F-2**, Table 13.3 in Appendix C). However, this change in

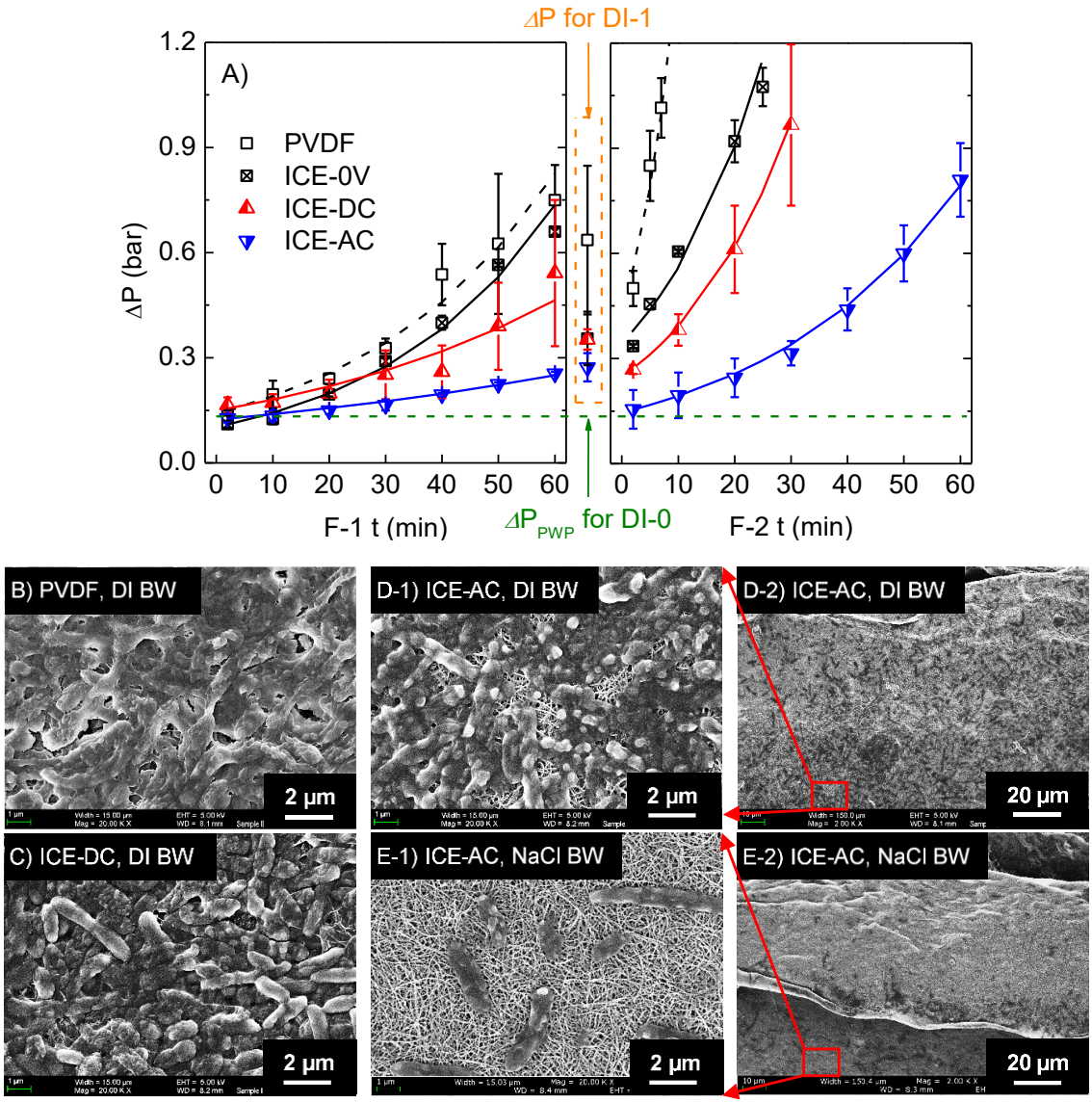

Figure 6.3. Fouling trends of PVDF with or without ICE in the absence or presence of potential. A) Δ*P* increase with filtration time of the control PVDF, ICE-0 V, ICE-DC and ICE-AC (10 kHz) using DI BW. SEM images of the membrane surfaces after F-2 and BW-2: B) control PVDF membrane post-DI-BW, C) ICE-DC post-DI-BW, D) ICE-AC post-DI-BW, and E) ICE-AC post-NaCl-BW. Experiments were completed using 10^8 CFU mL^{-1} filtration for 60 min or up to 1.1 bar in the absence or presence of 2 V DC or AC. A 10 min BW was carried out after each filtration cycle in the absence or presence of 8 V DC (for the DC filtration, polarity changed at 5 min) and 8 V AC (for the 2 V AC filtration).

pressure was not observed when starting the first bacterial filtration cycle (i.e. ΔP_0 for **F-1** was similar to ΔP_{PWP} for **DI-0** prior to membrane fouling). One hypothesis for the difference is that the electrostatic repulsion between the deposited bacteria may decrease during 155 mM NaCl filtration. The bacterial zeta potential has been reported to decrease by ~2/3 from solution of low (0.1 mM) to high ionic strength (~150 mM) due to electric double layer (EDL) compaction [40, 41]. Moreover, bacterial cells, both Gram-positive and Gram-negative, can shrink in

response to external ionic shock of 0.1–1 M by a few percent [42, 43]. Thus, *P. fluorescens* (Gram-negative) fouling layer may become thinner and result in a higher permeability in 155 mM NaCl than DI, i.e. ΔP_0 for **F-2** < ΔP for **DI-1**.

During **F-2**, the ΔP for all membranes except ICE-AC (ΔP = 0.81 bar at the end of **F-2**) increased to 1.1 ± 0.1 bar (maximum allowed). The average time to reach ΔP = 1.1 bar followed the order of control PVDF (67 min) < ICE-0 V (85 min) < ICE-DC (100 min) < ICE-AC (projected to be 129 min), and the latter three increased by 27, 49, and 93% from the control PVDF, respectively, resulting in a reduction of membrane fouling and an improvement of the membrane lifetime.

The fouling rate constant k for the control PVDF increased 4-fold from **F-1** (0.029 min^{-1}) to **F-2** (0.118 min^{-1}), meanwhile a smaller k increase (1.5 to 2.4-fold) was observed in experiments using ICE-PVDF in the absence and presence of electric potential. In all experiments, the greater k in **F-2** is likely caused by the remained bacteria on the membrane surface after **BW-1** and **DI-1**. Otherwise the ICE-PVDF had a lower k increase from **F-1** to **F-2** due to lesser total deposited bacteria after **F-1** and **BW-1** (Fig. 6.3 B–E). As a guideline, Fig. 13.7 in Appendix C summarizes all the ΔP values recorded during cycles 1 and 2 of the bacterial filtration experiment discussed above.

The *FRR* values (Table 6.1) provided further evidence for the antifouling efficacy. Using DI as the BW solution, the *FRR* was 18 and 43% for the control PVDF in **BW-1** and **BW-2**, respectively, and increased to 57 and 65% for the ICE-0 V. Increased reversible fouling with UF CNT surface modification was also observed for natural organic matter filtration and was attributed to CNT surface charge and roughness [44]. All the ICE-PVDF had a higher *FRR* (55–216% for **BW-1** and 1–51% for **BW-2**) than the control PVDF, ranking in the order of ICE-0 V > ICE-DC > ICE-AC. Despite the microbubble generation as an attempt to remove deposited bacteria, the ICE-DC had a lower *FRR* than ICE-0 V, and the bubble generation was very limited for ICE-AC. The reduced *FRR* for ICE-DC and ICE-AC was probably due to reduced fouling during filtration, i.e., there were less deposited bacteria to remove during BW.

In an attempt to increase the ICE-AC *FRR*, BW was also completed using 155 mM NaCl and an *FRR* ≥ 96% after both BW was observed, being 2–4 fold higher than that of BW using DI (BW using 155 mM NaCl was not applied to ICE-DC to avoid electrode oxidation and deterioration at 8 V DC). The *FRR* increase is confirmed by SEM analysis of the membranes post-BW. As displayed in Fig. 6.3 B–E, multilayer bacterial deposits were observed on the control PVDF and ICE-DC post-DI-BW, while sub-monolayer bacterial deposits were observed on the ICE-AC post-DI-BW (mostly individual bacteria) and post-NaCl-BW (mostly bare CNT surface). Lower magnification SEM (Fig. 6.3 D-2 and E-2) of the ICE edge indicated

an increasing bacterial density gradient away from the edge with a near uniform density >100 μm.

A higher *FRR* with 155 mM NaCl BW was observed for the control PVDF as well, 86 and 82% for **BW-1** and **BW-2**, respectively. Therefore, the *FRR* increase is primarily attributed to non-electroactive factors. As discussed previously, a reduction in electrostatic repulsion between the deposited bacteria and the bacterial cell shrinkage may result in a thinner fouling layer when using 155 mM NaCl in comparison to DI, which could be removed more easily.

Table 6.1. Δ*P* and *FRR* values for the control PVDF and the ICE-PVDF after 10^8 CFU mL^{-1} filtration and BW with DI or saline.

BW solution	Membrane	BW-1			BW-2		
		Δ*P* before BW (ΔP_f bar)	Δ*P* after BW (ΔP_c bar)	*FRR* (%)	Δ*P* before BW (ΔP_f bar)	Δ*P* after BW (ΔP_c bar)	*FRR* (%)
DI	**PVDF**	0.75 ± 0.10	0.64 ± 0.21	18 ± 3.7	1.15 ± 0.03	0.71 ± 0.19	43.2 ± 1.9
	ICE-0 V	0.66 ± 0.01	0.36 ± 0.08	***56.8*** ± 1.5	1.08 ± 0.06	**0.47** ± 0.10	***64.0*** ± 1.2
	ICE-DC	0.54 ± 0.21	0.36 ± 0.03	45.1 ± 2.9	1.14 ± 0.16	0.59 ± 0.14	54.2 ± 1.6
	ICE-AC	**0.25** ± 0.05	**0.22** ± 0.04	27.6 ± 4.1	**0.81** ± 0.01	0.52 ± 0.08	43.1 ± 1.3
155 mM NaCl	**PVDF**	0.56 ± 0.04	0.18 ± 0.02	86.1 ± 0.8	1.05 ± 0.05	0.29 ± 0.03	82.1 ± 0.5
	ICE-0 V	**0.26** ± 0.01	**0.11** ± 0.01	***114.6*** ± 1.8	**0.60** ± 0.01	**0.15** ± 0.01	***95.5*** ± 0.5

The lowest pressure before and after BW using DI and 155 mM NaCl are in **bold**.
The highest pressure recovery using DI and 155 mM NaCl BW are in ***bold and italic***.

6.3.5 ICE electric field modeling

The antifouling mechanisms at DC voltages have been discussed in **Membrane surface bacterial density and morphology**. Yet the mechanisms using AC, which had the best antifouling performance, should be different due to limited electrostatic, electroosmotic, electrophoretic, and electrochemical effects with frequently alternating polarity. A simplified COMSOL model of the ICE electric field was used to help elucidate the antifouling mechanism in the solution (Fig. 6.4), especially at AC potential. The estimated hydraulic velocity perpendicular to the membrane (v = flow rate/filter area) is ~45 μm/s. Since the permeability of the ICE-PVDF is very close to that of PVDF after compaction, the velocity field distortion over the membrane surface should be limited and was not considered.

The electric field strength during filtration (2 V) at ~0.1–0.5 and 0.8–0.9 mm above the surface is 1000 and 500 V/m, respectively. Assuming the electrostatic mobility of the bacterial cells is -1.0×10^{-8} $m^2/V\,s$ [40], the bacterial horizontal electro-migration velocity should be ~10

and 5 μm/s, a magnitude similar to the vertical velocity, in accordance with the hypothesis that electrophoresis is a possible fouling mitigation mechanism at DC potential. Nevertheless, EDL effects for the ICE were not considered in this model, which will develop as soon as the electrode surface gets charged and may greatly reduce the actual electric field strength in the solution.

The electric field distribution is nonuniform and its strength decreases with distance from the electrode edges, enabling a dielectrophoretic (DEP) mechanism. Negative dielectrophoresis is likely to occur for the bacteria in 155 mM NaCl and even DI [45, 46]. As a result, deposited bacteria would migrate away from the electric field. The DEP force is independent on the direction of the applied electric potential, thus DEP is effective with both DC and AC [47, 48]. Since 10 kHz AC effectively overcomes the EDL screening,[49] the DEP force will be greater with AC than DC, enhancing the antibiofouling performance. The bacterial density gradient at the ICE edges provides evidence for DEP during BW at 8 V AC. Bacterial properties and solution conductivity can significantly affect the DEP velocity (8700–64 μm/s) [50], and quantitative studies are limited. Thus, DEP on the scale of 10s μm/s (larger than electromigration) may be possible near the ICE under experimental conditions here.

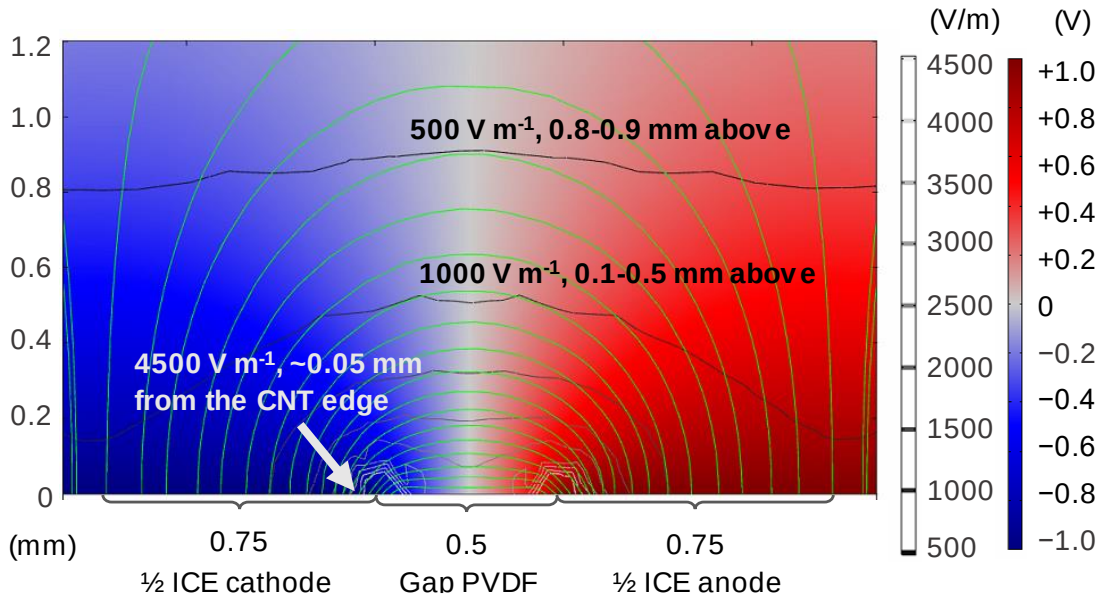

Figure 6.4. COMSOL simulation of the ICE electric field strength and electric potential distribution. The total voltage over the two adjacent filaments is set as 2 V. The electric potential is shown in color change from blue (−1 V) to red (+1 V) and the norm of electric field strength is presented with contour from light grey (4500 V/m) to dark grey (500 V/m). The green streamlines depict the direction and the electric field strength. No electric double layer or hydrodynamic effects are considered.

6.3.6 Summary of antifouling mechanisms

The ICE on PVDF membrane surface displayed antifouling properties at DC and AC electric potentials through filtration and BW cycles. In regard to the possible mechanisms involved in this electroactive fouling mitigation approach, we could conclude that: (1) dielectrophoretic effect in the solution between electrodes is an important antifouling mechanism and is improved under AC than DC; (2) electrophoretic effect between electrodes is possible yet will be limited by EDL screening; (3) electrostatic as well as electroosmotic effects at the electrode surface may contribute to the bacterial deposition reduction and thus fouling mitigation; (4) electrochemistry alters bacterial morphology but has a lesser effect on bacterial density than electrokinetics.

6.4 Conclusions

The ICE on commercial PVDF MF membranes were prepared by vacuum filtering CNT-Nafion solution through a laser-cut stencil. The ICE-PVDF membrane showed negligible permeability loss at < 1.1 bar and 25−36% higher average bacterial removal (~1 log) compared to the control PVDF.

Electric potentials of 2 V and 8 V DC were applied to the ICE during filtration using 10^7 CFU mL^{-1} and BW using DI, respectively. The deposited bacterial density on the ICE was altered by the presence and polarity of DC electric potential. The ICE anode and ICE cathode displayed 3 to 8-fold lower bacterial density than the control PVDF after filtration, and BW could further reduce the bacterial density on the ICE cathode (up to 75-fold lower than the control), displaying the best performance. Bacterial morphology was also affected by the applied potential. The deposited cells appeared dehydrated and deformed on the ICE anode after 60 min filtration at 2 V DC and significantly degraded after 10 min electrochemical BW at 8 V DC. In contrast, the deposited bacteria on the ICE cathode retained membrane integrity and morphology after filtration at 2 V DC and looked rougher after BW at 8 V DC, but less degraded than the bacteria on the ICE anode, indicating inactivation to different extents.

The ICE-PVDF membrane resulted in a lower fouling rate (34-75%) and a longer operation time (49-93%) than the control PVDF using 10^8 CFU mL^{-1} in the presence of 2 V DC and AC and the optimal *FRR* value was 96% during BW at 8 V AC using 155 mM NaCl.

According to electric field modeling and theoretical analysis, the antifouling performance was mainly due to electrokinetic effects, suggesting electrophoresis and dielectrophoresis as likely underlying mechanisms for the fouling reduction.

References

[1] B. Van Der Bruggen, C. Vandecasteele, T. Van Gestel, W. Doyen, R. Leysen, A review of pressure-driven membrane processes in wastewater treatment and drinking water production, Environmental Progress, 22 (2003) 46-56.

[2] G. Foley, A review of factors affecting filter cake properties in dead-end microfiltration of microbial suspensions, Journal of Membrane Science, 274 (2006) 38-46.

[3] F. Meng, S.-R. Chae, A. Drews, M. Kraume, H.-S. Shin, F. Yang, Recent advances in membrane bioreactors (MBRs): Membrane fouling and membrane material, Water Research, 43 (2009) 1489-1512.

[4] N.G. Cogan, S. Chellam, Regularized Stokeslets solution for 2-D flow in dead-end microfiltration: Application to bacterial deposition and fouling, Journal of Membrane Science, 318 (2008) 379-386.

[5] S.N. Jagannadh, H.S. Muralidhara, Electrokinetics methods to control membrane fouling, Industrial & Engineering Chemistry Research, 35 (1996) 1133-1140.

[6] T. Knoell, J. Safarik, T. Cormack, R. Riley, S.W. Lin, H. Ridgway, Biofouling potentials of microporous polysulfone membranes containing a sulfonated polyether-ethersulfone/polyethersulfone block copolymer: correlation of membrane surface properties with bacterial attachment, Journal of Membrane Science, 157 (1999) 117-138.

[7] F. Diagne, R. Malaisamy, V. Boddie, R.D. Holbrook, B. Eribo, K.L. Jones, Polyelectrolyte and silver nanoparticle modification of microfiltration membranes to mitigate organic and bacterial fouling, Environmental Science & Technology, 46 (2012) 4025-4033.

[8] Y. Liu, E. Rosenfield, M. Hu, B. Mi, Direct observation of bacterial deposition on and detachment from nanocomposite membranes embedded with silver nanoparticles, Water Research, 47 (2013) 2949-2958.

[9] R.W. Field, D. Wu, J.A. Howell, B.B. Gupta, Critical flux concept for microfiltration fouling, Journal of Membrane Science, 100 (1995) 259-272.

[10] P. Le-Clech, V. Chen, T.A.G. Fane, Fouling in membrane bioreactors used in wastewater treatment, Journal of Membrane Science, 284 (2006) 17-53.

[11] A.L. Lim, R. Bai, Membrane fouling and cleaning in microfiltration of activated sludge wastewater, Journal of Membrane Science, 216 (2003) 279-290.

[12] L. Guo, K. Ding, K. Rockne, M. Duran, B.P. Chaplin, Bacteria inactivation at a sub-stoichiometric titanium dioxide reactive electrochemical membrane, Journal of Hazardous Materials, 319 (2016) 137-146.

[13] W.R. Bowen, R.S. Kingdon, H.A.M. Sabuni, Electrically enhanced separation processes: the basis of in situ intermittent electrolytic membrane cleaning (IIEMC) and in situ electrolytic membrane restoration (IEMR), Journal of Membrane Science, 40 (1989) 219-229.

[14] A. Zhu, H.K. Liu, F. Long, E. Su, A.M. Klibanov, Inactivation of bacteria by electric current in the presence of carbon nanotubes embedded within a polymeric membrane, Applied Biochemistry and Biotechnology, 175 (2015) 666-676.

[15] A. Ronen, W. Duan, I. Wheeldon, S. Walker, D. Jassby, Microbial attachment inhibition through low-voltage electrochemical reactions on electrically conducting membranes, Environmental Science & Technology, 49 (2015) 12741-12750.

[16] L. Liu, J. Liu, B. Gao, F. Yang, Minute electric field reduced membrane fouling and improved performance of membrane bioreactor, Separation and Purification Technology, 86 (2012) 106-112.

[17] Q. Zhang, J. Nghiem, G.J. Silverberg, C.D. Vecitis, Semiquantitative performance and mechanism evaluation of carbon nanomaterials as cathode coatings for microbial fouling reduction, Applied and Environmental Microbiology, 81 (2015) 4744-4755.

[18] A.T. Poortinga, J. Smit, H.C. van der Mei, H.J. Busscher, Electric field induced desorption of bacteria from a conditioning film covered substratum, Biotechnology and Bioengineering, 76 (2001) 395-399.

[19] M. Hermansson, The DLVO theory in microbial adhesion, Colloids and Surfaces B: Biointerfaces, 14 (1999) 105-119.

[20] X.-B. Wang, Y. Huang, J. Burt, G. Markx, R. Pethig, Selective dielectrophoretic confinement of bioparticles in potential energy wells, Journal of Physics D: Applied Physics, 26 (1993) 1278.

[21] G.H. Markx, Y. Huang, X.-F. Zhou, R. Pethig, Dielectrophoretic characterization and separation of micro-organisms, Microbiology, 140 (1994) 585-591.

[22] C.D. Vecitis, M.H. Schnoor, M.S. Rahaman, J.D. Schiffman, M. Elimelech, Electrochemical multiwalled carbon nanotube filter for viral and bacterial removal and inactivation, Environmental Science & Technology, 45 (2011) 3672-3679.

[23] M.S. Rahaman, C.D. Vecitis, M. Elimelech, Electrochemical carbon-nanotube filter performance toward virus removal and inactivation in the presence of natural organic matter, Environmental Science & Technology, 46 (2012) 1556-1564.

[24] A.V. Dudchenko, J. Rolf, K. Russell, W. Duan, D. Jassby, Organic fouling inhibition on electrically conducting carbon nanotube–polyvinyl alcohol composite ultrafiltration membranes, Journal of Membrane Science, 468 (2014) 1-10.

[25] M.F.L. De Volder, S.H. Tawfick, R.H. Baughman, A.J. Hart, Carbon nanotubes: Present and future commercial applications, Science, 339 (2013) 535-539.

[26] C.-F. de Lannoy, D. Jassby, K. Gloe, A.D. Gordon, M.R. Wiesner, Aquatic biofouling prevention by electrically charged nanocomposite polymer thin film membranes, Environmental Science & Technology, 47 (2013) 2760-2768.

[27] F. Du, A. Hawari, M. Baune, J. Thöming, Dielectrophoretically intensified cross-flow membrane filtration, Journal of Membrane Science, 336 (2009) 71-78.

[28] S. Ibeid, M. Elektorowicz, J.A. Oleszkiewicz, Novel electrokinetic approach reduces membrane fouling, Water Research, 47 (2013) 6358-6366.

[29] Q. Zhang, C.D. Vecitis, Conductive CNT-PVDF membrane for capacitive organic fouling reduction, Journal of Membrane Science, 459 (2014) 143-156.

[30] F. Du, P. Ciaciuch, S. Bohlen, Y. Wang, M. Baune, J. Thöming, Intensification of cross-flow membrane filtration using dielectrophoresis with a novel electrode configuration, Journal of Membrane Science, 448 (2013) 256-261.

[31] M. Khayet, T. Matsuura, Membrane Distillation: Principles and Applications, 2011.

[32] M. Khayet, C.Y. Feng, K.C. Khulbe, T. Matsuura, Preparation and characterization of polyvinylidene fluoride hollow fiber membranes for ultrafiltration, Polymer, 43 (2002) 3879-3890.

[33] K. Ebert, D. Fritsch, J. Koll, C. Tjahjawiguna, Influence of inorganic fillers on the compaction behaviour of porous polymer based membranes, Journal of Membrane Science, 233 (2004) 71-78.

[34] P. Arribas, M. Khayet, M. García-Payo, L. Gil, Self-sustained electro-spun polysulfone nano-fibrous membranes and their surface modification by interfacial polymerization for micro- and ultra-filtration, Separation and Purification Technology, 138 (2014) 118-129.

[35] J.C.T. Lin, D.J. Lee, C.P. Huang, Membrane fouling mitigation: Membrane cleaning, Separation Science and Technology, 45 (2010) 858-872.

[36] D. Wu, M.R. Bird, The fouling and cleaning of ultrafiltration membranes during the filtration of model tea component solutions, Journal of Food Process Engineering, 30 (2007) 293-323.

[37] R. Hashaikeh, B.S. Lalia, V. Kochkodan, N. Hilal, A novel in situ membrane cleaning method using periodic electrolysis, Journal of Membrane Science, 471 (2014) 149-154.

[38] M. Dargahi, Z. Hosseinidoust, N. Tufenkji, S. Omanovic, Investigating electrochemical removal of bacterial biofilms from stainless steel substrates, Colloids and Surfaces B: Biointerfaces, 117 (2014) 152-157.

[39] M.C.V. Vela, S.A. Blanco, J.L. Garcia, E.B. Rodriguez, Analysis of membrane pore blocking models applied to the ultrafiltration of PEG, Separation and Purification Technology, 62 (2008) 489-498.

[40] M.C.M. Vanloosdrecht, J. Lyklema, W. Norde, G. Schraa, A.J.B. Zehnder, Electrophoretic mobility and hydrophobicity as a measure to predict the initial steps of bacterial adhesion, Applied and Environmental Microbiology, 53 (1987) 1898-1901.

[41] A.T. Poortinga, R. Bos, W. Norde, H.J. Busscher, Electric double layer interactions in bacterial adhesion to surfaces, Surface Science Reports, 47 (2002) 1-32.

[42] R.E. Marquis, Salt-induced contraction of bacterial cell walls, Journal of Bacteriology, 95 (1968) 775-781.

[43] E. Rojas, J.A. Theriot, K.C. Huang, Response of Escherichia coli growth rate to osmotic shock, Proceedings of the National Academy of Sciences, 111 (2014) 7807-7812.

[44] L.M. Bai, H. Liang, J. Crittenden, F.S. Qu, A. Ding, J. Ma, X. Du, S.D. Guo, G.B. Li, Surface modification of UF membranes with functionalized MWCNTs to control membrane fouling by NOM fractions, Journal of Membrane Science, 492 (2015) 400-411.

[45] J.A.R. Price, J.P.H. Burt, R. Pethig, Applications of a new optical technique for measuring the dielectrophoretic behavior of microorganisms, Biochimica et Biophysica Acta, 964 (1988) 221-230.

[46] R. Diaz, S. Payen, Biological cell separation using dielectrophoresis in a microfluidic device, Bio and Thermal Engineering Laboratory–University of California B (ed). https://people.eecs.berkeley.edu/~pister/245/project/DiazPayen.pdf, (2008).

[47] T.B. Jones, Basic theory of dielectrophoresis and electrorotation, Engineering in Medicine and Biology Magazine, IEEE, 22 (2003) 33-42.

[48] W.B. Betts, A.P. Brown, Dielectrophoretic analysis of microbes in water, Journal of Applied Microbiology, 85 (1999) 201s-213s.

[49] T.L. Sounart, T.A. Michalske, K.R. Zavadil, Frequency-dependent electrostatic actuation in microfluidic MEMS, Journal of Microelectromechanical Systems, 14 (2005) 125-133.

[50] J. Auerswald, H.F. Knapp, Quantitative assessment of dielectrophoresis as a micro fluidic retention and separation technique for beads and human blood erythrocytes, Microelectronic Engineering, 67 (2003) 879-886.

7

Nanocomposite membranes

GO-based materials implementation in water treatment applications

Although graphene oxide (GO) has been widely used in a variety of research fields, the potential for GO implementation remains controversial. Researchers commonly define GO as a 2D carbon nanomaterial with oxygen functionalities, but this definition is too loose and leads the community to compare results among significantly different nanomaterials. In order to overcome this challenge, here we suggest high throughput post-processing GO characterization techniques to rapidly and thoroughly define GO chemo-morphological properties. Then, based on characterization analysis and a clustering algorithm, we classified GO into six categories. The classification method was validated with GO samples obtained from different producers. The commercial samples were individually implemented to fabricate various macroscopic devices (e.g., membranes) and we observed that GO classified in the same category offered similar macroscopic performance. In contrast, samples from different categories resulted in a noticeable variation in macroscopic results, corroborating the importance of using standardized materials. The presented characterization and classification method will assist the research community by enabling a fair comparison between studies. Moreover, it will assist GO producers to target customers in a more effective manner by distributing GO with optimal properties for a specific application, supporting the leap of GO from lab to industry.

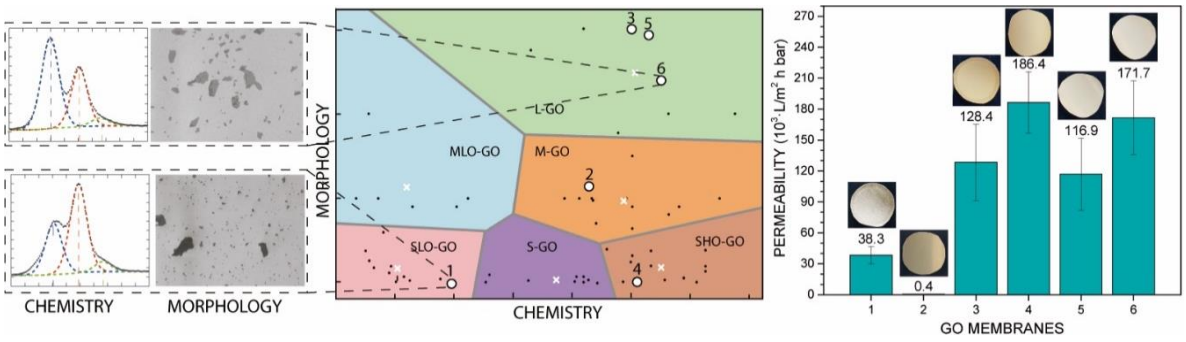

Graphene oxide standarization and classification: Methods to support the leap from lab to industry

7.1 Introduction

According to Aristotle, in order to explain the world and objects around us we need to recognize four causes: i) the matter determined by the material of the object; ii) the form determined by the shape of the object; iii) the agent determined by the transformation of the object; and iv) the end determined by the purpose of the object [1]. Although, this knowledge was professed more than 2000 years ago, there is analogism with modern science. In particular, in materials science and/or nanotechnology when we describe an object, we tend to refer to those four causes: i) the matter is the chemistry of the material; ii) the form is the morphology of the material; iii) the agent is the process through which a material is modified; and iv) the end is the functionality of the material.

For new nanomaterials, it is fundamental to well-define their morphology and chemistry since different chemo-morphological combinations will lead to diverse surface and quantum size phenomena. For this reason, nanomaterials such as carbon nanotubes (CNTs) are undergoing a standardization process, which tabulates all relevant CNTs properties and standard protocols for characterization [2]. A similar standardization process will be necessary for graphene oxide (GO), which can be thought as a single layer carbon sheet (i.e., graphene) decorated with oxygen functionalities, involving both basal-plane and edge-site chemical modification of graphene during oxidation and exfoliation. The standardization process can be included in the current effort to introduce a rational naming system for the two-dimensional carbon form [3].

GO has recently gained interest among academic researchers and industries. From the academic sector, the number of citations per year of scientific work whose title includes "graphene oxide" has increased by almost one order of magnitude (from ≈ 900 to ≈ 7000, see Fig. 7.1) in four years (2011–2015) [4]. From the industrial sector, the GO manufacturing capacity has increased by a factor of five over roughly three years, with a current yearly production capacity of ≈ 1000 tons/year [5, 6]. Moreover, the number of annual patents filed whose title contains "graphene oxide" has increased by an order of magnitude in four years (2011–2015) [7].

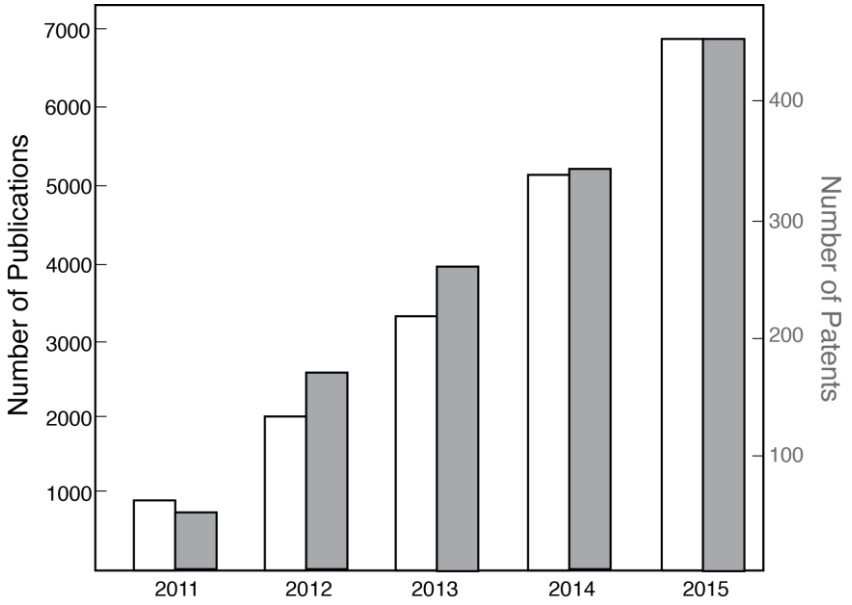

Figure 7.1. GO trends. Number of publications (white) and number of patents filled (gray), which title contains "graphene oxide", between 2011 and 2015.

The drive behind this increased interest is two-fold. First, the GO price per gram is about six orders of magnitude lower than pristine graphene, which opens different markets such as industrial applications. The price of GO is also steadily declining due to the development of scalable fabrication systems with current reactor capacity >100 tons/year, which leads companies to predict a GO price as low as a few cents per gram in the next five years. These factors also raise the interest of investors and producers who want to place themselves in the market before an explosion of growth dictated by successful demonstration of applications; similar to what recently happened with quantum dots, which found their market in the display industry [8].

Second, GO displays unique properties such as near-atomic thickness [9], the presence of oxy-groups allowing for rapid functionalization [10], scalable synthesis processes [11], and the possibility of controlled deposition of nano-thin films on a variety of substrates using solution-based casting techniques (e.g., vacuum filtration [12, 13] spin coating [14, 15], layer-by-layer [16], or doctor blade printing [17]). More importantly, the versatility and the possibility of tuning the primary GO properties (flake size and quantity of oxy-functionalities) led researchers to propose the use of GO in several fields such as energy storage [18, 19] separation processes [15, 20, 21], and drug delivery [22, 23], just to mention a few (readers can refer to exhaustive literature reviews of GO applications) [24]. In each specific application, the GO properties have been selected ad hoc to serve at best the functionality of the device in which GO is implemented. For example, in transparent conducting films, large-dimension and slightly-oxidized GO flakes are selected in order to enhance electron transport [25, 26]. Although slightly-oxidized GO flakes are also preferred for supercapacitor applications, recent studies explored the possibility

of exploiting surface GO oxy-functionalities to increase device pseudo-capacitance via red-ox reactions [27]. GO morphology is paramount for the enhancement of mechanical properties; for instance, large size GO flakes are preferred to maximize fiber reinforcement [28]. In membrane technology for water treatment, the number of oxy-functionalities and GO dimensions can be tailored accordingly to the contaminant of interest and desired permeability [20]; thus, the rational modification of the GO nanoproperties will allow controlled tuning of the permeability-selectivity tradeoff.

In order to enable successful commercialization and industrial application of GO, it is paramount that researchers and industries have a common understanding of GO nomenclature and properties, which can have a large impact on the application of interest, vida supra. However, from our experience, studies in the literature, and discussions with academics and GO producers, GO properties are extremely wide-ranging, source-dependent, and, in some of cases, are not even mentioned. In particular, the synthesis process plays a major role in determine GO properties. GO can be synthesized from 3D graphite flakes via the Hummers' method [29], which represents an evolution of two previous chemical exfoliation methods (Brodie and Staudenmaier) [10]. As it has been recently shown, even small tuning of the synthesis process (e.g., time and/or temperature of the oxidation process) can lead to significantly different GO properties [30]. One clear example illustrating how poor GO characterization can lead to confusion in the research field is the recent controversy on the water transport in GO laminates. On one hand, studies have reported fast water transport (FWT) in GO possibly due to the low wall friction experienced by water when traveling through regions of 2D pristine graphene capillaries [13, 31]; this is similar to FWT through 1D CNT due to a linear water-water dipole alignment parallel to the CNTs axis offering the lowest water-CNTs interaction [32]. On the other hand, surface friction might occur when water travels through GO nanochannels depending on the amount and type of GO basal plane oxy-groups [33-36]. The origin of this controversy most likely arises from the difference in nanoproperties of the compared GO materials. Thus, it is fundamental that GO properties are well characterized when proposing theories and/or in order to enable a fair comparison between research results.

This work here aims to initiate the GO standardization process offering: i) high-throughput and lab-accessible GO characterization protocols and ii) a GO classification according to properties based on a clustering algorithm. The classification is similar to what has been done for bulk materials, which are divided in sub-categories (e.g., high-density polymer versus low-density polymer). The standardized characterization protocols are then validated by six GO samples collected from different producers across two continents. Investigation of GO-based applications utilizing material from different producers is used to highlight the effect of the nanomaterial properties on the macroscopic performance of a device

7.2 Materials and methods

7.2.1 Materials

GO was acquired from six different producers across two continents. Depending on the producer, the GO was either received in powder form or in an aqueous solution. All the samples were then diluted in water to the same concentration (0.05 wt.%) and then subjected to the specific pre-treatment required by the producer; possible pre-treatments include sonication with a Branson sonicator (V = 1.9 L, *max. power* = 80 W, and f = 20 kHz) and pH adjustment with NaOH. The polyvinylidene difluoride (PVDF) membrane used as the support for the vacuum filtered GO thin film was purchased from Sterlitech (TriSep YMTM103001). The PVDF membrane was cleaned by ultrasonication in IPA for 5 min, then in DI for 5 min, and kept in IPA prior to use. *Escherichia coli B* (*E. coli*) CAROLINA™ 124300 (Carolina Biological Supply Company, Burlington, NC) was utilized as a model bacterium to evaluate the bacterial deposition on the GO membranes. BD Bacto™ tryptic soy broth (TSB), tryptic soy agar (TSA), NaCl (reagent grade), and ethanol (EtOH; laboratory grade) were purchased from VWR International (West Chester, PA). Formaldehyde (35% in water) was purchased from Sigma-Aldrich. Deionized (DI) water (>18 MΩ) was produced by a Nanopure Infinity ultrapure water system (Barnstead/Thermolyne) and was used to prepare solutions and rinse containers. Methylene blue (MB) hydrate (>95%) was purchased from Sigma-Aldrich and selected to evaluate the adsorption capacity of the different types of GO samples examined.

7.2.2 Characterization

7.2.2.1 XPS

The GO samples were analyzed by a Thermo Scientific K-Alpha XPS (ESCA). The X-rays were generated by a 12 keV electron beam and had a spot size of 400 μm. The O/C ratio calculation and peak deconvolution were performed by using the Thermo Scientific Avantage software. Three data points for each sample were taken. The dwell time was set to 10 ms for the survey spectra and 50 ms for the high-resolution (C1s) spectra. For each data point the number of scans were set to 5 and 10 for the survey scan and for the high-resolution scan, respectively. The XPS instrumental error for atomic composition is ± 1%, and the accuracy of the C1s peak fitting is ± 2%. Being aware of the possible GO chemical change caused by prolonged X-ray irradiation (>100 min) [37], the number of scans was minimized to obtain the same information in terms of oxidation percentage. In this way, the limited dwell time and a low scan number used here were not enough to chemically alter the GO.

7.2.2.2 UV-vis

The UV-vis absorbance spectra were obtained with a S-3100 SCINCO spectrophotometer. The wavelength range was from 200 to 1100 nm. The wavelength resolution was 0.95 nm. In order to avoid saturation of the absorbance signal, the samples were diluted to a concentration of 0.005 wt.%.

7.2.2.3 AFM

The thickness of the GO flake was measured with an Asylum Cypher AFM using an Olympus 200TS cantilever (resonance frequency ≈ 130 kHz). The images were acquired in amplitude modulation mode. The images in attractive (non-contact) and repulsive (contact) regime were obtained with a ratio between a set point amplitude and a free amplitude of 80% and 30%, respectively. The images were then flattened and a few scan lines were removed to increase the image quality using AR software from Asylum Research.

7.2.2.4 XRD

The GO crystallographic structure was analyzed with a Bruker D8 equipped with a two-dimensional VANTEC-500 detector. The spectra were obtained by the integration of the 2D images via EVA software. The integration time was 600 ms and two data points were obtained for each sample. The data were then smoothened with the MATLAB built-in smoothening function. The width of the GO nanochannels ($2h$) for each sample was determine using the Bragg's law:

$$2h = \frac{\lambda}{2 \cdot \sin\theta} \tag{7.1}$$

with a λ = 1.54 Å (i.e., wavelength of the Cu Kα).

7.2.2.5 ATR-FTIR

Infrared spectra were recorded using the ATR accessory for a Nicolet 670 Fourier Transform Infrared Spectrometer. The spectral resolution was 0.5–1 cm^{-1} over a range of 1000–4000 cm^{-1} and subsequently averaged over 16 scans, representing a single analysis interval of 12 s. A germanium crystal (no. 022-5450500, Pike Technologies) was employed as the ATR element and the GO samples were screw-pressed by the cap of the ATR cell, thereby bringing the samples into flush contact with the ATR crystal.

7.2.2.6 SEM

A Zeiss ULTRA Field Emission Scanning Electron Microscope with an In-lens secondary electron detector was used to characterize the GO morphology. The working distance, acceleration voltage, and aperture were set to 3–4 mm, 5 kV, and 30 μm, respectively. The statistical SEM image analysis in Fig. 7.4 was completed using ImageJ (see also Fig. 14.1 in

Appendix D) where ≈ 250 GO flakes from different SEM images were analyzed. The monolayer percentage was obtained by deconvoluting the normalized pixel intensity (i.e., 0–1) histograms in MATLAB (see Fig. 14.3 in Appendix D for more details). Pixels with higher intensity (brighter) represent monolayer flakes, whereas darker pixels represent the area characterized by two or more GO layers. The substrate background was discarded by applying a mask with the Magic Wand Tool in Photoshop. The GO solution needs to be diluted (<0.01 mg/mL) to avoid overlap of the deposited monolayer GO flakes, which would then be identified as a multilayer GO structures by the algorithm.

7.2.2.7 Zeta potential and zeta average

Both zeta potential (ζ-potential) and zeta average (ζ-avg) were evaluated using a Malvern Zetasizer ZS. The ζ-potential was calculated from the electrophoretic mobility, whereas ζ-avg was obtained with dynamic light scattering. This technique is based on the evaluation of particle Brownian motion, which is converted to a size distribution using the Stokes-Einstein relationship. In the Zetasizer software the solution was set to water and the material to carbon black. Three experiments for each sample were carried out.

7.2.2.8 Raman spectroscopy

Raman spectra were acquired using a WITec Confocal Raman Microscope/SNOM/AFM. The laser wavelength was 532 nm and the signal was acquired using a 0.5 s integration time of 10 spectra.

7.2.2.9 SCA

The static contact angle (*SCA*) measurements were completed with a Ramè-Hart 190 contact angle goniometer under ambient conditions. *SCA* were measured using 5 μL droplets and the data refer to the average of 5 measurements obtained with the Drop Analysis-DroSnake plugin in ImageJ.

7.2.3 GO classification method

The literature nanoscopic properties of GO were acquired by researching scientific articles utilizing the keywords graphene oxide, O/C ratio, length, dimension, and distribution. More than 300 peer-reviewed works (see supplementary text file for complete list in https://doi.org/10.1016/j.carbon.2018.02.091) were used to produce the histograms in Fig. 7.6 A and B. Each GO nanostructure included in this paper represents a GO characterization with both an O/C ratio and GO dimensions. Note that the length specified by the researcher was utilized (if a square flake was assumed) or it was estimated from the reported area assuming square flakes. A classification algorithm can be used here due to the independence of the chemistry and morphology variables (i.e., O/C ratio and length). The K-mean clustering

algorithm aims to minimize the loss function (L), defined as the sum of the distance of each observation from the centroid (x) of the cluster (k):

$$L = \sum_{k=1}^{K} \sum_{x \in k} (x - \mu_k) \tag{7.2}$$

where μ_k is the number of data points in the class k. A more comprehensive resource for further details on K-mean clustering can be found here [38]. In this study, the number of observations is equal to 60 (20% of the total dataset), which corresponds to works that reported both GO morphology and chemistry. The total number of clusters (K) is equal to 6. The number of clusters is chosen through the optimization "elbow" method (see Fig. 14.4 in Appendix D), where 6 is the minimum number of clusters to achieve a percentage of explained variance >90% [39]. This method allows removing any arbitrary decision on the number and definition of clusters which might be affected by bias. In contrast, the "elbow" method is derived from the statistical behavior of the data points. Note that for this classification only data points characterized by mean flake size <3 μm were considered, representing more than two thirds of the data found in the literature. The length for the remaining studies spans over two orders of magnitude and the information on the O/C ratio is often omitted, thus running a classification algorithm on this remaining data would not be feasible and thus has not been included here.

7.2.4 GO membrane fabrication and evaluation

7.2.4.1 GO membrane fabrication

After the GO pre-treatment suggested by the producers was performed, the six GO samples were diluted to the same concentration (≈ 0.05 wt.%). Then 1 mL of each of the six GO samples was added to 20 mL of deionized water. The GO solutions were then vacuum filtered and dried onto separate PVDF membranes.

7.2.4.2 Bacteria attachment experiments

E. coli was cultured in TSB by seeding from a TSA plate at 37°C and harvested at mid-exponential phase. After centrifugation (2 min at 10,000 rpm) and resuspension twice in 155 mM NaCl, the bacterial stock solution was diluted to an optical density of 0.15 at 600 nm (OD_{600} = 0.15) in saline (~10^8 CFU mL^{-1} by fluorescence microscopy enumeration) [40]. Finally, 500 mL of bacterial saline working solution was prepared with a concentration of 6×10^7 CFU mL^{-1} and 1/60 the volume of TSB was added to provide essential nutrients and avoid bacterial inactivation during the experiment. Graphene oxide membranes (GOMs) were placed in a glass beaker with 500 mL of the saline bacterial working solution. The bacterial-GOM suspension was maintained at room temperature and stirred for 20 h at 80–100 rpm. Once the bacterial experiment was concluded, GOMs were examined by SEM to determine surface bacterial density and morphology. SEM of bacterial samples was completed after they were fixed with

formaldehyde vapor for at least 12 h, dehydrated with 40-to-100% EtOH/DI solutions, dried at room temperature, and coated with 2 nm of Pt/Pd (80/20) (EMS 300T D Dual Head Sputter Coater).

7.2.4.3 Adsorption experiments

The adsorption of methylene blue (MB) was quantified using a S-3100 SCINCO UV-visible spectrophotometer. GO aqueous solutions with a total volume of 14 mL were prepared by adding 0.5 mg MB solution (volume 1 mL) and 1 mg GO solution (1:2 ratio) into plastic centrifuge tubes and then vortex-mixed. The volume of the GO solution was dependent on the product due to the different initial densities. The final concentration of the different components in the solution were 35.7 mg/L for MB and 71.4 mg/L for GO. The sample tubes with the GO suspension were shaken for 24 h in an Estella E24 Incubator Shaker at 25°C to reach the equilibrium. Then the adsorbent was separated from the solution by centrifugation at 10,000 rpm for 15 min. The absorbance of the supernatant was recorded at a wavelength of 608 nm (ε = 36,035 M^{-1} cm^{-1}). Finally, the adsorption capacity of the different GO samples was quantified as the log removal value (*LRV*):

$$LRV = \log_{10} \frac{C_0}{C_e} \tag{7.3}$$

where C_0 and C_e were initial and equilibrium concentrations of MB (mg/L), respectively.

7.2.4.4 GOM permeability

The wet flow curves of the GOMs were measured by the capillary flow porometry (CFP) method using a gas–liquid displacement Porometer (POROLUX™ 100, Porometer). CFP is based on the displacement of a wetting liquid inside a porous network by means of an inert gas flow. In this study, POREFIL® (Porometer, surface tension of 16 dyn/cm) was used as the wetting liquid agent, compressed air was used as the inert gas, and the pressure scan method within a pressure range of 0–5.5 bar (Fig. 14.6 in Appendix D) at room temperature was applied. Three different samples for each GOM were evaluated to obtain the final reported wet flow curve.

7.3 Results and discussions

7.3.1 GO chemistry

First, attention is focused on GO chemistry. A photo of the GO samples from different producers at a concentration of 0.01 wt.% in water is presented in Fig. 7.2-A. The samples have been ordered from darkest (1) to lightest (6), which also represents an increase of the extent of GO oxidation (O/C ratio values in Fig. 7.2-B). For example, when a carbon atom is oxidized,

the sp^2 conjugation of the carbon atom may be altered to sp^3, thus modifying the sp^2 mediated light absorption. Moreover, by retrofitting the O/C ratio in the photo, it was possible to build a color chart qualitatively indicating the extent of sample oxidation (Fig. 7.2-A right).

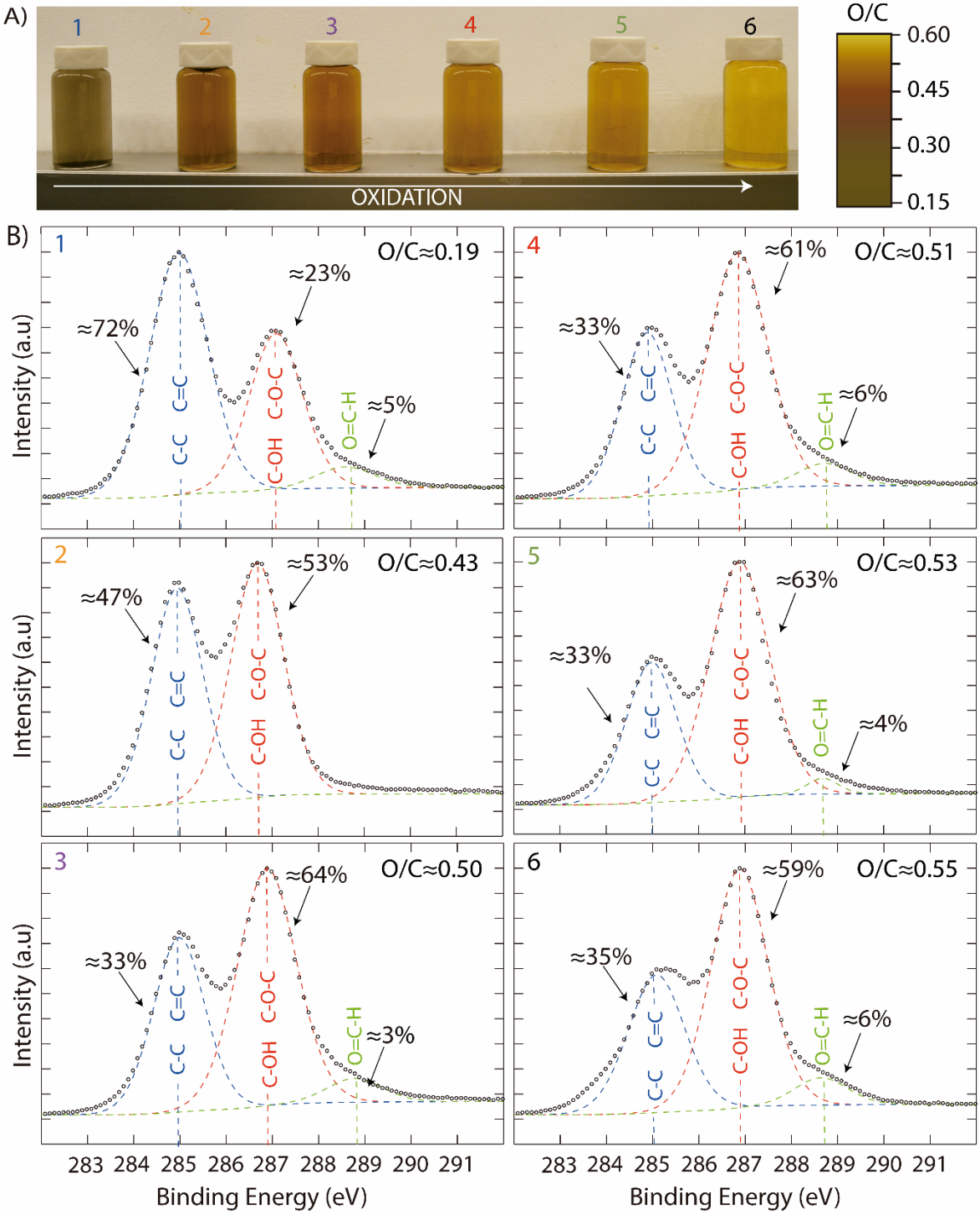

Figure 7.2. GO chemistry I. A) Photo of the six GO samples in solution (left). A color gradient relative to the O/C ratio (right). B) C1s spectra obtained by XPS analysis of GO samples. The data also display the percentage contribution of individual peak obtained by deconvolution and the O/C ratio.

To corroborate the extent of GO oxidation, XPS analysis of vacuum filtered GO thin films (see **Materials and methods**) was completed. The deconvolution of the C1s XPS spectra (Fig. 7.2-B) is based on one of the most accepted GO structural model (i.e., Lerf's model [41]) and it is characterized by three peaks: i) single (C–C) and double (C=C) carbon bonds centered at ≈ 285 eV; (ii) epoxide (C–O–C) and hydroxide (C–OH) functional groups centered at ≈ 287 eV; and (iii) carboxylate (O=C–OH) functional groups centered at ≈ 289 eV [42]. However, the relative percentage of the three peaks greatly varies depending on the sample. For example, Sample 2 is the only sample that does not display a carboxylate peak and the least oxidized sample (1) has a C–C/C=C contribution of 72%, while the most oxidized sample (6) is characterized by a C–C/C=C contribution of 35%. Concurrent with the decrease of sp^2 conjugation in Sample 6, an increase in C1s epoxide and hydroxide functionalities to almost 60% is also observed. Overall, the O/C ratio varies from 0.19 to 0.55 and confirms the large chemical variability of the six samples. It is worth noting that a lower oxidation extent can also be induced by a higher number of GO layers in a single flake that could hinder internal basal-plane oxidation. Other elements apart from O and C, such as N and S, were also observed in small percentages (see Table 14.1 in Appendix D for details) and are probably residuals of the synthesis process.

As seen in Fig. 7.2, XPS quantitatively characterizes the chemistry of GO thin films with limited and automated post-processing of the data (e.g., C1s peak deconvolution), leading to high-throughput measurements. The chemistry of GO thin films was also analyzed with spectroscopic techniques such as, UV-vis, ATR-FTIR, and Raman spectroscopy (Fig. 7.3). From the UV-vis spectra for Samples 2–6 in Fig. 7.3-A, it is possible to observe an absorbance peak around 220 nm representing the π-π* transition of the aromatic C=C bonds remaining from the original graphitic structure [43]. In contrast, Sample 1 is characterized by a redshifted peak (≈ 230 nm) due to its lower oxidation state [44], confirming a lower oxygen content compared to the other samples. Furthermore, Sample 1 also presents multiple shoulder peaks (blue rectangle in the inset zoom) related to multilayer GO structures [45], where the carbon planes can approach one another closely enough to allow π-π stacking, which also leads to a broader absorption peak in the region around 600 nm. Although the XPS analysis indicated that Samples 2–6 are characterized by a wide-range of oxidation states ($0.43 < O/C < 0.55$), the UV-vis fails to convey this information.

In Fig. 7.3-B, the FTIR spectra confirm the oxidation of GO with alkoxyl, epoxide, and carboxylate peaks centered at 1065, 1230, and 1730 cm^{-1}, respectively [46]. The other major peak centered at 1625 cm^{-1} is due to the presence of sp^2 domains. The FTIR spectra also display a broad absorbance band in the region 3200–3600 cm^{-1} related to OH stretching vibrations of adsorbed water for all the samples except for Sample 2 (i.e., the sample with no XPS carboxylate peaks). Although ATR-FTIR spectroscopy is able to quantify the concentration of gases via the

Lambert-Beer law, the quantification of the thin film materials' functionalities is challenging. The FTIR spectrum can be strongly influenced by the calibration curve, the morphology of the sample, and, in the case of ATR, also by the area of contact between the material and the germanium crystal. Thus, it is difficult to quantitatively compare the chemistry of different samples and the user can only report qualitative functionality information based on the presence or absence of peaks or relative change over time of a single sample. In summary, UV-vis and ATR-FTIR spectroscopy are useful techniques for confirming the GO oxidation state and identify functionalities, but are not able to quantify GO chemistry and oxy-functionalities since spectra from different samples are indistinguishable.

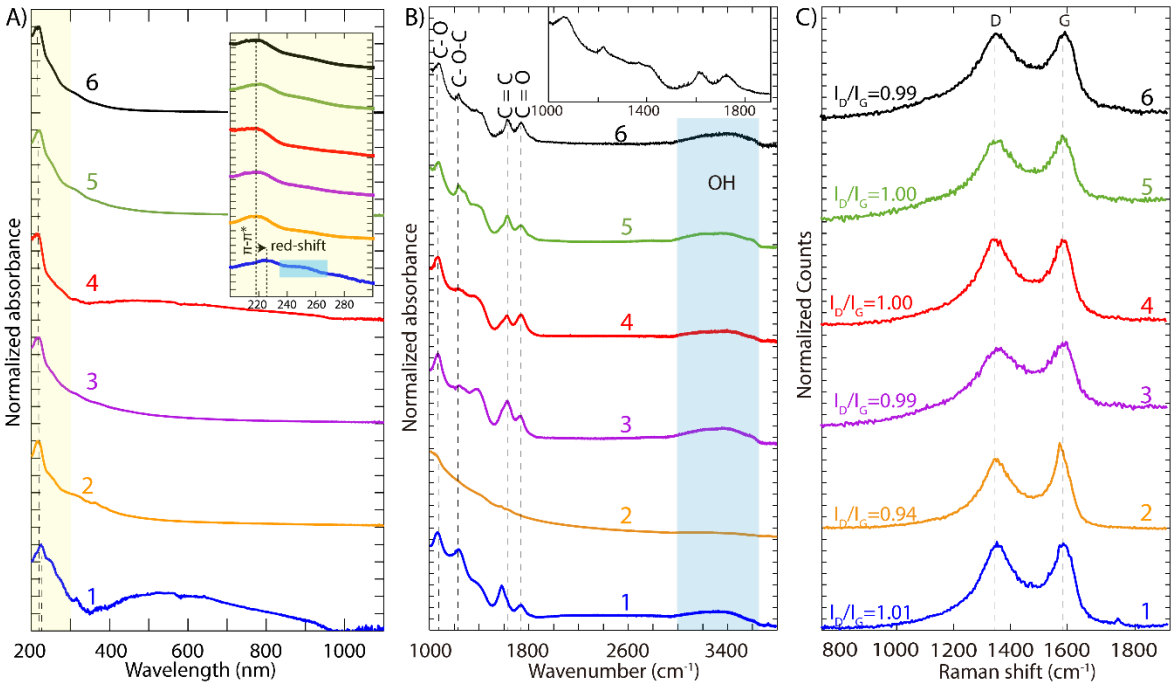

Figure 7.3. GO chemistry II. A) UV-vis, B) ATR-FTIR, and C) Raman spectra of the six GO samples.

Raman spectra have also been used by researchers to characterize GO [47]. In our case, the six Raman spectra samples are presented in Fig. 7.3-C and display a D-band at ~1350 cm^{-1}, representative of defects/disorder in the basal plane, and a G-band at ~1590 cm^{-1} representative of the in-plane sp^2 bond stretching [48]. A primary quantifiable Raman measurement is the D/G intensity ratio (I_D/I_G), which is a measurement of the defect density. However, all GO samples with different XPS oxidation states display $I_D/I_G \approx 1$, apart from Sample 2 which has a slightly lower defect density ($I_D/I_G \approx 0.94$); thus, Raman is not a suitable technique for quantifying the GO chemistry. Moreover, Raman spectroscopy tends to be a destructive technique [37] for a metastable material such as GO; even a short laser irradiation time (<2 s) would be sufficient to alter GO chemo-morphological structure and is likely responsible for the lack of Raman variation with oxidation state. In addition, during GO reduction, CO and CO_2 are liberated producing defects; thus, one cannot reliably characterize partially reduced GO samples with

Raman because the reduction converts one type of defect (oxy-groups) to another type (vacancies) produced during reductive deoxygenation.

Zeta potential (ζ-potential) can also be used to indirectly analyze the chemistry of materials in aqueous solutions. The ζ-potential of moderately stable GO dispersions (ζ-potential < -30 mV) in water at pH ≈ 7 is summarized in Table 7.1. The negative charge is connected to the ionization of the carboxylate functional groups, again indicating successful GO oxidation [49] and making aqueous GO dispersion stable from aggregation. For Sample 1, it was not possible to obtain reproducible ζ-potential values, since the material was not stable to aggregation and sedimentation in water. As observed by XPS, Sample 1 is characterized by the lowest extent of oxidation, which does not provide sufficient electrostatic repulsion to stabilize the colloidal solution, resulting in aggregation and subsequent settling of the GO dispersion (see Fig. 14.2 in Appendix D).

Static contact angle (*SCA*) provides information on the properties of a thin film, such as the GO chemistry, assuming that the morphology of GO film does not significantly vary (i.e., all thin films here are made with the same casting procedure). The *SCA* decreases from ≈ 60° to ≈ 25° with increasing oxidation state (from Sample 1 to Sample 6). This result is related to a higher affinity of water to more highly oxidized surfaces, due to the increase in hydrophilicity, in accordance with previous reports analyzing the wettability of GO in different oxidation states [50]. In particular, the presence of hydrophilic functional groups (e.g., hydroxyl) decreases the hydrophobic nature of pristine graphene and increases its surface energy. As stated for the UV-vis and ATR-FTIR techniques in Fig. 7.3, although ζ-potential and *SCA* can deliver useful qualitative information on the GO oxidation state, this information cannot be directly translated into quantifiable properties across samples.

Table 7.1. Zeta potential (ζ-potential), static contact angle (*SCA*), and zeta average (ζ-avg) of the six GO samples.

Sample	ζ-potential (mV)	*SCA* (°)	ζ-avg (nm)
1	NA	60.5 ± 2.1	NA
2	-38.1 ± 1.4	49.3 ± 1.7	596 ± 14
3	-32.4 ± 1.1	39.3 ± 3.3	1981 ± 224
4	-33.2 ± 0.3	31.1 ± 1.8	507 ± 13
5	-38.1 ± 1.4	25.7 ± 1.7	1503 ± 32
6	-29.7 ± 1.7	25.3 ± 2.3	1604 ± 216

7.3.2 GO morphology

After analyzing the GO chemistry, the attention is turned to techniques for characterizing GO flake morphology. SEM images and statistical data obtained by image processing are presented in Fig. 7.4. A representative SEM image for each of the samples is displayed in Fig. 7.4-A, whereas the statistical data in Fig. 7.4 B and C is based on multiple images (see **Materials and methods**). SEM image data analysis was used to quantify the flake size distribution (see Fig. 7.4-B and Fig. 14.1 in Appendix D for details). In Fig. 7.4-B, the flake areas have log-normal distributions (dashed red lines) characterized by a few larger flakes and more numerous smaller flakes. Noteworthy is the great extent of the variability of the average GO flake area between samples, which spans over an order of magnitude (e.g., from 0.2 to 9.3 μm^2). In particular, Samples 3, 5, and 6 are characterized by larger GO flakes than those in Samples 1, 2 and 4. This difference is also captured by zeta average (ζ-avg) hydrodynamic diameter measurements, which are >1500 nm and <600 nm for Samples (3, 5, 6) and (2, 4), respectively (Table 7.1). In the case of GO, ζ-avg measurements cannot be compared to the actual flake size measured by other techniques since they are assumed to be monodispersed samples with spherical or near-spherical shape (GO is 2D) that uniformly scatter light (GO is partially transparent) [51, 52]. For Sample 1, it was not possible to obtain a hydrodynamic value, since it is characterized by a poly-dispersivity index of 1, indicating that the sample likely contains aggregates that can sediment leading to a skewed size distribution (see Fig. 14.2 in Appendix D). In SEM images, GO flakes in the same image are characterized by different greyscale intensities: monolayer flakes appear brighter compared to multilayer aggregates. Using this intensity difference, we are able to quantify the percentage of monolayer for each sample (see Fig. 14.3 in Appendix D for details) [48]. GO Samples 2–6 have a monolayer percentage >78% confirming effective exfoliation and the 2D nature of GO. For Sample 1, SEM analysis confirms UV-vis and ζ-avg results, which indicated the presence of multilayer structures and large aggregates as only 15% of the flakes are monolayer and the intensity distribution displays multiple peaks related to flakes with various numbers of GO layers (e.g., multilayer).

Although SEM can quantify the percentage of monolayer structures and geometry of the GO flakes, the flake thickness is another important morphological parameter for a 2D material. XRD of a GO thin film is able to measure the separation distance (*2h*) between GO flakes due to GO's tendency to stack in a laminar fashion. XRD can give an approximation of the combined GO thickness including intercalants, such as water molecules, which will be remain unless specific and rigorous drying protocols are used. The GO separation distance varies ≈ 15% from Sample 1 to Sample 6 (from 7.9 to 9.1 Å) increasing with increasing GO oxidation and basal plane oxy-functionality (Fig. 7.5-A). Thereby, GO samples with higher extent of oxidation result in a less compacted thin film structure, whereas GO samples with lower extent

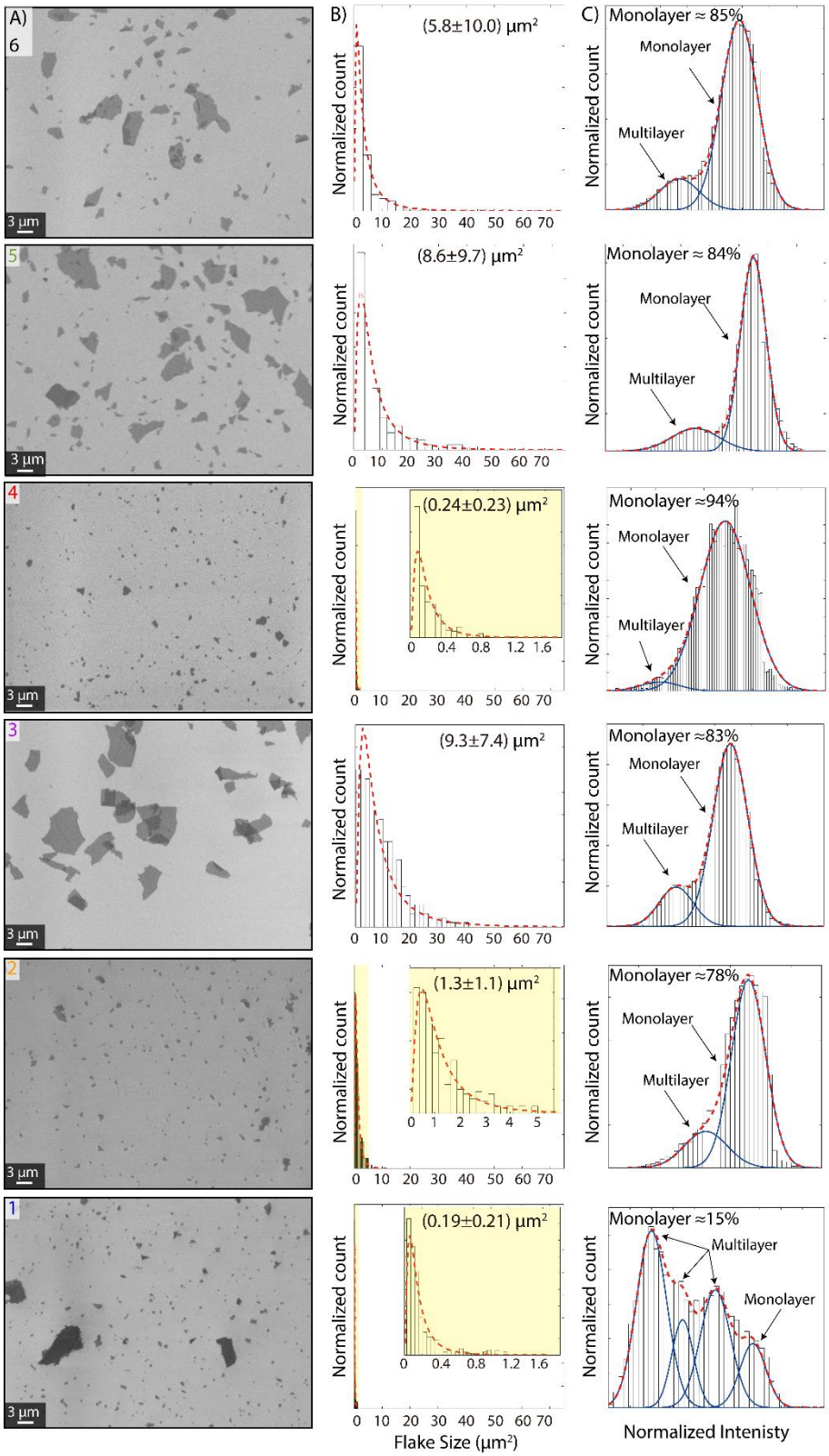

Figure 7.4. GO morphology I. A) SEM images of GO samples. B) GO flake size distribution fitted to a log-normal distribution (red dashed lines); yellow square represents zoom in for the smaller GO flakes (Samples 1, 2, and 4). C) Histograms of SEM image greyscale intensities that are deconvoluted to obtain mono-/multi-layer percentages.

of oxidation result in a more compacted thin film structure. Moreover, under ambient conditions GO samples with higher extent of oxidation will absorb more water molecules than the ones with lesser extent of oxidation. Considering that the graphene layer itself has a known vdW thickness of 0.34 nm and addition of oxygen groups can increase that thickness to 6–7 Å, any GO with a thickness larger than that is influenced by water adsorption. GO thickness can also be measured via AFM, however, AFM measurements can vary depending on the mode of operation and environmental conditions. As an example, GO morphology for Sample 5 obtained by operating the AFM in non-contact mode [53] (attractive regime, phase values above 90°) is displayed in Fig. 7.5-B. The GO monolayer thickness is ≈ 2 nm, which is considerably higher than the 1.5 nm thickness evaluated in contact mode [53] (Fig. 7.5-C, repulsive regime, phase values below 90°). Both values are in accordance with previously reported GO thickness [54]. AFM results may also be affected by the AFM tip geometry and ambient conditions (e.g., presence of humidity) [55], which will increase the thickness of the water layer trapped between the substrate and the GO flakes [56]. For this reason, AFM images comparing GO flakes from different producers are not presented here. However, AFM is useful for corroborating the monolayer nature of the GO observed by SEM.

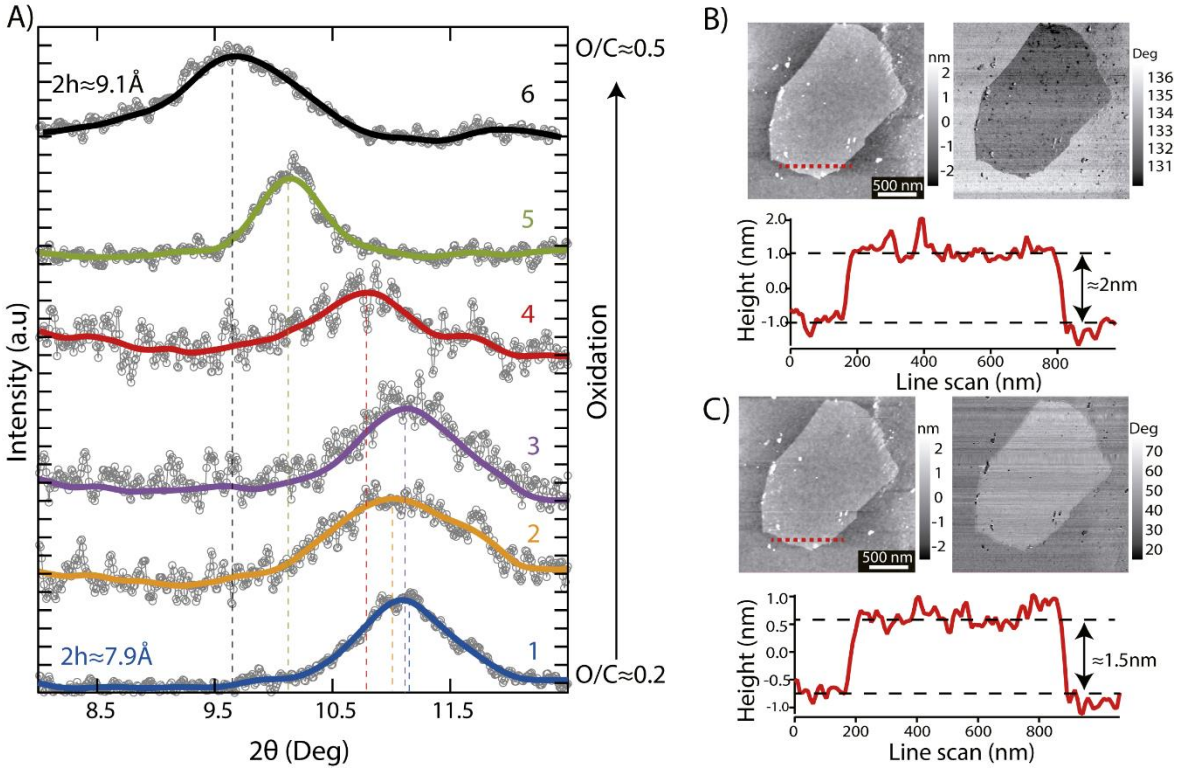

Figure 7.5. GO morphology II. A) XRD spectra for the six GO samples. AFM analysis in B) non-contact attractive and C) contact repulsive regime for a single GO flake.

7.3.3 GO characterization tools

All the tools used in this study to characterize the chemistry and morphology of GO are classified in Table 7.2. The information provided by the different techniques is divided between quantitative and qualitative; the latter should only be used in the GO prescreening phase and/or to obtain results in relative (and not absolute) terms that could validate quantitative measurements. To summarize, XPS is the primary tool to quantitatively analyze GO chemistry due to the ability to provide information regarding the oxidation state and the specific GO oxy-functionalities with minimal and automated data post-processing. Disregarding the time needed to pump down the XPS (pump and instrument dependent), an XPS measurement generally takes 1–2 min per sample. On the other hand, SEM is the primary tool to quantitatively characterize the GO morphology providing information on the monolayer nature and on the dimensions of the GO flakes. For SEM, the image acquisition generally takes 1–2 min per sample. Thus, the time required to quantitatively characterized the chemo-morphological GO properties is quite attractive. Other microscopy techniques, such as TEM or STEM, have not been included in this study as they would convey similar data obtained already by SEM on the

Table 7.2. Summary of the techniques used to characterize the GO chemistry and morphology.

Technique	Morphology	Chemistry	Notes
XPS	-	**Quantitative**	O/C atomic and oxy-functional group ratios via C1s peak deconvolution
Color chart*	-	Qualitative	Related to oxidation state
UV-vis*	Qualitative	Qualitative	Presence/extent of sp^2 conjugation and multilayer nature/structure
ATR-FTIR	-	Qualitative	Presence of specific oxy-functional groups and sp^2 conjugation
Raman	-	Qualitative	Defect and sp^2 conjugation, but destructive to sample
SCA	-	Qualitative	Wettability as indirect measure of oxidation & surface roughness
ζ-potential*	-	Qualitative	Surface charge as indirect measure of oxidation (deprotonated oxy-groups)
SEM	**Quantitative**	-	Flake size distribution and monolayer percentage via image analysis (see Appendix D)
XRD	**Quantitative**	Qualitative	Flake-to-flake separation influenced by the presence of oxy-groups
AFM	Semi-Quantitative	-	GO thickness highly sensitive to experimental and operation conditions
ζ-avg*	Semi-Quantitative	-	Hydrodynamic flake size distribution, skewed by spherical/opaque assumptions

*Refers to experiments conducted on GO dispersed in water.
In **bold** are highlighted the quantitative techniques.

GO morphology. However, TEM and STEM can give information regarding the atomic structure of GO [57] and the interaction between GO and other nanostructures, such as metal nanoparticles [58]. In regard to XRD, researchers can infer information on both chemistry and morphology from the separation distance *2h*, with a characterization time on the order of minutes per sample depending on the number of spectra acquired. Moreover, XRD does not require particular experimental conditions. The alternative techniques presented here such as ATR-FTIR, UV-vis, and Raman spectroscopy can deliver complimentary qualitative information on GO morphology and chemistry, which can be used for prescreening or as orthogonal measurements.

7.3.4 GO standardization and classification

Careful research of the GO literature (>300 peer-reviewed articles) was carried out in order to collect information on the chemistry and morphology of GO used in previous studies (see supplementary text file for complete list in https://doi.org/10.1016/j.carbon.2018.02.091). The O/C atomic ratio distribution for GO, reduced GO (RGO), and multilayer (i.e., nanoplatets) GO (MLGO) found in the literature are presented in Fig. 7.6-A. The distribution greatly varies as the O/C atomic ratio for GO and RGO are characterized by very different average values, 0.46 ± 0.13 and 0.16 ± 0.10, respectively. MLGO has an O/C similar to RGO due to its poor exfoliation. The variation in the dimension of the GO flake is even greater than the O/C atomic ratio and spans over five orders of magnitude as illustrated in Fig. 7.6-B. This variation is caused by the significant difference in the dimension of the starting materials (i.e., graphite flakes) [51] and/or processes such as sonication and centrifugation used during GO synthesis and post-processing [42, 59-61]. The large variation in the nanoscopic GO properties hinders a true comparison among scientific works and can generate confusion in the research community. For this reason, an initial attempt to statistically classify GO based on its chemo-morphological properties is presented in Fig. 7.6-C. The majority of the GO literature was researched in order to locate scientific works that characterized both GO chemistry and morphology and the data was classified using the K-mean clustering algorithm [38]. The basic idea behind K-mean clustering is to determine the minimum number of classes into which the data will be partitioned, and then perform computation to group data so that observations within a cluster are similar and observations in different clusters are dissimilar. Each cluster is characterized by a centroid, which is typically the mean of the data. The algorithm assigns each observation to one cluster randomly and then repeats the following two steps until the clusters do not change: i) for each cluster computes the centroid; ii) given the centroids, reassigns all the observation based on their closeness to centroids. Via this iterative process, a local minimum is found by minimizing a cost function (details in the **Materials and methods**). K-mean clustering classified the chemo-morphological data (black dots) into six categories: small and less oxidized

GO (SLO-GO in pink), small GO (S-GO, in purple), small and highly oxidized GO (SHO-GO, in brown), medium and less oxidized GO (MLO-GO, in blue), medium GO (M-GO, in orange), and large GO (L-GO, in green). By assuming a Gaussian distribution of data points, the centroid (white exes in Fig. 7.6-C) of each cluster is characterized by an O/C atomic ratio and a mean flake size as presented in the table in Fig. 7.6-D. According to this characterization, Sample 1 is classified as SLO-GO, Sample 2 as MGO, Sample 4 as SHO-GO, and Samples 3, 5 and 6 as L-GO. The fact that three samples felt in the same category could be an indication of a predominant GO synthesis method in industry, which yield nanomaterials with the same property. Note that the classification presented here can be refined with the introduction of data from future peer-reviewed publications. However, this classification could be used by producers to properly advertise their material and by researchers in presenting their work to allow for a more reliable comparison of results between different studies, and ultimately facilitating the rational development of GO based applications.

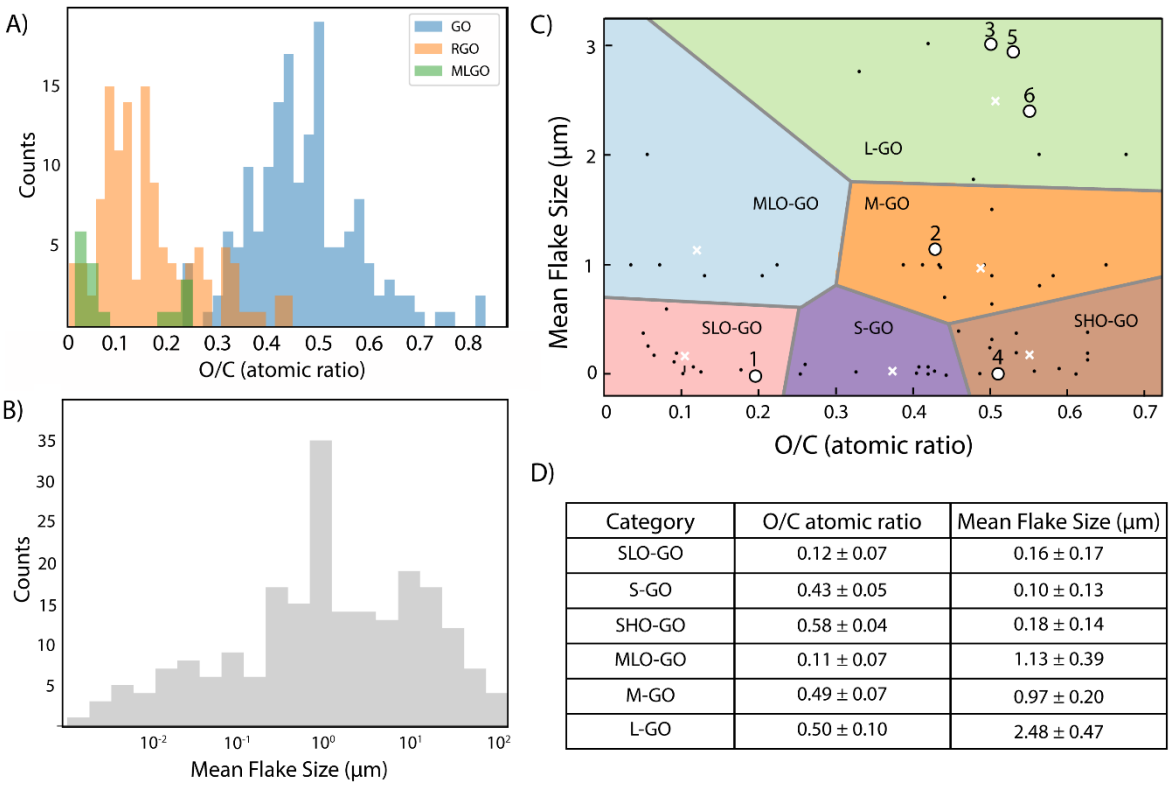

Category	O/C atomic ratio	Mean Flake Size (μm)
SLO-GO	0.12 ± 0.07	0.16 ± 0.17
S-GO	0.43 ± 0.05	0.10 ± 0.13
SHO-GO	0.58 ± 0.04	0.18 ± 0.14
MLO-GO	0.11 ± 0.07	1.13 ± 0.39
M-GO	0.49 ± 0.07	0.97 ± 0.20
L-GO	0.50 ± 0.10	2.48 ± 0.47

Figure 7.6. GO characterization in the literature. A-B) O/C atomic ratio and mean flake size distribution histograms. Each count represents a scientific work. C) K-mean classification of the GO characterization based on O/C atomic ratio and mean flake size. Every white "*x*" represents the centroid (mean) of each class, white circles represent GO samples used in this study, and black dots represent the chemo-morphological data obtained from literature review. D) The table lists the nanoscopic properties for the centroid of each category; the mean flake size of the samples used in this study was calculated from areas in Fig. 7.4 assuming a square GO flake.

Furthermore, the 2D material chemo-morphological properties might have a significant impact on the industrial device performance. For this reason, we investigated a number of GO-based applications with GO material from different producers. In particular, we focused on applications that are relevant for the use of GO in membrane separation processes, which has recently attracted the attention of many research groups [20, 33, 62]. The fabrication process (e.g., quantity of GO used in membranes and casting technique) was the same for all the membranes, and the tests were conducted by the same researcher reducing output variability related to experimental procedure. Thus, it is assumed that the variability in the results is primarily related to different GO properties.

7.3.5 GO applications

The first application evaluated was bacterial adhesion onto GO membranes (GOMs), which was motivated by recent reports indicating intrinsic antifouling properties of GOMs in water treatment applications (e.g., nanofiltration, forward osmosis, etc.) [63, 64]. The bacterial adhesion results are summarized in Fig. 7.7-A and Table 7.3. GOMs were immersed in a solution containing bacteria (*E. coli*) for 20 h (see **Materials and methods**) and the extent of bacterial deposition on the membrane surface was evaluated via SEM analysis. The variation in bacterial deposition behavior (bacterial adhesion ≈ 50% and >75%) is highlighted by comparison of SEM for Sample 6 (L-GO, Fig. 7.7-A left) and Sample 4 (SHO-GO, Fig. 7.7-A right). Representative images for the other samples can be found in Fig. 14.5 in Appendix D. By comparing images in Fig. 7.7-A, it is observed that larger GO flakes (Sample 6) result in increased deposition of *E. coli* as recently reported [65]. This trend was also observed for the other samples (Table 7.3) in which GOMs composed of L-GO lead to higher (1.5–2-fold higher) bacterial adhesion. The variation is likely connected to the higher number of intrinsic defects of smaller flakes that hinders bacterial adhesion. For example, it has been reported that the presence of higher defect surface density in small flakes as compared to large flakes will induce oxidative stress and reduce bacterial adhesion [65].

The second application was the use of GO for the adsorption of methylene blue (MB), which is often used as a representative molecule for cationic dye wastewaters. The adsorption of organic molecules is a fundamental parameter to evaluate when calculating the rejection properties of a filter or membrane. The introduction of MB in most GO solutions causes an instantaneous aggregation of GO flakes (see Fig. 7.7-B left and supplementary video in https://doi.org/10.1016/j.carbon.2018.02.091) due to GO surface charge neutralization [66, 67]. The GO MB aggregation phenomenon occurs in all samples, apart from Sample 1. The MB solution was in contact with the GO for 24 h, then the solution was centrifuged and the supernatant was extracted (Fig. 7.7-B right) to quantify the MB removal via UV-vis (see methods section for further details). The GO MB adsorption capacities are compared via the log removal

value (*LRV*) and summarized in Table 7.3. All GO samples have an average MB log removal capacity between 1.44 and 1.55 except for Sample 1 (SLO-GO), which has a log removal capacity of ≈ 1.1. Although Samples 4 and 1 are similarly characterized by small flakes, Sample 4 (SHO-GO) displays a 27% higher removal capacity compared to Sample 1 (SLO-GO); thus, the adsorption capacity cannot be connected to morphology. MB adsorption is more related to the GO surface charge due to the presence of oxy-functional groups [68, 69] i.e., the lesser number of oxy-functional groups for Sample 1 (O/C atomic ratio <0.2 as compared to 0.43–0.55 for Samples 2–6) results in a lesser MB adsorption capacity.

Although membrane permeability is a primary parameter in the design of membrane systems, recent studies report GOM permeabilities ranging over orders of magnitude [48]. The GOM permeability for the six different samples obtained by capillary flow porometry is displayed in Fig. 7.7-C left and Table 7.3. A large variation in the permeability (up to a factor of five) is observed, which is related to the variation in GO chemistry and morphology between samples.

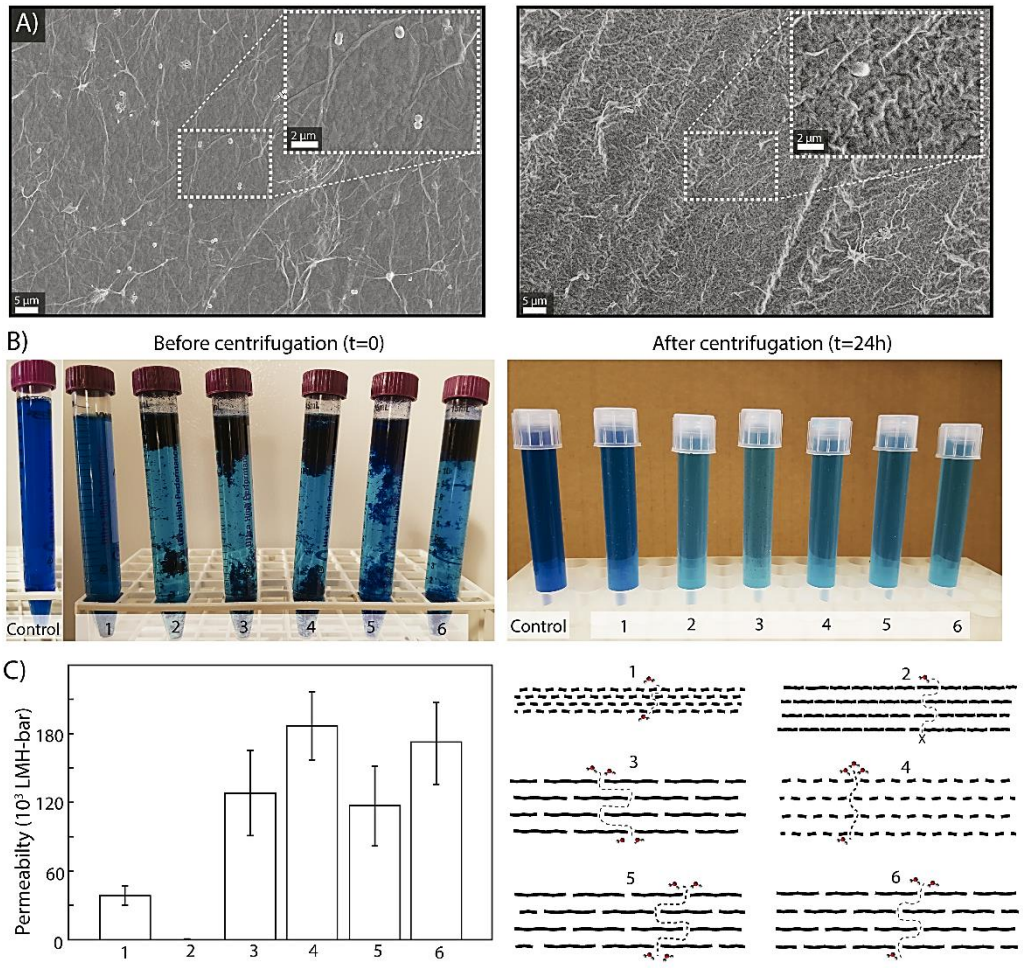

Figure 7.7. Performance comparison of GO toward macroscopic applications. A) Representative SEM images of *E. coli* bacteria adhesion onto GOMs (Samples 6 and 4, left and right image, respectively). B) MB adsorption of GO samples before (left) and after (right) centrifugation. C) Permeability data of GOMs at 5 bar (left) and schematic of their GO flake arrangement (right).

As recently proposed, GOM permeability is affected by two primary factors [70]: i) flake size, which is proportional to membrane pore tortuosity, thus inversely proportional to permeability; and ii) extent of oxidation, which is directly proportional to the width of GO nanochannels or interlayer separation distance (XRD data in Fig. 7.5-A), thus permeability. In summary, both GO chemistry and morphology will affect the GOM permeability and a scheme illustrating the individual effects of these two factors is displayed in Fig. 7.7-C right. Samples 3 and 5 have similar oxidation and flake size, leading to similar permeability results. Sample 4 displays the highest permeability value, predominantly due to both its high O/C ratio value (high nanochannels width) and small flake size (low tortuosity). Although Samples 4 and 6 exhibit similar permeability results, the cause is significantly different; for Sample 4 the permeability is partially originated by a small flake size (reduced tortuosity), whereas for Sample 6 the permeability is mostly driven by the increased O/C ratio (increased width of GO interlayer nanochannels), which compensates the larger flake size. Sample 1 displays a significant lower permeability due to the poor oxidation of the GO flakes leading to narrow GO nanochannels. Incorporation of GO into polymer membranes has been reported to enhance permeability by increasing overall membrane hydrophilicity [71]. Similarly, here the most hydrophilic GOM samples ($SCA < 40°$) have a higher permeability. In contrast, Sample 2 was nearly impermeable under 5 bar of applied pressure due to the absence of carboxylate functional groups (Fig. 7.2-B), which creates a compacted laminate structure and reduces wettability as corroborated by the absence of an O–H water vibration band in Fig. 7.3-B.

Table 7.3. Performance GO-based applications samples in terms of bacterial adhesion, adsorption properties, and permeability.

Sample	Category	Property		
		Bacterial adhesion *(bacteria/area)	**Adsorption (MB removal, *LRV*)**	**Permeability (10^3 LMH/bar)**
1	SLO-GO	46 ± 10	1.11 ± 0.17	38.3 ± 16.8
2	M-GO	53 ± 22	1.48 ± 0.17	0.5 ± 0.5
3	L-GO	77 ± 15	1.55 ± 0.17	128.4 ± 73.8
4	SHO-GO	51 ± 10	1.44 ± 0.17	186.3 ± 59.8
5	L-GO	100 ± 28	1.46 ± 0.16	116.9 ± 69.6
6	L-GO	75 ± 12	1.45 ± 0.15	171.6 ± 71.6

*Note this data have been normalized to 100 in order to increase readability. 100 bacteria/unit corresponds to 75 bacteria per 7000 μm^2.

7.4 Conclusions

By defining the most relevant characterization techniques, a vast-range of GO materials were classified into distinct categories according to their chemo-morphological properties. The classification process is based on GO chemistry and morphology determined by SEM image analysis and XPS spectra analysis. A K-mean clustering algorithm classified the chemo-morphological data into six categories SLO-GO, S-GO, SHO-GO, MLO-GO, M-GO, and L-GO. Although the classification relied on thorough literature research (>300 papers) for calibration, this work does not represent an ultimate classification process and could be extended and refined with other characterization techniques and more training data (e.g., future research investigations). The main goal of this work is to create momentum and raise awareness about the need of a GO standardization process and that the existing variation in device performance obtained from different research groups may be attributed to the highly variable properties of the GO starting material. This was highlighted in the last part of this work, in which GO-based applications yielded quite different results based on the diversity of what should have been, as advertised, the "same" GO material. This initial GO classification aims to facilitate the recognition of adequate material by setting standards for industrial GO producers. Concurrently, researchers will be able to make fair comparisons and increase the reproducibility of their and interlab results, leading to a higher signal to noise ratio in the development of GO materials for practical applications.

References

[1] Aristotle, Physics 2.3, 194b17-195b28.

[2] IEC, TC 113, (2016).

[3] A. Bianco, H.-M. Cheng, T. Enoki, Y. Gogotsi, R.H. Hurt, N. Koratkar, T. Kyotani, M. Monthioux, C.R. Park, J.M.D. Tascon, J. Zhang, All in the graphene family – A recommended nomenclature for two-dimensional carbon materials, Carbon, 65 (2013) 1-6.

[4] Web of Science, (2017).

[5] A. Zurutuza, C. Marinelli, Challenges and opportunities in graphene commercialization, Nature Nanotechnology, 9 (2014) 730-734.

[6] M. Peplow, Graphene booms in factories but lacks a killer app, Nature News, 522 (2015) 268-269.

[7] Espacenet, (2017).

[8] Y. Shirasaki, G.J. Supran, M.G. Bawendi, V. Bulović, Emergence of colloidal quantum-dot light-emitting technologies, Nature Photonics, 7 (2013) 13-23.

[9] K.S. Novoselov, V.I. Fal'ko, L. Colombo, P.R. Gellert, M.G. Schwab, K. Kim, A roadmap for graphene, Nature, 490 (2012) 192-200.

[10] D.R. Dreyer, S. Park, C.W. Bielawski, R.S. Ruoff, The chemistry of graphene oxide, Chemical Society Reviews, 39 (2010) 228-240.

[11] S. Park, R.S. Ruoff, Chemical methods for the production of graphenes, Nature Nanotechnology, 4 (2009) 217-224.

[12] Y. Han, Z. Xu, C. Gao, Ultrathin graphene nanofiltration membrane for water purification, Advanced Functional Materials, 23 (2013) 3693-3700.

[13] R.R. Nair, H.A. Wu, P.N. Jayaram, I.V. Grigorieva, A.K. Geim, Unimpeded permeation of water through helium-leak–tight graphene-based membranes, Science, 335 (2012) 442.

[14] J. Shen, G. Liu, K. Huang, Z. Chu, W. Jin, N. Xu, Subnanometer two-dimensional graphene oxide channels for ultrafast gas sieving, ACS Nano, 10 (2016) 3398-3409.

[15] Y. Wang, R. Ma, K. Hu, S. Kim, G. Fang, Z. Shao, V.V. Tsukruk, Dramatic enhancement of graphene oxide/silk nanocomposite membranes: Increasing toughness, strength, and young's modulus via annealing of interfacial structures, ACS Applied Materials & Interfaces, 8 (2016) 24962-24973.

[16] G.J. Silverberg, A.A. McClelland, S. Griesse-Nascimento, C. Girabawe, J.P. Kadow, L. Mahadevan, C.D. Vecitis, Controlling the roughness of Langmuir–Blodgett monolayers, The Journal of Physical Chemistry B, 121 (2017) 5078-5085.

[17] A. Akbari, P. Sheath, S.T. Martin, D.B. Shinde, M. Shaibani, P.C. Banerjee, R. Tkacz, D. Bhattacharyya, M. Majumder, Large-area graphene-based nanofiltration membranes by shear alignment of discotic nematic liquid crystals of graphene oxide, Nature Communications, 7 (2016) 10891.

[18] C. Ogata, R. Kurogi, K. Awaya, K. Hatakeyama, T. Taniguchi, M. Koinuma, Y. Matsumoto, All-graphene oxide flexible solid-state supercapacitors with enhanced electrochemical performance, ACS Applied Materials & Interfaces, 9 (2017) 26151-26160.

[19] J.J. Yoo, K. Balakrishnan, J. Huang, V. Meunier, B.G. Sumpter, A. Srivastava, M. Conway, A.L. Mohana Reddy, J. Yu, R. Vajtai, P.M. Ajayan, Ultrathin planar graphene supercapacitors, Nano Letters, 11 (2011) 1423-1427.

[20] B. Mi, Graphene oxide membranes for ionic and molecular sieving, Science, 343 (2014) 740.

[21] M. Fathizadeh, W.L. Xu, F. Zhou, Y. Yoon, M. Yu, Graphene oxide: A novel 2-dimensional material in membrane separation for water purification, Advanced Materials Interfaces, 4 (2017) 1600918.

[22] J. Liu, L. Cui, D. Losic, Graphene and graphene oxide as new nanocarriers for drug delivery applications, Acta Biomaterialia, 9 (2013) 9243-9257.

[23] Y. Wang, L. Polavarapu, L.M. Liz-Marzán, Reduced graphene oxide-supported gold nanostars for improved SERS sensing and drug delivery, ACS Applied Materials & Interfaces, 6 (2014) 21798-21805.

[24] V. Georgakilas, J.N. Tiwari, K.C. Kemp, J.A. Perman, A.B. Bourlinos, K.S. Kim, R. Zboril, Noncovalent functionalization of graphene and graphene oxide for energy materials, biosensing, catalytic, and biomedical applications, Chemical Reviews, 116 (2016) 5464-5519.

[25] C. Mattevi, G. Eda, S. Agnoli, S. Miller, K.A. Mkhoyan, O. Celik, D. Mastrogiovanni, G. Granozzi, E. Garfunkel, M. Chhowalla, Evolution of electrical, chemical, and structural properties of transparent and conducting chemically derived graphene thin films, Advanced Functional Materials, 19 (2009) 2577-2583.

[26] G. Eda, G. Fanchini, M. Chhowalla, Large-area ultrathin films of reduced graphene oxide as a transparent and flexible electronic material, Nature Nanotechnology, 3 (2008) 270-274.

[27] M. Jana, S. Saha, P. Khanra, P. Samanta, H. Koo, N. Chandra Murmu, T. Kuila, Non-covalent functionalization of reduced graphene oxide using sulfanilic acid azocromotrop and its application as a supercapacitor electrode material, Journal of Materials Chemistry A, 3 (2015) 7323-7331.

[28] M. Cano, U. Khan, T. Sainsbury, A. O'Neill, Z. Wang, I.T. McGovern, W.K. Maser, A.M. Benito, J.N. Coleman, Improving the mechanical properties of graphene oxide based materials by covalent attachment of polymer chains, Carbon, 52 (2013) 363-371.

[29] W.S. Hummers, R.E. Offeman, Preparation of graphitic oxide, Journal of the American Chemical Society, 80 (1958) 1339-1339.

[30] M.S. Chang, Y.S. Kim, J.H. Kang, J. Park, S.J. Sung, S.H. So, K.T. Park, S.J. Yang, T. Kim, C.R. Park, Guidelines for tailored chemical functionalization of graphene, Chemistry of Materials, 29 (2017) 307-318.

[31] J. Abraham, K.S. Vasu, C.D. Williams, K. Gopinadhan, Y. Su, C.T. Cherian, J. Dix, E. Prestat, S.J. Haigh, I.V. Grigorieva, P. Carbone, A.K. Geim, R.R. Nair, Tunable sieving of ions using graphene oxide membranes, Nature Nanotechnology, 12 (2017) 546-550.

[32] G. Zuo, R. Shen, S. Ma, W. Guo, Transport properties of single-file water molecules inside a carbon nanotube biomimicking water channel, ACS Nano, 4 (2010) 205-210.

[33] J.A.L. Willcox, H.J. Kim, Molecular dynamics study of water flow across multiple layers of pristine, oxidized, and mixed regions of graphene oxide, ACS Nano, 11 (2017) 2187-2193.

[34] A. Montessori, C.A. Amadei, G. Falcucci, M. Sega, C.D. Vecitis, S. Succi, Extended friction elucidates the breakdown of fast water transport in graphene oxide membranes, EPL (Europhysics Letters), 116 (2016) 54002.

[35] H. Dai, Z. Xu, X. Yang, Water permeation and ion rejection in layer-by-layer stacked graphene oxide nanochannels: a molecular dynamics simulation, The Journal of Physical Chemistry C, 120 (2016) 22585-22596.

[36] B. Chen, H. Jiang, X. Liu, X. Hu, Molecular insight into water desalination across multilayer graphene oxide membranes, ACS Applied Materials & Interfaces, 9 (2017) 22826-22836.

[37] M. Rogala, P. Dabrowski, P.J. Kowalczyk, I. Wlasny, W. Kozlowski, A. Busiakiewicz, I. Karaduman, L. Lipinska, J.M. Baranowski, Z. Klusek, The observer effect in graphene oxide – How the standard measurements affect the chemical and electronic structure, Carbon, 103 (2016) 235-241.

[38] C.M. Bishop, Pattern Recognition and Machine Learning, Springer-Verlag, New York, (2006).

[39] A. Hardy, An examination of procedures for determining the number of clusters in a data set, in: E. Diday, Y. Lechevallier, M. Schader, P. Bertrand, B. Burtschy (Eds.) New Approaches in Classification and Data Analysis, Springer Berlin Heidelberg, Berlin, Heidelberg, 1994, pp. 178-185.

[40] Q. Zhang, P. Arribas, E.M. Remillard, M.C. García-Payo, M. Khayet, C.D. Vecitis, Interlaced CNT electrodes for bacterial fouling reduction of microfiltration membranes, Environmental Science & Technology, 51 (2017) 9176-9183.

[41] A. Lerf, H. He, M. Forster, J. Klinowski, Structure of graphite oxide revisited, The Journal of Physical Chemistry B, 102 (1998) 4477-4482.

[42] C.A. Amadei, I.Y. Stein, G.J. Silverberg, B.L. Wardle, C.D. Vecitis, Fabrication and morphology tuning of graphene oxide nanoscrolls, Nanoscale, 8 (2016) 6783-6791.

[43] J.I. Paredes, S. Villar-Rodil, A. Martínez-Alonso, J.M.D. Tascón, Graphene oxide dispersions in organic solvents, Langmuir, 24 (2008) 10560-10564.

[44] B. Li, X. Zhang, P. Chen, X. Li, L. Wang, C. Zhang, W. Zheng, Y. Liu, Waveband-dependent photochemical processing of graphene oxide in fabricating reduced graphene oxide film and graphene oxide–Ag nanoparticles film, RSC Advances, 4 (2014) 2404-2408.

[45] Q. Lai, S. Zhu, X. Luo, M. Zou, S. Huang, Ultraviolet-visible spectroscopy of graphene oxides, AIP Advances, 2 (2012) 032146.

[46] S. Xia, M. Ni, T. Zhu, Y. Zhao, N. Li, Ultrathin graphene oxide nanosheet membranes with various *d*-spacing assembled using the pressure-assisted filtration method for removing natural organic matter, Desalination, 371 (2015) 78-87.

[47] D. Yang, A. Velamakanni, G. Bozoklu, S. Park, M. Stoller, R.D. Piner, S. Stankovich, I. Jung, D.A. Field, C.A. Ventrice, R.S. Ruoff, Chemical analysis of graphene oxide films after heat and chemical treatments by X-ray photoelectron and Micro-Raman spectroscopy, Carbon, 47 (2009) 145-152.

[48] C.A. Amadei, C.D. Vecitis, How to increase the signal-to-noise ratio of graphene oxide membrane research, The Journal of Physical Chemistry Letters, 7 (2016) 3791-3797.

[49] D. Li, M.B. Müller, S. Gilje, R.B. Kaner, G.G. Wallace, Processable aqueous dispersions of graphene nanosheets, Nature Nanotechnology, 3 (2008) 101-105.

[50] H. Li, Y. Huang, Y. Mao, W.L. Xu, H.J. Ploehn, M. Yu, Tuning the underwater oleophobicity of graphene oxide coatings via UV irradiation, Chemical Communications, 50 (2014) 9849-9851.

[51] J. Zhao, S. Pei, W. Ren, L. Gao, H.-M. Cheng, Efficient preparation of large-area graphene oxide sheets for transparent conductive films, ACS Nano, 4 (2010) 5245-5252.

[52] R. Xiong, K. Hu, A.M. Grant, R. Ma, W. Xu, C. Lu, X. Zhang, V.V. Tsukruk, Ultrarobust transparent cellulose nanocrystal-graphene membranes with high electrical conductivity, Advanced Materials, 28 (2016) 1501-1509.

[53] Á.S. Paulo, R. García, Unifying theory of tapping-mode atomic-force microscopy, Physical Review B, 66 (2002) 041406.

[54] S. Stankovich, D.A. Dikin, R.D. Piner, K.A. Kohlhaas, A. Kleinhammes, Y. Jia, Y. Wu, S.T. Nguyen, R.S. Ruoff, Synthesis of graphene-based nanosheets via chemical reduction of exfoliated graphite oxide, Carbon, 45 (2007) 1558-1565.

[55] S. Santos, A. Verdaguer, M. Chiesa, The effects of adsorbed water layers on the apparent height of nanostructures in ambient amplitude modulation atomic force microscopy, The Journal of Chemical Physics, 137 (2012) 044201.

[56] S. Santos, L. Guang, T. Souier, K. Gadelrab, M. Chiesa, N.H. Thomson, A method to provide rapid in situ determination of tip radius in dynamic atomic force microscopy, Review of Scientific Instruments, 83 (2012) 043707.

[57] S.H. Dave, C. Gong, A.W. Robertson, J.H. Warner, J.C. Grossman, Chemistry and structure of graphene oxide via direct imaging, ACS Nano, 10 (2016) 7515-7522.

[58] W. Shao, X. Liu, H. Min, G. Dong, Q. Feng, S. Zuo, Preparation, characterization, and antibacterial activity of silver nanoparticle-decorated graphene oxide nanocomposite, ACS Applied Materials & Interfaces, 7 (2015) 6966-6973.

[59] G. Gonçalves, M. Vila, I. Bdikin, A. de Andrés, N. Emami, R.A.S. Ferreira, L.D. Carlos, J. Grácio, P.A.A.P. Marques, Breakdown into nanoscale of graphene oxide: Confined hot spot atomic reduction and fragmentation, Scientific Reports, 4 (2014) 6735.

[60] U. Khan, A. O'Neill, H. Porwal, P. May, K. Nawaz, J.N. Coleman, Size selection of dispersed, exfoliated graphene flakes by controlled centrifugation, Carbon, 50 (2012) 470-475.

[61] X. Lin, X. Shen, Q. Zheng, N. Yousefi, L. Ye, Y.-W. Mai, J.-K. Kim, Fabrication of highly-aligned, conductive, and strong graphene papers using ultralarge graphene oxide sheets, ACS Nano, 6 (2012) 10708-10719.

[62] L. Huang, M. Zhang, C. Li, G. Shi, Graphene-based membranes for molecular separation, The Journal of Physical Chemistry Letters, 6 (2015) 2806-2815.

[63] M. Hu, B. Mi, Layer-by-layer assembly of graphene oxide membranes via electrostatic interaction, Journal of Membrane Science, 469 (2014) 80-87.

[64] H.M. Hegab, A. ElMekawy, T.G. Barclay, A. Michelmore, L. Zou, C.P. Saint, M. Ginic-Markovic, Fine-tuning the surface of forward osmosis membranes via grafting graphene oxide: Performance patterns and biofouling propensity, ACS Applied Materials & Interfaces, 7 (2015) 18004-18016.

[65] F. Perreault, A.F. de Faria, S. Nejati, M. Elimelech, Antimicrobial properties of graphene oxide nanosheets: Why size matters, ACS Nano, 9 (2015) 7226-7236.

[66] S.-T. Yang, S. Chen, Y. Chang, A. Cao, Y. Liu, H. Wang, Removal of methylene blue from aqueous solution by graphene oxide, Journal of Colloid and Interface Science, 359 (2011) 24-29.

[67] Y. Li, Q. Du, T. Liu, X. Peng, J. Wang, J. Sun, Y. Wang, S. Wu, Z. Wang, Y. Xia, L. Xia, Comparative study of methylene blue dye adsorption onto activated carbon, graphene oxide, and carbon nanotubes, Chemical Engineering Research and Design, 91 (2013) 361-368.

[68] G.K. Ramesha, A. Vijaya Kumara, H.B. Muralidhara, S. Sampath, Graphene and graphene oxide as effective adsorbents toward anionic and cationic dyes, Journal of Colloid and Interface Science, 361 (2011) 270-277.

[69] K. Krishnamoorthy, M. Veerapandian, K. Yun, S.J. Kim, The chemical and structural analysis of graphene oxide with different degrees of oxidation, Carbon, 53 (2013) 38-49.

[70] C.A. Amadei, A. Montessori, J.P. Kadow, S. Succi, C.D. Vecitis, Role of oxygen functionalities in graphene oxide architectural laminate subnanometer spacing and water transport, Environmental Science & Technology, 51 (2017) 4280-4288.

[71] S. Zinadini, A.A. Zinatizadeh, M. Rahimi, V. Vatanpour, H. Zangeneh, Preparation of a novel antifouling mixed matrix PES membrane by embedding graphene oxide nanoplates, Journal of Membrane Science, 453 (2014) 292-301.

8

Other preliminary results

8.1 Surface modification of ENMs by TiO_2 nanoparticles addition

8.2 Recycling industrial discarded RO membranes: towards a circular economy for sustainable growth

In this chapter a couple of future research directions are proposed based on some preliminary results. The first research line is the surface modification of polysulfone (PSU) electrospun nanofiber membranes (ENMs) by the addition of titanium dioxide nanoparticles (TiO_2 NPs), proposed in this PhD thesis as another possible way to reduce membrane organic fouling. To boost a circular economy in water filtration with membranes, a second research line is proposed based on recycling discarded RO membranes from industrial water treatment plants. This is assessed as a possible way to increase the sustainability of water treatment systems, improve membrane durability and reduce both membrane discharge to the environment and associated costs.

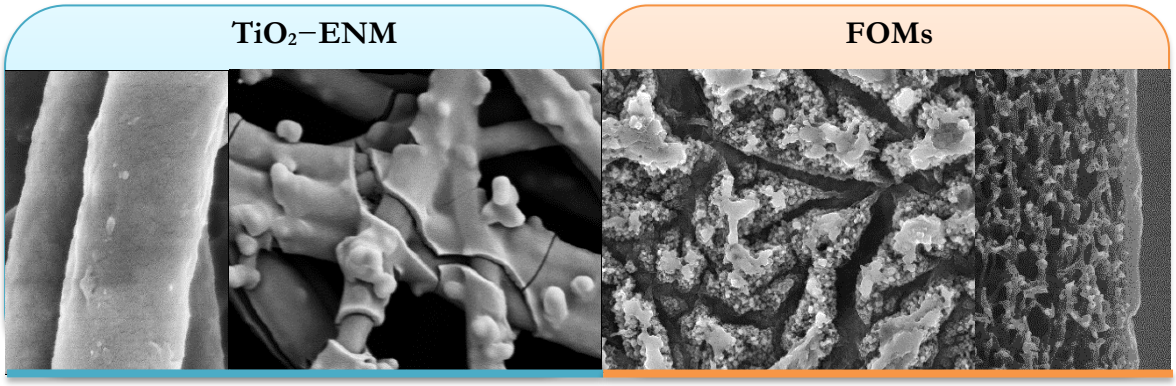

8.1 Surface modification of ENMs by TiO_2 nanoparticles addition

8.1.1 Introduction

The use of nanoparticles (NPs) in the manufacturing process of polymeric membranes has received much attention during last years, particularly to enhance membrane water permeability and reduce its fouling. Among various available inorganic NPs, nano-sized titanium dioxide (TiO_2) exhibits great potential because of its low-cost, low environmental impact, high hydrophilicity, good chemical stability and commercial availability. In addition, its excellent photocatalytic, antibacterial and self-cleaning properties under ultraviolet (UV) light make it interesting for wastewater treatment [1, 2].

In this section, nanocomposite membranes were developed by modifying the surface of PSU ENMs with TiO_2 NPs. The aim of this study was to enhance the water permeability and permeate quality of ENMs, when treating wastewaters containing organic matter and/or bacteria, and overall to improve their antifouling and antimicrobial characteristics.

8.1.2 Preliminary results

The first challenge for the development of TiO_2−ENM nanocomposite membranes is the preparation process. Two different methods were followed to prepare these nanocomposite membranes: i) blending the TiO_2 NPs in the nanofiber matrix via addition to the polymer solution followed by electropinning and ii) coating the TiO_2 NPs on nanofibrous membrane surface via controlled hydrolysis of titanium isopropoxide.

8.1.2.1 Polymer blended TiO_2−ENMs

The polymeric solution used to prepare PSU ENMs consisted on 20 wt% PSU dissolved in a mixture of 64 wt% *N, N*-dimethyl formamide (DMF) and 16 wt.% tetrahydrofuran (THF). The TiO_2 NPs, having a mean particle size of 21 nm, were then added to the casting solution so that their concentration was 0.2 wt.%. A previous study was conducted to determine the best solvent to disperse the TiO_2 NPs. TiO_2 powder was added to different solutions of 100% THF, 100% DMF and a 20%-80% THF-DMF mixture followed by ultrasonic vibration for 30 min.

The solutions were kept without stirring for 2 hours to check whether the TiO_2 NPs remained dispersed or not. Only in 100% DMF, TiO_2 NPs formed an homogeneous suspension after this waiting time (see Fig. 8.1.1). To prepare the PSU polymer solution containing TiO_2 NPs, these were dispersed in 20% DMF of the final polymer solution and then ultrasonicated for 30 min. The PSU polymer was dissolved in the remaining quantity of DMF together with THF by stirring at 60°C and 80 rpm for 10 h. Once the PSU was completely dissolved, both solutions were mixed and stirred at 60°C and 80 rpm for 5 h. The resulting polymer solution was used to prepare the polymer blended TiO_2−ENM nanocomposite membranes by electrospinning using the system described in Chapter 3. The electrospinning conditions were: a polymer solution flow rate of 2.5 mL/h, an electric voltage of 20 kV, a distance between the needle tip and the collector of 10 cm and an electrospinning time of 45 min.

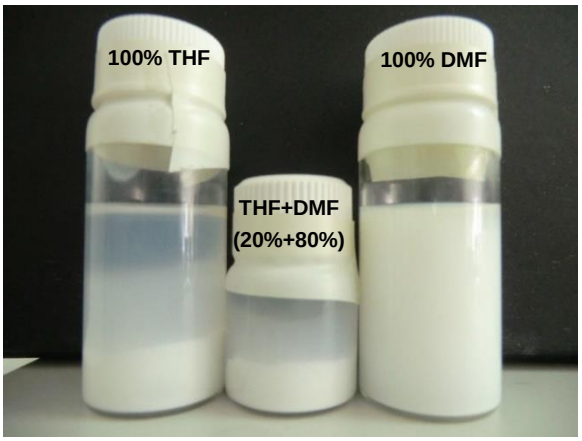

Figure 8.1.1. TiO_2 nanoparticles dispersed in different solvents.

The morphology as well as the distribution of the nanofibers on the surface of the unmodified PSU ENM and the polymer blended TiO_2−ENM nanocomposite membrane were similar (see Fig. 8.1.2 A and B). Under high SEM magnifications (Fig. 8.1.2 C and D), TiO_2 NPs embedded in the nanofibers of the polymer blended TiO_2−ENM nanocomposite membrane could be observed.

The mean nanofiber diameter ($\overline{\lambda_w}$) together with the nanofiber diameter distribution (i.e. histograms) of the unmodified PSU ENM and the polymer blended TiO_2−ENM nanocomposite membrane (see Fig 8.1.3) were determined using the obtained SEM surface images of the membranes (Fig. 8.1.2 A and B) and the software UTHSCSA Image Tool 3.0, following the procedure described in Chapter 4. The addition of the TiO_2 NPs in the polymer solution resulted in nanofibers with smaller diameters (0.74 μm compared to 0.85 μm of the unmodified PSU ENM). The incorporation of the TiO_2 NPs into the polymer solution increased its electrical conductivity, which resulted in an increase of the electric field strength between the needle tip and the collector during electrospinning. As a result, the electrified jet stretched more the nanofiber and reduced its diameter [3].

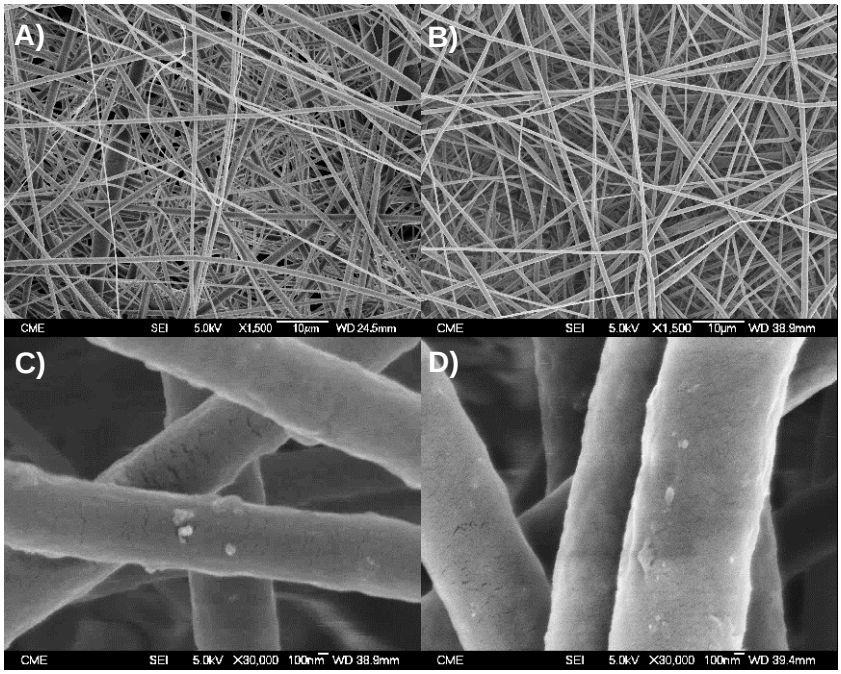

Figure 8.1.2. SEM surface images of the unmodified and modified membranes. A) PSU ENM at X1500 magnification, B) polymer blended TiO_2−ENM nanocomposite membrane at X1500 magnification, and C-D) nanofibers of the polymer blended TiO_2−ENM nanocomposite membrane containing TiO_2 NPs at X30000 magnification.

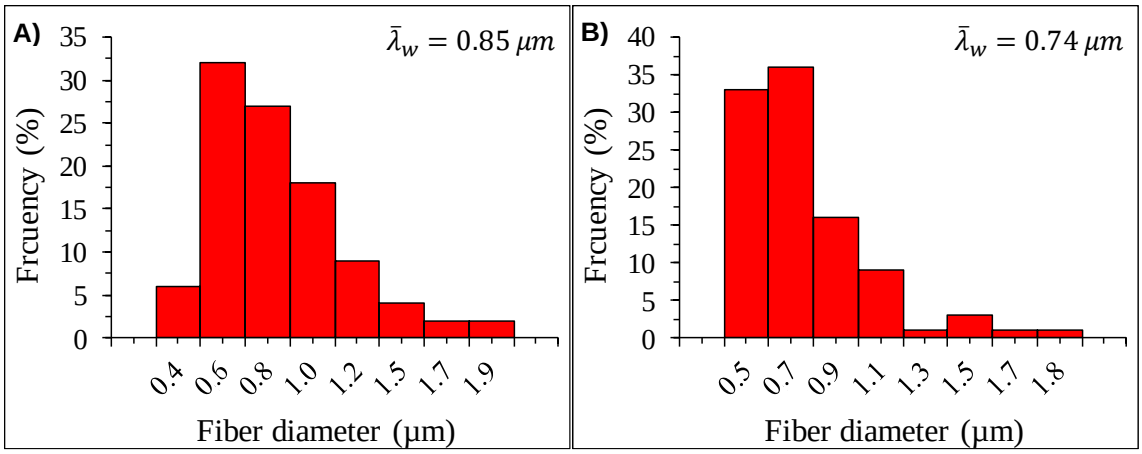

Figure 8.1.3. Nanofiber diameter distribution of the prepared membranes. A) PSU ENM and B) polymer blended TiO_2−ENM nanocomposite membrane.

8.1.2.2 Surface coated TiO_2−ENMs

The surface coated TiO_2−ENM nanocomposite membranes were prepared via filtration-steam hydrolysis. First, a solution containing 2.5 mL of titanium isopropoxide (TTIP) dissolved in 10 mL of pure ethanol was prepared by ultrasonic vibration for 5 min. An unmodified ENM was placed in a vacuum filtration setup (Millipore) having an inner diameter of 35 mm. To wet the ENM support, 10 mL ethanol was vacuum filtered through the ENM, followed by 12.5 mL

of the prepared TTIP/ethanol solution. Finally, water vapor at 65 °C was transported through the ENM for different hydrolysis exposure times to induce TiO_2 hydrolysis and to form a TiO_2 coated nanofilm on the surface of the ENM. The exposure time (t_h) was 1, 15 and 45 min and the resulting nanocomposite membranes were named, hereafter, TiO_2−ENM_N1, TiO_2−ENM_N15 and TiO_2−ENM_N45, respectively.

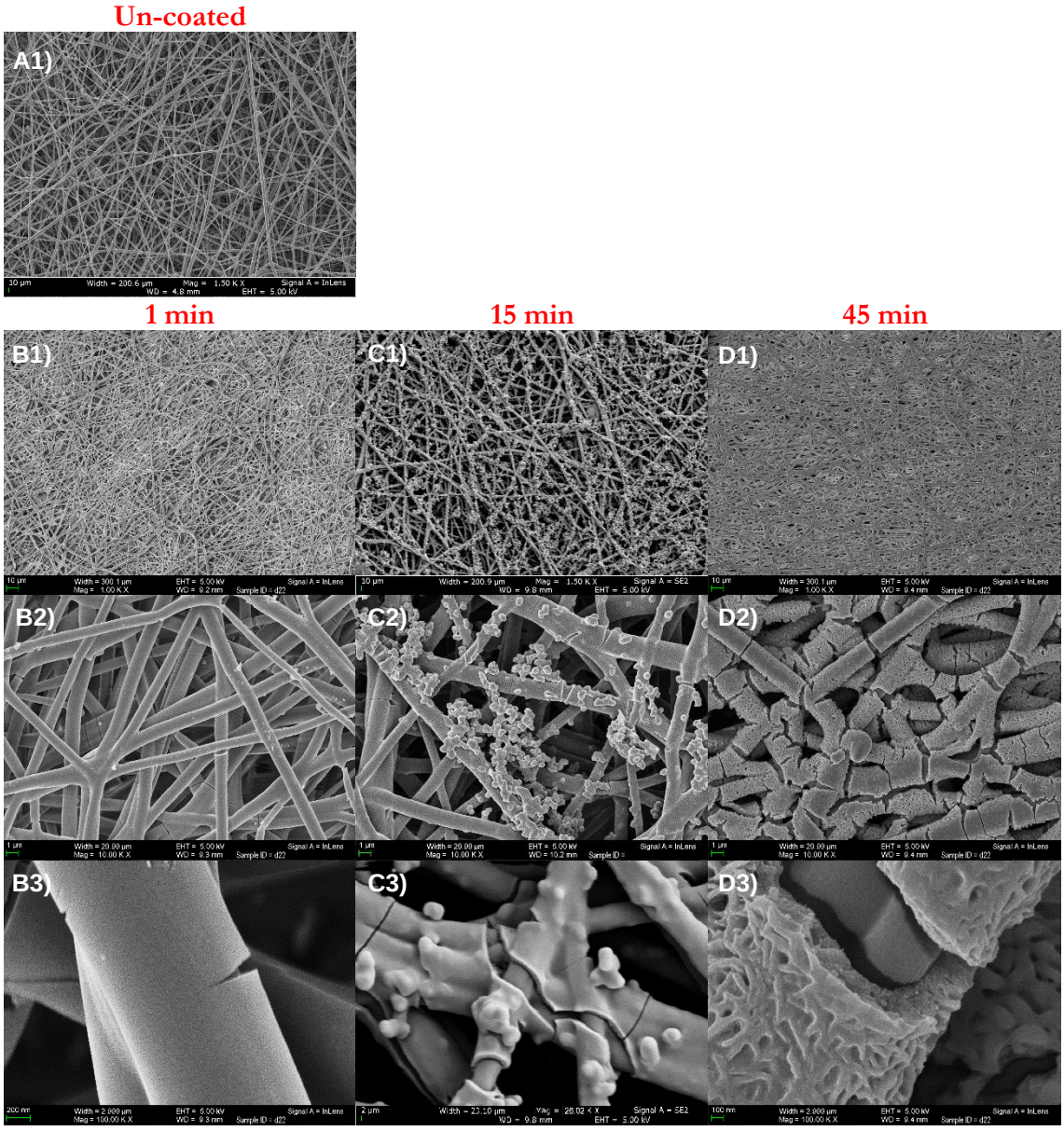

Figure 8.1.4. SEM surface images at different magnifications of the unmodified and the surface modified TiO_2 coated nanocomposite membranes with different hydrolysis exposure times. A1) Un-coated ENM supporting membrane at X1500; B1) TiO_2−ENM_N1 at X1000, B2) at X10000 and B3) at X100000; C1) TiO_2−ENM_N15 at X1500, C2) at X10000 and C3) at X26000; and D1) TiO_2−ENM_N45 at X1000, D2) at X10000 and D3) at X100000.

Fig 8.1.4 shows SEM surface images of the coated TiO_2−ENM nanocomposite membranes at various magnifications. Clear differences of the structural morphology of the TiO_2 coated nanocomposite membranes were observed for different hydrolysis exposure times. After 1 min of TiO_2 hydrolysis, the nanofibers of the membrane TiO_2−ENM_N1 were completely covered by a smooth and homogeneous TiO_2 layer, preserving the support nanostructure. With 15 min of TiO_2 hydrolysis, the nanofibers of the membrane TiO_2−ENM_N15 were covered by a thicker TiO_2 layer. In some areas the NPs seemed to be agglomerated, but the nanofiber network of the support was maintained visible. After 45 min of hydrolysis, a thick TiO_2 layer covered the nanofibers of the membrane TiO_2−ENM_N45, which clearly reduced the inter-fiber space of the membrane and resulted in a more compact and dense structure (Fig. 8.1.4 D1 and D2) compared to that of the membranes TiO_2−ENM_N1 and TiO_2−ENM_N15. Upon further magnification (Fig. 8.1.4-D3), it could be observed that the TiO_2 layer of the membrane TiO_2−ENM_N45 exhibited a rough surface with a ridge-and-valley morphology, very different to the smooth structure of the TiO_2 layer of the membrane TiO_2−ENM_N1 (see Fig 8.1.4-A3).

The thickness of the TiO_2 layer was estimated from the observed cracks on the SEM surface images using the image analysis software ImageJ. At least 50 measurements of the thickness were registered for each membrane. The estimated final thickness of the TiO_2 layer (δ_{NL}) was 100, 150 and 185 nm for the membranes TiO_2−ENM_N1, TiO_2−ENM_N15 and TiO_2−ENM_N45, respectively.

8.1.3 Future directions

As next step in this research line, a further characterization of the physicochemical properties of these membranes should be performed using attenuated total reflectance Fourier transform infrared spectroscopy (ATR-FTIR), X-ray photoelectron spectroscopy (XPS), atomic force microscopy (AFM) as well as porometry, water contact angle, and zeta potential measurements. The influence of the polymer blended and surface coated TiO_2 NPs on the surface hydrophilicity (e.g. using contact angle measurements), surface roughness (e.g. using AFM measurements) and surface charge density (e.g. using ζ-potential measurements) of the resultant nanocomposite membranes should also be investigated. In addition, filtration tests of model wastewater solutions containing organic matter and/or bacteria in the presence or absence of UV-light should be conducted. For these experiments, a new membrane module with a quartz crystal to illuminate the feed stream with UV-light during filtration should be designed and fabricated. Finally, the filtration and antifouling performance of the polymer blended and surface coated TiO_2−ENM nanocomposite membranes in the presence or absence of UV-light should be compared to the unmodified ENMs supports to evaluate the effectiveness of the TiO_2 NPs addition.

8.2 Recycling industrial discarded RO membranes: towards a circular economy for sustainable growth

8.2.1 Introduction

Water desalination has become an alternative to the conventional water sources and desalination plants make use of reverse osmosis (RO) technology via spiral-wound cylindrical modules. The lifespan of a RO membrane is estimated between 5 to 10 years [4]. Membrane lifespan strongly depends on fouling phenomena, which reduces water production rate, deteriorates water quality and increases energy consumption (i.e. increases the working pressure of the process). Consequently, the overall operational and maintenance costs of the desalination plants also increase. RO membrane modules are subsequently discarded and replaced by new ones whenever it is detected that the RO performance decreases irreversibly by more than 15%. Around 10–20% of membranes are annually replaced and disposed [5]. In addition, because RO technology grows continuously, the amount of waste from membrane disposal is gradually increased. Finding a way to recycle RO membranes would increase the sustainability of water treatment systems, improve the durability of the membranes and reduce the environmental costs associated with this technology.

Over the last decade, osmotically driven membrane processes (ODMPs), such as forward osmosis (FO) and pressure retarded osmosis (PRO), have attracted a special attention due to their potential to sustainably produce clean drinking water and energy [6]. Compared to the pressure driven membrane processes (PDMPs), FO and PRO offer the possibility to use osmotic pressure gradients in a wide range of applications, including water desalination, wastewater treatment and electric power generation [7]. In the case of FO, a high-concentration solution (i.e. draw solution, DS) is separated from a low-concentration solution (i.e. feed solution, FS) by a water-selective semipermeable membrane. As it is shown in Fig. 8.2.1, the concentration gradient between both the feed and draw solutions results in a transmembrane osmotic pressure. Consequently, unlike RO, in which mechanical energy is used for pumping the feed saline aqueous solution through a water-selective membrane to overcome the transmembrane osmotic pressure, in FO water flows spontaneously through the membrane from the low-concentration side to the DS side [8]. Some of the advantages of FO technology

over conventional RO process are its lower membrane fouling, less energy consumption and simpler membrane cleaning [9].

The membranes used in FO process are not ideal, and reverse solute permeate fluxes also occur through the membrane opposite to the direction of water permeate flux. This causes solute concentration polarization inside the membrane, known as internal concentration polarization (ICP) phenomenon, which significantly reduces the transmembrane osmotic pressure gradient and consequently, reduces membrane water permeability. The preparation of specific membranes is therefore essential for the development of FO technology. A suitable membrane for FO process should exhibit a high water permeability and a high solute rejection factor, a small resistance toward solute diffusion, high chemical stability, low ICP using thin and highly porous supports with low mass transfer resistance, and low susceptibility to fouling. It must have a hydrophilic character, a high porosity and low tortuosity factor (i.e. low structural parameter, *S*) [8, 10]. It is to be noted that the surface structure of the FO membrane facing the feed aqueous solution (i.e. active skin layer) is critical because it is directly associated with fouling tendency. Until now, three methods have been adopted to prepare polymeric FO membranes: the non-solvent phase inversion method, the interfacial polymerization (IP) on porous substrates to prepare thin film composite (TFC) membranes, and the layer-by layer (LbL) deposition of nanometer thick polycations and polyanions on porous charged substrates. A key advantage of the TFC approach is that the porous support and the thin film (i.e. active layer) can be separately optimized to achieve the best overall filtration performance and membrane stability [11, 12].

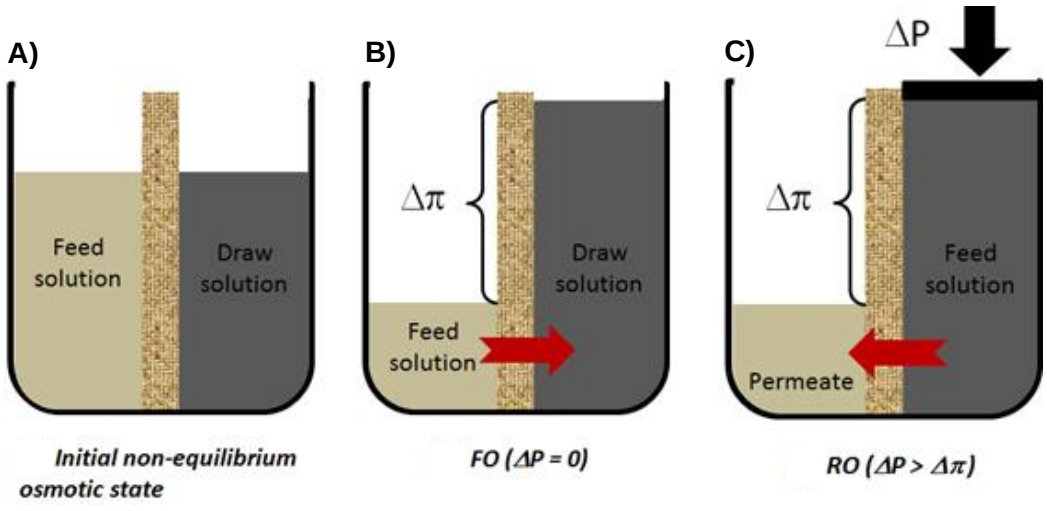

Figure 8.2.1. Illustration of FO and RO processes. A) Initial non-equilibrium osmotic state, B) FO process where no pressure is applied on the draw solution and C) RO process used for desalination of a saline feed solution by applying a hydrostatic pressure greater than the transmembrane osmotic pressure. Adapted from Arribas et al. [8], with permission from Elsevier.

The main objective of this work is to study different IP methods to modify the surface of disposed RO membranes (at laboratory scale) and transform them into polymeric TFC membranes for FO wastewater treatment (see Fig. 8.2.2). The achievement of this objective will provide important sociological and environmental advantages, since it will increase the sustainability of water treatment systems using membrane processes, improving their durability and decreasing the associated environmental costs by reducing wastes.

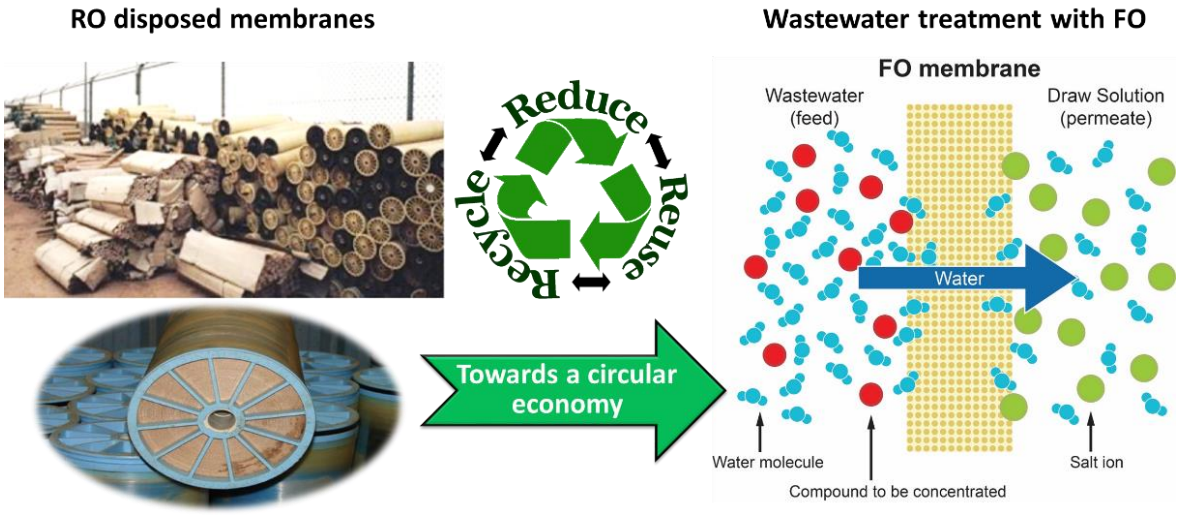

Figure 8.2.2. Illustration of the objective of this research study.

8.2.2 Materials and methods

8.2.2.1 Discarded RO modules for recycling

End-of-life discarded RO modules (TM720-400 by Toray Industries, Inc., Japan) of a classified real plant located in Almeria (Spain) were recycled in this study. These modules initially had a spirally wound polyamide (PA) thin film composite (TFC) membrane composed of three layers: i) a polyester (PE) support layer, ii) a polysulfone (PSU) layer and iii) a selective PA layer. These modules were used in the treatment of brackish water for more than three years. The discarded RO modules had a water permeability and salt rejection of 2.04 L/m^{2}h bar and 98.3%, respectively. After their autopsy, the RO membranes taken from these modules presented a clay-like appearance with a colloidal fouling texture composed by 84% inorganic and 16% organic compounds and the water contact angle of their active layer was 46° [13-15]. For recycling these membranes, a passive cleaning process under different NaClO dose levels (300,000−1049,000 ppm·h) and exposure times (48−88 h) was applied as described elsewhere [15-17], which ensured the total degradation of the PA layer of the end-of-life RO membranes. Therefore, these end-of-life RO membranes without an active PA layer were selected to be

transformed into recycled forward osmosis membranes (RFOMs) by modifying their surface via interfacial polymerization (IP) technique.

8.2.2.2 Preparation of new FO membranes

In this study, IP modification technique (see Chapter 5 and Appendix B for more details) was selected to create a PA layer on the surface of the cleaned end-of-life RO membranes. Different combinations of monomers and conditions of the IP process were considered to form the PA thin film layer. Particularly, the monomer trimesoyl chloride (TMC, Sigma-Aldrich) and the solvent hexane (Sigma-Aldrich, puriss., ≥99% (GC)) were used in all combinations to prepare the organic phase. For the aqueous phase, the monomers m-phenylenediamine (MPD, Sigma-Aldrich), triethylamine (TEA, Sigma-Aldrich), piperazine (PIP, Sigma-Aldrich) and polyvinyl acetate (PVA, Sigma-Aldrich) were used either separately or in a mixture to form the PA layer on the membranes surface.

Before IP modification, different pieces of the same discarded and cleaned RO membrane module were tested in FO. A lack of reproducibility of the FO permeation results was observed. Therefore, microfiltration (MF) commercial polyethersulfone (PES) membranes (Millipore), with similar characteristics to those of the supporting layers (i.e. PE+PSU) of the original RO membranes, were used as supports to perform a preliminary study in order to select the best IP method for the preparation of FO membranes (FOMs) (i.e. the IP method to follow in order to get an FOM membrane with the best overall FO performance). A total of five different FOMs were prepared under the conditions summarized in Table 8.2.1. These membranes were named as FOM1, FOM2, FOM3, FOM4 and FOM5. The IP reaction time was fixed at 15 min. The next step of this study would be the application of the selected IP method to develop RFOMs using the cleaned end-of-life RO membranes as support.

Table 8.2.1. Interfacial polymerization (IP) conditions applied to prepare the forward osmosis membranes (FOMs).

Membrane	IP method	Aqueuos phase			Organic phase		
		Material[1]	w/w (%)	t_{ap}[2] (min)	Material[1]	w/v (%)	t_{IP}[2] (min)
FOM1	IP1	MPD	2	60	TMC	0.25	15
FOM2	IP2	PIP	2	60	TMC	0.25	15
FOM3	IP3	MPD–TEA	1–1	60	TMC	0.25	15
FOM4	IP4	PIP–TEA	1–1	60	TMC	0.25	15
FOM5	IP5	PIP–PVA	1–1	60	TMC	0.25	15

[1]MPD: *m*-phenylenediamine; PIP: piperazine; TEA: triethylamine; PVA: polyvinyl acetate; TMC: trimesoyl chloride.

[2]t_{ap}: aqueous phase time; t_{IP}: polymerization reaction time.

8.2.2.3 Membranes surface characterization

The surface morphology of the membranes was analyzed by a field emission scanning electron microscope (FESEM, JEOL Model JSM-6335F) operated at 5 kV. Before conducting the SEM analysis, a thin gold layer of about 5 nm was sputtered on the membrane surface using an evaporator (EMITECH K550 X) for one minute under 25 mA.

8.2.2.4 FO commercial membranes

For sake of comparison and to check the filtration properties and the FO performance of the developed FOMs, three FO commercial membranes (FOCMs) were considered. Two FOCMs, an asymmetric PA TFC membrane (TFC-HTI) and a celluose triacetate (CTA) membrane (CTA-HTI), were supplied by Hydration Technology Innovations (HTI™, LLC, Albany, USA), and the third one was an Aquaporin FO flat sheet commercial membrane supplied by Sterlitech (Aquaporin).

8.2.2.5 FO experiments

A lab-made FO experimental device containing a Lewis cell was used to carry out the FO tests (see Fig. 8.2.3). The Lewis cell consisted on two stainless steel cylindrical chambers for the permeate and the feed solutions, each one with an internal volume of 300 mL. A membrane holder having an effective area of 9.1 cm^2 was placed between them. The FO experiments were conducted with the active layer of the FOMs facing the feed solution (AL-FS) and the bottom layer facing the permeate or draw solution. The feed and permeate solutions were kept at room temperature (about 24°C). The temperature inside each chamber was controlled by Pt100 sensors connected to a digital temperature indicator (Temperature Meßgerät pt100, PHYWE Systeme GmbH und Co. KG). Both chambers contained magnetic stirrers. The stirring speed of the feed and permeate solutions was fixed at 750 rpm using an electric motor with speed control (K50640, Kelvin S.A.).

Sodium chloride (NaCl, Scharlau Chemicals Co.) was used to prepare the permeate or draw solution (DS), whereas the organic foulant humic acid (HA, Fluka, Mw = 4.1 kDa) was employed to prepare the wastewater model feed solution (FS). The pH of the HA feed solution was adjusted to 11 (Metrohm pH/Ion meter 692) by adding 2 M hydrochloric acid (HCl, Sigma-Aldrich) aqueous solution. The FO tests were carried out using first low concentration DS and FS (i.e. 65 g/L NaCl and 10 mg/L HA, respectively) during 1 h (**cycle 1**) and subsequently, using high concentration DS and FS (i.e. 200 g/L NaCl and 100 mg/L HA, respectively) during one more hour (**cycle 2**). Both the electrical conductivity and the absorbance at 254 nm of the DS and FS were measured with a conductivity meter (Metrohm 712 **Ω**) and a spectrophotometer (Genesis 10S UV-Vis, Thermo Scientific Inc.), respectively.

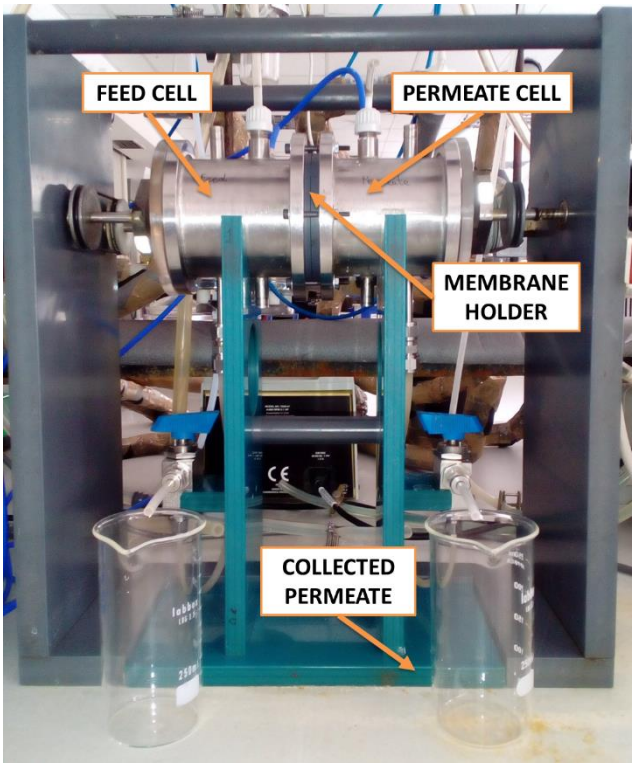

Figure 8.2.3. Experimental device used for the FO tests.

Using the corresponding calibration curves, the concentration of NaCl and HA of the DS and FS at the beginning (i.e. $C_0^{NaCl,\ DS}$, $C_0^{NaCl,\ FS}$, $C_0^{HA,\ DS}$, $C_0^{HA,\ FS}$) and at the end (i.e. $C_f^{NaCl,\ DS}$, $C_f^{NaCl,\ FS}$, $C_f^{HA,\ DS}$, $C_f^{HA,\ FS}$) of each cycle were determined.

In every cycle, the permeate flux (J), which goes throughout the membrane from the feed side to the permeate side, was measured as a function of time by weighing the mass of the permeate (m) collected over a period of time (Δt) on an electronic balance (AND GF-1200) and calculated as follows:

$$J\ (\mathrm{kg/m^2\,h}) = \frac{m}{A_{ef} \cdot \Delta t} \tag{8.2.1}$$

where A_{ef} is the effective membrane area.

The reverse salt permeate flux (J_S) was determinate using the following equation [18, 19]:

$$J_S\ (\mathrm{kg/m^2\,h}) = \left(C_f^{NaCl,\ FS} - C_0^{NaCl,\ FS}\right) \frac{V^{FS}}{A_{ef} \cdot t_{exp}} \tag{8.2.2}$$

where $C_0^{NaCl,\ FS}$ and $C_f^{NaCl,\ FS}$ are the initial and final salt concentration in the FS, respectively, V^{FS} is the total volume of the FS (which remained constant at 300 mL during the whole FO test), and t_{exp} is the total experimental time of the given cycle (60 min).

The HA and the salt rejection factors of the membranes (i.e. R_{HA} and R_S, respectively) at the end of the FO test were evaluated using the following equations:

$$R_{HA}\,(\%) = \left(1 - \frac{C_f^{HA,\ DS}}{C_f^{HA,\ FS}}\right) \cdot 100 \tag{8.2.3}$$

$$R_S\,(\%) = \left(1 - \frac{C_f^{NaCl,\ FS}}{C_f^{NaCl,\ DS}}\right) \cdot 100 \tag{8.2.4}$$

where $C_f^{HA,\ DS}$ and $C_f^{HA,\ FS}$ are the final HA concentration of the draw and feed solutions, respectively, and $C_f^{NaCl,\ FS}$ and $C_f^{NaCl,\ DS}$ are the final salt concentration of the feed and draw solutions, respectively.

The HA concentration factor (β_{HA}) and the salt dilution factor (γ_S), which were used to further evaluate the FO performance of the developed membranes, were described as follows:

$$\beta_{HA}\,(\%) = \left(\frac{C_f^{HA,\ FS}}{C_0^{HA,\ FS}} - 1\right) \cdot 100 \tag{8.2.5}$$

$$\gamma_S\,(\%) = \left(1 - \frac{C_f^{NaCl,\ DS}}{C_0^{NaCl,\ DS}}\right) \cdot 100 \tag{8.2.6}$$

8.2.3 Preliminary results

8.2.3.1 Surface characterization of FOMs

SEM images of the surface morphologies of the FOMs are shown in Fig. 8.2.4. The different IP methods used for the preparation of the membranes resulted in the formation of a PA thin film layer with different morphologies and structures. The membranes prepared with the monomers MPD and MPD–TEA in the aqueous phase (i.e. FOM1 and FOM3, respectively) displayed less rough surfaces than those of the membranes prepared with the monomers PIP, PIP–TEA and PIP–PVA (i.e. FOM2, FOM4 and FOM5, respectively). The membranes FOM1 and FOM3 showed a surface morphology with thin nodular-like-structures. It seemed that the addition of the acid acceptor TEA in the aqueous phase to prepare the membrane FOM3 resulted in a smoother and a flatter surface of the formed PA layer than that of the membrane FOM1. The membranes FOM2 and FOM5 exhibited a surface morphology with a thick nodular-like-structure. Apparently deep "channels" between these nodular-like-structures could also be observed. It is worth noting that the "channels" of the membrane FOM5 were oriented in a specific direction. The membrane FOM4 displayed a surface morphology with a ridge-and-

valley structure. These differences in the surface morphology of the FOMs are expected to affect their FO performance.

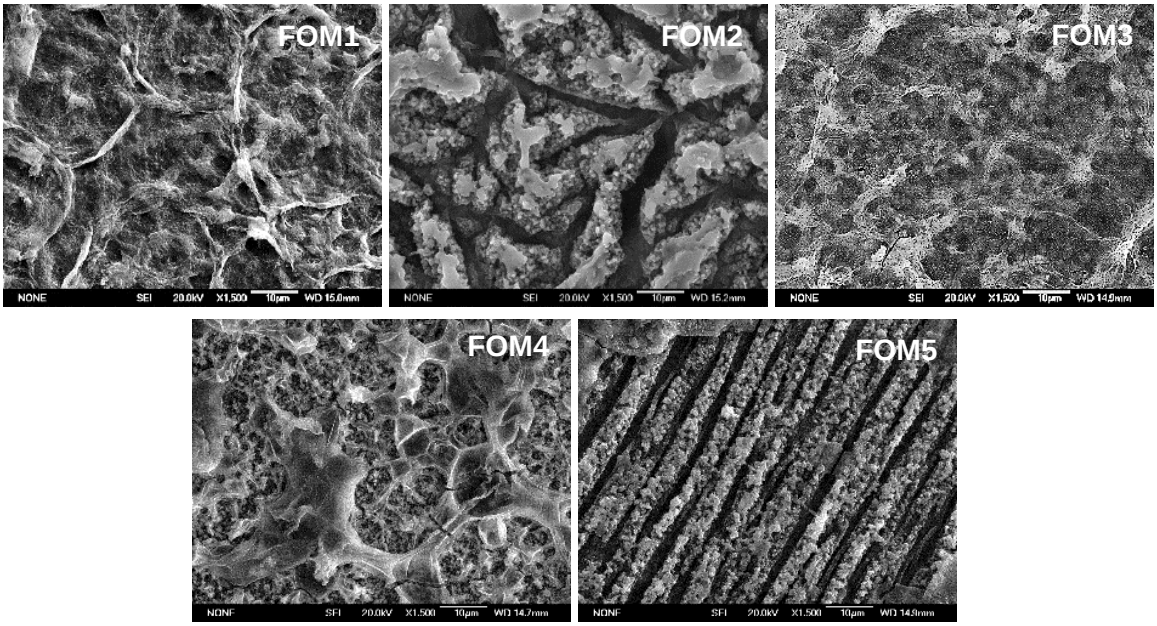

Figure 8.2.4. SEM surface images of the forward osmosis membranes (FOMs) at X1500.

8.2.3.2 FO performance

Fig. 8.2.5 A–C shows the permeate flux (J), the reverse salt permeate flux (J_S) and the permeate flux ratio (J_S/J) of the prepared FOMs and the FOCMs measured under low and high concentration conditions of the feed and draw solutions. A membrane with a good FO flux performance should display a J value as high as possible and a J_S value as low as possible, resulting therefore in a low J_S/J value.

For FO tests under high concentration (HC) conditions, all membranes (including FOMs and FOCMs) exhibited greater J and J_S values than those obtained under low concentration (LC) conditions (see Fig. 8.2.5 A and B). This is due mainly to the increase of the osmotic pressure of the permeate solution (i.e. the water chemical potential of the DS is lower at HC conditions than at LC conditions). The J values of all lab-made FOMs under LC (9.6–30.8 kg/m^2 h) and HC (13.8–41.8 kg/m^2 h) conditions were comparable or higher than those of the FOCMs (9.4–13.5 kg/m^2 h and 15.3–13.5 kg/m^2 h, respectively). Particularly, the membranes FOM1, FOM2, FOM3 and FOM4 had higher J values than those of the three tested FOCMs (i.e. CTA HTI, TFC HTI and Aquaporin). However, the J_S values of the membranes FOM2 and FOM4 were higher than those of the FOCMs, resulting in very similar J_S/J values compared to those of the CTA HTI and Aquaporin, respectively.

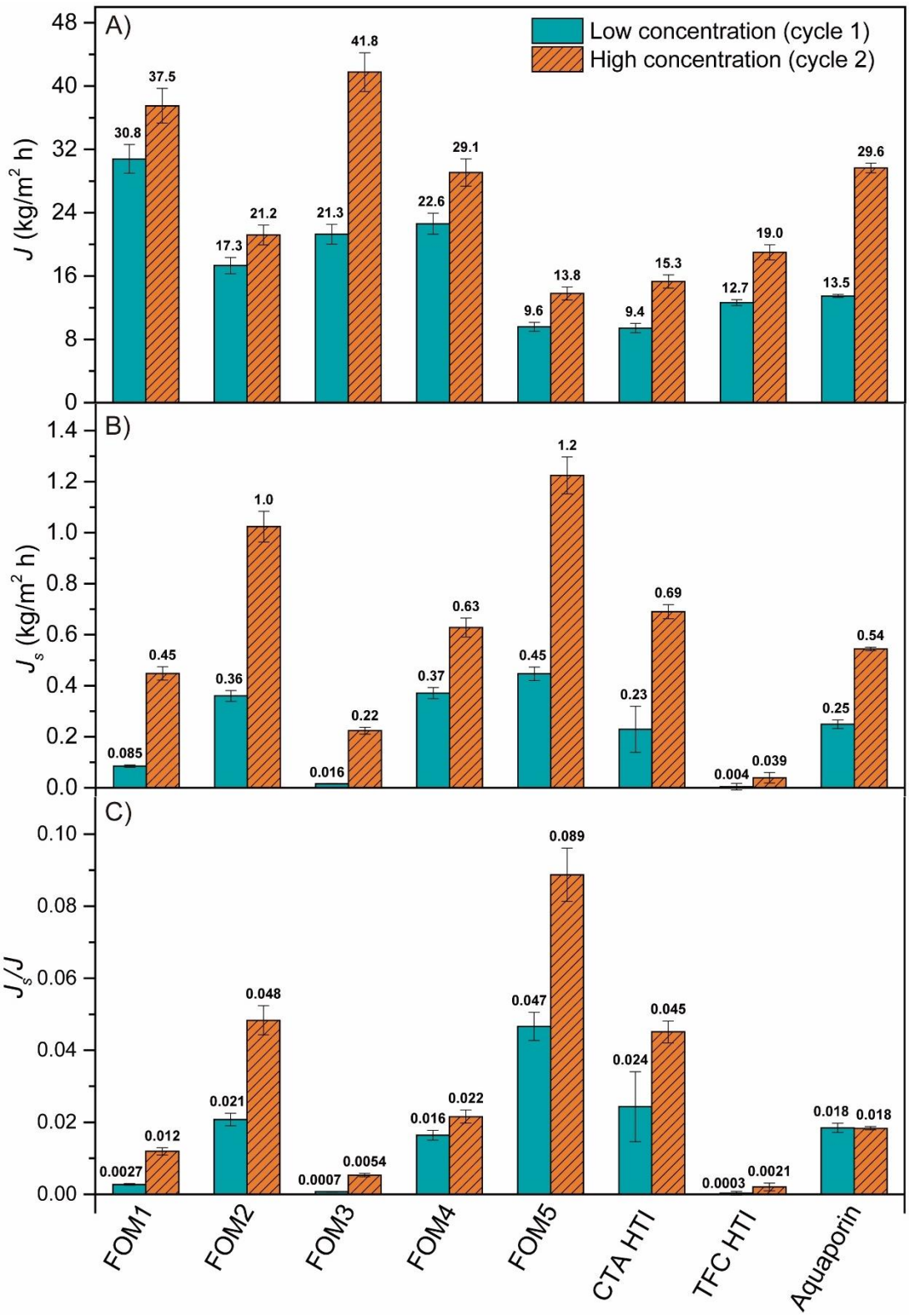

Figure 8.2.5. FO permeate fluxes of the prepared FOMs and the FOCMs. A) Permeate flux (J), B) reverse salt permeate flux (J_S) and C) permeate flux ratio (J_S/J). FO tests were conducted first under low concentration conditions (FS: 10 mg/L HA; DS: 65 g/L NaCl) during 1 h and then, under high concentration conditions (FS: 100 mg/L HA; DS: 200 g/L NaCl) during another 1 h. All tests were carried out with the active layer of the membranes facing the feed solution (AL-FS mode).

Table 8.2.2. FO characteristics of the prepared FOMs: final humic acid (HA) rejection factor (R_{HA}), final salt rejection factor (R_S), HA concentration factor (β_{HA}) and salt dilution factor (γ_S). FO tests were conducted first under low concentration (LC) conditions (FS: 10 mg/L HA; DS: 65 g/L NaCl) during 1 h and then under high concentration (HC) conditions (FS: 100 mg/L HA; DS: 200 g/L NaCl) during another 1 h. All tests were carried out with the active layer of the membranes facing the feed solution (AL-FS mode).

Membrane	FO characteristics							
	R_{HA} (%)		R_S (%)		β_{HA} (%)		γ_S (%)	
	LC	HC	LC	HC	LC	HC	LC	HC
FOM1	63.8 ± 0.5	97.6 ± 0.1	99.27 ± 0.01	98.81 ± 0.02	45.5 ± 1.8	5.4 ± 0.5	12.5 ± 1.2	16.3 ± 0.3
FOM2	96.4 ± 0.7	99.9 ± 0.1	97.81 ± 0.02	98.03 ± 0.02	12.2 ± 1.2	2.4 ± 0.3	13.8 ± 0.8	10.0 ± 0.8
FOM3	90.9 ± 0.4	98.9 ± 0.1	99.71 ± 0.01	99.16 ± 0.02	20.3 ± 1.3	4.3 ± 1.4	14.3 ± 0.9	16.0 ± 0.5
FOM4	97.7 ± 0.5	99.7 ± 0.1	97.78 ± 0.01	98.47 ± 0.02	16.3 ± 1.4	3.4 ± 0.2	14.2 ± 0.7	15.4 ± 0.1
FOM5	98.1 ± 0.9	99.9 ± 0.2	97.26 ± 0.03	97.82 ± 0.02	9.1 ± 1.0	1.2 ± 0.2	7.0 ± 0.6	8.3 ± 0.3

The membranes FOM1 and FOM3 exhibited very high J values under both LC (30.8 and 21.3 kg/m^2 h) and HC (37.5 and 41.8 kg/m^2 h) conditions, being 37–69% and 21–63% higher, respectively, than those of the FOCMs. In addition, the membranes FOM1 and FOM3 had lower J_S values under both LC (0.085 and 0.016 kg/m^2 h) and HC (0.45 and 0.22 kg/m^2 h) conditions than those of the commercial membranes CTA HTI (LC: 0.23 kg/m^2 h; HC: 0.69 kg/m^2 h) and Aquaporin (LC: 0.25 kg/m^2 h; HC: 0.54 kg/m^2 h). These differences in the J and J_S values resulted in a better FO flux performance of the membranes FOM1 and FOM3 compared to those of the commercial membranes CTA HTI and Aquaporin, exhibiting 85–97% and 33–88% lower J_S/J values under LC and HC conditions, respectively. The membrane FOM5 showed the lowest J values and the highest J_S values (consequently, the highest J_S/J values) under both LC and HC conditions compared to the rest of the lab-made FOMs. Although the membrane FOM5 exhibited J values comparable to the commercial membranes CTA HTI and TFC HTI, its high J_S values made it have the worst J_S/J values and, consequently, the worst FO flux performance among all tested membranes. In contrast, compared to the other membranes, the commercial membrane TFC HTI had the lowest J_S values resulting in the lowest J_S/J ratio although their J values were not high.

Taking into consideration all above mentioned comments, the membranes prepared with the IP1 and IP3 methods (i.e. FOM1 and FOM3, respectively) exhibited the most competitive FO flux performance.

Table 8.2.2 summarized other FO characteristics of the prepared FOMs including the final humic acid (HA) rejection factor (R_{HA}), the final salt rejection factor (R_S), the HA concentration factor (β_{HA}) and the salt dilution factor (γ_S). A membrane with a good FO performance for wastewater treatment should exhibit high R_{HA} and R_S values (i.e. it is able to keep the HA molecules in the FS and the salt in the DS) and consequently, the permeate flux (J) that goes through the membrane from the FS to the DS contains mainly water that will dilute the DS in the permeate side. Therefore, high β_{HA} and γ_S values are also expected for an FOM with a good FO performance.

The R_{HA} values of all FOMs under HC conditions were higher than those obtained under LC conditions, whereas R_S values under both LC and HC conditions were very similar and also very high (ranging from 97.3 to 99.7% and from 97.8 to 99.2%, respectively). In addition, the β_{HA} values of all FOMs under HC conditions were much lower than those obtained under LC conditions, whereas γ_S values were generally higher under HC conditions. It is to be noted that the HA concentration factor and salt dilution factor both depend not only on the good rejection factors of the FOMs (i.e. high R_{HA} and R_S values) but also on the corresponding membrane permeate fluxes J and J_S.

The R_{HA} values of the membranes FOM2, FOM4 and FOM5 under both LC and HC conditions were higher than those of the previously mentioned membranes with the best FO flux performance, i.e. FOM1 and FOM3, but their R_S values were lower. Moreover, the membranes FOM2, FOM4 and FOM5 exhibited up to 78–80% lower β_{HA} values under LC–HC conditions than those of the membranes FOM1 and FOM3, mainly due to their lower J values. Similar γ_S values were obtained for all FOMs, but the causes of these results were different for different membranes. The membranes FOM2, FOM4 and FOM5 exhibited high J_S values with R_S values lower than 97.8 and 98.5% under LC and HC conditions, respectively. Thus, the result in γ_S values ranging from 7.0 to 15.4% was partly due to the transport of salt solution from the permeate cell to the feed cell. On the contrary, the membranes FOM1 and FOM3 had low J_S values with R_S values higher than 99.3 and 98.8% under LC and HC conditions, respectively, together with high J and β_{HA} values. These results confirmed that their estimated γ_S values were mainly caused by the transport of permeate water through the membrane from the FS side to the DS side.

Both FOM1 and FOM3 membranes exhibited almost similar J values, higher than those of the other tested membranes. However, the HA rejection capacity (i.e. R_{HA} value) of the membrane FOM1 (63.8%) was much lower than that of the membrane FOM1 (90.9%) under LC conditions, which allowed the transport of a higher quantity of HA molecules from the FS side to the DS side. As a result, the HA concentration in the DS at the end of the FO experiment ($C_f^{HA,\ DS}$) conducted with the membrane FOM3 was as high as 6.8 mg/L, 5 times greater than that obtained with the membrane FOM1 (1.4 mg/L).

All the above mentioned results confirmed that the membrane FOM3 prepared with the combination of the monomers MPD and TMC in the presence of the acid acceptor TEA (i.e. IP3 method) exhibited the best and more competitive overall FO performance, with high values of J, R_{HA}, R_S, β_{HA} and γ_S together with low J_S values under both LC and HC conditions.

8.2.4 Future directions

Further characterization of the physicochemical properties of the different prepared FOMs should be performed to thoroughly understand the influence of the structure, morphology and chemical properties of the active layer (i.e. PA thin film layer) of these membranes on their overall FO performance. Characterization techniques such as ATR-FTIR, XPS and AFM should be carried out, as well as porometry, water contact angle, and zeta potential measurements.

The next step of this research line would be the surface modification of disposed RO membranes following the selected IP3 method to transform them into RFOMs and use them in wastewater treatment by FO technology. The study of their overall FO performance should be carried out and correlated with their structural and chemical characteristics. It is expected that the application of IP to modify disposed and cleaned RO membranes would improve the FO performance of the resultant TFC membranes compared to that of the disposed unmodified and cleaned RO membranes. Finally, a comparison of the FO performance of the prepared RFOMs with that of the FOCMs and other lab-made FOMs should be done to confirm the possibility to reuse discarded RO membranes for their application in FO technology, extend their lifetime and contribute to a circular economy and sustainability in membrane science and related materials.

References

[1] A.L. Linsebigler, G. Lu, J.T. Yates, Photocatalysis on TiO_2 surfaces: Principles, mechanisms, and selected results, Chemical Reviews, 95 (1995) 735-758.

[2] Z. Xu, T. Wu, J. Shi, K. Teng, W. Wang, M. Ma, J. Li, X. Qian, C. Li, J. Fan, Photocatalytic antifouling PVDF ultrafiltration membranes based on synergy of graphene oxide and TiO_2 for water treatment, Journal of Membrane Science, 520 (2016) 281-293.

[3] N. Bhardwaj, S.C. Kundu, Electrospinning: A fascinating fiber fabrication technique, Biotechnology Advances, 28 (2010) 325-347.

[4] J. Landaburu-Aguirre, R. García-Pacheco, S. Molina, L. Rodríguez-Sáez, J. Rabadán, E. García-Calvo, Fouling prevention, preparing for re-use and membrane recycling. Towards circular economy in RO desalination, Desalination, 393 (2016) 16-30.

[5] L.F. Greenlee, D.F. Lawler, B.D. Freeman, B. Marrot, P. Moulin, Reverse osmosis desalination: Water sources, technology, and today's challenges, Water Research, 43 (2009) 2317-2348.

[6] L. Huang, N.-N. Bui, M.T. Meyering, T.J. Hamlin, J.R. McCutcheon, Novel hydrophilic nylon 6,6 microfiltration membrane supported thin film composite membranes for engineered osmosis, Journal of Membrane Science, 437 (2013) 141-149.

[7] J.T. Arena, B. McCloskey, B.D. Freeman, J.R. McCutcheon, Surface modification of thin film composite membrane support layers with polydopamine: Enabling use of reverse osmosis membranes in pressure retarded osmosis, Journal of Membrane Science, 375 (2011) 55-62.

[8] P. Arribas, M. Khayet, M.C. García-Payo, L. Gil, 9 - Novel and emerging membranes for water treatment by electric potential and concentration gradient membrane processes, in: A. Basile, A. Cassano, N.K. Rastogi (Eds.) Advances in Membrane Technologies for Water Treatment, Woodhead Publishing, Oxford, 2015, pp. 287-325.

[9] S. Lee, C. Boo, M. Elimelech, S. Hong, Comparison of fouling behavior in forward osmosis (FO) and reverse osmosis (RO), Journal of Membrane Science, 365 (2010) 34-39.

[10] D. Emadzadeh, W.J. Lau, T. Matsuura, A.F. Ismail, M. Rahbari-Sisakht, Synthesis and characterization of thin film nanocomposite forward osmosis membrane with hydrophilic nanocomposite support to reduce internal concentration polarization, Journal of Membrane Science, 449 (2014) 74-85.

[11] P. Arribas, M. Khayet, M.C. García-Payo, L. Gil, Self-sustained electro-spun polysulfone nano-fibrous membranes and their surface modification by interfacial polymerization for micro- and ultra-filtration, Separation and Purification Technology, 138 (2014) 118-129.

[12] P. Arribas, M.C. García-Payo, M. Khayet, L. Gil, Improved antifouling performance of polyester thin film nanofiber composite membranes prepared by interfacial polymerization, Journal of Membrane Science, 598 (2020) 117774.

[13] S. Molina, R. García Pacheco, L. Rodríguez-Sáez, E. García-Calvo, E. Campos, D. Martínez, J. de la Campa, J. de Abajo, Transformation of end-of-life RO membranes into recycled NF and UF membranes, surface characterization, in: International Desalination Asociation Word Congress, IDAWC15, San Diego, California, 2015.

[14] R. García Pacheco, E. García-Calvo, E. Campos, D. Zarzo, Life+13 transfomem: Conversion of end-of-life reverse osmosis membrane into recycled ultrafiltration and nanfiltration membranes, in: XI AEDYR International Congress, FuturEnviro, Valencia, Spain, 2015, pp. 35-41.

[15] R. García-Pacheco, J. Landaburu-Aguirre, P. Terrero-Rodríguez, E. Campos, F. Molina-Serrano, J. Rabadán, D. Zarzo, E. García-Calvo, Validation of recycled membranes for treating brackish water at pilot scale, Desalination, 433 (2018) 199-208.

[16] S. Molina, J. Landaburu-Aguirre, L. Rodríguez-Sáez, R. García-Pacheco, J.G. de la Campa, E. García-Calvo, Effect of sodium hypochlorite exposure on polysulfone recycled UF membranes and their surface characterization, Polymer Degradation and Stability, 150 (2018) 46-56.

[17] R. García-Pacheco, J. Landaburu-Aguirre, S. Molina, L. Rodríguez-Sáez, S.B. Teli, E. García-Calvo, Transformation of end-of-life RO membranes into NF and UF membranes: Evaluation of membrane performance, Journal of Membrane Science, 495 (2015) 305-315.

[18] S. Lim, M.J. Park, S. Phuntsho, L.D. Tijing, G.M. Nisola, W.-G. Shim, W.-J. Chung, H.K. Shon, Dual-layered nanocomposite substrate membrane based on polysulfone/graphene oxide for mitigating internal concentration polarization in forward osmosis, Polymer, 110 (2017) 36-48.

[19] N.Z.S. Yahaya, M.Z.M. Pauzi, N. Mu'ammar Mahpoz, M.A. Rahman, K.H. Abas, A.F. Ismail, M.H.D. Othman, J. Jaafar, Chapter 10 - Forward osmosis for desalination application, in: A.F. Ismail, M.A. Rahman, M.H.D. Othman, T. Matsuura (Eds.) Membrane Separation Principles and Applications, Elsevier, 2019, pp. 315-337.

9

Conclusions

This PhD thesis explored the development of different types of membranes for water treatment applications including: i) nanostructured membranes (chapters 3 and 4), ii) thin film composite membranes (chapters 5 and 8) and iii) nanocomposite membranes (chapters 6, 7 and 8). Provided that the major obstacle that limits the effective application of membranes in water treatment is fouling phenomenon, different strategies were adopted to develop membranes with enhanced antifouling properties. These applied strategies include membrane surface modification by interfacial polymerization technique (IP), the use of novel materials in membrane preparation such us carbon nanotubes (CNTs), graphene oxide (GO) and TiO_2 nanoparticles (NPs), and the application of electro-active methods during filtration. The more important and interesting results presented in this dissertation are summarized below.

It was elucidated in Chapter 2 that the use of membrane technology for water treatment is constantly growing thanks to the discovery and development of novel and advanced materials for membrane fabrication and modification. However, it was shown that there are still some involved phenomena in water filtration applications that need further improvements (e.g. reduction of both temperature and concentration polarization effects, enhancement of both membrane fouling resistance and long-term operation, etc.). The engineering and development of new advanced membranes could therefore result in more sustainable, economical, and effective solutions for the continuous increasing demands of desalination and treatments of different emerging types of wastewaters.

In Chapter 3, electrospun nanofiber membranes (ENMs) were successfully prepared by electrospinning using the polymer polysulfone (PSU) and the mixture of solvents *N, N*-dimethyl formamide (DMF) and tetrahydrofurane (THF). The effects of different electrospinning parameters (i.e. polymer flow rate, F; electric voltage, V; distance between the needle tip and the collector or gap, G; and electrospinning fabrication time, t_e) on the structure and morphology of the membranes were studied and the membrane fabrication conditions were optimized. The

PSU ENMs were used for the treatment of humic acid (HA) model solutions of 15 mg/L at two different pH values (3 and 11) using cross-flow microfiltration (MF). It was found that the PSU ENMs were not selective (α = 0%) under acidic conditions (pH 3) mainly due to the reduction of the electrostatic repulsion between the HA molecules and the membrane surface, which consequently increased the adsorption of HA molecules to the membrane surface. Under basic conditions (pH 11), both the HA molecules and the PSU ENMs were negatively charged, so that the electrostatic repulsive forces between them increased, reducing the adsorption of HA to the membrane surface and obtaining HA separation factors up to 60%. Permeate fluxes and separation factors measurements were used to elucidate the fouling mechanisms that take place on the membranes under the two different pH conditions. Although the PSU ENMs demonstrated their suitability for wastewater treatment, the overall filtration performance of the membranes could be further improved. In addition, the high organic irreversible fouling factors of the membranes (FR_{IR} up to 99%) suggested the need to enhance their antifouling properties.

Based on the conclusions drawn from Chapter 3, PSU ENMs with improved filtration performance for wastewater treatment were prepared in Chapter 4. The enhancement of the filtration performance of the membranes was achieved by applying a suitable heat post-treatment (HPT) after electrospinning. The HPT induced bonding between the nanofibers and increased the thickness of the nanofibers, which mainly improved the structural integrity of the membrane and decreased the inter-fiber space. These structural changes led to reduced permeate fluxes and better separation factors of the membranes. The pure water permeability (*PWP*) of all prepared PSU ENMs were 3 to 100-fold higher than those achieved by other lab-made ENMs used for particulate removal and up to 63-fold greater than those of commercial flat sheet membranes typically used in MF processes. These values confirm the structural advantages of the ENMs over traditional water filtration membranes, such as their interconnected nanofiber structure with an open pore morphology, their high surface area to volume ratio and their high void volume fraction (i.e. high porosity). As a result, the developed membranes allowed the use of lower pressures to obtain the same water production rate, reducing therefore energy consumption during filtration.

Compared to the PSU ENMs prepared in Chapter 3, the heat-treated optimized PSU ENM with the highest filtration performance in Chapter 4 showed a 4.5 times greater final permeate flux (after conducting the HA filtration test at pH 11) and a 18.2% higher final separation factor. In addition, under the same filtration procedure, the heat-treated optimized PSU ENM had up

to 38% better filtration performance than that of the commercial PES MF membrane (HPWP, Millipore). These results verified the good performance of the prepared PSU ENMs for wastewater treatment by MF. However, the organic irreversible fouling factors of these PSU ENMs were still very high (FR_W ranged from 81.9 to 99%).

In Chapter 5, the interfacial polymerization (IP) surface modification technique was used to successfully enhance the antifouling properties of the heat-treated optimized PSU ENMs. First, polyester (PE) thin film nanofiber composite (TFNC) membranes were prepared by reacting bisphenol A (BPA) and trimesoyl chloride (TMC) under different IP reaction times. The formation and growth process of the PE thin layer on ENMs was elucidated. By correlating the physicochemical properties of the prepared PE TFNC membranes with their filtration performance and antifouling properties, the optimum IP reaction time was determined. The so prepared membrane had a smooth surface and a water permeability as high as 213.0 $L/m^2 h$ bar with a 72.5% HA separation factor. The enhanced antifouling performance of this membrane against HA foulant allowed 90% recovery of its initial water flux after HA filtration (FR_W ~10%). The low fouling tendency of this membrane may result in a long lifetime of the membrane and the reduction of the maintenance costs.

PE thin layers were also successfully formed on other supporting membranes under the optimal IP reaction time. The ENM supports with a smaller size of the inter-fiber space and a higher hydrophobicity favored a faster IP reaction forming a rougher, denser and higher cross-linked PE layer and resulting in PE TFNC membranes with lower filtration performance indexes and worse antifouling properties. Similar surface morphology as well as filtration and antifouling performance were observed when using as a support the commercial PES MF membrane (HPWP, Millipore) mainly due to their smaller pore size compared to ENM supports, also causing a faster IP reaction.

Polyamide (PA) TFNC and PA thin film composite (TFC) membranes with improved antifouling properties were also successfully prepared by the IP reaction of piperazine (PIP) and TMC in the presence of trimethylamine (TEA) on ENMs and on commercial PES MF membranes (HPWP, Millipore), respectively. In terms of filtration performance, PA TFNC membranes showed much higher permeability values than other lab-made PA TFNC and PA TFC membranes and comparable or lower separation factors and antifouling properties.

The advantages of ENMs for filtration were confirmed again, since all PE or PA surface modified membranes prepared on ENM supports had a higher filtration performance than

those prepared on conventional MF commercial membranes. Particularly, the best PE TFNC membrane (PE TFNC1_15) exhibited comparable antifouling performance to previously reported PE TFC membranes with two orders of magnitude greater water permeability and 6–33% better separation factor. Compared to other PA TFC membranes, it had 34–83% greater antifouling performance and 10–71 times higher water permeability with only 17–27% lower separation efficiency.

In chapters 6 and 7, the surface of commercially available MF membranes was modified with carbon-based nanomaterials (carbon nanotubes, CNT, and graphene oxide, GO, respectively) and the resulting nanocomposite membranes were used for the disinfection of wastewater containing bacteria. In Chapter 6, interlaced CNT electrodes (ICE) were successfully formed on the surface of commercial polyvinylidene fluoride (PVDF) MF membranes by vacuum filtration of a CNT-Nafion solution through a laser-cut stencil. The surface of the resultant ICE-PVDF membrane exhibited antifouling properties at DC and AC electric potentials during filtration and backwash (BW) cycles. Compared to the unmodified PVDF membranes, the application of a DC or AC voltage on the ICE during dead-end filtration through the modified ICE-PVDF membranes inactivated and degraded bateria and reduced its attachement to the membrane surface. Bacterial deposition was reduced mainly due to the electrostatic and electroosmotic effects that occurred on the electrode surface, whereas bacterial morphology was greatly altered by electrochemistry.

Compared to the unmodified PVDF membranes, the antifouling properties of the modified ICE-PVDF membranes also resulted in higher fouling resistance and longer filtration operation time (i.e. higher membrane lifespan) in the absence and presence of applied voltage. A model of the ICE elctric field showed how the electrophoretic effect between the electrodes and the dielectrophoretic effect in the solution were involved in the electroactive fouling mitigation of the modified membranes. Under optimal filtration operating conditions, the modified ICE-PVDF membranes reduced the fouling rate by 75% and increased the membrane operation time by 93% compared to the unmodified membrane. After two filtration cycles and under optimal BW conditions, the modified membranes with ICE on the surface could recover up to 96% of the water permeate flux. This result highlights that this novel technique offers a promising solution to microbial fouling control during filtration.

In Chapter 7, a standardization process of the GO starting material was proposed offering high-throughput characterization techniques and clustering algorithms that were able to identify

six classes of GOs based on their chemo-morphological properties (i.e. O/C ratio and mean flake size). The classification method was validated with six GO samples obtained from different producers. GO membranes (GOMs) were successfully prepared by vacuum filtration of different GO suspensions through PVDF MF membranes. The experimental study showed that those applications based on GOs from the same class tended to have the same macroscopic performance (i.e. methylene blue adsorption, bacterial attachment, and permeability). In contrast, GO samples from different classes resulted in a remarkable variation of the macroscopic results. For instance, large variations in the intrinsic antifouling capacity of GOMs made with different classes of GOs (bacterial adhesion ≈50% and >75%) as well as their permeability (up to a factor of five) were shown and related to the differences between the chemo-morphological properties of the GOs. These results corroborate the importance of using standardized materials. The presented GO characterization and classification method will support the research community by enabling a reasonable comparison between scientific investigations. In addition, it will assist GO producers to target customers more effectively by distributing GO with optimal properties for a specific application, supporting the leap of GO from lab to industry.

Finally, in Chapter 8 some preliminary results of different future research directions were discussed. It was shown that the structure and morphology of the surface modified TiO_2-ENMs were very different depending on the followed method to incorporate TiO_2 nanoparticles to the membrane as well as on the modification conditions (i.e. exposure time). Due to these morphological and structural differences, the filtration and antifouling performances are expected to be different as well.

FO membranes (FOMs) were successfully prepared on commercial PES MF membranes using different IP methods. These membranes were used for the treatment of wastewater containing organic matter. The FO filtration tests conducted at low and high concentration conditions demonstrated the good FO flux performance of 4 out of the 5 prepared FOMs compared to that of the commercial FO membranes (i.e. CTA HTI, TFC HTI, Aquaporin). The IP method performed with the combination of the monomers m-phenylenediamine (MPD) and TMC in the presence of TEA resulted in very promising membranes that exhibited a competitive overall FO filtration performance. For instance, the so prepared membrane had up to 36.6% higher permeate flux and 94% lower reverse salt permeate flux than that of the commercial Aquaporin membrane. The next step in this research line would consist in the

surface modification of disposed RO membranes following the previously selected IP method to transform them into recycled FOMs (RFOMs) and use them in wastewater treatment by FO. This possibility can extend the lifetime of the discarded RO membranes and incorporate them as a value chain within a society of circular economy.

It is to be noted that membrane technologies have undergone significant development during last decades, driven by available advanced materials, new technologies, changes of environmental regulations, increasing demand of water supply and sanitation, etc. Therefore, it is expected that membrane science and its related technologies will play a more important role in the future of different industrial sectors (pharmaceutical, chemical, medicine, bioengineering, microelectronics, etc.). The availability of novel tailored membranes with specific properties and new membrane processes offer important tools for the design of appropriate and alternative production systems for a sustainable growth.

10

Future research projects

This chapter proposes interesting topics and research lines derived from the concluding reflections and questions emerged from this PhD thesis.

The filtration performance of PSU ENMs when treating wastewater containing organic matter was greatly improved by the application of a suitable heat post treatment (HPT) (Chapter 4). However, the irreversible organic fouling of these membranes still remained high. Different HPTs were investigated resulting in a wide variety of ENMs with different morphological and structural characteristics, which were directly correlated to their filtration properties and antifouling performance. It would be interesting to develop a theoretical fouling model to predict and quantify the degree of organic fouling of these ENMs based on their structural morphology (i.e. size of the inter-fiber space, diameter of the nanofibers, membrane thickness, porosity, tortuosity, surface roughness, etc.). Although different fouling models have been developed for porous MF and UF membranes, there is no fouling model that explains fouling mechanisms of ENMs. An adequate model could help identify the type of structure and morphology that intrinsically results in better antifouling characteristics.

The present PhD thesis showed that increasing the membrane surface charge density and reducing the membrane surface roughness could reduce membrane fouling with both organic compounds and microorganisms. However, the antifouling properties of all developed membranes in this dissertation were mainly evaluated in short-time laboratory tests with model solutions of single organic compounds such as HA or with model bacterial suspensions such as *Pseudomonas fluorescens* or *Escherichia coli*. Research studies on the estimation of the antifouling properties of surface modified membranes with real multi-component feed streams are still lacking, especially for long-term applications. It would be interesting to first test model solutions that contain organic matter and bacteria with concentrations similar to those of real solutions using the developed membranes in this PhD thesis. Then, these membranes should be tested for long-term filtration using realistic feed streams and operating conditions. The study and optimization of the operating conditions (i.e. flow rate, pressure, temperature, etc.) for different

feed stream characteristics (i.e. solute concentration, pH, ionic strength, etc.) may also serve as a starting point for further improvements of the membrane separation process to reduce membrane fouling and achieve a better long-term membrane performance optimization of the operating conditions (i.e. flow rate, pressure, temperature, etc.) for different feed stream characteristics (i.e. solute concentration, pH, ionic strength, etc.) may also serve as a starting point for further improvements of the membrane separation process to reduce membrane fouling and achieve a better long-term membrane performance.

The design of new membrane modules with improved hydrodynamic conditions during filtration, so that membrane fouling is reduced, would also be an interesting research area. For instance, the development of new cross-flow membrane modules with an internal design that generates turbulences near the membrane surface would help preventing adhesion of foulants on the membrane surface and consequently would reduce fouling. In addition, the possibility of using a bigger filtration system with different membrane modules working in parallel or in series could be explored with the aim of increasing the overall water production or water quality of the filtration application, respectively.

The polyester (PE) thin film nanofiber composite (TFNC) membranes developed in Chapter 5 showed a better antifouling performance than the polyamide (PA) TFNC membranes. For this reason, new monomers could be investigated to form different types of PE layers on ENMs. In addition, the preparation of polyesteramide (PEA) TFNC membranes that encompasses the advantages of both PE membrane (i.e. higher antifouling performance) and PA membrane (i.e. better selectivity) would be a fascinating research area.

Using the idea of an interlaced electrode design for the electro-active biofouling mitigation in Chapter 6 as starting point, different geometries and patterns of the carbon nanotubes (CNT) surface electrodes as well as CNT loadings could be explored in order to improve the electrical conductivity of the electrodes, strengthen the generated electric field and consequently, increase the electrokinetic and electrochemical effects on the membrane surface and reduce further biofouling. In addition, taking into account that the lowest biofouling on the surface modified ICE-PVDF membranes was achieved when operating at an alternate current (AC) of 2 V, it would also be interesting to investigate the influence of AC frequency on biofouling mitigation mechanisms to further enhance biofouling control and reduce energy consumption during filtration.

The surface modification of ENMs using different types of nanoparticles (NPs) such as silicon dioxide (SiO_2), silver (Ag), alumina (Al_2O_3), zirconium dioxide (ZrO_2), zinc oxide (ZnO), zeolite, and other nanomaterials (NMs) such as CNT, titanium nanotubes (TNT) and graphene oxide (GO) or even mixtures of them could also be studied to improve both the filtration and antifouling performance of ENMs. Moreover, the development of a new generation thin film

nanofiber nanocomposite (TFNN) membranes using ENMs as a support and embedding NPs or other nanomaterials in the polymeric top thin film layer during the interfacial polymerization (IP) process could be another interesting research line that deserves future exploration. The thin film nanocomposite (TFN) membranes that have already been developed on phase inversion MF and UF membrane supports by other research groups showed improved water permeability without compromising solute separation. In addition, depending on the characteristics of the added NPs and NMs, improvements of the surface charge properties as well as the antifouling and antimicrobial characteristics were also reported. This concept of TFNN membranes would combine the important properties of conventional membrane polymers (e.g. flexibility, ease of manufacture, high packing-density modules) and the advantages of the ENMs (e.g. high porosity, large surface area to volume ratio, low flow resistance, high permeability) with the unique functionality of molecular sieves (e.g. tunable hydrophilicity, charge density, pore structure, and antimicrobial capability together with better chemical, thermal, and mechanical stability). It would also introduce additional tunable parameters in membrane engineering, which could result in advanced high-performance membranes.

The development of nanotechnology and the use of NMs (e.g. TiO_2 NPs, Ag NPs, ZnO NPs, CNT, GO, fullerenes, etc.) in water treatment applications is growing at a significant speed. Therefore, the exposure to NMs is increasing too. The toxicity and other effects of these NMs on humans, animals and the environment in general is an issue of large concern worldwide that has to be explored in our future research. Generally, the goal of using NMs in membrane technology for water purification is to make water adequate and safe to drink, so any concerns regarding their toxicity must be seriously considered and addressed. The stability of these NMs during realistic long-term filtration experiments, as well as the possible accumulation of these NMs and their leaching into drinking water should be carefully monitored following the up-to-date established regulations. For the types of NMs for which no scientific data of their harmfulness is available, the doses in drinking water to which an individual can safely be exposed has to be determined. Thus, clear and adequate legislation about NMs in water and their potential risks on the life of living beings must be developed.

11

Appendix A

Supplementary information of Chapter 4

Fig. 11.1 shows some examples to understand the way to evaluate the damage of the membranes due to the heat post-treatment (HPT). As it can be observed in Fig. 11.1, almost the entire surface of some of the membranes after the HPT step was burned (Fig. 11.1-A, red color). These membranes could not be used in filtration. Other membranes had only few burned spots on the surface, making their surface heterogeneous and not desirable for filtration tests (Fig. 11.1-B, yellow color). Finally, some membranes did not show visual damage and were therefore good candidates to be used for water treatment (Fig. 11.1-C, green color).

Fig. 11.2 shows, as an example, how to evaluate the degree of networking and interconnectivity of the PSU ENMs after the application of the HPT. Firstly, the total number of the nanofiber intersections were quantified using their corresponding SEM surface images. Subsequently, the intersections in which the nanofibers are clearly fused together were identified. In this way, the degree of networking (*DN*) of each PSU ENM is given by the percentage ratio between these two values (i.e. *DN* = bonding points between nanofibers/total nanofibers intersections). Images of Fig. 11.2 show two examples of the nanofibers structure on the surface of PSU ENMs treated with a medium (230ºC/60 min) and a high (230ºC/75 min) HPT. The yellow circles represent some normal intersections between nanofibers while the red circles represent points with fused nanofibers, i.e. bonding points between nanofibers.

Fig. 11.3 summarizes the nanofiber diameter distributions (i.e. nanofiber diameter histograms) of the treated PSU ENMs, obtained by statistical analysis applied on the nanofiber diameter measurements evaluated by UTHSCSA Image Tool 3.0 software.

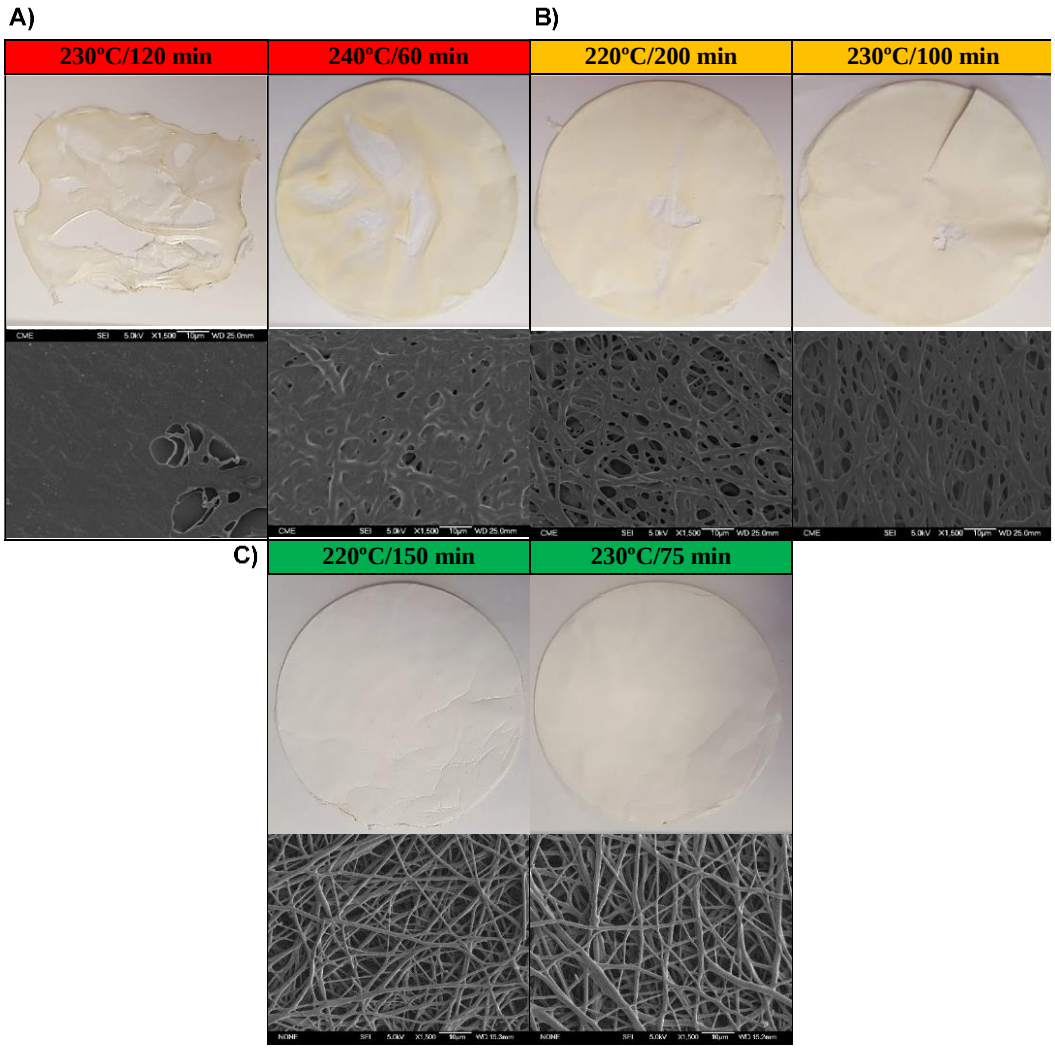

Figure 11.1. Visual criterion to evaluate the damage of the membranes due to the HPT. Pictures of the PSU ENMs after the HPT (top) with their corresponding SEM image of the surface (bottom). A) Membranes graded with 0 points, B) 5 points and C) 10 points.

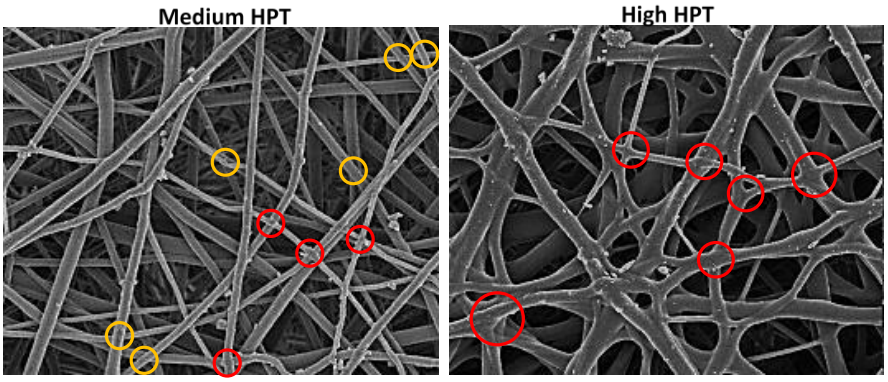

Figure 11.2. Evaluation of the degree of networking and interconnectivity of the PSU ENMs after the application of the heat post-treatment (HPT). SEM images of the nanofibers structure on the surface of PSU ENMs treated with a medium (230°C/60 min) and a high (230°C/75 min) HPT. The yellow circles represent some normal intersections between nanofibers while the red circles represent points with fused nanofibers.

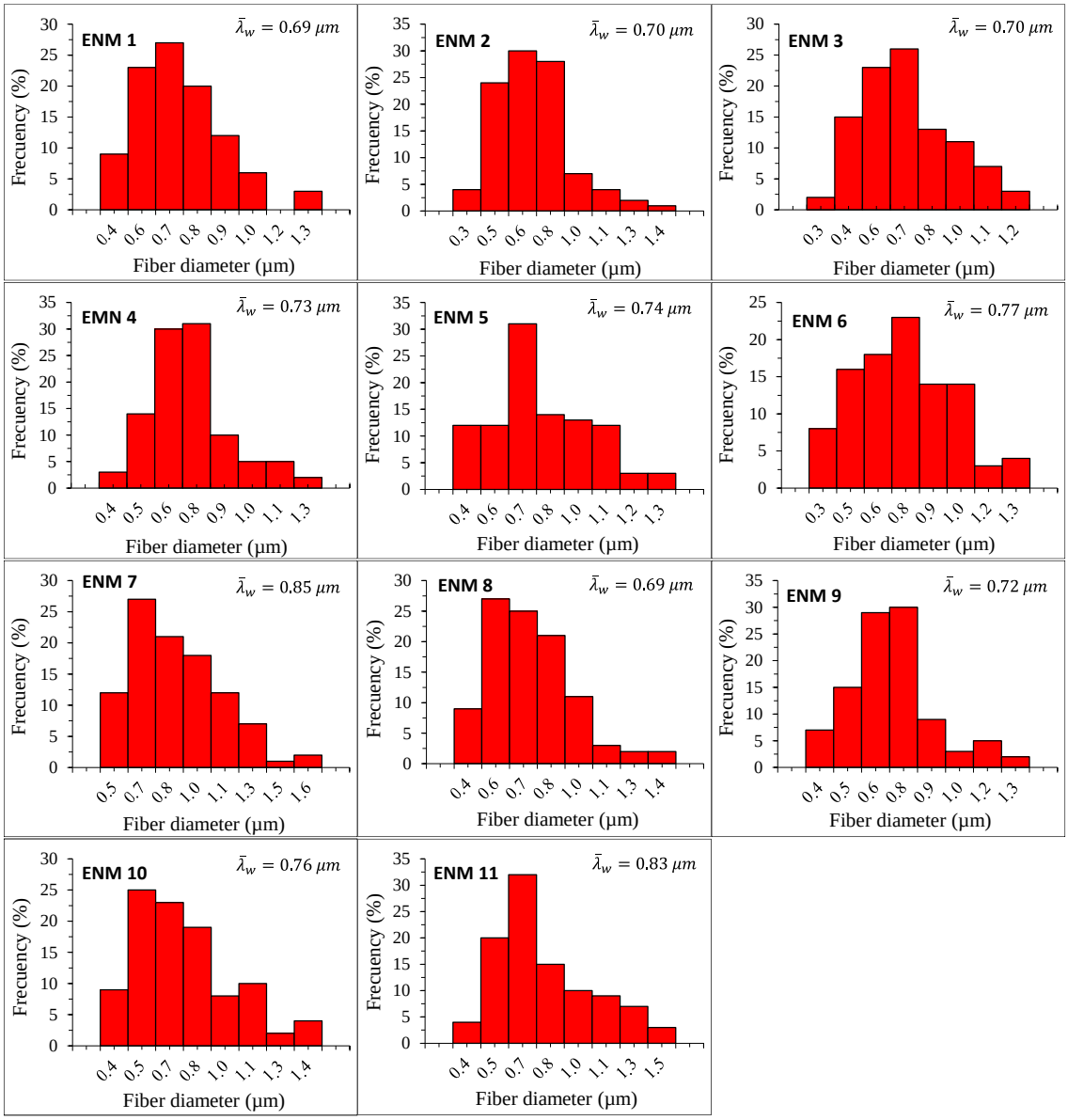

Figure 11.3. Nanofibers diameter histograms of the treated PSU ENMs.

Fig. 11.4 is a sketch showing the effects of the heat post-treatment (HPT) on the nanofiber diameters and the size of the inter-fiber space of the ENMs. ENMs after fabrication via electrospinning had a thickness of about 900 ± 50 μm. To carry out the HPT, the ENMs are attached to a copper support and introduced in a ceramic oven. After the HPT is completed, the thickness of the ENMs was reduced and varied in the range of 80–380 μm. One of the main effects observed with the increase of the HPT temperature or time was the increase of the nanofiber diameters ($\overline{\lambda_w}$) of the membranes along with a decrease of the mean size of the inter-fiber space ($\overline{d_f}$), i.e. nanofibers became flatter and thicker along the membrane, resulting in a decrease in the mean size of the inter-fiber space.

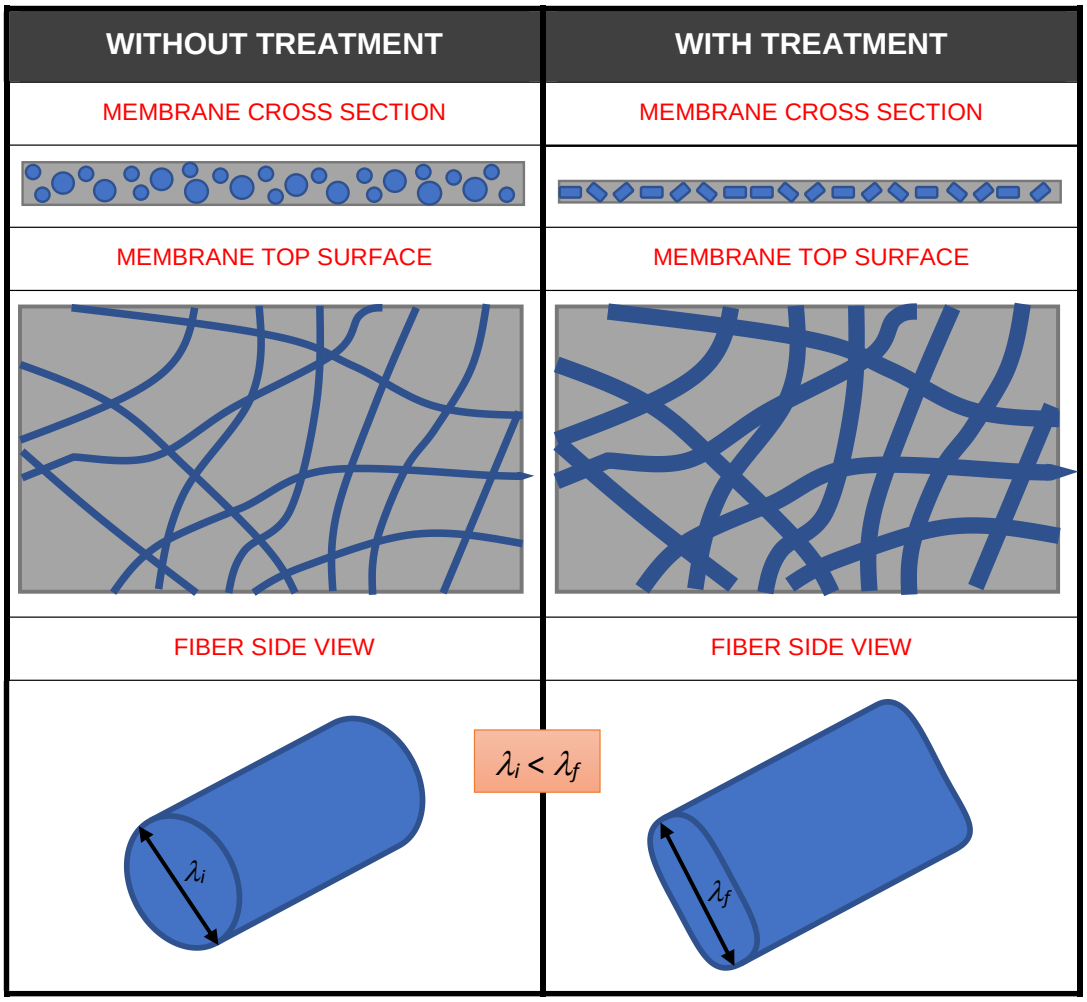

Figure 11.4. Sketch of the effects of the heat post-treatment (HPT) on the nanofiber diameters and the size of the inter-fiber space of the ENMs. The parameters λ_i and λ_f represent the initial and final diameter of the nanofibers, respectively.

Fig. 11.5 shows as an example some of the techniques used for the analysis of the fouling of the PSU ENMs. From the FTIR analysis (see Fig. 11.5-A) it can be observed the appearance of characteristic peaks of the humic acid (HA) on the spectra of the ENM after HA microfiltration (MF) (indicated with black arrows over the graph), what confirms the presence of HA in the membranes after filtration. The surface and the cross-section of the self-sustained PSU ENMs were examined by a field emission scanning electron microscope (FESEM, JEOL Model JSM-6330F) equipped with an energy dispersive spectrometer (EDS, Oxford Instruments X-Max). The accumulation of HA on the surface of the ENMs can be observed from the SEM bottom image of Fig. 11.5-B. EDS in mapping mode together with the software INCA (Oxford Instruments) were used to determine the elemental composition of the ENMs before and after HA MF along the cross-section of the membrane samples. This elemental analysis was performed in three differentiate areas: the bottom side (i.e. facing the permeate), the center side and the top side (i.e. facing the feed). The cross-section SEM images of Fig. 11.5-C correspond

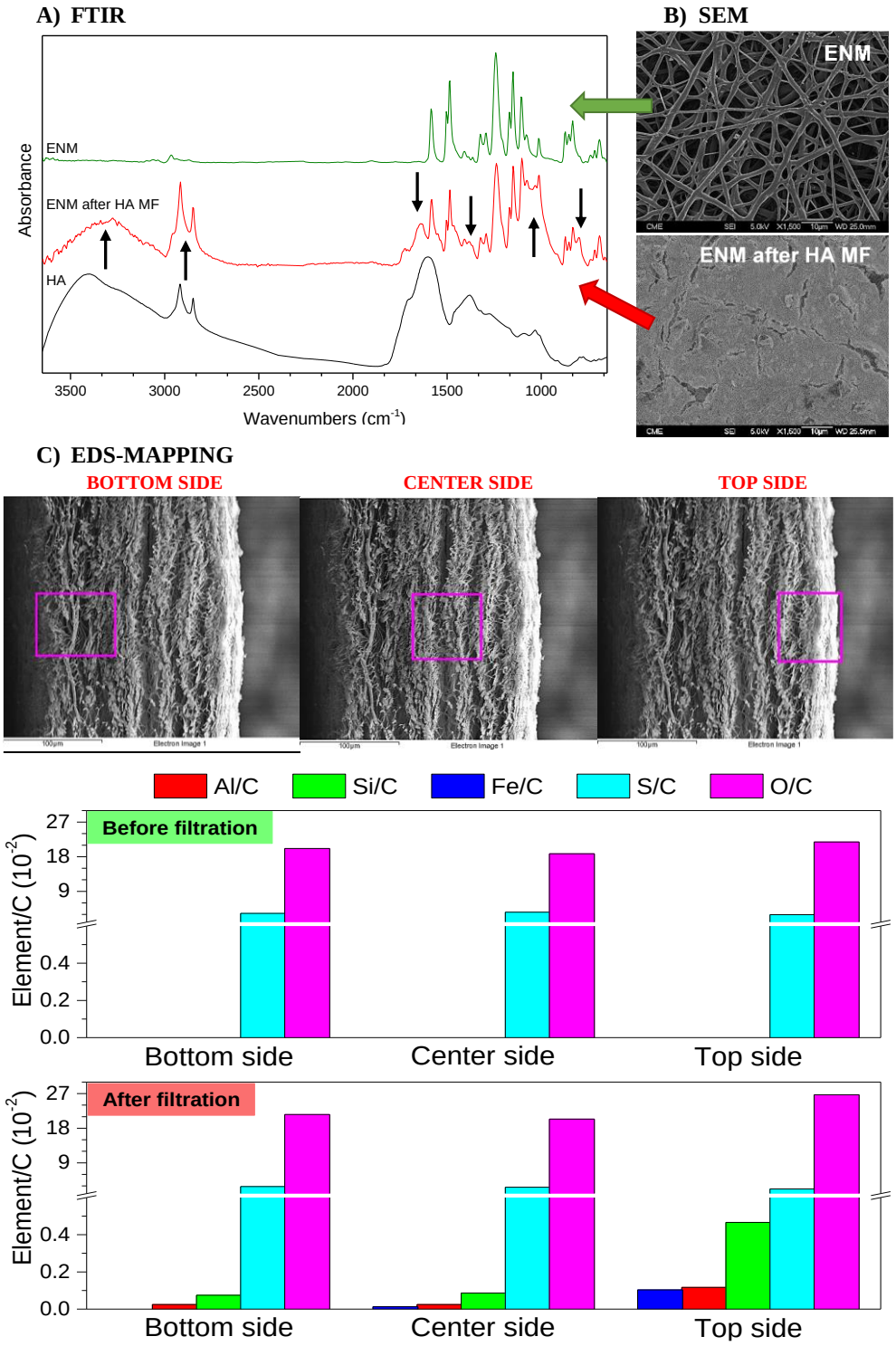

Figure 11.5. Example of the characterization analysis of the organic fouling of the PSU ENMs. A) FTIR spectra of the HA and the ENM before and after filtration, B) SEM surface images of the ENM before and after filtration (X1500), and C) SEM cross section images of the ENM after filtration taken during the EDS mapping analysis in the bottom, centre and top sides of the membrane. The graph under the images summarizes the relative percentage (i.e. Element/C) of the atomic composition of the ENM before and after HA MF in the bottom, center and top sides.

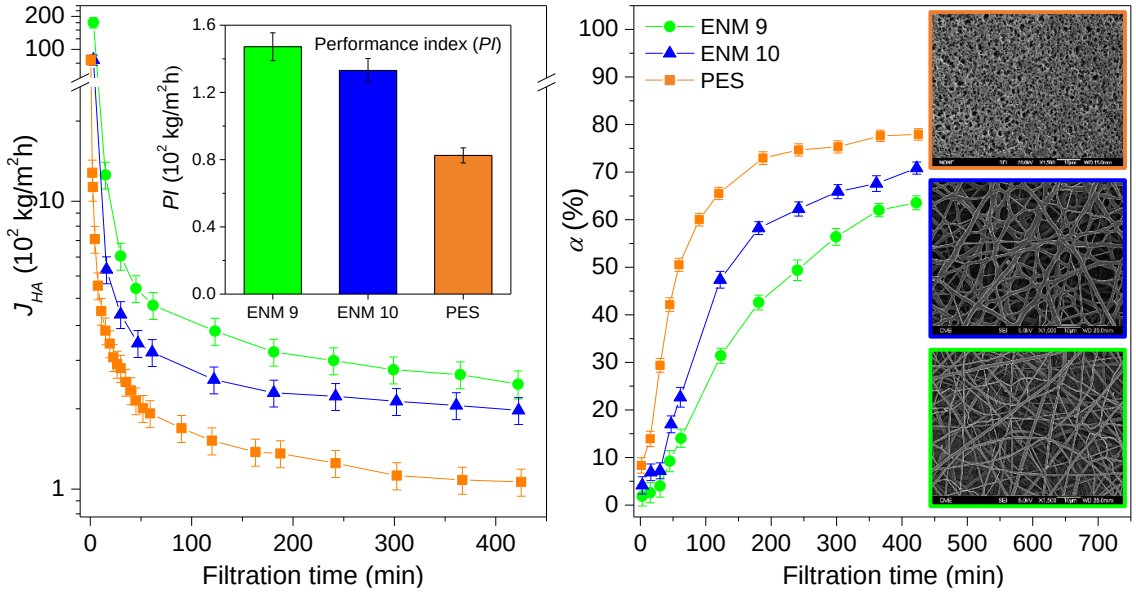

Figure 11.6. Humic acid permeate flux (J_{HA}), separation factor (α) and performance index (PI) of the PSU ENMs 9 and 10 prepared with a HPT of 230°C/60 min and 230°C/75 min, respectively, and PES MF commercial membrane. The filtration tests were conducted with 15 mg/L HA feed aqueous solution at pH 11 and 10^5 Pa transmembrane pressure (ΔP). The inset pictures are SEM surface images of the membranes before HA MF test.

to the PSU ENM after HA MF. The elemental analysis areas are highlighted with a pink square over the cross section SEM images. The graph under these images summarizes the relative percentage (i.e. Element/C) of the atomic composition of the ENM before and after HA MF in the three areas of interest. Before HA filtration, the relative percentage concentration of sulfur (S/C) and oxygen (O/C) detected in the membrane was practically the same in the three areas of interest, i.e. there was a homogeneous distribution of these elements across the membrane. In addition, the concentration ratio of O/C across the membrane was higher than that of S/C, which is in concordance with the chemical formula of the PSU (i.e. $C_{27}H_{46}O_4S_1$). After HA filtration, a 13 to 25% decrease of the S/C ratio and a 7 to 22% increase of the O/C ratio across the membrane were observed as well as the emergence of new elements such as aluminum (Al), silicon (Si) and iron (Fe) coming from the HA. It is worth noting that the O/C ratio was higher in the top side (0.27) than that of the bottom and center sides (0.21 and 0.20, respectively), probably due to the higher accumulation of HA in the top side of the membrane. In the same way, the concentration ratio of the new elements (i.e. Al/C, Si/C, Fe/C) was not homogeneous across the membrane. Although the analysis shows that fouling occurs along the whole cross-section of the membrane, the accumulation of these elements increase in the order: bottom side<center side<top side, being the Al/C, Si/C and Fe/C concentration ratios 79, 84 and 100% higher, respectively, in the top side than in the bottom side.

Fig. 11.6 shows the main results of the filtration parameters analyzed during the HA MF tests conducted with the heat-treated optimized PSU ENMs 9 and 10 (i.e. HPT of 230°C/60 min and 230°C/75 min, respectively) and the PES MF commercial membrane. SEM surface images of the membranes before HA MF test are included to realize the initial differences in the morphological structure of the membranes.

12

Appendix B

Supplementary information of Chapter 5

12.1 Polyester thin film nanofiber composite membranes prepared with different polymerization reaction times and supports

Fig. 12.1 shows the SEM surface images at X300 magnification of the polyester (PE) thin film nanofiber composite (TFNC) membranes prepared on ENM1 support with different interfacial polymerization (IP) reaction times. While increasing the IP reaction time from 5 to 15 min, the inter-fiber space of the ENM1 support was progressively covered with the PE layer resulting in a less rough surface. For 15 min IP reaction time, the membrane PE TFNC1_15 showed a smooth surface. With a further increase of the IP reaction time to 20 min, the entire surface of the membrane was covered by a rough PE layer with nodular structure (PE TFNC1_20).

In sections 5.3.1.1 and 5.3.2.1 of Chapter 5 it was shown that a change in the chemical structure of the PE thin film layer formed on the membranes surface led to a change of its morphology. Particularly in section 5.3.1.1, when studying the influence of the polymerization reaction time on the physicochemical properties of PE TFNC membranes, a change in the chemical structure of the membrane PE TFNC1_20 (t_{IP} = 20 min) with respect to the membrane PE TFNC1_15 (t_{IP} = 15 min) was demonstrated due to the appearance of carboxylic acid groups, which changed the film layer morphology from smooth to rough with nodular structure. In the same way in section 5.3.2.1, when looking at the influence of the different supporting membranes (ENM1, ENM2, PES) on the PE thin film formation and on its physicochemical caracteristics, the FTIR spectra of the membranes PE TFNC2_15 and PE TFC_15 revealed new peaks compared to the FTIR spectra of the membrane PE TFNC1_15, with also indicated the presence of carboxylic acid groups on the membranes.

These carboxilic acid groups were hypothisized to be incorporated as a mixture of 1,3,5-benzene tricarboxylic acid and 1,3-benzene dicarboxylic acid. As a result, in the FTIR spectra of the membranes PE TFNC1_20 (Fig. 12.2-A), PE TFNC2_15 and PE TFC_15 (Fig. 12.2-B), the peak assigned to the C=O stretching vibration of the ester group at 1720 cm^{-1} became broader than that of the membrane PE TFNC1_15 due to a new contribution centered at 1698 cm^{-1} (i.e. characteristic of the –COOH group). In addition, a broad contribution between 2300 and 2700 cm^{-1} and a narrow peak at 3110 cm^{-1} appeared.

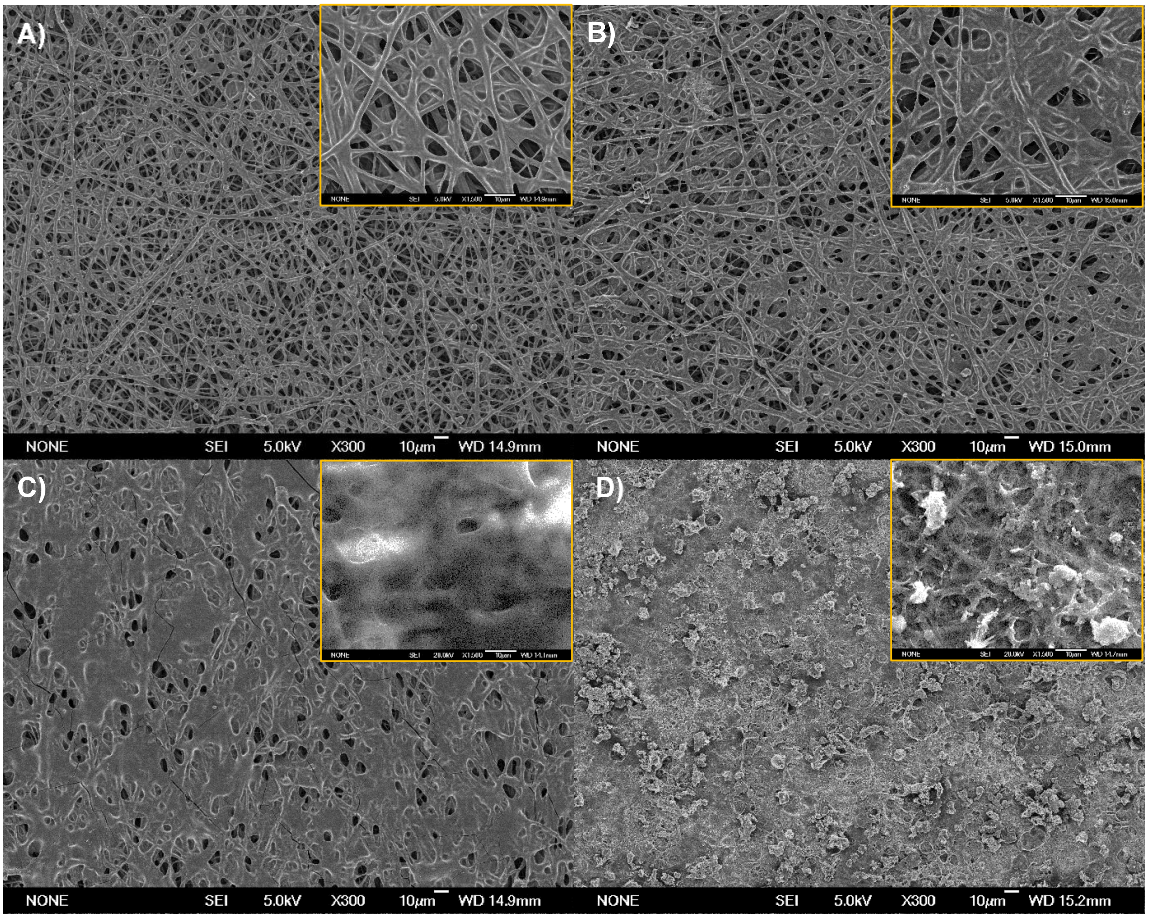

Figure 12.1. Influence of the polymerization reaction time on the morphological and structural characteristics of polyester (PE) thin film nanofiber composite (TFNC) membranes. SEM surface images at X300 magnification of the PE TFNC membranes prepared on ENM1 with IP reaction times of A) 5 min (PE TFNC1_5), B) 10 min (PE TFNC1_10), C) 15 min (PE TFNC1_15) and D) 20 min (PE TFNC1_20). The inset micrographs are SEM surface images of the membranes at X1500 magnification. The PE TFNC membranes were prepared by reacting BPA and TMC as described in Fig. 5.2-A of Chapter 5.

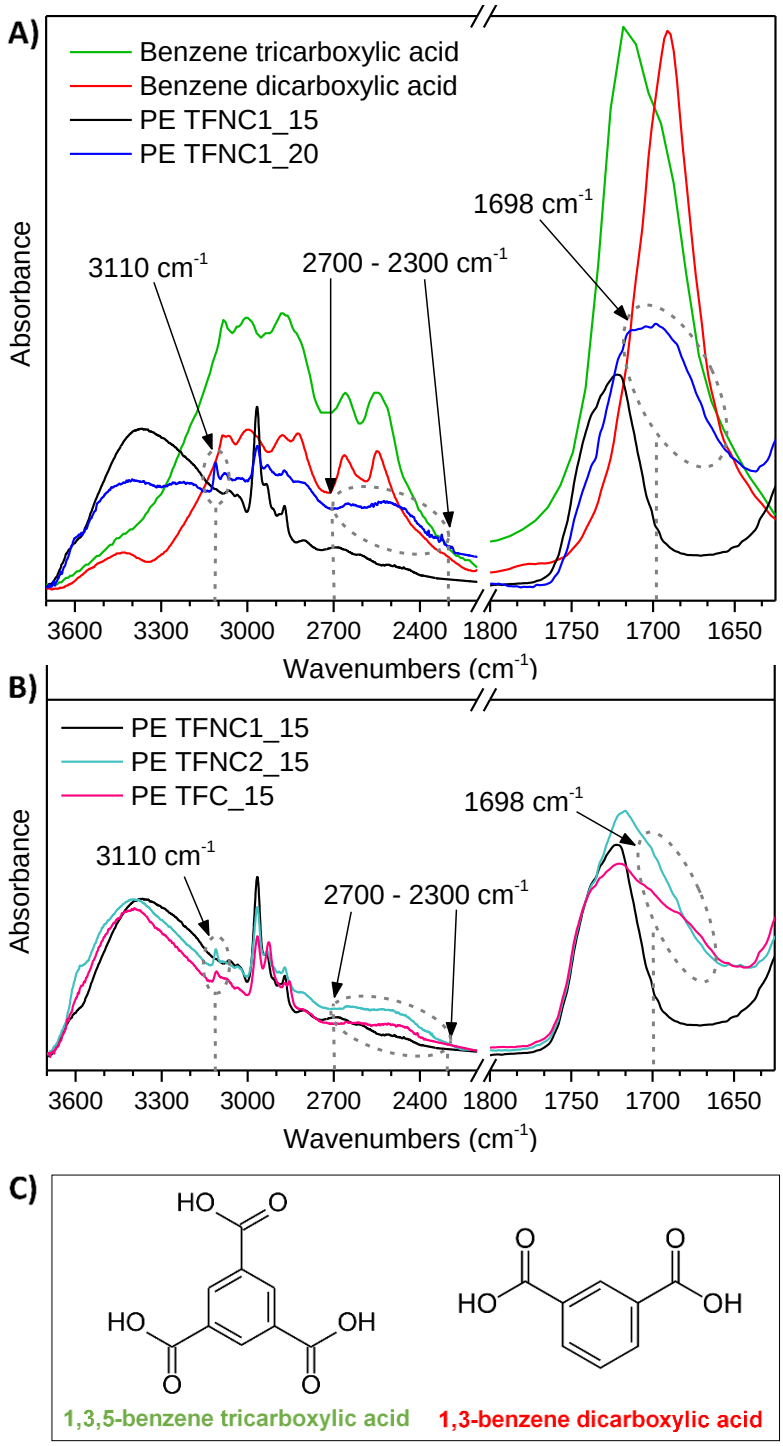

Figure 12.2. Influence of the polymerization reaction time and the different supporting membranes on the chemical composition of polyester (PE) thin film composite (TFC) membranes. FTIR spectra in the range 3700–1625 cm^{-1} of A) 1,3,5-benzene tricarboxylic acid, 1,3-benzene dicarboxylic acid, and the PE TFNC membranes prepared by PE surface modification on ENM1 support with IP reaction times of 15 min (PE TFNC1_15) and 20 min (PE TFNC1_20). B) FTIR spectra in the range 3700–1625 cm^{-1} of the PE TFC membranes prepared by PE surface modification on different supports (ENM1, ENM2, PES) with 15 min IP reaction time (PE TFNC1_15, PE TFNC2_15, PE TFC_15). C) Chemical structure of 1,3,5-benzene tricarboxylic acid and 1,3-benzene dicarboxylic acid.

12.2 Procedure to select the interfacial polymerization approach to prepare the polyamide thin film composite membranes

Table 12.1 summarizes all different combinations of monomers and conditions of the interfacial polymerization (IP) approaches considered to prepare the polyamide (PA) and the polyester (PE) thin film composite (TFC) membranes using as support the microfiltration (MF) commercial polyethersulfone (PES) membrane.

12.2.1 Preliminary selection of the more adequate IP approaches

The good filtration performance of the membrane PE TFC_15 was already demonstrated in section 5.3.2.2 of Chapter 5. This membrane was therefore used as a reference to evaluate the properties of the PA TFC membranes. A total of twelve different PA TFC membranes were prepared under the conditions summarized in Table 12.1. These membranes were named considering the combination of the used monomers (i.e. PE, PA1, PA2, PA3, PA4 and PA5), the type of the membrane (i.e. TFC) and the IP reaction time (i.e. 5, 10 and 15 min). Porometer measurements were conducted to get the wet curves of the membranes, which were used to calculate their permeability. Fig. 12.3 displays the permeability curve of all PA TFC membranes together with that of the membrane PE TFC_15. The SEM images of Fig. 12.4 show the differences in the surface morphology and structure of the membranes at X1500 magnification.

To select an adequate IP approach, the PA TFC membranes with a similar permeability to that of the membrane PE TFC_15 taken as reference were considered. Fig. 12.3 shows that regardless of the IP reaction time, all developed membranes with the combination of monomers PA3 (i.e. PA3 TFC_5, PA3 TFC_10) and PA5 (i.e. PA5 TFC_5, PA5 TFC_10) exhibited very low permeability compared to the membrane PE TFC_15. Therefore, the IP approaches followed to prepare these membranes were discarded. The membranes PA1 TFC_15, PA2 TFC_15 and PA4 TFC_10 were also discarded because of their low permeability. The membranes PA1 TFC_5 and PA2 TFC_5 exhibited a higher permeability than that of the membrane PE TFC_15, but resulted in a lower separation factor during HA filtration, so that these membranes were also discarded. Finally, the membranes PA1 TFC_10, PA2 TFC_10 and PA4 TFC_5 showed permeability curves very similar to the membrane PE TFC_15. Therefore, these membranes were selected for further characterization.

Table 12.1. Combination of monomers and interfacial polymerization (IP) conditions considered to prepare polyester (PE) and polyamide (PA) thin film composite (TFC) membranes.

Combination code	TFC type	Aqueuos phase				Organic phase			
		Material[1]	Chemical structure	w/w (%)	t_{ap}[2] (min)	Material[1]	Chemical structure	w/v (%)	t_{IP}[2] (min)
PE	Polyester	BPA	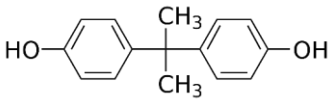	2	60	TMC	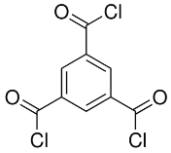	0.25	15
PA1	Polyamide	MPD	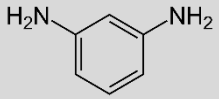	2	60	TMC	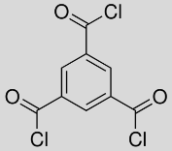	0.25	5, 10, 15
PA2	Polyamide	MPD–TEA	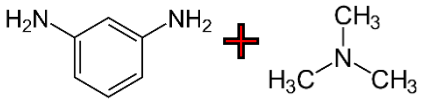	1–1	60	TMC	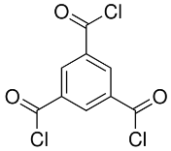	0.25	5, 10, 15
PA3	Polyamide	PIP	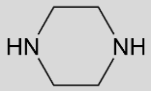	2	60	TMC	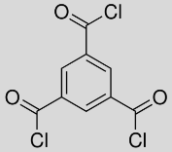	0.25	5, 10
PA4	Polyamide	PIP–TEA	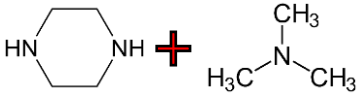	1–1	60	TMC	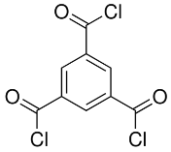	0.25	5, 10
PA5	Polyamide	PIP–PVA	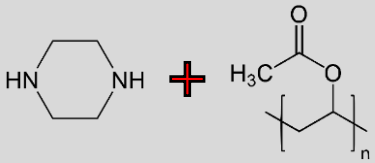	1–1	60	TMC	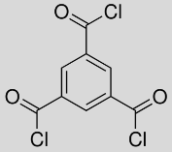	0.25	5, 10

[1]BPA: bisphenol A; MPD: *m*-phenylenediamine; TEA: triethylamine; PIP: piperazine; PVA: polyvinyl acetate; TMC: trimesoyl chloride.
[2]t_{ap}: aqueous phase time, t_{IP}: polymerization reaction time.

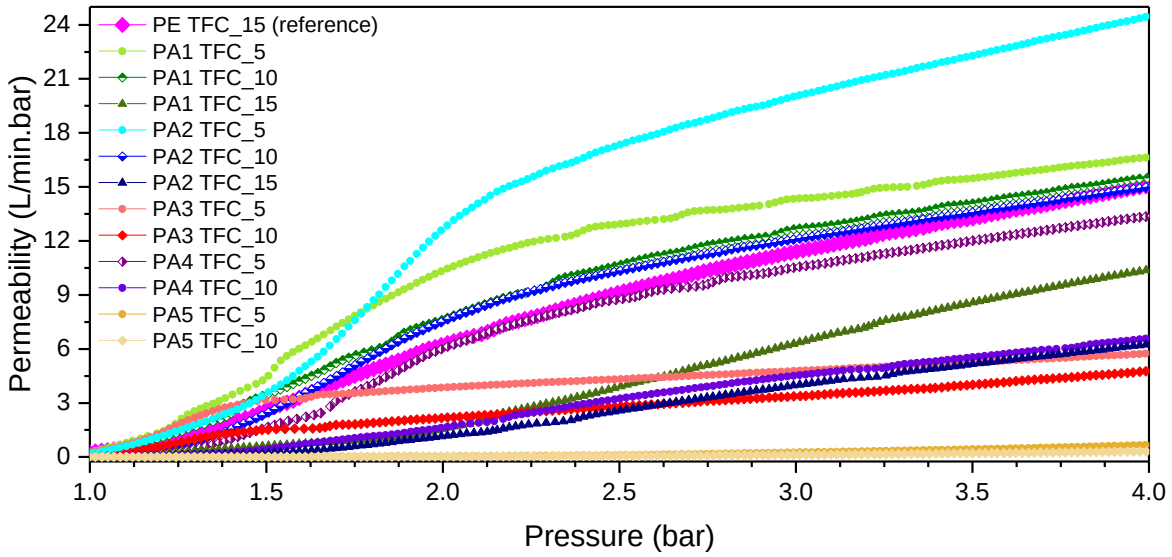

Figure 12.3. Permeability of all polyester (PE) and polyamide (PA) thin film composite (TFC) membranes. The permeability values were calculated from the wet curve of the membranes tested using Porometer.

SEM images in Fig. 12.4 showed that the surface morphologies of the membranes PA1 TFC_10 (Fig. 12.4-B2) and PA2 TFC_10 (Fig. 12.4-C2) were similar to that of the membrane PE TFC_15 (Fig. 12.4-A1): rough with nodular structure. However, different sizes of the nodular structure were observed for the latter membranes. The size increased in the order: PE TFC_15 < PA1 TFC_10 < PA2 TFC_10. The surface morphology of the membrane PA4 TFC_5 (Fig. 12.4-E2) was also rough with granular-like-structure morphology and no visible open pores.

12.2.2 Physicochemical properties of the pre-selected polyamide thin film composite membranes

Fig. 12.5 shows the structural morphology of the membrane PE TFC_15 taken as reference and the PA TFC membranes (PA1 TFC_10, PA2 TFC_10 and PA4 TFC_5) selected for further characterization. Different surface structures can be seen at the SEM surface images of the PA TFC membranes taken at X10000 magnification. For instance, voids of small diameter appeared within the nodular structure of the membranes PE TFC_15 and PA2 TFC_10, whereas the membrane PA1 TFC_10 exhibited a smooth surface with no voids. The cross section SEM images were used to determine the thickness of the PE and PA layers formed on the membranes using ImageJ free software. At least 50 measurements were taken for each membrane. The estimated final thickness of the thin film layer (δ_{TFC}) of the membranes PE TFC_15, PA1 TFC_10, PA2 TFC_10 and PA4 TFC_5 was 1.18, 1.46, 0.68 and 2.05 μm, respectively.

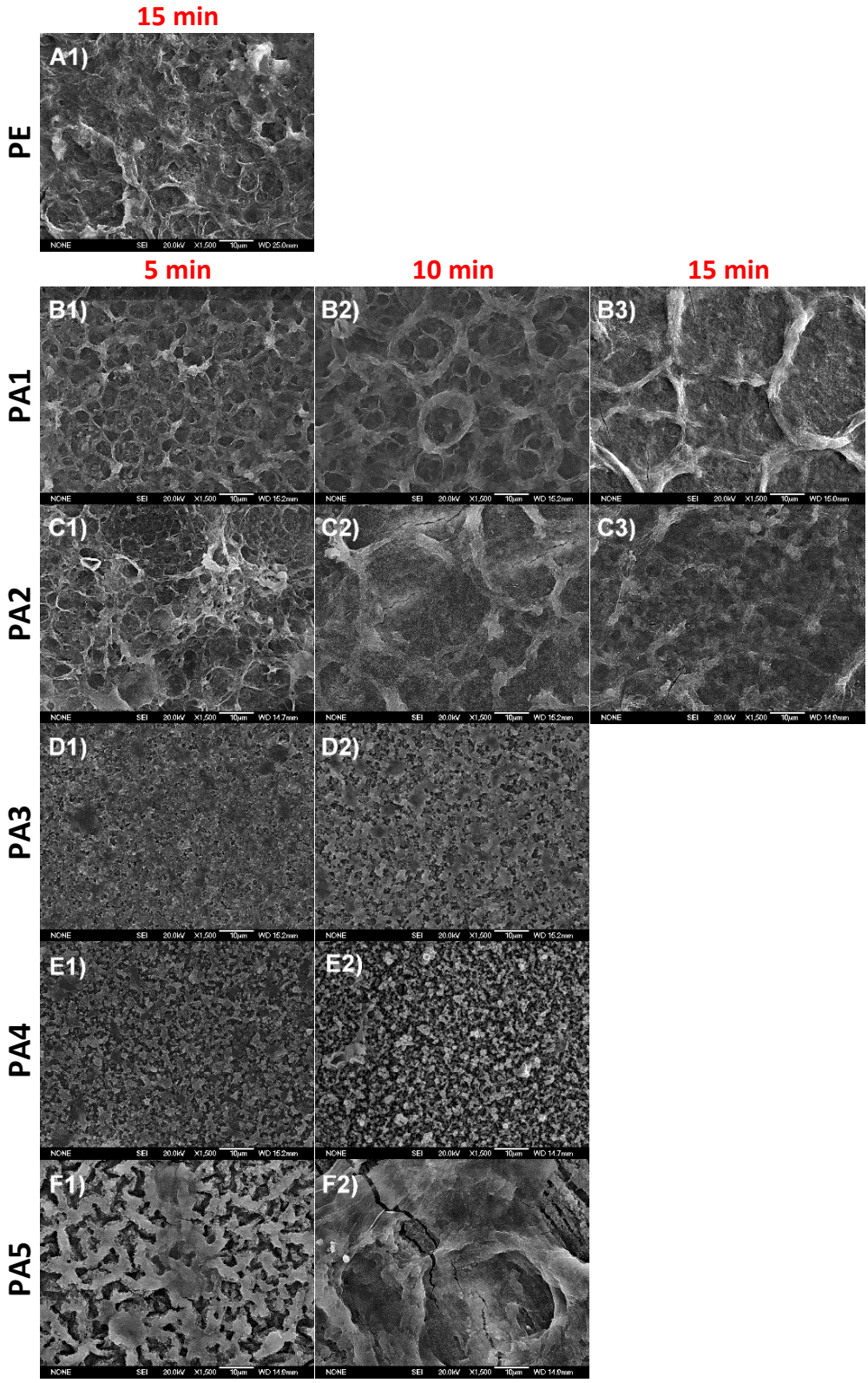

Figure 12.4. SEM surface images at X1500 magnification of all polyester (PE) and polyamide (PA) thin film composite (TFC) membranes. A1) PE TFC_15, B1) PA1 TFC_5, B2) PA1 TFC_10, B3) PA1 TFC_15, C1) PA2 TFC_5, C2) PA2 TFC_10, C3) PA2 TFC_15, D1) PA3 TFC_5, D2) PA3 TFC_10, E1) PA4 TFC_5, E2) PA4 TFC_10, F1) PA5 TFC_5 and F2) PA5 TFC_10.

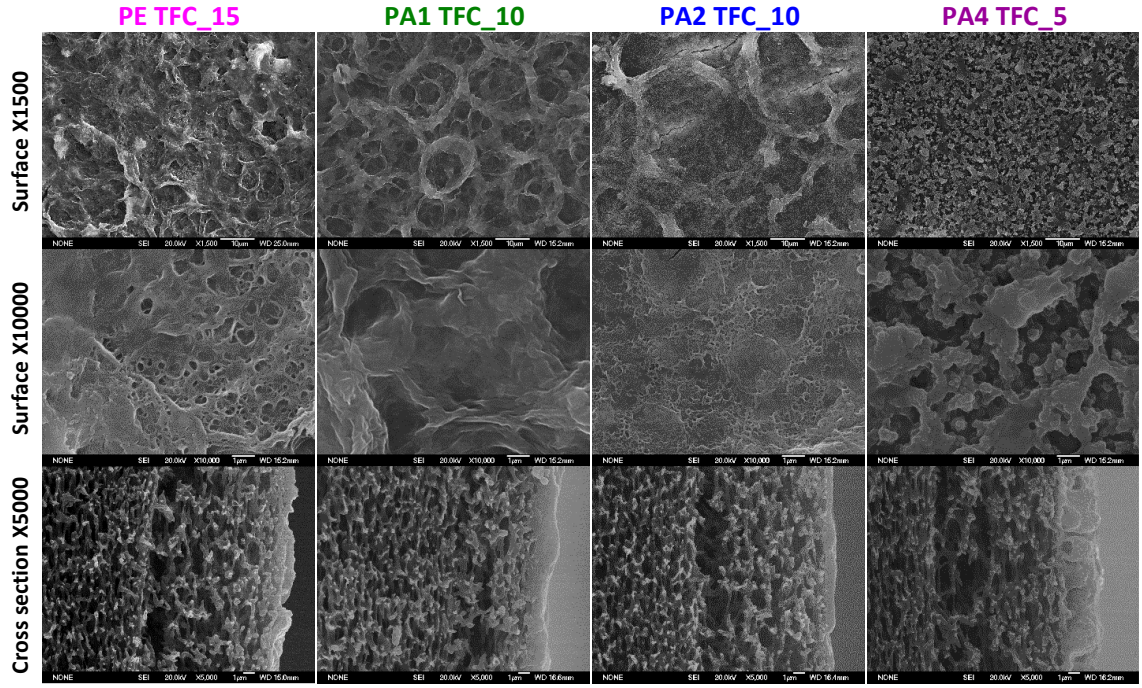

Figure 12.5. SEM surface and cross section images at different magnifications of the polyester (PE) and pre-selected polyamide (PA) thin film composite (TFC) membranes.

Fig. 12.6 displays the physicochemical properties of the unmodified supporting membrane (PES) and the pre-selected surface modified PA TFC membranes (PA1 TFC_10, PA2 TFC _10, PA4 TFC_5). A clear reduction of the mean pore size ($\overline{d_f}$) of the PA TFC membranes compared to the PES support was observed in Fig. 12.6-A (left). This reduction of $\overline{d_f}$ was 7.2% for PA1 TFC_10, 5.3% for PA2 TFC _10 and 9.0% for PA4 TFC _5 (see Table 12.3). The $\overline{d_f}$ value of the PA TFC membranes decreases in the order PA2 TFC_10 (543 nm) > PA1 TFC_10 (532 nm) > PA4 TFC_5 (521 nm). The trend of the pore size reduction of these membranes was consistent with the increase of the thickness of their corresponding PA layer.

Fig. 12.6-B shows the FTIR spectra of the PES support and the PA TFC membranes. Table 12.2 provides the peak assignments of the IR bands for these membranes. The FTIR spectra of the PES support showed peaks at 1321, 1298 and 1148 cm^{-1}, which were attributed to the asymmetric and symmetric stretching vibration of S=O bonds of the PES based polymer. Other characteristic strong IR bands of the PES substrate appeared at 1577, 1485 and 1239 cm^{-1}, which correspond to the C=C aromatic in-plane ring bend stretching vibration, the C‑H stretching vibration of the methyl group (CH_3–C–CH_3) and the C–O–C asymmetric stretching of aryl–O–aryl group, respectively. In addition, the weaker peaks in the range of 1125–870 cm^{-1} were due to skeletal aliphatic C–C stretching and aromatic hydrogen bending/rocking, whereas those in the region 865–825 cm^{-1} were assigned to the in-phase out-of-plane hydrogen deformation of para-substituted phenyl groups.

It is worth quoting that the combination of the monomers PA1 (i.e. MPD-TMC) and PA2 (i.e. MPD/TEA-TMC) formed fully aromatic PA TFC membranes, whereas PA3 (i.e. PIP/TEA-TMC) created a semi-aromatic PA TFC membrane [1] (Fig. 12.7). These differences were associated mainly to the different character of the amine monomers used for the IP process (i.e. MPD is an aromatic amine while PIP is an aliphatic amine). Thus, chemical structure differences between the membranes PA1 TFC_10 and PA2 TFC_10 compared to the membrane PA4 TFC_5 were expected and confirmed by the peaks of their corresponding FTIR spectra. TEA is only an acid acceptor used in the IP process to accelerate the MPD-TMC or PIP-TMC reaction by removing HCl generated as by-product during the amide bond formation. In general, the addition of TEA was expected to promote the cross-linking and film formation [2-4].

Compared to the PES support, the FTIR spectra of the membranes PA1 TFC_10 and PA2 TFC_10 showed three peaks at ~1660, 1609 and 1541 cm^{-1}, characteristic of the PA thin layer. The peak at 1660 cm^{-1} (amide I band) was assigned to the C=O stretching, C–N stretching and C–C–N deformation vibration in a secondary amide group. The peak at 1609 cm^{-1} (aromatic amide) was attributed to the N–H deformation, C=C ring stretching vibration and aromatic ring breathing. The peak at 1541 cm^{-1} (amide II band) corresponds to the C–N stretching and N–H in-plane bending vibration of the amide group (–CONH). In addition, two weak peaks, assigned to the amide III and amide V bands, respectively, appeared at ~1386 and 783 cm^{-1}. Moreover, the detected broad adsorption peak in the range 3150–3700 cm^{-1}, centred at ~3313 cm^{-1} for the membrane PA2 TFC_10 and at 3328 cm^{-1} for the membrane PA1 TFC_10, corresponded to the O–H stretching vibration of carboxylic acid group (–COOH) and the N–H stretching vibration of residual amine groups. The two weak peaks appeared at ~1715 and 1443 cm^{-1} were due to the C=O stretching vibration of carboxylic acid group and the C–O stretching together with the O–H bending vibration of carboxylic acid, respectively.

In contrast to the membranes PA1 TFC_10 and PA2 TFC_10, the aromatic amide (1609 cm^{-1}), the amide II (1541 cm^{-1}) and the amide V (783 cm^{-1}) bands were not detected in the FTIR spectra of the membrane PA4 TFC_5. The amide I band was shifted to a lower wavenumber (peak centered at 1614 cm^{-1} with a significant contribution at 1630 cm^{-1} instead of the peak found at 1661 cm^{-1} for the fully aromatic membranes). The amide III band was also shifted to a lower wavenumber (1378 cm^{-1} instead of 1386 cm^{-1}), whereas the broad peak of the O–H stretching vibration of carboxylic acid group (–COOH) and the N–H stretching vibration of residual amine groups was shifted to a higher wavenumber (~3393 cm^{-1}), probably due to the absence or much lower quantity of residual amine groups in the semi-aromatic membrane. The peak assigned to the C–O stretching and O–H bending vibration of carboxylic acid group of

the membrane PA4 TFC_5 appeared at a similar wavenumber 1443 cm^{-1} to that of the membranes PA1 TFC_10 (1441 cm^{-1}) and PA2 TFC_10 (1443 cm^{-1}).

From the comparison of the FTIR spectra of all pre-selected PA TFC membranes in the ranges 1200–1050 cm^{-1} and 900–850 cm^{-1}, it was observed a gradual reduction of the intensity of the characteristic peaks of the PES support following the order PA2 TFC_10 > PA1 TFC_10 > PA4 TFC_5. This result agrees well with the increasing thickness of the PA thin layer (δ_{TFC}) of these membranes (Table 12.3). In addition, the higher intensity of the characteristic peak of the amide I band of the membrane PA4 TFC_5 compared to that of the membranes PA1 TFC_10 and PA2 TFC_10 indicated its higher degree of crosslinking, which is in accordance with the XPS results of the PA TFC membranes (Fig. 12.8 and Table 12.4).

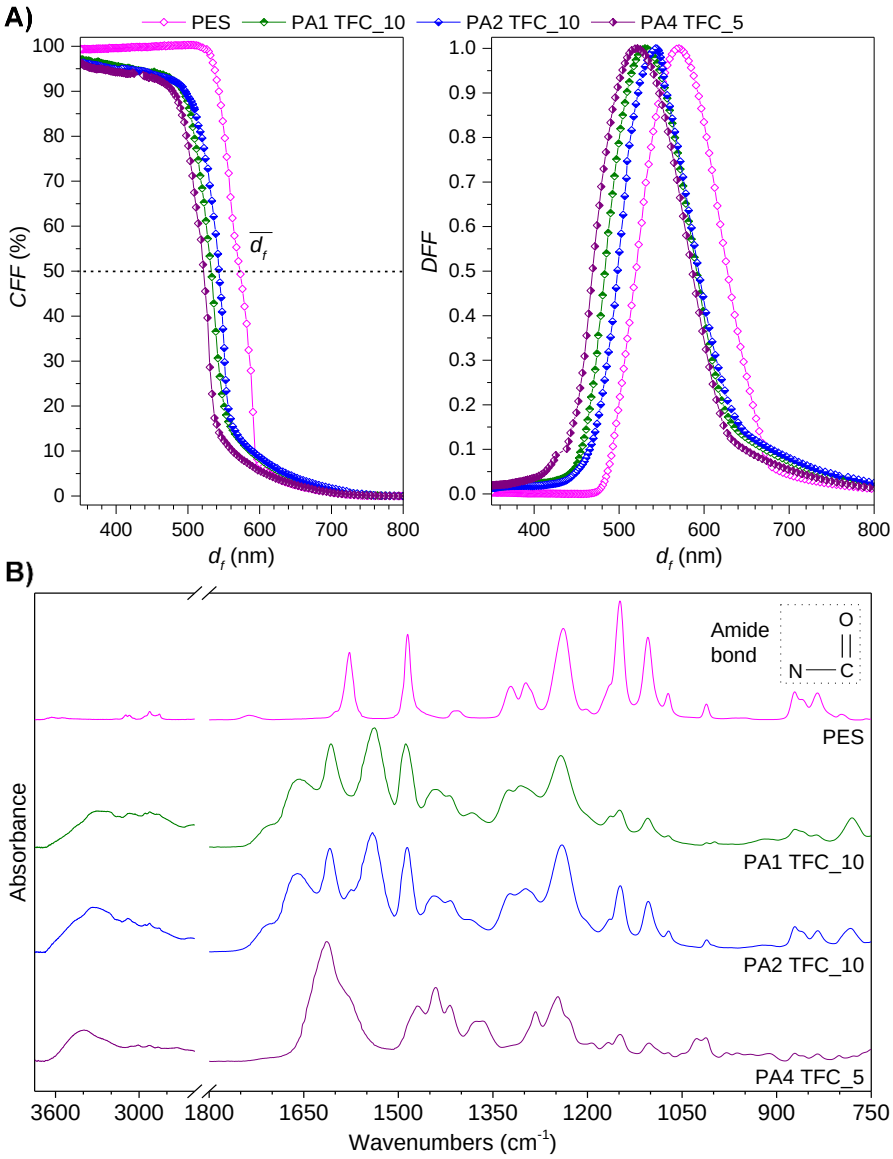

Figure 12.6. Physicochemical properties of the unmodified supporting membrane and the pre-selected polyamide (PA) thin film composite (TFC) membranes. A) Normalized differential (*DFF*) and cumulative (*CFF*) pore size distributions, and B) FTIR spectra of the PES support and the PA TFC membranes (PA1 TFC_10, PA2 TFC_10, PA4 TFC_5).

Table 12.2. Peak assignments of the IR spectra of the unmodified supporting membrane and the pre-selected polyamide (PA) thin film composite (TFC) membranes.

Peak assignments	Wavenumbers (cm^{-1})	Polymers*	REF.
In-phase out-of-plane hydrogen deformation of para-substituted phenyl groups/Aliphatic C–H rocking	835, 858	PES	[1, 5]
Skeletal aliphatic C–C/aromatic hydrogen bending/ rocking	872, 1011, 1073, 1104	PES	[5, 6]
C–SO_2–C symmetric stretching vibration	1148	PES	[1, 5, 6]
C–O–C asymmetric stretching of aryl–O–aryl group	1239	PES	[1, 5, 6]
S=O stretching vibration	1298	PES	[5, 6]
C–SO_2–C asymmetric stretching vibration	1321	PES	[5, 6]
C=C aromatic in-plane ring stretching vibration	1407	PES	[5]
C–H stretching vibration of CH_3–C–CH_3 group	1485	PES	[5, 6]
C=C aromatic in-plane ring stretching vibration	1577	PES	[1, 5, 6]
Polyamide (amide V)	780, 783	PA1, PA2	[5, 7]
Stretching vibration of sulfonic group/C–O stretching vibration of ester groups	1027	PA4	[1]
N–H in-plane bending coupled with C–N stretching/ C–H and N–H deformation vibration of amide bond formation (–CONH) (amide III band)	1283	PA4	[8]
N–H in-plane deformation coupled with C–N stretching of amide bond formation (–CONH) (amide III band)	1383, 1386, 1378	PA1, PA2, PA4	[9, 10]
C–O stretching/O–H bending vibration of carboxylic acid/bending vibration of methylene group (–CH_2–)	1441, 1443, 1441	PA1, PA2, PA4	[6, 11-13]
C–N stretching /N–H in-plane bending vibration of amide group (–CONH) (amide II band)	1538, 1541	PA1, PA2	[1, 5-7, 13, 14]
Protonated amino group (–NH^{3+})/C–C and C–N in plane stretching vibration/ C–N stretching or N–H bending vibration of amide group (amide II band)	1575	PA2	[14-17]
C–C and C–N in plane stretching vibration/ C=O stretching vibration of carboxylic acid salt	1580 (shoulder)	PA4	[15, 18]
N–H deformation/C=C ring stretching vibration/ aromatic ring breathing (aromatic amide)	1607, 1609	PA1, PA2	[1, 5-7, 13, 14]
C=O stretching/C–N stretching vibration of amide bond formation (–CONH) (amide I band)	1614 (peak) 1630 (shoulder)	PA4	[1, 11, 15, 19, 20]
C=O stretching/C–N stretching/C–C–N deformation vibration of amide bond formation (–CONH) (amide I band)	1656, 1660	PA1, PA2	[1, 5-7, 13, 14]
C=O stretching vibration of carboxylic acid group	1715, 1715	PA1, PA2	[5-7]
O–H stretching of carboxylic acid group (–COOH)/ N–H stretching vibration of residual amine groups	3328, 3313 (broad)	PA1, PA2	[1, 5, 16]
O–H stretching of carboxylic acid group (–COOH)/ N–H stretching vibration of residual amine groups	3393 (broad)	PA4	[1, 15, 20-22]

*PES: polyethersulfone; PA1, PA2 and PA4 are different types of polyamides obtained from the monomer combinations summarized in Table 12.1. The colors are used to clarify the link between a specific wavenumber and its corresponding polymer.

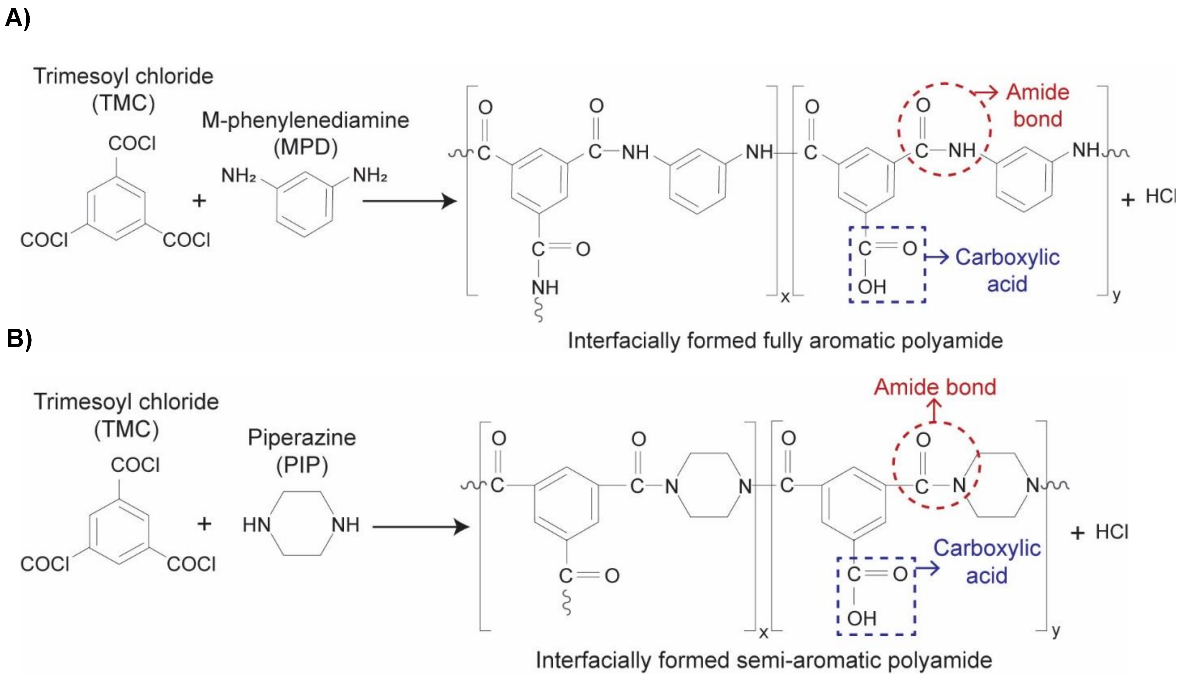

Figure 12.7. Schematic of the mechanism of the interfacial polymerization (IP) reaction of different amine monomers with TMC. A) Aromatic MPD amine reacts with TMC to form a fully aromatic PA TFC membrane and B) aliphatic PIP amine reacts with TMC to form a semi-aromatic PA TFC membrane. x in polymer chain represents the cross-linked part of the resulting polymer and y represents the linear part. x + y = 1. If x = 1, the resulting polyamide is fully cross-linked (i.e. all carbonyl groups formed amide linkages), and if y = 1, the resulting polyamide is fully linear (i.e. one carbonyl group formed carboxylic acid).

Table 12.3. Physicochemical properties and filtration performance of the unmodified supporting membrane (PES) and the pre-selected polyamide (PA) thin film composite (TFC) membranes (PA1 TFC_10, PA2 TFC_10, PA4 TFC_5): mean pore size ($\overline{d_f}$), PA thin layer thickness (δ_{TFC}), zeta potential (ζ-potential), mean humic acid (HA) permeate flux ($\overline{J_{HA}}$), final HA separation factor (α_f) and performance index (PI).

Membrane	Physicochemical properties			Filtration performance		
	$\overline{d_f}$ (nm)	δ_{TFC} (μm)	ζ-potential * (mV)	$\overline{J_{HA}}\left(\frac{kg}{m^2h}\right)$	α_f (%)	$PI\left(\frac{kg}{m^2h}\right)$
PES	573 ± 6	-	-46.4 ± 0.1	269 ± 30	84.0 ± 1.2	98 ± 11
PA1 TFC PES_10	532 ± 6	1.46 ± 0.31	-39.9 ± 0.4	6.4 ± 0.3	70.7 ± 1.2	5.1 ± 0.2
PA2 TFC PES _10	543 ± 3	0.68 ± 0.15	-46.0 ± 0.4	7.3 ± 0.2	66.8 ± 1.4	5.4 ± 0.2
PA4 TFC PES_5	521 ± 6	2.05 ± 0.29	-34.8 ± 0.2	5.7 ± 0.2	91.0 ± 1.1	5.8 ± 0.2

*Values at pH=10.

The surface chemistry of the PA TFC membranes was analyzed by a Thermo Scientific K-Alpha XPS (ESCA) with X-rays generated by a 12 kV electron beam with a spot size of 400 μm. The C, O and N atomic percentages of the different membranes were quantified using the Thermo Scientific Avantage software. Three data points were taken for each membrane sample.

The final atomic percentages of the different elements of each membrane were calculated as the average of the three data points together with their standard deviation. The results of the XPS surface elemental analysis of the pre-selected PA TFC membranes are shown in Fig. 12.8 and summarized in Table 12.4.

According to prior studies [19, 23-26], the O/N ratio allows to quantify the degree of crosslinking of the PA layer. Theoretically, for a fully cross-linked PA layer the O/N ratio is 1:1 while for a linear PA layer it is 2:1 (Fig. 12.7). The fully cross-linked structure implies that each carboxyl group of TMC is bonded to an amine monomer forming an amide linkage. Therefore, all O and N atoms are associated (i.e. three O atoms correspond to three N atoms). However, the fully linear structure leaves one carboxyl group without bonding to an amine monomer forming a carboxylic acid. This structure has two N atoms corresponding to four O atoms. The total theoretical O/N ratio can be therefore calculated as follows [24, 25]:

$$\mathrm{O/N} = \frac{3x+4y}{3x+2y} \tag{12.1}$$

where x and y represent the cross-linked and linear portions of the resulting polymer, respectively. As a result, the crosslinking degree (*CD*) of the pre-selected PA TFC membranes can be estimated as follows [24, 25]:

$$CD\ (\%) = \frac{x}{x+y} \cdot 100 \tag{12.2}$$

From the XPS data, the calculated O/N ratio of the membranes PA1 TFC_10, PA2 TFC_10 and PA4 TFC_5 was 1.24, 2.0 and 1.20, respectively. From Eqs. (12.1) and (12.2), the obtained *CD* of the membranes PA2 TFC_10 and PA4 TFC_5 was 67.9 and 72.7% (i.e. partial cross-linked structure), whereas that of the membrane PA1 TFC_10 was 0% (i.e. fully linear structure). The increasing order of the *CD* of the PA TFC membranes (PA2 TFC_10 < PA1 TFC_10 < PA4 TFC_5) followed the previously mentioned increasing order of their δ_{TFC} values (Table 12.3). A higher crosslinking degree corresponded to a higher thickness of the PA layer.

Table 12.4. XPS surface elemental analysis and crosslinking degree (*CD*) estimation of the pre-selected polyamide (PA) thin film composite (TFC) membranes.

Membrane	Atomic percentage			Relative ratio O/N	*CD* (%)
	C (%)	O (%)	N (%)		
PA1 TFC PES_10	75.04 ± 0.51	13.84 ± 0.18	11.12 ± 0.34	1.24	67.9
PA2 TFC PES _10	73.08 ± 0.23	17.94 ± 0.30	8.98 ± 0.06	2.00	0
PA4 TFC PES _5	72.72 ± 0.43	14.86 ± 0.42	12.41 ± 0.14	1.20	72.2

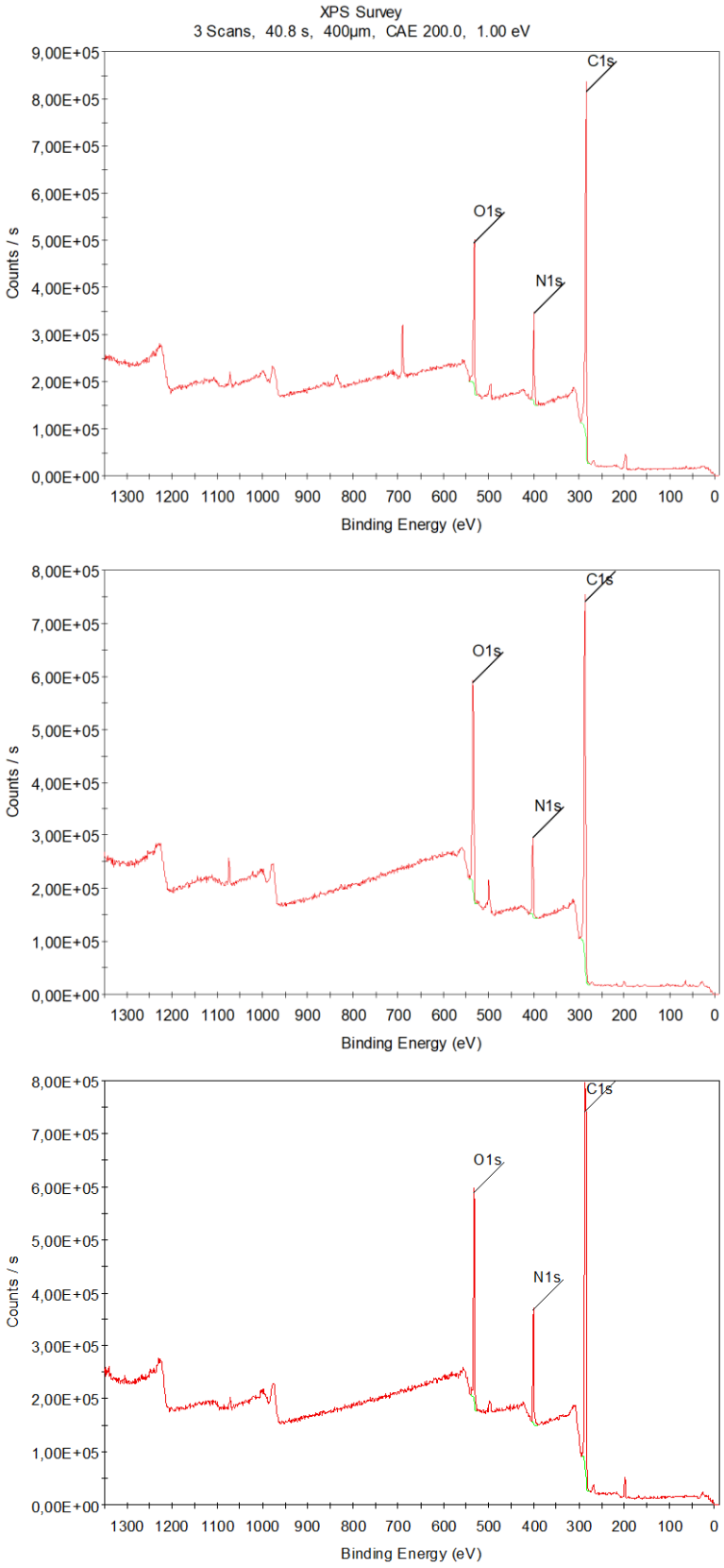

Figure 12.8. XPS spectra of the pre-selected polyamide (PA) thin film composite (TFC) membranes. A) PA1 TFC_10, B) PA2 TFC_10 and C) PA4 TFC_5.

12.2.3 Filtration performance of the pre-selected polyamide thin film composite membranes

Fig. 12.9 shows the filtration results of both the supporting membrane (PES) and the pre-selected PA TFC membranes (PA1 TFC_10, PA2 TFC_10 and PA4 TFC_5). Table 12.3 summarizes some filtration data together with some physicochemical properties of these membranes. A good correlation was found between the filtration properties of the PA TFC membranes and their morphological and chemical structures. It was observed a decrease of $\overline{J_{HA}}$, PA2 TFC_10 (7.3 kg/m^2 h) > PA1 TFC_10 (6.4 kg/m^2 h) > PA4 TFC_5 (5.7 kg/m^2 h), following the same order than the increase of α_f, PA2 TFC_10 (66.8%) < PA1 TFC_10 (70.7%) < PA4 TFC_5 (91.0%) (Fig. 12.9-A). This trend agreed with the reduction of the mean pore size ($\overline{d_f}$) of the membranes and with both the increase of the thickness of the PA layer (δ_{TFC}) and its crosslinking degree (*CD*) (Tables 12.3 and 12.4). Therefore, the membrane PA4 TFC_5, with the thickest and highest cross-linked PA thin layer was the membrane that exhibited the lowest HA permeate flux, the highest HA separation factor and the greatest filtration performance (Fig. 12.9 and Table 12.3).

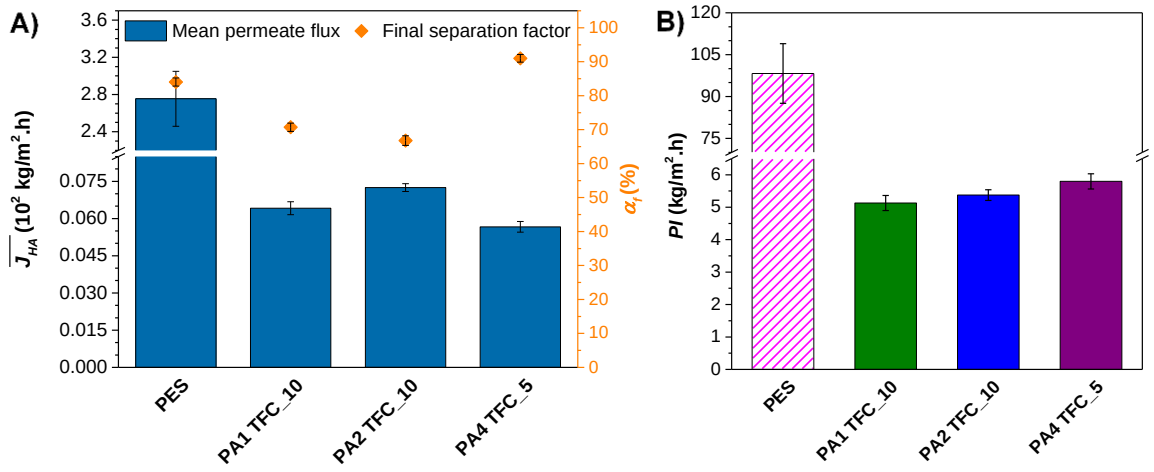

Figure 12.9. Filtration properties of the unmodified supporting membrane and the pre-selected polyamide (PA) thin film composite (TFC) membranes. A) Mean humic acid (HA) permeate flux ($\overline{J_{HA}}$) together with final HA separation factor (α_f), and B) performance index (*PI*) of the PES support and the PA TFC membranes (PA1 TFC_10, PA2 TFC_10, PA4 TFC_5). The filtration tests were conducted with 15 mg/L HA feed aqueous solution at pH 11 and 10^5 Pa transmembrane pressure.

The ζ-potential of the membranes PA1 TFC_10, PA2 TFC_10 and PA4 TFC_5 was -39.9, -46.0 and -34.8, respectively. The decrease of the negative surface charge of these membranes followed the order PA2 TFC_10 > PA1 TFC_10 > PA4 TFC_5, which was consistent with the increase of their respective *CD*. The negative surface charge of this type of PA TFC membranes could be attributed to the deprotonation of carboxyl groups (–COOH → –COO$^-$) dissociated from unreacted acid chlorides of TMC [12, 19]. Therefore, a higher *CD* indicated a lower

amount of carboxyl groups available to be deprotonated, which would be the reason of the lowest negative surface charge of the membrane PA4 TFC_5 compared to the membranes PA1 TFC_10 and PA2 TFC_10. It is known that the presence of carboxylic acid groups (–COOH) on the membrane surface increases its hydrophilicity [11, 20, 27]. Therefore, the membrane PA2 TFC_10 with a fully linear structure of the PA layer and 0% crosslinking degree was assumed to have a higher number of –COOH groups on its surface and, consequently, a higher hydrophilicity. The latter assumption agrees well with the higher permeate flux exhibited by the membrane PA2 TFC_10.

All pre-selected PA TFC membranes exhibited similar filtration performance (Fig. 12.9-B). However, the membrane PA4 TFC_5 achieved the highest *PI* value (5.8 kg/m^2 h) with a very high HA separation factor (91.0%). Therefore, the IP approach followed to develop the membrane PA4 TFC_5 was selected to prepare the PA TFC membranes on ENM1 and PES supports in the present study. These IP conditions were 5 min reaction time of 1% w/w PIP, 1% w/w TEA (acid acceptor) and 0.25% w/v TMC.

12.3 Polyester *versus* polyamide thin film composite membranes

Fig. 12.10 shows, as an example, the granular structure formed within the inter-fiber space of the membrane PA TFNC1_5, which was prepared by reacting PIP and TMC in presence of TEA for 5 min as described in Fig. 5.2-B of Chapter 5.

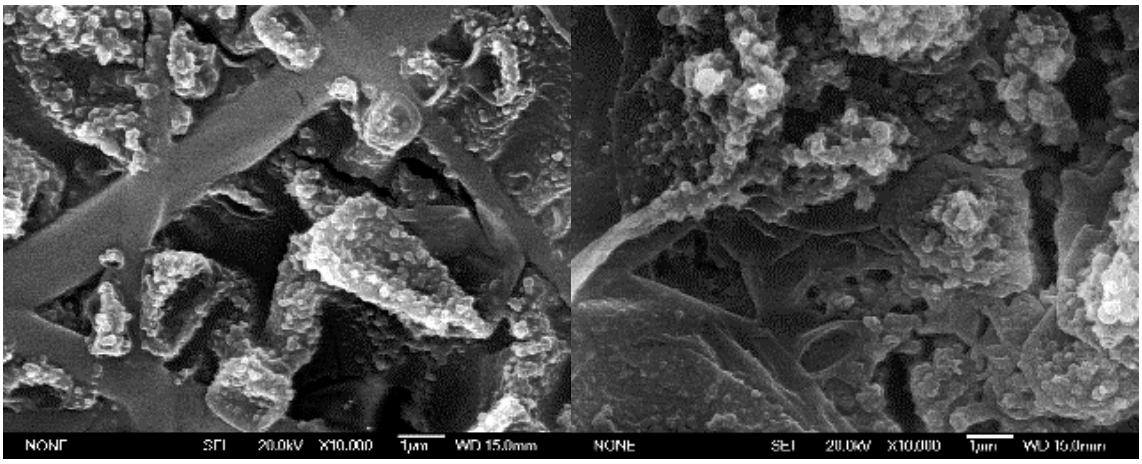

Figure 12.10. SEM images taken at X10000 magnification showing the granular structure formed within the inter-fiber space of the membrane PA TFNC1_5.

References

[1] C.Y. Tang, Y.-N. Kwon, J.O. Leckie, Effect of membrane chemistry and coating layer on physiochemical properties of thin film composite polyamide RO and NF membranes: I. FTIR and XPS characterization of polyamide and coating layer chemistry, Desalination, 242 (2009) 149-167.

[2] A.L. Ahmad, B.S. Ooi, Optimization of composite nanofiltration membrane through pH control: Application in CuSO4 removal, Separation and Purification Technology, 47 (2006) 162-172.

[3] A.K. Ghosh, B.-H. Jeong, X. Huang, E.M.V. Hoek, Impacts of reaction and curing conditions on polyamide composite reverse osmosis membrane properties, Journal of Membrane Science, 311 (2008) 34-45.

[4] C. Klaysom, S. Hermans, A. Gahlaut, S. Van Craenenbroeck, I.F.J. Vankelecom, Polyamide/polyacrylonitrile (PA/PAN) thin film composite osmosis membranes: Film optimization, characterization and performance evaluation, Journal of Membrane Science, 445 (2013) 25-33.

[5] P.S. Singh, S.V. Joshi, J.J. Trivedi, C.V. Devmurari, A.P. Rao, P.K. Ghosh, Probing the structural variations of thin film composite RO membranes obtained by coating polyamide over polysulfone membranes of different pore dimensions, Journal of Membrane Science, 278 (2006) 19-25.

[6] N.-N. Bui, M.L. Lind, E.M.V. Hoek, J.R. McCutcheon, Electrospun nanofiber supported thin film composite membranes for engineered osmosis, Journal of Membrane Science, 385-386 (2011) 10-19.

[7] M. Fathizadeh, A. Aroujalian, A. Raisi, Effect of lag time in interfacial polymerization on polyamide composite membrane with different hydrophilic sub layers, Desalination, 284 (2012) 32-41.

[8] B.R. Singh, D.B. DeOliveira, F.-N. Fu, M.P. Fuller, Fourier transform infrared analysis of amide III bands of proteins for the secondary structure estimation, Proc. SPIE 1890, Biomolecular Spectroscopy III, 1993.

[9] H. Li, W. Shi, Q. Du, R. Zhou, H. Zhang, X. Qin, Improved separation and antifouling properties of thin-film composite nanofiltration membrane by the incorporation of cGO, Applied Surface Science, 407 (2017) 260-275.

[10] H.S. Lee, S.J. Im, J.H. Kim, H.J. Kim, J.P. Kim, B.R. Min, Polyamide thin-film nanofiltration membranes containing TiO_2 nanoparticles, Desalination, 219 (2008) 48-56.

[11] J. Rezania, V. Vatanpour, A. Shockravi, M. Ehsani, Preparation of novel carboxylated thin-film composite polyamide-polyester nanofiltration membranes with enhanced antifouling property and water flux, Reactive and Functional Polymers, 131 (2018) 123-133.

[12] A. Akbari, E. Aliyarizadeh, S.M. Mojallali Rostami, M. Homayoonfal, Novel sulfonated polyamide thin-film composite nanofiltration membranes with improved water flux and anti-fouling properties, Desalination, 377 (2016) 11-22.

[13] A. Prakash Rao, S.V. Joshi, J.J. Trivedi, C.V. Devmurari, V.J. Shah, Structure–performance correlation of polyamide thin film composite membranes: effect of coating conditions on film formation, Journal of Membrane Science, 211 (2003) 13-24.

[14] G.-R. Xu, J.-N. Wang, C.-J. Li, Polyamide nanofilm composite membranes (NCMs) supported by chitosan coated electrospun nanofibrous membranes: Preparation and separation performance research, Desalination, 328 (2013) 31-41.

[15] J. Xiang, Z. Xie, M. Hoang, K. Zhang, Effect of amine salt surfactants on the performance of thin film composite poly(piperazine-amide) nanofiltration membranes, Desalination, 315 (2013) 156-163.

[16] Y. Song, F. Liu, B. Sun, Preparation, characterization, and application of thin film composite nanofiltration membranes, Journal of Applied Polymer Science, 95 (2005) 1251-1261.

[17] K.Y. Wang, T.-S. Chung, G. Amy, Developing thin-film-composite forward osmosis membranes on the PES/SPSf substrate through interfacial polymerization, AIChE Journal, 58 (2012) 770-781.

[18] N.-W. Oh, J. Jegal, K.-H. Lee, Preparation and characterization of nanofiltration composite membranes using polyacrylonitrile (PAN). II. Preparation and characterization of polyamide composite membranes, Journal of Applied Polymer Science, 80 (2001) 2729-2736.

[19] Y. Li, Y. Su, J. Li, X. Zhao, R. Zhang, X. Fan, J. Zhu, Y. Ma, Y. Liu, Z. Jiang, Preparation of thin film composite nanofiltration membrane with improved structural stability through the mediation of polydopamine, Journal of Membrane Science, 476 (2015) 10-19.

[20] N. Misdan, W.J. Lau, A.F. Ismail, Physicochemical characteristics of poly(piperazine-amide) TFC nanofiltration membrane prepared at various reaction times and its relation to the performance, Journal of Polymer Engineering, 35 (2015) 71-78.

[21] A.L. Ahmad, B.S. Ooi, Properties–performance of thin film composites membrane: study on trimesoyl chloride content and polymerization time, Journal of Membrane Science, 255 (2005) 67-77.

[22] Y. Li, Y. Su, Y. Dong, X. Zhao, Z. Jiang, R. Zhang, J. Zhao, Separation performance of thin-film composite nanofiltration membrane through interfacial polymerization using different amine monomers, Desalination, 333 (2014) 59-65.

[23] C.Y. Tang, Y.-N. Kwon, J.O. Leckie, Probing the nano- and micro-scales of reverse osmosis membranes–A comprehensive characterization of physiochemical properties of uncoated and coated membranes by XPS, TEM, ATR-FTIR, and streaming potential measurements, Journal of Membrane Science, 287 (2007) 146-156.

[24] O. Akin, F. Temelli, Probing the hydrophobicity of commercial reverse osmosis membranes produced by interfacial polymerization using contact angle, XPS, FTIR, FE-SEM and AFM, Desalination, 278 (2011) 387-396.

[25] M. Tian, C. Qiu, Y. Liao, S. Chou, R. Wang, Preparation of polyamide thin film composite forward osmosis membranes using electrospun polyvinylidene fluoride (PVDF) nanofibers as substrates, Separation and Purification Technology, 118 (2013) 727-736.

[26] J. Xu, H. Yan, Y. Zhang, G. Pan, Y. Liu, The morphology of fully-aromatic polyamide separation layer and its relationship with separation performance of TFC membranes, Journal of Membrane Science, 541 (2017) 174-188.

[27] M. Jahanshahi, A. Rahimpour, M. Peyravi, Developing thin film composite poly(piperazine-amide) and poly(vinyl-alcohol) nanofiltration membranes, Desalination, 257 (2010) 129-136.

13

Appendix C

Supplementary information of Chapter 6

CNT properties

The CNT used in this study has an average length of 100 μm, an average diameter of 15 nm (5–30 nm), and 5% residual iron according to manufacturer specification.

PVDF and PC membrane preparation before ICE deposition

It is worth noting that the cleaning procedure of the PVDF membrane explaining in this study (ultrasonication in IPA for 5 min, then in DI for 5 min, and kept in IPA prior to use) was applied before the preparation of the ICE. PVDF membrane is hydrophobic, then the deposition of the CNT on the membrane surface was easily and better developed when the membrane was previously wet. Two different wetting/cleaning experiments were tried, consisting in either only immersed the PVDF membrane in IPA (method 1) or ultrasonicated in IPA (5 min), then in DI (5 min), and kept in IPA (method 2) before ICE deposition. It was observed by electric conductivity measurements over the ICE that the method 2 reduced the resistivity of the ICE channels about 41 to 53%, thus improving their conductivity. These results were consistent for different volumes of the CNT solution used for ICE preparation. As high conductivity is desirable for the applied cell potential over the ICE to improve the effectiveness of the bacterial electrochemical filtration, it was decided to use the method 2 as wetting/cleaning procedure.

On the other hand, PC membrane was hydrophilic, then wetting step was not necessary for a properly ICE deposition on the membrane surface.

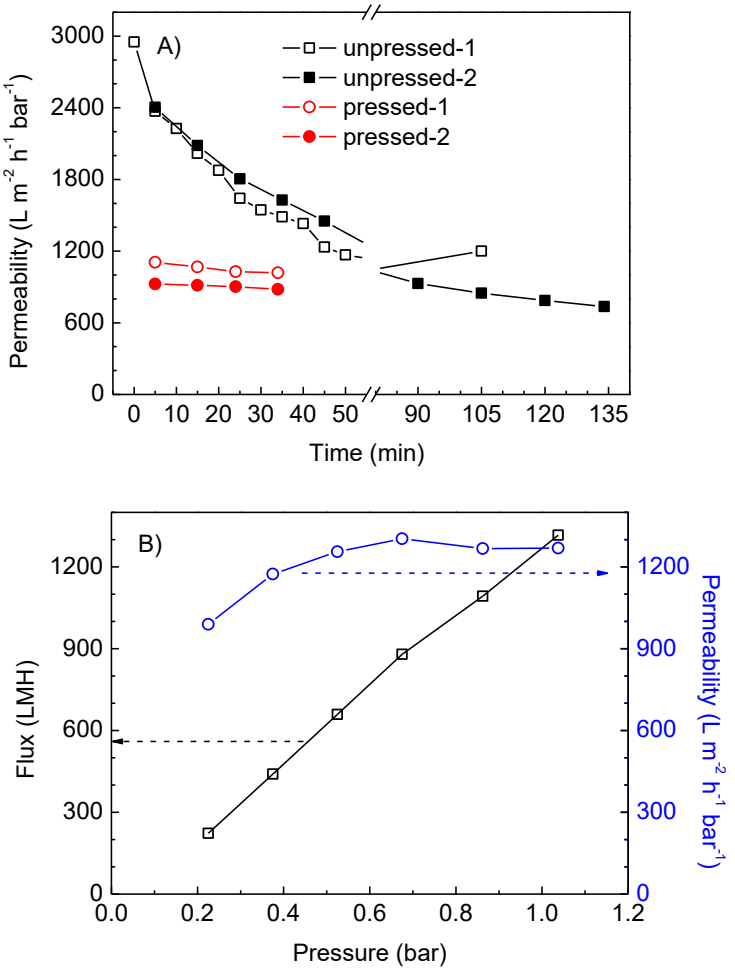

Figure 13.1. Time-dependent permeability of the unpressed and mechanically-pressed PVDF membranes. A) Permeability change with filtration time for the unpressed and pressed PVDF membranes (after 100 min DI filtration, the unpressed membranes had a similar stable permeability to the pressed membranes) and B) flux and permeability versus pressure for the pressed PVDF membranes.

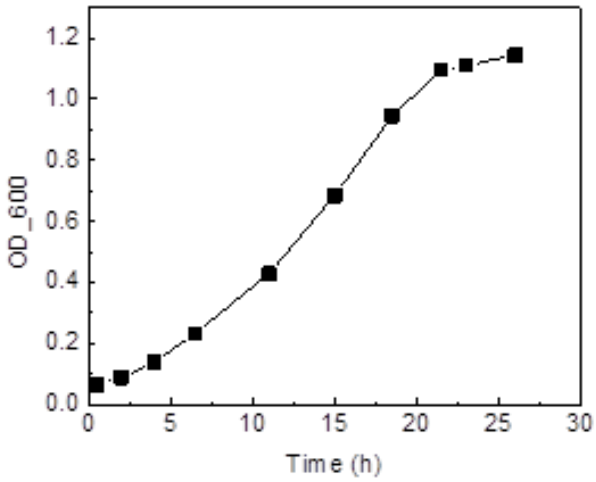

Figure 13.2. Growth curve of the *P. fluorescens* in TSB by seeding from a TSA plate at 30°C. It can be told that 18 h is mid-to-late exponential phase and is able to provide high biomass yield.

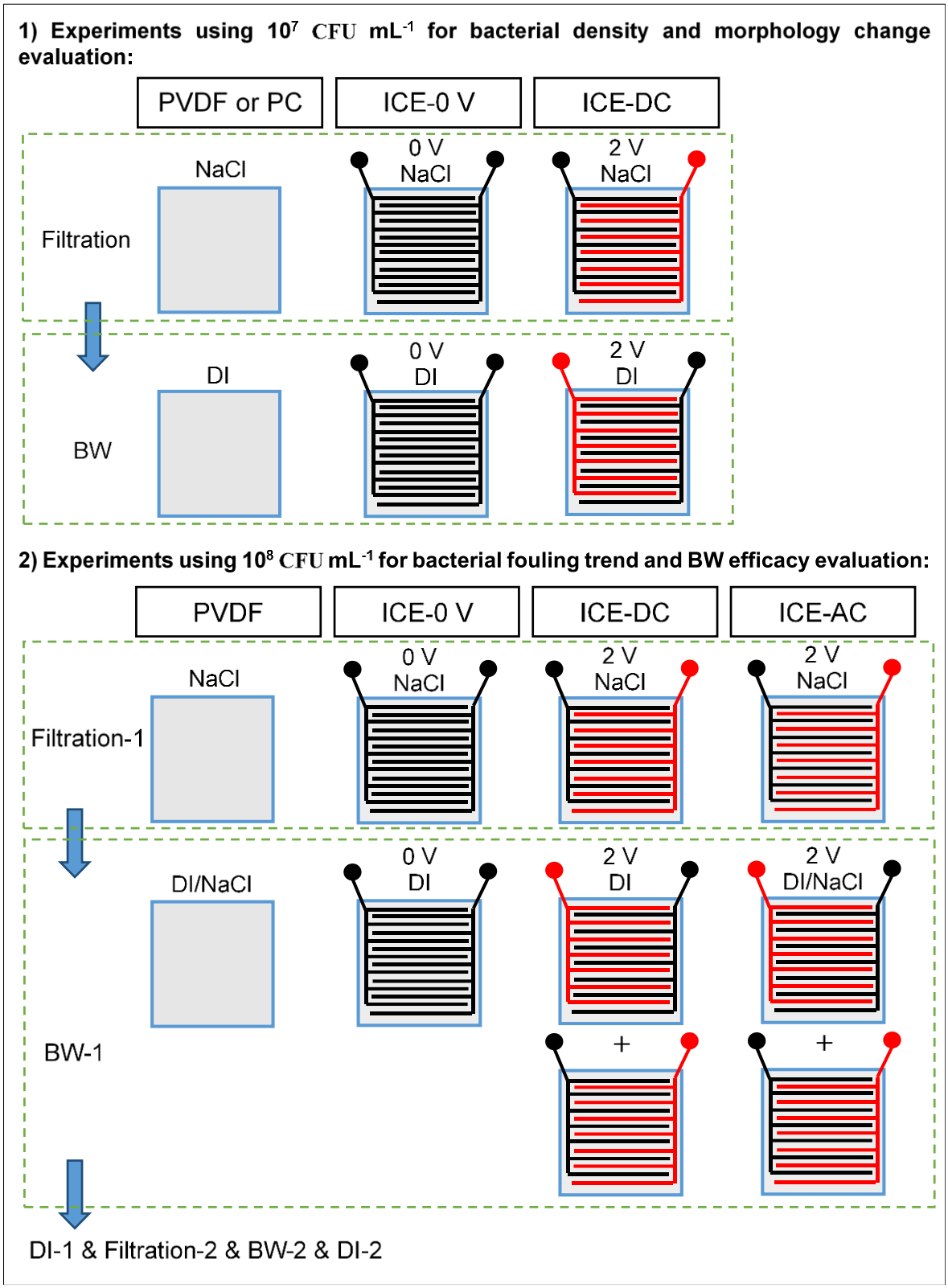

Figure 13.3. Bacterial filtration experimental protocol diagram. Protocol 1 was used to evaluate bacterial removal, surface density, and morphology post-filtration. Protocol 2 was used to evaluate bacterial fouling trend and backwash efficacy.

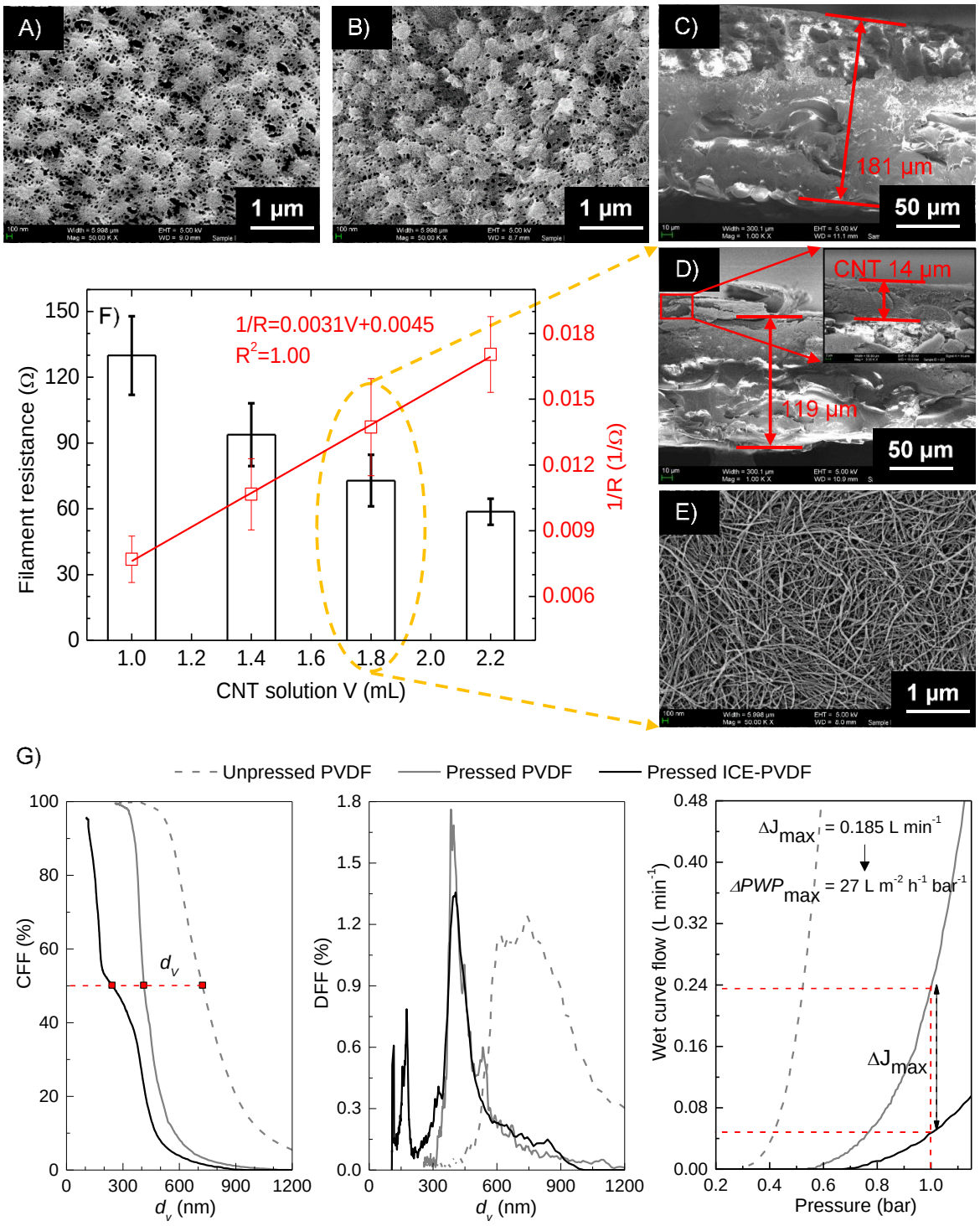

Figure 13.4. Cross-sectional and superficial morphology of the PVDF and ICE-PVDF membranes. SEM images of: A, B) top surface of unpressed and pressed PVDF membranes, respectively, and C, D) cross-section of unpressed PVDF and pressed PVDF membrane with ICE on top, respectively, E) top surface of the ICE. F) Electric resistance of a single ICE filament with varying CNT-Nafion volume and G) cumulative pore size distribution (*CFF*), differential pore size distribution (*DFF*), and wet curve flow of the unpressed PVDF, pressed PVDF, and pressed ICE-PVDF measured by gas-liquid displacement porometer.

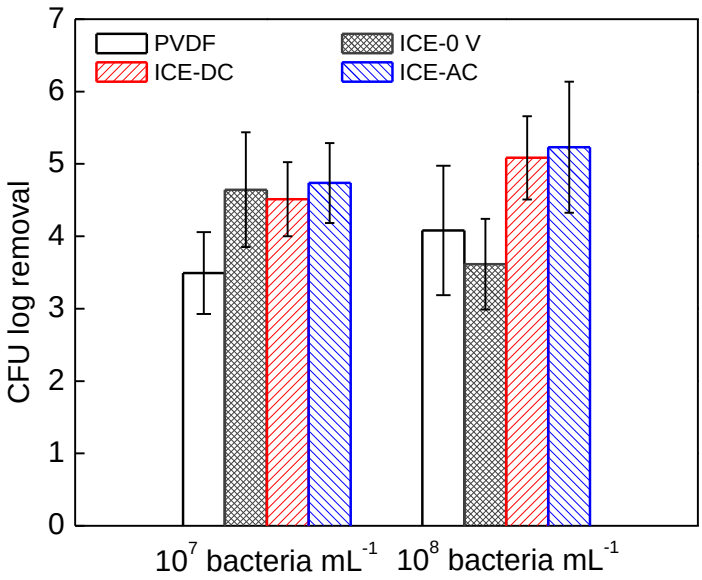

Figure 13.5. Bacterial removal by the PVDF membranes with or without ICE in the presence or absence of applied voltage. Experiments were completed by filtering 10^7 or 10^8 CFU mL^{-1} in 155 mM NaCl solution at the flow rate of 1.2 mL/min (i.e. J = 163.6 L/m^2 h). Feed and permeate samples were taken after 30 min of filtration to determine CFU. The error bars are used to describe the ranges of the data instead of confidence intervals.

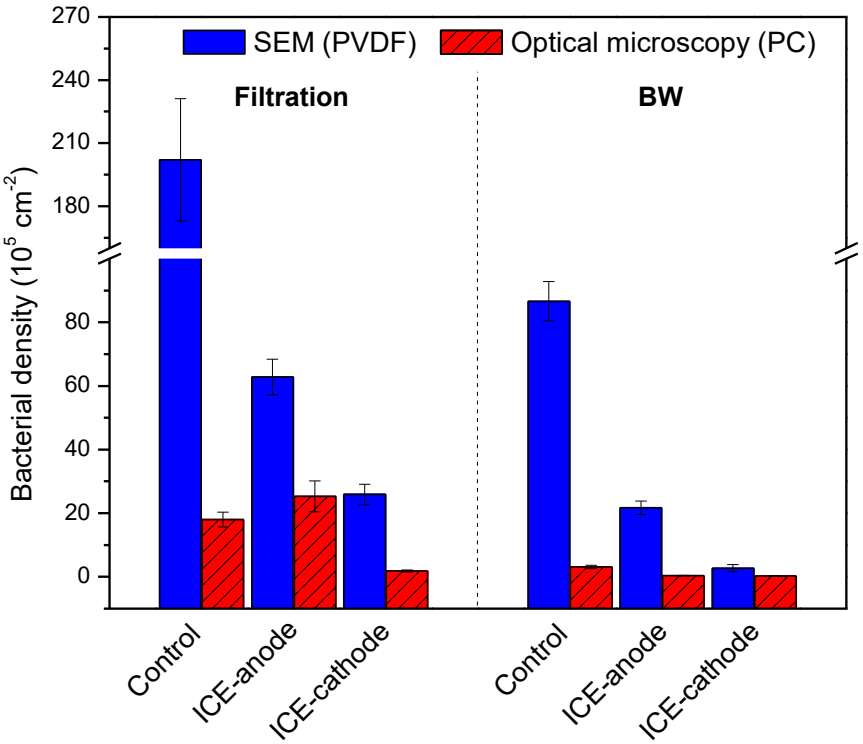

Figure 13.6. Bacterial density on PVDF and PC membrane surfaces with or without ICE after filtration and BW. Experiments were completed by filtering 10^7 CFU mL^{-1} in 155 mM NaCl solution for 60 min at the flow rate of 1.2 mL/min (i.e. J = 163.6 L/m^2 h) and BW at the same flow rate for 10 min with DI water. For the PVDF and PC with ICE, 2 V DC and 8 V DC (with the reversed polarity) were applied during filtration and BW, respectively.

By optical microscopy, there were 18.0 ± 2.3 and 3.1 ± 0.5 × 10^5 CFU/cm^2 on the control PC before and after BW. In comparison, the bacterial density increased by 41% on the ICE anode (25.3 ± 4.9 × 10^5 CFU/cm^2) and decreased by 90% on the ICE cathode (1.8 ± 0.3 × 10^5 CFU/cm^2) after electrochemical filtration at 2 V DC. After BW, the bacterial density further decreased on the anode (0.4 ± 0.1 × 10^5 CFU/cm^2) and cathode (0.3 ± 0.1 × 10^5 CFU/cm^2), 87 and 90% lower than the control, respectively.

The PVDF, PC, and ICE have notable difference in surface hydrophobicity (DI contact angle was 83.5, 65.9, and 118.7°, respectively) and surface roughness (smooth, shiny & very smooth, and rough, respectively), thus the bacterial deposition will vary e.g., there were an order of magnitude greater bacterial density on PVDF versus PC. Plus, the result is also dependent on the bacterial counting technique (SEM and fluorescence microscopy follow very different sample preparation procedures).

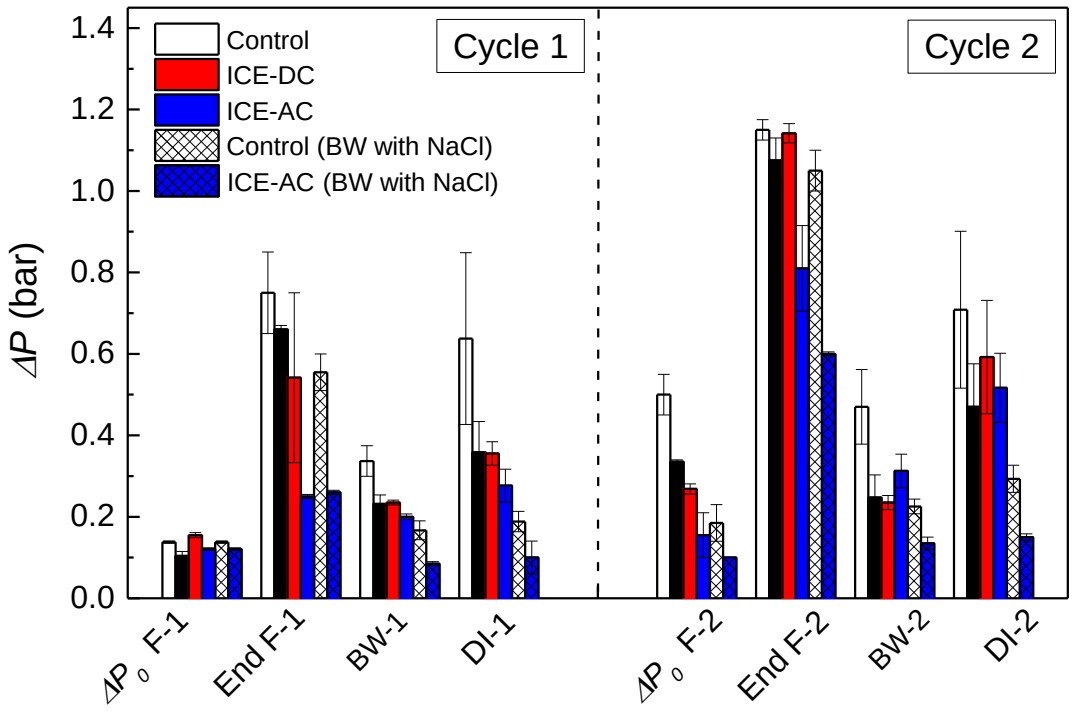

Figure 13.7. Δ*P* values for the control PVDF and the ICE-PVDF in different steps of the bacterial filtration test. Experiments were completed using 10^8 CFU mL^{-1} filtration for 60 min or up to 1.1 bar in the absence or presence of 2 V DC or AC. A 10 min BW with DI or saline solution was carried out after each filtration cycle in the absence or presence of 8 V DC (for the DC filtration, polarity was reversed in comparison to filtration for the first 5 min and then reversed again for the final 5 min to clean both electrodes) or 8 V AC (for the 2 V AC filtration). DI water was filtered for 10 min after each BW cycle to determine the fouling resistance recovery (*FRR*) of the process. For all, bacteria filtration, BW filtration and DI water filtration, the flow rates were kept at 1.2 mL/min (i.e. J = 163.6 L/m^2 h). Experimental procedure diagram is displayed in Fig. 13.3, Protocol 2.

Table 13.1. Membrane morphology characterization and pure water permeability of PVDF membranes with or without ICE.

Membrane	Morphological characteristics					Filtration properties
	δ (μm)	ε_S (%)	ε_V (%)	d_S (nm)	d_V (nm)	*PWP* (L/m² h bar)
PVDF unpressed	181 ± 6	15.7 ± 1.4	52.8 ± 2.2	44 ± 4	722 ± 59	2950 ± 323
PVDF pressed	119 ± 3	8.1 ± 0.9	39.0 ± 4.5	31 ± 4	412 ± 13	935 ± 71
ICE pressed	14 ± 1	25.5 ± 4.1	-	52 ± 10	175 ± 7	--
ICE-PVDF pressed	123 ± 6	-	31.4 ± 7.5	-	245 ± 14	902 ± 12

Table 13.2. Welch's t-test summary of the bacterial removal under different conditions.

Influent		PVDF	ICE-0 V	ICE-DC
10^7 CFU mL^{-1}	**ICE-0 V**	0.134		
	ICE-DC	**0.070**	0.251	
	ICE-AC	0.134	0.89	0.713
10^8 CFU mL^{-1}	**ICE-0 V**	0.655		
	ICE-DC	0.409	**0.247**	
	ICE-AC	0.423	0.286	0.879

Table 13.3. Bacterial density on the PVDF and PC membrane surfaces with or without ICE after 10^7 CFU mL^{-1} filtration and DI BW.

Surfaces	Conditions	Characterization technique	
		SEM for PVDF membranes (10^5 cm^{-2})	Optical microscopy for PC membranes (10^5 cm^{-2})
Control	Filtration	202.1 ± 29.1	18.0 ± 2.3
	BW	86.6 ± 6.2	3.1 ± 0.5
ICE	Filtration anode, 2 V DC	62.8 ± 5.6	25.3 ± 4.9
	BW cathode, 8 V	2.7 ± 1.1	0.3 ± 0.1
	Filtration cathode, 2 V DC	25.9 ± 3.2	1.8 ± 0.3
	BW anode, 8 V	21.7 ± 2.1	0.4 ± 0.1

Table 13.4. Exponential fitting results of the pressure increase of the control PVDF and ICE-PVDF after 10^8 CFU mL^{-1} filtration and DI BW.

Membrane	Filtration-1		Filtration-2	
	ΔP_0 (bar)	k (min^{-1})	ΔP_0 (bar)	k (min^{-1})
PVDF	0.138 ± 0.003	0.029 ± 0.001	0.427 ± 0.060	0.108 ± 0.012
ICE-0 V	**0.104** ± 0.011	0.033 ± 0.002	0.338 ± 0.025	0.0489 ± 0.0002
ICE-DC	0.155 ± 0.006	0.019 ± 0.003	0.245 ± 0.001	0.0455 ± 0.0005
ICE-AC	0.121 ± 0.003	**0.0123** ± 0.0005	**0.138** ± 0.005	**0.0299** ± 0.0009

The lowest values in each column are in **bold**.

14

Appendix D

Supplementary information of Chapter 7

Table 14.1 summarizes the results of the XPS analysis. Note that O/C atomic ratio in Fig. 7.2 in the Chapter 7 is obtained by calculating the average for each of the samples. Some of the samples contained sulfur (S), which might be a residual of the oxidation process. The nitrogen (N) can be connected to atmospheric adsorption.

Table 14.1. XPS percentage peak area data for the six samples. The standard deviation for the atomic ratio of each element is ± 1%.

Sample	Test	C1s (%)			Atomic percentage (%)			
		C–O	C–C C=C	C=O	C	O	N	S
1	a	24.36	70.29	5.35	79.62	14.14	2.44	0.8
	b	23.39	71.83	4.77	78.38	16.62	4.11	0.89
2	a	53.33	46.67	0	68.27	29.81	1.42	0
	b	52.33	47.67	0	68.76	29.95	1.29	0
	c	53.44	46.56	0	67.96	29.68	1.97	0.38
3	a	56.49	40.69	2.82	66.6	33.4	0	0
	b	56.63	40.08	3.29	66.05	33.43	0.53	0
4	a	64.45	33.01	2.54	65.25	33.8	0	0.96
	b	65.72	31.41	2.87	65.81	33.86	0	0.33
	c	63.25	32.99	3.76	65.66	33.88	0	0.46
5	a	62.94	33.83	3.23	63.79	34.15	1.02	1.04
	b	64.9	32.84	2.25	64.02	34.16	0.87	0.95
	c	63.23	33.32	3.46	63.86	34.86	0.27	1.01
6	a	59.43	34.15	6.42	63.75	35.56	0	0.69
	b	59.82	34.72	5.46	63.69	35.25	0.49	0.57
	c	61.6	33.4	5.01	63.17	34.8	1.27	0.75

Fig. 14.1 left represents an SEM image of GO flakes cast on silica. Fig. 14.1 right represents the same image analyzed by ImageJ in order to determine the size distribution of the GO flake.

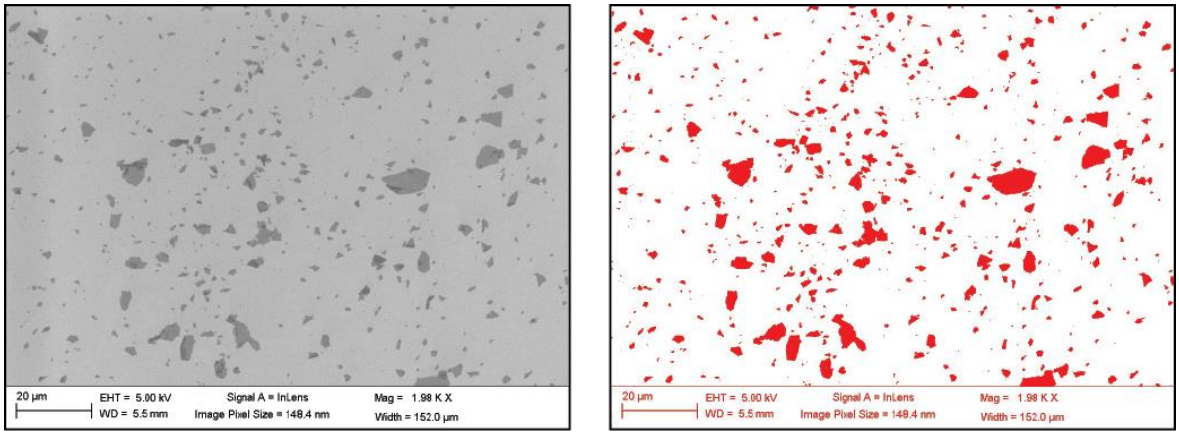

Figure 14.1. SEM of monolayer GO and flake size distribution via ImageJ analysis.

Fig. 14.2 presents the settling of GO flakes in Sample 1. The photo was taken 10 minutes after the injection of GO and highlights the pure colloidal stability of Sample 1.

Figure 14.2. Aggregation and settling of GO in Sample 1.

Fig. 14.3 represents the technique used for determining the GO layer percentage. In the first step, the substrate (silica) is changed to white. Then an intensity histogram is generated followed by deconvolution of the histogram into monolayer and multilayer peaks. The monolayer percentage is then calculated by considering the relative area under each peak in the histogram.

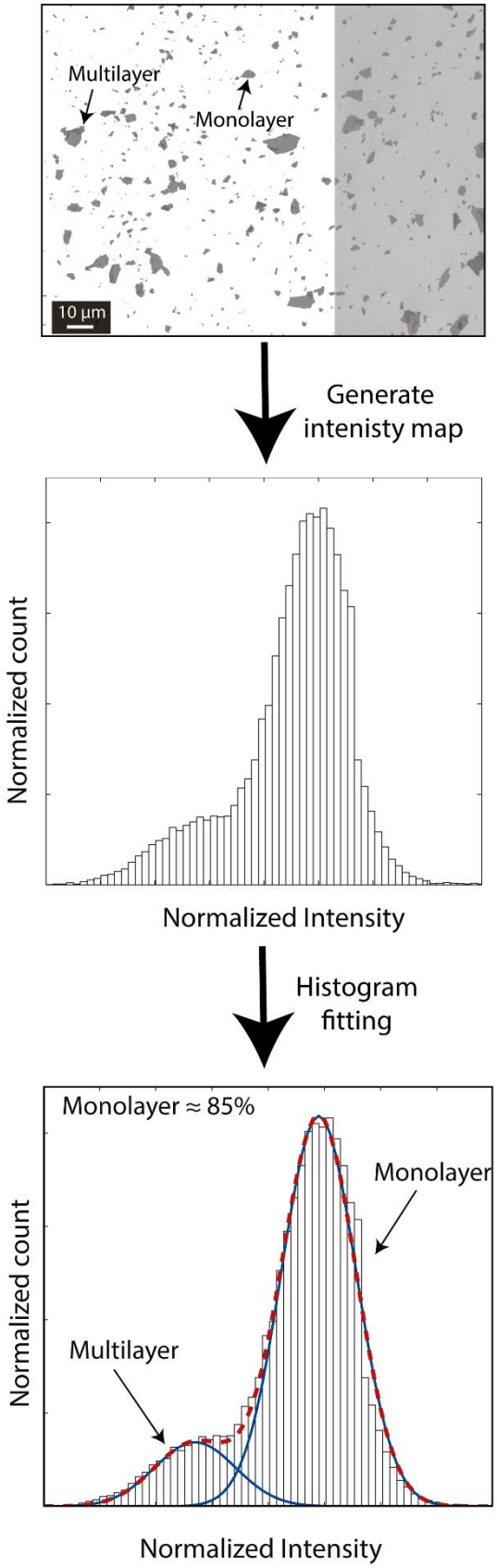

Figure 14.3. GO monolayer percentage evaluation.

Fig. 14.4 represents the elbow method used to determine the optimal number of clusters used in Fig. 7.6 in Chapter 7. Six is the lowest number of clusters to achieve 90% of variance explained.

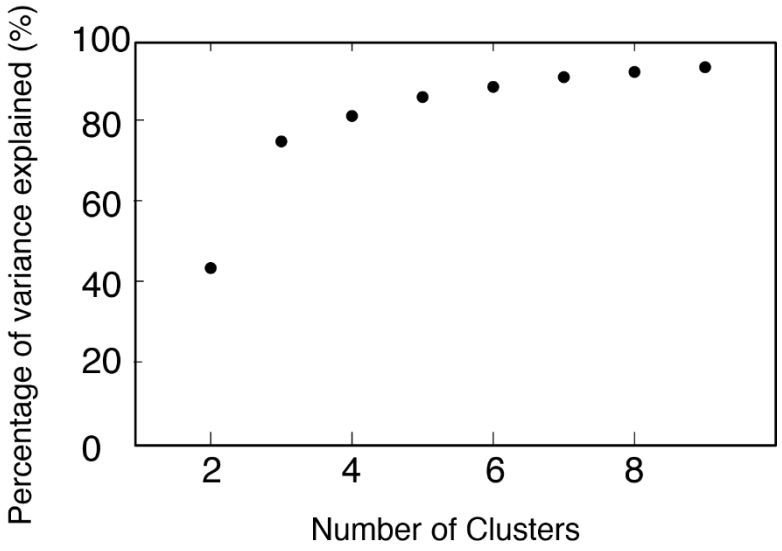

Figure 14.4. Elbow method to determine the optimal number of clusters.

Fig. 14.5 collects representative SEM images of bacterial adhesion for Samples 1, 2, 3 and 5. Please refer to Fig. 7.7 in Chapter 7 for Samples 4 and 6.

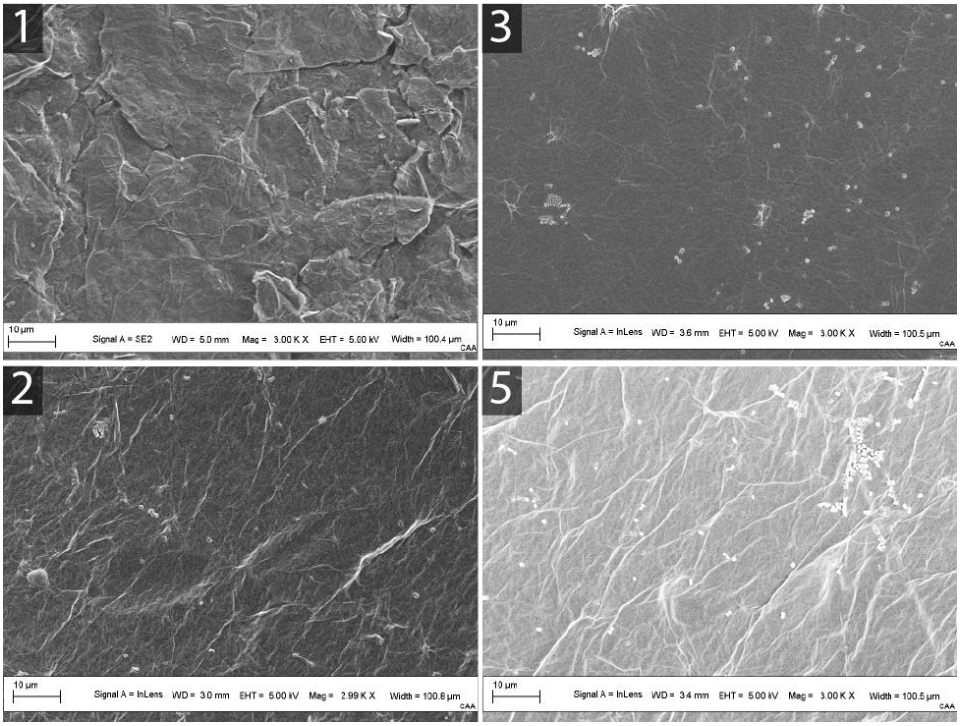

Figure 14.5. Representative SEM images of *E. coli* bacteria adhesion onto GOM surfaces. The samples are identified by numbers.

Fig. 14.6 represents the permeability curve of the six GOMs. The applied pressure was varied from 0 to 5.5 bar. The data contained in Fig. 7.7-C in Chapter 7 refers to permeability evaluated at 5 bar in Fig. 14.6.

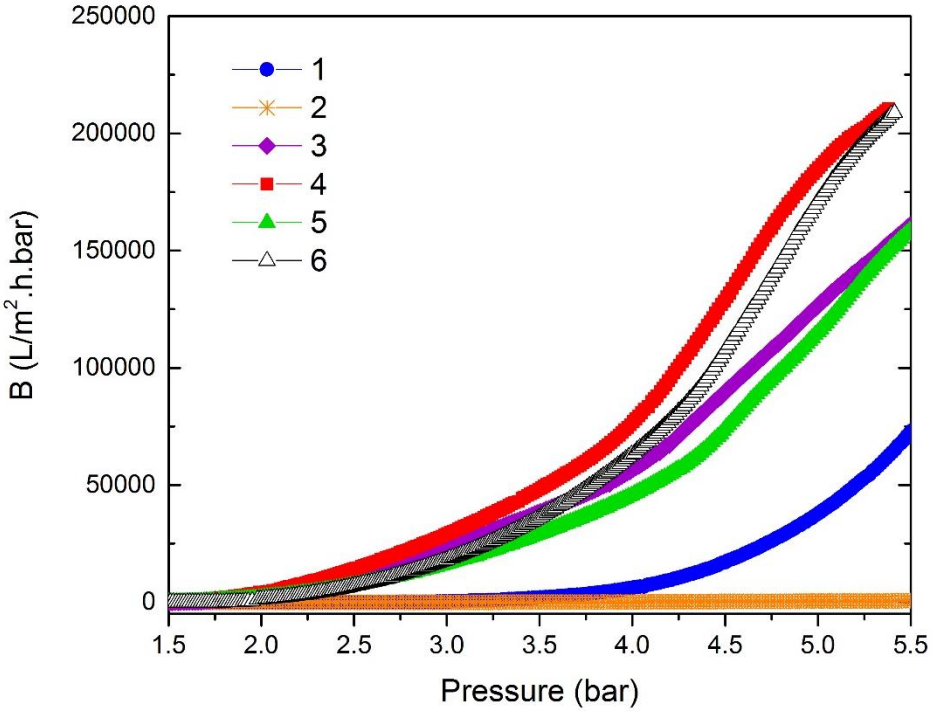

Figure 14.6. Permeability (*B*) for the six GOM samples as function of applied pressure.

Abbreviations and symbols

Abbreviations

ABE	Acetone-butanol-ethanol
Ac	Acetone
AC	Alternating current
ADMH	3-allyl-5,5-dimethylhydantoin
AFM	Atomic force microscopy
Ag	Silver
AGMD	Air gap membrane distillation
Al	Aluminium
AL-FS	Active layer facing the feed solution
Al_2O_3	Aluminium oxide/Alumina
AP	Aqueos phase
AQP	Aquaporin
AQP-Z	Aquaporin Z
ATR	Attenuated total reflectance
ATR-FTIR	Attenuated total reflectance Fourier transform infrared spectroscopy
BP	Bucky-paper
BPA	Bisphenol A
BPID	Pipiperidine
BSA	Bovine serum albumin
BW	Backwash
β-CD	β -cyclodextrin
C	Carbon

CA	Cellulose acetate
CDADO	Carboxylated aromatic diamine-diol
CFP	Capillary flow porometry
CFU	Colony forming unit
CMCNa	Sodium carboxymethyl cellulose
CNF	Cellulose nanofiber
CNT	Carbon nanotube
C–C	Single carbon bond
C=C	Double carbon bond
$–CH_2–$	Methylene group
$CH_3–C–CH_3$	Methyl group
–C=O	Polyester bond
C–O–C	Epoxide functional bond
C–OH	Hydroxide functional bond
–CONH	Amide bond/Amide group
–COO–	Ester bond
–COOH	Carboxylic acid group
CS	Chitosan
CTA	Cellulose triacetate
CTAB	Cyltrimethylammonium bromide
2D	Two-dimensional
3D	Three-dimensional
DABSA	2,5-diaminobenzene sulfonic acid
DAPI	4', 6-diamidino-2-phenyindole dilactate
DBA	3,5-diaminobenzoic acid
DC	Direct current
DCMD	Direct contact membrane distillation
DEP	Dielectrophoresis

DI	Deionized
DMAP	4-dimethylaminopyridine
DMF	*N, N*-dimethyl formamide
DNA	Deoxyribonucleic acid
DS	Draw solution
E. coli	Escherichia coli
ED	Electrodialysis
EDL	Electric double layer
EDS	Energy dispersive spectrometer
EDX	Energy dispersive X-ray spectroscopy
EfOM	Effluent organic matter
ENM	Electrospun nanofibrous membrane
EO	Electroosmosis
EP	Electrophoresis
EPS	Extracellular polymeric substances
EtOH	Ethanol
FA	Fly ash
Fe	Iron
Fe_3O_4	Ferrous ferric oxide
FESEM	Field emission scanning electron microscopy
FO	Forward osmosis
FOCM	Forward osmosis commercial membrane
FOM	Forward osmosis membrane
FS	Feed solution
FTCS	1H, 1H, 2H, 2H-perfluorododecyltrichlorosilane
FTIR	Fourier transform infrared spectroscopy
FWT	Fast water transport
GA	Gallic acid

GLA	Glutaraldehyde
GO	Graphene oxide
GOM	Graphene oxide membrane
HA	Humic acid
HC	High concentration
HCl	Hydrochloric acid
HF	Hollow fiber
HPECMs	Homogeneous polyelectrolyte complex membranes
HPE	Hyperbranched polyester
HPEI	Hyperbranched polyethylenimine
HPT	Heat post-treatment
ICE	Interlaced carbon nanotube electrode/s
ICP	Internal concentration polarization
IP	Interfacial polymerization
IPA	Isopropanol/Isopropyl alcohol
IR	Infrared
LbL	Layer-by-layer
LC	Low concentration
L-GO	Large graphene oxide
LMH	Units of $L/m^2 h$
MB	Methylene blue
MBA	*N,N´*-methylenebis(acrylamide)
MD	Membrane distillation
MF	Microfiltration
M-GO	Medium graphene oxide
MLGO	Multilayer graphene oxide
MLO-GO	Medium and less oxidized graphene oxide
MMMs	Mixed matrix membranes

MPD	*m*-phenylenediamine
MWCNT	Multiwalled carbon nanotube
MWCO	Molecular weight cut-off of the membrane
N	Nitrogen
NA	Not applicable
$NaBH_4$	Sodium borohydride
NaCl	Sodium chloride/Salt
NaClO	Sodium hypochlorite
NaOH	Sodium hydroxide
NF	Nanofiltration
NHE	Normal hydrogen electrode
NMs	Nanomaterials
NPs	Nanoparticles
NOM	Natural organic matter
NTSC	Naphthalene-1,3,6-trisulfonylchloride
O	Oxygen
OC	Optimized conditions
O=C–OH	Carboxylate functional group
OD	Osmotic distillation
ODMP	Osmotically driven membrane process
OD_{600}	Optical density at 600 nm
–OH	Hydroxyl group
OP	Organic phase
O&M	Operation & maintenance
PA	Polyamide
PAA	Polyacrylic acid
PAH	Poly (allylamine hydrochloride)
PAI	Polyamide-imide

PAMAM	Amine-functional polyamidoamine
PAMAM G2	NH_2-terminated amine-functional polyamidoamine
PAN	Polyacrylonitrile
PAS	Polyarylsulfone
PBI	Polybenzimidazole
PC	Polycarbonate
Pd	Paladio
PDA	Polydopamine
PDDA	Poly(diallyl dimethylammoniumchloride)
PDMC	Poly(2-methacryloyloxy ethyl tri-methylammonium chloride)
PDMP	Pressure-driven membrane process
PDMS	Polydimethylsiloxane
PE	Polyester
PEA	Polyesteramide
PEC	Polyelectrolyte complex
PEG	Polyethylene glycol
PEI	Polyethyleneimine
PEN	Pentaerythritol
PES	Polyethersulfone
PET	Polyethylene terephthalate
PEVP	Poly(*N*-ethyl-4-vinylpyridiniumbromide)
P. fluorescens	Pseudomonas fluorescens
PI	Polyimide
PIP	Piperazine
PLA	Poly (lactic acid)
PMA	Phosphomolybdic acid
PNIPAAm	Poly(*N*-isopropylacrylamide)
PP	Polypropylene

PRO	Pressure retarded osmosis
PSS	Poly(sodium 4-styrenesulfate)
PSU	Polysulfone
Pt	Platino
PTFE	Polytetrafluoroethylene
PU	Polyurethane
PV	Pervaporation
PVA	Polyvinyl alcohol
PVAm	Polyvinylamine
PVC	Polyvinyl chloride
PVDF	Polyvinylidene fluoride
PVDF-HFP	Polyvinylidene fluoride-co-hexafluoropropylene
PVP	Poly(1-vinylpyrrolidone)
PVP-g-SiO_2	Poly(1-vinylpyrrolidone)-grafted-silica
RED	Reverse electrodialysis
RFOM	Recycled forward osmosis membrane
RGO	Reduced graphene oxide
RNA	Ribonucleic acid
RO	Reverse osmosis
S	Sulfur
SDS	Sodium dodecyl sulfate
SE	Seriol (2-Amino-1, 3-propanediol)
SEM	Scanning electron microscopy
SGMD	Sweeping gas membrane distillation
S-GO	Small graphene oxide
SHO-GO	Small and highly oxidized graphene oxide
Si	Silicon
SiO_2	Silicon dioxide/Silica

SLO-GO	Small and less oxidized graphene oxide
SMMs	Fluorinated surface modifying macromolecules
SPES	Sulfonated polyethersulfone
SPPBES	Sulfonated copoly (phthalazinone biphenyl ether sulfone)
SPTA	Sulfophthalic acid
STEM	Scanning transmission electron microscopy
TA	Tannic acid
TEA	Trimethylamine
TEM	Transmission electron microscopy
TEOA	Triethanolamine
TF	Thin film
TFC	Thin film composite
TFN	Thin film nanocomposite
TFNC	Thin film nanofiber composite
TFNN	Thin film nanofiber nanocomposite
THF	Tetrahydrofurane
TiO_2	Titanium dioxide/Titania
TMC	Trymesoyl chloride
TMBPA	Tetramethyl bisphenol A
TNT	Titanium nanotubes
TOCNs	TEMPO-oxidized cellulose nanofibrils
TSA	Tryptic soy agar
TSB	Tryptic soy broth
TTIP	Titanium isopropoxide
UF	Ultrafiltration
UV	Ultraviolet
UV-vis	Ultraviolet-visible spectroscopy or spectrophotometry
VMD	Vacuum membrane distillation

XPS	X-ray photoelectron spectroscopy
XRD	X-ray diffraction
Zn	Zinc
ZnO	Zinc oxide
ZrO_2	Zirconium dioxide/Zirconia

Symbols

A_{ef}	Effective filtration area
B	Permeability
CD	Crosslinking degree
C_e	Equilibrium concentration
C_f	Concentration of the feed solution
CFF	Cumulative filter flow distribution/Cumulative inter-fiber space or pore size distribution
C_p	Concentration of the permeate solution
C_r	Concentration of the retentate solution
C_0	Initial concentration
$C_0^{HA,\ DS}$	Initial concentration of humic acid in the draw solution
$C_0^{HA,\ FS}$	Initial concentration of humic acid in the feed solution
$C_f^{HA,\ DS}$	Final concentration of humic acid in the draw solution
$C_f^{HA,\ FS}$	Final concentration of humic acid in the feed solution
$C_0^{NaCl,\ DS}$	Initial concentration of salt in the draw solution
$C_0^{NaCl,\ FS}$	Initial concentration of salt in the feed solution
$C_f^{NaCl,\ DS}$	Final concentration of salt in the draw solution
$C_f^{NaCl,\ FS}$	Final concentration of salt in the feed solution
d	Interplanar distance
d_f	Inter-fiber space or pore size

$\overline{d_f}$	Mean size of the inter-fiber space or mean pore size
DFF	Differential filter flow distribution/ Differential inter-fiber space or pore size distribution
DN	Degree of networking
d_S	Superficial mean pore size
d_V	Volumetric mean pore size
f	Frequency
F	Polymer solution flow rate
FC	Frequency count
FD_0	Initial permeate flux decline
FRR	Fouling resistance recovery
FR_W	Irreversible fouling factor
FWHM	Full width at half-maximum
G	Air gap or distance between the needle tip and the collector
h	Width of the bins
h	Height of the carbon nanotube filaments
2h	Width of the graphene oxide nanochannels or separation distance between graphene oxide flakes
I	Electric current or intensity
I_D/I_G	Ratio of the intensity of the D-band and the G-band
J	Permeate flux
J_f	Final permeate flux
J_{HA}	Humic acid permeate flux
$\overline{J_{HA}}$	Average of all humic acid permeate fluxes of the filtration test
J_{HA_0}	Initial humic acid permeate flux
J_{HA_f}	Final humic acid permeate flux
J_{HA}/J_{w0}	Ratio of the humic acid permeate flux and the initial water flux

J_i	Initial permeate flux
J_S	Reverse salt permeate flux
J_S/J	Ratio of the reverse salt permeate flux and the permeate flux
J_{w0}	Initial water permeate flux
J_{wf}	Final water permeate flux
k	Fouling rate constant
k	Cluster or class
K	Number of clusters
L	Loss function
l	Length of the carbon nanotube filaments
LEP	Liquid entry pressure
LRV	Log removal value
m	Mass of permeate collected over a period of time
m	Number of bins (disjoint categories)
MPS	Mean pore size
Mw	Molecular weight
N	Number of samples in the statistical set
PI	Performance index
PWP	Pure water permeability
R_{HA}	Humic acid rejection factor
R_S	Salt rejection factor
S	Structural parameter
SCA	Static contact angle
s_w	Weighted standard deviation of the nanofiber diameters
$\overline{s_w}$	Average of the weighted standard deviation of the nanofiber diameters
T	Temperature

t	Time
t_{ap}	Aqueous phase time
t_c	Critical time
t_{exp}	Experimental time
t_h	Hydrolysis exposure time
t_{IP}	Polymerization reaction time
t_e	Electrospinning time
v	Hydraulic velocity perpendicular to the membrane
V	Volume
V	Electric voltage
V^{FS}	Volume of the feed solution
V_{rms}	Root mean square voltage
w	Width of the carbon nanotube filaments
x	Centroid (mean) of each class k
$\Delta\delta$	Experimental error of the thickness
ΔP	Transmembrane pressure
ΔP_0	Initial transmembrane pressure (before fouling, at time 0)
ΔP_c	Transmembrane pressure of a clean membrane (after backwash)
ΔP_f	Final transmembrane pressure (after fouling & before backwash)
ΔP_{PWP}	Transmembrane pressure when measuring pure water permeability
Δt	Period of time
ΔV	Permeate volume collected over a period of time
α	Separation factor
$\bar{\alpha}$	Average of the separation factor for the entire filtration process
α_f	Final separation factor
β_{HA}	Humic acid concentration factor
γ_S	Salt dilution factor

δ	Thickness
δ_{NF}	Thickness of the nanofilm
δ_{TFC}	Thickness of the thin film layer
ε	Molar absorbance coefficient
ε	Void volume fraction or porosity
ε_S	Superficial porosity
ε_V	Volumetric porosity
λ	Wavelength
λ_0	Dominant characteristic of the statistical set that corresponds to the highest peak
λ_c	Bin characteristic or bin center
λ_i	Initial diameter of the nanofiber (before heat post-treatment)
λ_f	Final diameter of the nanofiber (after heat post-treatment)
λ_w	Weighted arithmetic mean of the nanofiber diameters
$\overline{\lambda_w}$	Average of the weighted arithmetic mean of the nanofiber diameters
μ_k	Number of data points in the class k
2θ	Diffraction angle
θ	Half of the diffraction angle
θ_w	Water contact angle
ϱ	Bulk resistivity
ϱ_m	Density of the membrane
ϱ_{pol}	Density of the polymer material
ϱ_{PSU}	Density of the polysulfone
ζ-avg	Zeta average
ζ-potential	Zeta potential

List of figures

Figure 1.1. Cross-flow and dead-end configurations for a membrane filtration process……5

Figure 1.2. Biofouling formation sequence……...7

Figure 1.3. Strategies to reduce organic and microbial adhesion on the membrane surface to mitigate fouling. These strategies include: A) increased surface charge density, B) increased surface hydrophilicity, C) reduced surface roughness, and D) enhanced hydrodynamics conditions……9

Figure 1.4. Mechanism of interfacial polymerization (A–D)……...10

Figure 1.5. Membranes developed in this PhD thesis for the treatment and disinfection of different types of waters containing organic matter and bacteria……16

Figure 2.1. SEM images of electrospun polyacrylonitrile/polyethylene terephthalate (PAN/PET) membrane: (a) PAN/PET membrane (cross-section) and (b) PAN/PET membrane infused with polyvinylamine (PVAm) grafted cellulose nanofiber (CNF) (top view). (c) TEM image taken at a small section of the cellulose network containing pores and individual polymer chains with spaghetti-like configuration. Reprinted from Wang et al. [4], with permission from Elsevier……29

Figure 2.2. (a) Mechanisms of formation of triangle-shape tri-bore hollow fiber membranes. (b) SEM images of Matrimid® tri-bore hollow fiber membranes using different dope compositions. Adapted from Wang et al. [6], with permission from Elsevier……30

Figure 2.3. Reaction procedure for preparation of PVP grafted silica nanoparticles (PVP-g-SiO_2). Reprinted from Song and Kim [22], with permission from Elsevier……32

Figure 2.4. SEM cross-section images of: (a) neat polyethersulfone (PES) membrane and PES membrane with (b) 15 wt% diaminobenzoic acid (DBA) and (c) 15 wt% gallic acid (GA). Reprinted from Mehrparvar et al. [24], with permission from Elsevier……33

Figure 2.5. SEM cross-section images of the GO-blended polyvinylidene fluoride (PVDF) membranes with (a) 0 and (b) 0.3 wt% graphene oxide (GO). Reprinted from Wang et al. [25], with permission from Elsevier……33

Figure 2.6. Field emission scanning electron microscopy (FESEM) images of Ag/FA/PU (M1) mat (obtained from 1 h stirring solution) at different magnifications (a) lower magnification, (b)

higher magnification (inset is FESEM EDX of Ag/FA/PU (M1) mat). Reprinted from Pant et al. [37], with permission from Elsevier……36

Figure 2.7. FESEM images (A and B, scale bar 100 nm) and confocal fluorescence microscopy images (a and b, scale bar 50 mm) of different membranes with AQP-Z incorporated membrane (called LPR 400). Reprinted from Li et al. [44], with permission from Elsevier……37

Figure 2.8. Schematic illustration of hydrophilic coating with dendritic polymers on the polyamide (PA) active layer of thin film composite reverse osmosis (TFC RO) membrane. Reprinted from Xu et al. [46] and Sarkar et al. [52], with permission from Elsevier……39

Figure 2.9. Schematic diagram for synthesis of the terpolymer P(MDBAC-r-Am-r-HEMA) (a) and surface modification of reverse osmosis (RO) membranes (b). Reprinted from Ni et al. [56], with permission from Elsevier……40

Figure 2.10. (a) Schematic diagram of the interfacial polymerization process used to fabricate the patterned thin film composite (TFC) membranes. The monomers *m*-phenylenediamine (MPD) and trymesoyl chloride (TMC) react to form a highly crosslinked polyamide (PA) layer at top of the patterned polyethersulfone (PES) ultrafiltration (UF) membrane used as a support. SEM images of the non-patterned (b) and patterned (c) TFC membrane surface after 24 h of $CaSO_4$ filtration experiment. Reprinted from Maruf et al. [70], with permission from Elsevier……..42

Figure 2.11. (a) Schematic dual-layer hydrophobic/hydrophilic hollow fiber membranes: (1) Cross-section of dual-layer hollow fiber membranes, (2) temperature distribution across dual-layer hydrophobic/hydrophilic membranes, and (3) temperature distribution across dual-layer hydrophobic/hydrophilic membranes filled with high thermal conductivity fillers blended into the inner-layer. (b) SEM images of the inner-layer filled with graphite, Cloisite NA^+ and MWCNTs. Reprinted from Su et al. [76], with permission from Elsevier……46

Figure 2.12. SEM images of the polytetrafluoroethylene (PTFE) hollow fiber membrane prepared by a stretching ratio of 220%: (a) X27 cross-section, (b) X1000 inner-surface, and (c) X1000 outer-surface. Reprinted from Zhu et al. [78], with permission from Elsevier……47

Figure 2.13. Mechanism for the fluorosilanization on the surface of polyvinylidene fluoride (PVDF) membranes with and without TiO_2. (a) Hydrolyzation of 1H, 1H, 2H, 2H-perfluorododecyltrichlorosilane (FTCS), (b) interaction of the hydroxyl groups with the surface of TiO_2 can form covalent bonds of Si–O–Ti, (c) the intermolecular crosslinking between the tri-silanols can lead to a 2D network of polysiloxane, (d) condensation of tri-silanols in the solution in absence of TiO_2 coating, and (e) surface SEM image of FTCS–PVDF membrane. Reprinted from Razmjou et al. [101], with permission from Elsevier……50

Figure 2.14. (a) Schematic method used for preparation of superhydrophobic polyvinylidene fluoride electrospun nanofibrous membranes (PVDF ENMs) ((1) PDA-modification; (2) silver nanoparticle coating; (3) 1-dodecanethiol hydrophobic modification). (b) SEM images of un-modified PVDF ENMs ((a1), (a2)), integral modified PVDF ENMs (I-PVDF (b1), (b2)), and surface modified PVDF ENMs (S-PVDF (c1), (c2)). Reprinted from Liao et al. [109], with permission from Elsevier……52

Figure 3.1. Schematic diagram of electrospinning set-up……75

Figure 3.2. Scheme of the micro/ultra-filtration experimental set-up: (1) Membrane module; (2) double jacketed container; (3) circulation pump; (4) three steps stopcock; (5) pressure and flow control valves; (6) pre-filter; (7) flow-meter; (8) manometer; (9) pressure indicator; (10) permeate container; (11) emptying valve……78

Figure 3.3. SEM images of PSU ENMs without heat post-treatment for three different polymer solution flow rates (V = 18 kV and G = 15 cm): A) ENM 1 (F = 1 mL/h), B) ENM 2 (F = 1.5 mL/h) and C) ENM 3 (F = 2 mL/h). All images were taken at the same magnification X1500……80

Figure 3.4. SEM images of PSU ENMs without heat post-treatment for two electric voltages (F = 2.5 mL/h and G = 10 cm): A) ENM 5 (V = 18 kV), B) ENM 6 (V = 20 kV). Both images were taken at the same magnification X1500……...81

Figure 3.5. SEM images of PSU ENMs without heat post-treatment for two different air gap distances (F = 2 mL/h and V = 18 kV): A) ENM 3 (G = 15 cm) and B) ENM 4 (G = 10 cm). Both images were taken at the same magnification X1500……...82

Figure 3.6. ATR-FTIR spectra of 20% PSU ENMs with different fabrication parameters and water absorbance spectra……82

Figure 3.7. SEM images of ENM 2 (F = 1.5 mL/h, V = 18 kV and G = 15 cm) taken at X1500: A) Without heat post-treatment, B) with heat post-treatment and their respective nanofiber diameter distributions……83

Figure 3.8. ATR-FTIR spectra of the PSU polymer and ENM 4 with and without heat post-treatment (HPT) at 220°C for 2 h……84

Figure 3.9. SEM images of ENM 9 (F = 2.5 mL/h, V = 20 kV and G = 10 cm): A) Without IP at X1500, D) E) with IP at X80 and X1500 respectively, B) and C) Cross section of ENM 9 with IP at X200 and X5000 respectively……..86

Figure 3.10. ATR-FTIR spectra of the PSU ENM 9 unmodified and modified by IP (F = 2.5 mL/h, V = 20 kV and G = 10 cm)……..86

Figure 3.11. XRD patterns of PSU polymer, phase inversion PSU membrane and PSU ENM 9 unmodified and modified by IP……...87

Figure 3.12. Feed and permeate concentration measurements during the filtration test of PSU ENM 8 with a heat post-treatment at 205°C for 30 min using 15 mg/L HA solution at different environment conditions: A) pH = 3; B) pH = 11. The shown images in A and B correspond to the surface of PSU ENM 8 after HA filtration tests……89

Figure 3.13. Separation factor (α) of PSU ENM 8 with heat post-treatment at 205°C for 30 min during the filtration tests of 15 mg/L HA solution at different pH values, 3 and 11……90

Figure 3.14. A) Permeate fluxes (J_{w0}, J_{HA}) and B) irreversible fouling factors (FR_W) of PSU ENM 8 with heat post-treatment at 205°C for 30 min during the filtration test of 15 mg/L HA solution at different pH values, 3 and 11. ($\Delta P = 10^5$ Pa; J_{wf} (pH 3) = 1.03×10^2 kg/m^2 h; J_{wf} (pH 11) = 0.69×10^2 kg/m^2 h)……..91

Figure 3.15. A) Permeate fluxes (J_{w0}, J_{HA}) and B) irreversible fouling factors (FR_W) of PSU ENM 9 unmodified and modified by interfacial polymerization (IP) with a heat post-treatment at 200°C for 75 min during the filtration test of 15 mg/L HA solution at pH 11. ($\Delta P = 10^5$ Pa; J_{wf} (ENM 9 without IP) = 2.53×10^2 kg/m^2 h; J_{wf} (ENM 9 with IP) = 0.31×10^2 kg/m^2 h)…..93

Figure 3.16. Separation factor (α) of PSU ENM 9 unmodified and modified by IP with heat post-treatment at 200°C for 75 min during the filtration tests of 15 mg/L HA solution at pH 11. The shown images correspond to the surface of the unmodified and modified PSU ENM 9 after HA filtration test……93

Figure 4.1. 3D surface graph showing the result of the preliminary evaluation of the PSU ENMs treated with different heat post-treatments (HPTs)……...109

Figure 4.2. SEM images of the surface of PSU ENMs prepared with a HPT time of 60 and 90 min at a HPT temperature of 210, 220 and 230°C. All images were taken at X1500 magnification……....111

Figure 4.3. SEM images of the surface of PSU ENMs prepared with a HPT temperature of 220 and 230°C at different HPT times (from 45 to 180 min). All SEM images were taken at X1500 magnification……112

Figure 4.4. Effects of HPT temperature and time on the morphological characteristics of PSU ENMs: A) weighted arithmetic mean of the fiber diameters ($\overline{\lambda_w}$), B) void volume fraction (ε) and C) water contact angle (θ_w). Contact angles micrographs in C) are added as supporting information of the graphics……...114

Figure 4.5. Effects of HPT temperature (A) and time (B) on the mean size of the inter-fiber space ($\overline{d_f}$), the inter-fiber space distribution or differential filter flow (*DFF*) and the cumulative filter flow distribution (*CFF*) of the PSU ENMs……115

Figure 4.6. Humic acid permeate flux (J_{HA}), separation factor (α) and irreversible fouling factor (FR_{IR}) of the PSU ENMs prepared with a HPT temperature of 210, 220 and 230°C for 90 min HPT time (A), and with 230°C HPT temperature for 45, 60, 75 and 90 min HPT time (B). The filtration tests were conducted with 15 mg/L HA feed aqueous solution at pH 11 and 10^5 Pa transmembrane pressure (ΔP)……...119

Figure 4.7. Humic acid permeate flux (J_{HA}), separation factor (α) and irreversible fouling factor (FR_{IR}) of the PSU ENMs prepared at different HPT conditions. The filtration tests were conducted with 15 mg/L HA feed aqueous solution at pH 11 and 10^5 Pa transmembrane pressure (ΔP)……122

Figure 4.8. Performance index (*PI*) of the PSU ENMs prepared with different HPT conditions……122

Figure 5.1. Schematic illustration of the preparation process of polyester and polyamide thin film composite membranes by interfacial polymerization……...138

Figure 5.2. Schematic of the interfacial polymerization reaction of different monomers. A) Bisphenol A and trimesoyl chloride react to form polyester (PE) and B) piperazine and trimesoyl chloride in presence of acid acceptor triethylamine to form polyamide (PA)……139

Figure 5.3. Influence of the polymerization reaction time on the morphological and structural characteristics of polyester thin film nanofiber composite membranes. A) SEM surface images at X1500 magnification, B) mean pore size ($\overline{d_f}$), C) normalized differential (*DFF*) and cumulative (*CFF*) pore size distributions, and D) FTIR spectra of the unmodified supporting membrane (ENM1) and the surface modified PE TFNC membranes prepared with reaction times of 5 min (PE TFNC1_5), 10 min (PE TFNC1_10), 15 min (PE TFNC1_15) and 20 min (PE TFNC1_20). The PE TFNC membranes were prepared by reacting BPA and TMC as described in Fig. 5.2-A……..143

Figure 5.4. Influence of the polymerization reaction time on the bondings and bonding ratio of polyester thin film nanofiber composite membranes. A) Area under the peak at 1720 cm^{-1} corresponding to the –C=O fuctional group (i.e. CO bonding), B) area under the peak at 3355 cm^{-1} corresponding to the –OH fuctional group (i.e. OH bonding), and C) area bonding ratio of these two functional groups (i.e. OH/CO)……148

Figure 5.5. Influence of the polymerization reaction time on the filtration properties of polyester thin film nanofiber composite membranes. A) Humic acid permeate flux (J_{HA}) and B) separation factor (α) as a function of filtration time of the unmodified supporting membrane (ENM1) and the surface modified PE TFNC membranes prepared with reaction times of 5 min (PE TFNC1_5), 10 min (PE TFNC1_10), 15 min (PE TFNC1_15) and 20 min (PE TFNC1_20). C) Irreversible fouling factors (FR_W), and D) photographs of the membranes after the filtration tests carried out with 15 mg/L HA feed aqueous solution at pH 11 and 10^5 Pa transmembrane pressure……...150

Figure 5.6. Influence of the supporting membrane on the morphological and structural characteristics of polyester thin film composite membranes. A) SEM surface images at X1500 magnification, B) mean pore size ($\overline{d_f}$), C) normalized differential (*DFF*) and cumulative (*CFF*) pore size distributions, and D) FTIR spectra of the unmodified supporting membranes (ENM1, ENM2, PES) and the surface modified membranes (PE TFNC1_15, PE TFNC2_15, PE TFC_15, respectively). All membranes were prepeared with 15 min reaction time of BPA and TMC as described in Fig. 5.2-A…….156

Figure 5.7. Influence of the supporting membrane on the filtration properties of polyester thin film composite membranes. A) Humic acid permeate flux (J_{HA}) and B) separation factor (α) as a function of filtration time of the unmodified supporting membranes (ENM1, ENM2, PES) and the surface modified membranes (PE TFNC1_15, PE TFNC2_15, PE TFC_15, respectively). C) Performance index (*PI*) and D) photographs of the membranes after filtration tests carried out with 15 mg/L HA feed aqueous solution at pH 11 and 10^5 Pa transmembrane pressure……....158

Figure 5.8. Morphological and structural characteristics of polyamide thin film composite membranes prepared on different supports. A) SEM surface images at X1500 magnification, B) mean pore size ($\overline{d_f}$), C) normalized differential (*DFF*) and cumulative (*CFF*) pore size distributions, and D) FTIR spectra of the unmodified supporting membranes (ENM1, PES) and their respective surface modified membranes (PA TFNC1_ 5, PA TFC_5). The PA TFC membranes were prepared with 5 min reaction time of PIP and TMC in presence of the acid acceptor TEA as described in Fig. 5.2-B……161

Figure 5.9. Comparison of the filtration properties of polyester and polyamide thin film composite membranes prepared on different supports. A) Humic acid permeate flux (J_{HA}) and B) separation factor (α) as a function of filtration time of the unmodified supporting membranes (ENM1, PES) and their respective surface modified polyester (PE TFNC1_15, PE TFC_15) and polyamide (PA TFNC1_5, PA TFC_5) TFC membranes. C) Performance index (*PI*), and

D) photographs of the membranes after the filtration tests carried out with 15 mg/L HA feed aqueous solution at pH 11 and 10^5 Pa transmembrane pressure……163

Figure 6.1. Schematic for interlaced CNT electrodes (ICE) fabrication on MF membranes. 1) Top casing, 2) stencil, 3) MF membrane, 4) porous sinter, 5) bottom casing, 6) MF membrane with ICE post-fabrication, 7) container casing, 8) pump connection, 9) filtrate container, and 10) base……177

Figure 6.2. Bacterial density and morphology on membrane surfaces with or without ICE after filtration and BW. SEM images of the control PVDF and ICE surfaces: A) Filtration control PVDF, B) BW control PVDF, C) filtration ICE anode, D) cathodic BW of ICE anode during filtration, E) filtration ICE cathode, and F) anodic BW of ICE cathode during filtration. Experiments were completed by filtering 10^7 CFU mL^{-1} in 155 mM NaCl solution for 60 min at the flow rate of 1.2 mL/min (i.e. J = 163.6 $L/m^2 h$) and BW at the same flow rate for 10 min with DI water. For the ICE-PVDF, 2 V DC and 8 V DC (with the reversed polarity) were applied during filtration and BW, respectively……...183

Figure 6.3. Fouling trends of PVDF with or without ICE in the absence or presence of potential. A) ΔP increase with filtration time of the control PVDF, ICE-0 V, ICE-DC and ICE-AC (10 kHz) using DI BW. SEM images of the membrane surfaces after F-2 and BW-2: B) control PVDF membrane post-DI-BW, C) ICE-DC post-DI-BW, D) ICE-AC post-DI-BW, and E) ICE-AC post-NaCl-BW. Experiments were completed using 10^8 CFU mL^{-1} filtration for 60 min or up to 1.1 bar in the absence or presence of 2 V DC or AC. A 10 min BW was carried out after each filtration cycle in the absence or presence of 8 V DC (for the DC filtration, polarity changed at 5 min) and 8 V AC (for the 2 V AC filtration)……185

Figure 6.4. COMSOL simulation of the ICE electric field strength and electric potential distribution. The total voltage over the two adjacent filaments is set as 2 V. The electric potential is shown in color change from blue (−1 V) to red (+1 V) and the norm of electric field strength is presented with contour from light grey (4500 V/m) to dark grey (500 V/m). The green streamlines depict the direction and the electric field strength. No electric double layer or hydrodynamic effects are considered……188

Figure 7.1. GO trends. Number of publications (white) and number of patents filled (gray), which title contains "graphene oxide", between 2011 and 2015……198

Figure 7.2. GO chemistry I. A) Photo of the six GO samples in solution (left). A color gradient relative to the O/C ratio (right). B) C1s spectra obtained by XPS analysis of GO samples. The

data also display the percentage contribution of individual peak obtained by deconvolution and the O/C ratio……...205

Figure 7.3. GO chemistry II. A) UV-vis, B) ATR-FTIR, and C) Raman spectra of the six GO samples……207

Figure 7.4. GO morphology I. A) SEM images of GO samples. B) GO flake size distribution fitted to a log-normal distribution (red dashed lines); yellow square represents zoom in for the smaller GO flakes (Samples 1, 2, and 4). C) Histograms of SEM image greyscale intensities that are deconvoluted to obtain mono-/multi-layer percentages……...210

Figure 7.5. GO morphology II. A) XRD spectra for the six GO samples. AFM analysis in B) non-contact attractive and C) contact repulsive regime for a single GO flake……211

Figure 7.6. GO characterization in the literature. A-B) O/C atomic ratio and mean flake size distribution histograms. Each count represents a scientific work. C) K-mean classification of the GO characterization based on O/C atomic ratio and mean flake size. Every white "*x*" represents the centroid (mean) of each class, white circles represent GO samples used in this study, and black dots represent the chemo-morphological data obtained from literature review. D) The table lists the nanoscopic properties for the centroid of each category; the mean flake size of the samples used in this study was calculated from areas in Fig. 7.4 assuming a square GO flake……..214

Figure 7.7. Performance comparison of GO toward macroscopic applications. A) Representative SEM images of *E. coli* bacteria adhesion onto GOMs (Samples 6 and 4, left and right image, respectively). B) MB adsorption of GO samples before (left) and after (right) centrifugation. C) Permeability data of GOMs at 5 bar (left) and schematic of their GO flake arrangement (right)……...216

Figure 8.1.1. TiO_2 nanoparticles dispersed in different solvents……228

Figure 8.1.2. SEM surface images of the unmodified and modified membranes. A) PSU ENM at X1500 magnification, B) polymer blended TiO_2−ENM nanocomposite membrane at X1500 magnification, and C-D) nanofibers of the polymer blended TiO_2−ENM nanocomposite membrane containing TiO_2 NPs at X30000 magnification……229

Figure 8.1.3. Nanofiber diameter distribution of the prepared membranes. A) PSU ENM and B) polymer blended TiO_2−ENM nanocomposite membrane……229

Figure 8.1.4. SEM surface images at different magnifications of the unmodified and the surface modified TiO_2 coated nanocomposite membranes with different hydrolysis exposure times. A1) Un-coated ENM supporting membrane at X1500; B1) TiO_2−ENM_N1 at X1000, B2) at

X10000 and B3) at X100000; C1) TiO_2−ENM_N15 at X1500, C2) at X10000 and C3) at X26000; and D1) TiO_2−ENM_N45 at X1000, D2) at X10000 and D3) at X100000……...230

Figure 8.2.1. Illustration of FO and RO processes. A) Initial non-equilibrium osmotic state, B) FO process where no pressure is applied on the draw solution and C) RO process used for desalination of a saline feed solution by applying a hydrostatic pressure greater than the transmembrane osmotic pressure. Adapted from Arribas et al. [8], with permission from Elsevier……234

Figure 8.2.2. Illustration of the objective of this research study……235

Figure 8.2.3. Experimental device used for the FO tests……..238

Figure 8.2.4. SEM surface images of the forward osmosis membranes (FOMs) at X1500…240

Figure 8.2.5. FO permeate fluxes of the prepared FOMs and the FOCMs. A) Permeate flux (J), B) reverse salt permeate flux (J_S) and C) permeate flux ratio (J_S/J). FO tests were conducted first under low concentration conditions (FS: 10 mg/L HA; DS: 65 g/L NaCl) during 1 h and then, under high concentration conditions (FS: 100 mg/L HA; DS: 200 g/L NaCl) during another 1 h. All tests were carried out with the active layer of the membranes facing the feed solution (AL-FS mode)……241

Figure 11.1. Visual criterion to evaluate the damage of the membranes due to the HPT. Pictures of the PSU ENMs after the HPT (top) with their corresponding SEM image of the surface (bottom). A) Membranes graded with 0 points, B) 5 points and C) 10 points……260

Figure 11.2. Evaluation of the degree of networking and interconnectivity of the PSU ENMs after the application of the heat post-treatment (HPT). SEM images of the nanofibers structure on the surface of PSU ENMs treated with a medium (230ºC/60 min) and a high (230ºC/75 min) HPT. The yellow circles represent some normal intersections between nanofibers while the red circles represent points with fused nanofibers……260

Figure 11.3. Nanofibers diameter histograms of the treated PSU ENMs……...261

Figure 11.4. Sketch of the effects of the heat post-treatment (HPT) on the nanofiber diameters and the size of the inter-fiber space of the ENMs. The parameters λ_i and λ_f represent the initial and final diameter of the nanofibers, respectively……..262

Figure 11.5. Example of the characterization analysis of the organic fouling of the PSU ENMs. A) FTIR spectra of the HA and the ENM before and after filtration, B) SEM surface images of the ENM before and after filtration (X1500), and C) SEM cross section images of the ENM after filtration taken during the EDS mapping analysis in the bottom, centre and top sides of

the membrane. The graph under the images summarizes the relative percentage (i.e. Element/C) of the atomic composition of the ENM before and after HA MF in the bottom, center and top sides…….263

Figure 11.6. Humic acid permeate flux (J_{HA}), separation factor (α) and performance index (PI) of the PSU ENMs 9 and 10 prepared with a HPT of 230°C/60 min and 230°C/75 min, respectively, and PES MF commercial membrane. The filtration tests were conducted with 15 mg/L HA feed aqueous solution at pH 11 and 10^5 Pa transmembrane pressure (ΔP). The inset pictures are SEM surface images of the membranes before HA MF test……264

Figure 12.1. Influence of the polymerization reaction time on the morphological and structural characteristics of polyester (PE) thin film nanofiber composite (TFNC) membranes. SEM surface images at X300 magnification of the PE TFNC membranes prepared on ENM1 with IP reaction times of A) 5 min (PE TFNC1_5), B) 10 min (PE TFNC1_10), C) 15 min (PE TFNC1_15) and D) 20 min (PE TFNC1_20). The inset micrographs are SEM surface images of the membranes at X1500 magnification. The PE TFNC membranes were prepared by reacting BPA and TMC as described in Fig. 5.2-A of Chapter 5…….268

Figure 12.2. Influence of the polymerization reaction time and the different supporting membranes on the chemical composition of polyester (PE) thin film composite (TFC) membranes. FTIR spectra in the range 3700–1625 cm^{-1} of A) 1,3,5-benzene tricarboxylic acid, 1,3-benzene dicarboxylic acid, and the PE TFNC membranes prepared by PE surface modification on ENM1 support with IP reaction times of 15 min (PE TFNC1_15) and 20 min (PE TFNC1_20). B) FTIR spectra in the range 3700–1625 cm^{-1} of the PE TFC membranes prepared by PE surface modification on different supports (ENM1, ENM2, PES) with 15 min IP reaction time (PE TFNC1_15, PE TFNC2_15, PE TFC_15). C) Chemical structure of 1,3,5-benzene tricarboxylic acid and 1,3-benzene dicarboxylic acid……269

Figure 12.3. Permeability of all polyester (PE) and polyamide (PA) thin film composite (TFC) membranes. The permeability values were calculated from the wet curve of the membranes tested using Porometer…….272

Figure 12.4. SEM surface images at X1500 magnification of all polyester (PE) and polyamide (PA) thin film composite (TFC) membranes. A1) PE TFC_15, B1) PA1 TFC_5, B2) PA1 TFC_10, B3) PA1 TFC_15, C1) PA2 TFC_5, C2) PA2 TFC_10, C3) PA2 TFC_15, D1) PA3 TFC_5, D2) PA3 TFC_10, E1) PA4 TFC_5, E2) PA4 TFC_10, F1) PA5 TFC_5 and F2) PA5 TFC_10…….....273

Figure 12.5. SEM surface and cross section images at different magnifications of the polyester (PE) and pre-selected polyamide (PA) thin film composite (TFC) membranes……...274

Figure 12.6. Physicochemical properties of the unmodified supporting membrane and the pre-selected polyamide (PA) thin film composite (TFC) membranes. A) Normalized differential (*DFF*) and cumulative (*CFF*) pore size distributions, and B) FTIR spectra of the PES support and the PA TFC membranes (PA1 TFC_10, PA2 TFC_10, PA4 TFC_5)……276

Figure 12.7. Schematic of the mechanism of the interfacial polymerization (IP) reaction of different amine monomers with TMC. A) Aromatic MPD amine reacts with TMC to form a fully aromatic PA TFC membrane and B) aliphatic PIP amine reacts with TMC to form a semi-aromatic PA TFC membrane. x in polymer chain represents the cross-linked part of the resulting polymer and y represents the linear part. x + y = 1. If x = 1, the resulting polyamide is fully cross-linked (i.e. all carbonyl groups formed amide linkages), and if y = 1, the resulting polyamide is fully linear (i.e. one carbonyl group formed carboxylic acid)……...278

Figure 12.8. XPS spectra of the pre-selected polyamide (PA) thin film composite (TFC) membranes. A) PA1 TFC_10, B) PA2 TFC_10 and C) PA4 TFC_5……280

Figure 12.9. Filtration properties of the unmodified supporting membrane and the pre-selected polyamide (PA) thin film composite (TFC) membranes. A) Mean humic acid (HA) permeate flux ($\overline{J_{HA}}$) together with final HA separation factor (α_f), and B) performance index (*PI*) of the PES support and the PA TFC membranes (PA1 TFC_10, PA2 TFC_10, PA4 TFC_5). The filtration tests were conducted with 15 mg/L HA feed aqueous solution at pH 11 and 10^5 Pa transmembrane pressure……...281

Figure 12.10. SEM images taken at X10000 magnification showing the granular structure formed within the inter-fiber space of the membrane PA TFNC1_5……..282

Figure 13.1. Time-dependent permeability of the unpressed and mechanically-pressed PVDF membranes. A) Permeability change with filtration time for the unpressed and pressed PVDF membranes (after 100 min DI filtration, the unpressed membranes had a similar stable permeability to the pressed membranes) and B) flux and permeability versus pressure for the pressed PVDF membranes……...288

Figure 13.2. Growth curve of the *P. fluorescens* in TSB by seeding from a TSA plate at 30°C. It can be told that 18 h is mid-to-late exponential phase and is able to provide high biomass yield…….288

Figure 13.3. Bacterial filtration experimental protocol diagram. Protocol 1 was used to evaluate bacterial removal, surface density, and morphology post-filtration. Protocol 2 was used to evaluate bacterial fouling trend and backwash efficacy……...289

Figure 13.4. Cross-sectional and superficial morphology of the PVDF and ICE-PVDF membranes. SEM images of: A, B) top surface of unpressed and pressed PVDF membranes, respectively, and C, D) cross-section of unpressed PVDF and pressed PVDF membrane with ICE on top, respectively, E) top surface of the ICE. F) Electric resistance of a single ICE filament with varying CNT-Nafion volume and G) cumulative pore size distribution (*CFF*), differential pore size distribution (*DFF*), and wet curve flow of the unpressed PVDF, pressed PVDF, and pressed ICE-PVDF measured by gas-liquid displacement porometer…….290

Figure 13.5. Bacterial removal by the PVDF membranes with or without ICE in the presence or absence of applied voltage. Experiments were completed by filtering 10^7 or 10^8 CFU mL^{-1} in 155 mM NaCl solution at the flow rate of 1.2 mL/min (i.e. J = 163.6 L/m^2 h). Feed and permeate samples were taken after 30 min of filtration to determine CFU. The error bars are used to describe the ranges of the data instead of confidence intervals……...291

Figure 13.6. Bacterial density on PVDF and PC membrane surfaces with or without ICE after filtration and BW. Experiments were completed by filtering 10^7 CFU mL^{-1} in 155 mM NaCl solution for 60 min at the flow rate of 1.2 mL/min (i.e. J = 163.6 L/m^2 h) and BW at the same flow rate for 10 min with DI water. For the PVDF and PC with ICE, 2 V DC and 8 V DC (with the reversed polarity) were applied during filtration and BW, respectively……291

Figure 13.7. ΔP values for the control PVDF and the ICE-PVDF in different steps of the bacterial filtration test. Experiments were completed using 10^8 CFU mL^{-1} filtration for 60 min or up to 1.1 bar in the absence or presence of 2 V DC or AC. A 10 min BW with DI or saline solution was carried out after each filtration cycle in the absence or presence of 8 V DC (for the DC filtration, polarity was reversed in comparison to filtration for the first 5 min and then reversed again for the final 5 min to clean both electrodes) or 8 V AC (for the 2 V AC filtration). DI water was filtered for 10 min after each BW cycle to determine the fouling resistance recovery (*FRR*) of the process. For all, bacteria filtration, BW filtration and DI water filtration, the flow rates were kept at 1.2 mL/min (i.e. J = 163.6 L/m^2 h). Experimental procedure diagram is displayed in Fig. 13.3, Protocol 2……292

Figure 14.1. SEM of monolayer GO and flake size distribution via ImageJ analysis……...296

Figure 14.2. Aggregation and settling of GO in Sample 1……296

Figure 14.3. GO monolayer percentage evaluation……...297

Figure 14.4. Elbow method to determine the optimal number of clusters……298

Figure 14.5. Representative SEM images of *E. coli* bacteria adhesion onto GOM surfaces. The samples are identified by numbers……298

Figure 14.6. Permeability (B) for the six GOM samples as function of applied pressure…….299

List of tables

Table 2.1. Membrane separation processes used for water treatment together with their driving force and main fields of applications……...26

Table 2.2. Characteristics of the different pressure-driven membrane processes……28

Table 2.3. DCMD performance of different single and dual layer hollow fiber membranes fabricated in the literature……...48

Table 2.4. Pervaporation performance of various polyelectrolyte membranes (PECMs) for dehydration of isopropanol (IPA) and ethanol (EtOH) at 70°C……...56

Table 3.1. Electrospinning parameters used to prepare PSU ENMs using a polymer solution mixture of 20% PSU + 16% THF + 64% DMF: polymer solution flow rate (*F*), electric voltage (*V*), distance between the needle tip and the collector or gap (*G*), electric current or intensity (*I*) and electrospinning time (t_e)……79

Table 3.2. Mean nanofiber diameter of the PSU ENMs prepared with and without heat post-treatment and their corresponding weighted standard deviation……...84

Table 3.3. Water contact angles (θ_w) of PSU ENMs prepared with heat post-treatment……85

Table 3.4. Diffraction angles of each diffractogram (2θ), full width at half-maximum (*FWHM*) and inter-planar distance (d)……...88

Table 4.1. Prepared PSU ENMs with different heat post-treatments and their corresponding morphological characteristics: thickness (δ), weighted arithmetic mean of the nanofiber diameters ($\overline{\lambda_w}$) with its corresponding weighted standard deviation ($\overline{s_w}$), water contact angle (θ_w), void volume fraction (ε) and mean size of the inter-fiber space ($\overline{d_f}$)……110

Table 4.2. Filtration performance of PSU ENMs prepared with different heat post-treatments: initial water permeate flux (J_{w0}), mean humic acid (HA) permeate flux ($\overline{J_{HA}}$), final HA permeate flux (J_{HA_f}), final HA separation factor (α_f), irreversible fouling factor (FR_W) and performance index (*PI*)……..118

Table 4.3. Morphological characteristics and filtration performance of lab-made ENMs and commercial MF membranes: thickness (δ), void volume fraction (ε), mean pore size (*MPS*),

mean nanofiber diameter ($\overline{\lambda_w}$), transmembrane pressure (ΔP), pure water permeability (PWP), initial water permeate flux (J_{w0}), initial permeate flux (J_i), final permeate flux (J_f), final water flux (J_{wf}), final separation factor (α_f) and irreversible fouling factor (FR_W)……125

Table 5.1. Morphological and filtration properties of the unmodified supporting membranes: heat post-treatment temperature (T), heat post-treatment time (t), thickness (δ), weighted arithmetic mean of the nanofiber diameters ($\overline{\lambda_w}$) and its corresponding weighted standard deviation ($\overline{s_w}$), water contact angle (θ_w), void volume fraction (ε), mean pore size ($\overline{d_f}$) and pure water permeability (PWP)……136

Table 5.2. Interfacial polymerization conditions used to prepare the polyester and polyamide thin film composite membranes……137

Table 5.3. Physicochemical properties and filtration performance of the unmodified supporting membranes and the polyester and polyamide thin film composite membranes: mean pore size ($\overline{d_f}$), zeta potential (ζ-potential), initial water permeate flux (J_{w0}), mean humic acid (HA) permeate flux ($\overline{J_{HA}}$), final HA permeate flux (J_{HA_f}), mean HA separation factor ($\overline{\alpha}$), final HA separation factor (α_f), irreversible fouling factor (FR_W) and performance index (PI)……144

Table 5.4. Peak assignments of the IR spectra of the unmodified supporting membranes and the polyester and polyamide thin film composite membranes……146

Table 5.5. Interfacial polymerization conditions, physicochemical properties and filtration and antifouling performance of different reported polyester and polyamide thin film composite membranes: molecular weight cut off ($MWCO$), mean pore size (MPS), zeta potential (ζ-potential), transmembrane pressure (ΔP), pure water permeability (PWP), final separation factor (α_f) and irreversible fouling factor (FR_W)……...152

Table 6.1. ΔP and FRR values for the control PVDF and the ICE-PVDF after 10^8 CFU mL^{-1} filtration and BW with DI or saline……...187

Table 7.1. Zeta potential (ζ-potential), static contact angle (SCA), and zeta average (ζ-avg) of the six GO samples……...208

Table 7.2. Summary of the techniques used to characterize the GO chemistry and morphology……..212

Table 7.3. Performance GO-based applications samples in terms of bacterial adhesion, adsorption properties, and permeability……217

Table 8.2.1. Interfacial polymerization (IP) conditions applied to prepare the forward osmosis membranes (FOMs)……236

Table 8.2.2. FO characteristics of the prepared FOMs: final humic acid (HA) rejection factor (R_{HA}), final salt rejection factor (R_S), HA concentration factor (β_{HA}) and salt dilution factor (γ_S). FO tests were conducted first under low concentration (LC) conditions (FS: 10 mg/L HA; DS: 65 g/L NaCl) during 1 h and then, under high concentration (HC) conditions (FS: 100 mg/L HA; DS: 200 g/L NaCl) during another 1 h. All tests were carried out with the active layer of the membranes facing the feed solution (AL-FS mode)……242

Table 12.1. Combination of monomers and interfacial polymerization (IP) conditions considered to prepare polyester (PE) and polyamide (PA) thin film composite (TFC) membranes……...271

Table 12.2. Peak assignments of the IR spectra of the unmodified supporting membrane and the pre-selected polyamide (PA) thin film composite (TFC) membranes……277

Table 12.3. Physicochemical properties and filtration performance of the unmodified supporting membrane (PES) and the pre-selected polyamide (PA) thin film composite (TFC) membranes (PA1 TFC_10, PA2 TFC_10, PA4 TFC_5): mean pore size ($\overline{d_f}$), PA thin layer thickness (δ_{TFC}), zeta potential (ζ-potential), mean humic acid (HA) permeate flux ($\overline{J_{HA}}$), final HA separation factor (α_f) and performance index (*PI*)……...278

Table 12.4. XPS surface elemental analysis and crosslinking degree (*CD*) estimation of the pre-selected polyamide (PA) thin film composite (TFC) membranes……279

Table 13.1. Membrane morphology characterization and pure water permeability of PVDF membranes with or without ICE……...293

Table 13.2. Welch's t-test summary of the bacterial removal under different conditions……293

Table 13.3. Bacterial density on the PVDF and PC membrane surfaces with or without ICE after 10^7 CFU mL^{-1} filtration and DI BW……293

Table 13.4. Exponential fitting results of the pressure increase of the control PVDF and ICE-PVDF after 10^8 CFU mL^{-1} filtration and DI BW……...294

Table 14.1. XPS percentage peak area data for the six samples. The standard deviation for the atomic ratio of each element is ± 1%……295